



<https://theses.gla.ac.uk/>

Theses Digitisation:

<https://www.gla.ac.uk/myglasgow/research/enlighten/theses/digitisation/>

This is a digitised version of the original print thesis.

Copyright and moral rights for this work are retained by the author

A copy can be downloaded for personal non-commercial research or study, without prior permission or charge

This work cannot be reproduced or quoted extensively from without first obtaining permission in writing from the author

The content must not be changed in any way or sold commercially in any format or medium without the formal permission of the author

When referring to this work, full bibliographic details including the author, title, awarding institution and date of the thesis must be given

Enlighten: Theses

<https://theses.gla.ac.uk/>
research-enlighten@glasgow.ac.uk

GEOMETRIC ACCURACY TESTING, EVALUATION AND APPLICABILITY

OF

SPACE IMAGERY

TO

THE SMALL SCALE TOPOGRAPHIC MAPPING OF THE SUDAN

BY

ABDELAZIM ELNIWEIRI HASSAN ELNIWEIRI

B.Sc. Eng. (Honours)

Thesis Submitted for the Ph.D. Degree
in Photogrammetry and Remote Sensing
to the
University of Glasgow.

Volume I

Department of Geography and Topographic Science.
October, 1988.

ProQuest Number: 10998219

All rights reserved

INFORMATION TO ALL USERS

The quality of this reproduction is dependent upon the quality of the copy submitted.

In the unlikely event that the author did not send a complete manuscript and there are missing pages, these will be noted. Also, if material had to be removed, a note will indicate the deletion.



ProQuest 10998219

Published by ProQuest LLC (2018). Copyright of the Dissertation is held by the Author.

All rights reserved.

This work is protected against unauthorized copying under Title 17, United States Code
Microform Edition © ProQuest LLC.

ProQuest LLC.
789 East Eisenhower Parkway
P.O. Box 1346
Ann Arbor, MI 48106 – 1346

**TO
IHSAN AND SAHAR**

CONTENTS

	Page
ACKNOWLEDGEMENTS.	XI
ABSTRACT.	XIII
1. CHAPTER 1	
Introduction.	
1.1 Introduction.	1
1.2 Stating the Problem.	3
1.3 The Topography of the Sudan.	3
1.4 Status of Topographic Mapping in the Sudan.	5
1.5 Thesis Organization.	12
2. CHAPTER 2	
Space Remote Sensing.	
2.1 Remote Sensing.	15
2.2 Electromagnetic Energy Radiation.	15
2.2.1 Electromagnetic Spectrum.	16
2.2.2 Electromagnetic Energy Source.	17
2.2.3 E.M.Energy Interactions with the Atmosphere.	18
2.2.3.1 Atmospheric Scattering.	19
2.2.3.2 Atmospheric Absorption.	19
2.3 Remote Sensors.	20
2.3.1 Photographic Systems.	20
2.3.1.1 Frame Cameras.	21
2.3.1.2 Panoramic Cameras.	25
2.3.2 Television Cameras.	27
2.3.3 Electro-optical Sensor Systems.	29
2.3.3.1 Optical Mechanical Line Scanners.	31
2.3.3.2 The Multispectral Line Scanner.	32
2.3.3.3 Solid State Array Based Systems.	33
2.3.4 Microwave Imaging Radars.	35

3.5	Analytical Instrumentation.	73
3.5.1	Zeiss Jena Stecometer C II.	73
3.5.2	Kern DSR-II Analytical Stereoplotter.	75
3.5.2.1	Computer Control of the DSR-II	77
3.5.2.2	Controlling Software	78
3.5.3	The Wild Avioplan OR-1 Orthophoto Unit.	78
3.5.3.1	Data Pre-processing for the Avioplan OR-1.	81
3.6	Summary.	81
4.	CHAPTER 4	
	Landsat MSS and TM Scanner Systems.	
4.1	Introduction.	83
4.2	Optical Mechanical Scanner Design.	83
4.2.1	Rotating Mirror Units.	84
4.2.2	Oscillating Mirror Units.	84
4.2.3	Spectral Separation Techniques.	84
4.3	Displacements and Distortions in Scanner Images.	85
4.3.1	Displacements Caused by the Panoramic Nature of the Scanning.	85
4.3.2	Distortions Due to Non-linear Mirror Sweep.	88
4.3.3	Displacements Caused by Platform Motion and Attitude.	88
4.3.4	Relief Displacements in Scanner Imagery.	92
4.3.5	Displacements Caused by Earth Curvature and Rotation.	94
4.4.1	Landsat MSS Sensor.	95
4.4.2	Landsat MSS Data Processing.	98
4.5	Landsat TM Sensor.	100
4.5.1	Internal Calibration.	102
4.5.2	Electronic Module.	103
4.5.3	TM Ground Segment.	103

4.5.3.1	GSFC Preliminary Processing	103
4.5.3.2	TM Image Processing System at GSFC.	104
4.5.3.3	Final Processing at EROS Data Centre.	104
4.5.4	TM User Products.	105
4.6	Ground Resolution of MSS and TM Images	105
4.7	Geometrical Analysis of Landsat Scanner Images.	106
4.7.1	Projective 3D Transformation Models.	108
4.7.1.1	Collinearity Equation Models.	109
4.7.1.2	Simplified Projective Models.	111
4.7.2	Two-dimensional Transformation Techniques.	115
4.8	Planimetric Test Procedure.	120
4.9	Summary.	121
5. CHAPTER 5	MSS and TM Images Geometric and Interpretation Tests	
5.1	Introduction.	122
5.2	Planimetric Accuracy Test of MSS Images over Sudan.	123
5.2.1	Linear Conformal Transformation Results.	127
5.2.2	Affine Transformation Results.	127
5.2.3	Polynomial Transformations Results.	128
5.2.4	Analysis of the Results.	131
5.3	Planimetric Accuracy Test of TM images over Sudan.	132
5.3.1	Geometric Accuracy Tests of Whole TM Scene.	134
5.3.1.1	Linear Conformal Transformation Results.	134
5.3.1.2	Affine Transformation Results.	135
5.3.1.3	Polynomial Transformation Results.	135
5.3.2	Geometric Accuracy Tests of TM Quarter Scenes.	137
5.3.3	Overall Results of TM Accuracy Tests over the Red Sea Hills Test Area.	139

5.4	Planimetric Accuracy Test of TM Images of South East England.	140
5.5	Interpretation of MSS Images over the Sudan.	147
5.5.1	Interpretation of MSS Images over the Nile Test Area.	148
5.5.2	Interpretation of MSS Images over the Red Sea Hills Area.	156
5.6	Interpretation of TM Images over the Sudan.	159
5.7	Conclusions.	160

6. CHAPTER 6. Linear Array Scanners.

6.1	Introduction.	162
6.2	Geometry of Linear Array Images.	163
6.3	Stereoscopic Linear-array Data Acquisition.	166
6.4	MOMS Sensor System.	168
6.4.1	MOMS-1 Experiment.	169
6.4.2	MOMS Image Processing.	171
6.4.2.1	Radiometric Correction.	171
6.4.2.2	Geometric Correction.	171
6.5	SPOT HRV Sensors.	172
6.5.1	Description of HRV Sensors.	172
6.5.2	SPOT Image Processing and Products.	175
6.6	Planimetric Image Rectification and Transformation.	176
6.7	Three-dimensional Transformation.	176
6.8	Summary.	181

7. CHAPTER 7 Geometric Accuracy and Interpretation Tests of MOMS Images.

7.1	Introduction.	183
7.2	Test Area.	184
7.3	Test Procedure.	187
7.4	Accuracy Test Results.	188
7.4.1	Linear Conformal Transformation Results.	188
7.4.2	Affine Transformation Results.	189

7.4.3	Polynomial Transformation Results.	190
7.4.4	Analysis of the MOMS Geometric Accuracy Test Results.	192
7.4.5	SPOT Geometric Accuracy Test Results.	193
7.5	Interpretation of MOMS Images.	195
7.6	Summary and Conclusion.	199
8.	CHAPTER 8	
	Landsat RBV Systems.	
8.1	Introduction.	200
8.2	Geometric Distortion in RBV Images.	203
8.2.1	Geometric Distortions Introduced by the Optical Unit.	203
8.2.2	Distortions Introduced by the Electronic Unit.	203
8.3	Landsats -1 and -2 RBV Systems.	206
8.4	Landsat-3 RBV System.	206
8.5	Data Reception and Processing.	209
8.6	Rectification and Transformation of RBV Images.	211
8.6.1	Pre-rectification of RBV Images.	211
8.6.2	Planimetric Transformation of RBV Images.	213
8.6.3	Three Dimensional Transformation of RBV Images.	213
8.7	Summary.	219
9.	CHAPTER 9	
	Geometric Accuracy and Interpretation Tests of RBV Images.	
9.1	Introduction.	220
9.2	Test Areas.	227
9.3	Coordinate Measurement.	228
9.3.1	Monoscopic Measuring Procedure.	228
9.3.2	Stereoscopic Measuring Procedure.	229
9.4	Planimetric Accuracy Test Results.	229
9.4.1	Red Sea Hills Test Area Results.	230

9.4.1.1	Linear Conformal Transformation Results.	230
9.4.1.2	Affine Transformation Results.	230
9.4.1.3	Polynomial Transformation Results.	231
9.4.2	Alaskan Test Area Results.	233
9.4.2.1	Linear Conformal Transformation Results.	233
9.4.2.2	Affine Transformation Results.	234
9.4.2.3	Polynomial Transformation Results.	234
9.5	Planimetric Accuracy Test Summary.	237
9.6	Published Tests and Applications.	238
9.7	Height Accuracy Test Results.	239
9.8	Results of the Interpretation Tests.	241
9.8.1	Interpretation Results of the RBV Images over Sudan.	241
9.8.1.1	Interpretation of RBV Images over the Nile Test Area.	241
9.8.1.2	Interpretation of RBV Images over the Red Sea Hills Area.	246
9.8.2	Interpretation Results of RBV Images over Alaska.	246
9.8.3	Other Interpretational Tests of Landsat-3 RBV Imagery.	247
9.9	Conclusion.	249

10. **CHAPTER 10** **Space Photographic Systems.**

10.1	Introduction.	250
10.2	Considerations of Space Photography.	251
10.3	Photographic Films.	255
10.4	High Definition Films.	256
10.5	Multispectral Photographic Systems.	257
10.6	Space Photography Experiments.	258
10.6.1	Metric Camera (MC) Experiment.	259
10.6.2	Large Format Camera (LFC) Experiment.	261
10.6.3	Russian Space Photographic Systems.	264

11.7.1	Interpretation of MC Photographs over the Nile Test Area.	297
11.7.2	Interpretation of MC Photographs over the Red Sea Hills Test Area.	304
11.7.3	The Results from Other Interpretational Tests of MC Photography.	303
11.7.4	Interpretation of the LFC Photos over the Red Sea Hills Test Area.	308
11.7.5	The Results from Other Interpretational Tests of the LFC Photography	311
11.8	Conclusion	312
12. CHAPTER 12	Orthophotographs and Orthophoto Maps from Space Photography	
12.1	Introduction.	313
12.2	Development of Orthophotography	313
12.2.1	Instruments based on Optical Projection.	315
12.2.2	Optical Transfer Devices.	316
12.2.3	Electronic Transfer Devices.	317
12.3	Digital Terrain Models (DTMs).	319
12.4	Digital Terrain Data Acquisition.	320
12.4.1	Land Surveying Methods of DIM Data Acquisition.	320
12.4.2	DIM Data Acquisition Based on Contour Digitization.	320
12.4.3	Photogrammetric Methods of DIM Data Acquisition.	321
12.5	Space Orthophotography over the Sudan.	323
12.5.1	CRISP Package.	323
12.5.2	SCOP Package.	328
12.5.3	SORA-OP Package.	331
12.6	Space Orthophotography Experiments.	333
12.6.1	Planimetric Accuracy Test of the Produced Orthophotograph.	334
12.6.2	Accuracy of the Generated DIM and Contours.	336

12.6.2.1 PANACEA Package.	336
12.6.2.2 Accuracy of the Interpolated DTM.	343
12.7 Conclusions	344
13. CHAPTER 13	Conclusions and Recommendations.
13.1 General	346
13.2 The Potential Contribution of the TM.	346
13.3 The Potential Contribution of the MOMS and SPOT.	346
13.4 Assessment of TM, MOMS and SPOT Images.	349
13.5 The Potential Contribution of Space Photographic Systems.	350
13.6 Near-future Space Imaging Systems.	353
13.7 Recommendations.	355
13.8 Final Note.	356
BIBLIOGRAPHY.	357
APPENDICES.	

ACKNOWLEDGMENTS

The author wishes to express his sincere gratitude to his supervisor, Professor G. Petrie for suggesting this topic for investigation and his continuous advice, help and supervision throughout the years of this research. He also wishes to acknowledge that, without the continuous encouragement, wide knowledge and experience, and extensive contacts of his supervisor, this research would have never been executed and presented in its present form.

The freedom in the use of the facilities available in the department granted by the former and the present heads of the department, Professor I. B. Thompson and Professor J. Tivy, is gratefully acknowledged and highly appreciated.

The author also wishes to acknowledge the help received from the Topographic Science staff who are always ready to help, particularly Mr. B.D.F. Methley, Mr. D.A. Tait, Mr. J. Shearer and Mr. I. Gerrard.

Sincere thanks are also due to:

University of Khartoum, Sudan, for the financial support received during the period in which this research has been conducted.

Professor R. Welch of the University of Georgia and the former president of the American Society of Photogrammetry and Remote Sensing for expressing his interest in the project and sending the topographic map sheets covering the Georgia test area.

The National Engineering Laboratories (NEL), East Kilbride, for allowing the author the free use of their Zeiss Stecometer CII stereocomparator. The help received from Mr. Nick Welch during this period is also appreciated.

Department of Civil Engineering, City University, for allowing the author to use their computer programs in checking his results. The help received from Dr. Mike Cooper and Mr. Jerry Clark during the use of these programs is also acknowledged.

Dr. M.A. Abdelghafar and brother Mohammed Shafi for their generosity and hospitality during the last six months of this research.

The numerous friends in Glasgow for their encouragement and support.

Finally my sincere gratitude to my wife Ihsan who supported and encouraged me during the hard days of the research.

ABSTRACT

The geometric accuracy, interpretability and the applicability of using space imagery for the production of small-scale topographic maps of the Sudan have been assessed. Two test areas have been selected. The first test area was selected in the central Sudan including the area between the Blue Nile and the White Nile and extending to Atbara in the Nile Province. The second test area was selected in the Red Sea Hills area which has modern 1:100,000 scale topographic map coverage and has been covered by six types of images, Landsat MSS TM and RBV; MOMS; Metric Camera (MC); and Large Format Camera (LFC).

Geometric accuracy testing has been carried out using a test field of well-defined control points whose terrain coordinates have been obtained from the existing maps. The same points were measured on each of the images in a Zeiss Jena Stereocomparator (Stecometer C II) and transformed into the terrain coordinate system using polynomial transformations in the case of the scanner and RBV images; and space resection/intersection, relative/absolute orientation and bundle adjustment in the case of the MC and LFC photographs. The two sets of coordinates were then compared. The planimetric accuracies (root mean square errors) obtained for the scanner and RBV images were: Landsat MSS ± 80 m; TM ± 45 m; RBV ± 40 m; and MOMS ± 28 m. The accuracies of the 3-dimensional coordinates obtained from the photographs were: MC:- X= ± 16 m, Y= ± 16 m, Z= ± 30 m; and LFC:- X= ± 14 m, Y= ± 14 m, and Z= ± 20 m.

The planimetric accuracy figures are compatible with the specifications for topographic maps at scales of 1:250,000 in the case of MSS; 1:125,000 scale in the case of TM and RBV; and 1:100,000 scale in the case of MCMS. The planimetric accuracies (vector ± 20 m) achieved with the two space cameras are compatible with topographic mapping at 1:60,000 to 1:70,000 scale. However, the spot height accuracies of ± 20 to ± 30 m - equivalent to a contour interval of 50 to 60 m - fall short of the required heighting accuracies for 1:60,000 to 1:100,000 scale mapping.

The interpretation tests carried out on the MSS, TM, and RBV images showed that, while the main terrain features (hills, ridges, wadis, etc.) can be mapped reasonably well, there was an almost complete failure to pick up the cultural features - towns, villages, roads, railways, etc. - present in the test areas. The high resolution MOMS images and the space photographs were much more satisfactory in this respect though still the cultural features are difficult to pick up due

to the buildings and roads being built out of local material and exhibiting little contrast on the images.

CHAPTER 1

Introduction

1.1 Introduction

At the present time, every country in the world faces an increasing demand for maps to meet the various and different requirements of developments such as the survey and management of natural resources, the monitoring and planning of the environment, the provision of geo-referenced data concerning human activities, etc. All of these must be based on accurate and up-to-date topographic maps. The current status of world mapping in general illustrates the need for much to be done especially in the developing countries which still do not have medium scale maps, if indeed they have any useful maps at all. According to a United Nations study in 1976 (U.N. World Cartography, 1976), the world-wide deficit in maps at scale of 1:50,000 is about 63.4% of the total possible coverage at this scale; while that in maps at scale of 1:100,000 is about 48.2% of the total coverage at the same scale. In a paper by Konecny et al (1979) repeated by Ihemadu(1985), the percentages of the actually mapped Earth's surface at various scales were estimated to be:

Scale	Percentage
1:1,000,000	85%
1:250,000	35%
1:100,000	15% to 20%
1:25,000	5%

In the developed countries, map coverage percentages are definitely higher than these coverage estimations, but the pace of development in many areas has caused the maps to be out of date. Thus revision has become obligatory if these maps are to be useful. A study prepared for the German government estimated that 50% of the existing German maps need revision and that map revision is required every 3 years in some areas of the developed countries (Konecny, 1983). Although map revision at large scales in most of these countries must be done in a piece-meal fashion by land survey methods since the developments themselves are

usually randomly located, certain less developed areas in some of these countries, especially those with large areas such as U.S.A and Canada, may sometimes be subjected to a specific massive development programme which requires aerial photographic projects to be planned and executed for the sole purpose of map revision of these areas. It is generally believed that for timely revision other economical and fast means must be sought to cope with these demands.

In the Third World countries, the situation is far worse. Due to factors relating to their economies and political conflicts and also because of the vast area of many individual countries, much of which comprises desert, dense forests, mountainous terrain, etc and is therefore uninhabited or inaccessible, map coverage is often very limited. Furthermore some of the maps available in these countries have been prepared from information gathered by administrative officials as sketches of boundaries and the main natural and man-made features in the area for administrative purposes (Stone, 1982; Bailey 1957). The resulting maps are at very small scales and often none too accurate. Also they do not contain the topographic information needed for regional planning and development purposes. In many other cases, photogrammetric mapping to a good standard has been undertaken but the coverage is both limited and patchy, often being associated with the coverage of small areas in each of which a specific development project is being undertaken. Systematic topographic mapping is the exception rather than the rule.

In general, it is realized by the developing countries that the only way to rectify the situation is to increase the rate of mapping and map revision. At the moment, it seems that one way of doing this is to utilize the capabilities of remote sensing technology in acquiring images of the Earth's surface from space which can be used for the stated purposes.

With the repeated coverage capability of space remote sensing systems, it also seems logical to consider using their images for map revision in the developed countries, particularly where one considers the current trend in modern cartography to using automated systems which lend themselves quite nicely to the handling of digital data.

In the Third World countries, space remote sensing presents new challenges and problems since the amount of detail which can serve as control for image transformation is often very little and the contrast between man-made features, i.e buildings, roads, railway lines, and the ground may be negligible which makes these features hardly discernible.

In addition to this, the lack of funds to buy modern equipment and machines for the processing of remote sensing data, and the limited number of skilled personnel are disadvantages from which most of these countries suffer.

1.2 Stating The Problem

In this research, a thorough investigation of the possibility of producing topographic maps from the available space images acquired by various sensors for the developing countries and employing methods which are affordable by these countries has been carried out. Taking the author's home country (Sudan) as the test area presents a great opportunity for him to acquire experience and knowledge of the kind of problems that he will undoubtedly face during his work dealing with the topographic mapping of his own country.

1.3 The Topography of the Sudan

Sudan is the largest country in Africa. It extends from $3^{\circ} 30'$ to 23° of latitude north of the Equator, and from 22° to 38° of longitude east. Three distinguishable areal zones can be recognized in terms of its physical geography and vegetation. These occur as three east-west belts running from the south to the north of the country, made up of the tropical zone, ($3^{\circ} 57'$ to about 8° N), the semi-arid zone (8° to 16° N), and the arid zone north of the 16° parallel of latitude.

Much of Sudan's topography is characterised by the vast flat plains of the Nile surrounded by low hills and areas of elevated terrain, Fig. 1.1. However, along the Red Sea coast, a narrow coastal plain no more than 30 km wide soon gives way to a relatively narrow strip of hills (200 km wide) rising up to over 2,000 m. The drainage divide between the Nile and the Red Sea plain lies less than 50 km from the coast. Also in the south-east of the country, the interior plains give way to the high plateau of Ethiopia. The main rivers flowing off this high plateau, such as the Blue Nile, Atbara, Setit, Gash, Angar, Akabo and Kurum, have all cut deep into the basement metamorphic complex.

Southern Sudan shares an area of high ground with Northern Uganda which rises to a height of over 3,000 m in the Imatong mountains at the border. This high ground continues north-westwards along the Zaire & Central African Republic borders towards Chad to form the Congo/Nile drainage divide. A further area of high ground is formed in Western

Darfur by the volcanic masses of Jebel Maira, which rises to over 3,000 m, and the Meidob hills. Streams flowing off this high ground drain south-east towards Bahr ElArab and the White Nile or westward through the Wadis Tiwal, Azum and Kadja to the Chari and into Lake Chad.

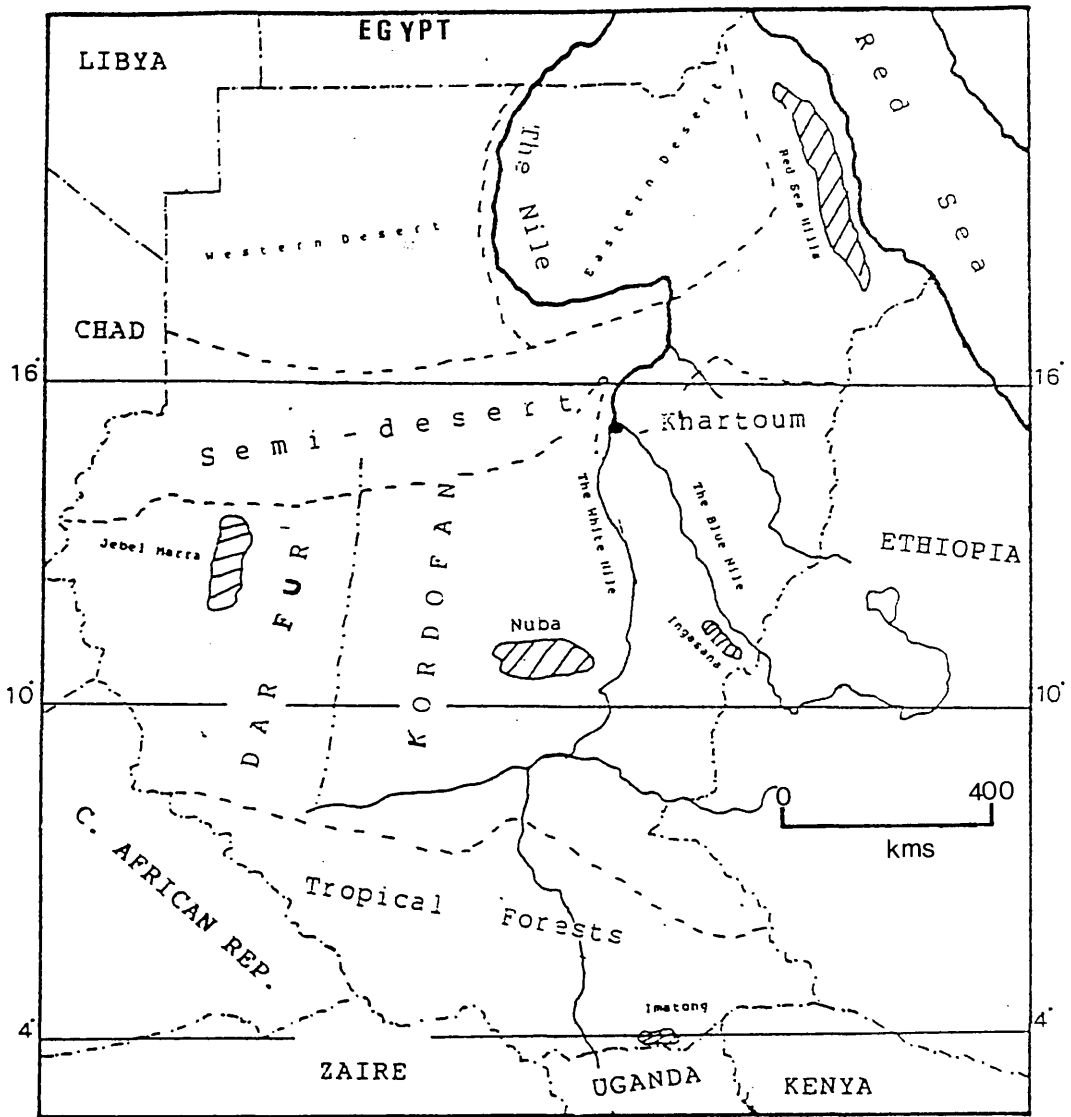


Fig. 1.1 Topographic Features of the Sudan.

Throughout the central plains, isolated granite hills or Jebels rise above the main plain surface as in the case of the Ingasana Hills in the Blue Nile province and the Nuba mountains of Southern Kordofan.

As can be seen in Fig. 1.1, large parts of the country can be categorized as inaccessible areas. The north-western desert outlined in the figure is a dead area with few human activities and no development

taking place. This is mainly due to the nature of the desert which is characterized by the scarcity of water and vegetation cover and massive amounts of loose sand soil. The same remarks can be made about the north-eastern desert. Further south, sand dunes which are in continuous motion in the northern and central parts of the Kordofan and Darfur regions make transportation in these areas extremely difficult if not impossible. Since the economic activities in many developing countries are mainly based on rain-fed farming and grazing, this area is almost totally abandoned in terms of human occupation. Being so and given its extent, it is very difficult and costly to use aerial photography in mapping such areas especially when one considers the difficulties in carrying out the field work associated with this mapping.

Still further south, the presence of dense humid tropical rain forests creates another inaccessible area. These forests coupled with the poor seasonal roads, the lack of alternative communication facilities and the fragile political situation make the mapping of this area extremely difficult. And above all, the sheer size of the country itself, compared with its economic capabilities, presents a big challenge in terms of mapping it using conventional photogrammetry.

1.4 Status of Topographic Mapping in the Sudan

The Sudan Survey Department (SSD), established in 1899, is responsible for the country's topographic mapping and surveying activities. Looking first at the provision of the basic control network, the main landmarks in Department's surveying history can be summarized as being the completion in 1954 of the part of the Arc of the 30th Meridian first-order chain that crosses Sudan; the establishment of the Sudanese part of the 12th Parallel chain; and the establishment of various secondary triangulation chains along the Red Sea Hills and Western Sudan. Recently a densification of the control network has been carried out by the British Military Survey Service using satellite doppler fixing for individual stations. Of course, all of these activities were widely spread over the period since the establishment of the SSD due to its concern with many other surveying activities, especially cadastral surveys.

Soon after its establishment at the turn of the 20th century, the Anglo-Egyptian government of the Sudan was faced with the problem of governing and administering a vast country with poor transport and communication services and, most vitally, no maps. Hence the SSD was established and assigned the task of executing two urgently needed survey and mapping projects. One was the compilation of a series of

1:250,000 scale maps to satisfy the urgent demands of administration, military activities and development. The other was the surveying and demarcation of the cultivated land plots and the preparation of the associated property maps along the whole of the Nile from Khartoum to Wadi Halfa on the Egyptian border for taxation purposes in the first place and for land registration in the second. By the year 1908, all the sheets at 1:250,000 scale, for which the data were gathered by the method of route surveys, were published for the whole country. The resulting maps were therefore mainly planimetric maps which showed very little detail away from the routes and the settlements along these routes. They contained no contouring; instead the topography was depicted by rough form lines to show the general features of the relief. These maps were required to be executed very quickly; therefore no attention was paid to the establishment of control chains. In fact, all mapping activities in the Sudan before World War II were characterized by the quick execution of mapping tasks on a local basis for specific development projects, such as Gezira, Gash and Tokar irrigation schemes, without paying attention to the control survey of the country as a whole.

In 1935, the observations of the Sudanese part of the first-order triangulation chain of the Arc of the 30th Meridian, which joins Alexandria in Egypt to Capetown in South Africa were started. This chain runs north-south along the centre of the country. Work on this chain was soon halted by the War, when priority was again given to topographic mapping, but this time for military purposes. Trimetrogon photography of the whole country north of 8° N latitude with the exception of the north western desert was carried out by the American Air Force. Some of this photography was used by the SSD to prepare 1:100,000 scale planimetric maps of about 80,000 square miles in the "Sudd" area of the Upper Nile province; and a further 20,000 square miles of the Kosti area were mapped by the U.S Geological Survey (Wright, 1951 & 1967; Gorani, 1980).

The work on the Arc of the 30th Meridian was resumed in 1952 by the U.S Army Map Service with the help of the SSD and was completed in a period of fifteen months (Mills, 1955; Gorani, 1980). With the completion of this chain, the first first-order triangulation chain in Sudan was established. In 1953, the concept of the Arc of the 12th Parallel chain was introduced by the Scientific Council of Africa South of the Sahara via one of its resolutions at a meeting held in Bukava (Congo). This chain was to help provide more and better data for defining the shape of the Earth and to provide a geodetic control reference for the various individual surveys in the area (Yater, 1970).

Immediately after independence, in 1956, a U.N aid programme was used to establish the Sudanese part of the Arc of the 12th Parallel. The task was again executed by the Americans in co-operation with the SSD. More first- and second-order chains were also established by the Americans along the Red Sea Hills. Short second-order chains were also established in Central and Western Sudan during the 1970s. More recently, further densification of the control has been executed by the British Military Survey using satellite doppler fixing. The overall control network in the Sudan is shown in Fig. 1.2.

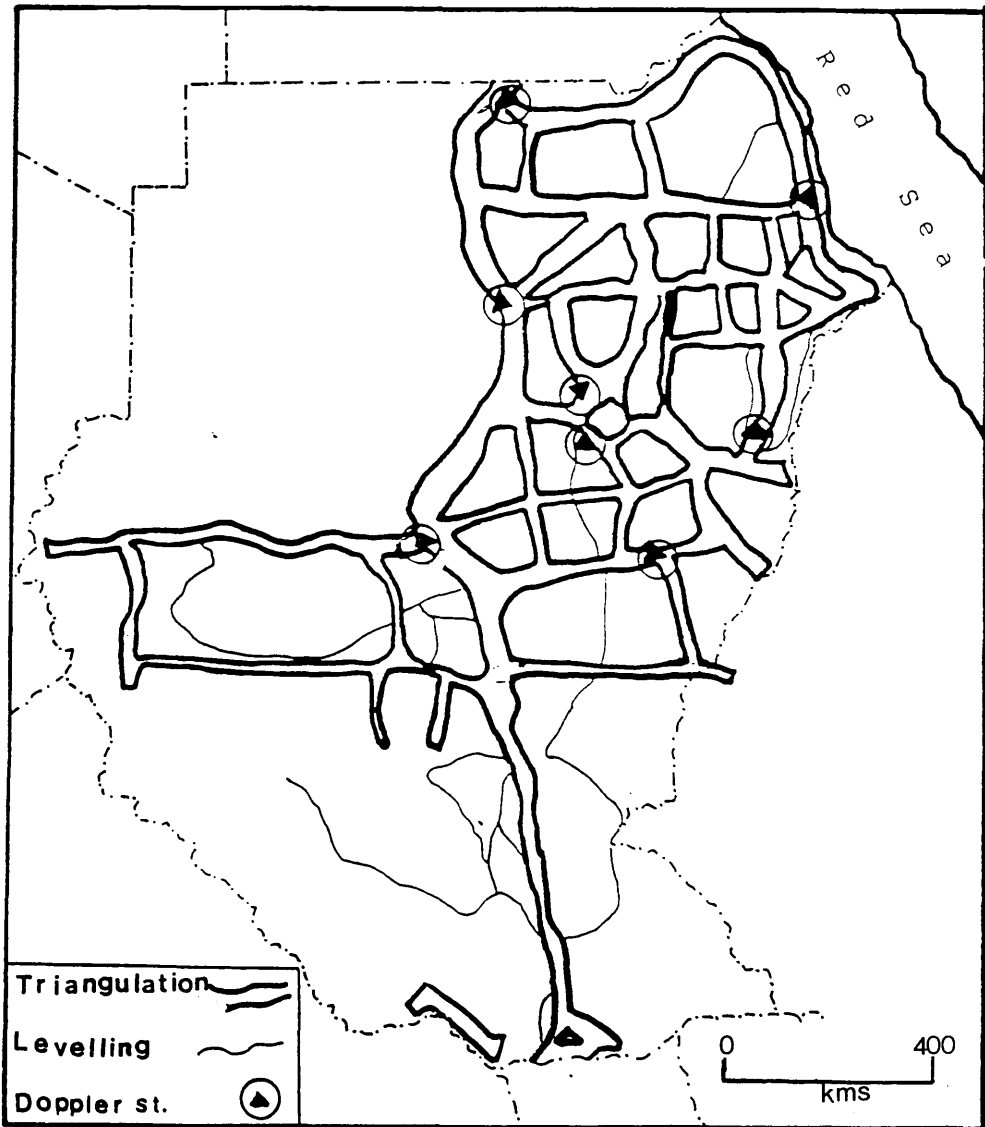


Fig. 1.2 Control Network of the Sudan.

At the moment, the status of the topographic mapping of the Sudan can be summarized as follows:

i) 1:250,000 Series: This consists of 172 sheets which give complete coverage of the whole country. Most of these sheets are printed in 3 to 4 colours with the exception of some which cover desert areas which are printed in black only. The maps in this series are the products of a recent revision (1970 - 1976) of the original 1:250,000 scale route maps produced earlier under the Anglo-Egyptian government. Although this revision took advantage of the established control network and the data acquired in the developing areas, in many parts of the country, especially the north-western desert and the tropical forests, the revision was by no means comprehensive and only major changes of administrative boundaries and names were added.

ii) 1:100,000 Series: In the early 1970s, it was decided that the 1:250,000 scale maps were too small in scale to provide the information needed for the feasibility studies, investigations and planning of the development projects of the Five Year Plan announced by the Government. Therefore a 1:100,000 scale series was to be produced to fulfil this demand and to serve as the basic series for other smaller-scale map production. The total coverage of the Sudan at this scale requires 920 sheets. Aerial photography and photogrammetric methods were considered as the quick and easy means for the production of the maps. In fact, a simple calculation will reveal that to accomplish this task unbelievably large financial and technical resources would have to be secured. Therefore, selected important areas in which investigations needed to be carried out for various Earth resources and development projects, were given priority.

The U.N Development Programme (UNDP) was requested to help in the execution of this mapping programme and an agreement between the UNDP and the Sudan Government was signed in 1970. Through this agreement, the UNDP was directly concerned with the establishment of the infrastructure needed to carry out the field control, photo-interpretation, photogrammetric work, and cartographic preparation of the maps. As a result, the Survey Department was equipped with new stereo-plotting machines such as Wild A7, A8, and A10 Autographs and several B8S Aviographs for the photogrammetric compilation of these maps. The aerial photography itself was a direct responsibility of the SSD, for which purpose, it was equipped with a Twin Otter Series 300

survey plane equipped with a Wild NF2 navigation sight, Decca Doppler radar equipment, a Wild RC10 camera with a super-wide-angle lens and a Wild RC8 wide-angle camera.

Besides the aerial survey component provided by the UNDP, the project also resulted in the setting up of a comprehensive map production facility at the SSD Headquarters in Khartoum, including a reprographics unit, printing press, etc. Training was also provided for selected SSD personnel in various foreign countries. In spite of all this considerable investment and a substantial effort on the part of the UNDP and SSD personnel, only a limited map coverage has resulted from this project, with a few sheets published mainly for the area around Khartoum and the Sinkat-Haiya area in the Red Sea Hills. The many difficulties encountered by the SSD have included lack of foreign currency to purchase materials, spare parts, etc; the poor economic situation in the country causing budgetary restrictions resulting in limited field survey work, flying restrictions, etc; the shortage of trained personnel, many of whom have gone to work in the neighbouring oil producing states (Saudi Arabia, Libya, the Gulf States, etc.); and the long periods of civil war, especially in the south of the country.

In addition to this UNDP supported programme, a joint survey and mapping project was agreed with the British Directorate of Overseas Surveys (DOS) in which the production of a block of 1:100,000 sheets covering the Red Sea Hills was undertaken by the DOS (now O.S.D. as part of the Ordnance Survey). The result of these two projects is that about 55 sheets have been produced in this series, most of them by DOS. Fig. 1.3 shows the coverage of the published sheets in the 1:100,000 scale series amounting to a small percentage of the whole in relation to the area of the Sudan. The same situation repeats itself in most of the Third World countries as depicted in the publication and index maps published yearly by DOS.

iii) 1:25,000 Scale Series: A limited number of sheets has been produced in this series to cover parts of the Khartoum Province. The production of this limited coverage was suddenly decided upon by the Government for military reasons soon after the Libyan backed military rebellion in 1976. Therefore, these sheets were classified as secret documents and kept in the Security Headquarters where they could only be made available to users by special request. This has been so till 1985 when the Security

Organization was dismantled.

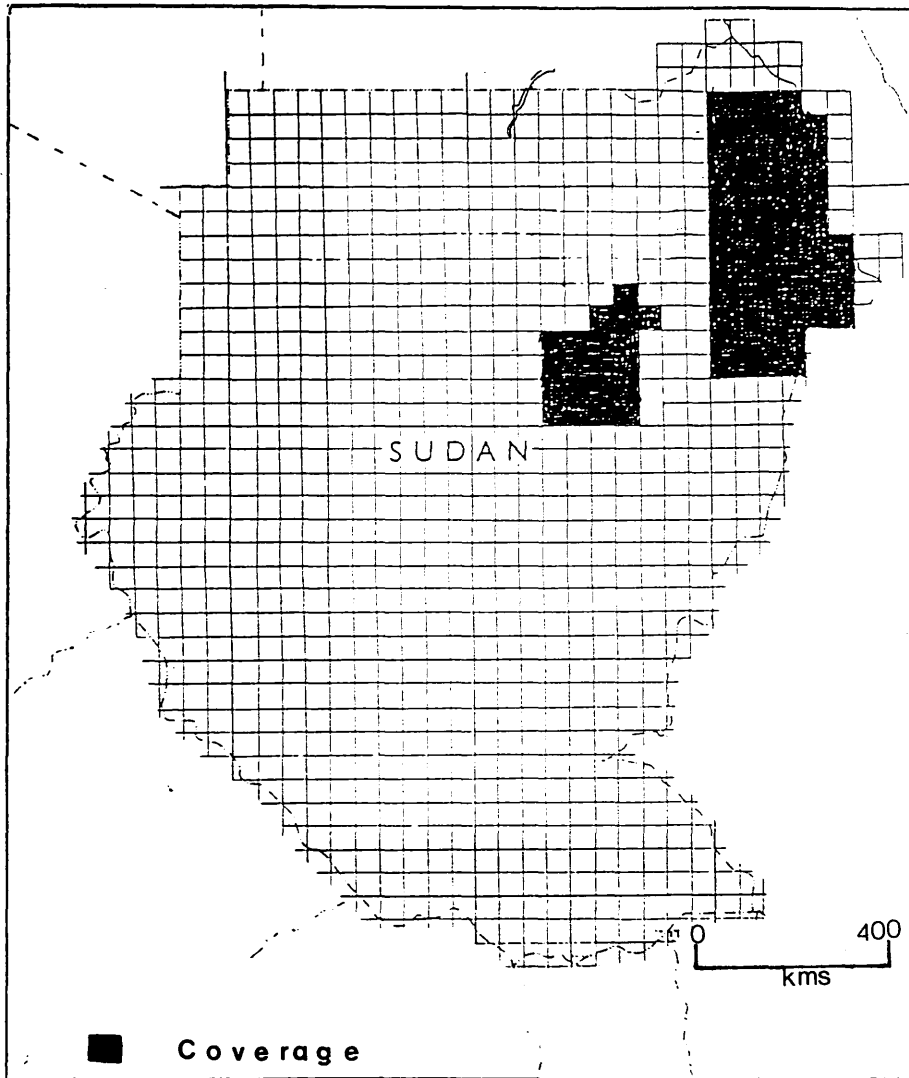


Fig. 1.3 1:100,000 scale Map Coverage in the Sudan.

From the above description, it is clear that the Sudan is a good example of the developing countries since it suffers from all the factors that make topographic mapping using conventional aerial photogrammetric methods, a real challenge. Considering the vast area of the country, the use of space imagery appears to offer a solution to some of the problems of topographic mapping in the Sudan. Although the scale and resolution of space imagery is less than would be achieved

from airborne platforms, many of the developing countries are not in any desperate need of very detailed large scale maps and plans. Instead they have an urgent need for medium to small scale topographic map cover to support the first-time developing process. The Sudan in particular has a large land area, much of which is flat or has a limited range of relief and contains little detail. So small scale line maps or image maps are quite appropriate mapping products. As mentioned above, this has already been realized by the SSD in deciding on the production of a 1:100,000 scale series to serve as its basic coverage of the whole country. Since much of the Sudan is desert or semi-arid land, the weather is often cloud-free so that the problems of acquiring imagery from space are not present in the same way as happens with the cloudy areas of the tropics or those areas with a maritime temperate climate such as the U.K.. This good weather, in addition to the factors discussed above, makes the Sudan a favourite choice to represent the developing countries in this investigation since there is a great probability of finding cloud-free space imagery from various space imaging systems.

With space imagery, several map or image map sheets at the 1:100,000 scale can be produced from a single image or stereo-model which results in a dramatic reduction in the photogrammetric operations which are required to produce these sheets as compared with those necessary to prepare maps from aerial images. The reduction in the number of the images required to map a certain area also brings benefit in terms of the reduced provision of control points which, as shown above, is a major consideration in the inaccessible areas. The use of space images in the topographic mapping will also lift the burden of planning and executing individual imaging projects from the backs of the economically crippled developing countries. This is because these images are made available from world-wide remote sensing programmes which are planned and executed by the developed countries. In addition to the above, an immense wealth of space imageries is already available and waiting to be exploited.

Therefore, it seems quite timely and appropriate to investigate the capabilities of the various existing remote sensing systems in this present project and to determine what contribution each of these systems can offer in respect of the topographic mapping of the developing countries in general and the Sudan in particular. This investigation can also provide an insight into what may be expected from future systems as well as to determine what can be achieved from the available images.

1.5 Thesis Organization

This thesis is organised in such a way that the general aspects of remote sensing are presented first. Then the various individual systems are described and tested using imagery taken over a common test area in the Red Sea Hills. Those systems with no stereoscopic imaging capabilities are described first of all and a series of tests of their planimetric accuracy and their interpretability for topographic mapping will be reported upon. Following this, an investigation of the various space photographic systems which permit stereoscopic imaging and the results of tests using images taken with these systems are then presented and the results are analyzed in detail. Finally the conclusion and recommendations resulting from all these experimental data are given in the last chapter.

In Chapter 2, the various fundamental aspects of remote sensing, including the characteristics of the electromagnetic spectrum and its interaction with the atmosphere and Earth's surface, are covered and the various types of sensors and satellite imaging systems are described with particular reference to those used in the author's experimental work. This is followed by Chapter 3 in which the considerations of topographic mapping such as planimetric and height accuracy specifications, and contour intervals are stated. The test areas selected for this investigation, the acquisition of the test data and its accuracy, and the equipment used in the experimental work are also described.

In Chapter 4, the Landsat MSS and TM systems are described in some detail followed by a geometrical analysis of line scanner imagery in which the mathematical models which have been suggested by various investigators for their transformation into the map system are reviewed. The specific mathematical models and procedures followed in conducting the planimetric tests in this investigation are described and the reasons for adopting them are explained. This leads directly to Chapter 5, in which first of all the planimetric accuracy and interpretability tests carried out on MSS and TM images are reported followed by an analysis of the results obtained including a comparison with the results obtained by other investigators in various test areas.

The German MOMS and the French SPOT-HRV systems are described in Chapter 6. The geometry of these push broom scanners is discussed and the mathematical models for the reduction of the images obtained by them are derived. Again this leads to Chapter 7, in which the results of the planimetric accuracy and interpretation tests of MOMS images

are explained and analyzed. A discussion and the prediction of the accuracy that could be obtained from the French SPOT-1 satellite images over Sudan had these been available for testing is also given.

In Chapter 8, the RBV system is described with particular reference to those carried aboard Landsats 1,2 and 3. The geometry of the RBV camera is analysed and the mathematical models which can be used for the RBV imagery rectification are given and discussed. The various arrangements of the stereo-models which can be formed from images on adjacent orbit tracks are also discussed. Finally, the mathematical models and test procedure followed in the height accuracy tests are explained. As before, this leads to an associated Chapter 9 in which the test areas selected for the geometric accuracy test of RBV imagery, and the procedures followed in image coordinate measurement for the planimetric and height tests are described. The results of the accuracy test are presented and analyzed, followed by the results of the interpretation that has been carried out to establish the amount of detail contained in the RBV images.

Chapter 10 discusses the various space photographic systems. First the considerations of space photography are reviewed and explained followed by a general description of the various photographic films available for the use in space photography. A survey of the past Earth orbiting space photography experiments is then given followed by a description of the Metric Camera (MC), the Large Format Camera (LFC) and the recent Russian space photographic systems. This is followed by a discussion of the geometric aspects of space photographs and the mathematical models used in analytical photogrammetry for mensuration of these photographs. Finally, the photogrammetric operations carried out on the MC and LFC photographs in this investigation are outlined and the test procedure is explained. This serves as an introduction to Chapter 11 in which the results obtained from the accuracy and interpretation tests of the MC and LFC photographs are presented and analyzed. The results of the accuracy tests are presented and discussed first. Then the accuracy tests carried out by other investigators on the MC and LFC as well as the Russian cameras are discussed, analyzed and compared with the results obtained in this investigation. Finally, the results of the interpretation tests are presented and discussed.

In Chapter 12, the theoretical aspects of orthophotography and a survey of orthophoto production instruments are given as an introduction to the orthophotography experiments conducted by the author on the MC photographs. This is followed by a discussion of Digital Terrain Models (DTM) and their collection and utilization, as an introduction

to the generation of a DTM, its accuracy test and the contouring experiments carried out by the author on the profiling data gathered from the MC photographs. Then the actual experiments are described and the results presented and analyzed.

Finally, in Chapter 13, the conclusions which can be drawn from this investigation and the associated series of experimental tests are presented together with recommendations and suggestions for further investigations and systems development. Several Appendices explaining some of the mathematical formulae and the computer programs used in this investigation are also included.

CHAPTER 2

Space Remote Sensing

2.1 Remote Sensing

Remote sensing is generally defined as the science and art of obtaining information about an object, area, or phenomenon through the analysis of data acquired by a device that is not in physical contact with the object, area, or phenomenon under investigation. However the term remote sensing is usually applied to the acquisition from a considerable distance of image data about the Earth's surface, its resources and the surrounding atmosphere and its subsequent analysis.

A more detailed and descriptive definition of remote sensing is that "Remote sensing denotes the joint efforts of employing modern sensors, data processing equipment, information theory and processing methodology, communication theory and devices, space and airborne vehicles, and large system theory and practice for the purpose of carrying out aerial or space surveys of the Earth's surface" (Baker and Mikhail, 1975).

For most analysis and mapping of the Earth's surface and its resources and particularly for topographic mapping, the main form of remotely sensed data is that measured and recorded in terms of the variation in electromagnetic energy distribution reflected or emitted from the surface and generated in the form of images. These can then be measured or interpreted by the field scientists or topographic scientists concerned with the analysis or mapping.

2.2 Electromagnetic Energy Radiation

The electromagnetic state at a point can be expressed by two vectors - E, the electric field, and H, the magnetic field - each orthogonal to the other. Electromagnetic radiation is a dynamic form of energy in which these fields propagate in a wave-like configuration through space at a constant speed. The interrelations between these fields along their propagation path are expressed by the well known Maxwell equations. The major implication of these is that changes in the fields E or H propagate through space with a speed equal to the constant value c, which is known as the speed of light and has a measured value of 2.9979×10^8 m/s.

2.2.1 Electromagnetic Spectrum

Electromagnetic waves are usually categorized by their wavelength and its location within the electromagnetic spectrum. Fig. 2.1 shows the various regions of the electromagnetic radiation spectrum used in remote sensing.

The entire band of wavelengths (λ) between 0.3 and 15 micrometers (μm) is referred to as the optical portion of the electromagnetic spectrum, since electromagnetic waves in this portion can be refracted and focussed using lenses and prisms.

The wavelengths (λ) in the optical portion lying between 0.3 and 1.0 μm constitute the photographic region where photographic emulsions can be utilized to record the data. The human eye is sensitive to wavelengths between 0.4 and 0.7 μm within the photographic region; hence this portion is referred to as the visible region.

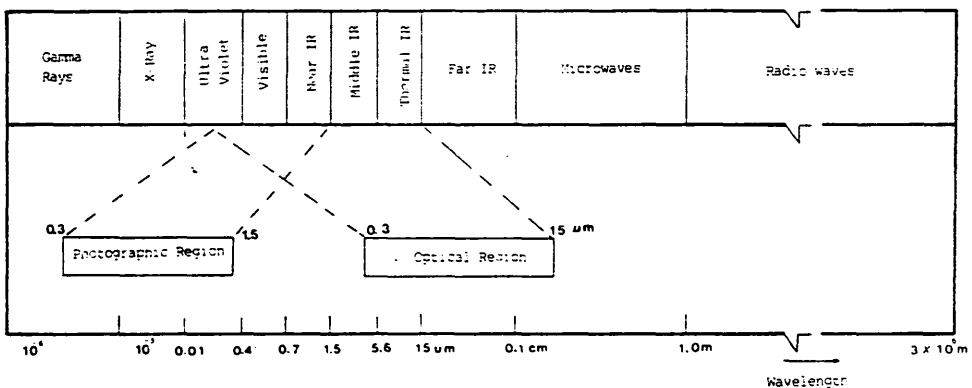


Fig. 2.1 Electromagnetic Spectrum.

At wavelengths below 0.4 μm exists the ultraviolet region and above 0.7 μm is the infrared region. This latter region is further classified into four sub-regions - the near infrared covering wavelengths between 0.7 and 1.5 μm ; the middle infrared, lying between 1.5 and 5.6 μm ; the thermal infrared between 5.6 and 15 μm ; and beyond the optical region comes the far infrared region covering wavelengths between 15 μm . to 0.1 cm. Energy coming from the Earth in the first two of these infrared regions is dominated by that reflected by the Earth's surface features, while in the other two infrared regions, the energy is dominated by the energy emitted from the Earth's surface.

The infrared region is followed by the microwave region between wavelengths 0.1 cm. and 10 m. Beyond the 10 m. wavelength are the radio waves. The energy reflected or emitted from the terrain at these microwave and radio wavelengths is detected using an aerial or antenna instead of the optical elements used at the shorter wavelengths.

2.2.2 Electromagnetic Energy Source

All matter at temperatures above the absolute zero (0° K. or -273° C.) continuously emits electromagnetic radiation. For an ideal radiator which totally absorbs and re-emits all energy incident upon it or an ideal emitter which emits all the energy from its thermal activity, the energy emitted is given by the Stefan-Boltzmann law as:

$$W = s.T^4$$

where:

W is the total energy emittance from the body in watts/sq. m;
s is Stefan-Boltzmann constant (5.6697×10^{-8} watt $m^{-2} \text{ }^{\circ}$ K); and
T is the absolute temperature of the body.

These ideal bodies are hypothetical and are called blackbodies. The total energy emitted therefore varies significantly with small variations of the temperature. In addition, the spectral distribution of the emitted radiation also varies with the temperature of the emitting body. Fig. 2.2 shows the emitted energy distribution for blackbodies at various temperatures. The area under each curve gives the total energy emitted at the respective temperatures.

From Fig. 2.2 it is clear that, as the temperature increases, the black body radiation distribution curve peak shifts towards shorter wavelengths. The wavelength at which the peak occurs is given by Wien's displacement law as:

$$\Delta \lambda = A/T, \text{ where } A=2898 \text{ } \mu\text{m } ^{\circ}\text{K.}$$

The major source of electromagnetic energy is the Sun. The Sun emits electromagnetic energy similar to that emitted by blackbodies at temperature of $6,000^{\circ}$ K. The energy distribution curve for blackbodies at this temperature in Fig. 2.2 shows that the maximum emittance occurs at the wavelengths about 0.5 micrometres. Upon striking the Earth's surface, some of the Sun's energy is reflected back to be sensed by the remote sensor (in the presence of the Sun), some is scattered, and the

rest is absorbed and subsequently emitted by the Earth's surface features. The Earth's surface emittance approximates that of a blackbody at a temperature of about 300°K. This means that the Earth's maximum emittance occurs at a wavelength of about 9.7 micrometres which is in the thermal infrared region. For this reason, thermal infrared sensing is often used in studying Earth's surface properties related to its temperature.

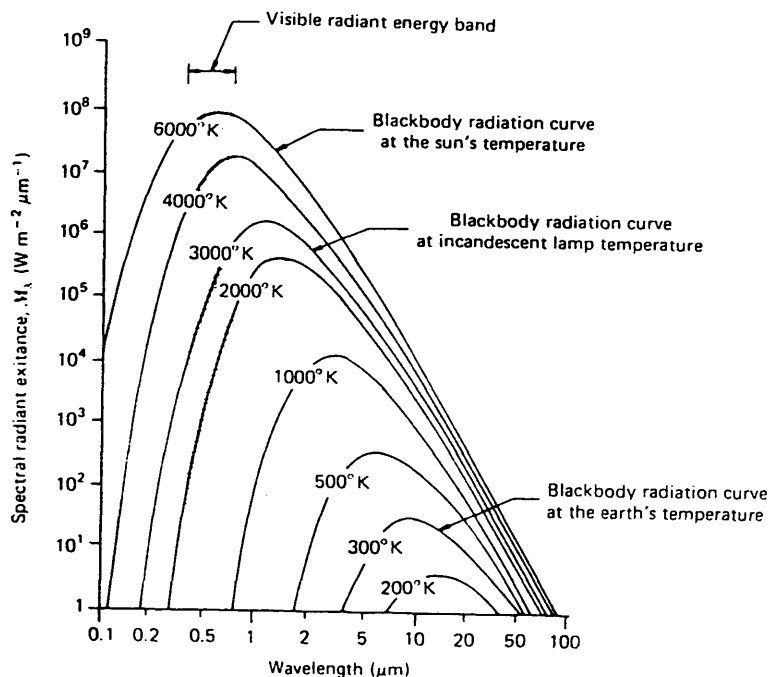


Fig. 2.2 Emitted Energy Distribution from Blackbodies.

2.2.3 E.M Energy Interactions with the Atmosphere

All radiation detected by remote sensors passes through some or all of the atmosphere layers, once or twice depending on the electromagnetic region being sensed and on the sensor's altitude. In space remote sensing, the radiation passes twice through the full thickness of the atmosphere in its path from the Sun to the Earth's surface and from there to the sensor for the reflective region and just once in its path from the Earth's surface to the sensor for the emitted region.

2.2.3.1 Atmospheric Scattering

In its path through the atmosphere, some of the electromagnetic radiation is scattered, some is completely lost by absorption and the rest passes through. Different types of scattering may occur depending on the atmosphere's molecular composition and suspended particles. Unpredictable diffusion of the blue region radiation occurs due to the interaction of the electromagnetic radiation with the molecules of the atmosphere and the tiny particles suspended in it.

When the diameters of the atmospheric suspended particles are equal to the energy wavelengths being sensed, as in the case of water vapour and dust suspension, Mie scattering occurs to affect remote sensing at wavelengths longer than the blue region and hazy images will result. When the suspended particles are greater in diameter than the wavelengths of the radiation being sensed, as in the case of clouds and water droplets, all radiation in the visible and near to middle infrared regions is scattered nonselectively making remote sensing of Earth's surface impossible at these wavelengths.

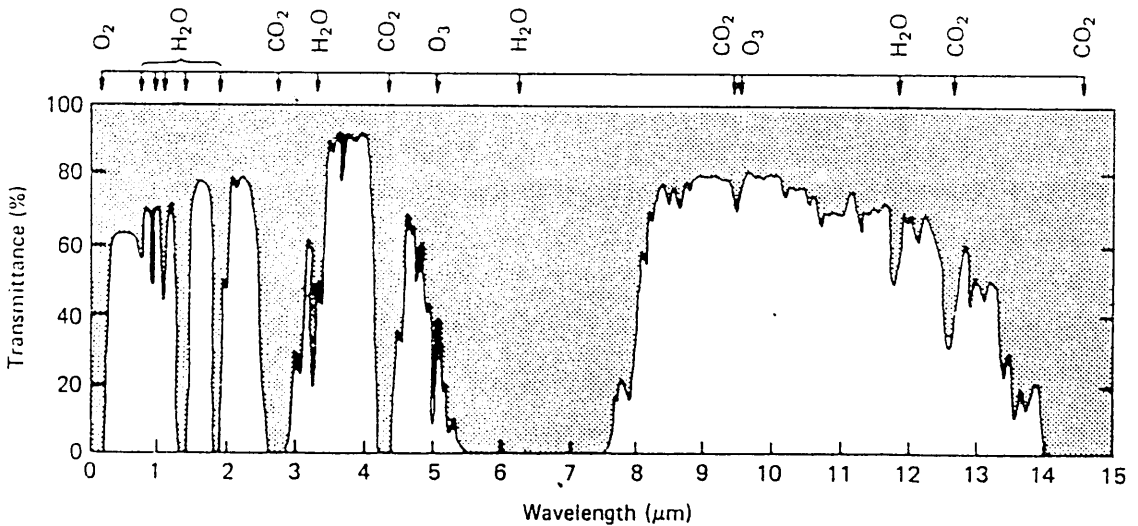


Fig. 2.3 Atmospheric Windows.

2.2.3.2 Atmospheric Absorption

Atmospheric absorption results in a complete loss of energy to the atmospheric constituents at certain wavelengths. Absorbing constituents of atmosphere are water vapour, carbon dioxide and ozone. The effects of atmospheric absorption restrict remote sensing to these regions

where minimal or no atmospheric absorption occurs - referred to as atmospheric windows. Fig. 2.3 shows these atmospheric windows and the absorbing constituent in each non-window region. From Fig. 2.3, the first atmospheric window covers the visible and near infrared regions. This is the window used for remote sensing in the region of reflected solar radiation. The second and third windows cover the wavelength regions from 3.0 to 5.0 μm and from 8.0 to 14.0 μm respectively in the middle and thermal infrared regions of the electromagnetic spectrum. The fourth window is in the microwave region covering wavelengths between 1 mm to 1 m.

2.3 Remote Sensors

Sensors can be classified into two broad categories as imaging sensors which are capable of presenting the data gathered about the Earth's surface in a pictorial form, and non-imaging sensors which produce measurements of various phenomena, such as atmospheric temperature variation. In this investigation, only imaging sensors are discussed since they supply the input data for the photogrammetric operations carried out for map production.

Imaging sensors can be further classified into active sensors and passive sensors. Active sensors are those capable of generating their own carrier field radiation. Hence with these sensors it is possible to control the way in which the radiation is directed, spectrally distributed and polarized, and the way in which it is allowed to vary in time or phase. Upon striking the Earth's surface, the radiation is reflected back to be measured by the sensor for the determination of the direction from which it has been reflected, its spectral distribution, and its time variation and phase of return after it has undergone alterations due to its interaction with the Earth's surface features. Passive sensors on the other hand rely on the natural radiation reflected or emitted from the Earth's surface. This radiation cannot be controlled in the same manner as the radiation generated by an active sensor, and therefore suitable radiation conditions must occur and may have to be waited for before sensing takes place. In this discussion, sensors will be discussed under four main categories. These are: (i) photographic systems; (ii) television cameras; (iii) electro-optical scanners; and (iv) microwave imaging radars.

2.3.1 Photographic Systems

Photographic systems record reflected electromagnetic energy variations as image data on sensitive films. Therefore they are

restricted in operation to the photographic region of the spectrum. Photographic systems may consist of one or more photographic cameras. Basically there are three types of photographic cameras that are available for remote sensing applications. These are frame cameras, panoramic cameras, and strip cameras. Strip cameras were originally developed for low altitude reconnaissance aerial photography where a strip photograph is taken for interpretation purposes. Since no advantages, for which the stable geometry of frame photography may be sacrificed, will be gained from the use of strip cameras in space, there is little prospect of them being employed in space remote sensing.

2.3.1.1 **Frame Cameras**

A frame camera is one in which the entire frame is exposed through a lens which is fixed relative to the focal plane. This exposure can only take place when the shutter is opened to allow the radiation to strike the sensitive film. There are two types of frame cameras-the reconnaissance type and the metric or mapping type . The difference in the design of the two types is dictated by the difference in the fields of applications within which each type is used. The metric camera is a calibrated camera in which the geometric characteristics are optimized to provide the very high degree of precision required for topographic mapping, while in reconnaissance cameras, resolution and image definition are optimized- often at the cost of the camera's geometric characteristics and stability. Since this investigation is concerned solely with topographic mapping, only the mapping camera design will be discussed. The principle, construction and main parts of a mapping camera are shown in Fig. 2.4 and discussed below.

(1) **Camera Body**

The camera body houses the camera drive mechanism which provides the motions necessary to set and trigger the shutter, to operate the film flattening system and to wind on the film between exposures. A small electric motor provides the power for the driving mechanism.

(2) **Lens Cone Assembly**

The lens cone supports the entire lens assembly including the filter. It prevents any light other than that passing through the lens from reaching the film. In mapping cameras, the lens cone supports an inner cone (spider) made of low thermal expansion metal. This inner cone holds the lens assembly at a distance equal to the focal length of the

lens from its upper surface which defines the focal plane of the camera. On this upper surface, the fiducial marks are located in fixed positions.

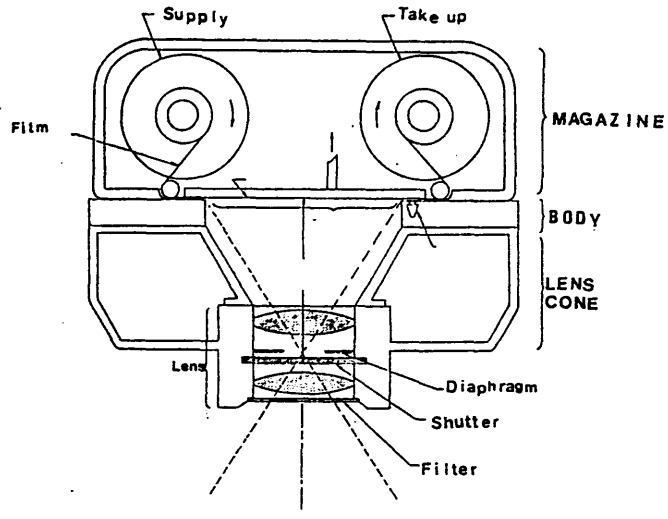


Fig. 2.4 Frame Camera.

The lens assembly is the most important part of the camera since the geometric and radiometric quality of the resulting photographs depends on the characteristics, the design, and the alignment of its optical elements. Every single lens has optical aberrations which affect the quality of the image. These aberrations depend on the design of the lens and the quality of the glass from which the lens is cut. To reduce the effects of these aberrations, the actual lens is made up of a combination of component lenses made from different types of glass. These individual lenses are arranged in such a way as to give the best possible image for the whole format. For mapping cameras, the lens should be almost distortion free. A filter may be used in front of the lens to prevent a selected range of radiation from reaching the film to achieve photography within single narrow bands or to reduce the atmospheric haze by filtering out the scattered blue light.

(3) Shutter Assembly

The shutter assembly consists of the shutter and the diaphragm. The shutter controls the interval of time during which the radiation from the ground scene is allowed to pass through the lens. The function of the diaphragm is to control the size of the bundle of rays which may

pass through to the film. For geometric reasons, mapping cameras must have a between-the-lens type of shutter. As the name indicates, the between-the-lens shutter is positioned or inserted through a slot in the space between the front and rear elements of the lens. One of the common designs of shutters used in modern cameras is the rotary type employing a series of continuously rotating discs. Each disc has a cut-away section so that, when these cut-aways mesh, they form an aperture which allows exposure to be made. The speed of the rotating discs is controllable, such that the desired exposure and the intervals between exposures can be selected.

An example of this type of shutter is the Zeiss Aerotop shutter which has four rotating discs. The working principle of this shutter is shown in Fig. 2.5. The required moment of exposure is selected by the fifth plate and the capping disc which are controlled by the intervalometer. The usual possible exposures are in the range of 1/100 to 1/1,000 of a second.

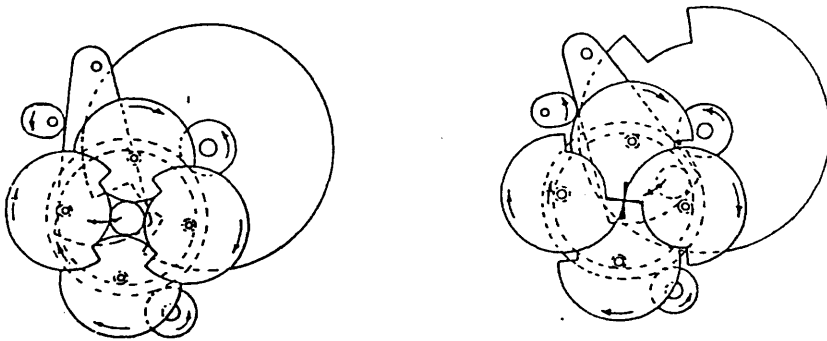


Fig. 2.5 Working Principle of the Aerotop Shutter.

(4) Camera Magazine

This is the light tight container which contains the film and the film winding mechanism which advances the necessary amount of film between exposures. This amount is measured by the number of revolutions made by the metering roller. When the correct amount has been advanced, a clutch is engaged to stop the take up spool from advancing the film any further. Various film flattening mechanisms are possible, such as

the vacuum flattening method which is widely used especially with metric cameras, e.g in the Wild and Zeiss Oberkochen mapping cameras.

(5) **Image Motion Compensation**

The forward motion of the platform during the exposure time causes a relative image motion in the focal plane proportional to the product of the platform ground speed (V) and the exposure time (t) for a given altitude (H) and camera focal length (f). The image relative speed (v_i) is given by:

$$v_i = V \times f/H \quad \dots\dots\dots(2.2)$$

If t is the exposure time, then the image motion (m) usually expressed in millimetres is

$$m_i = V \times t \times f/H \quad \dots\dots\dots (2.3)$$

This image motion may cause degradation in image quality if not compensated for. Obviously it will occur when the platform's speed is great enough and/or if long exposures times need to be used. For a satellite moving at a ground speed of 7.5 km/sec. at 250 km of altitude, a shutter speed of 1/500 sec. will result in an image motion of 18 micrometres if the focal length of the taking camera is 305.0 mm. This image motion results in a slightly blurred image if not compensated for. This was the case in the Metric Camera which is described in Chapter 10.

One obvious method of image motion compensation (IMC) is to move the film in the focal plane during the exposure time with a speed equal to the image motion speed so that the resultant relative motion between the film and the image becomes zero. This is the most convenient way of implementing IMC on these mapping cameras which are equipped with a compensation system such as the latest Zeiss Jena LMK, Zeiss Oberkochen RMK and Wild RC-20 models. In cameras equipped with a register glass and a pressure plate, the film is clamped between the two plates and all three elements are driven together by the IMC motor. After the exposure has been made, the pressure plate is lifted immediately and both plates return to their starting positions without pulling the film back with them. The cycle of exposure is started by imparting an intervalometer pulse to a variable speed motor to start driving the

film transport at IMC speed. The rate at which the variable speed motor will run is selected automatically utilizing the platform's speed and altitude data. When the film-transport system reaches IMC speed, it produces a pulse to operate the camera shutter while the film is moving. At the end of the exposure, the IMC device powers the metering rollers to advance the film for the next exposure.

An alternative method is to move the lens assembly in a direction opposite to the direction of flight at a speed equal in magnitude image motion speed. However this is more difficult to achieve and control, therefore it is not commonly used. A third method is to rotate the whole camera in such a way that the optical axis points towards the same ground point throughout the duration of the exposure. This technique has been used with the Skylab S-190B Earth Terrain Camera in the early 1970s.

The geometry of the resulting frame photographs is that of a central projection and it is described mathematically by the well known collinearity equations. A detailed discussion of these equations is given in Chapter 10 and Appendix A.

2.3.1.2 Panoramic Cameras

The principle of panoramic photography is to scan the Earth's surface across the direction of flight and to expose the film through a narrow slit which scans the focal plane from one end to the other. The mechanical approaches to this scanning divides panoramic cameras into:

(1) Direct Scanning (Rotating Lens) Cameras

The principle of scanning in this camera, as shown in Fig. 2.6, is based on the use of a lens which rotates about its rear nodal point to scan the Earth's surface across the direction of flight. Attached to the lens is a scanning arm (tube) on top of which is a narrow slit having a length equal to the width of the focal plane. The scanning arm rotates with the lens so that the slit scans the film across the direction of flight. The film is accurately positioned in the focal plane, which is part of a circle whose radius equals the focal length of the lens, by two small rollers located at the slit end of the scanning arm. The slit width determines the exposure which each point in the image receives for a given lens sweeping rate. Only the central part of the lens is used to form the image, hence the sharpest possible image results throughout the image format.

A variant of this design is that of the split-scan panoramic camera in which the scanning is carried out by two lens assemblies. One lens is made to point to the left while the other is made to point to the right of the flight track. A common drive mechanism drives both lenses to ensure simultaneous left and right scanning. In both these designs, after the photograph has been exposed, the lens returns to its starting position, with the slit being capped, to complete the cycle of one exposure. IMC is achieved by moving the lens at image motion speed in the direction opposite to the direction of flight. Examples of rotating lens panoramic cameras are the Itek HyAc and Fairchild KA-82. No examples of the use of such cameras for civilian purposes have been reported, although it is an open question as to whether they have been used by reconnaissance satellites for military intelligence purposes.

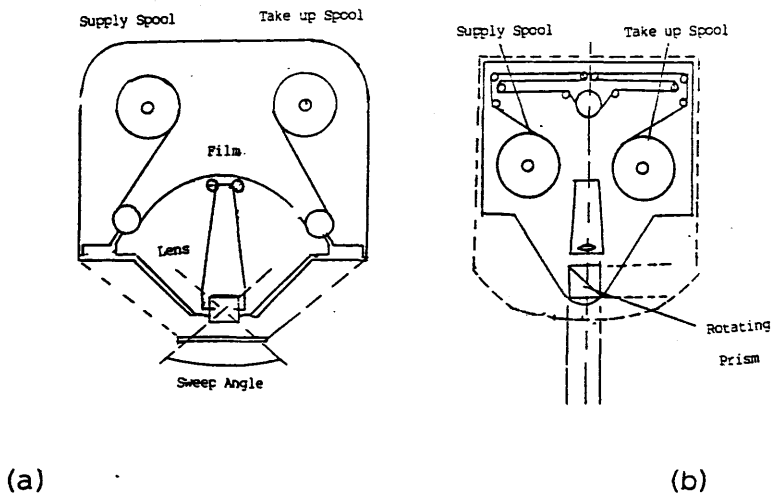


Fig. 2.6 Principle of Panoramic Cameras.

(2) **Rotating Prism Panoramic Camera**

An alternative design of panoramic camera is shown in Fig. 2.6b. Scanning of the ground scene is achieved by rotating a double dove prism, whose diagonal surfaces are aluminized and cemented together, in front of a stationary lens. The prism rotates at a uniform rate to reflect the light rays coming from a series of narrow ribbons of the scene one at a time so that they pass through the lens to focus on the film. The film is continuously advanced by the rotation of the

cylindrical drum around which it passes. Again IMC is carried out by translating the lens longitudinally at a continuously varying rate during the time of exposure.

(3) Rotating Optical Bar Panoramic Camera

This type of camera was designed in an attempt to combine the high resolution of the rotating lens type with rapid cycling speeds. As shown in Fig. 2.7, the optical path inside the camera is made horizontal by two mirrors. The whole optical bar, the lens and the two mirrors, rotates continuously around the optical axis at a constant speed, which obviates the need to start and stop the rotating lens as in the rotating lens type. The film is placed on a cylindrical focal plane. The supply spool continuously revolves, supplying film to a series of rollers and the take up spool continuously revolves to take up exposed film. An example of this type of camera is the Itek KA-80 which was used in the last three missions of the Apollo lunar flights.

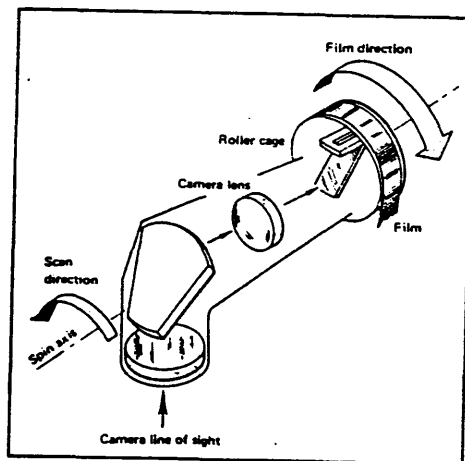


Fig. 2.7 Optical Bar Panoramic Camera.

2.3.2 Television Cameras

Although television cameras do not record electromagnetic radiation on sensitive films but instead convert it to video signals, they are often regarded as being similar to photographic cameras since they are also restricted in operation to the photographic region and the whole frame of the image is formed simultaneously on the target

when the shutter is opened so that geometrically they are identical to frame cameras. Television cameras are one of the most commonly used instruments in space remote sensing systems operating in the photographic region of the spectrum. This results from their small size and weight, their lack of moving parts and the ease with which their data can be telemetered to Earth. Examples include the television cameras used in the Mariner series of planetary missions and the APT (Automatic Picture Transmission) and AVCS (Advanced Vidicon Camera System) cameras used in weather satellites.

Television cameras first form frame images of the ground scene on a light sensitive target through the use of an optical lens system and then by sweeping an electron beam in a raster pattern across the target, the image is transformed into a series of video signals. The actual operation depends on the type of tube used in the system. Vidicon tubes are commonly used in space remote sensing since their dwell time is long enough to allow the scanning of the target. The vidicon tube, Fig. 2.8, has a photoconductive target onto which the image formed by the optical lens of the camera is focussed. The conductance of successive points on the target varies with the intensities of the light rays forming the image of the scene. A beam generated by the electron gun then sweeps the photoconductive layer in a raster pattern generating an electric current proportional to the target conductance and hence to the light intensities in the scene. This current flows to the signal electrode and from there the data may either be transferred and stored on magnetic tape or transmitted directly to the ground.

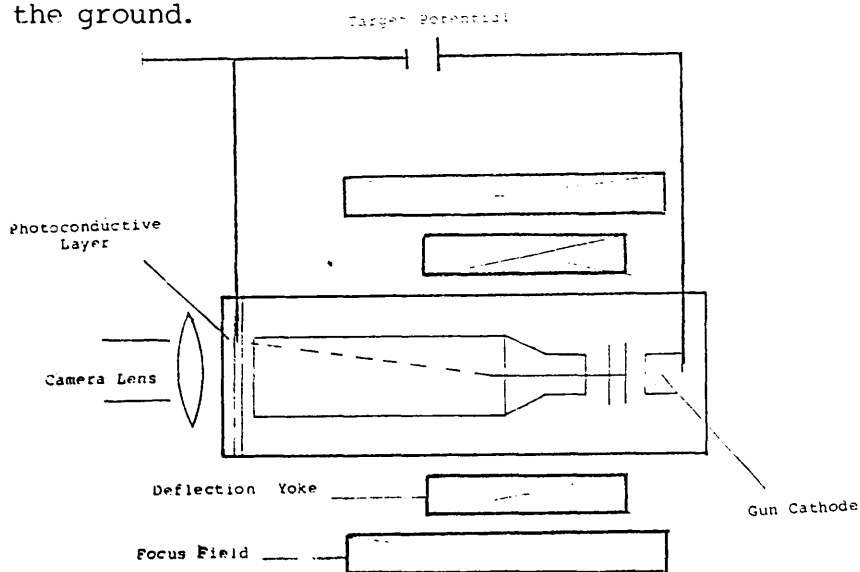


Fig.2.8 Vidicon Tube.

Return Beam Vidicon (RBV) tubes are relatively high resolution

vidicon tubes. The photoconductive layer allows the focussed image to be stored for a relatively long period (more than 0.1 second), thus allowing shuttered operation of the camera. The conductance of the layer again varies with the intensities of light in the image. An electron beam generated by the electron gun then sweeps the photoconductive layer in a raster pattern and is being reflected continuously from the photoconductor and returned to the aperture of an electron multiplier. The signal being output from the multiplier is then passed to an analogue-to-digital convertor to allow it to be stored on tape. This type of tube generally has a higher signal-to-noise ratio and better resolution than the vidicon. Television cameras having this particular type of vidicon tube have been carried on board the first three satellites of the Landsat series and will be discussed in detail in Chapter 8.

2.3.3 **Electro-Optical Sensor Systems**

As the name implies, electro-optical sensors operate in the optical region and utilize solid state detectors instead of the photographic films used in the photographic cameras systems or the video-based technology of the television cameras. Optical mechanical line scanners and solid state array systems are examples of sensors falling into this category. The heart of an electro-optical sensor is its electronic radiation detectors. Two types of electronic detectors are normally distinguished - thermal detectors and quantum detectors.

(a) Thermal detectors rely on the temperature increase which occurs in certain heat sensitive materials as a result of radiation absorption, which in turn produces electrically monitorable variations in the material properties of the detector. The sensitivity of thermal detectors to electromagnetic radiation tends to be low and the response time, i.e. the elapsed time from the moment the radiation is focussed on the detector to the moment a signal output is produced, is long.

(b) Quantum detectors are those in which the incident photon of radiation interacts directly with the electronic energy levels within the detector material to produce free charge carriers. The advantage of these detectors is that they are very sensitive to radiation and individual photons produce a significant response within a short time. They can be classified further into photoemissive and photoconductive detectors and photodiodes.

(i) In the photoemissive detectors such as photomultipliers, the incident photons excite electrons within the photosensitive

materials in such a manner that they are emitted through the surface barrier. So they are inherently limited in response to those spectral regions where the individual photon energies are sufficient to overcome the binding energies of the electrons in the photosensitive material.

(ii) In photoconductive detectors, an incident photon with energies greater than the energy gap of the material produces free charge carriers which cause the resistance of the material to vary inversely with the number of incident photons.

(iii) In photodiodes, the sensitive material contains a p-n junction which modifies its electrical properties proportionally to the incident radiation flux striking the junction. The effect of the incident radiation can therefore be monitored and expressed either as a photovoltage value or as a photoconduction value. The p-n junction has a highly conductive p-region with mobile positive charges (electron-holes) and a highly conductive n-region with free negative charges (electrons). At the interface between the two regions, free positive charges in the p-region diffuse into the n-region where they annihilate the free electrons, leaving behind fixed ions. These ions create an electric field between the two regions forming the depletion region. This depletion region acts as the insulator of a capacitor since it is surrounded by two highly conductive regions, Fig. 2.9a.

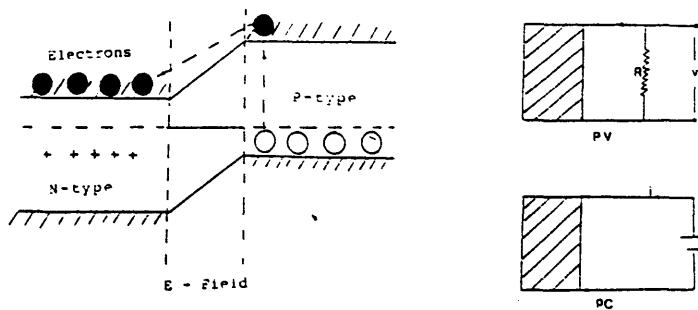


Fig. 2.9 Principle of Photodiodes.

When a radiation flux strikes the p-region of the junction and if that radiation is of a sufficient energy to raise electrons from inner levels of the material in the p-region into the conduction bands, extra electron-holes will be created through freeing these electrons. If the freed electrons diffuse

into the depletion region, the electric field will accelerate it across to be deposited into the n-region. In the photovoltaic mode, the electron deposition can be monitored as a voltage across a load resistance. In the photoconductive mode, an external voltage is applied to the diode in the same direction as the internal field, hence increasing the depletion region. This increases the probability that the electron-holes will be produced in the depletion region with faster effects on the external circuit of the photodiode (Fig. 2.9b). The change in the electric field which occurs in the photovoltaic mode doesn't occur in the photoconductive mode since, once the charges cross the depletion region, equilibrium is established by a current flow in the external circuit of the photodiode.

2.3.3.1 Optical Mechanical Line Scanners

The principle and construction of optical mechanical line scanners is shown in Fig. 2.10. The mirror oscillates or rotates to scan the Earth's surface in a series of relatively very narrow strips in the direction transverse to the flight direction. The image is continuously built up from these narrow strips as the platform moves forward in its line of flight. The radiation received from the Earth's surface is focussed onto the sensitive area of the detector.

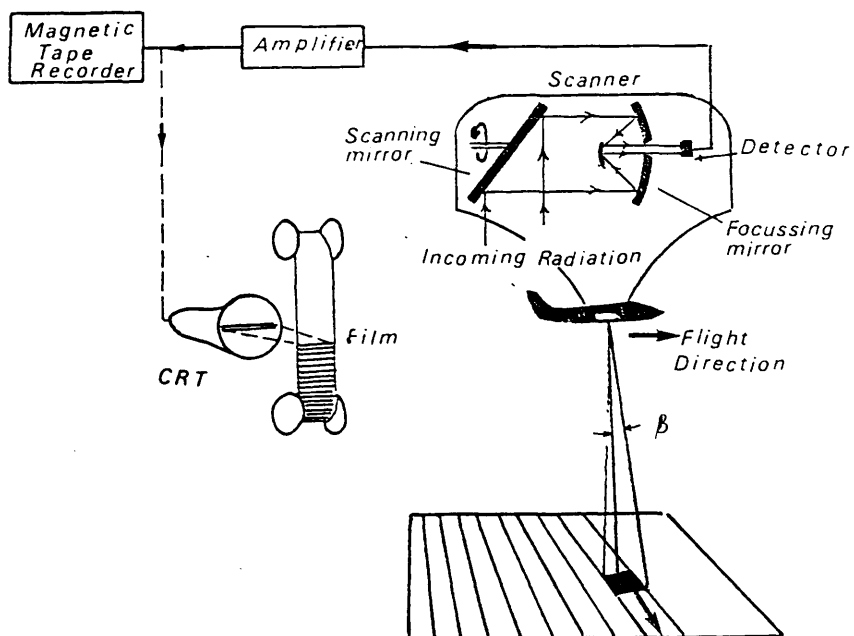


Fig. 2.10 Principle of Optical-mechanical Scanners.

The size of the detector and the rate at which the signal of the detector signal is sampled, together with the flight altitude, determine the specific ground area element detected at any particular moment (Fig.2.10). This small ground area element is known as the scanner's Instantaneous Field Of View (IFOV). The intensity of the output electrical (video) signal of the detector is proportional to the amount of the received radiation. This signal is then passed to the analogue-to-digital convertor to be encoded and is then telemetered to the receiving ground station or recorded using an on-board video or digital tape recorder. The recorded tapes may later be recovered or replayed and the data transmitted to the ground.

Examples of spaceborne optical mechanical line scanners are the Very High Resolution Radiometers (VHRR) on board the National Oceanic and Atmospheric Administration (NOAA) weather satellites which operate in the $\lambda=10.5$ to $12.5 \mu\text{m}$ band of the thermal infrared region, and those carried on the Heat Capacity Mapping Mission (HCMM) which operated in the visible and near infrared ($\lambda = 0.5$ to $1.1 \mu\text{m}$) and in the thermal infrared ($\lambda=10.5$ to $12.5 \mu\text{m}$) parts of the spectrum respectively.

2.3.3.2 The Multispectral Line Scanner

The multispectral line scanner is an optical mechanical line scanner in which multiple detectors (each of which is sensitive to a single specified spectral band) are used to image the same ground scene in different spectral bands. Fig. 2.11 shows the principle of the scanning operation, which is similar to that of the optical mechanical scanner discussed in Section 2.3.3.1, and the array of detectors of the multispectral line scanner.

The radiation from the scene is separated into discrete wavelengths bands by a grating and spectral filters and the radiation from each band is directed onto the specific detector sensitive to this radiation. The output signal from each detector is then encoded and telemetered to the ground receiving station or recorded on a multitrack tape on board the platform. Examples of spaceborne multispectral scanners are the Multi-Spectral Scanner (MSS) series which have been carried onboard the first five satellites of the Landsat series and the Thematic Mapper (TM) used on Landsats 4 and 5. A more detailed discussion of these two sensors will be given in Chapter 4.

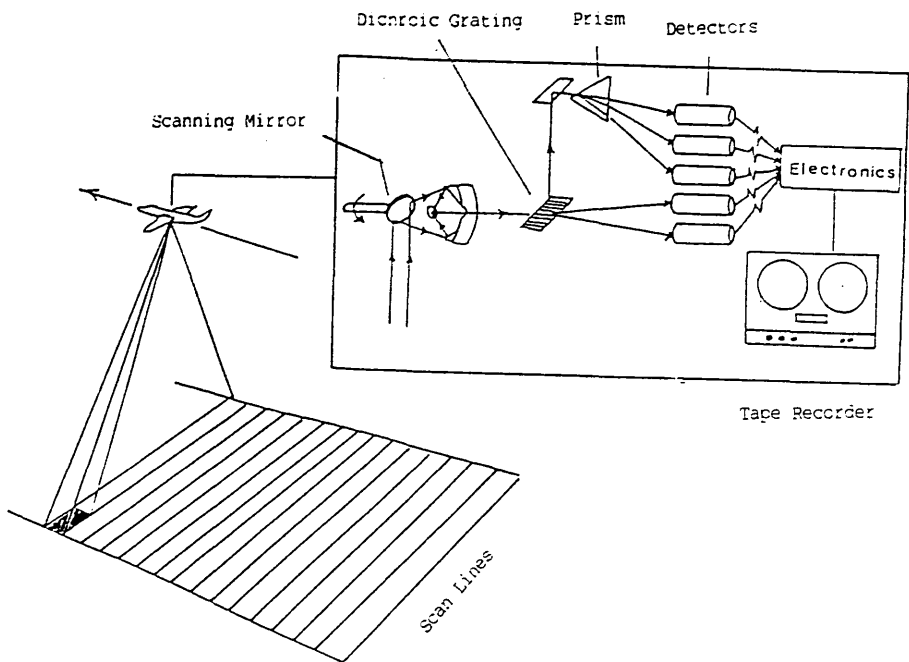


Fig. 2.11 Principle of Multispectral Line Scanners.

2.3.3.3 Solid State Array Based Systems

These are the systems which employ either linear or areal arrays of solid state detectors. Most of solid state array systems employ Charge Coupled Devices (CCD) as detectors. A CCD in its elementary form consists of closely spaced Metal Oxide Semiconductor (MOS) capacitors formed by depositing metal electrodes or gates over an oxidized silicon substrate. The MOS and the silicon substrate are pulsed into deep depletion forming potential pockets at the interface. The incident photons liberate charge-carriers (electrons) from the atoms of the substrate or the deposited MOS as explained in the photodiode detectors above. These electrons are stored in the depletion pockets and when an electrical input signal is applied, they are transferred serially to the output element. Again CCDs are available which use one or other of two modes of operation - the photoconductive (PC) and photovoltaic (PV) modes. In the PV mode, a power source is connected to a load resistance and to the detectors so that any variation in the charge carrier electron concentration produces a variation in voltage across the load resistor. In the PC mode, a p-n junction separates the charge carriers of opposite sign produced by the incident photons so that, as in the case of photoconductive diodes, no power source is required.

(1) Linear Array Systems

Instead of imaging very narrow strips of the ground by the mechanical scanning of the optical viewing system of a sensor pixel by pixel as in the optical mechanical scanners, a whole linear strip of the terrain can be imaged simultaneously by using a linear array of detectors arranged in the cross-track direction, see Fig. 2.12. Each detector in the array receives radiation from a corresponding ground element (pixel). The ground coverage is produced in the normal way of scanning by the forward motion of the platform but, in this case, in the manner of a pushbroom. The HRV scanner used in the French SPOT satellite and the German MOMS device mounted on the SPAS platform deployed from the American Space Shuttle are two examples of these systems.

Compared with the optical mechanical scanners, imaging devices employing solid state linear arrays produce images of far better geometric quality since there are no moving parts. Furthermore, linear array systems are lighter in weight, more compact, and consume less power (Petrie, 1985).

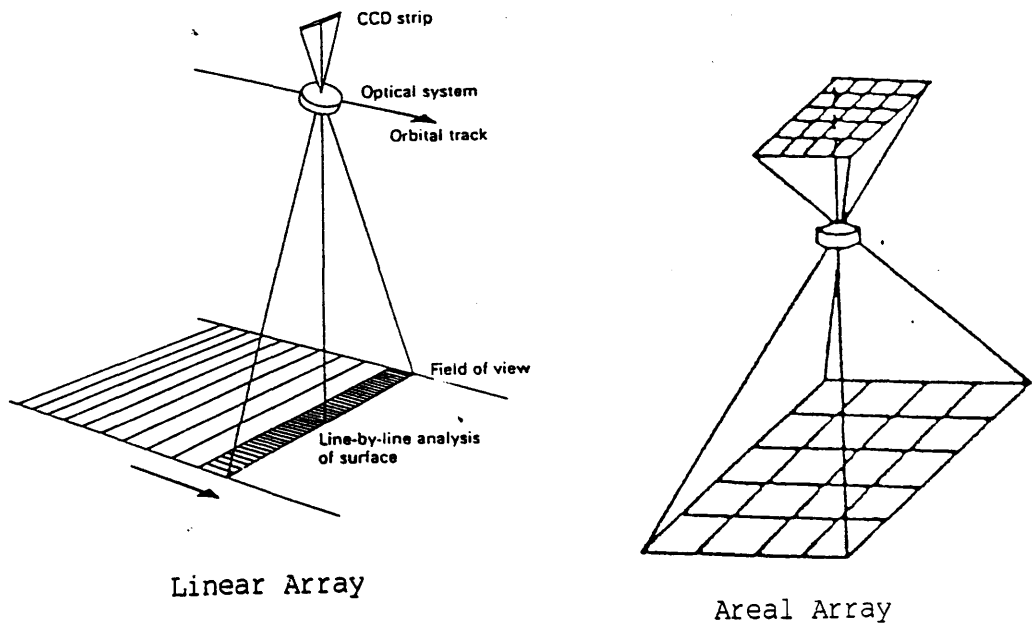


Fig. 2.12 Principle of Array Sensors.

(2) **Areal Array Systems**

In these systems, the solid state detectors are arranged in a matrix so that the whole field of view is imaged simultaneously to produce a synoptic view of the Earth's surface. Geometrically speaking, the image which is produced is similar to that produced by a photographic frame camera. The signal from each individual detector is then encoded serially and transmitted. This type of sensor is sometimes known as solid state framing camera or a staring device as opposed to a scanning device. The solid state framing camera on the UOSAT (OSCAR-9) satellite manufactured by GEC in the U.K. is one example of this type of sensor. It uses a 288x385 areal array of Charged Coupled Devices (CCDs). Still higher resolution CCD areal arrays of 800x800 and 1125x1125 have been developed for high definition television (HDTV).

Sensors employing solid state areal arrays may be expected to produce images of very high geometric fidelity. Since the object is imaged instantaneously, all those types of distortions associated with the mechanical scanning process within individual scan lines will be eliminated.

2.3.3.4 **Microwave Imaging Radars**

In general, microwave sensors have the advantage of being capable of producing images of the Earth in all weather conditions and by day and night. Passive microwave radiometers are scanners which have been developed to produce images of the terrain using the Earth's emitted radiation at microwave lengths, but in practice have been little used. By contrast, microwave imaging radars are active devices in which the ground is illuminated by a beam or a pulse generated by a source mounted in an aircraft or spacecraft.

Radar (Radio Detecting and Ranging) was originally developed as a means of using microwaves to detect the presence of moving objects (aircraft, ships, etc) and to determine their positions for military purposes. Their principle of operation entails transmitting short bursts of microwave energy from a ground station in the direction of interest and recording the strength of reflections received from the objects lying within a narrow field in that specific direction. Different types of airborne radar were then developed for various applications such as Doppler radar for position fixing and monitoring moving objects, B-scan radar which is fixed on the nose of military planes for detecting flying objects within the field of view ahead, etc.

However in the context of mapping, which is the principal concern of this investigation, imaging radars are those of most interest. Imaging radars have evolved from the Plan Position Indicator (PPI) type of radar which was originally developed for air navigation purposes. In the PPI, a rotating antenna is made to scan the area of the Earth's surface located directly underneath the platform using circular scans (Fig. 2.13). However the resulting image is very distorted and too poor to be considered for mapping (Ali, 1982). For better image quality and less distorted imagery, the Side Looking Radar (SLR) was developed.

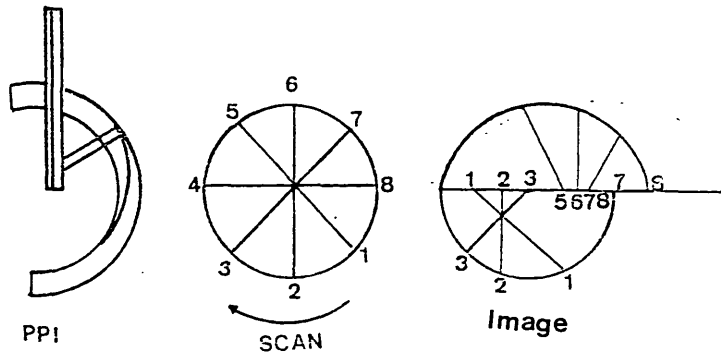


Fig. 2.13 Principle of PPI Radar.

In the SLR, a rectilinear antenna, Fig. 2.14, is fixed parallel to the longitudinal axis of the platform and made to emit microwave energy towards the ground to one side away from the flight line. The main elements of an SLR are:

- i) A high powered transmitter which produces short bursts of electric energy at a fixed frequency;
- ii) an antenna consisting of a dipole and a reflector. The reflector is in the form of a parabolic cylinder with its long diameter in the along-track direction. Therefore, the antenna transmits a fan shaped beam of energy towards the ground and receives the returning reflections. A transmitting-receiving multiplexer or switch connects the antenna alternately to the transmitter and the receiver;
- iii) The receiver which picks up the reflected signals from the ground detected by the antenna and amplifies them before passing the result to a display or recording unit.

When the transmitted burst, or pulse, hits the Earth's surface, as

shown in Fig. 2.14, a series of reflections are generated sequentially off successive terrain objects. These reflections reach the antenna in a form of stream of pulses in time sequence according to the slant distances of the reflecting objects from the antenna. This stream of pulses is picked up by the receiver, amplified, and transformed into a series of electric signals, the intensities of which are proportional to those of the received pulses. These electric signals, together with the electronically measured time, may be used to control the brightness and position of the flying spot of a cathode ray tube (CRT) so creating an image of the line on the face of the tube. A continuous strip image is built up from the individual imaged narrow strips of the terrain as the platform moves forward.

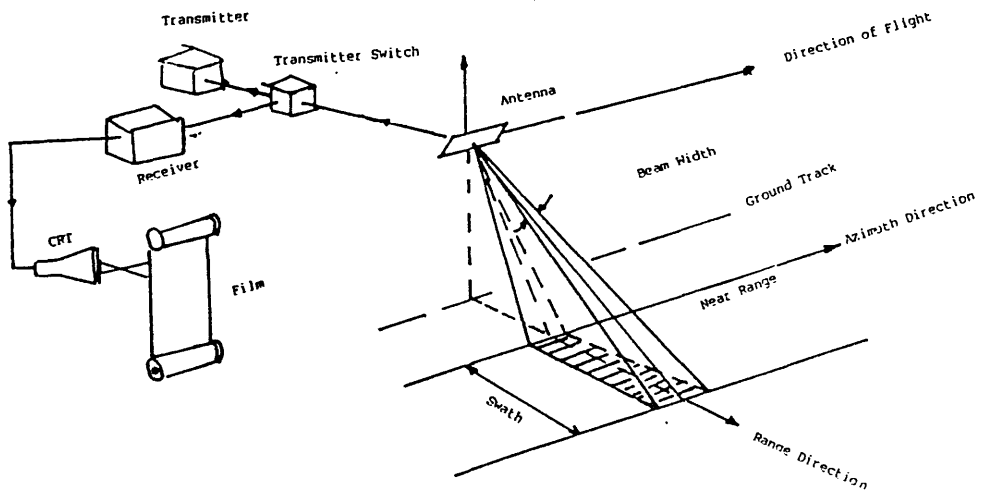


Fig. 2.14 Real Aperture SLR.

In the context of mapping, system ground resolution is an important factor. Ground resolution can be defined as the smallest terrain object which is discernible in the image or the smallest distance between two terrain objects that is required for these objects to be imaged by the imaging system as separate objects. In SLR images, the resolution in the range (cross-track) direction is different to that in the azimuth (along-track) direction. Range resolution is dependent on the pulse duration, so that the shorter the pulse duration, the better the resolution, but short pulse duration results in little transmitted energy and hence, weak returns and consequently diminished image content. On the other hand, azimuthal resolution depends on the wavelength of the transmitted energy and the length of the antenna (aperture). To improve the range resolution, microwave energy

comprising short wavelengths and/or a long antenna should be used. However, short wave length microwave energy is susceptible to atmospheric attenuation and back scatter.

Originally SLRs were of the real aperture type in which the radar aperture is determined by the physical length of the antenna. But the physical length of antenna is limited by the practical problem as to what can be carried on the aircraft and the effect that it has on the aircraft's aerodynamics. This physical limitation left no room for an improvement of the resolution of images acquired with real aperture radar (Ali, 1982; Chen, 1985; Lillesand & Kiefer, 1987). These limitations, coupled with the demands of high resolution radar imagery, led to the development of Side-looking Synthetic Aperture Radar (SAR).

The idea of SAR is based on the fact that, when an object is linearly traversed by a radar beam, a one-to one correspondence exists between the along-track coordinate and the instantaneous Doppler shift of the radar signal after being reflected by the object. This fact was first noticed by Wiley of the Goodyear Aircraft Corporation (now the Goodyear Aerospace Corporation) in the early fifties (Sherwin et al, 1962; Brown and Porcello, 1969; Ali, 1982). A SAR set transmits a series of coherent microwave pulses, each one of which, upon striking the Earth's surface, results in a series of reflections from terrain objects in a direction transverse to the direction of the platform motion. Each reflected signal is received back and compared with the coherent reference wave of a stable oscillator. Frequency shifts are determined for each reflection. These shifts determine the position of the reflecting object relative to the platform at each moment during the period in which that object falls within the beam width. SAR therefore differs from real aperture radar in that it uses a method of signal processing of the reflected microwave pulses to achieve fine azimuth resolution. The effect of this processing is that effectively it synthesizes a very long antenna. Fig. 2.15 depicts the process of synthesizing this long antenna. Acquiring SAR data requires rather complex integrated navigational and control systems on board the platform.

The basic concept of recording SAR data is to measure the amplitude and the frequency of the signal generated by comparing the returned signals with the reference signal for each object and recording these values on a magnetic tape or on photographic film. Conversion of these recorded data to an image form involves very complex equipment and processing operations.

Because of the large ranges over which images have to be acquired, only SARs are of practical value in space remote sensing within the context of this investigation. A SAR system was carried on board Seasat launched on 26th of June 1978 and more recently two SAR systems have been flown in two separate Shuttle missions on experimental basis designated Shuttle Imaging Radar A and B (SIR-A, SIR-B).

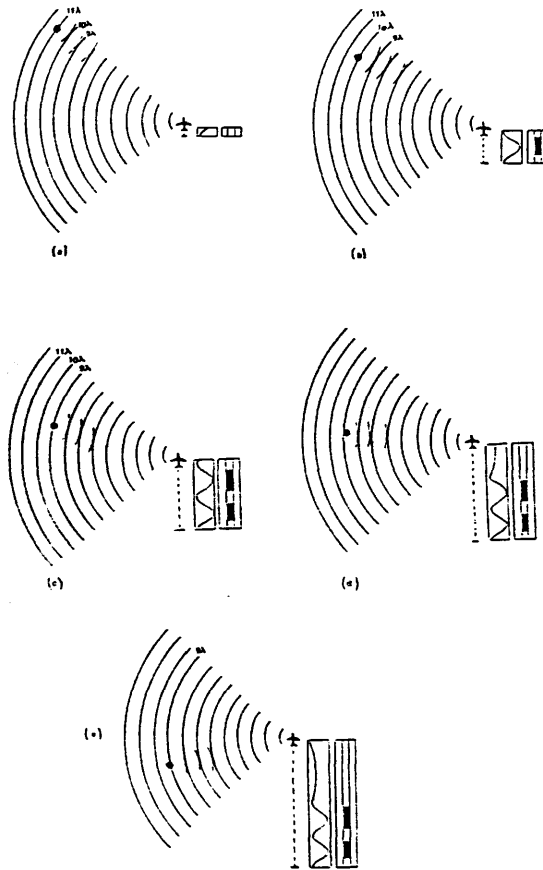


Fig. 2.15 Principle of SAR System.

From the review of imaging technology contained in Section 2.3, it is obvious that numerous imaging systems exist which can be used for the acquisition of images of the Earth from satellites and considered for mapping applications. This is the field of enquiry of the author's research project. However, due to the lack of availability of microwave imagery over the Sudan, the project has of necessity been slightly restricted to cover optical systems only - though, as has been shown, this still covers a large number of devices or systems.

2.4 Launched Space Sensor Systems

Over 2,000 satellites and spacecraft have been launched since the launch of the Russian Sputnik in 1957. These include planetary observation, scientific, telecommunication, navigation, weather, military intelligence and civilian Earth observation satellites. However for Earth's surface mapping only the weather, military and civilian Earth observation satellites are of interest. The great majority of this group comprise weather satellites on which sensors having ground resolution of the order of kilometres are normally operated. Since for the application of space imageries to topographic mapping and most Earth resource monitoring and mapping, the ground resolution of the acquiring sensor should be less than 100 m, weather satellites have no role to play in this particular context. This leaves the small number of military and civilian Earth observation satellites and spacecraft to be considered. Information about the military intelligence satellites as well as their imageries has not been made available to civilian users, so that only the civilian Earth observation satellites and spacecraft are of interest in this investigation.

Several civilian space Earth Observation systems have been launched since 1970. Some of these systems have been flown for several days to provide limited coverage of the Earth's surface on experimental missions, while others have been flown to provide repetitive data for the duration of their operational life which may be a period of several years. Some satellites or manned spacecraft have contained several imaging sensors; others have only had a single sensor mounted on-board. Certain sensors have been mounted in manned spacecraft and the images recovered together with the crew. Other sensors have been mounted in dedicated unmanned satellites and the resulting images telemetered to ground receiving stations.

The exciting experience of observing the Earth from space was initiated by the manned space programmes of the 1960s (Mercury, Gemini and Apollo). The photographs of the Earth's surface taken by the crews during the Mercury and Gemini missions were the first to demonstrate to civilian users the feasibility of space imagery. Mission GT-4 in the Gemini series included the first formal photographic experiment which resulted in the acquisition of 39 near-vertical overlapping photographs of the south-western U.S.A, Northern Mexico and other areas of North America, Africa and Asia for geological purposes (NASA, 1967a; NASA, 1967b; NASA, 1968; Doyle, 1970; Lowman, 1969; Doyle, 1975; ASP, 1980). With the success of this experiment, subsequent missions included a

number of similar experiments concerned with the observation of various geographic phenomena. Many of these missions, especially these undertaken with manned spacecraft, have resulted in large numbers of photographs being acquired using hand held cameras. Interesting and valuable though these are, they have not been taken in a manner which allows them to be used for systematic mapping. More significant in the mapping context are the Apollo, Soyuz, Landsat, Skylab, Seasat, Space Shuttle and Spot satellite programmes in which specially designed or configured mapping systems have been orbited. These Earth observation space systems will be discussed in chronological order in the following paragraphs.

2.4.1 Apollo Earth Orbiting Systems

The Apollo programme was initiated by the U.S National Aeronautics and Space Agency (NASA) in the 1960s with the landing of a man on the Moon and his safe return to Earth as the primary objective. During this programme, several preliminary flights were made over the Earth to determine and demonstrate the possibility of fulfilling this objective. In the context of the topographic mapping of the Earth's surface, certain of the Apollo Earth-orbiting flights (Apollo 6 & 9) which were made prior to the lunar orbiting and landings are of special interest. Apollo 6 carried a Hasselblad 500 EL camera. The camera was bracket-mounted in the hatch window of the command module. Several strips of near-vertical photographs were acquired across North America, the Atlantic and West Africa and were used by many scientists for geologic, hydrographic and geographic interpretation investigations (Wobber, 1970; Doyle, 1975).

In Apollo 9, the first experiment was conducted to acquire multi-spectral photography of the Earth's surface. A battery of four 70 mm Hasselblad cameras, which were electrically driven and triggered to ensure synchronization, were used in this experiment. Three of these cameras carried black-and-white films which were appropriately filtered to produce photographs in the green, red and near IR parts of the spectrum while the fourth exposed false colour IR film. Some 140 sets of photographs were thus obtained covering parts of the South-western, South-central and South-eastern U.S.A as well as parts of Mexico and the Caribbean-Atlantic area which were again used by scientists in various fields. Since the photoscales of Apollo photographs have been in the region of 1:2,000,000 and smaller, the main cartographic products have been very small-scale mosaics, photomaps and thematic maps (Thrower, 1970; Petrie, 1974).

In 1975, the joint American-Russian Apollo-Soyuz Test Project (ASiP) was carried out in which an Apollo spacecraft joined up with a Russian Soyuz spacecraft orbiting the Earth. During this project, hand-held 35 mm Nikon and 70 mm Hasselblad cameras were used to photograph areas which were selected on the basis of their interest to specialists in the fields of geology, desert studies, oceanography and meteorology. Another 70 mm Hasselblad camera with an f=60 mm or 100 mm lens was used to acquire 60% overlapping photographs. This camera was bracket-mounted in the spacecraft window. However the quality of these photographs was not as good as these of the previous missions. Again these photographs were used for various scientific investigations, particularly geologic investigations. Very-small scale mosaics and photomaps were also made from these photographs for parts of the U.S.A (Doyle, 1975; El-Baz, 1977).

2.4.2 Soyuz Earth Orbiting Systems

The Soyuz satellite series which has been gradually developed by the U.S.S.R since the 1960s have carried several remote sensing devices. Although details are lacking, it is believed that most were photographic cameras whose films are recovered together with the cosmonauts returning from Soyuz missions. The best known in this series are Soyuz 9 and 22. Photographs from Soyuz 9 were used for the production of photomaps of the Caspian Sea area. Soyuz 22 carried a Zeiss Jena MKF-6 six-channel multispectral camera. The MKF-6 consists of a basic body carrying six f=125 mm lenses each with its colour filter and shutter assembly. Attached to this basic body are six film magazines corresponding to the six lens assemblies. The basic body of the MKF-6 on board Soyuz 22 was mounted on a swivel-frame to facilitate the rocking of the camera during the time of exposure to ensure image motion compensation. The photo-format of the MKF-6 is 55x 81 mm. The MKF-6 camera was mounted such that the long side was perpendicular to the direction of flight. From the altitude of 256 km at which Soyuz was flown, this gave a ground coverage of 117x170 km per photograph. Although the photo-scale was very small, the high resolving power of the camera resulted in very good quality photographs which were used for geological mapping and vegetation studies (Herda, 1978; Zickler, 1978; Konecny, 1980; Curran, 1985).

2.4.3 Landsat Sensor Systems

Landsat programme was initiated with the launch of Landsat-1 in 1972. The sensor systems in the satellites launched in this programme to date include: (i) an RBV system; (ii) a Multispectral Scanner (MSS)

system; and (iii) a Thematic Mapper (TM) system.

Each of the first generation of these satellites comprising Landsats -1, -2, and -3 was launched into a Sun synchronous, near polar orbit at an altitude of approximately 919 km. The orbital inclination was about 99° to the Equator so as to achieve coverage of most of the Earth's surface while the orbital period was such as to ensure that the angle between the Sun, the Earth's centre and the satellite was maintained at 37.5° to give repeatable solar illumination conditions. This was done to help in the comparison of images of the same scene acquired at different dates for the monitoring of changes in vegetation, land use, etc and to facilitate the mosaicing of images from adjacent tracks. The satellites crossed the Equator every 103 minutes. The Earth rotates a distance of 2,760 km at the Equator during this period so the following satellite track was situated at this distance to the west of the previous one when it crossed the Equator. Each satellite completed 14 orbits in 24 hours after which the next orbit was flown adjacent to the first orbit from the previous day, see Fig. 2.16.

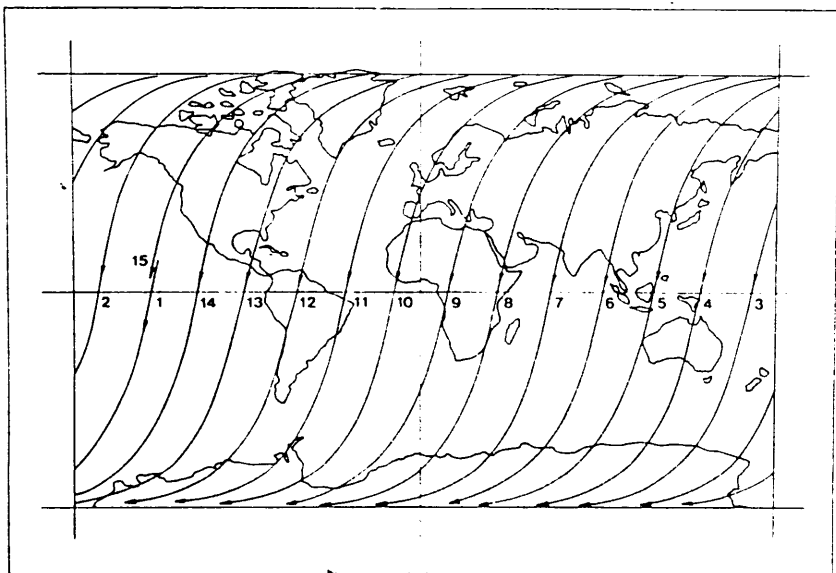


Fig. 2.16 Landsat-1, 2 & 3 Orbital Tracks.

Entire coverage of the Earth would have been obtained in 18 days if the weather was cloud free. Landsat-1 was operated between 23rd of July 1972 and 6th of January 1978; while Landsat-2 operated over the period between 22nd of January 1975 and 25th of February 1982. Both of these satellites carried an identical payload consisting of a 4-channel multispectral scanner (MSS) and three boresighted RBV television cameras. Landsat-3 operated over the period between 5th March 1978 and

31st March 1983. It carried a 5-channel multispectral scanner (MSS) equipped with an additional channel operated for thermal infrared sensing and two high resolution RBV television cameras (instead of three) arranged in such a way that they acquired adjacent ground scenes. Table 2.1 gives the band assignment, scene format, and ground resolution for these sensors. The geometric aspects of these MSS and the RBV systems will be discussed later in more detail in Chapters 4 & 5; and Chapters 8 & 9 respectively.

The data acquired by these sensors were either transmitted directly to a receiving station when the satellite was within the range of that ground station or stored on tape recorders for later transmission to data centres in the U.S.A. Fig. 2.17 shows the locations of operational Landsat ground receiving stations throughout the world.

Satellite Sensor	Landsat-1 and -2	Landsat-3
RBV	<p>Three RBV multispectral cameras (80 m ground pixel size)</p> <p>Band 1: $\lambda=0.475 - 0.575 \mu\text{m}$ (blue-green) Band 2: $\lambda=0.580 - 0.680 \mu\text{m}$ (yellow-red) Band 3: $\lambda=0.690 - 0.830 \mu\text{m}$ (red-near IR)</p>	<p>Two RBV single band cameras (30 m ground pixel size)</p> <p>$\lambda=0.505 - 0.750 \mu\text{m}$ (visible to near IR)</p>
MSS	<p>4- Channel MSS scanner (80 m ground pixel size)</p> <p>Band 4: $\lambda=0.50 - 0.60 \mu\text{m}$ (green) Band 5: $\lambda=0.60 - 0.70 \mu\text{m}$ (red) Band 6: $\lambda=0.70 - 0.80 \mu\text{m}$ (red-near IR) Band 7: $\lambda=0.80 - 1.10 \mu\text{m}$ (Near IR)</p>	<p>5-Channel MSS scanner (80 m ground pixel size)</p> <p>Band 1: $\lambda=0.50 - 0.60 \mu\text{m}$ Band 2: $\lambda=0.60 - 0.70 \mu\text{m}$ Band 3: $\lambda=0.70 - 0.80 \mu\text{m}$ Band 4: $\lambda=0.80 - 1.10 \mu\text{m}$</p> <p>(120 m ground pixel size) Band 5 $\lambda=10.40-12.50 \mu\text{m}$ (Thermal IR)</p>

Table 2.1 Band Assignments in Landsat-1, 2 & 3 Sensors.

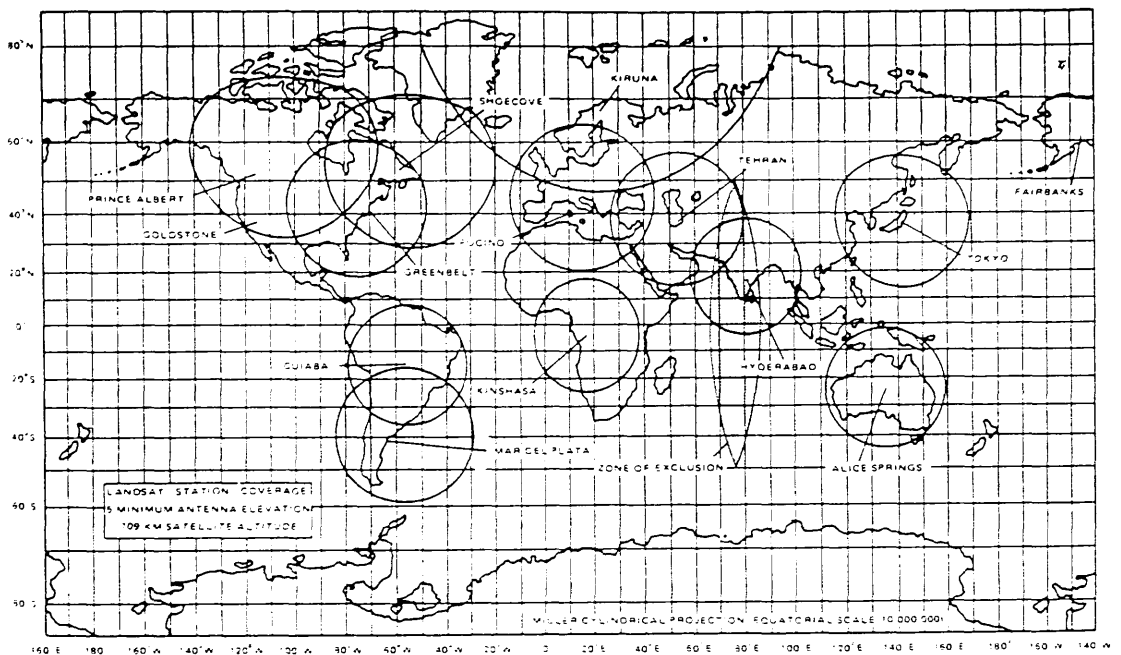


Fig. 2.17 Landsat Ground Receiving Stations.

The second generation of Landsat series was initiated on 16th July 1982 with the launch of Landsat-4 in a near polar, Sun synchronous orbit, at an altitude of 705 km and an inclination of 98.2° . The orbital period of the satellite is 99 minutes to provide coverage of the entire Earth between 81° N and 81° S latitudes in 16 days. In each orbital track the satellite crosses the Equator at 9.45 local time. The effects of the satellite being orbited at 200 km lower than the previous Landsats are that:

- (i) a wider angle of view is used to provide the 185 km cross-track swath;
- (ii) the total Earth coverage is provided in 233 ground tracks (14 tracks per day) with adjacent tracks being separated by a 7-day period instead of being acquired on successive days as in the previous Landsats;
- (iii) successive tracks are separated by 2,752 km at the Equator; and
- (iv) that the adjacent tracks overlap by about 7.6% at the Equator.

The satellite carried a 4-channel multispectral scanner (MSS) identical to those carried on board the first three satellites to provide a continuation of the MSS data acquisition. It also carried the Thematic Mapper (TM), which is a 7-channel multispectral scanner of a different design to that of the MSS. Table 2.2 lists the wavelengths covered by each of the bands and their respective ground resolutions for the TM.

Wavelength Bands (um)	Ground Pixel Size (m)
Band 1 $\lambda = 0.45 - 0.52$	30
Band 2 $\lambda = 0.52 - 0.60$	30
Band 3 $\lambda = 0.63 - 0.69$	30
Band 4 $\lambda = 0.76 - 0.90$	30
Band 5 $\lambda = 1.55 - 1.75$	30
Band 6 $\lambda = 10.40 - 12.50$	120
Band 7 $\lambda = 2.08 - 2.35$	30

Table 2.2 TM Wave Bands and their Respective Pixel Sizes.

Landsat-5, carrying identical sensors was launched on 1st March 1984 in an orbit having the same specification, but at an eight days phase to that of Landsat-4 such that the two satellites together cover the Earth every 8 days. For both satellites, the time interval between adjacent tracks is seven days - see Fig. 2.18. The MSS and TM are aligned so that they scan the same 185 km wide ground swath directly below the orbital path with a sidelap between the scenes from adjacent orbits ranging from 7.3% at the Equator to 84% at 80° N or S.

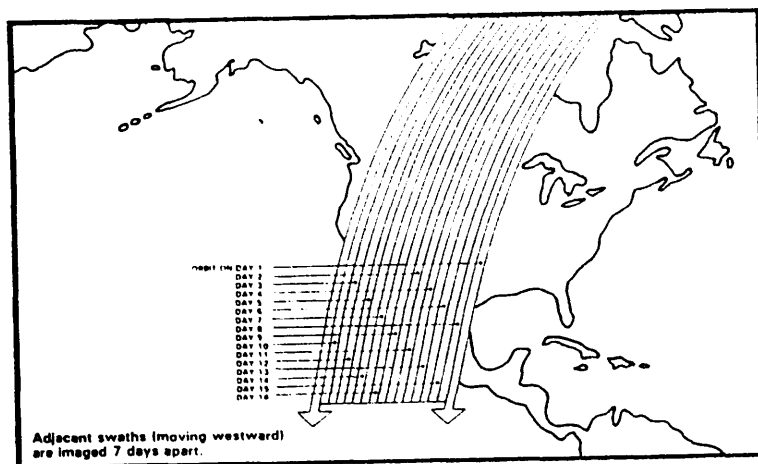


Fig. 2.18 Landsat-4 & 5 Orbital Tracks.

Landsats -4 and -5 were designed to use a communication system called the Tracking and Data Relay Satellite System (TDRSS) for transmitting the acquired image data, tracking data and ground commands to and from the ground stations. TDRSS consists of two communication satellites in geosynchronous orbit and a centralized ground receiving station located at White Sands, New Mexico. The first TDRSS satellite (TDRS-East) was put into orbit on 17th April 1983 using NASA's Space Shuttle Challenger (Mission STS-6), and was positioned over the Equator at 41° west longitude at an altitude of 35,890 km. The second TDRS satellite (TDRS-West) was lost when the Space Shuttle Challenger was destroyed in the Shuttle disaster in February 1986. TDRS-East itself later failed, so the TDRSS system, which was designed to eliminate the frequent failures experienced with the tape recorders on board the first three Landsats, hasn't had the chance to demonstrate its capabilities. A more detailed description of the TM sensor and its geometric characteristics is given in Chapter 4.

2.4.4 Skylab Sensor Systems

The search for a space imaging system that could provide images suitable for small-scale topographic mapping was begun by NASA with the launch of Skylab on May 14, 1973. Skylab was put into a circular orbit at 435 km above the Earth and, among many other scientific experiments, six remote sensing systems were carried on board forming the Earth Resources Experiment Package (EREP). Three of these systems were imaging sensors and therefore they are of interest in the context of this investigation. These are:

- i) the S-190A multi-spectral photographic camera system;
- ii) the S-190B Earth Terrain Camera (ETC); and
- iii) the S-192 Conical Multispectral Scanner.

The S-190 A and B cameras were the photographic components of EREP. The S-190A system consisted of six Itek 70 mm film cameras, each with its own optical system having a $f=6$ in. (152 mm) lens, shutter assembly and film transport assembly, mounted on a common mount and synchronised to give six photos of the same ground scene at 1:2,850,000 scale over the spectral range $\lambda=0.4$ to $0.9 \mu\text{m}$ with 38 to 79 m ground resolution depending on the altitude of the satellite at exposure. Its objective was to photograph various parts of Earth's surface in

different spectral bands to test space photography for various remote sensing applications.

The S-190B camera built by Actron Industries was a modified Hycon KA-74 reconnaissance camera equipped with a bidirectional focal plane shutter and vacuum film flattening. IMC was achieved by rocking the entire camera in its mount during exposure. The camera was equipped with an $f=18$ in. (460 mm), $f/4$ lens having a maximum radial distortion of 10 μm . Negative images of 11.5x11.5 cm format were exposed giving a ground resolution of 17 to 30 m depending on the satellite altitude. Discussion of the results achieved by various investigators using the photographs obtained by these cameras will be given in Chapter 11.

The S-192 multispectral scanner collected imagery of the Earth using a rotating mirror equipped with a conical scan. A spherical mirror was the major element of a folded reflecting telescope which had a 17 inch aperture. The electromagnetic energy received from the scene simultaneously irradiated thirteen imaging detectors, each responding to a specific wavelength band. Data from this scanner consisted of computer compatible tapes of raw or calibrated data with ancillary information such as tape format descriptions, calibration data, time, and spacecraft attitude. S-192 images were used mainly for interpretative and quantitative studies in various scientific fields (NASA, 1974; Curran, 1985).

2.4.5 **Seasat - SAR System**

Seasat was launched on June 26, 1978 to observe the Earth's oceans by means of several sensors designed to monitor surface winds, waves and temperature. In the context of this present investigation into mapping, the primary interest in Seasat must be in its Synthetic Aperture Radar (SAR). This was used primarily to image ocean waves, sea ice and coastlines but also obtained images of several land areas and as a result could be used for mapping experiments. Seasat was launched in a near polar orbit at an altitude of 800 km. The satellite orbit was designed to provide optimum coverage of oceans, but its tracks did cross land areas, thereby offering the opportunity to acquire 25 m resolution radar imagery of Earth's land surface. The Seasat SAR generated imagery across a 100 km swath at a distance of 230 to 330 km to one side of the satellite track. It only operated for 98 days but during this period, about 500 passes were acquired. Seasat SAR data could be acquired only when the satellite was within the sight of the five ground receiving stations located in California, Alaska, Florida, Newfoundland, and Britain. Thus the land areas covered are all in the

Northern Hemisphere including these parts of North America and Western Europe which lay within the range of the five ground stations.

2.4.6 Space Shuttle Sensor Systems

The Space Shuttle was conceived and operated by NASA as a re-usable space transporter which could place experimental scientific satellites and operational communication, navigation and remote sensing satellites in orbit. In the context of topographic mapping, the following imaging systems launched by the Shuttle are of great interest:

(i) Shuttle Imaging Radars (SIR)

Two experimental imaging radars were launched on board the NASA's Space Shuttle Challenger to continue the series of radar experiments which began with the launch of SAR on board Seasat as described above. SIR-A was launched on 12th, November 1981 in an orbit inclined approximately 40° to the Equator and at an altitude of 245 km to obtain images of areas that are difficult to obtain due to constant cloud cover or dense forests or both. SIR-A is a SAR which differs from the Seasat SAR in that its antenna is made to illuminate the ground at a larger look angle - 47° to 53° compared with the 20° to 26° of the Seasat SAR. The acquired data were recorded on-board the Shuttle on an optical tape recorder. SIR-A obtained imagery over about 10 million sq. km of the Earth's surface during the 8 hours of its operation. It acquired imagery over a number of tropical, arid and mountainous regions which were imaged for the first time (Taranik & Thome, 1980; ASP, 1980; Lillesand & Kiefer, 1987; Campbell, 1987).

SIR-B was orbited on the Space Shuttle Mission STS-41G which was launched on 5th October, 1984. It was operated over a period of 8 days. The principal difference between the SIR-A and SIR-B systems was that the latter was equipped with an antenna that could be tilted mechanically to illuminate the Earth's surface at varying look angles (between 15° and 60°). This was done to study the effect of different illumination geometries on the data to allow decisions to be made about the design of future space imaging radar systems. SIR-B was equipped with a digital data handling subsystem (DDHS) in addition to the usual optical recorder. The DDHS was designed to allow the digital data to be relayed to the ground receiving stations using the TDRSS system. Due to the failure of the TDRS-East and the loss of the TDRS-West, the digital data received from the DDHS covered only about 6 million sq. km. However, the optical recorder capacity was

enough to store the data during the days of operation. Like Seasat, both SIR-A and SIR-B were operated in the L-band ($\lambda=23$ cm) of the microwave spectrum (Taranik & Thome, 1980; ASP, 1980; Lillesand & Kiefer, 1987; Campbell, 1987; Wise & Trinder, 1987).

(ii) **The Metric Camera (MC)**

The Metric Camera (MC) is a modified Zeiss Oberkochen RMK 30/23 camera which was sponsored by the German Aerospace Research Establishment (DFVLR) and flown as part of the European Space Agency (ESA) Spacelab-1 experiment on board the Space Shuttle Mission STS-9. With a lens of focal length of 305.128 mm and an orbital altitude of 250 km, the MC acquired photographs at 1:820,000 scale. The 23 cm x23 cm format yielded ground coverage of 189x189 sq. km per frame.

(iii) **Large Format Camera (LFC)**

LFC is a 23 cm x46 cm. format photographic camera built by Itek Optical Systems under contract to Johnson Space Center (JSC). LFC was flown on board the Space Shuttle mission STS-41G. At the orbital altitude of 250 km and using the same focal length of 305.0 mm, the photo-scale is again 1:820,000, but the ground coverage per frame is 189x378 sq. km arising from the enlarged format of 23x46 cm. The additional benefit of the large format is that stereomodels with larger base:height ratio can be formed compared with these resulting from the use of the 23 cm x 23 cm format. Both systems are described in detail in Chapter 10.

(iv) **Modular Opto-electronic Multispectral Scanner (MOMS)**

MOMS is a two channel pushbroom scanner, using a CCD linear array, each detector having a pixel size of 16 μ m x 16 μ m and operating in the visible and near infrared region of the spectrum. MOMS was developed by the German Messerschmitt-Bolkow-Blohm (MBB) company as a series of experimental sensors sponsored by the West German government. The first instrument in this series to be used in space (MOMS-1) was flown on an experimental basis in two of the Space Shuttle missions. The first of these missions took place in June 1983 during Shuttle Mission STS-7, while the second took place nearly 7 months later in February 1984 during Mission STS-11/41-B. The specification of MOMS is given in Table 2.3. The MOMS system will be discussed in more detail in Chapters 6 & 7.

Sensor:	Reticon CCPD 1728
CCDs/line	4
Pixel Size	16 μ m x 16 μ m
Ground Pixels/line	6912
Channel 1	$\lambda = .575 - .625 \mu$ m
Channel 2	$\lambda = .825 - .975 \mu$ m
Ground Pixel Size	20 m from 300 km altitude
Total Field of View	26.2 $^{\circ}$
Swath Width	138 km

Table 2.3 Specifications of MOMS-1.

2.4.7 The "Systeme Probatoire d'Observation de la Terre" (SPOT)

SPOT is a space imaging system which has been conceived and designed by the French Centre National d'Etudes Spatiales (CNES). The SPOT satellite consists of two parts: the SPOT "bus", a standard multipurpose platform, and a payload. The various subsystems of the SPOT bus perform the essential functions of power supply, orbit control, and data transmission. SPOT-1 was launched by Ariane-1 on 22nd February 1986 into a Sun-synchronous, near polar (98.77 $^{\circ}$ inclination) orbit at an altitude of 818.269 km. It crosses the Equator going from north to south at about 10:30 am local solar time. Complete coverage of the Earth is produced in 26 days.

Its payload consists of two identical High Resolution Visible (HRV) imaging instruments, two magnetic-tape data recorders and a telemetry transmitter. The HRV is a pushbroom type scanner which uses linear arrays of CCDs to image individual lines of the ground simultaneously. The HRV sensor is designed to operate either in a panchromatic mode over a broad waveband ($\lambda=0.51$ to 0.73μ m) or in a multispectral mode on three narrow wavebands ($\lambda=0.50 - 0.59 \mu$ m, $0.61 - 0.68 \mu$ m, and $0.79 - 0.89 \mu$ m respectively). The light rays from the ground scene which is being imaged enter the HRV via a plane mirror that is steerable by ground control to view ground scenes on either side of the ground track through an angle relative to the vertical up to 27 $^{\circ}$ in 45 steps of 0.6 $^{\circ}$ each. This capability allows off-nadir viewing in addition to the nadir i.e. vertical viewing (Fig. 2.19) which makes it possible to acquire stereoscopic imagery with a large

base to height ratio. SPOT will be described and discussed in some detail in Chapters 6 and 7.

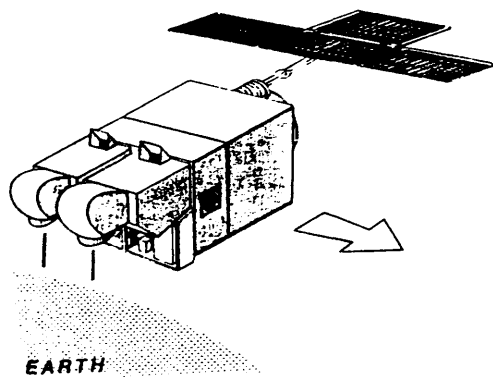


Fig. 2.19a SPOT-1 Satellite System.

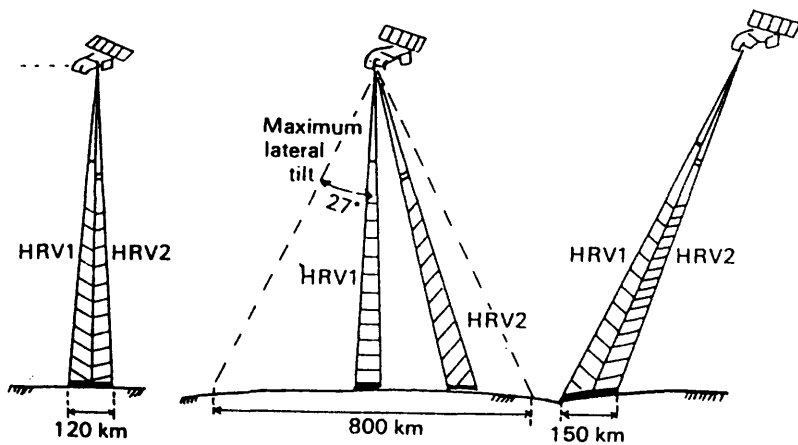


Fig. 2.19b SPOT-1 Stereoscopic Viewing Capability.

2.5 **Summary**

In the above account, the basic physics and theoretical aspects of remote sensing have been explained in general terms and the various types of imaging sensors have been reviewed and described. This was followed by a survey of Earth observation satellites and spacecraft systems. In the next Chapter, topographic mapping specifications concerning map accuracy and information content will be discussed together with the realization of these specifications using photogrammetric methods. Finally, descriptions of (i) the test areas which have been selected for the tests carried out in this investigation; (ii) the topographic maps covering these test areas; and (iii) the analytical instruments used in the tests will be given.

CHAPTER 3

Map Specifications, Test Areas and Photogrammetric Instrumentation

3.1 Introduction

Having reviewed the possible space imaging systems which can be considered for topographic mapping operations in Chapter 2, it is vital next to consider the main criteria which govern such mapping - especially those concerned with the content, completeness and accuracy of topographic mapping. In this investigation, the completeness and the accuracy of the planimetric and height information which can be extracted photogrammetrically from space images are of prime interest. Thus the realization of topographic map content and accuracy specifications through photogrammetric operations will be discussed in some detail to help later to analyze the results of the various interpretational and geometrical (planimetric and planimetric/height) tests which have been carried out to assess their suitability for this purpose. This is followed by a description of the areas selected for the tests and the analytical photogrammetric instruments used in the tests.

3.2 Topographic Mapping Considerations

The content and the accuracy standards specified for topographic mapping vary from one country to another but almost invariably they are stated in terms: (a) of the percentage completeness of the content and (b) of the degree of departure of the points shown on the map from their correct positions. The principal concerns of a topographic map specification include:

- (i) the specification of the content of the map, including the individual features to be included and how they are to be depicted, and the specific contour interval to be used in the sheet or series;
- (ii) the completeness of the map detail which determines whether any feature or detail defined in the specification has been omitted or missed or whether the map content is complete;
- (iii) the positional (planimetric) accuracy of the detail shown in the map; and

(iv) the height (vertical) accuracy both in terms of spot heights and contours.

3.2.1 **Specification and Completeness of Map Detail**

The completeness of the factual information or content addresses both the question of the content of the map and the correctness of the description of the features existing in the area which is covered by the map. This is usually verified by a field check of the plotted map before its final publication. Topographic features which are usually shown in medium- and small-scale maps, include among many others:

(i) cultural features such as roads, railway lines, ferry terminals, power and communication lines, bridges and dams, buildings, parks and sport fields;

(ii) land forms such as hills, sand dunes, valleys, marshes, etc;

(iii) water bodies such as seas, rivers, lakes, reservoirs, creeks and ditches; and

(iv) vegetated areas such as woods, forests, pasture, areas of bush, etc. and agricultural areas which include big irrigated schemes, rain-fed cultivated areas, private farms and gardens.

The extraction of these features from space imagery depends to a considerable extent on the ground resolution of this imagery expressed in metres per line pair for photographic systems, or in metres per pixel for electro-optical systems or radars. However, no matter which value is selected for the ground resolution of the imaging system, some details which are required to be included in the maps, will be too fine to be discerned on the images. The size of discernible features on a particular image depends on the resolution and hence on the scale of the image. In very general terms, as the image scale becomes smaller, as is the case in high altitude space imagery, the requirement for high resolving power increases. If the 0.1 mm figure, which is widely accepted as the finest detail that can be plotted on the map, is considered, it can provide an estimation for the scales of maps that can be produced from certain imagery by computing the scale at which the ground resolution of the imagery is represented by 0.1 mm.

However the interpretability of the topographic features on a particular space image will vary from one part of the country to another. This is so since urban areas, rural areas and uncultivated areas each have different types of buildings, road patterns, etc. Even if the buildings have the same size and shape, the context in which they occur may be a critical matter. An individual building may be extremely important in a remote area and would need to be detected and mapped accurately, whereas in an urban area it would not be marked individually but simply be part of a large agglomeration such as a built-up area. In general, the most critical matters are the detection and interpretation of fine cultural features and the internal detail of settlements. It has been estimated that to extract these features from monoscopic space imagery for mapping at 1:50,000 and 1:100,000 scales, the ground pixel sizes required are 3 m and 7 m respectively (Doyle, 1975; Konecny et al., 1982). For the stereoscopic extraction of these features for mapping at the same scales, the ground pixel sizes required are 6 m and 14 m respectively. Therefore the values of ground resolution required for 1:50,000 scale topographic mapping from space using photographic systems are 8 m and 17 m respectively for the monoscopic and stereoscopic utilization of the photographs. The corresponding ground resolution values required for mapping at 1:100,000 scale are 20 m and 40 m respectively.

In general, the percentage of map information which can be extracted from a particular type of image determines the suitability of that image for topographic mapping. This suitability is determined through interpretation tests in which all features which are shown on an existing map of the test area at a particular scale are listed and classified. Then a comprehensive search for these features is conducted on the image covering the test area. The percentage of features which can be detected and identified is then calculated. If this percentage is more than 75% and preferably higher (say 85% to 90%), one can say that topographic mapping can be carried out using this type of image with the rest of the features supplemented by other methods - particularly through field completion by a topographer or surveyor using the photogrammetric plot as a base.

3.2.2 Planimetric Accuracy Specification

The planimetric accuracy of a topographic map is best evaluated by finding the errors at a number of individual well-defined points whose positional coordinates are known accurately (say from a large scale map) and then judging the result against a standard specification set by the mapping authorities of the country for which the map is being

produced. Several attempts had been made by various American mapping agencies to draw up standard map accuracy specifications which led finally to the specification of the U.S. National Map Accuracy Standards (NMAS) (Marsden, 1960). Thus in the course of this debate, the American Society of Photogrammetry (ASP) recommended that, for topographic maps prepared by photogrammetric methods, the planimetric accuracy should be such that 95% of all well-defined detail be within 0.5 mm of their correct positions at the publication scale. However the U.S.G.S recommended that 90% (instead of 95%) of well-defined points should be within 0.5 mm from their correct positions at the publication scale. The Federal Board of Surveys and Maps (FBSM) recommended two classes of accuracy:

(i) Class A in which 90% of well-defined cultural and drainage features should be plotted within 0.6 mm of their correct positions at publication scale; and

(ii) Class B in which 90% of the well-defined points should be plotted within 1.0 mm of their correct positions at publication scale.

Applying the usual statistical methods at the 90% confidence level, the adoption of the above two limits meant that the planimetric standard error (m_{p1}) in Class A should be less than or equal to ± 0.4 mm, while that in Class B should be ± 0.6 mm.

From these various recommendations, the NMAS accuracy specifications were developed. These specifications require that for maps at 1:20,000 scale or larger, 90 per cent of the planimetric details present on the map (omitting those details which are unavoidably displaced by exaggerated symbols) should lie within 0.5 mm of their true planimetric positions (Petrie, 1974; 1978; 1985). Applying the usual statistical methods, at the 90% confidence level, this is equivalent to a standard error (m_{p1}) of ± 0.3 mm. This planimetric accuracy specification has been adopted by NATO and many other countries. However, for many developing countries, the specification recommended by the FBSM for Class B maps is quite enough. Applying the specification to each of the various map scales required by the national mapping agency gives the planimetric accuracy requirement (tolerance) for each map scale in ground terms.

3.2.3 Contour Interval and Accuracy Specifications

Relief is most often represented on topographic maps by contours

supplemented by spot heights. The basic requirements of relief representation by contours call for the specification of contour interval (C.I) as well as the contour (m_c) or spot height accuracy (m_h).

3.2.3.1 Contour Interval

The contour interval adopted for a specific map scale not only varies from one country to another but may also vary from one area to another within a single country, depending on the character of the terrain. One of the ideas of expressing the C.I by a formula that takes into consideration map scale and the type of the terrain is that suggested by Imhof (1965) as:

$$C.I = n \cdot \log n \cdot \tan \alpha \quad \dots\dots\dots(3.1)$$

where $n = \sqrt{S_m/100 + 1}$

α =slope angle of the terrain; e.g. $\alpha=45^\circ$ represents highly mountainous terrain; $\alpha=26^\circ$ for medium mountainous terrain; and $\alpha=9^\circ$ for relatively flat terrain.

S_m = map-scale number.

In a paper based on a UN (1983) study about the practice of selecting contour intervals in topographic mapping, Ghosh (1987) studied the frequency of the contour intervals used in world mapping and concluded that the most used contour intervals at each of the commonly used map scales are as given in Table 3.1.

Map-scale	Contour Interval (m)
1:5,000	2, 5
1:10,000	2, 5, 10
1:20,000	5, 10
1:50,000	10, 20, 40
1:100,000	20, 50

Table 3.1 Most Used Contour Intervals.

For the 1:100,000 scale, a contour interval of 50 m may be considered for hilly areas while the contour interval of 20 m is for terrain with gentle slopes. In developing countries, the selection of countour intervals of 30 m instead of 20 m for flat areas and of 60 m

instead of 50 m for hilly areas in 1:100,000 scale maps may be quite satisfactory and, given the size of unmapped areas, saves a lot of effort and money.

3.2.3.2 Contour and Spot Height Accuracy

The specification of contour accuracy also varies from one country to another. In the U.S.A, the NMAS states that "not more than 10% of the elevations tested shall be in error by more than one-half the contour interval. In checking elevations taken from the map, the apparent vertical error may be decreased by assuming a horizontal displacement within the permissible horizontal error for a map of that scale" (Marsden, 1960). This means that 90% of elevations either read for points along contour lines or interpolated from the contours should lie within half the contour interval of their true elevations. This is equivalent to a standard error (m_h) of $\pm 0.3 \times C.I.$

European height accuracy standards have generally been based on a concise statement of the permissible vertical error and the allowable horizontal shift, expressed in a single formula. This statement based on the suggestions of Karl Koppe (Singels, 1968) who first noticed the high correlation between height error and terrain gradient and used a simple empirical law for expressing the height error. According to Koppe, the height accuracy is given by:

$$m_c = A + B \cdot \tan \alpha \quad \dots\dots\dots(3.2)$$

where A = allowable standard error in flat terrain (m_h);
 B = the planimetric (drafting) standard error of the contour (m_{pl}); and
 α = Angle of slope.

The North Atlantic Treaty Organization (NATO) (Singels, 1968) has adopted a system of categorizing maps into two classes according to the reliability of their contour information. The contour accuracies are specified such that the standard error value specified for a Class I map at a specific map scale is also considered as the standard error value acceptable for Class II map at the immediately larger scale, e.g. the standard error value specified for a Class I map at 1:50,000 scale is equal to that specified for Class II map at 1:25,000 scale. According to this scheme, the accuracy specifications for maps at 1:50,000 scale are $(6+15\tan \alpha)$ and $(12+30\tan \alpha)$ for Classes I and II respectively. The height accuracy specifications for maps at 1:100,000 scale are $(12+30\tan \alpha)$ & $(24+60\tan \alpha)$ for Class I and Class II

respectively.

For the spot heights included in a topographic map, the accuracy required is usually about one-fifth to one-eighth of the required contour interval (Tham,1968). So for a map at the map scale which requires contours to be plotted at a contour interval of 30 m, the accuracy of the spot heights shown on the same map is required to be within the range ± 6 m to ± 4 m.

A number of different methods have been used to test and determine the actual accuracy of contours on maps. The resulting accuracy statements may be expressed in terms of the positional reliability of the contour lines, or as the correctness of the heights read from them. Most of these evaluation methods are discussed in Ackermann (1978), Thompson (1979) and Imhof (1965). In practice, the contour accuracy testing of a map is done by establishing a number of discrete points spread in a regular manner over the map and then interpolating the height values at these points from the contour lines. These interpolated values are compared with the "true" height values of these points and the result is judged against the official specification.

3.2.3.3 Overall Requirements for Topographic Mapping at Small Scales

The overall requirements for topographic mapping at small scales are summarized by Doyle (1984) and given in Table 3.2 which lists the contour interval (C.I); the contour accuracy (m_c) requirement (as defined above); the planimetric accuracy (m_{pl}) requirement; the spot height measurement accuracy (m_h) requirement (again as defined above); and the ground resolution (G.R) required at each specific scale within the range of the small and medium scale topographic maps that might be expected to be compiled from space imagery. However, as noted above, the contour intervals used at each particular map scale may vary from one country to another depending on the terrain, degree of development, etc.

Scale No.	C.I m	m_c m	m_{pl} m	m_h m	Gr. Resolution	
					m/lp	m/pixel
500,000	50	17.0	150	15	71	29
250,000	25	8.5	75	8	36	14
100,000	20	6.8	30	6	14	6
50,000	10	3.0	15	3	7	3

Table 3.2 Overall Requirements for Small Scales Map and Photomap Production (Doyle,1984).

3.3 Photogrammetric Considerations in Mapping

Photogrammetry is capable of providing the topographic data in any one of three forms:

(i) In graphical form in the familiar shape of the topographic map with lines, symbols and so on to represent planimetric detail. The height and relief forms of the terrain are represented by spot heights and contours.

(ii) In photographic form as orthophotographs or orthophotomaps. The orthophotograph is a correctly-scaled photographic image from which all relief and displacements have been removed, while the orthophotomap is an orthophotograph which has been enhanced by the addition of symbols, lines, colour, text, etc. Contours are also included in most orthophotomaps.

(iii) In digital form giving the X, Y, Z coordinates of all measured data together with header codes and attribute data which describe the type of feature which has been measured and interpreted. Additionally height information can be provided in the form of a digital terrain model, contours or digital terrain profiles.

Turning from the specifications for topographic mapping to the main factors which concern those responsible for the actual execution of the mapping using photogrammetric methods, there are quite a number of considerations which determine the applicability and suitability of remotely sensed images to topographic mapping. Among these interrelated factors, the photographic scale and ground resolution, the geometrical quality of the imagery and the monoscopic or stereoscopic measuring capability are major concerns.

3.3.1 Image Scale and Ground Resolution

The ground resolution may be defined as the minimum size for an object to be shown on a specific image. To a considerable extent, this defines the amount of topographic detail which can be extracted from the image of the terrain and also has its impact on the accuracy of measurements. The scale of an image acquired from a specific satellite altitude depends on the equivalent focal length of the sensor, while the ground resolution in that image depends both on the image

scale and the resolving power of the sensor system. In the case of electro-optical sensors and radars, the ground resolution is determined by the finite size of the IFOV and the rate at which the detectors are sampled. The IFOV itself is determined by the detector "aperture" size. In photographic systems, three parameters determine the resolving power of the whole system and hence the ground resolution of the acquired photographs. These are the resolving power of the lens; the resolving power of the film and the degree to which image motion is present. To obtain fine ground resolution with the enormously increased altitudes of satellites, two approaches seem to be possible.

(i) Since the ground resolution depends partly on image scale, an improvement can be achieved by increasing the focal length in proportion to the increase in the satellite altitude. But with the increase in the focal length and a given image format, the field angle will be reduced which results in a small base:height ratio which will give rise to difficulties in the 3D mensuration of these images. With the increased scale and ground resolution derived from the use of the larger focal length lens, the exposure time should be brief to avoid the effects of image motion or else the ground resolution will deteriorate and the improvement gained by the use of the long focal length lens will be lost. With brief exposure times, the energy admitted through the lens might not be sufficient to result in the desired good quality photographs.

(ii) With the focal length being kept constant, the ground resolution can be improved by improving the resolving power of the system either by making better lenses or using slower fine-grained films or by a combination of both. Improving the resolving power of the lens calls for a wider aperture to admit sufficient energy during the brief exposure time and to narrow the normal field angles since the resolution tends to fall away from the optical axis.

However this brings its own set of difficulties. A wide aperture of $f/4$ with a long focal length of say $f=60$ cm, means that the dimension (diameter) of each lens element is 15 cm ($60/4$) which results in problems of manufacture, assembly, weight and expense. This may be compared with $f/4$ for a standard $f=15$ cm lens used in a wide angle aerial survey camera which gives a diameter of 3.75 cm. On the other hand, the use of slower films requiring a long exposure time, calls for a very efficient FMC mechanism to prevent the deterioration of the resolution by image

motion. For a long time most photogrammetrists did not realize that this alternative solution was viable. The Americans were the first to realize that through the use of fine grained film in cameras equipped with FMC, the resolution will shoot up to above 100 lp/mm (Brock, 1976). Hence the ground resolution will be much better than that in photographs having the same scale which are acquired by cameras with no FMC which cannot utilize such films. As will be discussed in more detail later, this was demonstrated clearly by the photographs taken by the LFC which compensates for the forward motion by moving the film in the direction of image motion. Although these photographs have the same scale as that of the photographs acquired by the MC with no FMC, their ground resolution is incomparably better as will be shown in Chapter 12. These experiences have in fact led to the widespread adoption of FMC mechanisms in the most recent designs of aerial survey cameras e.g. the Zeiss Jena LMK, the Wild RC20 and the Zeiss Oberkochen RMK 23/30, the last of which is planned to be orbited in the next Spacelab mission. The inclusion of an FMC mechanism allows the use of a wide spectrum of films to achieve fine ground resolution and to satisfy various mapping objectives.

In general, a balanced combination of these two approaches is the practical and certain solution to this problem. In the LFC, the combination of moderately long focal length and the use of slow films with FMC proved to be more effective than the use of the same long focal length with faster films with no FMC from the same altitude. Fig. 3.1 gives the scales and ground resolution of imagery taken by systems having different focal lengths from various satellite altitudes. It is clear that the systems which have short focal lengths and wide angle coverage have little applicability since the extremely small scale gives rise to difficulties in identifying detail and therefore very little information can be extracted from them. As the scales get smaller, the ground resolution of a particular system becomes coarser by the same proportion. However it can also be seen that, for a given focal length and orbital altitude giving the same scale, the ground resolution can be greatly increased through the application of the measures (FMC and slow, fine grained film) discussed above.

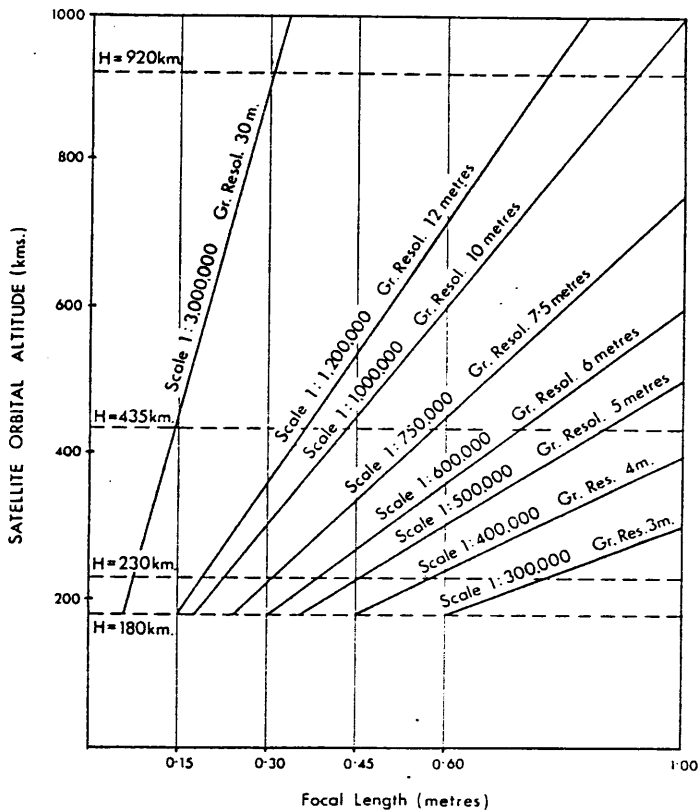


Fig. 3.1 Scale and Ground Resolution of Space Images.
(for Camera/Film Resolution of 100 lp/mm)

3.3.2 Geometrical Quality

The geometrical quality addresses the question of the stability of the internal geometry of the sensor and the occurrence, the magnitude and the pattern of geometric distortions inherent in the image. As mentioned previously in Chapter 2, a mapping camera has a superior geometrical stability and the resulting photographic images are based on the relatively simple geometry of a central projection. The inherent distortions of the image due to the optical lens can easily be compensated for, once they have been determined by calibration. Furthermore the image displacements present in these photographs due to tilt and relief can be compensated for relatively easily.

On the other hand, scanner imageries have complex geometry since they are formed through the process of scanning the Earth's surface in both directions (along-track and cross-track) in the case of optical mechanical scanners and in the along-track direction as in the case of linear array scanners. Thus the optical imaging elements are in motion

throughout the scanning process. Furthermore, since the exposure of the image is a sequential procedure which proceeds either pixel by pixel or line by line, the image is subjected to the additional displacements produced by changes in the orientation of the sensor during exposure in a manner which does not occur with a camera where the whole frame image is exposed simultaneously. The calibration of scanners is notoriously difficult and often unsatisfactory. Nevertheless both optical and digital rectification methods have been developed to eliminate the distortions and displacements inherent in these scanner images. The geometrical quality of the final result can be judged by the accuracy to which the content of this image can be transformed into a map projection system or by how accurately the ground coordinates of a set of points can be determined from this image.

Another related factor which may affect the contribution of space images to topographic mapping is the accuracy of the satellite tracking and the position, height and attitude determination systems used with a particular satellite. This may sometimes become very important for mapping inaccessible and developing regions of the world which do not have basic survey or maps, and where ground control points are not available for the transformation and rectification of the images.

3.3.3 Stereoscopic Measurement

Photogrammetric methods of map making are based on the use of stereoscopic images, especially if heights and contours have to be determined. Some of the sensor systems in this investigation lack the capability of acquiring overlapping stereoscopic images. This is because topographic mapping was not one of their mission objectives and so the systems were not designed to satisfy the requirements of stereo-photogrammetry. Relief displacements in these monoscopic images can however be eliminated especially when digital terrain model data are available from another source.

Many different and sometimes conflicting considerations regarding the stereoscopic use of space images in topographic mapping need to be taken into account in trying to assess the most suitable system for acquiring these images. However these considerations are largely related to the scale and the ground resolution of the imagery on the one hand and the stereoscopic geometry, especially the base:height (B:H) ratio, on the other. These are especially important given the situation that space imagery is taken from a minimum altitude of 180 km and often from much greater altitudes.

Both the scale (f/H) and the base:height ratio (B/H) are taken into account in the formula which relates the stereoscopic measurement of parallax (dp) in the stereo-model to the difference in height (Δh) in the terrain:

$$\Delta h = \frac{H}{f} \cdot \frac{H}{B} \cdot dp \dots\dots\dots (3.3)$$

where f is the focal length;
 H is the orbital altitude; and
 B is the base.

It is clear from equation (3.3) that, for a given photographic scale, large base:height ratios are desirable to achieve good heighting accuracy. This requirement appears to contradict that for large image scale and high ground resolution. Thus with a super-wide-angle camera which gives large base:height ratios, the resulting scales of space photography are too small to be useful. By contrast, with narrow-angle vertical photography, while the scale and resolution may be adequate, the resulting base:height ratio is too small to permit useful height and contour measurements to be made. Therefore if a standard-format narrow-angle camera is to be used for stereoscopic photography, a suitable base:height ratio may be obtained from convergent photographs. However the use of such photographs gives rise to many special difficulties both of a geometric nature and due to the differing scales and convergencies which exist on each of the photographs making up a stereopair. However, as will be seen later, it has proved to be possible to combine an increased angular coverage and a better base:height ratio with a useful scale and ground resolution by increasing the image format- as has been done with the NASA Large Format Camera (LFC). The larger side of the format in this camera was oriented in the direction of the flight such that stereo-models with base:height (B:H) ratios up to 1.2 can be formed by a suitable selection of the photographs making up the model from the same orbit track.

The accuracy of measuring spot heights on photographic images in a high precision stereoplotter using good quality imagery is usually from 1:5,000 (0.2%o) H to 1:15,000 (0.067%o) H, where H is the flying altitude (Petrie 1974; 1984). From practical experience, the minimum contour interval possible is assessed at 3.3x these values (Petrie, 1974), thus giving a minimum interval of 0.6%o H or 0.2%o H for the above height measuring accuracy values. The minimum contour intervals

for orbital altitudes are shown in Fig. 3.2. Contour intervals of 36 m or 40 m will result for the minimum orbital altitude (180 km.) taking 0.2‰ H as the possible contour interval. Comparing the values of Fig. 3.2 with those given for contour intervals in Table 3.2 shows clearly that there is potentially a large shortfall in the conventional photogrammetric contouring possible from orbital imagery.

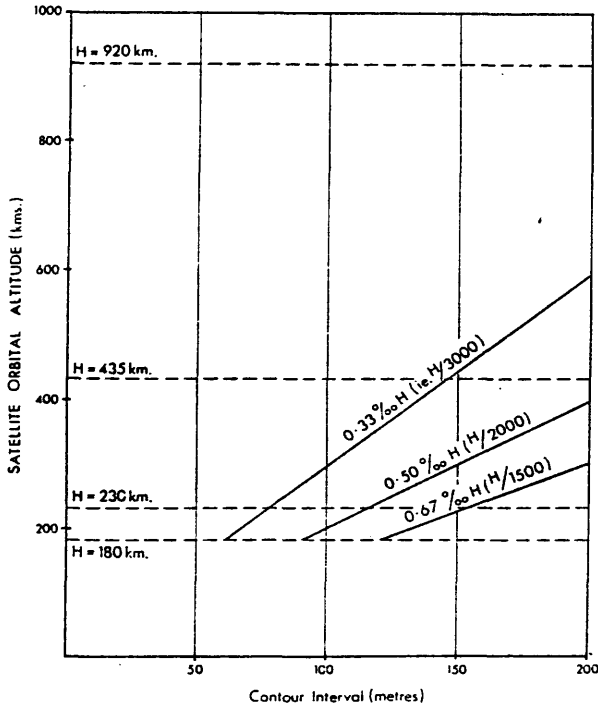


Fig. 3.2 Height Accuracy and Contour Interval.

In general, the fulfilment of the accuracy specification in the small scale topographic maps which are compiled photogrammetrically from space imagery, in particular that for planimetric accuracy, is much easier than the fulfilment of the specification of map content and completeness. As discussed above, there is a reasonable possibility for an Earth-orbiting remote sensing system, which has Earth resources observation or topographic mapping as an objective, to provide images which satisfy the accuracy specification for medium- to small-scale topographic mapping. On the other hand, whether the ground resolution needed to image the fine cultural detail required to be shown on these maps is feasible or not is a question which still remains to be answered. Several recent space imaging systems (MC, LFC, TM, SPOT and MOMS) can be considered to be steps forward in the direction of fulfilling this resolution requirement. To what extent each of these systems has indeed achieved this aim is the subject of the series of interpretation tests carried out in this present research. At the same

time, the planimetric and, where applicable, height accuracy of the information extracted from their images is the subject of the series of accuracy tests.

3.4 Test Areas

Parts of the Sudan for which suitable images had been acquired by various space sensor systems were selected as test areas. Luckily the Sudan has large areas of desert and semi-desert with little cloud cover located relatively close to the Equator and fall within the orbits of those satellites launched with low orbital inclinations. Thus it was possible to find specific areas which had been covered by several different types of image. The final selection of these areas was dictated by the availability of topographic maps at 1:100,000 scale or larger and the desire to select areas which represent typical developed and underdeveloped parts of the country. Another area was selected for the test of the space photographs over a well developed area in a developed country (U.S.A) to provide a comparison between the results obtained using photographs of the Sudan test areas with those obtainable over an area in a developed country which had very well defined detail.

For the height accuracy test of the RBV images, an area which has good-quality RBV images having a lateral overlap of the order of 60% is needed. As will be shown in Chapter 9, RBV images with 60% lateral overlap could only be acquired by Landsat-3 over areas at latitudes greater than 48° N/S. A search for these images was conducted by interrogating the Earthnet Image archive data base through the On-line Data Availability (LEDA) facility. Another search was conducted through the National Remote Sensing Centre (NRSC) at the Royal Aircraft Establishment (RAE) in Farnborough and the Environmental Remote Sensing Application Centre (ERSAC), Livingston. After considerable time and effort, good quality images were eventually found covering part of the state of Alaska in the U.S.A..

3.4.1 Sudan Test Areas

For the purpose of this investigation, it was necessary to choose areas where good topographic maps and images from most of the space remote sensing systems were available. As shown in Chapter 1, the only areas in the Sudan which fulfil the requirement for good map coverage are those in the Red Sea Hills area and that part of the Nile Valley located around Khartoum. As can be seen from Fig. 3.3, part of the Metric Camera photography acquired during orbital path no.3 covers a

strip over Sudan stretching from $8^{\circ} 50'$ N latitude, 29° E longitude to $21^{\circ} 40'$ N, $37^{\circ} 30'$ E. This strip covers parts of both of these well mapped areas. In addition, three strips of LFC photography and a strip of MOMS imagery cover the Red Sea Hills area only. These are in addition to the Landsat MSS, RBV and TM images which were available over both these candidate areas.

Therefore, these two areas are the obvious if not the only choice for the investigation on topographic mapping from space imagery to be carried out over the Sudan. Furthermore these two test areas have the advantage of representing the two extreme cases in developing countries. The Red Sea Hills area is one with little population and little development due to natural factors such as water scarcity and hilly, heavily dissected terrain. By contrast, the Nile/Gezira test area is mostly flat and is heavily populated, including big cities and townships which, as in most of the developing countries, are located near water sources, i.e. along river banks and streams. In addition, it has a dense rural population and development along the Nile and the irrigated area of the Gezira.

i) Red Sea Test Area

This is a predominantly hilly area with height variation from 300 m. to 3,000 m. above mean sea level. This area can be considered one of the poorest areas in Sudan. Water scarcity and low annual rainfall together with the ruggedness of the terrain represent the main hardship factors in the area. Thus the population in this area is at the lowest level with occasional small villages and semi-nomadic camps scattered across the area. Accordingly cultural features are at the lowest level of density. A single railway line crosses this area running from the interior down to Port Sudan situated on the coast of the Red Sea, while a two lane surfaced road connecting Khartoum to Port Sudan via Wad Medani and Kessala represents the other main transport feature in this area. A few narrow unsurfaced roads or tracks interconnect the scattered settlements in the area. Topographic features take the forms of hills, ridges, valleys, basins, plains and very small seasonal streams in wadis.

ii) Nile Test Area

This is the area extending between latitudes $14^{\circ} 20'$ N and 18° N and longitudes 32° E and $34^{\circ} 30'$ E, shown as area B in Fig. 3.3. This area includes three of the biggest cities in Sudan (Khartoum, Khartoum North, and Omdurman) which form the capital; the northern part of the

Gezira triangle lying between the Blue and White Niles and including both of these rivers; the northern areas of Khartoum Province; and the southern areas of the Nile Province up to Atbara city located on the bank of the River Atbara. This area is an example of the sort of densely populated area which can be found in developing countries, although away from the banks of the Nile in the north, the area is lightly populated with scattered small villages and townships. A great variety of well-defined detail is present in this area, including various types of communication lines such as surfaced roads of different gauges, railway lines, tracks, bridges, ferry terminals and the various other cultural features which one might expect in densely populated cities and townships.

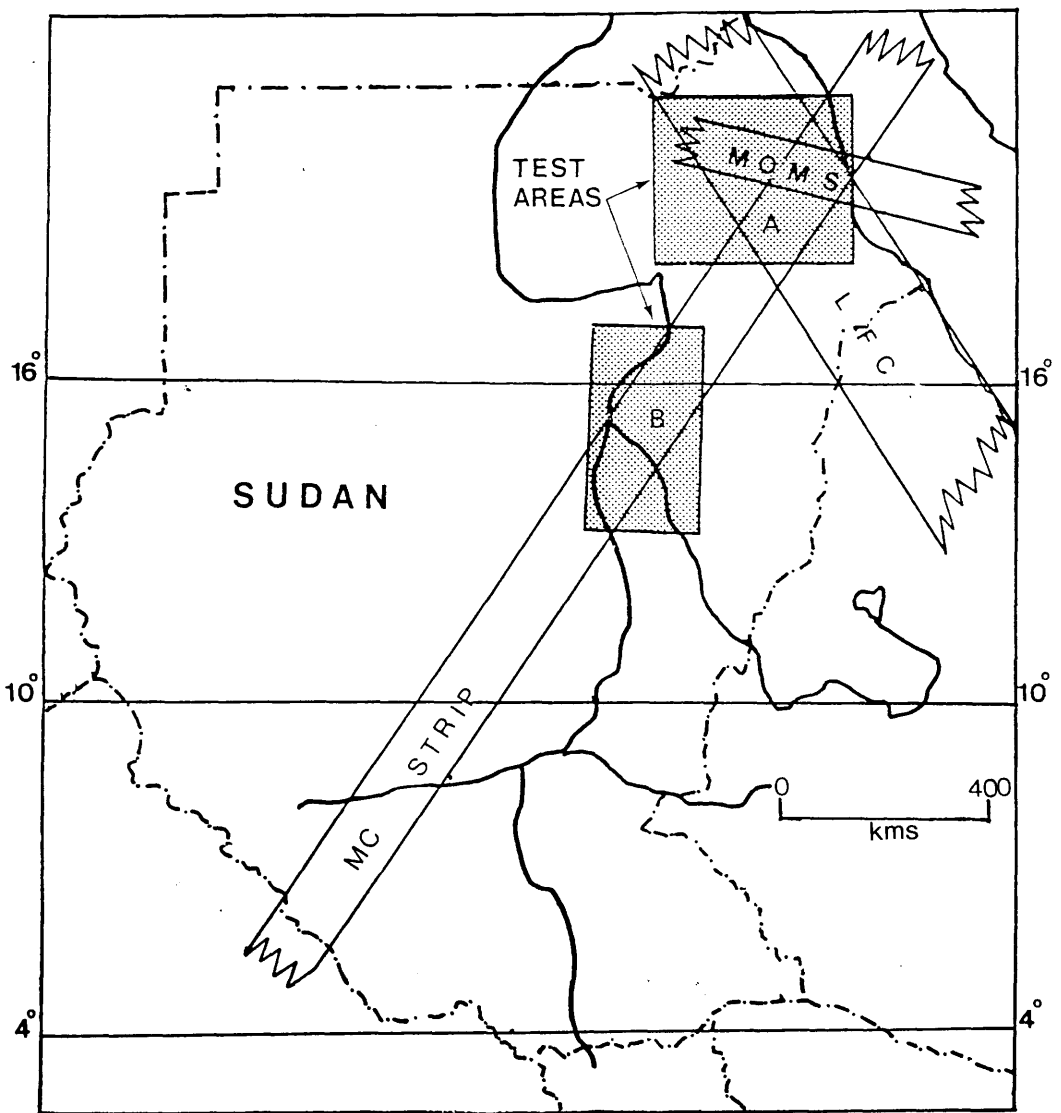


Fig. 3.3 Sudan Test Areas.

3.4.1.1 Accuracy of Sudan 1:100,000 Scale Topographic Maps

Both of the Sudan test areas are covered by 1:100,000 scale topographic maps with 20 m contour interval. As mentioned in Chapter 1, some of these maps were published by the SSD, but the majority were published by DOS. These maps were compiled from 1:40,000 scale wide-angle and 1:60,000 scale super-wide-angle aerial photography both taken from flying height of 5500 m. Wild A7, B8S and Kern PG-2 stereoplotters were used in the compilation of these maps. The accuracy (m_{p1}) of the planimetric detail plotted in these maps is estimated to be about ± 30 m (Simmons, 1976).

The magnitude of errors which are contributed by various sources to the error in contours were estimated by Simmons to be as follows:

- $m_h = \pm 0.8$ m (0.15 % H -the r.m.s.e. of height in single models);
- $m_t = \pm 2.5$ m (the r.m.s.e. in height due to aerotriangulation & adjustment),
- $m_p = \pm 1.6$ m and ± 2.4 m (the r.m.s.e. in the planimetric positions of the pass points, for WA and SWA photography respectively);
- $m_i = \pm 0.8$ m and ± 1.2 m (the r.m.s.e. in planimetry due to the instrument and the operator using WA & SWA photography.); and
- $m_d = \pm 10$ m (0.1 mm on map - the r.m.s.e. in planimetry due to plotting)

The standard error of the contours is then estimated from:

$$m_c^2 = + (m_h^2 + m_t^2) + (m_p^2 + 2 \times m_i^2 + m_d^2) \cdot \tan^2 \alpha \dots\dots\dots (3.4)$$

where α is the slope angle which was estimated to be an average figure of 18° taking into account all types of terrain likely to be encountered in the Sudan (Simmons, 1976).

With the wide-angle photography, this results in $m_c = \pm 4.25$ m, while with the super-wide-angle photography, it results in $m_c = \pm 4.28$ m. From this, it is clear that these values are good enough to allow the maps to be used in this investigation.

For the purpose of accuracy testing, well-defined image points were identified on the relevant topographic map sheets and the Universal Transverse Mercator (UTM) grid coordinates carefully scaled off using an accurate engineering scale on which the scale divisions were read through a magnifying lens. Every point was scaled off three times. Whenever the ground coordinates of the set of points selected

were found to fall within two different U.T.M zones, they were transformed into a common zone with the longitude separating the two zones acting as central meridian. The image coordinates of those points selected in the image under test were later measured monoscopically or stereoscopically (depending on the type of image) on the Zeiss Stecometer CII owned by the National Engineering Laboratories (N.E.L) at East Kilbride.

3.4.2 Georgia Test Area

To provide a comparison between the results obtained over the Sudan with those obtainable over well-defined detail in a well-mapped and developed area of the world, another test area was selected. This was part of the state of Georgia in the U.S.A extending between latitudes 31° N and $32^{\circ} 30'$ N and longitudes $81^{\circ} 15'$ W and $82^{\circ} 40'$ W. This area can be considered as a representative sample of a highly developed area since it contains the variety and density of detail which are usually associated with those areas. Well-defined details include motorways and road intersections and roundabouts, railway intersections and embankments, bridges, airports and airfields, field corners, etc. The terrain in this area can be categorized as being fairly flat with relief ranging between 3 and 60 m above mean sea level.

The 1:24,000 scale topographic maps of this area published by the U.S.G.S were obtained through the good offices of Professor Welch of the University of Georgia. The contour interval in these maps is 10 ft. (3 m). From the U.S NMAS specifications mentioned above, the planimetric accuracy (m_{p1}) and the contour accuracy (m_c) of these maps are ± 7.0 m and ± 1.0 m respectively. This means that the coordinates of the control and check points interpolated from these maps are more than accurate for the purpose of this investigation.

3.4.3 Alaska Test Area

In addition to the main test area (Sudan Red Sea Hills area) used in this investigation, the area extending between latitudes 64° to $66^{\circ} 15'$ N and longitudes $146^{\circ} 30'$ to $148^{\circ} 50'$ W in the state of Alaska, USA was selected primarily for the height determination test using RBV imagery. As explained previously, such a test cannot be carried out over the Sudan since the RBV images do not have sufficient stereo-overlap at latitudes close to the Equator. The selection of this particular area was dictated by the availability of cloud free RBV frames and the percentage of overlap between subscenes from adjacent satellite paths. This area can be characterised as hilly with a relief

variation ranging from 100 to 700 m. above datum. The density of detail in the area is not much greater than that encountered in the Red Sea area. Details such as road intersections, ridges, small water bodies were used as control and check points.

Topographic maps of the area at 1:63,360 scale and with 50 ft (15 m) contour interval were obtained. These maps were published by the USGS. Applying the NMAS specifications, the planimetric and contour accuracies may be estimated to be $m_{pl} = \pm 19$ m and $m_h = \pm 5$ m respectively. Again these maps are sufficiently accurate for the purpose of this investigation.

3.5 Analytical Instrumentation

Three analytical photogrammetric instruments were used in the mensuration stages of this investigation. Firstly, a Zeiss Jena Stecometer C II stereocomparator was used for the measurement of the image coordinates of the control and check points in the series of planimetric and height accuracy tests. Secondly, a Kern DSR-1 analytical stereoplotter was used for the generation of digital terrain profiles which are, as will be shown in Chapter 12, necessary for the production of contour lines and an orthophotograph. Finally the computer-controlled Wild Avioplan OR-1 orthophotoprinter was used for the production of the test orthophotograph.

3.5.1 Zeiss Jena Stecometer C II

Comparators are instruments which measure image coordinates which are later input to a computer program to carry out one of the photogrammetric operations which will eventually give the object space coordinates as output. Fig. 3.4 shows the overall arrangement of the high precision Stecometer C II stereocomparator built by Carl Zeiss Jena and used for most of the measurements of the space images.

Two photo carrier plates situated next to each other on the upper stage can accommodate image frames up to 24 cm x 24 cm in size. The images are viewed simultaneously from below by means of a dual microscope with a fixed viewing system to give a stereoscopic model. The two carrier plates can be translated jointly by the movement of the lower stage in the x-direction to measure x-coordinates (x_1), while the optical viewing system can be shifted in the y-direction to measure y-coordinates (y_2). The left hand carrier plate can be shifted separately in the y-direction to provide a displacement between the two photos, e.g. to measure or eliminate y-parallax (py_1). The right hand carrier

plate can be moved in the x-direction to produce a displacement between the two photos i.e. to measure x-parallax (px_2) or height. This arrangement allows the measurement of the image coordinates as x_1 , y_2 , px_2 and py_1 . The movements for x_1 and y_2 are driven by variable speed motors via the machine handwheels to take the measuring marks to the vicinity of the point to be measured. The selection of the slower motor-driven motion is done by pushing the x_1 and y_2 handwheels inwards till they click, then giving a gentle push in the direction of the translation required. The measuring mark is then brought into contact with the surface of the model at the point to be measured through the manual rotation of the handwheels (providing x and y movements) and footdisks (controlling the px and py movements).

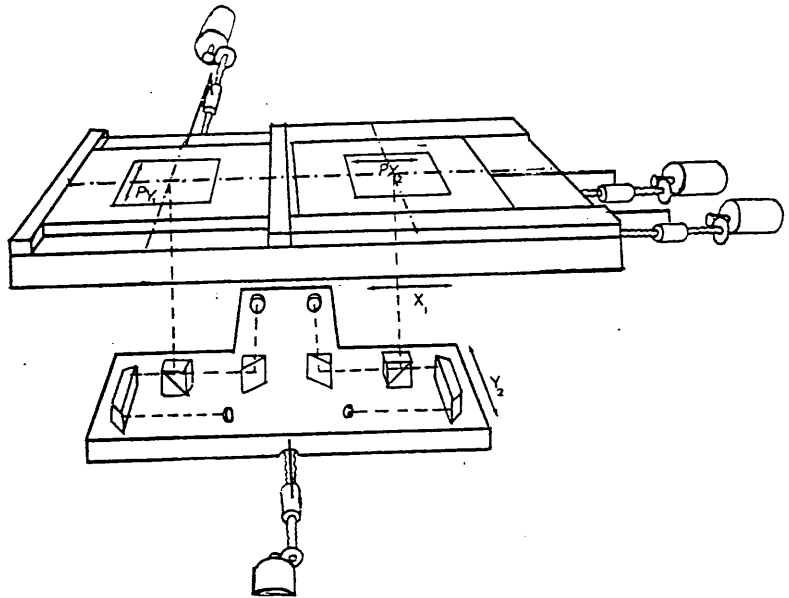


Fig. 3.4 Overall Arrangement of Stecometer C II.

Three magnification ratios - 4.8x, 9.6x, and 18x - are available and seven choices of measuring marks are possible. The choices of measuring marks comprise 3 different sizes of point-shaped mark; 3 ring-shaped marks of different diameters; and one cross-mark. These allow the operator to select the particular measuring mark that suits the size and shape of the point to be measured. The values of x_1 , y_2 , px_2 and py_1 are generated by means of rotary encoders with a resolution or least count of 2 μ m. In the case of the Stecometer at N.E.L. used for the majority of the test measurements, these coordinate values are sent to the recording unit, which is a Cromemco System 3 microcomputer (Fig. 3.5). The coordinate values are displayed on the screen of the microcomputer so that the operator can view them and decide whether to accept them or to make a further refinement of the pointing. When the values are acceptable, a foot pedal is pressed to record the data on to

a floppy disk.



Fig. 3.5 Zeiss Jena Stecometer C II System of N.E.L..

3.5.2.1 Kern DSR-II Analytical Stereoplottter

As mentioned above, a Kern DSR-1 system owned by the Institute of Advanced Architectural Studies, University of York, was used for the collection of the digital terrain height data required for part of the experimental work. In contrast to the Stecometer C II stereocomparator, the DSR-II, as shown in Fig. 3.6, is an analytical plotter in which an oriented, parallax-free model can be achieved.

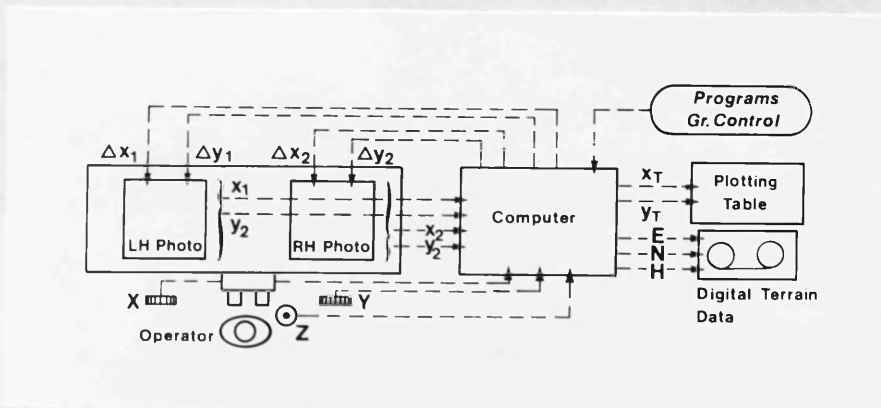


Fig. 3.6 Overall Arrangement of the DSR-II.

By moving the measuring mark over the surface of the stereo-model via the mechanical rotation of the handwheels and the foot disk, the operator generates X, Y, Z or E, N, H object space coordinates which are continuously forwarded to the computer. Thus the machine follows the object coordinates primary approach favoured by the majority of manufacturers of analytical plotters. Resident in the computer are programs to determine and maintain the complete relationship between object space and image space by executing algorithms such as the collinearity equations. These programs receive, as input, changes in object space coordinates and compute corresponding changes in image coordinates. The computed changes of image space coordinates are then input to the servo systems that move the image plates such that the stereomodel is maintained and the operator sees it in 3D. The positions of the two plates are measured by encoders and fed back to the computer as x_1 , y_1 , x_2 and y_2 coordinates to be used in the computation.



Fig. 3.7 Kern DSR-11 Analytical Plotter.

3.5.2.2 Computer Control of the DSR-11

The computer control of the DSR-11 is based on the distributed computing concept which is implemented by using a DEC PDP-11 computer as the main control computer (p1); a DEC LSI-11/2 based 16 bit microprocessor (p2) for the major real-time computational tasks, and the less powerful Intel 8085 microprocessors (p3) for smaller tasks. Fig. 3.8 shows this distributed computer architecture of the DSR-11

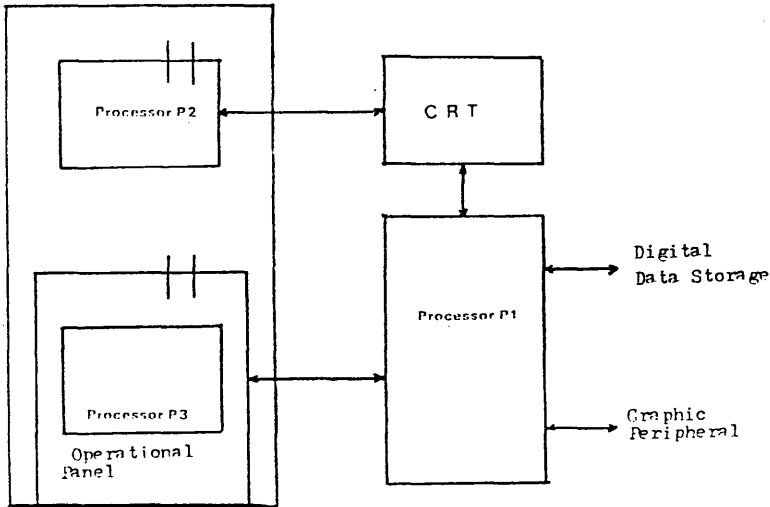


Fig. 3.8 Distributed Computer Architecture of the DSR-11

The main control computer (p1) is a PDP 11 - typically a Q-bus machine such as the 11/23 or 11/73 models. This computer stores the DSR-1 operating system and the main programs which do not require real-time operation. Also it controls the flow of communication between various elements of the DSR and the operator.

The plate processor (p2) has the job of maintaining the position of the stage plates as commanded by the controlling computer (p1) or directly through the motions of the operator input devices. The real-time program that controls this is downloaded from the p1 machine upon starting up the operating system. It can drive the plates individually or in stereoscopic mode, depending on the commands and parameters received from the p1 machine. In stereoscopic mode, this processor is capable of recomputing the plate coordinates of the required points and commanding the plates to move to their locations. At the same time, it presents the present plate coordinates to a standard DEC parallel interface which links it to the control computer p1. The servomotors that provide the motion of the plates operate in a closed loop which allows the plate processor to directly control the speed and

acceleration of the plates.

The third processor (p3) is the operator control panel (OCP) processor which is based on an Intel 8085 microprocessor and has its program stored locally. Its function is to display messages and prompts to the operator and returns and accepts his responding keystrokes and commands as well as communicating with the p1 processor.

The DSR-II operator control consists of the DEC VT100 terminal for interaction with the control processor p1 and the operator control panel (OCP). On the OCP, there are separate controls for the illumination of both images and both floating marks and for varying the floating mark size. There are also switches to select the manual drive device: i.e either handwheels or trackball, for X and Y movements; footdisk for Z. Two other switches allow separate selection of the manual motion speed at 1, 2, or 4 times the programmed rate for the X, Y, and Z motions (which is selected through the DSR operating system). In addition to the OCP, there are the two actual hand wheels and a trackball for the X and Y motions, plus a foot disk and a height drum for the Z motion, all of whose signals are sent to p1. Two foot pedals acting as recording switches are also included (Fig. 3.7).

3.5.2.3 Controlling Software

The controlling computer can be programmed to carry out the sequence of photogrammetric operations that are required in a particular project. Kern supplies the DSR-II operating system residing in the control computer (p1) to control the DSR-II. Kern software includes inner, relative and absolute orientation, instrument test procedures, profiling program, etc. Several third party software packages are also available. In this investigation, a software package developed for close range photogrammetry applications by the Technical University of Graz and the Graz Research Centre denoted as CRISP (for Close Range Imagery Software Package) was used. CRISP will be explained in some detail in Chapter 12.

3.5.3 The Wild Avioplan OR-1 Orthophoto Unit

As mentioned above, a Wild Avioplan OR-1 Orthophotoprinter was used for the production of the test orthophotograph at the Institute of Photogrammetry, Technical University of Vienna. The Wild OR-1 is an analytically controlled orthophotoprinter based on the optical transfer principle. However unlike other devices built on this same principle, such as the Zeiss Jena Topocart/ Orthophot, it is wholly computer

photographs. The X, Y, Z coordinates are supplied by an existing digital terrain model (DTM) or gathered as digital terrain profiles on a stereoplotter in a separate prior step. A regular grid DTM covering the area of the orthophotograph is interpolated from these digital terrain data at a suitable grid interval. The interpolated X, Y, Z coordinate data are then fed to a Data General mini-computer which, using the known values of the exterior orientation of the photograph acquired via the collinearity condition equations, computes the corresponding image coordinates x' , y' for each grid node in an off-line step. The result of this computational step is a set of digital terrain data recorded as x' , y' , Z which are needed for the production of the orthophotograph. The regular grid of the DTM is now represented by irregular profiles on the image plane as shown in Fig. 3.9.b. These data are then fed to the on-line controlling computer. For each line element m between two image points representing two grid nodes on the terrain, the computer computes the coordinates of the mid point x'_{m12} , y'_{m12} , of each line element and drives the photo carriage to that point. The angle θ through which the line element needs to be rotated and the value of the differential magnification M_{m12} are also computed via the following set of equations:-

$$\begin{aligned}
 x'_{m12} &= (x'_1 + x'_2)/2 \\
 y'_{m12} &= (y'_1 + y'_2)/2 \\
 \tan \theta &= (y'_2 - y'_1) / (x'_2 - x'_1) \\
 M_{m12} &= K / \sqrt{(x'_2 - x'_1)^2 + (y'_2 - y'_1)^2}
 \end{aligned}
 \dots\dots\dots (3.5)$$

where K is the slit width.

The photo carriage is an xy cross-slide in which x is the primary motion. The motors and spindles which drive the two components of this carriage are completely enclosed, a small motor driving each spindle through a belt drive. Each spindle is permanently engaged by a ball race in a mount attached to the carriage. On the end of each spindle is a rotary encoder. Pulses from each encoder are counted electronically and provide the respective coordinates of the actual position of the carriage. These coordinates are continuously compared with that given by the computer. The differences between the two sets are converted by a digital/analogue convertor to voltages which, after amplification, are applied to the respective DC motor that drives each carriage so as to reduce the difference to null. Within the y-carriage is a k-

turntable which holds the photo carrier. The cams of the basic zoom lens unit are operated by hand using a control knob on the front face of the projection unit to give a magnification range of 0.33x to 3x which, with the original 2x fixed magnification of the optical system, gives a total magnification range of 0.66x to 6x. The terrain zoom cams are driven continuously by a servo motor under the control of the computer to maintain the magnification at the desired value. The interchangeable slit masks are mounted on a holder at the rear of the projection unit and are coupled mechanically by a sleeve to a light-tight slide in the drum housing. A standard slit width of 0.1mm is used for black-and-white orthophotograph printing and another of 0.3mm for colour orthophotographs.

The drum enclosed in its housing is rotated to correspond to the scan motion. The maximum film format which can be accommodated on the drum is 970mm in the Y-direction by 780mm in the X-direction giving an orthophoto size of 900mmx750+one scan width mm.

3.5.3.1 Data Pre-processing for the Avioplan OR-1

From the above description of the OR-1, it is clear that two essential preparatory data processing steps need to be carried out on the digital terrain model (DTM) data gathered on the DSR-1. These are:

- a) the interpolation of a set of dense profile lines that represent the straight parallel lines on the orthophoto plane from the digital terrain model data as described above; and
- b) the derivation of the image plane positions of the straight parallel lines defined on the orthophoto plane.

The interpolation of the straight lines was carried out using the Stuttgart Contour Program (SCOP), while the determination of the corresponding image positions of these lines was done using the SORA-OP (Software for Off-line Rectification with the Avioplan - Orthophoto and Stereo orthophoto). These two programs will be discussed in some detail later in Chapter 12.

3.6 Summary

In this chapter, the map content and accuracy requirements and specification were explained and the realization of these requirements using photogrammetric methods has been discussed. This has been done to help in understanding the capabilities of space sensor systems as

determined through the series of accuracy and interpretation tests reported in the following chapters. A description of the test areas selected for these tests has also been given. Finally the analytical photogrammetric instruments which have been used in this investigation have also been described and their working principles explained. In the following chapter, the characteristics of the Landsat MSS and TM images will be described and the geometry of their images explained. The mathematical models employed for the transformation of these images will be reviewed in general and those used specifically in this investigation together with the procedures employed in their application will be explained in detail.

CHAPTER 4

Landsat MSS and TM Scanner Systems

4.1 Introduction

The first MSS on Landsat-1 proved to be a successful step into space remote sensing for many scientists working in different fields. This success established the MSS as the standard sensor for all the satellites of the Landsat series which followed. NASA continued supervising, managing and operating the series through the 1970s and early 1980s till the U.S National Oceanic and Atmospheric Administration (NOAA) of the Department of Commerce was given the responsibility for managing and developing all American civil operational satellites in January 1983. Later in September 1985, the operational and processing activities associated with the Landsat satellites were privatized. The Earth Observation Satellite Company (EOSAT) was formed as a joint venture of the RCA Corporation and the Hughes Aircraft Company and is now responsible for the development, control and scheduling of the satellites, the processing of their image data, and the marketing, sales and distribution of the final products. As already discussed in Chapter 2, thus far there have been five satellites launched in the series. Each of them carried an MSS as part of its payload, while Landsats 4 and 5 have also been equipped with TM, an optical mechanical scanner of improved resolution recording in a larger number of spectral bands. In the following paragraphs, the general aspects of the design of optical mechanical scanners are described followed by the description and the geometrical analysis of Landsat MSS and TM images.

4.2 Optical Mechanical Scanner Design

The primary function of the scanning unit in an optical mechanical line scanner is to focus the radiation coming from a narrow strip of ground across the flight line onto a bank of detectors. The incident radiation is separated onto several spectral bands. The radiation in each spectral band is then directed to the detector which is responsive to it. There are many ways of accomplishing the mechanical scanning, but the simplest and most common are shown in Fig. 4.1, in which the scanning units are classified into rotating mirror and oscillating mirror scanning units.

Fig. 4.1

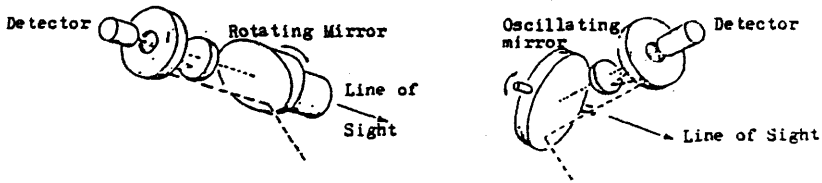


Fig. 4.1 Scanning Mechanism in Optical-Mechanical Scanners.

4.2.1 Rotating Mirror Units

The simplest arrangement in this group is that in which a mirror is made to rotate through 360° around an axis which is oriented along the direction of flight. During part of this rotation, the radiation coming from the Earth's surface is reflected to pass along the optical axis of the objective lens of the scanner to be focussed on the detectors situated in the focal plane. This optical axis is oriented across the direction of flight as shown in Fig. 4.1. The other part of the rotation cycle may be used for exposing the detectors to the calibration lamps.

4.2.2 Oscillating Mirror Units

In this type of device, the mirror is driven by a cam or some suitable alternative to linearly scan the Earth's surface at right angles to the flight direction. At the end of scanning period, the mirror is given an impulse to return in the opposite direction in a similarly linear manner. As will be shown later in this chapter, this arrangement is used in the Landsat MSS systems.

4.2.3 Spectral Separation Techniques

Multispectral sensing is achieved by simultaneously sensing the spectral information over a range of wavelengths using many detectors, each sensing a specific spectral band. The separation of the incident

radiation into selected spectral bands is done by using suitable filters in conjunction with a row of detectors, each with a different spectral response.

An alternative which is common in airborne scanners is to use dispersing elements, i.e prisms or gratings, with detectors so positioned as to receive the dispersed radiation. Dichroic mirrors are employed to separate the visible from the infrared region or to subdivide the infrared region into narrow bands.

4.3. Displacements and Distortions in Scanner Images

The positions of the terrain features shown on scanner images should have a simple relation with the actual positions of these features on the Earth and with those depicted on a map. However, before these images can be considered to be in their correct cartographic positions, the geometrical displacements and distortions associated with the scanning and printing processes must be removed. Most of the distortion associated with the scanning process can be summarized as the following:

4.3.1 Displacements Caused by the Panoramic Nature of the Scanning

The basic geometry of an optical mechanical scanner is shown in Fig. 4.2. As the scanning mirror scans the Earth's surface, the forward motion of the platform allows the build up of a continuous strip image from the successive scan lines. During the scanning, the terrain within a scan line is viewed successively by the fixed IFOV as discrete pixels. The scan angle θ varies to bring these discrete pixels into the scanner's optical system.

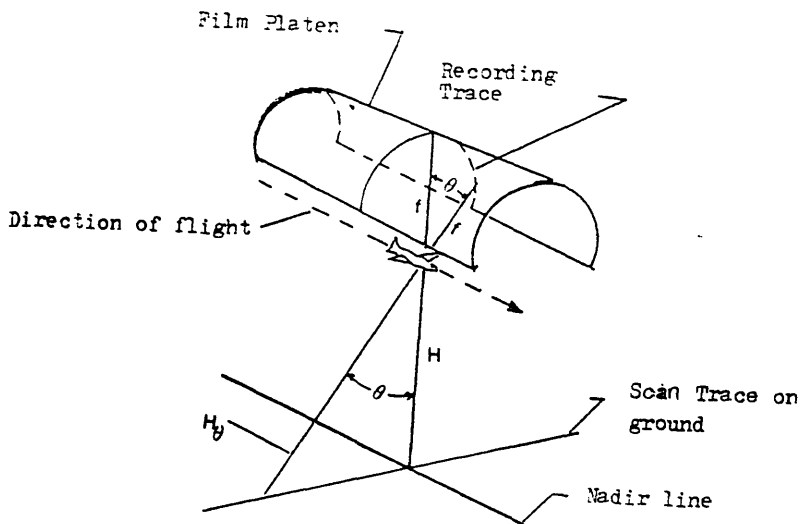


Fig. 4.2 Basic Geometry of Scanner Imagery.

Since the equivalent focal length of the scanner remains unchanged while the distance between the sensor and the imaged discrete pixel increases with $\sec \theta$, the actual area covered by the IFOV varies with the scan angle θ . Fig. 4.3 shows the variation of ground pixel size with the scan angle and the distortion caused by this variation in the resulting image.

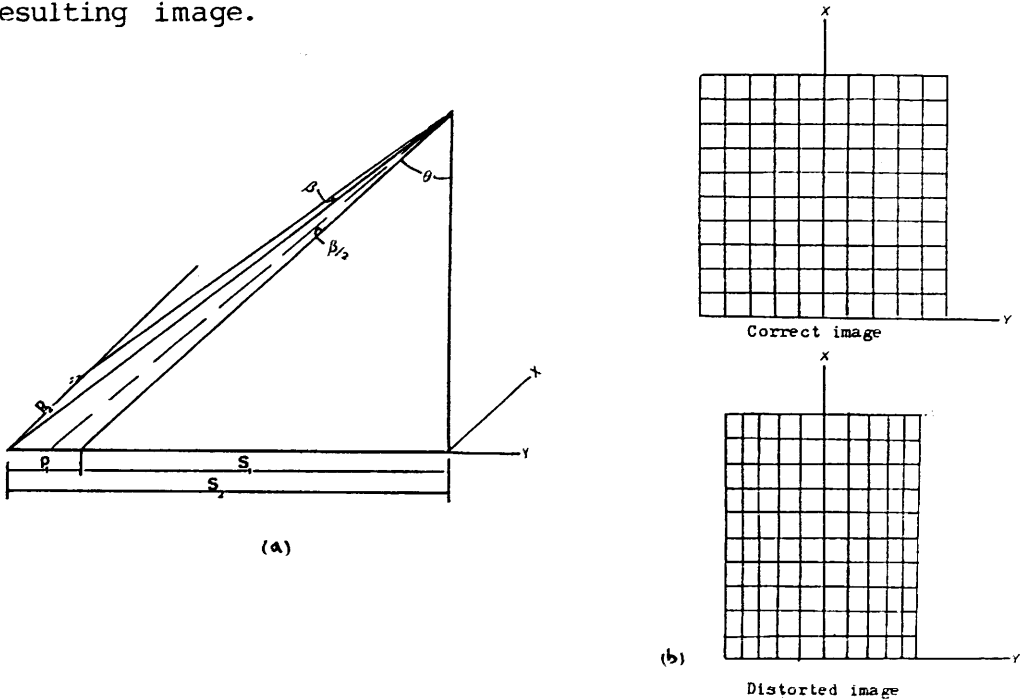


Fig. 4.3a Variations in Ground Pixel Size with Scan Angle.
 Fig. 4.3b Panoramic Distortion in Scanner Images.

As can be seen in Fig. 4.3a, the dimensions of the square ground pixel at the nadir point of a scan line are equal to $H.B \times H.B$. The dimension of the ground pixel at scan angle θ can be computed as follows:

In the scan direction (Y-direction), the dimension (P_1) of the ground pixel is, as shown in Fig. 4.3a, the distance $S_2 - S_1$. From the figures:

$$S_2 = H. \tan (\theta + B/2)$$

$$S_1 = H. \tan (\theta - B/2)$$

i.e
$$S_2 = H. \frac{\tan \theta + \tan B/2}{1 - \tan \theta \tan B/2}$$

..... (4.1)

$$S_1 = H. \frac{\tan \theta - \tan B/2}{1 + \tan \theta \tan B/2}$$

Since B/2 is a very small angle, tan B/2 can be taken to be equal to B/2. Substituting in equations (4.1):

$$S_2 = H. \frac{\tan \theta + B/2}{1 - B/2 \tan \theta}$$

$$S_1 = H. \frac{\tan \theta - B/2}{1 + B/2 \tan \theta}$$

Hence:

$$P1 = H.B. \frac{1 + \tan^2 \theta}{1 - B^2 \tan^2 \theta}$$

Since B² is very small, the term B².tan² θ can be ignored which results in:

$$P1 = B.H.\sec^2 \theta \quad \dots\dots\dots (4.2)$$

The X- direction dimension (P2) of the ground pixel at scan angle θ can similarly be computed to give:

$$P2 = B.H.\sec \theta. \quad \dots\dots\dots (4.3)$$

The result of representing various sizes of ground area element by the same image pixel gives rise to a cylindrical (panoramic) distortion and scale compression in the across track direction as shown in Fig. 4.3b.

In the direction of flight, the varying size of the instantaneous area covered in a single scan line with the scan angle results in scan lines taking the shape of a bow tie as shown in Fig. 4.4a. These scan lines overlap at the edges of the image on both sides of the nadirline. The overall effect of the panoramic distortion on the resulting image is shown in Fig. 4.4b (Lillesand and Kiefer, 1979).

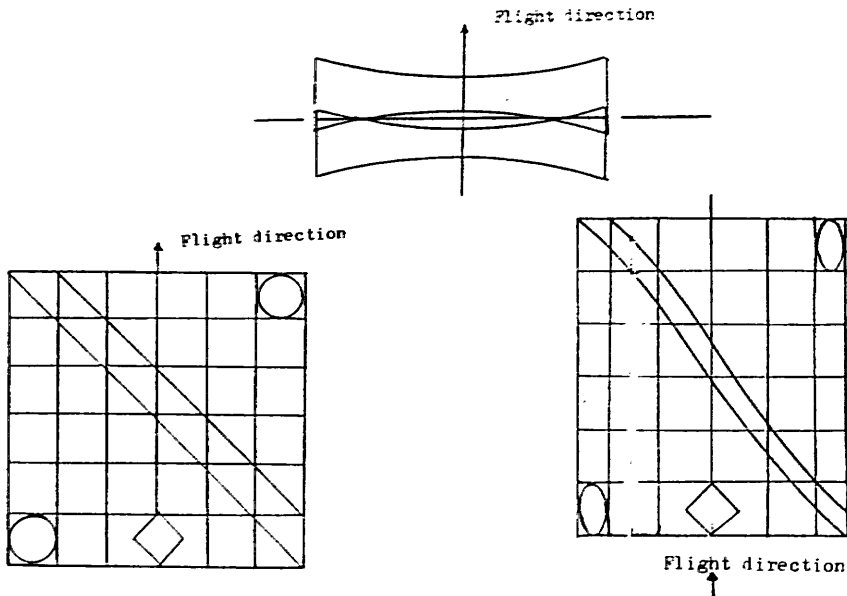


Fig. 4.4a Effects of Panoramic Distortion in the Flight Direction.
 Fig. 4.4b The Overall Effect of the Panoramic Distortion.

In airborne scanners with wide angles of coverage operated from relatively low altitudes, the resulting displacements are large. However in spaceborne scanner systems, the maximum scan angle is small while the altitude is very large, so the magnitude of this distortion is almost negligible. Thus for Landsats 1, 2 and 3, the orbital altitude (H) is 920 km; the maximum scan angle (θ) is 5.7° ; and the IFOV is 86 urad. Along the nadir line, the ground pixel size is 79 m x 79 m, while at the edge of the image on both sides of the nadir line, the pixel size is about 79.8 m x 79.4 m.

4.3.2 Distortions Due to Non-linear Mirror Sweep

The mechanical rocking of the scanning mirror inevitably produces slight variations in the scanning angular speed during the scan. The non-linear motion of the mirror can be determined by pre-flight calibration and a correction to the distortions introduced by this non-linear motion can be incorporated in the processing procedures using the calibration data. The residual distortions after this correction are negligible.

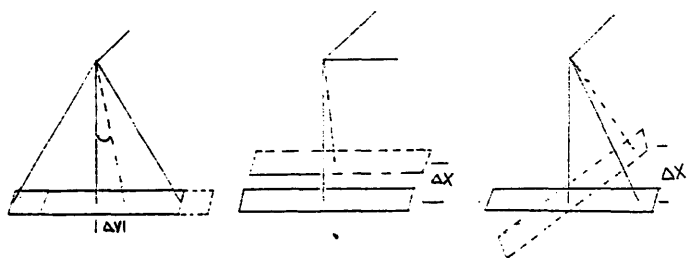
4.3.3 Displacements Caused by Platform Motion and Attitude

Anomalies in the platform motion such as velocity changes, changes in flying altitude and variation in the platform attitude during the

scanning process are serious sources of geometric distortion in scanner imagery.

The platform is supposed to move forward at a constant nominal velocity. Any change in this nominal velocity during the scanning process results in a scale distortion in the direction of flight. This is so because the ground area over which the satellite has moved during the period in which a specific number of lines forming the image has been scanned changes. In spaceborne scanners, this is not a severe problem since the satellite's forward velocities are much more stable than those of aircraft.

The attitude of the platform may change continuously during the scanning process so that every line scan has its own set of exterior orientation parameters. A continuous record of the satellite attitude is therefore required for the rectification of scanner imagery, otherwise alternative methods of rectification have to be sought (Derenyi and Konecny 1964). The parameters which describe the attitude of any platform may be taken as the rotation angles w (roll - about the along track axis); ϕ (pitch - about the across track axis); and k (yaw - about the vertical axis). The effects of the continuous change in these rotation angles, w , ϕ and k on the image at the nadirline are shown in Fig. 4.5.



- (i) Displacement due to Roll (w).
- (ii) Displacement due to Pitch (ϕ).
- (iii) Displacement due to Yaw (k).

Fig. 4.5 Effects of Satellite Attitude on MSS Images.

Changes in roll (w) introduce displacements in scan direction (y -direction). The magnitude of the displacement in ground position in Y of a point at the nadirline is given by:

$$\Delta Y = H \cdot d\omega \quad \dots\dots\dots (4.4)$$

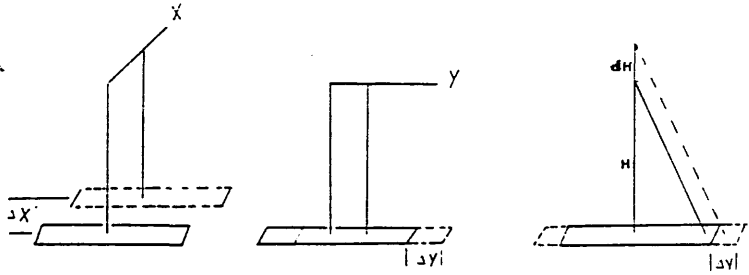
Changes in the pitch (θ) introduce displacements in the direction of flight (the x-direction). As can be seen from Fig. 4.5, the magnitude of the displacement of the X ground position of a point at the nadirline is given by:

$$\Delta X = H \cdot d\theta \quad \dots\dots\dots (4.5)$$

Changes in yaw (k) do not introduce any displacement at the nadirline. At points on both sides of the nadirline and at scan angle θ changes in yaw introduce displacement in the X- terrain coordinate. The magnitude of this displacement is given by:

$$\Delta X = H \cdot \tan \theta \cdot dk \quad \dots\dots\dots (4.6)$$

Besides the displacements produced by these changes in attitude, a further series of displacements will result from the translations (dX_0 , dY_0) from the nominal or correct sub-satellite track and from the variation in orbital height (dH_0) from the desired value.



- (i) Displacement due to X- Translation
- (ii) Displacement due to Y- Translation
- (iii) Displacement due to Change in Altitude.

Fig. 4.6 Effect of Satellite Position and Altitude Variation.

If the displacement from the sensor's nominal X- coordinate position (i.e the translation in the direction of flight) at the instant of imaging the scan line is dX_0 , then the magnitude of the displacement of the X ground position of any point at the nadirline is:

$$\Delta X = dX_0 \quad \dots\dots\dots (4.7)$$

Again if the displacement of the sensor from its nominal Y-coordinate position (the translation in the scan direction) is dY_0 , then the displacement at a point on the nadirline in the y-direction is:

$$\Delta Y = dY_0 \quad \dots\dots\dots(4.8)$$

Any change in the nominal flying altitude (dH_0) of the platform which is supposed to be a constant will result in scale distortion. As shown in Fig. 4.6, the resulting displacement within a scan line at a particular point occurs in the scan direction, i.e in the y-coordinate of that point.

The magnitude of displacement which is caused by the change in the altitude of the platform at any point as can be seen in Fig. 4.6 is given by:

$$\Delta Y = dH_0 \tan \theta \quad \dots\dots\dots(4.9)$$

Summarizing all these different effects gives rise to the following equations along the nadir line.

$$\begin{aligned} \Delta X &= dX_0 + H.d\phi + H.\tan \theta.dk \\ \Delta Y &= dY_0 - H.dw + dH_0.\tan \theta \end{aligned} \quad \dots\dots\dots(4.10)$$

The effects of the positional displacements and attitude variation on image points away from the nadirline are more complex than those at the nadirline. However, the overall effects of displacements which result from the platform positional and attitude parameters on the ground coordinates of points shown on scanner images can be expressed by mathematical formulae. These formulae can be derived from those applied in photogrammetry for frame photography with the consideration of the special conditions that exist in scanner images. For vertical frame photography, the equations for these displacements are as:

$$\begin{aligned} \Delta X &= dX_0 + x'/f.dH + y'/fH.dk + H(1+x'^2/f^2).d\phi - x'y'/f^2.H.dw \\ \Delta Y &= dY_0 + y'/f.dH - x'/fH.dk + x'y'/f^2H.d\phi - H(1+y'^2/f^2).dw \end{aligned} \quad \dots\dots\dots(4.11)$$

where x', y' are image coordinates and f is the focal length. Since the

x' coordinate in scanner images is zero considering a single scan line, equations (4.11) reduce to:

$$X = dx_0 + y'/fH \cdot dk + H \cdot d\phi \dots\dots\dots (4.12)$$

$$Y = dy_0 + y'/f \cdot dH - H(1+y^2/f^2) \cdot dw$$

Substituting $\tan \theta = y/f$, equations (4.11) become:

$$X = dx_0 + H \cdot \tan \theta \cdot dk + H \cdot d\phi \dots\dots\dots (4.13)$$

$$Y = dy_0 + \tan \theta \cdot dH - H(1+\tan^2 \theta) \cdot dw$$

Equations (4.13) are in fact similar to equations (4.10) with the effect of the variation of roll angle (w) at points away from the nadir line being added.

These rotation angles may change from ^{one} point to another within a scan line and also from one scan line to another depending on the rate at which these changes occur. The effect of the displacements in the platform positional coordinates and the variations in the parameters of its attitude on the resulting image are shown in Fig. 4.7. Again because space satellites are much more stable than aircraft, these displacements are very small in space scanner images. The changes within a scan line in the attitude angles (dw , $d\phi$ and dk) of a spacecraft are very small - again in contrast to the situation encountered with airborne scanners. For example, the rate of change in the attitude of Landsat 1, 2, 3 is in the order of +0.015 degree per second (U.S.G.S, 1979).

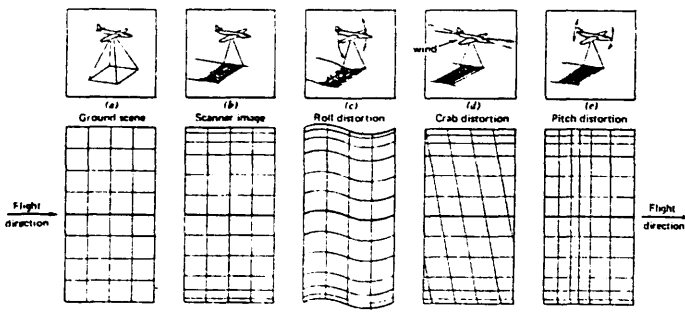


Fig. 4.7 Image Displacements Due to Platform Motion.

4.3.4 Relief Displacements in Scanner Imagery

Variations in terrain height will cause image displacements in scanner images. The magnitude of these displacements depends on the

relief variation, the flying altitude and the scan angle at which a specific point is located. Relief displacement will be particularly significant at large scan angles. Relief displacement (Δr) in a vertical frame photograph is radial from the nadir point and directly proportional to the distance (r) of the image point from the nadir point.

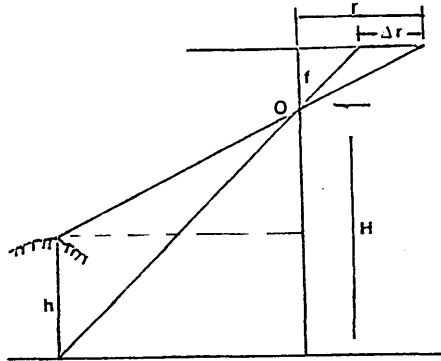


Fig. 4.8 Relief Displacements in Frame Photography.

As can be seen in Fig.4.8, relief displacement in vertical frame photography is given by:

$$\Delta r = rh/H \quad \dots\dots\dots(4.14)$$

where r is the radial distance of the image point from the principal point (or nadir point);
 h is the height of the image object; and
 H is the flying altitude.

In the case of scanner images, the situation is significantly different due to the nature of scanning. Fig. 4.9 shows relief displacement in scanner images. Since the scanner image is scanned line by line and each scan line has its own central projection geometry, this relief displacement can only occur in the scan direction.

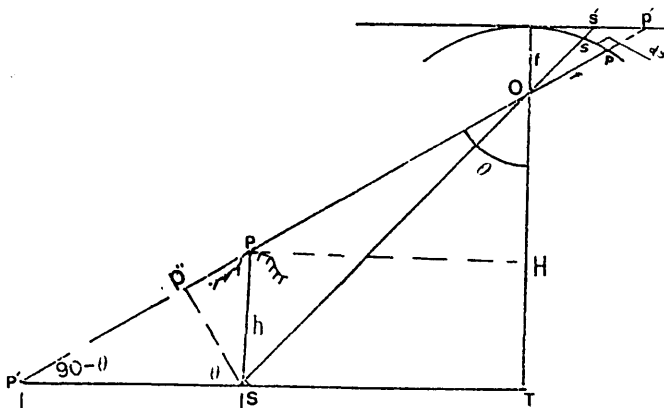


Fig. 4.9 Relief Displacements in Scanner Images.

An object point P having an elevation h above datum is imaged at image point p as if it is at point P' on the datum. The bottom point S of the object is imaged at image point s. The distance dy is the relief displacement caused by the difference in height between the two points of the object. From Fig. 4.9 dy can be computed as:

$$dy/P'S = f/OP''$$

i.e $dy/(h \sin \theta) = f/(H \cdot \sec \theta)$

$$dy = (fh/H) \cdot \sin \theta \cdot \cos \theta \quad \dots\dots\dots (4.15)$$

The magnitude of this displacement on the ground is the distance P'S given by $h \tan \theta$. In spaceborne scanner systems, the scan angles are often very small, e.g 5.7 degrees in MSS and 7.8 degrees in TM. Therefore relief displacements are often negligible except in very hilly areas. As an example, extreme relief variation in the Sudan Red Sea Hills area is about 600 m. In Landsat MSS images, the maximum Y-coordinate error introduced by the relief displacement at the edges of the image on both sides of nadirline, as a result of this particular relief variation is about 60 m. Since the ground pixel size in MSS images is 79 m, the error introduced by relief displacement which is less than 79 m can be ignored.

4.3.5 Displacements Caused by Earth Curvature and Rotation

In space scanner images, the ground area covered by a particular image is very large compared with that of airborne scanner images. The larger the area of the ground covered by the image, the more significant is the curvature of the Earth's surface. This Earth's surface curvature causes image displacements. Since the image is formed line by line, these displacements occur only in the direction of scan (Y-direction). The displacement at any image point can be computed assuming a particular spheroid to represent the Earth. As can be seen in Fig. 4.10, the actual ground distance swept by the scanner is d_3 . The distance d_3 is imaged on the scanner image as if it is the distance d_2 . Thus the displacement caused by the Earth's curvature is $d_3 - d_2$ which can be computed as:

$$L = (H+R) \cdot \sin \theta.$$

$$\sin \eta = L/R = (H+R)/R \cdot \sin \theta.$$

but $\eta = \theta + \zeta$

Thus:

$$d_3 = R \zeta = R(\sin^{-1}(R+H)/R \cdot \sin \theta - \theta) \\ = H(\theta + (V^2 + V) \cdot \theta^3/6)$$

where $V = (H+R)/R$

$$d_2 = H \cdot \tan \theta = H \cdot (\theta + \theta^3/3)$$

$$d_3 - d_2 = H \cdot \theta^3/3 \cdot ((V^2 + V)/2 - 1) \dots\dots\dots (4.16)$$

For example, Earth's curvature displacements at the edges of the MSS images amount to about 70 m. However, these displacements are taken care of during the image processing as will be explained later.

Furthermore during the period required to image the whole frame of scanner image, the Earth continuously rotates beneath the orbital plane. Thus the area covered by the image frame takes a rhomboid shape rather than a square one (Fig. 4.10). To remove this distortion, successive swaths in the image must be displaced towards the west edge by the amount $Y = H_e X$, where H_e is the change in the nominal satellite heading due to the Earth's rotation. Again this displacement is taken care of during the image processing.

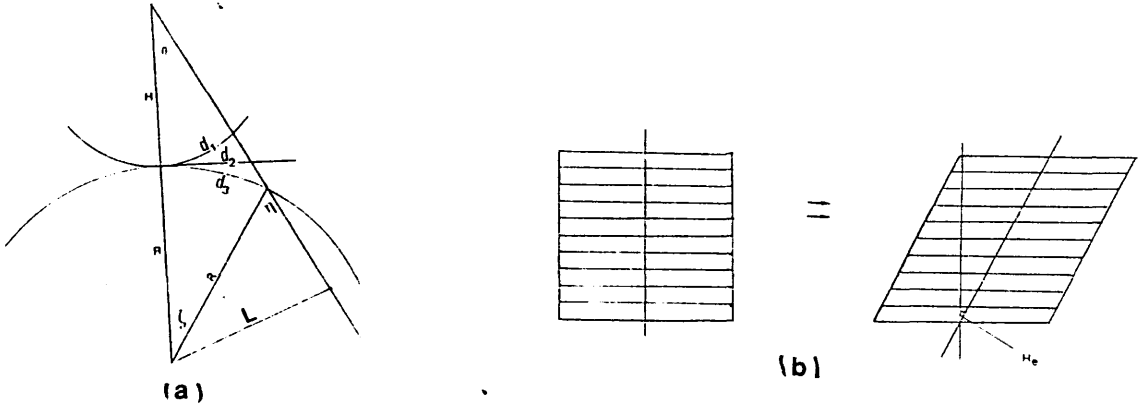


Fig. 4.10 Earth Rotation Displacement.

4.4 Landsat MSS Sensor and Data

4.4.1 Landsat MSS Sensor

The MSS used in four of the five Landsat missions launched to date is a four channel scanner operating in the visible and near infrared regions. Only Landsat-3 had an additional channel in the thermal infrared part of the spectrum. The principal components of MSS scanner are shown in Fig. 4.11.

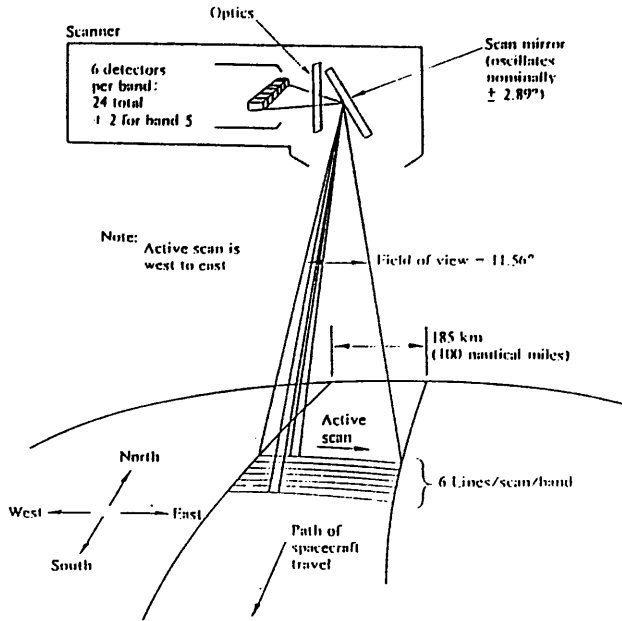


Fig. 4.11 Landsat MSS Scanner.

During the day, the oscillating mirror of the scanner continuously scans the Earth's surface in 185 km swaths across the satellite track giving an angular coverage of 11 degrees. Reflected solar radiation received from the Earth's surface is reflected by the mirror into reflecting telescope optics and focussed on the ends of a fibre optic bundle located in the focal plane of the telescope. The size of the fibre optic bundles and the focal length of the telescope determine the IFOV of the sensor. The ground pixel size resulting from the IFOV is 79x79 m for each of the usual four bands and 237x237 m for the fifth band of Landsat-3. The radiation is then separated by filters into the appropriate spectral bands before each band is focussed on to four rows of six photomultiplier detectors. Thus six scanlines are acquired per swath in each band. With the satellite moving forward in its orbit, a continuous strip image of the Earth's surface is obtained.

The scanning pattern is illustrated in Fig. 4.12a. During each scan, the voltage produced by each detector is sampled every 9.95 microseconds during the retrace period. For one detector, approximately 3,300 samples are taken along an individual scan line. Thus the instantaneous pixel size of 79x79 m moves about 56 m over the ground between each sample. As shown in Fig. 4.12b, this makes the effective ground pixel size of the scanner equal to 56x79m. The analogue signals produced by each detector are converted into digital values (0 - 63) representing 64 different brightness values of the sensed area of an

individual pixel. These values are formatted into a 15 megabit data stream before transmission to ground stations. The scanning mirror oscillates at a frequency of 13.62Hz to scan from west to east and retrace as the satellite travels southward in its orbit. This corresponds to a period of 73.42 milliseconds, giving 36.71 milliseconds for each of the scan and retrace motions.

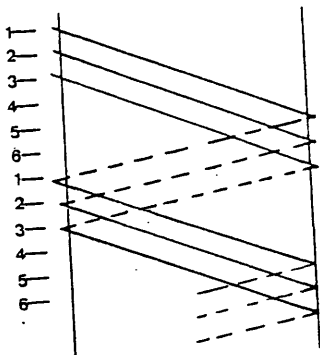


Fig. 4.12a Scanning Pattern of Landsat MSS.

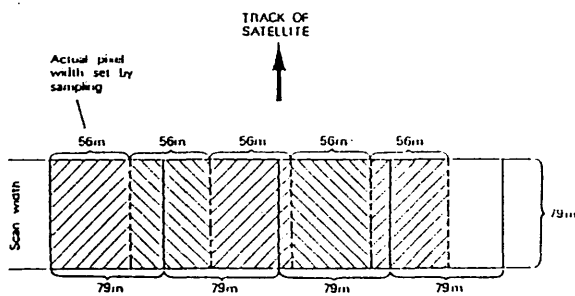


Fig. 4.12b Sampling of the Along Scan Data.

During retrace, the incident radiation is blanked out by the mechanical shutter and during every other mirror retrace, the individual detectors in the four bands are exposed to a rotating variable density wedge filter illuminated by on-board calibration lamps to provide the calibration data required for each detector. The calibration data for the two detectors of Band 8 (the thermal infrared band) used in Landsat 3 were provided by exposing them to a temperature reference during mirror retraces when Bands 4 to 7 were not being exposed to the calibration lamps. To avoid data being acquired during the non-linear part of the mirror oscillation, the data acquisition is made during the middle 33.0 milliseconds of the scan period. As mentioned above, the analogue signal of each detector is converted to digital values of brightness. When the satellite is within the sight of a ground receiving station, the digital data are directly transmitted from the satellite to the station in real-time. Over locations remote from a receiving station, two on-board tape

recorders are used to store up to 60 minutes of data. The recorded data are then transmitted to the ground when the satellite passes over a ground receiving station.

At the ground receiving stations, the received data are stored on magnetic tapes for subsequent processing. During image processing, the continuous strip MSS imagery is transformed to individual framed images, each covering a ground area of 185km x 185km. These are produced as hard copy on photographic film or kept in digital form on computer compatible tapes (CCTs)

4.4.2 Landsat MSS Data Processing

As shown in Fig. 4.13, Landsat MSS image processing comprises the so-called annotation and correction steps. In the annotation step, the spectral bands are assigned to their respective images and the time and date of acquisition, orbit number, Sun azimuth and elevation; etc. are attached to the product. In the correction step, first a radiometric correction is made using the calibration data. Next a geometric correction is made within each band in which the various systematic displacements and distortions discussed above are removed and adjustments are also made so that the accurate registration of images of the same ground scene from different bands is obtained.

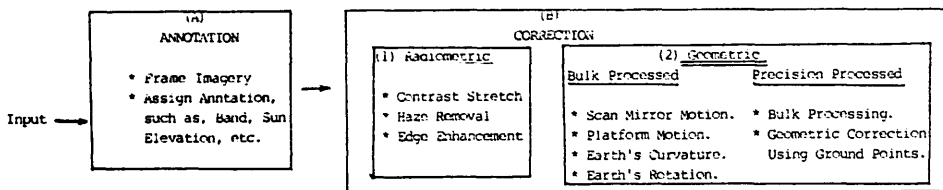


Fig. 4.13 MSS Image Data Processing.

The accuracy with which the geometric correction is made varies from one processing facility to another. In NASA's processing facility at the Goddard Space Flight Centre (GSFC), in which the images used in this investigation were processed, two different levels of geometric

correction are applied to yield three different classes of images (bulk-processed, precision-processed and intensive-processed). In bulk-processed images, correction of the above discussed systematic distortions is made using calibration and satellite control data only. In precision-processed images, ground control points are identified in the images and utilized to further refine the geometric corrections applied in the bulk processing. When the precision processing is applied to the digital images, the resulting digital images are called intensive-processed images. The images which have been used in this investigation were bulk processed.

Bulk image processing is based on the computation of a rhombus image border defining the image frame and centered on the Earth's surface at the location of the centre of the required image. The centre of the image is determined from the satellite ephemeris and the telemetered satellite pitch and roll. The border is oriented at an azimuth determined by the satellite heading plus the telemetered satellite yaw angle. As the film writer exposes an MSS image within the computed image border, extensive geometric corrections for (1) panoramic distortion; (2) scan non-linearity, jitter; (3) change in satellite attitude; (4) change in satellite altitude; (5) Earth curvature; and (6) Earth rotation are applied to the scanning beam. The major distortions among these are those caused by Earth curvature and Earth rotation.

The locations of 9 x 9 grid points within the image are used for the computation of the systematic distortions. Thus the distortions caused by the satellite attitude and altitude are computed at these grid points based on the telemetered data. The corrections at other image points are interpolated from these grid point values before being corrected for by applying small correcting deflections to the scanning beam. The images are fitted to a Space Oblique Mercator (SOM) map projection system with the satellite orbit as central meridian, while tick marks on these images may be given in either the UTM projection or in the geographic coordinate system of latitude and longitude.

Bulk-processed MSS images are produced on film using devices such as Laser Beam Recorder (LBR). The LBR exposes the film by a high energy laser beam scanning a series of lines across the film. As it scans, the beam intensity is modulated by the sensor data read from magnetic tape. The basic deflection pattern of the beam is supplied by the internal controller of the LBR. Additional deflection and intensity modulation are applied through a special digital computer. Intensity modulation is computed in the digital computer in the radiometric

correction step using sensor calibration data, while the deflections are computed as corrections to the systematic distortions inherent in the image. As discussed above, these systematic corrections are computed using calibration data, altitude and attitude data and the satellite ephemeris.

4.5 Landsat TM Sensor

The Thematic Mapper (TM) is an advanced type of multispectral scanning sensor designed to achieve higher image resolution, extended spectral coverage, improved geometric fidelity and greater radiometric resolution compared with those obtained with the MSS. As mentioned in Chapter 2, TM data are sensed in seven spectral bands simultaneously with Bands 1 to 5 and Band 7 having an IFOV of 30m on the ground while Band 6 has an IFOV of 120m. Table 2.2 gives the spectral ranges of the seven bands. TM is mounted on the spacecraft with its optical axis lying in the across track direction. Fig. 4.14 shows the optical and electronic subsystems of the TM sensor.

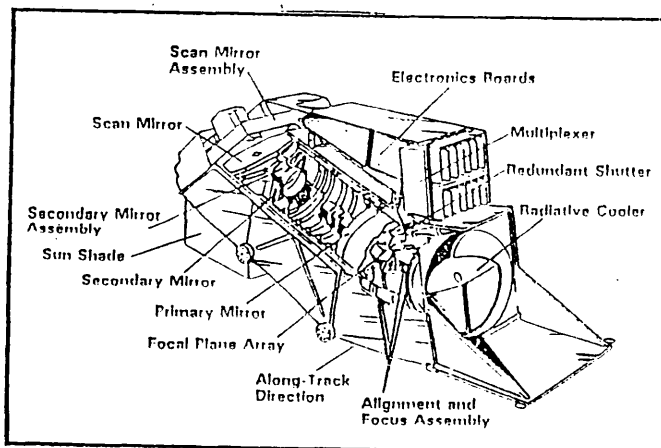


Fig. 4.14 TM Sensor.

Directly above the sunshade aperture is the scan mirror assembly including the mirror drive mechanism and scan monitor hardware. The scan mirror oscillates in the across-track direction to scan the Earth's surface from west-to-east in the forward direction and from east-to-west in the reverse direction, during the descending (daylight) portion of the orbit. In both directions, it allows the radiation coming from the Earth to pass along the telescope to be focussed on the detector arrays. The scan mirror is designed to scan equal ground areas at all scan angles and to operate linearly over a scan angle of 7.7 degrees. At the end point of each scan, about 10.7 milliseconds

turnaround time elapses before the next scan begins. A scan angle monitor on the scan mirror passes signals to the timing mechanism in the multiplexer to indicate the beginning, midscan, and end of the period of the scan mirror's travel while data are being taken in the forward scan direction. Equivalent signals are generated for the beginning, midscan, and end of the reverse scan. A line stop signal indicating the end of the formatting period is buffered and retransmitted to the Scan Line Corrector (SLC) to reset itself for the next scan. A second signal, delayed from the line stop signal by a programmable period, acts as a synchronization signal to the calibration shutter. These are scan angle monitor pulses which provide for synchronization of the scan line corrector, calibration shutters, filter shutter, and dc restore circuits (USGS & NOAA, 1984)

The SLC consists of a pair of parallel beryllium mirrors mounted at an angle of 45° with respect to the telescope optical axis. The whole subsystem rotates about an axis normal to the scan mirror oscillation axis to rotate the line of sight of the TM backward along the ground track direction to compensate for the forward motion of the spacecraft. This allows the scan mirror to produce straight scan lines perpendicular to the ground track. During the turnaround period, when the SLC receives the line stop signal, it jumps to its reset position so that the next set of scan lines is parallel to the previous one with no gaps and no double imaging.

The radiation coming from the Earth's surface then passes through f/6.0 Ritchey-Chretien telescope with $f = 243.8$ cm. With the IFOV of 42.5 urad, this focal length gives an image pixel size of 104 μm . From the satellite altitude of 705 km, this gives a ground pixel size of 30 m. The telescope uses a 41.15 cm aperture diameter primary mirror and a 15.7 cm. aperture diameter secondary mirror to correct for spherical aberration and coma simultaneously. Both mirrors are fabricated from ultra low expansion titanium silicate glass which is silver coated by SiO_2 . The telescope focusses the radiation on the prime focal plane.

The prime focal plane detector array consists of the silicon detectors and preamplifier components for the first four visible spectral bands located at the prime focus of the primary telescope. For each of these four bands, the detector assembly consists of an array of 16 monolithic silicon detectors to convert the sensed scene energy into low level electrical signals which are then amplified. Fig. 4.15 shows the detector arrangement used in these arrays.

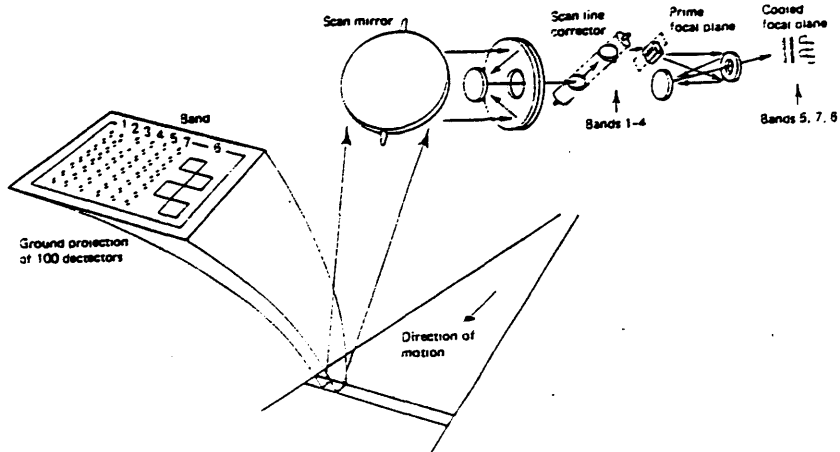


Fig. 4.15 Detector Arrangement in the TM Sensor.

The relay optics mechanism consisting of a folding mirror and a spherical mirror is used to transfer the scene energy onto a second focal plane located in the radiative cooler, i.e. in the cooled focal plane array. These two mirrors are mounted in a graphite composite structure containing cylindrical assemblies that provide a capability for the on-orbit alignment and focus of the cooled focal plane (with detectors for Bands 5 to 7) with respect to the prime focal plane. The relay system has an optimum demagnification of 0.5 to allow the use of smaller detectors in the cooled focal plane.

The detector assembly in the cooled focal plane consists of a 16-element monolithic indium antimonide (InSb) detector for each of Bands 5 and 7 arranged in a manner similar to those of the prime focal plane. Finally a 4-element monolithic mercury-cadmium-telluride (MgCdTe) detector is provided for Band 6 (the thermal band). The cooled focal plane can be maintained at any one of three selectable temperatures - 90° K, 95° K, and 105° K - to within $+0.2^{\circ}$ K using a thin film heater.

4.5.1 Internal Calibration

The on-board calibrator is mounted in front of the prime focal plane and consists of three tungsten filament lamps for Bands 1 to 5, and Band 7; a blackbody for Band 6, and a flex-pivot-mounted resonant shutter. The shutter oscillates at the same time frequency as the scan mirror. Thus the shutter introduces the calibration source energy and a black dc restoration surface into the detector field of view during the

turnround time of each scan mirror cycle. An imaging scheme is used on the output end of the shutter to ensure uniform calibration without stray radiation. Thus the method for transmitting radiation to the moving calibration shutter allows the lamps to provide radiation independently and to contribute proportionally to the illumination of all detectors.

4.5.2 **Electronic Module**

This contains the power supply, the printed circuit boards containing the drives and control electronics for all mechanisms and heaters, the command and telemetry distribution and collection circuitry, the signal processing postamplifiers that limit the system frequency response, and the multiplexer. The multiplexer encodes all the radiometric data, multiplexes the outputs from all the detectors and converts them to digital data in the form of 8-bit words that comprise the 84.9 Mbps stream transmitted to the Earth.

4.5.3 **TM Ground Segment**

The ground segment activity of the TM system consists of three main parts. The first covers the TM data reception, recording on magnetic tapes and transmission to GSFC. The second covers the processing facilities comprising the TM Image Processing System (TIPS) at the GSFC. Finally the third involves the archiving, final processing and distribution of the final products carried out at NOAA's EROS Data Centre (EDC). Since privatization, the archiving, final processing and distribution of Landsat images have been handled by EOSAT.

4.5.3.1 **GSFC Preliminary Processing**

At GSFC, the TM data received from Landsat will first have been recorded on high density magnetic tapes (HDT). In preparation for the image processing, the GSFC then generates directories of these digital tapes together with mirror scan correction data, quality information, and a systematic correction data (SCD) tape. This systematic correction data (NASA, 1984) involves:

- (i) correcting and validating the mirror scan and PCD data recorded earlier;
- (ii) making provision for image framing by generating a series of scene centre parameters;
- (iii) synchronizing the telemetry data with the video data;
- (iv) estimating the deviation from the linear motion of the scan

- mirror and the scan line correction mechanism;
- (v) generating benchmark systematic correction matrices for specified map projections; and
- (vi) producing along- and across-scan high-frequency scan line matrices representing the image data.

All these data are processed and reformatted into a digital tape (SCD) which is used during the geometric correction process.

4.5.3.2 **TM Image Processing System at GSFC**

After the preparation of input data, the TM data on the HDT and the corresponding SCD tape are input to TIPS.

- (i) TIPS screens the raw TM data;
- (ii) reads in the image data required for the specific scene;
- (iii) builds histograms from the brightness values in the scene;
- (iv) extracts radiometric calibration values; and
- (v) selects control point neighbourhoods in preparation for the radiometric and geometric correction computations.

Radiometric lookup tables are then calculated using computed gain and offset values. TIPS also computes geometric correction matrix values based on the SCD and control point correlation information. Header, annotation, and trailer data are also formatted at this stage.

Finally TIPS documentates, aligns and converts the data from band-interleaved-by-pixel (BIP) to band-interleaved-by-line (BIL) format; then applies radiometric corrections to the data using the lookup tables generated earlier; appends the geometric correction information; and writes a partially processed TM archive data tape (HDT-AT).

During the initial product generation, TIPS reformats the BIL tape to BSQ format, applies the geometric corrections computed during archive generation above, and creates the necessary header, annotation, and trailer data files. The fully processed data **are** then written on a High Density Tape denoted HDT-PT.

4.5.3.3 **Final Processing at EROS Data Centre**

The final products include either partially or fully processed digital data produced as CCTs or fully processed data written on 241-mm wide film. These can be generated directly from the corresponding HDT-AT's (partially processed) or HDT-PTs (fully processed) data

written on High Density Tapes which have been sent to the TM Tape Archive. However, CCT-As and CCT-Ps are also shipped to the NOAA Landsat Archive in Sioux Falls where they are stored and can be duplicated for the user requesting a specific product. A 241-mm film master is also shipped to the NOAA archive, where it may be used to create the user's film product. Since privatization, user requests have been handled by EOSAT through the EROS Data Centre. This will remain the case until the EOSAT processing facility now being built in Maryland is completed when all processing activities will be carried out and supervised by EOSAT.

4.5.4 **TM User Products**

At the moment, TM data are distributed by EOSAT through the EROS Data Centre. TM products which are available to the user are as follows:

i) Photographic products are available in 241-mm film full scenes in monochrome (black-and-white) or colour. For each scene, seven monochrome images are available, while colour composites of these images are available in any three colour combinations.

ii) Digital products are available on CCTs at densities of 6,250 or 1,600 bits per inch. One quadrant of scene data is contained on one 6,250-bpi or three 1,600-bpi CCTs. These come in four options:

- 1- BSQ or BIL format;
- 2- Radiometrically corrected data ("A") or both radiometrically and geometrically corrected data ("P");
- 3- Nearest neighbour or cubic convolution resampling; or
- 4- the Space Oblique Mercator, the Universal Transverse Mercator (UTM) or the Polar Stereographic map projection.

4.6 **Ground Resolution of MSS and TM Images**

Performance values for Landsat sensors are often quoted as pixel sizes based on the IFOVs of these sensors. As mentioned above for the MSS, the ground pixel size is about 79 m, while for the TM the ground pixel size is 30 m. However, these values can be misleading when a comparison between different sensor systems is attempted and provide no indication of the percentage of information which can be extracted from images acquired by these sensors for a given geographical area. A more definitive comparison between various sensors can be made using the modulation transfer functions (MTFs) of these sensors. In order to

make this comparison relevant to the low contrast conditions prevailing in an operational environment, the MTFs should be scaled down to a modulation of 0.23 (1.6:1) target contrast. It is known that for a normal observer to resolve low contrast targets at the resolution limit, a modulation of 5% to 10% is required (Welch and Pannell, 1982). Therefore, the spatial frequencies corresponding to 10% modulation can be accepted as measures of system resolution. Using the MTF curves of the MSS and the TM, Welch and Pannell (1982) estimated the ground resolution at low contrast to be 120 m and 48 m for the MSS and the TM respectively.

4.7 Geometrical Analysis of Landsat Scanner Images

Many investigators have discussed the geometry of optical mechanical scanners in general and derived mathematical models for the photogrammetric rectification of their imagery. Some have developed methods and equipment to rectify these images. A brief summary of some of those efforts would seem to be appropriate before commencing the analysis of the MSS and TM scanner imagery.

In a series of papers, Derenyi & Konecny, (1964; 1966) first applied a photogrammetric approach to the imagery produced by optical mechanical scanners. At that time, these were entirely airborne scanners. These papers dealt with the basic recording system, the scan angle effects of varying resolution size and panoramic displacement mentioned in Section 4.3.1 and the dynamic nature of the image acquisition, scale variation and orientation found in scanning system. The study of the exterior orientation effects was based upon a modification of Hallert's differential formulae of equations (4.11) for frame photography. In the second of the two papers, the authors presented projection equations which considered the dynamic nature of the imagery as the elements of exterior orientation of scanner imagery change from ^{one} point to another. These equations constitute the basis for a strict image rectification procedure if the orientation elements are known for every instant of image acquisition. These elements may be provided by satellite positioning and attitude control systems capable of providing satellite position and attitude to very high accuracies. These equations were then linearized utilizing Taylor's series expansion with some approximation for the variables involved.

In a further series of papers, Konecny (1970; 1972; 1974; 1975; 1976) summarized the basic projective relationships associated with various remote sensing systems. These papers dealt with methods of approximate relative orientation and the rectification of images

recorded with dynamic systems. Also they discussed the accuracies which may be expected utilizing these systems. The last of these papers (Konecny, 1976) provides an excellent summary of most of the work done on the geometry of non-conventional remote sensing systems up till then.

Another paper by Taylor (1971) provided a useful insight into the rectification procedures for infrared scanner images. Rectification equations were derived from basic projection equations by first assuming a perfect orientation case, and then analysing the image displacements which were produced after subsequent perturbations in roll, pitch, and yaw.

Markarian et al, (1971) presented a scheme which utilized general polynomials for the rectification of digitized imagery. The concept of treating the data as an uncorrected input used to generate a rectified output array was used, and the principle of digitally "stepping" on the output array and placing gray scale values from the corresponding positions in the distorted input array was advocated. Further it was recommended that the nearest neighbour be used as the gray scale value from the input array, rather than to attempt the interpolation of gray scale values.

From this short review, one concludes that the mathematical models expressing the basic geometry of the scanner imagery had been well developed even before the launch of Landsat-1. However, further interest in the geometric aspects and cartographic applications of optical mechanical scanners is evidenced by the increase in the published literature in those fields in the early 1970s following the launch of Landsat-1.

As early as 1970, Colvocoresses analyzed image distortions and displacements in MSS imagery for five possible sources, namely Earth's curvature, atmospheric refraction, exterior orientation angular elements, terrain relief and map projection. He concluded that the effect of atmospheric refraction is negligible and that of the terrain relief would be minimal except in extreme cases.

Forrest, (1974) examined the cartographic application of space scanner imagery in some detail. He considered the scanner geometry, resolution, and the use of ground control points extracted from existing maps to resect for sensor orientation elements to achieve a precision beyond that obtainable from satellite ephemeris data.

A series of papers by Kratky, (1972a; 1972b; 1974) addressed the geometric problems in MSS imagery from a photogrammetric point of view. He derived functional formulae to account for the continuous variation in the orientation of scanning systems. After presenting the basic collinearity equations, he investigated the use of polynomials and harmonic functions to approximate the variation in orientation with time. These equations were presented in matrix form for a resection computation to solve for the coefficients of these functions. Because of the smoother motions of spacecraft, it was possible to incorporate small angle approximations into the analysis yielding simplified equation forms.

Wong (1975) investigated the use of the two-dimensional polynomials which he had developed earlier for use with television systems, for the planimetric rectification of MSS images. He explained the ease with which this rectification can be carried out to obtain satisfactory results with Landsat MSS images. Since then, the use of polynomials in the rectification and transformation of satellite scanner images has become most common.

Several mathematical models have been used by various investigators to model the residual distortions in the bulk processed MSS imagery in the course of their rectification and accuracy testing. These mathematical models are either of the 3D projective type developed from the rigorous geometrical analysis of MSS imagery or they follow a 2D interpolative approach using polynomials of various degrees. The polynomials have been implemented in computer programs in which points on the images were measured and fitted to the corresponding ground coordinates to determine the accuracy of the fit and hence to identify the most effective terms which could be used to reduce the errors present in the image. These effective terms are then taken together to form a specific mathematical model for use with space scanner imagery. These mathematical models could also be used for the rectification of the imagery in digital form in a process similar to that used in the precision processing of the images.

4.7.1 Projective 3D Transformation Models

These are based on the knowledge or an estimate of the effects of the exterior orientation elements on the geometry of the imagery. In these methods, an attempt is made to model and estimate the parameters of the functions assumed to represent the behaviour of the scanner orientation elements.

4.7.1.1 Collinearity Equation Models

The collinearity condition implies that the perspective centre of an imaging system, an object point and its corresponding image point all lie on a straight line. The mathematical equations which describe or enforce this condition are known as collinearity equations and represent the heart of analytical photogrammetry. Fig. 4.16 illustrates the collinearity condition in conventional frame photography.

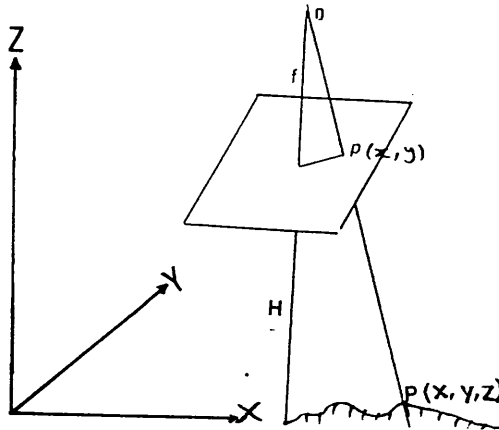


Fig. 4.16 Collinearity Condition in Frame Photography.

The standard collinearity equations expressing this case are as:

$$x = -f \frac{m_{11}(X-X_0) + m_{12}(Y-Y_0) + m_{13}(Z-Z_0)}{m_{31}(X-X_0) + m_{32}(Y-Y_0) + m_{33}(Z-Z_0)} \dots\dots\dots(4.17)$$

$$y = -f \frac{m_{21}(X-X_0) + m_{22}(Y-Y_0) + m_{23}(Z-Z_0)}{m_{31}(X-X_0) + m_{32}(Y-Y_0) + m_{33}(Z-Z_0)}$$

- where x, y are the image coordinates of point p ;
- X, Y, Z are the ground coordinates of point p ;
- X_0, Y_0, Z_0 are the ground coordinates of the exposure station;
- f is the focal length of the camera; and
- $m_{11}, m_{12}, \dots\dots\dots m_{33}$ are elements of the rotation matrix expressed as functions of orientation parameters w, ϕ, k .

Line scanner images differ from frame photography in that, instead of the whole image being acquired instantaneously by allowing the radiation coming from the ground scene to pass through the lens and

expose the whole of photographic film, the image is acquired line by line. As can be seen from Fig. 4.17, with the continuous variation of orientation elements, each scan line will have a separate set of orientation parameters and therefore requires a separate set of collinearity equations.

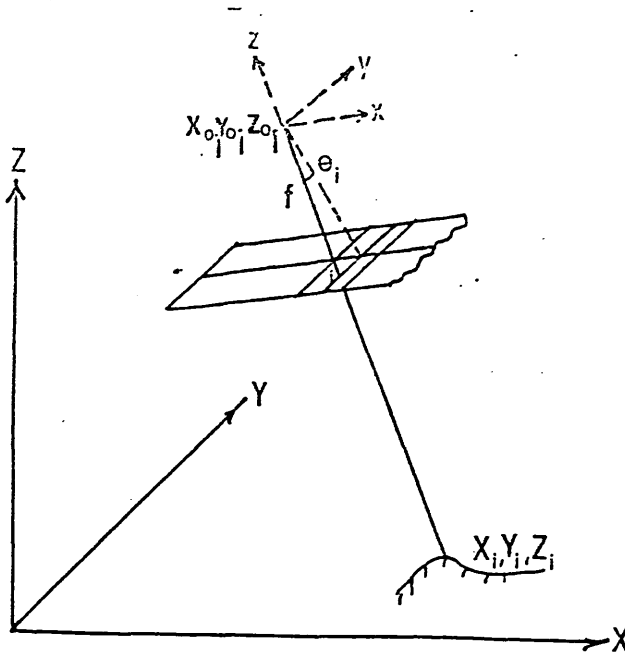


Fig. 4.17 Collinearity Condition in Scanner Image.

Hence each scan line has to be considered separately and therefore the x-coordinate of all points within one scan line is always zero. Furthermore, the y-coordinate can be expressed in terms of the equivalent focal length and the scan angle as $y = f \cdot \tan \theta$. The collinearity equations for a scan line can therefore be expressed as:

$$0 = -f \frac{m_{11}(X-X_0) + m_{12}(Y-Y_0) + m_{13}(Z-Z_0)}{m_{31}(X-X_0) + m_{32}(Y-Y_0) + m_{33}(Z-Z_0)} \dots\dots\dots (4.18)$$

$$f \tan \theta = -f \frac{m_{21}(X-X_0) + m_{22}(Y-Y_0) + m_{23}(Z-Z_0)}{m_{31}(X-X_0) + m_{32}(Y-Y_0) + m_{33}(Z-Z_0)}$$

These represent most closely the actual physical situation as it occurs during scanning. As mentioned above, the orientation parameters and the position of the projection centre vary continuously with time and so a continuous record of these parameters or a method to evaluate

them is required if the collinearity equations are to be used in the image rectification. In practice, the measurement and recording of these parameters to a satisfactory accuracy is very difficult. However in spaceborne scanner systems, the orientation parameters can be recorded at selected points (anchor points) along the satellite path using a subsystem such as the Attitude Control and Measurement system used in the Landsat series. The measured values are then telemetered to the ground receiving station together with the image data. The positions of the projection centres at the same anchor points can be provided by the satellite tracking system. The values of the exterior orientation parameters at points between the selected anchor points can be computed using mathematical models that express the variation of these parameters as functions of time, i.e with changes in the x-coordinate. After an assumption of appropriate functions to represent the behaviour of the exterior orientation elements, a solution may be obtained using sufficient object space control points. Normally an iterative technique using the updated estimates from each preceding iteration is utilized. Once the coordinates and tilts of the projection centres have been determined, the coordinates of any other previously unknown points may be measured and calculated.

Since the functions may not represent accurately the variation in the exterior orientation elements with respect to the x-coordinate of the image, it is often recommended to treat the image in sections. In this case, it is necessary to introduce some constraints at the section interfaces to ensure that the same results are obtained for each element lying on either side of the junction. A limitation to this model is that some exterior orientation elements are highly correlated so that recovery of all the elements may not be possible. Also it is necessary to ensure that the relief displacement in hilly areas should be compensated for if this model is to give an accurate result, especially with airborne scanner images.

4.7.1.2 Simplified Projective Models

Since the recovery of the exterior orientation parameters, based upon the scanner collinearity equations and ground control points is not possible for each individual scanline, the use of such equations requires an approximation. Thus other methods for scanner imagery resection have been sought in which the resection accuracies might approach those obtainable by the collinearity equations. One such method is the use of parametric formulæ derived from the collinearity equations after some assumptions. One set of these formulae is that developed by Kratky (1971) to express the distortions in MSS images

taking into account the effects of scanner geometry, panoramic distortion, Earth rotation, satellite orbit, satellite attitude and map projection.. In the development of these formulæ Kratky used the following third degree polynomials to describe the attitude of the satellite:

$$\begin{aligned} k &= k_0 + a_1 x + a_2 x^2 + a_3 x^3 \\ \emptyset &= \emptyset_0 + b_1 x + b_2 x^2 + b_3 x^3 \\ w &= w_0 + c_1 x + c_2 x^2 + c_3 x^3 \end{aligned}$$

Kratky's formulae take the following form:

$$\begin{aligned} \Delta x &= (dX/m + f\emptyset_0) + x(dm/m + fb_1) + yk_0 + a_1xy + a_2x^2y + b_2x^2f + \\ &\quad a_3x^3y + b_3x^3f. \\ \Delta y &= dY/m - ydH/H + (f + y^2/f)w_0 + x(f + y^2/f)c_1 + x^2(f + y^2/f)c_2 \\ &\quad + x^3(f + y^2/f)c_3. \end{aligned}$$

..... (4.19)

where: dX, dY are corrections to the map coordinates (X, Y) of a ground control point;

m, dm are the scale factor and its correction respectively;

H, dH are the satellite altitude and its correction;

f is the effective focal length of the satellite;

x, y are the image coordinates of a point; and

$\Delta x, \Delta y$ are the distortion values in the point x, y coordinates.

Equations (4.19) can be rearranged as:

$$\begin{aligned} \Delta x &= (dX/m + f\emptyset_0) + x(dm/m + fb_1) + yk_0 + a_1xy + a_2x^2y + b_2x^2f + \\ &\quad a_3x^3y + b_3x^3f. \\ \Delta y &= (dY/m + fw_0) + c_1fx - (dH/H)y + (w_0/f)y^2 + c_2fx^2 + (c_1/f)xy^2 \\ &\quad + c_3fx^3 + (c_2/f)x^2y^2 + (c_3/f)x^3y^2. \end{aligned}$$

..... (4.20)

Equations (4.20) are two polynomials taking the following general form:

$$\begin{aligned} \Delta x &= a_0 + a_1x + a_2y + a_3 xy + \dots + a_7x^3y \\ \Delta y &= b_0 + b_1x + b_2y + b_3 xy + \dots + b_8x^3y^2 \end{aligned}$$

..... (4.21)

Therefore polynomials in the form of equations (4.21) can be used to transform the image to the required ground space, in which case, no attempt is made to compute the values of the exterior orientation parameters.

Other simplified projective formulae can be derived from Hallert's equations for frame photographs (equations (4.11)) but which take into account scanner geometry. These equations are derived from the consideration of the effects of very small deviations of exterior orientation parameters from the ideal situation of vertical frame photographs and assuming flat terrain. Similarly if the satellite is assumed to be orbiting over a flat terrain at a constant altitude, the overall effects of exterior orientation parameters on the ground coordinates of the points are as shown in equations (4.13). From equations (4.13), the transformation from image space to the object space can be approximated by the following form of equations which are shown to express the displacements caused by the platform motion and attitude (Derenyi, 1974; Baker & Mikhail, 1975).

$$\begin{aligned}
 X &= X_0 + dX_0 + Hd\phi + H\tan\theta dk \\
 Y &= Y_0 + dY_0 + H\tan\theta + \tan\theta dZ_0 - H(1 + \tan^2\theta)dw \\
 &\dots\dots (4.22)
 \end{aligned}$$

where X, Y are ground coordinates of a point;

X_0, Y_0, Z_0 are the coordinates of the scanner at the moment of imaging the reference scan line, i.e the scan line in which the point is located;

dX_0, dY_0 are the changes in X_0, Y_0 with time;

θ is the scan angle;

H is the satellite altitude; and

w, ϕ and k are the roll, pitch and yaw angles respectively.

Again the exterior orientation parameters may be provided at selected anchor points and the variation of these parameters within the image can then be computed as functions of time (i.e in terms of x-coordinate) from these anchor points. Any number of polynomial forms may be defined to represent the variation of the exterior orientation elements within the image. As an example, the assumption may be made that the change in each orientation element varies as a linear function of x within each section. Then:

$$\begin{aligned}
X_0 &= a_x + b_x x \\
Y_0 &= a_y + b_y x \\
&\cdot \\
&\cdot \\
&\cdot \\
k &= a_k + b_k x
\end{aligned}
\tag{4.23}$$

These relationships may be substituted directly into equations (4.22) and after regrouping the following equations result.

$$\begin{aligned}
X &= (X_0 + a_x - Ha_\phi) + (a_x - Hb_\phi)x - Ha_k \tan\theta - Hb_k x \tan\theta \\
Y &= (Y_0 + a_y + Ha_w) + (b_y + Ha_w)x + (H + a_z) \tan\theta + b_z x \tan\theta + \\
&\quad Ha_w \tan^2\theta + Hb_w x \tan^2\theta
\end{aligned}
\tag{4.24}$$

If the first two terms of the series expansion are taken for $\tan\theta$, i.e., $\tan\theta = \theta + 1/3 \theta^3$, and using $\theta = y/f$ where f is the effective principal distance, the resulting polynomials are:

$$\begin{aligned}
X &= a_1 + a_2 x + a_3 y + (a_3/3c_2)y^3 + a_4 xy + (a_4/3f^2)xy^3 \\
Y &= b_1 + b_2 x + b_3 y + (b_3/3c_2)y^3 + b_4 xy + (b_4/3f)xy^3 + b_5 y^2 + \\
&\quad (2b_5/3f^2)y^4 + (b_5/9f^4)y^6 + b_6 xy^2 + (2b_6/3f^2)xy^4 + (b_6/9f^4)xy^6
\end{aligned}
\tag{4.25}$$

The last two terms of the second equation of equations (4.25) will be zero if the system is roll stabilized. Again equations (4.25) take the form of a 2D transformation, since they can be written as in equations (4.24) and used for the transformation of scanner images without the need for the computation of the exterior orientation parameters.

$$\begin{aligned}
E &= a_1 + a_2 x + a_3 y + a_4 xy + a_5 y^3 + a_6 xy^3 \\
N &= b_1 + b_2 x + b_3 y + \dots + b_7 y^2 + b_8 y^4 + b_9 y^6 + \\
&\quad b_{10} xy^2 + b_{11} xy^6
\end{aligned}$$

where E, N are easting and northing of a point;
 x, y are the corresponding image coordinates; and
 a's, b's are the transformation parameters.

4.7.2. **Two-dimensional Transformation Techniques**

In practice, however, the collinearity equation approach has not been used too much, both because of the lack of familiarity of the remote sensing community with such a photogrammetric approach and the fact that its implementation is difficult without giving an appropriate improvement in the accuracy of the final result. Thus as an alternative, two-dimensional (2D) image transformation formulae have been widely used for image rectification. These formulae are applied to determine the type and magnitude of the image distortions at selected ground control points from which correction values can then be computed for the rest of the image using interpolative techniques. In these techniques, the coordinate differences (discrepancies) between corrected and uncorrected image coordinates are assumed to be a realization of a two-dimensional stochastic field and attempts are made to obtain estimates for these differences by non-parametric interpolative methods. With these methods, no effort is made to estimate the parameters associated with orientation. Instead the common approach is to use the mathematical formulae as transformation models. Using the ground control points, the parameters of the transformation model are computed. Then the computed parameters are substituted back in the transformation model which is then used to compute the unknown coordinates of the points of which the image coordinates have been measured. As mentioned above, in practice, simple 2D transformations, particularly polynomial transformations, are used for this purpose. The choice of the order of the polynomials in a particular image transformation is determined by the degree of accuracy required for the particular application, the number of control points required to achieve that accuracy, and the computational facilities available.

The polynomials which are most commonly used for scanner image transformation are those originally derived by Wong (1968) to express the geometrical distortions in television cameras. In 1975, Wong used these polynomials to carry out the transformation of MSS images and demonstrated the ease with which they can be incorporated in a computer program. He also showed that quite satisfactory results can be obtained with less computational effort compared to the projective models

discussed above. Wong's polynomials take the following form:

$$\begin{aligned}
 E &= a_0 + a_1x + a_2y + a_3xy + a_4x^2 + a_5y^2 + a_6x^2y + a_7xy^2 \\
 &\quad + a_8x^3 + a_9y^3 + a_{10}x^3y + a_{11}xy^3 + a_{12}x^4 + a_{13}y^4 + \\
 &\quad a_{14}x^2y^2 + a_{15}x^3y^2 + a_{16}x^2y^3 + a_{17}x^5 + a_{18}y^5 + a_{19}x^3y^3 \\
 N &= b_0 + b_1x + b_2y + b_3xy + \dots + \\
 &\quad \dots + \\
 &\quad \dots + b_{19}x^3y^3 \\
 &\hspace{20em} \dots \dots \dots (4.27)
 \end{aligned}$$

where a_i, b_i ($i=0$ to 19) are the transformation parameters.

Each of the equations of either the E or N coordinates in equations (4.27) includes the following terms (taking E as the example):

- a constant term, e.g. a_0 (1 term)
 - linear terms, e.g. a_1x and a_2y (2 terms)
 - second-order terms, e.g. $a_3xy; a_4x^2; a_5y^2$ (3 terms)
 - third-order terms, e.g. $a_6x^2y; a_7xy^2; a_8x^3; a_9y^3$ (4 terms)
 - fourth-order terms, $a_{10}x^3y; a_{11}xy^3; a_{12}x^4; a_{13}y^4; a_{14}x^2y^2$ (5 terms)
- etc.

Thus the number of terms of one specific order in the equations will always be one greater ($n+1$) than the order of the terms, (n) e.g. there are five fourth-order terms, four third-order terms, etc.

It is most helpful when deciding which of these terms to use in the transformation and rectification of the imagery, to understand the effects of the individual terms of equations (4.27) on the transformation and the pattern of distortion or displacements which can be corrected by each of these terms. Figs. 4.18 and 4.19 show the shifts in E and N which will result from the use of the individual correction terms in each of the two equations above.

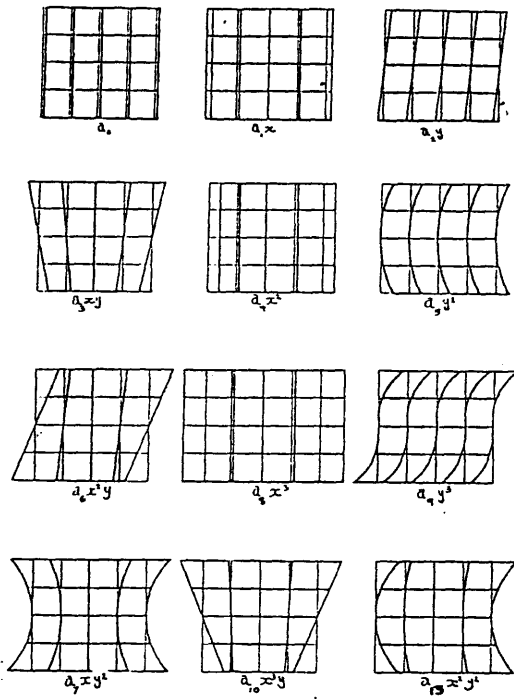


Fig. 4.18 Corrections Introduced in Eastings.

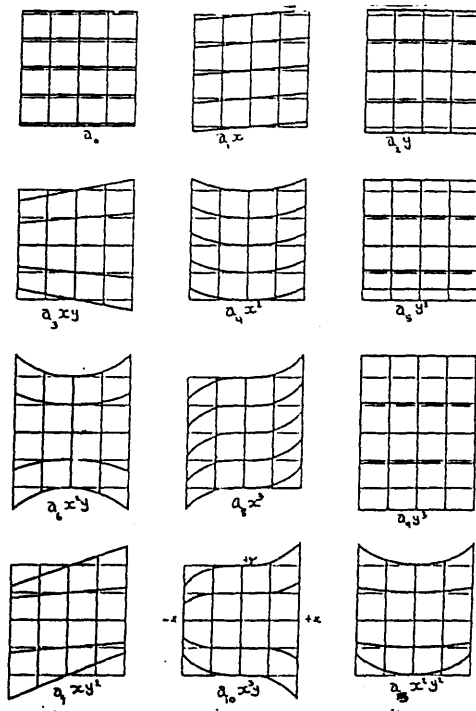


Fig. 4.19 Corrections Introduced in Northings.

In this investigation, Wong's two-dimensional (2D) image transformation methods will be applied. As has been shown above, the maximum relief displacement in the test area is less than the ground pixel size of the image. Thus it appeared quite appropriate to apply such a two-dimensional transformation in the accuracy tests. Using a set of control points, the transformation parameters are computed by fitting the image coordinates of these control points to their respective ground coordinates using a least squares solution. The transformation parameters are then used to transform the image coordinates of a set of check points into the ground coordinate system, the residuals at these points being computed as the differences between the computed coordinate values and the given ground coordinates. The various transformations carried out in this test and the procedure followed in their execution are as follows:

(1) **Linear Conformal Transformation**

This simple linear transformation was used to transform the measured scanner image coordinates of points into the corresponding set of terrain coordinates and provide an appropriate measure for the accuracy of the bulk processed MSS images over the test area before any attempt was made to use higher order terms. The transformation parameters are computed by fitting the image to the known ground coordinates of well distributed control points. These parameters are then used to compute the ground coordinates of any other measured point in the image. The computed ground coordinates are compared with the corresponding terrain coordinates of check points which have been scaled from the maps and the root mean square errors (r.m.s.e) values are computed. The linear conformal transformation is expressed mathematically as:

$$\begin{aligned}
 E_i &= ax_i - by_i + c \\
 N_i &= bx_i + ay_i + d
 \end{aligned}
 \dots (4.28)$$

where E_i & N_i are the easting and northing coordinates respectively of point i ;

x_i & y_i are the corresponding image coordinates; and
 a , b , c and d are the transformation parameters.

(2) **Affine Transformation**

An affine transformation has also been carried out to detect and correct any affinity present in the imagery. For space scanner images,

the affine transformation models or corrects first order distortions such as the effects of non-orthogonality and scale differences between the along track and scan directions caused by scanning process and Earth rotation or generated during the processing and production of the image. The transformation is formulated mathematically as:

$$E_i = a_0 + a_1 x_i + a_2 y_i$$

$$N_i = b_0 + b_1 x_i + b_2 y_i$$

.....(4.29)

Where a's and b's are the transformation parameters.

(3) Polynomial Transformation

As mentioned above, the polynomials of equations (4.27), which were developed and used by Wong (1975), have been used for the planimetric accuracy tests of space images. Various degree polynomial transformations have been carried out using Wong's polynomials. Table 4.1 lists the various transformations carried out for the planimetric test in this investigation.

TRANSFORMATION	1	x	y	xy	x ²	y ²	x ² y	xy ²	x ³	y ³	x ³ y	xy ³	x ⁴	y ⁴	x ² y ²	x ³ y ²	x ² y ³	x ⁵	y ⁵	x ³ y ²	
LINEAR CONFORMAL	/	/	/																		
AFFINE	/	/	/																		
POLYNOMIAL:																					
4 terms	/	/	/	/																	
5 "	/	/	/	/	/																
6 "	/	/	/	/	/	/															
7 "	/	/	/	/	/	/	/														
8 "	/	/	/	/	/	/	/	/													
9 "	/	/	/	/	/	/	/	/	/												
10 "	/	/	/	/	/	/	/	/	/	/											
11 "	/	/	/	/	/	/	/	/	/	/	/										
12 "	/	/	/	/	/	/	/	/	/	/	/	/									
13 "	/	/	/	/	/	/	/	/	/	/	/	/	/								
14 "	/	/	/	/	/	/	/	/	/	/	/	/	/	/							
15 "	/	/	/	/	/	/	/	/	/	/	/	/	/	/	/						
16 "	/	/	/	/	/	/	/	/	/	/	/	/	/	/	/	/					
17 "	/	/	/	/	/	/	/	/	/	/	/	/	/	/	/	/	/				
18 "	/	/	/	/	/	/	/	/	/	/	/	/	/	/	/	/	/	/			
19 "	/	/	/	/	/	/	/	/	/	/	/	/	/	/	/	/	/	/	/		
20 "	/	/	/	/	/	/	/	/	/	/	/	/	/	/	/	/	/	/	/	/	/

Table 4.1 The Various Transformations Applied in the Planimetric Test.

4.8 Planimetric Test Procedure

The procedure shown in Fig.4.20 was followed in the planimetric accuracy test of MSS, TM, MOMS and RBV images in this investigation. The measured image coordinates are in the arbitrary comparator coordinate system. These measured coordinates have been used directly in the testing procedure.

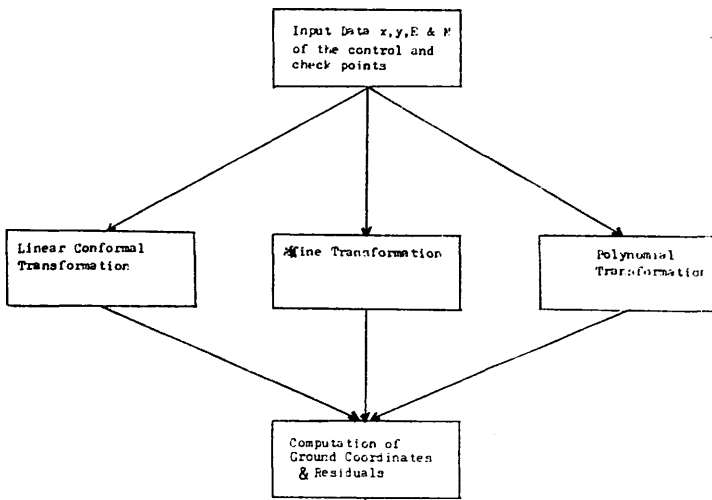


Fig. 4.20 Planimetric Test Procedure.

The linear conformal transformation was executed by a computer program called LINCON written in FORTRAN 77 by Dr. Hsu of ESRIN, Frascati, Italy which is available in the Departmental program library. A description of the program will be given in Appendix B.1.1.

The affine transformation was executed by selecting the first three terms incorporated in a computer program called POLYTRANS which carries out polynomial transformation. This FORTRAN 77 program was also written by Dr. Hsu and modified by the author to execute Wong's polynomials.

The third step in Fig. 4.20 is the application of the polynomial transformations. As mentioned in Section 4.6.1.2, the polynomial transformations in this investigation were carried out using the 20-term polynomials of equations (4.27). These polynomials were incorporated in the FORTRAN 77 computer program POLYTRANS. This program executes a loop of transformations. In the first loop, the first three terms of the polynomials, amounting to an affine transformation, are used. Then in each following loop, an additional polynomial term is added until the last term is reached. In each of these loops, the transformation is carried out and the r.m.s.e. values in Easting,

Northing and Vector are computed in both the ground coordinate system and at image scale. The r.m.s.e. values provide a measure of the effect that adding each term has on the transformation.

All these transformations were carried out in two steps. In the first step, all measured points in an image were used as control points for the computation of the transformation parameters i.e. no check points were used. In the second step, a set of well distributed points were selected and used as control points which were used to compute the transformation parameters. These were then used to transform the rest of the points which are considered as check points. The r.m.s.e values have been computed for both the control and check points. The specific results and experiments of applying these polynomial transformations to the planimetric accuracy tests of MSS, TM, MOMS and RBV imageries will be discussed in more detail in the respective chapters.

4.9 **Summary**

In this chapter, the Landsat MSS and TM scanner systems have been described, the geometry of scanner imagery explained, and the various approaches which may be used to carry out the rectification and the transformation of the images produced by the Landsat scanners have been reviewed. The transformations used in the planimetric tests carried out in the present project have also been outlined. In the next chapter, the procedure followed in the accuracy and interpretation tests of the MSS and the TM images is explained in more detail, the results obtained are given, analyzed and compared with the results obtained by other investigators over different test areas before a conclusion about their contribution to the topographic mapping in Sudan is reached.

CHAPTER 5

MSS & TM Images Geometric and Interpretation Tests

5.1 Introduction

Until recently, the MSS and TM scanners were the only sensors which have operated successfully in long-life Earth observation satellites. Therefore an immense wealth of data has been acquired by these systems and virtually every part of the world has good, cloud-free images acquired over it. It is, therefore, quite appropriate to test the applicability of these images to the topographic mapping of the world's developing areas and to the Sudan in particular. Thus geometrical accuracy and interpretation tests have been carried out by the author on images acquired by these systems over the Sudan test areas described in Chapter 3.

Geometrical accuracy tests were conducted on images covering part of the Sudan Red Sea Hills test area. As described in Chapter 4, the accuracy test procedure comprises selecting well defined and identified points on each scene, measuring image coordinates of these points using the Stecometer, scaling the corresponding ground coordinates off the 1:100,000 scale topographic maps of the area and carrying out a series of planimetric transformations using some of the selected points as control points. The rest of the points were considered as check points for which the ground coordinates were computed using the transformation parameters determined using the control points. The root mean square errors (r.m.s.e) were computed for both the control and the check points in each transformation carried out. These r.m.s.e values were compared and analyzed to draw conclusions about the geometric qualities of these images and their possible rectification for use in the topographic mapping of Sudan and similar areas.

Following the geometrical accuracy test, a simple interpretation test was carried out over both the Red Sea Hills and the Nile test areas so as to establish the amount of information available on these images and to match this with the requirements for the content of small scale (1:100,000 to 1:250,000) topographic maps. In the following paragraphs, the results of the tests carried out on MSS images are described and discussed first, followed by those from the corresponding tests carried out on the TM images. Finally the results of the interpretation tests are reported for both MSS and TM images.

5.2 Planimetric Accuracy Test of MSS Images over the Sudan

Three MSS images or scenes were used for the MSS tests. The first two were scenes E-1285-07295-Band-7 and E-1357-07283-Band-7 having Worldwide Reference System (WRS) values of path-184/row-047 and path-184/row-046 respectively. The first of these two scenes was acquired by

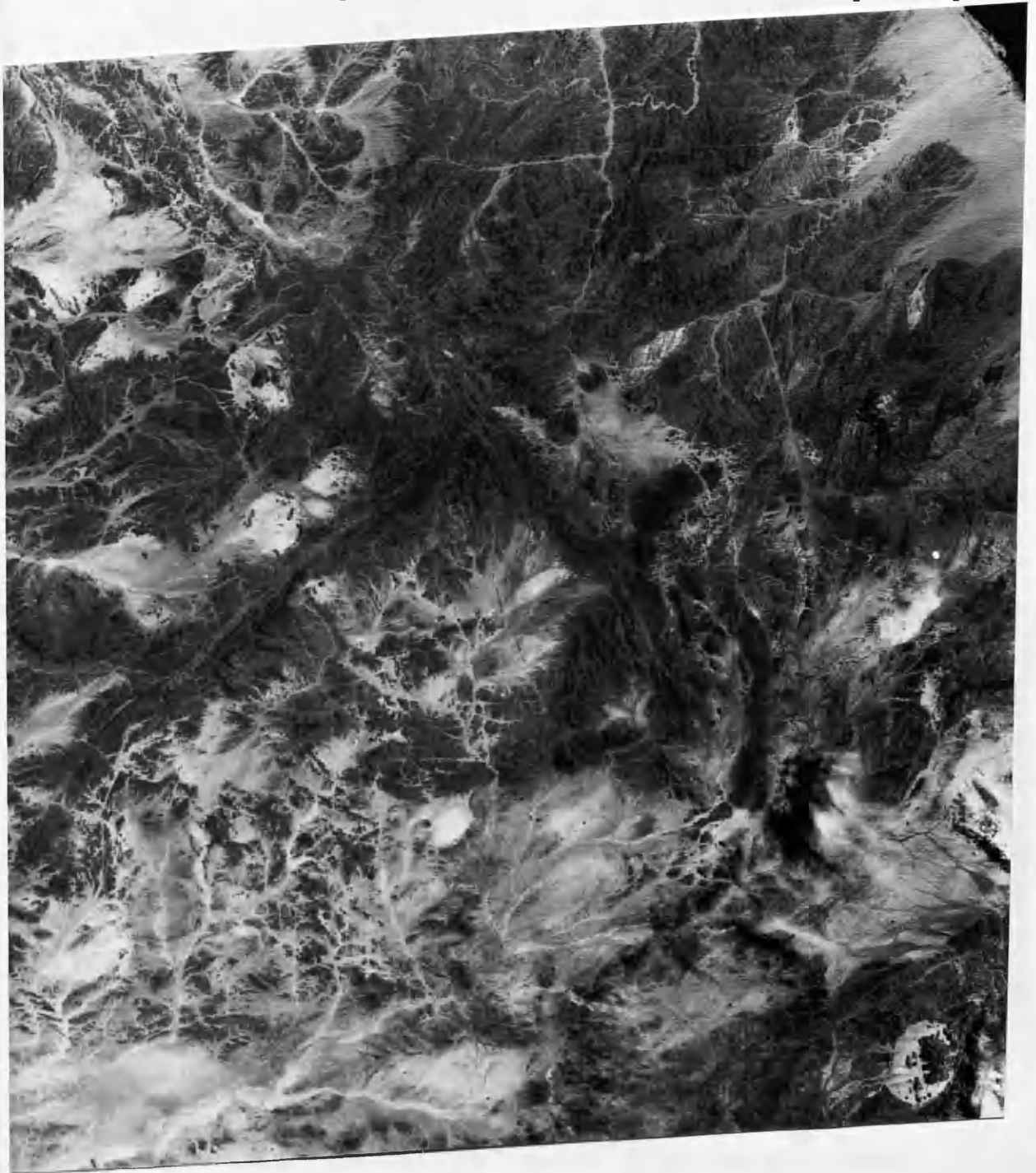


Fig. 5.1 MSS Scene E-1285-07295 Band-7 1:1,000,000 Scale Print.

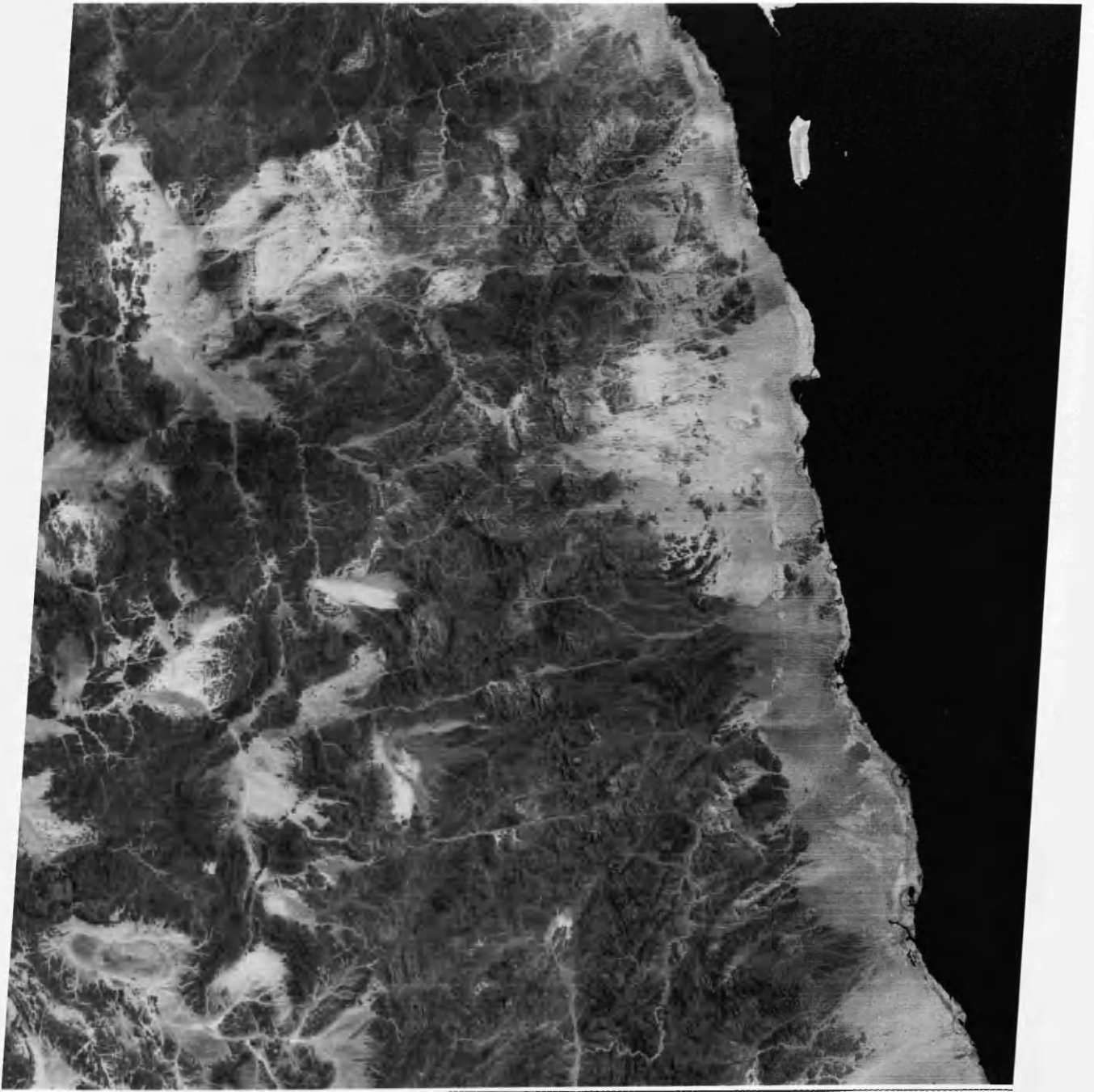


Fig. 5.2 MSS Scene E-1357-07283 Band-7 1:1,000,000 Scale Print.

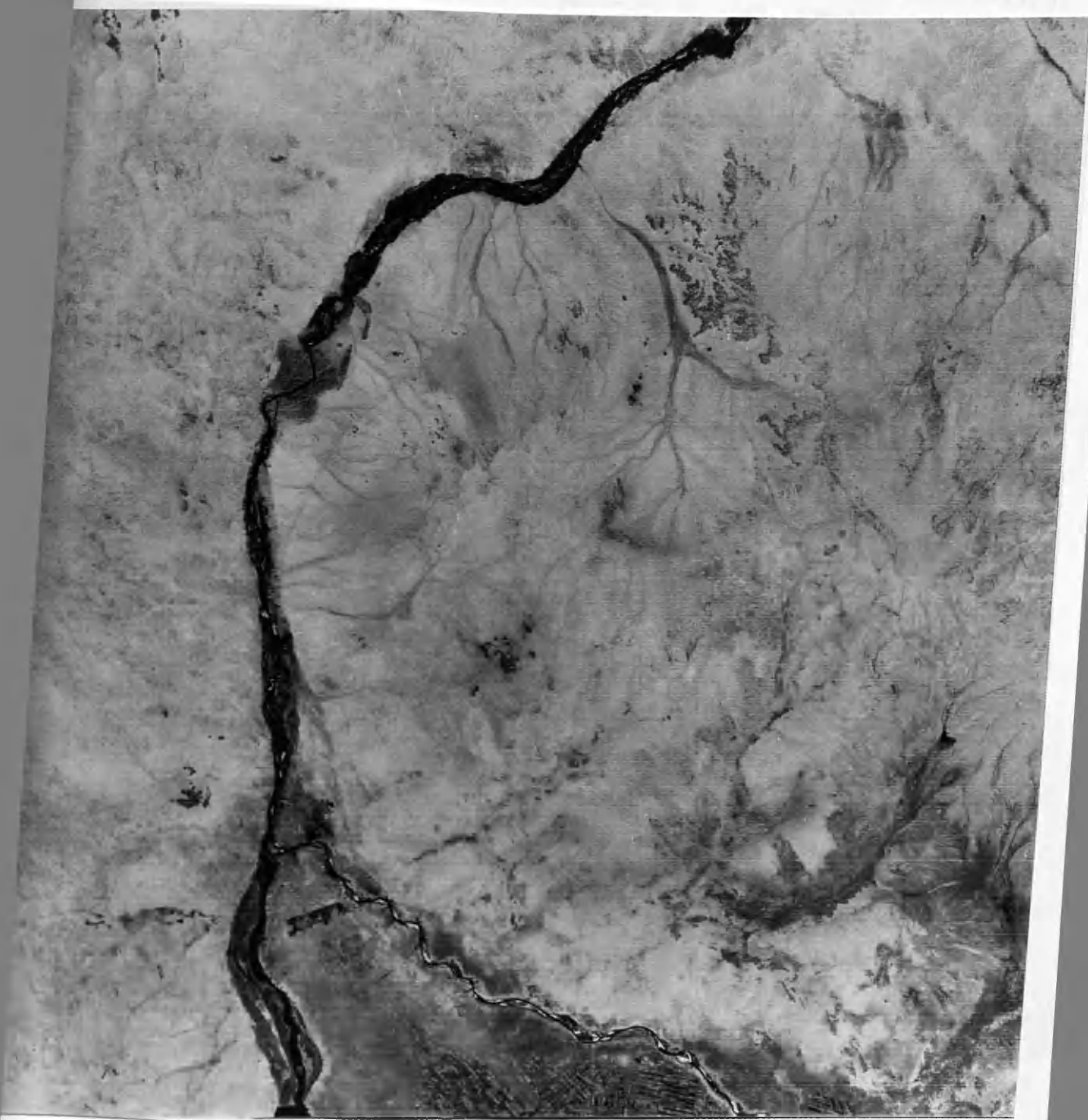


Fig. 5.3 MSS Scene E-2319-07275 Band-5 1:1,000,000 Scale Print.

Landsat-1 on 4th May 1973 while the other was acquired by the same Landsat on 15th July 1973. The two scenes cover the part of the Red Sea Hills test area extending between latitudes 18° N and 21° N and longitudes $35^{\circ} 30'$ E and $37^{\circ} 30'$ E. The third scene is Scene E-2319-07275-Band-5 with WRS values of path-186/row-049, acquired by Landsat-1 on 7th, Dec. 1975, covering the part of the Nile test area extending between latitudes 15° N and 17° N and longitudes 32° E and 34° E and including the three big cities of the capital triangle and the northern part of Gezira. All three scenes were utilized in the interpretation tests, but only scene E-1285-07295-7 could be used for the planimetric accuracy test since it was the only one for which topographic maps of the whole area of the scene were available. Figs. 5.1 to 5.3 show the 1:1,000,000 prints of these three MSS scenes.

A set of 130 points, as well-defined as possible, were selected over the whole area of the scene used for the geometric accuracy test. The points were selected to be as evenly distributed over the area as possible to produce results that would show the pattern of distortion over the whole image. The ground coordinates of these points were carefully scaled off the 1:100,000 scale topographic map using an engineering glass scale which is equipped with magnifiers and following the procedure outlined in Section 3.4.1. Coordinates can be measured to 0.1 mm at map scale using this device. Therefore the accuracy of these coordinates is estimated to be about ± 10 m in ground terms.

Image coordinates were measured monoscopically on the Stecometer as has been described in Section 3.5.1. The diapositive was aligned on the left carrier plate such that the comparator x-axis passes through the two horizontal corner marks of the image, i.e. the image x-axis is taken to be along the scan direction and the y-axis is along the flight direction. The measuring procedure was started by loading the measuring program (STECA) into the computer memory. Following this, the selected image points were then measured one by one and their coordinates recorded. Three pointings were made at each point and whenever the readings in any of these pointings were different from the mean of the three pointings by more than 10 μ m, they were discarded and a new pointing was substituted. The 9.6x-magnification eyepiece was found to be suitable. Any larger magnification makes the granularity of the emulsion more profound and the image more difficult to point to.

The test operations which have been described in Chapter 4 were carried out on this scene. As mentioned in Chapter 4, two sets of linear conformal, affine, and polynomial transformations have been carried out in the planimetric accuracy test of MSS images. All 126

points (4 points have been rejected for misidentification) were used as control points in the first set of transformations to determine geometric accuracy over the whole image. In the second set of transformations, a set of 50 points well distributed over the whole scene were selected as control points for use in the linear conformal, affine and polynomial transformations. The distribution of the control points selected was such that, in transforming the whole scene as a whole to the ground coordinate system, the resulting transformation parameters represent the best fit of the image to the ground reference system. The remaining 76 points were used as check points. Following those transformations, the results were analyzed and the residuals at all the points were plotted to see whether they depicted any systematic errors.

5.2.1 Linear Conformal Transformation Results

Using all the 126 points as control points with the linear conformal transformation resulted in r.m.s.e values of ± 259 m, ± 261 m and ± 367 m in easting (E), northing (N) and vector (V) respectively. The pattern of the residuals which have resulted from this transformation is given in Fig. C.1 and shows the systematic nature of the residual distortions in the bulk-processed MSS images. Clearly the dimension and the distribution of these values resulting from the simple linear conformal transformation are much too large to be acceptable for any of the map scales (1:100,000 to 1:250,000) being considered in this investigation. The second linear conformal transformation, which was carried out using the set of 50 well distributed points as control, has resulted in r.m.s.e values of ± 274 m, ± 306 m, and ± 411 m in easting (E), northing (N) and vector (V) respectively at the control points. At the 76 check points, the corresponding r.m.s.e values are ± 204 m, ± 279 m and ± 346 m in easting, northing and vector respectively. As can be seen in Fig. C.2, the pattern of the residuals which resulted from this linear conformal transformation also shows that there is a systematic distortion in the image which needs to be compensated for if better results are to be obtained. A substantial part of this distortion appeared to be due to a scale affinity confirming what has been noticed and shown by Wong (1975). Therefore, the affine transformation carried out after the linear conformal transformation should cater for this type of error.

5.2.2 Affine Transformation Results

The first affine transformation was carried out using all the measured 126 points as control points. This has resulted in r.m.s.e.

values of ± 86 m, ± 97 m & ± 130 m in easting, northing and vector respectively. Compared with the r.m.s.e. values which have resulted from the linear conformal transformation, it is clear that an improvement of 216 m in the vector planimetric position has occurred with the application of the affine transformation. The pattern of the residuals which have resulted from this transformation is shown in Fig. C.3.

The execution of the second affine transformation using the set of 50 well distributed points which have been selected as control for the second set of transformation has resulted in r.m.s.e values of ± 93 m, ± 110 m, and ± 144 m in easting, northing and vector respectively at the control points. The corresponding values for the set of check points are ± 87 m, ± 93 m, and ± 127 m respectively. As expected, a substantial improvement occurred due to the compensation for the scale affinity by this transformation. Although MSS bulk-processed images are supposed to be corrected for this scale affinity during NASA's bulk-processing procedures, as shown by these values, a considerable amount of residual affinity still exists in these images. Again these values, while they represent a considerable improvement, are still too large to be tolerated in topographic mapping over the scale range being considered in this investigation. Furthermore, as shown in Figs. C.3 and C.4, the pattern of the residuals which have resulted from the affine transformation shows that there are systematic distortions still remaining to be compensated for. Hence, the polynomial transformations were carried out to determine the best planimetric accuracy which can be achieved for the MSS images over Red Sea Hills Area and the specific terms of the 20-term polynomials of equations (4.25) which would be effective in correcting this residual distortion.

5.2.3 Polynomial Transformations Results

The r.m.s.e values which have resulted from the various polynomial transformations using all the 126 measured points as control are listed in Table 5.1. These values show that an improvement of 3 m has occurred with the application of the 4th term (xy); a second improvement of 5 m has occurred with the application of the 6th term (y^2); a third substantial improvement (3 m) has occurred with the application of the 8th term (xy^2); and a fourth substantial improvement (17 m) has occurred with the application of the 10th term (y^3). The last substantial improvement (5 m) has occurred with the application of the 14th term (y^4). Polynomial terms higher than the 14th term had no significant effect in the transformation. As mentioned above, the image y-axis was taken in the direction of flight. Therefore it is clear that

substantial improvements occurred with the application of terms which include the along track image coordinates.

Transformation	No. of Pts	r.m.s.e E	r.m.s.e N	r.m.s.e V
LINEAR CONFORMAL	126	259.21	260.50	367.49
AFFINE	"	85.86	97.37	129.83
POLYNOMIALS:				
4 terms $x y$	"	84.57	94.17	126.57
5 terms x^2		84.80	93.99	126.59
6 terms y^2		73.30	70.68	101.82
7 terms $x^2 y$		73.57	70.82	102.12
8 terms $x y^2$		72.37	67.50	98.96
9 terms x^3		72.43	67.77	99.19
10 terms y^3		59.06	56.16	81.50
11 terms $x^3 y$		58.55	56.30	81.22
12 terms $x y^3$		58.30	56.53	81.21
13 terms x^4		58.32	56.65	81.30
14 terms y^4		55.93	52.85	76.95
15 terms $x^2 y^2$		56.06	52.68	76.92
16 terms $x^4 y$		55.81	52.91	76.91
17 terms $x y^4$		55.90	51.36	75.91
18 terms x^5		56.09	51.58	76.20
19 terms y^5		56.03	51.77	76.29
20 terms $x^3 y^3$		55.99	51.54	76.11

Table 5.1 MSS Red Sea Area Hills Transformation Results (all control).

Transformation	CONTROL POINTS			CHECK POINTS				
	No. of Pts.	r.m.s.e E	r.m.s.e N	r.m.s.e V	No. of Pts.	r.m.s.e E	r.m.s.e N	r.m.s.e V
LINEAR	50	274.40	305.71	410.80	76	203.69	279.15	345.59
AFFINE	"	93.22	109.66	143.93	"	86.54	93.16	127.15
POLYNOMIALS:								
4 terms $x y$	"	93.74	104.87	140.66	"	84.60	90.30	123.74
5 terms x^2	"	94.55	106.03	142.07	"	85.55	89.92	124.12
6 terms y^2	"	77.37	75.71	108.23	"	74.94	69.72	102.36
7 terms $x^2 y$	"	78.26	76.49	109.43	"	74.98	70.56	102.97
8 terms $x y^2$	"	77.03	72.62	105.86	"	74.32	67.77	100.58
9 terms x^3	"	77.95	73.34	107.03	"	74.57	68.45	101.22
10 terms y^3	"	65.87	56.51	86.79	"	57.87	58.68	82.42
11 terms $x^3 y$	"	63.42	55.73	84.43	"	59.73	59.58	84.36
12 terms $x y^3$	"	63.83	55.79	84.78	"	58.66	61.02	84.64
13 terms x^4	"	64.69	56.52	85.91	"	58.68	61.21	84.80
14 terms y^4	"	60.10	52.20	79.60	"	56.96	57.97	81.27
15 terms $x^2 y^2$	"	60.08	52.84	80.01	"	58.05	57.70	81.85
16 terms $x^4 y$	"	59.75	53.57	80.25	"	57.75	57.70	81.64
17 terms $x y^4$	"	60.45	50.38	78.69	"	57.56	58.86	82.33
18 terms x^5	"	60.97	50.95	79.45	"	58.04	58.93	82.71
19 terms y^5	"	60.65	51.20	79.38	"	58.60	59.16	83.27
20 terms $x^3 y^3$	"	61.66	51.26	80.18	"	58.60	59.63	83.60

Table 5.2 MSS Red Sea Hills Area Transformation Results.

Table 5.2 lists the results of the various polynomial transformations which have been carried out using the set of the selected well distributed 50 points as control points. As can be seen from Table 5.2, again substantial improvements in the results have occurred with the application of the 4th, 6th, 8th, 10th and 14th terms. In particular, an improvement of 4 m has occurred with the application of the 4th term (xy). An additional improvement of 21 m has occurred with the application of the 6th term (y^2), while improvements of about 2 m and 21 m have occurred with the application of the 8th (xy^2) and the 10th term (y^3) respectively. The last substantial improvement has occurred with the application of the 14th term (y^4). These terms introduce substantial corrections to the residual distortions inherent in the MSS image having the patterns shown in Fig. 5.4.

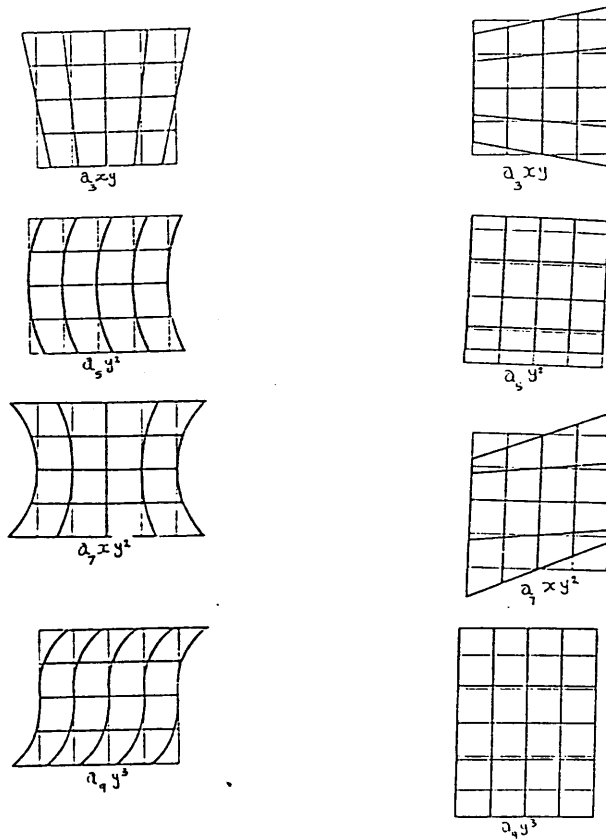


Fig. 5.4 Distortion Pattern in MSS image.

Figs. C.5 to C.14 show the patterns of residuals after the transformations with which a substantial improvement has taken place. The 14-term polynomial transformation has resulted in minimum r.m.s.e. values at both the control and the check points. These minimum values are ± 60 m, ± 52 m and ± 80 m in easting, northing and vector at the

control points and values of ± 57 m, ± 58 m and ± 81 m. in the easting, northing and vector at the check points. These values represent the best planimetric accuracy which can be obtained from the MSS image taken over the Sudan Red Sea Hills test area.

5.2.4 Analysis of the Results

Table 5.3 lists some of the published results of testing MSS bulk-processed images over various test areas carried out by several investigators throughout the period since 1973 using film transparencies. Comparing those results with these obtained over Sudan reveals that the accuracies obtainable from the MSS image taken over Sudan are worse by about 30 m than the best of those obtained over developed areas. However considering that hill tops, ridges, rocks and points along the confluences of dry stream network were selected and scaled off the 1:100,000 scale topographic maps in the Red Sea Hills area to serve as control and check points, while road intersections, railway junctions, bankings, fields and buildings corners, bridges, etc. for which the ground coordinates were either given by ground survey methods or scaled off medium- or even large-scale maps, were used for the same purpose in well developed areas, the difference between these results may be considered not that significant. This is especially justified when one considers that the 79 m ground resolution (pixel size) of the sensor means that objects of sizes less than that are extremely difficult to be resolved, although some experiences (Trinder and Nasca, 1976; Fleming, 1976) showed that linear features in this category can sometimes be seen. However, with the control and check points in the Red Sea Hills area being not that well-defined, pointing to these points during measurement of the image coordinates was bound to be of low certainty. Therefore the result of using this type of points is bound to be slightly worse than the best of those results which are obtained over developed areas.

TRANSFORMATION	CONTROL POINTS				SOURCE
	No. of: Pts.	r.m.s.e E	r.m.s.e N	r.m.s.e: V	
LINEAR	4	-	-	192	Colvocoresses, 1973
"	181	94	67	115	Wong, 1975
AFFINE	15	-	-	163	Bahr & Schuhr, 1974
"	33	-	-	151	" " " 1974
"	181	74	67	100	Wong, 1975
"	64	-	-	70	Trinder, Nasca 1976
"	31	83	124	-	Steiner, Kirby 1977
POLYNOMIALS					
6 terms	15	-	-	112	Bahr & Schuhr, 1974
"	33	-	-	106	" " " , 1974
"	10	59	87	106	" " " , 1975
16 terms	-	42	39	57	Forrest, 1975
20 terms	181	37	44	57	Wong, 1975
Parametric	64	-	-	66'	Trinder, 1976

Table 5.3 A Summary of MSS Published Transformation Results.

However, in all cases, it must be made clear that these results are those resulting from purely numerical methods applied to the measured coordinates of a limited number of well defined points. For mapping purposes, these techniques would have to be applied over a whole image using a computer controlled output, e.g. a laser-beam recorder. Presumably it is possible to produce images in which the distortions in the detail are corrected to the accuracy shown. However, the justification of any effort to be put into topographic mapping from MSS images even at very small scales is dependent on the amount of information which can be extracted from these images. In many maps, this matter is more critical than the planimetric accuracy of this information. Theoretically, the 79 m ground pixel size leaves little doubt that the amount of this information which can be depicted on an image map is bound to be limited to those terrain features which are of this order of size. Although, as mentioned above, some experiences showed that linear features of a size less than 79 m have been detected, there is no possibility of detecting many of the cultural features which are required to be shown on topographic maps. However, the actual contribution that MSS images may make towards topographic mapping varies from one area to another depending on the degree of development. The potential contribution of MSS images to the topographic mapping of the Sudan is discussed in Section 5.5 which gives the results of interpretation tests carried out on the Sudan test images.

5.3 Planimetric Accuracy Test of TM Images over the Sudan

A TM scene was selected and acquired for this test. This was scene E-50127-07302 with the path/row values 172 and 046 acquired by Landsat-4 on 6th July, 1984, processed by TIPS and reproduced at EROS Data Centre on 240 mm film transparencies. This scene covers part of the Red Sea Hills test area described in Section 2.6. Only Band 4 (Fig. 5.5) of this scene shows terrain detail clearly since some kind of noise appears as fog in the other bands covering the scene and reducing the amount of detail which can be seen and interpreted.

For the geometrical accuracy test, a set of 98 points were selected on the Band 4 image to be as well distributed over the scene as possible. All of these points are either well defined points on ridges, hill tops, or they are points occurring on the dry natural drainage streams flowing down and between these hills. No detail can be picked out on the sandy plains as the high reflectance sand appears as a uniformly white image hiding all detail in the area. Image coordinates

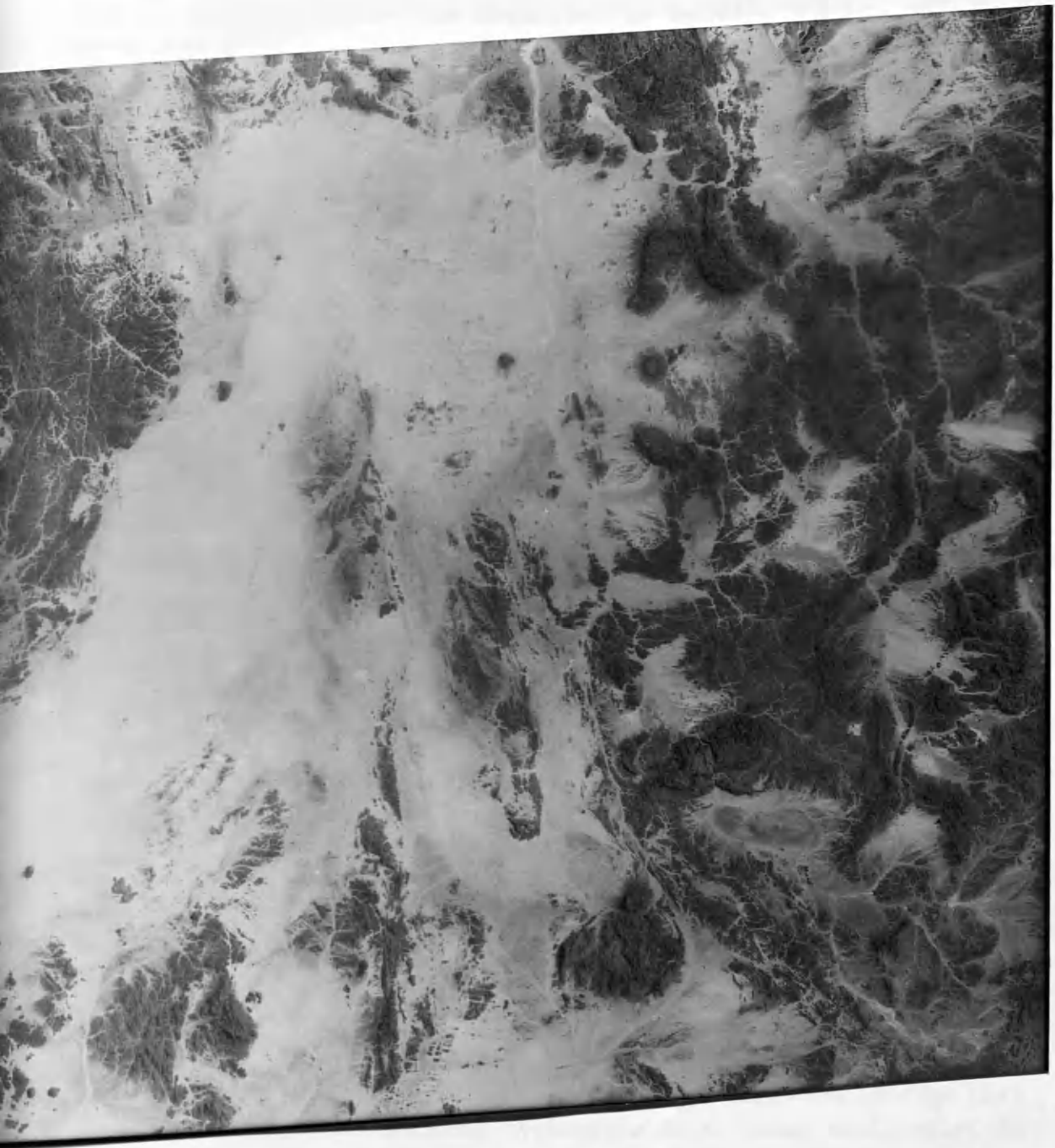


Fig. 5.5 TM Red Sea Hills Scene 1:1,000,000 Scale Print.

were again measured on the Stecometer at N.E.L, East Kilbride using the same technique which was applied in the MSS planimetric test and described above. Ground coordinates were scaled off the topographic maps in the same manner as described in Section 3.4.1.1. The test operations of Section 4.7 which are used in the test of the MSS image above were again used in testing the TM image.

5.3.1 Geometric Accuracy Tests of Whole TM Scene

In this accuracy test, the whole of the TM image taken over the Sudan Red Sea Hills area is considered as a unit in the first instance. In the initial set of transformations carried out in this test, the whole scene has been transformed to the ground coordinate system using all the 98 points as control points. In the second set of transformations, a set of 40 well distributed points were used as control points and the whole scene was transformed again to the ground coordinate system using these 40 points. The remaining 58 points were used as check points.

5.3.1.1 Linear Conformal Transformation Results

The use of all the 98 points measured as control in the linear conformal transformation has resulted in r.m.s.e. values of ± 46 m, ± 44 m and ± 64 m in easting, northing and vector respectively. The pattern of the residuals which have resulted from this transformation are shown in Fig. C.15. As can be seen from Fig. C.15, these residuals reveal the systematic nature of the distortion in the image.

In the second linear conformal transformation, the set of 40 well distributed points were used as control points with the remaining 58 points used as check points. The r.m.s.e. values which resulted after the linear conformal transformation were ± 42 m, ± 45 m, and ± 61 m in eastings, northings and vector respectively at the control points and corresponding values of ± 38 m, ± 38 m and ± 54 m at the check points. The pattern of the residuals which have resulted from the linear conformal transformation of the TM image is depicted in Fig. C.16 which shows that some residual systematic distortions still exist in the image despite the fact that the geometric correction in TIPS processing facility is considered to be very rigorous. Again a substantial part of this distortion is considered to be due to scale affinity from which all optical-mechanical scanner images are known to suffer. The affine transformation was then carried out to cater for scale affinity.

5.3.1.2 Affine Transformation Results

The r.m.s.e. values which have resulted from the execution of affine transformation using all the 98 points as control are ± 25 m, ± 30 m and ± 39 m in easting, northing and vector respectively. An improvement in the planimetric accuracy of 25 m has occurred with the compensation for scale affinity through the application of the affine transformation.

The corresponding r.m.s.e. values which have resulted from the affine transformation using the set of 40 well distributed points as control are ± 25 m, ± 34 m, and ± 42 m in eastings, northings, and vector respectively at the control points. The corresponding values at the check points are ± 24 m, ± 32 m, and ± 40 m respectively. These values again show that a substantial drop in the values of the r.m.s.e. has occurred. As can be seen from Fig. C.17, once again the pattern of the residuals which resulted from the affine transformation shows that there are still some systematic errors which can be eliminated by the application of the polynomial transformation.

5.3.1.3 Polynomial Transformation Results

In the first set of polynomial transformations, all the 98 points were used as control. Since no improvement had occurred in the transformation of the MSS image with the application of polynomial terms higher than the 14th term, in these transformations of the TM imagery only polynomials of 4 to 14 terms were used giving some reduction in the computational effort required for the tests. The r.m.s.e. values which have resulted with each of these transformations are listed in Table 5.4. As can be seen from Table 5.4, while the r.m.s.e. values in easting remained virtually constant, the r.m.s.e. values in northing continued to improve. This improvement occurred very slowly and no significant improvement has occurred with the application of polynomial terms higher than the 10th.

In the second set of polynomial transformations, the reduced set of 40 points was used as control points. Since it was found in the previous set of polynomial transformations that no improvement in the results has taken place with the application of terms higher than the 10th term, polynomials of 4 to 10 terms were used in this set of transformations. Table 5.5 lists the r.m.s.e. values at both the control points and check points which have resulted from each of the polynomial transformations. Again no significant improvement has occurred with the application of a specific term. Instead the improvement continued very slowly each time a term was added. In

general, the improvement which have occurred with the application of the 10-term polynomials over the results of the affine transformation amounted to about 2 m. From these r.m.s.e. values of ± 30 m, ± 38 m, and ± 48 m can be taken to represent the planimetric accuracy of information taken from TM images over Sudan Red Sea Hills and like areas. Fig C.18 to Fig. C.24 show the pattern of the individual residuals which resulted from each of these transformations. As can be seen from these figures, the overall pattern of residuals remained the same with each of the various polynomial transformations, but it is clear that some local systematic distortions still exist in the image. Therefore, the scene was divided into four quarter-scenes and the above transformations were carried out on each individual quarter-scene.

Transformation	No. of Pts	r.m.s.e E	r.m.s.e N	r.m.s.e V
LINEAR CONFORMAL	98	44.87	50.84	67.81
AFFINE	"	34.53	42.26	54.57
POLYNOMIALS:				
4 terms $x y$	"	34.33	42.39	54.54
5 terms x^2	"	31.97	41.12	52.09
6 terms y^2	"	31.81	34.66	47.04
7 terms $x^2 y$	"	31.90	34.48	46.97
8 terms $x y^2$	"	32.04	34.55	47.12
9 terms x^3	"	31.00	34.35	46.27
10 terms y^3	"	31.09	33.66	45.82
11 terms $x^3 y$	"	31.23	33.52	45.81
12 terms $x y^3$	"	31.03	31.56	44.26
13 terms x^4	"	31.20	31.82	44.57
14 terms y^4	"	31.40	32.38	45.10

Table 5.4 TM Red Sea Hills Area Transformation Results (all control).

Transformation	CONTROL POINTS			CHECK POINTS				
	No. of Pts.	r.m.s.e E	r.m.s.e N	r.m.s.e V	No. of Pts.	r.m.s.e E	r.m.s.e N	r.m.s.e V
LINEAR	40	44.61	50.29	67.22	58	41.29	54.55	68.41
AFFINE		34.94	41.66	54.83		31.87	41.69	52.48
POLYNOMIALS:								
4 terms $x y$		33.80	42.08	53.98		31.15	41.31	51.74
5 terms x^2		30.64	41.47	51.57		28.16	39.57	48.56
6 terms y^2		31.01	32.33	44.80		28.34	38.74	48.00
7 terms $x^2 y$		30.69	32.73	44.87		29.82	38.53	48.73
8 terms $x y^2$		29.20	33.44	44.39		26.99	31.67	41.61
9 terms x^3		29.20	33.44	44.39		29.00	38.00	47.80
10 terms y^3		28.80	33.01	43.81		29.96	38.05	48.43

Table 5.5 TM Red Sea Hills Area Transformation Results (whole scene)

5.3.2 Geometric Accuracy Tests of the TM Quarter Scenes

The results obtained with each of these quarter-scenes are summarized in Tables 5.6 to 5.9. The r.m.s.e. values which have resulted from the linear conformal transformation of the first quarter-scene are +39 m, +35 m and +53 m in easting, northing and vector at the control points and corresponding values of +47 m, +49 m, and +68 m at the check points. For the second quarter-scene, the r.m.s.e. values at the control points are +38 m, +46 m and +60 m in easting, northing and vector respectively. The corresponding values at the check points are +34 m, +41 m and +54 m. The r.m.s.e. values which have resulted for the third quarter-scene are +36 m, +37 m and +52 m at the control points and +35 m, +44 m and +65 m at the check points. Finally the r.m.s.e. values which have resulted from the linear conformal transformation of the fourth quarter-scene are +25 m, +25 m and +35 m at the control points and +21 m, +27 m and +34 m at the check points.

The differences in the planimetric accuracy obtained from each of these quarter-scenes are partially due to the differences in the distribution of the control points on the individual quarter-scene and partially due to the differences in the pattern of local distortion in each of these quarter-scenes. The pattern of residuals which have resulted from the linear conformal transformation for each individual quarter-scene are shown in Figs. C.25 to C.28. These patterns show the local systematic distortion in each quarter-scene to have different patterns. However these values give average r.m.s.e. values of +35 m, +36 m and +51 m in eastings, northings, and vector respectively at the control points and corresponding values of +38 m, +40 m, and +55 m at the check points from the linear conformal transformation.

The corresponding average r.m.s.e. values in easting, northing and vector of the control and check points after affine transformation are +30 m, +32 m & +43 m and +31 m, +36 m & +47 m respectively. Figs. C.29 to C.32 show the patterns of the residuals which have resulted from the affine transformation on each of the four quarter-scenes. Finally the average r.m.s.e. values which have resulted from the 7-term polynomial transformation, which was found to be satisfactory, are +25 m, +30 m & +39 m at the control points and +32 m, +31 m & +44 m at the check points. With the application of terms higher than the 7th term, the results got worse in the second, third and fourth quarter-scenes. The results from the first quarter-scene got worse with the application of terms higher than the 8th term. As can be seen from Tables 5.8 and 5.9, while the r.m.s.e. values in northings at the check points got worse with the application of the 8th to 10th terms in the third

quarter-scene, the r.m.s.e. values in the eastings at the check points got worse in the fourth quarter-scene. This is mainly due to the poor distribution of the control and check points in these quarter-scenes.

Transformation	CONTROL POINTS			CHECK POINTS				
	No. of Pts.	r.m.s.e. E	r.m.s.e. N	r.m.s.e. V	No. of Pts.	r.m.s.e. E	r.m.s.e. N	r.m.s.e. V
LINEAR	14	39.54	35.10	52.88	17	47.00	49.28	68.11
AFFINE		35.06	33.44	48.58		34.95	39.34	52.62
POLYNOMIALS:								
4 terms x y		35.23	33.20	48.41		34.94	39.12	52.45
5 terms x		33.42	33.06	47.01		34.86	38.22	51.73
6 terms y		33.39	32.47	46.58		34.93	36.30	50.37
7 terms x y		28.43	32.47	43.16		37.34	36.29	52.07
8 terms x y		28.43	29.60	41.04		37.35	32.62	49.59
9 terms x		26.38	23.98	35.65		49.34	58.92	76.85
10 terms y		26.12	22.54	34.50		55.22	40.96	68.75

Table 5.6 TM Red Sea Hills Area Transformation Results (Quadrant 1).

Transformation	CONTROL POINTS			CHECK POINTS				
	No. of Pts.	r.m.s.e. E	r.m.s.e. N	r.m.s.e. V	No. of Pts.	r.m.s.e. E	r.m.s.e. N	r.m.s.e. V
LINEAR	15	38.34	45.73	59.71	18	34.37	41.19	53.65
AFFINE		30.88	36.36	47.70		33.19	35.74	48.78
POLYNOMIALS:								
4 terms x y		29.72	36.13	46.79		33.47	35.06	48.47
5 terms x		28.43	36.12	45.97		30.72	35.11	46.66
6 terms y		28.42	31.89	42.72		30.76	32.31	44.61
7 terms x y		28.17	31.36	42.15		29.22	30.67	42.37
8 terms x y		24.89	29.95	38.95		33.57	31.91	46.31
9 terms x		20.04	28.57	34.90		54.16	32.14	62.98
10 terms y		18.97	26.75	32.80		55.90	37.57	67.35

Table 5.7 TM Red Sea Hills Area Transformation Results (Quadrant 2).

Transformation	CONTROL POINTS			CHECK POINTS				
	No. of Pts.	r.m.s.e E	r.m.s.e N	r.m.s.e V	No. of Pts.	r.m.s.e E	r.m.s.e N	r.m.s.e V
LINEAR	15	36.18	37.22	51.91	14	34.88	44.35	65.42
AFFINE		27.38	31.06	41.41		34.89	39.85	52.96
POLYNOMIALS: 4 terms x y		27.38	31.06	41.41		34.89	39.85	52.96
5 terms x		25.91	30.11	39.72		34.77	38.53	51.90
6 terms y		20.59	29.64	36.09		35.84	37.07	51.56
7 terms x y		20.20	29.55	35.79		35.62	36.30	50.86
8 terms x y		19.97	27.91	34.32		37.83	40.98	55.77
9 terms x		19.57	29.33	35.26		37.01	52.29	66.06
10 terms y		20.11	34.37	39.83		36.24	55.47	66.26

Table 5.8 TM Red Sea Hills Area Transformation Results (Quadrant 3).

Transformation	CONTROL POINTS			CHECK POINTS				
	No. of Pts.	r.m.s.e E	r.m.s.e N	r.m.s.e V	No. of Pts.	r.m.s.e E	r.m.s.e N	r.m.s.e V
LINEAR	17	24.97	25.41	35.63	19	20.86	27.19	34.27
AFFINE	"	24.70	25.38	35.42	"	19.36	28.96	34.84
POLYNOMIALS: 4 terms x y	"	23.00	25.96	34.68	"	22.38	28.14	35.96
5 terms x	"	23.38	26.47	35.32	"	25.22	24.69	35.29
6 terms y	"	23.24	27.55	36.05	"	25.31	24.39	35.15
7 terms x y	"	24.08	27.58	36.61	"	26.96	19.08	33.03
8 terms x y	"	14.66	24.82	28.82	"	39.20	21.40	44.66
9 terms x	"	15.30	22.17	26.94	"	40.00	23.90	46.60
10 terms y	"	16.24	22.13	27.45	"	36.71	23.46	43.57

Table 5.9 TM Red Sea Hills Area Transformation Results (Quadrant 4).

5.3.3 Overall Results of TM Accuracy Tests Over the Red Sea Hills Test Area

In general, these results when compared with the planimetric accuracy requirements of Table 3.2 mean that planimetric information can be derived from TM images which is sufficiently accurate to satisfy mapping requirements at the scale range considered in this investigation. Alternatively planimetrically accurate image maps of scales 1:100,000 and smaller can be produced from TM imagery. The amount of detail which could be extracted from the TM images is undoubtedly much greater than that from MSS images. The size of the individual detail which could be extracted is also much smaller, but there are still, however, many cultural and man-made features which are required to be shown on maps at these scales which cannot be provided by the TM images. This point will be considered in more detail later in this chapter.

5.4 Planimetric Accuracy Test of TM Images of South East England

A further geometric accuracy test of TM images has been carried out in the Department of Geography and Topographic Science by Isong (1987). The two test areas used in this test are located in South East England.

i) London Test Area: which is the area of 95km by 88 km covered by quadrant 3 of TM scene track-201/row-024. A great variety of detail such as motorways, roads of various gauges, railway lines, rivers, reservoirs, woods and forests exist in this area. The test was carried out on the Band 4 TM image of quadrant 3 acquired on 12th April, 1984 by Landsat-5, shown in Fig. 5.5. The scene was processed by ESA Earthnet processing facility at Kiruna. The quality of the image was very good.

ii) Kent Test Area: This is the 95km by 88 km area covered by quadrant 4 of the same TM scene track-201/row-024. The test was carried out on the Band 3 image of this quadrant, shown in Fig. 5.6, which was acquired on 12th April, 1984 and processed at Kiruna. The quality of this image is good but 40% of the image covers the sea and many parts of the remaining land area are covered by forests. Therefore difficulties were experienced in selecting well distributed points to serve as control and check points. Again well defined points on motorways, railway lines, roads, rivers, reservoirs, airports, etc. were identified and selected.

Image coordinates of the points selected on these images for the test were measured on the Stecometer at N.E.L. The corresponding ground coordinates were scaled off the 1:50,000 scale Ordnance Survey (O.S.) topographic maps of these areas using the same engineering scale which was used by the present author. Linear conformal, affine and 4- to 10-term polynomial transformations were carried out on the images. The results obtained in this test are summarized in Tables 5.10 and 5.11.

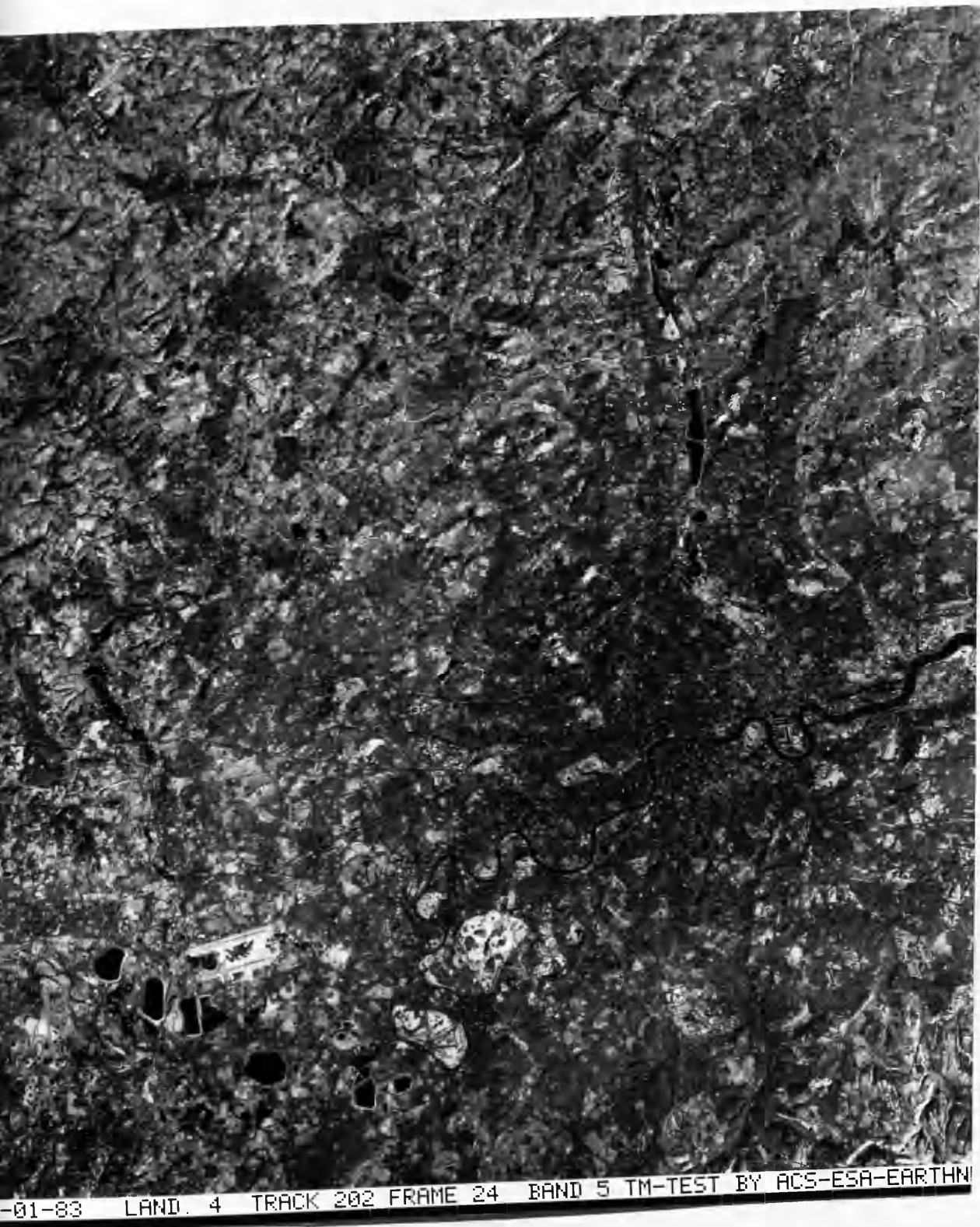


Fig. 5.6 TM London Scene 1:500,000 Scale Print.



Fig. 5.7 TM Kent Scene 1:500,000 Scale Print

Transformation	CONTROL POINTS			CHECK POINTS				
	No. of Pts.	r.m.s.e E	r.m.s.e N	r.m.s.e V	No. of Pts.	r.m.s.e E	r.m.s.e N	r.m.s.e V
LINEAR	20	14.37	12.70	19.81	30	14.36	15.18	20.90
AFFINE	"	14.70	12.97	19.60	"	14.66	15.18	21.10
POLYNOMIALS: 4 terms $x y$	"	15.14	11.22	18.84	"	14.64	14.78	20.76
5 terms x^2	"	15.60	11.12	19.16	"	14.77	13.96	20.33
6 terms y^2	"	14.91	11.29	18.71	"	15.22	13.72	20.49
7 terms $x^2 y$	"	15.48	11.10	19.05	"	15.21	14.80	21.25
8 terms $x y^2$	"	15.04	11.24	18.78	"	15.93	15.13	21.97
9 terms x^3	"	16.78	11.43	20.30	"	14.42	14.75	20.63
10 terms y^3	"	15.84	11.35	19.49	"	15.42	15.88	22.13

Table 5.10 TM London Area Transformation Results.

Transformation	CONTROL POINTS			CHECK POINTS				
	No. of Pts.	r.m.s.e E	r.m.s.e N	r.m.s.e V	No. of Pts.	r.m.s.e E	r.m.s.e N	r.m.s.e V
LINEAR	20	19.70	21.97	29.51	30	22.76	23.95	33.04
AFFINE	"	18.85	21.77	28.80	"	21.91	21.67	30.82
POLYNOMIALS: 4 terms $x y$	"	19.31	22.28	29.48	"	22.24	21.75	31.13
5 terms x^2	"	19.71	22.30	29.76	"	22.60	22.93	32.30
6 terms y^2	"	20.29	22.88	30.58	"	22.28	22.68	31.79
7 terms $x^2 y$	"	21.05	21.87	30.36	"	22.20	26.00	34.19
8 terms $x y^2$	"	20.49	22.29	30.28	"	21.61	25.64	33.53
9 terms x^3	"	22.19	23.17	32.08	"	23.01	26.07	34.77
10 terms y^3	"	21.36	23.96	32.10	"	23.31	25.27	34.39

Table 5.11 TM Kent Area Transformation Results.

The comparison of the results of the planimetric accuracy tests which have been carried out on the TM image over Sudan (Tables 5.4 to 5.9) with those obtained from the tests carried out on TM images over South East England reveals how relatively poor the geometric quality of the NASA TM image over Sudan is compared with the ESA TM image over England.

Comparing the image qualities of the London and Kent TM images (Figs. 5.6 and 5.7) with that of the Sudan Red Sea Hill TM image (Fig 5.5) shows how comparatively poor is the quality of the latter. In addition to this, the points which were selected as control and check points in the Red Sea Hills area are as described above, i.e. mainly hill tops, ridges, points on dry streams, etc. These points, although they were found to be as well defined as possible in this area, are by no means as well defined as the road intersections, railway junctions, bridges, airports and field corners, etc. which are easily found in the developed world. This difference in the quality of points between the points which have been used in the Red Sea Hills area and those used in the two English areas undoubtedly has its effect in the results of the Red Sea Hills area tests. Furthermore, the ground coordinates in the English test areas were scaled off the 1:50,000 scale Ordnance Survey topographic sheets while those in the Red Sea Hills area were scaled off the 1:100,000 scale maps as described above. The comparison of the results over the Red Sea area with those over the London and Kent areas reveals that the differences in the planimetric accuracy values which are obtained with high order polynomials are in the order of 10 to 20 m which seems to be too large despite all the disadvantages which, as discussed above, exist in the Red Sea Hills area. The comparison also reveals that, while no improvement occurred at all in the planimetric accuracy by using high order polynomials on the images of the English test areas, some improvement has occurred with the application of these polynomials in the transformation of the whole scene of the Red Sea Hills area. This may be due to the the rigorous systematic corrections carried out in the ESA Processing Facility as compared with these applied by the NASA facilities. In general, the poorer results which have been obtained over Sudan appear to result from the poor radiometric quality of the image and the less rigorous geometrical corrections which were carried out during processing. With a better quality image, one may expect these r.m.s.e. values to drop to the same level as those obtained on the Kent area.

As part of the Landsat Image Quality Analysis programme (LIDQA) organized by NASA, geometric accuracy tests have been carried out on Landsat-4 & -5 TM digital data by several other investigators. Fusco

et al, (1985) reported the results of an investigation carried out by ESA Earthnet in which a comparison between ESA Earthnet and NASA TM products was conducted. In that investigation, two TM scenes were tested. The first was that covering the area of Detroit having WRS path 16/row 31. A system processed digital image of this scene was acquired from NASA. The raw data of the same scene were transferred to the ESA Processing Facility and a system processed image was again produced. A set of 22 points were selected and their image coordinates were measured in both images. The ground coordinates of these points were measured on USGS 1:24,000 scale topographic maps. Affine transformation was carried out on both images. The results obtained gave r.m.s.e. values of ± 18.34 m, ± 22.81 m and ± 29.27 m in cross-track, along-track and vector respectively for the NASA product and corresponding values of ± 22.24 m, ± 25.89 m and ± 34.13 m for the ESA product.

The other scene tested by Fusco et al was that covering the southern part of France and having WRS path 197/row 29. The image data were received from Landsat 5 by both a NASA ground station and the Earthnet Fucino station. A set of 85 points were selected to perform an image to image transformation between the ESA processed and NASA processed images of this scene. Again affine transformation was carried out. The whole scene was first transformed to the NASA whole image, then the image was divided into 4 quarter-scenes and each quarter-scene was transformed to its corresponding quarter-scene. The results obtained from these transformation are listed in Table 5.10.

	No. of points	r.m.s.e. (m) (cross-track)	r.m.s.e. (m) (along track)	r.m.s.e. (m) (vector)
Full scene	85	14.12	22.48	25.22
Quad 1	19	10.48	14.50	17.00
Quad 2	23	12.58	15.64	19.06
Quad 3	21	11.34	11.80	15.51
Quad 4	22	13.65	13.22	18.08

Table 5.12 TM NASA/ESA Comparison Results (Fusco, et al (1985)).

The plot of the residuals showed local systematic errors in the four quarter-scenes. The pattern of these systematic errors differs from one quarter-scene to another as noticed by the present author over the Sudan Red Sea Hills area. From these results, Fusco et al concluded

that while the geometrical corrections carried out in the ESA Processing Facility are very rigorous, the presence of the systematic errors indicates that there are some residual errors in the NASA processed images which may be related to the transformation of the image into SOM projection. This conclusion confirms the effect which has been noticed by the present author.

Thormodsgard et al. (1983) reported r.m.s.e. values of up to $\pm 1,000$ m in the positional accuracy of image points determined from the computed longitude/latitude tick marks on TM images which are originally estimated from the satellite tracking data.

Goodenough et al. (1988) used ground control points with image coordinates measured on hard copy images for the transformation to obtain r.m.s.e. values as high as ± 200 m. Colvocoresses, (1986), after noticing that far better results have been obtained by several investigators using digital TM data, pointed out that the results obtained by Goodenough reflect errors which are introduced by the Digital-to-Analogue Processor which controls the operation of the film writer. Therefore despite the fact that the digital image from which the hard copy is produced has been rectified, the hard copy image contains distortions caused by these errors introduced after the image has been rectified.

Geometric testing of TM P digital data was carried out by Welch et al. (1985) on two American test areas in Georgia and Iowa states. Using polynomials of first to fifth order for the transformations of the whole $185 \text{ m} \times 185 \text{ m}$ scene, planimetric r.m.s.e. values ranging from ± 25 m to ± 28 m were obtained. With subscenes (quarter scenes) and the same polynomial transformations, planimetric r.m.s.e. values ranging from ± 19 m to ± 27 m were obtained. In both tests, Welch noticed that first and second order polynomials give superior results to those utilizing higher order polynomials in TM image rectification. This confirms what was noticed by the present author in the results of the planimetric accuracy tests of the TM image over the Red Sea Hills area.

Hardy (1985) reported r.m.s.e. values of ± 16 m and ± 23 m in eastings and northings respectively for the first order polynomial transformation (affine) of TM P digital data using 28 control points. For the second order polynomials, he obtained r.m.s.e. values of ± 13 m and ± 19 m in eastings and northings respectively. Corresponding values of ± 13 m and ± 16 m and ± 9 m and ± 12 m were obtained with the third and fourth order polynomials respectively. In all these transformations, no check points were used and the r.m.s.e. values given were computed at

the control points.

All these results confirm that, from the point of view of geometric accuracy, TM data can be used for topographic mapping at scales 1:100,000 and smaller. The extent of the contribution of TM data at these scales, however, depends on the area being mapped. Image maps have been produced from the TM digital data by the U.S Geological Survey (U.S.G.S). In these image maps, the enhancement, rectification and resampling were carried out on the digital data before the image map has been finally printed. Accuracy tests carried out on these image maps are reported by Colvocoresses (1985) to have resulted in planimetric r.m.s.e values ± 24 m and ± 28 m for the 1:100,000 scale Dyersburg and Washington DC image maps respectively.

5.5 Interpretation of MSS Images over the Sudan

Although topographic mapping can be carried out using digitally enhanced images in which geometric and radiometric corrections as well as contrast and edge enhancements have been carried out, the resulting image map will be used and interpreted visually. Although the pixel size of MSS imagery is 79 m, the ground resolution for low contrast images is estimated to be in the order of 120 m (Welch and Pannell, 1982). This is most likely to be the case in the many areas in the developing countries where the contrast is often low and therefore MSS imagery can hardly be useful for the topographic mapping at 1:250,000 scales and larger unless the terrain morphology is the prime feature and no cultural features are present. Wong (1975) concluded that the MSS imagery is limited by resolution rather than by its geometric fidelity and therefore he does not recommend them for mapping at scales larger than 1:500,000. Trinder and Nasca (1976) have been more successful in detecting cultural features which are mostly linear such as roads, railways, pipelines, etc. on the MSS imageries in Australia where they see it as being quite useful in the revision of the Australian topographic map series at 1:250,000 scale.

However several very substantial topographic mapping projects in the developing countries have been carried out by various mapping agencies. For example, the complete coverage of Libya at 1:250,000 scale (127 sheets) has been produced by the Earthsat Corporation (USA) from digitally enhanced and produced MSS colour imageries; and a set of 1:250,000 scale maps were produced by the DOS for part of the Antarctic (Swithenbank & Lane 1975; Read & Lane, 1976; Petrie, 1985). This is in addition to the various thematic mapping projects carried out by a number of other agencies.

The experience of Hunting Surveys in using MSS imagery for several mapping projects in Africa and the Middle East as reported by Leatherdale (1978) showed that man-made features such as settlements, communication lines, bridges, etc. are the most difficult features to detect from MSS images, while coastlines, mud flats, lakes, reservoirs, very large canals and swamps are the features which are most readily and easily detected. Between these two extremes come agricultural land use, vegetation, forests and moorlands, rough pasture, rock and sandy deserts with various degrees of detectability which can generally be described as adequate. Leatherdale (1978) also reported that the rate of success in detecting man-made features is disappointing even in digitally enhanced MSS imagery.

Interpretation of MSS images over Sudan was carried in the Department of Geography and Topographic Science as part of the work done in collaboration with Sudan Survey Department (Abdalla, 1982; Petrie, 1985). A similar interpretation was carried out by the author with the use of the collateral information shown on 1:100,000 topographic maps of the area and which are also required to be shown in smaller scale, i.e. 1:250,000 scale maps.

The interpretation was carried out by first making a comprehensive list of the features and detail that are shown on 1:100,000 scale topographic maps of each test area. Then the detection and identification of these features was attempted using a mirror stereoscope. Features which were not detected using the stereoscope despite prior expectations were tried again in the Stecometer. The result of this interpretation is as follows:

5.5.1 Interpretation of MSS Images over the Nile Test Area

A false colour mosaic covering the Nile test area was published by the Regional Remote Sensing Facility, Nairobi. The mosaic was constructed from four Landsat MSS scenes. These were Scenes 1214-07362, 1214-07364, 1215-07420 and 1215-07423 which were acquired by Landsat-1 in February, 1973. This mosaic has been used in addition to the Landsat MSS scene shown on Fig. 5.3 for the interpretation test over the Nile test area.

The features which are shown on the 1:100,000 scale maps of this area and which are listed for the interpretation test fall into five groups. These are (1) lines of communication; (2) cultural features; (3) hydrology; (4) relief forms; and (5) vegetation.

1) Lines of Communication:

Lines of communication that are usually shown on 1:100,000 scale maps include, roads, streets, tracks, telephone lines, power lines, and rail roads. Telephone and power lines are not expected to appear on space images. Lines of communication which are shown on the 1:100,000 scale maps of the Nile test area include hard surfaced roads, unsurfaced roads, tracks, bridges, ferry terminals, and railway lines. The results of the search for each of these on the MSS image are as follows:

i) Surfaced Roads:

These are usually surfaced with asphalt or tar macadam and are 8 to 16 m. wide. A strip of bare land is kept along each side of these roads. North of Khartoum, a strip of fertile land along the eastern bank of the Nile, which is densely populated and heavily cultivated is served by one of these surfaced roads that runs through this strip up to Elgiali. Along the west bank of the Nile, a similar strip of fertile land extends almost parallel to that on the eastern bank. Along the edge of this strip and separating fertile land from the semi-desert land away from the Nile, runs a short surfaced road. Both of these surfaced roads are shown on the 1:100,000 scale topographic maps of the area. On the MSS image, the detection of both of these roads proved not to be possible on both the MSS scene and the mosaic despite the sharp contrast between these roads and the surrounding background especially on the western bank where the area adjacent to the road is open bare land and the contrast between the road and the background sand soil is very sharp.

In the area between the Blue and White Niles south of Khartoum, details are very dense. Along the western bank of the Blue Nile, a surfaced road runs through the very narrow strip of bare land separating the cultivated land of Gezira Irrigation Scheme and the narrow strip of fertile land along the river bank. Again this road is shown on the 1:100,000 scale topographic maps covering the area. Parts of this road were detected where the pattern of the surrounding detail such as the regular pattern of the cultivated plots assisted in this detection. But in general, an almost complete failure was experienced in the detection of this major road.

Another surfaced road runs almost parallel to the eastern bank of the White Nile between Khartoum and Jebel Awlia. An extension of this road to Kosti further south is at present under construction. While the road is shown on the 1:100,000 topographic maps of the area, a complete failure to detect it on the MSS image was experienced. In this respect, the contrast between the road and the light black clay soil is very poor despite the fact that small parts of the road run through stretches of cultivated areas.

ii) Unsurfaced Roads and Tracks:

Many unsurfaced roads and tracks interconnecting the various villages and the townships in the Nile test area are shown on the 1:100,000 scale topographic maps. A complete failure to detect any of these on the MSS image was experienced. Unsurfaced roads are expected to be very difficult to detect since they are nothing but the trace of the repeated passage of lorries and trucks. The precise locations of these roads at any specific moment of time are often selected by drivers according to the circumstances (sand conditions, etc) prevailing at that time and the locations of small villages in the area which can also change. Therefore these roads have no planned or permanent locations with respect to the other detail in the area. In Gezira area, some of these roads run beside large canals and through the uncultivated land between cultivated plots of land. In this case, it was the strip between the two cultivated plots or the prominence of the canals that are actually shown rather than the roads themselves. No space imagery can be expected to show tracks since these are extremely narrow and continuously changing in location.

iii) Bridges:

These include five bridges ranging in widths between 10 to 20 m. These are the Medani bridge across the Blue Nile just north of Wad Medani, the main town of the south end of the Gezira; the Burri bridge across the Blue Nile connecting Khartoum to Khartoum North; the Omdurman bridge across the Nile connecting Khartoum North to Omdurman; the Blue Nile bridge for trains, cars and light vehicles between Khartoum and Khartoum North; and the White Nile bridge across the White Nile connecting Khartoum to Omdurman. The first three bridges are of concrete construction while the other two are made up of a steel framework and wooden

floor. In addition to these, there is a dam/bridge across the White Nile further up the river at Jebel Awlia. These bridges are shown on the 1:100,000 scale topographic maps. These bridges are also clearly shown on the MSS image with the exception of Medani bridge which was under construction at the time these images were taken.

iv) Railway Lines:

All railway lines in the Nile test area are shown on the 1:100,000 scale topographic maps. Railway lines in Sudan are of the narrow gauge, single track type running through the fairly flat plains. Therefore very few embankments, cuttings, or high bridges can therefore be found along their course. In general, these lines exhibit only a very slight contrast with their surrounding environment as they are laid on a slightly elevated strip of ground made of the local soil. Although this low contrast does make it very difficult to detect these lines, some parts of the line that goes south from Khartoum through the Gezira area to Wad Medani were detected. Again this was due to the pattern or alignment of detail on both sides of the railway line. The other railway line goes north from Khartoum to Atbara where it splits into two branches. One branch continues north to Wadi Halfa right on the northern border with Egypt. The other branch runs to the east first through the semi-desert and desert and then through the Red Sea Hills down to Port Sudan on the coast of the Red Sea. A complete failure to detect this main railway line was experienced even though part of this line runs through the narrow cultivated fertile strip of land along the eastern bank of the Nile. The failure to detect this part of the railway is due to the irregular pattern of the surrounding detail compared to the chequerboard pattern of the Gezira area.

v) Ferry Terminals:

In this test area, ferries are usually small boats used for transportation between cities on opposite banks of the river. They are mainly crossing ferries connecting cities directly opposite to each other. Due to the changing level of water in the Nile, these ferries often have no permanent terminal locations since they are selected where it is convenient and safe for passengers to board and leave them. Despite these changing locations, the approximate positions of the ferry terminals are shown on the 1:100,000 scale topographic maps of the area using

symbols. However, whatever the case, these terminals cannot be expected to show up on the MSS images since they are often small in area and have poor contrast with the surrounding area.

2) Cultural Features:

Cultural features that are shown on the 1:100,000 scale topographic maps covering the Nile test area include cultivated lands, big cities, towns and villages, cemeteries, airfields, pipelines, parks and recreation areas, wells, fountains, etc.

i) Cultivated Areas:

Cultivated areas are shown on the 1:100,000 scale topographic maps covering the Nile test area as area symbols of various green shades. South of Khartoum, cultivated areas are mostly big irrigated schemes such as the Gezira Irrigation Scheme, Gunied Sugar Cane Scheme, and White Nile Pump Schemes. These schemes are well planned such that the area of each scheme is divided into large units supplied with water from the main canal by 2 to 4 m wide water channels. These units are further divided into plots each of about 10 acres area. All these cultivated areas are shown on the 1:100,000 scale topographic maps as large blocks of area symbols. The main canals supplying water to these schemes are also shown. On the MSS image, these schemes show up quite clearly, but the individual units are not quite distinguishable. Instead large blocks of cultivated areas are shown against uncultivated plots located besides them which make the area appear as a large chequerboard. The regular pattern of the cultivated plots made it possible to detect the unsurfaced roads which traverse them with the prior knowledge from the maps as to where they run. Small villages within this area appear as uncultivated areas where the pattern of cultivated plots is suddenly broken giving an irregularly shaped bare land area. These villages are often located beside irrigation canals where administrative and irrigation monitoring stations have first been established by the irrigation scheme authorities. Other smaller cultivated areas along the banks of the White and Blue Niles which are mostly private farms can also be detected. The large green belt comprising forest sheltering Khartoum and Soba Agricultural Research Farm are also clearly shown and can be detected quite easily.

North of Khartoum, cultivated areas are mainly restricted to the

narrow strips of fertile land along the Nile banks with the exception of small irrigated schemes. Again these cultivated areas are shown on the topographic maps covering the area. On the MSS image, these show up quite clearly as a continuous light black strip with the river running in the middle as a dark black line. In general, cultivated lands show up quite clearly on the MSS image. In the irrigated schemes, the image shows the cultivated plots at the time it was taken in a manner which it is not possible to show on topographic maps. Therefore, cultivated areas were easily detected and delimited everywhere on the Band 5 MSS ($\lambda = 0.6$ to 0.7 μm) image. This is because of the high absorption of energy by vegetation at these wavelengths relative to other surrounding features. However, the delimitation of the narrow clay strips along the river shores which are usually submerged during the flooding season is difficult. This is because the vegetation along these shores extends right to the water line and with these shores being saturated with water, the black tone of the vegetation is readily confused with the dark black colour of the water.

ii) Built-up Areas and Settlements:

Built up areas in the Nile test area comprise big cities such as the three cities of the capital, Wad Medani and Atbara; small towns as Hasaheisa, Kamleen, Maseed, Jebel Awlia, and Shendi; and numerous smaller villages which are scattered throughout the area. All the big cities and towns are shown on the 1:100,000 scale topographic maps of the area as large blocks of buildings. Important internal features are shown using symbols. The smaller villages are shown on the topographic maps using symbols since they are often very small in area. On the MSS image, the big cities and towns could be detected, but the villages can only be detected where they are surrounded by cultivated land or their position is guessed at from the detection of the roads that converge towards them. However, the ease with which these towns were detected depends on the size and the surrounding background of each individual town. The internal detail of the cities and towns can be detected only where they are regular in pattern and occupy a considerable area. In Khartoum and Khartoum North, some of the internal details could be detected - especially the industrial centre in Khartoum North. Detection of streets and roads was found to be very difficult and often not possible. In Omdurman, detection of internal details is more difficult if not impossible. This is because most of the buildings are built

from the local earth and therefore the contrast between these buildings and the background is extremely poor.

iii) Cemeteries:

Big cemeteries in Khartoum and Khartoum North were detected as areas of bare ground having irregular shapes surrounded by blocks of building. In all cases, detection of cemeteries requires collateral information to identify these bare grounds as cemeteries. Cemeteries which are located at cities outskirts were not detected.

iv) Airfields:

The two main airports in this area are the Khartoum International Airport and Wadi Saidna Military Airport. The runways in both of these are long, wide and surfaced using either concrete or tar macadam. Both of these airports showed up very clearly on the MSS image, but the details of aircraft parking areas and passenger halls could not be distinguished. However, these parking areas and halls are also not shown on the 1:100,000 scale topographic maps either.

Smaller cultural features i.e. wells, springs, tanks and towers are not expected to be shown on the MSS images since they all have small areas compared to the 79 m pixel size of the MSS images. By contrast, these important features are shown on the 1:100,000 scale topographic maps using symbols.

3) Hydrology

In the Nile test area, the hydrological features which are shown on the 1:100,000 scale maps include rivers, falls, canals, wide irrigation channels, water bodies, dams, islands and dry streams.

i) Rivers:

As expected, these appear quite clear and sharp on the Band 5 MSS image because of the high absorption of energy by water at these wavelengths. The land/water boundary was very sharp and no difficulty was experienced in detecting and delineating the rivers. This is because of the sharp difference in the amount of energy reflected by the land as compared with the water. In addition to the Blue, the White and the main Nile rivers which

represent the major life vein of the area, at Wad Medani in the south of the test area, there is the river Rahad which again showed up quite clear and sharp. This is a seasonal river, becoming nearly dry with water pools forming here and there in the dry season. During the rainy season which starts in early May and lasts till early November, this river floods. This particular MSS image was acquired just after the rainy season ended. Therefore the river appears very sharp and the water/land boundary defining its actual width can easily be delineated.

ii) Water Bodies:

These exist mainly along the White Nile and the courses of the main Nile. A wide area along the White Nile banks is submerged when the river floods and, when the flood season ends, water pools will be created scattered over this previously submerged area. These water pools usually don't last long but since this MSS image was acquired immediately after the flood season, they appear as sharp black spots with a lighter dark tone surrounding them. These light black tone areas could be cultivated areas since virtually all the area is seasonally cultivated. However, these small seasonal pools are not shown on the 1:100,000 scale topographic maps. Instead all the area which is submerged during flooding is filled with a light green tint.

iii) Dry Streams:

These are the natural drainage systems which drain the rain water to the rivers. Since the terrain in the Nile test area is generally made up of very flat plains, these dry streams are very complex, ranging from 1m wide streams which drain the water into bigger streams which in turn drain into still bigger streams which are up to 10m wide. Wide dry streams appear very sharp with a complexity which it could never be possible to show on line maps. This is again due to the fact that the image was acquired immediately after the rainy season in Sudan.

4) Relief Features:

As mentioned above, the Nile test area is mainly very flat with only a few low hills scattered about such as Jebel Awlia on the eastern bank of the White Nile south of Khartoum; Karrari and Markhiat north of Omdurman; and a series of hills in the North such as Jebel Um Ali, Nagaa and Musawarat. Sand dunes dominate the semi desert area with

gravel beds appearing as wadis in this area. These relief features are shown on the 1:100,000 scale topographic maps using contours and shades of brown colour. All these hills were easily detected on the MSS image of the area, but no information about the relief heights could be extracted. Instead a generalized form of relief could be shown.

5) Vegetation

The vegetation which is shown on the 1:100,000 scale topographic maps covering the Nile test area includes scattered trees, scrub, orchards and woodlands. Interpretation of these elements is generally affected by the season during which the images were acquired. At the time this image was acquired, tree leaves start to fall but despite this, the woodlands appear quite clear and can easily be detected and delineated. The delineation of woodlands is noticeably easier in the Elghaba area and in the Khartoum green belt where these woods have a more or less regular shape with buildings right at their edges. Scattered trees are not expected to be detected and scrubs can only be detected where they grow on dry stream beds with the ground underneath saturated with water. Orchards exist along the Nile banks but they cannot be differentiated from cultivated lands.

Summing up, there was an almost complete failure to find roads, railways, villages, water tanks and many other point and line features. Instead a generalized pattern of the relief and many of the natural drainage features as well as the irrigation canals and irrigated areas showed up quite clearly. The result of this interpretation is summarized in Table 5.13, which shows that the percentage of information which can be extracted from MSS images of the Nile test area does not exceed the range of 35% to 40% of those required to be shown on 1:100,000 scale topographic maps. As discussed in Chapter 3, with this percentage it is not feasible at all to use MSS images in the topographic mapping of this area at 1:100,000 scale. Even if 1:250,000 scale maps are considered, the percentage of information which can be extracted from MSS images to the total required to be shown on the map does not exceed 40% by a large margin. Therefore it is again not feasible to use these images for topographic map compilation at this scale.

5.5.2 Interpretation of MSS Images over the Red Sea Hills Area

The part of the Red Sea Hills test area which is covered by the MSS image in this investigation, is generally very hilly with sandy valleys in the west and a narrow sandy coastal plain in its eastern part. In

general, the area is thinly populated and hence there are few cultural features. The dominant items of information required for mapping are therefore relief forms, dry streams, surface materials, the coast line and several islands.

The main lines of communication present in the Red Sea Hills area at the time of acquisition of this image included an unsurfaced main road that connects Port Sudan, Kassala, Wad Medani and Khartoum, several smaller internal surfaced and unsurfaced roads in Port Sudan city and a single gauge railway line.

Unfortunately the part of the coastal plain area which is covered by the MSS images in this investigation is located north of Port Sudan. Hence there was no possibility of detecting the part of the Port Sudan - Kassala unsurfaced road and the railway line that traverse the coastal plain before crossing the hills at Summed (Summit). In the hills themselves, a disappointing failure was experienced in the detection of these lines and the locations of the main road and the main railway line can only be guessed by the alignment of features along their courses.

Small unsurfaced roads and tracks interconnecting the villages and small towns in this area are shown on the 1:100,000 scale topographic maps of the area. These roads and tracks were not expected to be detected on MSS images since they follow the dry streams and wadis which are mainly highly reflective sandy beds. Therefore the contrast between the roads and the highly reflective sands is extremely poor. In practice, this negative expectation was fulfilled.

Unfortunately all the big settlements in the Red Sea Hills test area fall outside the area covered by these images with the exception of Sinkat and Haya. With the aid of the topographic maps of the area, these can be detected but as small towns, their internal detail cannot be recognized. Once again without the collateral information given by existing map, these towns could never have been detected, identified and mapped.

As mentioned above, the most dominant features in the area are relief forms, dry streams, coast line and islands. Relief forms such as hills, rocks, ridges, and cliffs are shown very clearly and no difficulty was experienced in detecting all of these forms. However, the highly reflective sandy valleys appear as almost uniformly white areas filtering out all possible detail in these valleys. On the other hand, the network of dry streams shows up very clearly as in the Nile

test area. The coast line, islands and bays of the Red Sea coast are shown quite clearly as well. A summary of the results of this interpretation is given in Table 5.13

FEATURES SHOWN ON 1:100,000 MAPS	MSS PARTIUM TEST AREA: RED SEA TEST AREA				TM RED SEA TEST AREA	
	DETECTED	IDENTIFIED	DETECTED	IDENTIFIED	DETECTED	IDENTIFIED
Communication:						
Hard surfaced roads	1	0	-	-	2	2
Unsurfaced roads	0	0	0	0	0	0
tracks	0	0	0	0	0	0
Footpaths	0	0	0	0	0	0
Streets	0	0	0	0	-	-
Bridges	1	0	0	0	-	-
Ferry terminals	0	0	0	0	-	-
Railways	1	0	0	0	2	0
Railway stations	0	0	0	0	0	0
Culture:						
Cultivated land	3	3	2	0	2	0
Big cities	3	1	1	0	2	1
Towns	1	0	0	0	0	0
Villages	0	0	0	0	0	0
Ruins	0	0	0	0	0	0
Electrical stations	0	0	0	0	0	0
Pipelines	0	0	0	0	0	0
Powerlines	0	0	0	0	0	0
Wells	0	0	0	0	0	0
Storage tanks	0	0	0	0	0	0
Cemeteries	0	0	0	0	0	0
Airports	3	3	0	0	3	3
Landing Grounds	0	0	0	0	1	1
Hydrology:						
Rivers	3	3	-	-	-	-
Falls	3	1	-	-	-	-
Canals	3	3	-	-	-	-
Irrigation channels	1	0	-	-	-	-
Water bodies	3	1	-	-	-	-
Dams	3	3	-	-	-	-
Reservoirs	3	1	-	-	-	-
Hydrography:						
Tidal flats	*	*	*	*	*	*
Reefs	*	*	*	*	*	*
Rocks	3	0	3	0	3	1
Near shore bathymetry	0	0	0	0	0	0
Water depth	0	0	0	0	0	0
Marsh	3	3	-	-	-	-
Harbours	-	-	3	3	3	3
Small harbours	3	1	3	1	3	2
Shore line	3	3	3	3	3	3
Islands	3	3	3	3	3	3
Relief forms:						
Sand dunes	3	0	3	0	3	0
Gravel beds	1	0	1	0	2	0
Elevated grounds	3	3	3	2	3	3
Contours	0	0	0	0	0	0
Vegetation:						
Woodlands	3	1	1	0	1	0
Scattered trees	0	0	0	0	0	0
Scrub	0	0	0	0	0	0
Orchards	2	0	0	0	0	0
Others:						
Administrative boundaries	0	0	0	0	0	0
Rest houses	0	0	0	0	0	0
Triangulation pillars	0	0	0	0	0	0

0 = NOT; 1 = SOMETIMES; 2= OFTEN; 3 = YES; - = NOT AVAILABLE; AND * = REQUIRES REPEATED AVERAGE

Table 5.13 MSS Interpretation results.

In general, despite the fact that details are scarce in this area, the amount of information which can be extracted from MSS images in this area is again disappointing and the use of these images in the small scale topographic mapping of the area is again not feasible in light of the minimum criteria which have been specified in Chapter 3.

5.6 Interpretation of TM Images over the Sudan

The part of the Red Sea Hills area which is covered by the TM image in this investigation does not differ from that covered by the MSS images, which are discussed above, in respect of the various features which exist in each area. As mentioned above, this area is very hilly with sandy plains on both sides of the hill range. The area is also thinly populated and therefore very few cultural details are shown on the 1:100,000 scale topographic maps covering the area. In general, the main features which are shown on these maps include relief forms such as hills, ridges, rock dykes, valleys, etc as the dominant features. Other features such as wadis, khors, dry streams, and tracks traversing the narrow plains between the hills and the wide sandy plain to the west, are also shown on the maps. Settlements in the area mainly comprise a very few small villages which are more like nomadic camps than villages. These villages or camps are not shown on the maps explicitly but their locations are indicated by other cultural features such as wells after which these camps are often named.

Unfortunately not a single surfaced or unsurfaced road exists in the area covered by this TM image. However surfaced roads would be expected to show up quite clearly on the TM images should there be any. All the lines of communication that exist in the area and are shown on the topographic maps are unsurfaced tracks. These tracks follow the courses of the wadis, khors and dry streams since they are mainly formed by the repeated passage of the nomads with their camels looking for pasture along the beds of these khors and wadis. These tracks are not expected to be detected on space images as they exhibit no contrast with the highly reflective sandy background.

The small villages are also not expected to be detectable on the TM image since they are usually small in area and the few buildings or tents within each individual village are often scattered far apart from one another. However, as mentioned above, these villages are not shown explicitly on the topographic maps of the area. The relatively big and permanent villages such as those existing in the Nile test area and the southern part of the Red Sea Hills might be expected to be more detectable on the TM image than on the MSS image.

As mentioned above, wadis, khors, and dry streams which are shown on the 1:100,000 scale maps can easily be detected everywhere with the exceptions of those which run over the highly reflective plains. In fact, the complexity with which these khors and dry streams are shown on the TM image is far superior to that shown on the topographic maps. Other hydrological features such as rivers, water bodies, coast lines, etc are also expected to show up very clearly on the TM images since no difficulty was experienced in their detection on the MSS images.

All the above mentioned relief features do in fact show up very clearly on the TM image and no difficulty was met in their detection. Even the individual fine details of the hills such as the ridges and individual small peaks and cliffs can easily be detected. By contrast, the sandy valleys show up as a uniform white tone hiding any possible detail in the area. Even the khors and dry streams which show up quite clearly everywhere else are completely hidden in these sandy plains. This is generally because of the high reflectivity of the sandy soil in these plains.

No vegetation exists in this area apart from the scattered leafless trees and bushes which grow in such an environment. However, vegetation is expected to show up very clearly on the TM images - especially in the near IR bands.

In general, the amount of information which might be extracted from the TM images over Sudan will differ from one part of the country to another depending to the degree of development. In some parts of the Sudan such as the area covered by the TM image in this investigation, the amount of information present on the TM image does not differ much from that on the MSS images. In other parts such as the Nile test area - especially the Khartoum and Gezira areas, the amount of information which can be extracted from the TM images should be much greater than that obtained from the MSS images. However, while the TM image might be quite sufficient for mapping the first type of area, the amount of information which can be extracted for the second type of area is still very much less than the minimum requirement of the topographic mapping specified in Chapter 3.

5.7 Conclusions

The conclusions one reaches from these tests can be summarized as follows: with the 30 m ground resolution and the much improved geometric fidelity available with the TM images it seems that trying to apply MSS images to the topographic mapping of the Sudan at any scale

within the scale range mentioned above is not worth the time and effort that would need to be put into it. This is so, despite the fact that, there is very little gain in terms of the amount of information which can be extracted from the TM images in areas such as the part of the Red Sea Hills area covered by the TM image in this investigation. As the results above show, the TM image could provide the basic information that is required to be shown on maps at these scales with sufficient planimetric accuracy. However the smaller man-made features cannot be extracted from TM images which is a major limitation. However in the case of many developing areas still in the early stages of development, these features are rather limited in any case, even though they are important. For this reason, the author believes that the starting point in the process of topographic mapping for many developing areas at the moment could be image maps derived from TM images if only because of their widespread availability and comparatively low cost. On these image maps, other information could be added as time goes on. However, the other approach could be to utilize space imagery of a higher resolution such as that available from linear array scanners and photographic cameras. The results of geometric accuracy tests and interpretation tests using such images will be considered in the chapters which follow this one.

CHAPTER 6

Linear Array Scanners

6.1 Introduction

Recently the attention of the topographic mapping community interested in the possibilities of mapping from space imagery has to a large extent been centred on the development and implementation of solid state arrays as a replacement of mechanical scanners in space remote sensing. Photodiodes, phototransistors, and Charge Coupled Devices (CCDs) can all be fabricated using microelectronic techniques into linear or two dimensional arrays. CCDs differ from the other two devices in that they use analogue charge transfer readout while others use digital multiplexing. Linear array systems simultaneously image a complete narrow strip of the terrain instead of sweeping it out sequentially as with MSS and TM devices. Ground coverage is produced in the usual way by the platform forward motion. By comparison with optical-mechanical scanners, linear array systems are far superior in respect of their higher precision and constant geometry; their direct optoelectronic conversion of image points into electrical signals; their minimal weight and small dimension; their low power consumption; and their high radiometric sensitivity. In general, in the context of scanner imagery, linear array systems offer the following advantages over the optical mechanical scanners:

(i) Since no mechanical scanning devices are needed for the imaging process, all the distortions and disturbances caused by these parts in optical-mechanical scanner images, and which contribute to the degradation of the image resolution, are eliminated. Therefore, the absence of these distortions and disturbances creates an improved situation for the acquisition of high resolution images. However, this improved resolution is still by no means near the resolution of photographic systems.

(ii) The more stable geometry of the arrays and of the imaging process, compared with the situation in the case of optical mechanical scanners, and the stability of the silicon structure result in very simple patterns of distortions in the acquired images. Therefore this stability provides the basis for the acquisition of scanner images which can be used for the reasonably accurate mapping of the features present on the Earth's surface. Again photographic systems are superior in stability than linear array scanners, but in the context of

scanner images the geometry of linear array images represent a significant improvement.

(iii) Very high radiometric sensitivity is possible arising from the longer dwell time on the area from which the signal is continuously gathered while it is being imaged on the focal plane. In addition, the small size of the individual solid state detector element makes it possible to have an array with a great number of detector elements in the focal plane of the sensor. Since the signal gathering capability of any sensor increases proportionally to the number of detectors onto which the radiation from a certain ground area is focussed, the radiometric accuracy of the linear array sensors is superior to that of the optical-mechanical scanners.

As mentioned in Chapter 2, a German experiment was conducted in 1983/84 using a sensor called the Modular Opto-electronic Multispectral Scanner (MOMS) which employed this technology. Only two years later, the first operational space imaging system based on linear array technology was launched. This was the French SPOT-1 HRV, the first in a planned series of Earth observation satellite systems. In the following paragraphs, the geometry of images which are acquired by linear array scanners is explained and the mathematical models and procedures used in their rectification and transformation are outlined and discussed. Following this, MOMS is described in detail followed by a description of the SPOT-1 HRV sensors- since these two systems represent the current state-of-the-art in linear array sensor technology.

6.2 Geometry of Linear Array Images

As mentioned in Chapter 2, in linear array systems, the whole scan-line across the flight direction is imaged simultaneously by an optical lens onto the focal plane. The rays coming from this scan-line are focussed by the lens onto a row of detectors located at the focal plane as shown in Fig. 6.1. As the platform moves in its path, new scan lines are continuously acquired as individual units. The image is therefore built up from these scan lines. Hence one set of collinearity equations relates all image points within this scan-line to their corresponding ground points. As the platform moves in its orbit, orientation elements continuously vary with time. Therefore, a new set of collinearity equations is needed for each scan-line.

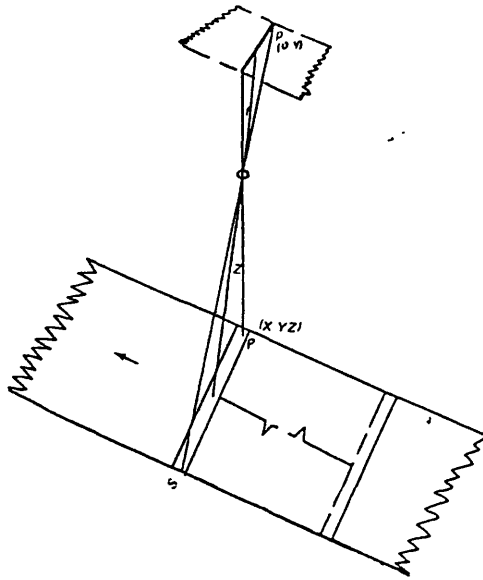


Fig. 6.1 Geometry of Linear Array Images.

In general, the collinearity equations can be written in the following form to accommodate this dynamic nature of the image:

$$\begin{aligned}
 0 &= -f \cdot \frac{m_{11s}(X_p - X_{os}) + m_{12s}(Y_p - Y_{os}) + m_{13s}(Z_p - Z_{os})}{m_{31s}(X_p - X_{os}) + m_{32s}(Y_p - Y_{os}) + m_{33s}(Z_p - Z_{os})} \\
 Y_p &= -f \cdot \frac{m_{21s}(X_p - X_{os}) + m_{22s}(Y_p - Y_{os}) + m_{23s}(Z_p - Z_{os})}{m_{31s}(X_p - X_{os}) + m_{32s}(Y_p - Y_{os}) + m_{33s}(Z_p - Z_{os})} \\
 &\dots\dots\dots(6.1)
 \end{aligned}$$

where X_p , Y_p , and Z_p are the ground coordinates of a point p which is imaged on scan-line s;

X_{os} , Y_{os} , and Z_{os} are the coordinates of the projection centre at the instant of imaging scan-line s expressed in the terrain coordinate system;

m_{11} to m_{33} are the elements of the rotation matrix which expresses the orientation of the platform at that instant; and

f is the focal length of the optical system of the scanner.

The image y-coordinate of the point (y_p) is taken along the scan line from the centre of the scan-line, and it is given by:

$$y_p = (i - (n-1)/2) \cdot \text{pixel width}$$

in which i is pixel number; and

n is the total number of pixels in the array.

The image x-coordinate of any point in the scan line is taken to be equal to zero since only a single scan-line is considered in equations 6.1.

Before enforcing these equations, all inherent systematic distortions and displacements within each scan line should be compensated for. These distortions and displacements are caused by the variations in the satellite attitude and altitude and the curvature and rotation of the Earth.

The image format resulting from a constant yaw error (Δk) is shown in Fig. 6.2a. As can be seen from this figure, the scan lines in the resulting image remain parallel to each other, but the area covered by the image format is skewed. This is similar to the effect of the Earth's rotation. On the other hand, if the yaw error varies with time the scan lines in the image will not remain parallel and displacements will be introduced as shown in Fig. 6.2b.

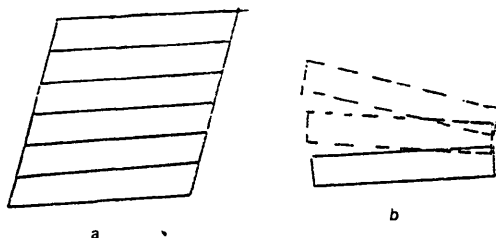


Fig. 6.2 Effects of Yaw Angle Error in Linear Array Images.

A fixed pitch error ($\Delta \theta$) has no effect in the image, but a time varying pitch angle creates gaps and overlaps as shown in Chapter 4.

Changes in the spacecraft altitude (ΔH) from the nominal value result in a scale error as in the case of optical-mechanical scanners.

Scale error can also result from the changes in the satellite velocity (Δv) as shown in Chapter 4. However in space linear array systems, the most serious of these are the distortions caused by Earth's curvature and the displacements caused by Earth's rotation. The Earth's curvature introduces distortions which are similar to those in frame photography, but can occur only in the scan direction, i.e in the y-coordinate direction, since each scan line is considered as a separate unit. This distortion is given by:

$$dy = Hy^3 / (2Rf^2) \quad \dots (6.2)$$

where H is the platform altitude;
 R is the Earth radius of curvature; and
 f is the focal length of the scanner.

6.3 Stereoscopic Linear-array Data Acquisition

The idea of stereoscopic linear array data acquisition was introduced by Colvocoresses of the U.S.G.S. who gave various configurations for an automated mapping satellite based on the linear array technology (Colvocoresses, 1979; 1980). Following this, the Germans planned a linear array mapping system based on a slightly modified configuration, while the French introduced the different configuration which is used in the SPOT HRV sensors for acquiring overlapping images from different satellite paths. In general, the various configurations of linear array sensors with which stereoscopic imaging can be achieved fall into one or other of the following three groups:

i) Two or more linear array systems are used that are oriented to produce vertical, fore, and/or aft images. Stereomodels can then be formed from the along track vertical and forward pointing images, from the vertical and backward pointing pair of images or from the forward and backward pointing pair of images. An infinite choice of base:height ratios (B:H) is possible depending on the angle α of convergence of the fore and aft array systems. Small B:H ratios will result in very poor height accuracy. On the other hand, too large B:H ratios results in problems such as dead areas, intolerable vertical exaggeration etc. (Welch, 1983). There are several possible stereo configurations for the linear array sensors in this group. These were the configurations originally introduced by Colvocoresses (1980) as alternatives to be used in stereo imaging using linear

array sensors. Fig. 6.3 shows these various configurations. The stereo and multispectral configuration shown in Fig. 6.3d was that originally selected to be flown on the proposed Mapsat (Colvocoresses, 1980) and Stereosat (Welch, 1981) systems which in the end were not funded or implemented.

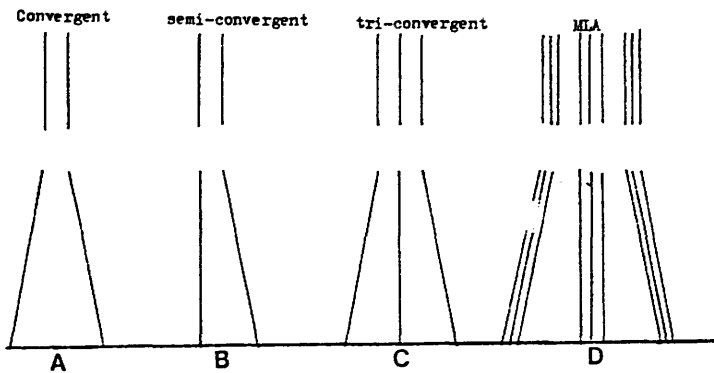


Fig. 6.3 Along Track Stereo Linear Array Systems.

ii) In the second configuration group, forward, vertical and backward pointing images are acquired as in the first group above. But instead of using three separate camera systems, three parallel linear array lines located at the focal plane of a single optical system such that light rays having an angle of incidence α come to focus onto array lines A and C, while those coming from the nadir direction focus onto array line B (Fig. 6.4). This has been suggested for future applications of MOMS (Hofmann, 1985).

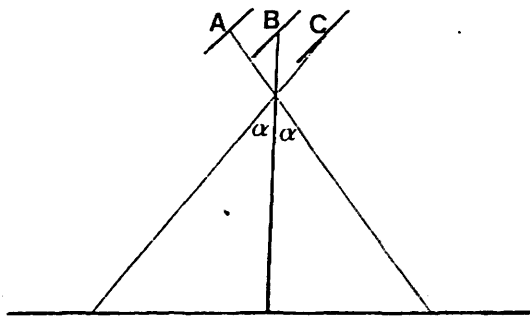


Fig. 6.4 Configuration of Multi Array System.

iii) A system with an adjustable viewing angle may be used so that the scanner can be pointed to produce laterally off-nadir (i.e tilted) images as well as vertical images. In this case, stereomodels are formed from laterally overlapping images which

have been acquired from different satellite paths at different times or dates. This configuration is being utilized in SPOT HRV sensors (Baudoin, 1984; Lillesand et al, 1987).

6.4 MOMS Sensor System

The MOMS sensor system was developed by Messerschmitt-Bolkow-Blohm (MBB) for the West German Ministry of Research and Technology under contract from the German DFVLR and with the scientific guidance of the University of Munich. It is a new design of scanner based on solid state linear arrays. The detector elements in these arrays are Reticon CCDs with 1728 pixels per array. CCDs possess the high quantum efficiency and broad band spectral response characteristics of silicon detectors over the spectral region lying between $\lambda=400$ to 1000 nm (MBB, 1984).

MOMS was designed on a modular basis to satisfy a wide spectrum of regional and global remote sensing applications (Bodechtel, et al, 1986). This modularity is evidenced in that:

i) Each spectral channel has a separate optical unit of varying configuration which may ^{be} implemented through the exchange of lenses and/or spectral filters.

ii) The focal plane array assembly in each spectral channel can be varied with regard to the number and type of arrays required to meet an individual mission specification. The incorporation of up to 6 CCD arrays per line is achieved by using two lens systems as shown in Fig. 6.5.

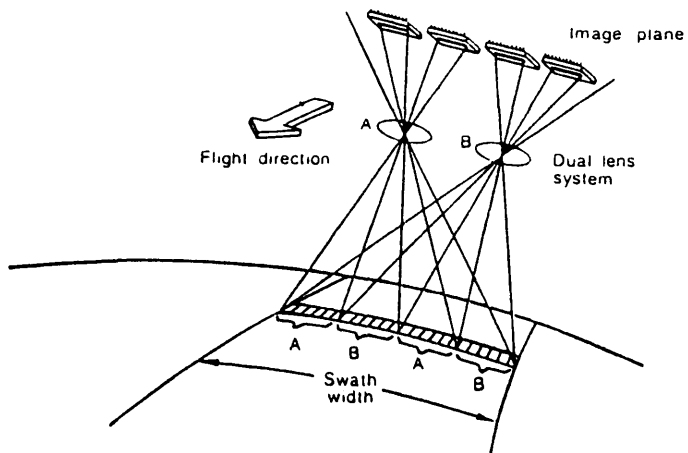


Fig. 6.5 The MOMS Optical System.

iii) The possibility exists to give a different orientation to the modules of the scanner, for example it may be tilted to allow off-nadir viewing at various angles for the acquisition of overlapping images either in the along track or the scan direction.

This modular construction allows the system to be adapted to suit different mission types, specifications, and objectives. Coupled with the possibility of retrieving the sensor being realized by the Space Shuttle, this resulted in an imaging system which was optimized for experimenting with and testing of linear array sensors for various scientific applications. The first two experiments utilizing MOMS were mounted on the SPAS pallet which was deployed from the Space Shuttle Missions STS-7 in June 1983 and STS-11 in February, 1984. Both experiments were designated MOMS-1.

6.4.1 **MOMS-1 Experiment**

The objective of MOMS-1 experiments was to demonstrate the applicability of high resolution CCD linear array data to topographic and thematic mapping over the scale range of 1:50,000 to 1:100,000. As shown in Fig. 6.6, MOMS-1 sensor consists of four major parts:

i) two optical modules mounted on a rigid plate, each with two objective lenses, four sensor arrays, and associated shutters, control, and readout electronics;

ii) a power box for the overall power supply;

iii) a logic box containing electronic modules to control major sensor functions and the real-time correction and formatting of the digital data stream; and

iv) a Bell and Howell MARS-1428 LT-3B high density digital tape (HDT) recording unit. This unit is kept in a pressurized environment inside a specially-built container mounted on the pallet. Due to the experimental nature of these missions, the recording capability was limited to 30 minutes.

The characteristics and parameters which were specified to meet the objectives of the MOMS-1 experiment were given in Table 2.3.

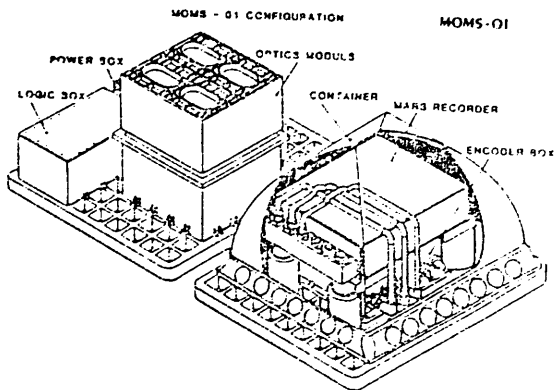


Fig. 6.6 MOMS-1 Experiment Components.

During the flight period, the information and commands for imaging were controlled by the MOMS operation team at NASA's mission control centre at Houston and by the mission specialists onboard the Shuttle. Fig. 6.7 shows the overall flow of this information. The data supplied by weather satellites were used to decide which targets were cloud free. A globally distributed set of test sites were located between 28° $30'$ north and south latitudes (the orbital inclination of the Space Shuttle). In this way, potentially a large variety of conditions and phenomena could be imaged, and in practice, this was actually achieved.

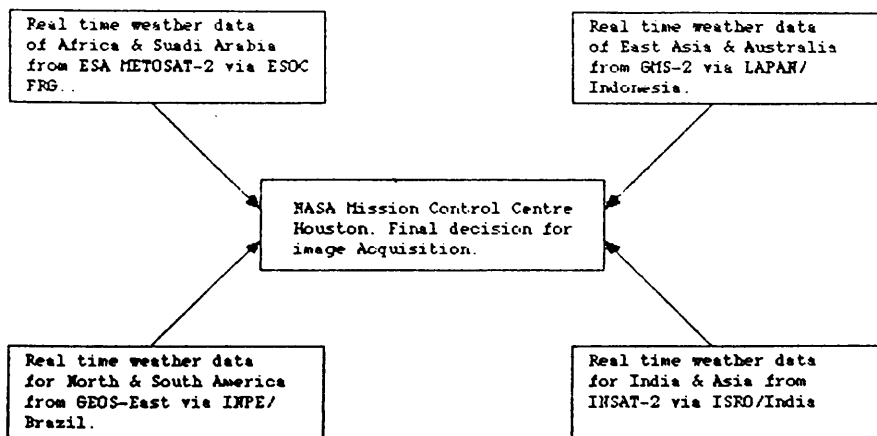


Fig. 6.7 Overall Flow of Information and Commands.

6.4.2 MOMS Image Processing

The processing of the MOMS image data was carried out at the West German Remote Sensing Data Centre at DFVLR. Quick look images were produced from the HDT before the data were transferred to standard 1,600 bpi CCTs. Radiometric and geometric corrections were applied to produce system corrected digital data on CCTs. From these system corrected digital data, hard copies can be produced upon request as transparencies and paper prints. The overall flow of MOMS image processing is shown in Fig. 6.8.

6.4.2.1 Radiometric Correction

Linear array systems have the disadvantage that each of the individual elements in the sensor arrays has a different radiometric response. Therefore, corrections to smooth out these differences in the image, so that the brightness values in the image can relate to the radiations reflected by each point in the imaged ground scene, are necessary. These corrections are carried out based on the variations in response noted during calibration. Any differences in the responses of the individual pixels within an array which are not compensated for give rise to image striping parallel to the flight direction.

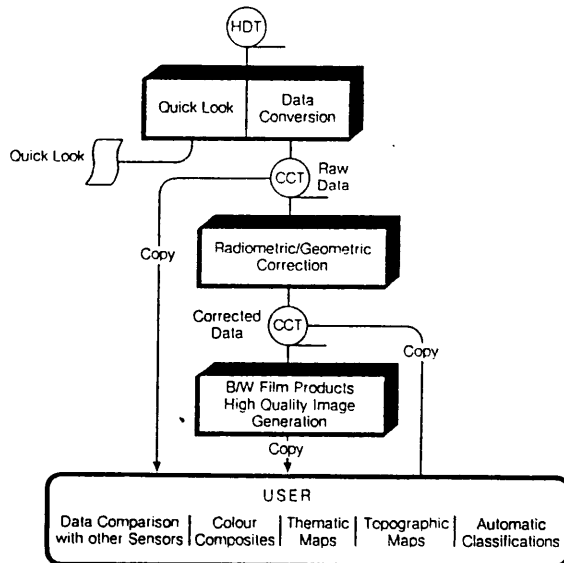


Fig. 6.8 Processing Operations of MOMS-1 Image Data.

6.4.2.2 Geometric Correction

Geometric correction was also carried out during processing at DFVLR using calibration and recorded satellite positional and attitude

data. The calibration data were used in the correction for the distortions which are associated with the geometry of the scanner itself and its optical system. The satellite positional and attitude data were used in the correction for the distortion introduced in the images by the variations in the positional and attitude parameters of the platform. The effects of Earth's rotation and curvature were also eliminated.

6.5 SPOT HRV Sensors

As mentioned in Chapter 2, SPOT is an operational satellite system initiated by the launch of SPOT-1 in 1986. The SPOT satellite and its imaging sensor were conceived by the French Institut Geographique National (IGN). Two identical High Resolution Visible (HRV) sensors operating in the visible region of the electromagnetic spectrum with the capability of acquiring either panchromatic and/or multispectral image data, represent the main part of the SPOT-1 payload. Since these represent the first long life operational space linear array imaging system and are bound to have a great impact on the type of small scale topographic mapping which is the main concern of this thesis, a detailed description is included in this chapter.

6.5.1 Description of HRV Sensors

The HRV sensor consists of an optical assembly which focusses the image of the scan-line on a linear array of CCDs. These CCDs are then sampled at an appropriate time by the electronic sampling systems as the satellite moves along its orbit to provide a continuous strip image of the Earth's surface. Fig. 6.9 shows the optical and detecting system of the HRV sensor. The optical system is a folded catadioptric telescope with an equivalent focal length (f) of 1,082 mm and an aperture of $f/3.5$.

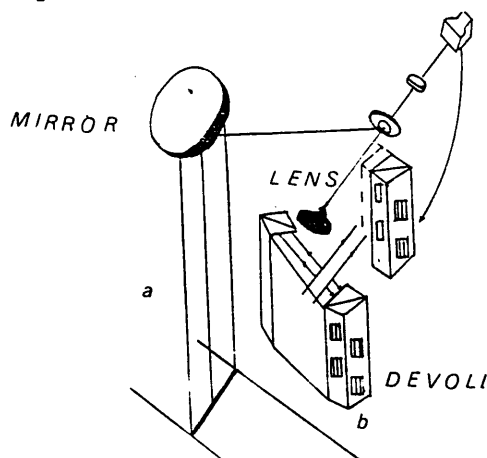


Fig. 6.9 SPOT-1 HRV Optical and Electronic Components.

The reflected solar radiation coming from the Earth's surface is reflected through 90° at the telescope entrance by a plane elliptical mirror to enter the telescope. It is this mirror, mounted on bearings and driven by a stepper motor, that permits HRV to record off-nadir imagery over an angular range of $\pm 27^\circ$ (Lillesand et al, 1987). As far as topographic mapping is concerned, the off-nadir viewing capability gives the major advantage of acquiring overlapping images of the ground surface with various base:height (B:H) ratios from neighbouring satellite orbits, Fig. 6.10.

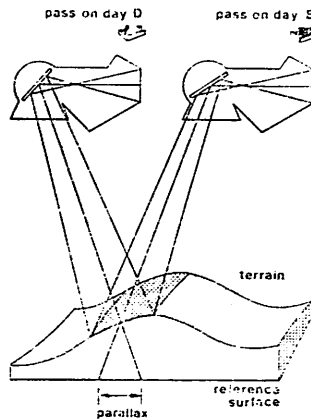


Fig. 6.10 SPOT Stereoscopic Image Acquisition Capability.

The spherical collector mirror collects and focusses the received radiation on the linear array of detectors located at the focal plane of the telescope. The aberrations of this spherical mirror are corrected by a lens doublet mounted just behind the entrance pupil. The field curvature distortion inherent in such an optical combination is corrected by a field lens mounted just before the focal plane of the telescope. When used in its multispectral mode, a focal plane beam-splitter separates the incident radiation into three narrow spectral bands - $\lambda=0.5 - 0.59 \text{ um}$; $\lambda=0.61 - 0.68 \text{ um}$; and $\lambda=0.79 - 0.89 \text{ um}$.

The detection system of the HRV sensor consists of an assembly of four detector arrays. These four arrays are accurately positioned in a staggered configuration as shown in Fig. 6.9b. These assemblies recombine the four quarter-line images to produce a full line image covering the entire 60 km field without discontinuity. As can be seen in Fig. 6.9, four assemblies of detectors (DEVOLI) are used, one for

the panchromatic channel and one for each of the three multispectral channels.

When the HRV sensor is used in multispectral mode, two CCD pixels are used to produce a single image pixel. This means that the ground pixel size in the multispectral images is 20 m instead of the 10 m of the panchromatic mode.

The signals generated by the CCD arrays are sampled by two separate electronic systems, one for each of the panchromatic and multispectral modes. The panchromatic system samples the four arrays of the panchromatic channel. The 10 m ground pixel of the panchromatic mode demands a very high CCD sampling rate. To cope with this high sampling rate, the panchromatic electronic system consists of four identical "chains" operating in parallel so that each can sample one array during the full sampling period. All the image data are then multiplexed to generate the output serial bit stream in a definite format.

By contrast, the multispectral system samples the 12 (3x4) arrays corresponding to the multispectral channel. In the multispectral electronic sampling system, given the 20 m ground pixel size, the sampling rate for an individual scan line is half that of the panchromatic one. Therefore two CCD arrays can be sampled sequentially by only a single electronic chain of the same design as that used for sampling an individual CCD array used in the panchromatic mode. The total multispectral sampling system therefore consists of 6 (2x3) sampling chains.

Each of the panchromatic and the multispectral sampling systems is associated with its own sequencer to synchronize all operations of sampling and output organization. The rate at which bits are output by the panchromatic sampling electronics is one-third greater than that of the multispectral sampling electronics. To overcome this, the panchromatic sampling system includes a data compression function which ensures that the system output bit-rate is identical to that of the multispectral sampling electronics.

Each of the two HRV instruments can operate in either the multispectral mode or the panchromatic mode. Since the bit-rate that can be transmitted by the telemetry subsystem is limited to 50 megabits/sec. only two of the four possible modes can be used at a time. The data are transmitted on X-band transmission frequency (8.025 to 8.4 GHz), so that any receiving station equipped to receive this frequency can receive HRV data. Two on-board recorders are used to

store image data over areas outside the range of receiving stations for later play back and transmission to the Toulouse and Kiruna receiving stations.

6.5.2 SPOT Image Processing and Products

Basically there are five levels of SPOT image processing which try to answer the requirements of a wide spectrum of users. These are:

i) Level 1A which ^{are} essentially raw data, since the only processing performed is the equalization of the responses of the detectors using calibration data.

ii) Level 1B in which ^tradiometric and geometric system corrections are carried out. The positional accuracy of this product is estimated to be $\pm 1,500$ m. for nadir viewing.

iii) Level 1P in which contrast enhancement is carried out in addition to the system correction. The small influences of roll, pitch, and nonlinear movement of the satellite are eliminated and the size of the images is enlarged to give 1:266,000 scale images in the 22.5 cm x 22.5 cm standard aerial format by resampling with a pixel size of 25 μ m on the image (which gives a 6.7 m ground pixel size).

iv) Level 2 in which precision processing is carried out. Radiometric corrections are carried out as in level 1B, but in addition to the normal system correction based on calibration and telemetred data, a geometric correction is based on the use of 6 to 9 ground control points for each scene. The image is fit to a map projection system such as Lambert Conformal, Transverse Mercator, etc. Positional accuracy of the produced image is estimated to be ± 50 m. for nadir viewing.

v) Level 2S in which scene registration processing using land marks is executed. Registration between scenes of the same area after this processing is carried out is estimated to be about ± 0.5 pixel.

All the above processing levels are available as full scenes or quarter scenes recorded on CCT, film and/or print. One full scene can be recorded on one 6,250 bpi (byte per inch) CCT or on two or three 1,600 bpi CCTs with a maximum capacity of 32 M bytes. Photographic products are also available with various processing levels.

6.6 Planimetric Image Rectification and Transformation

Planimetric image rectification may be performed using the procedures described in Chapter 4 for the rectification and transformation of MSS & TM images. Since the geometry of the images acquired by linear array systems is much stable than those acquired by optical-mechanical scanners, one expects that simple transformation models should result in an accuracy which is sufficient for the purposes of topographic mapping. In this investigation, the same methods and mathematical models for linear conformal, affine and polynomial transformations described in the planimetric testing of MSS and TM images in Chapters 4 and 5 were again used for the testing the MOMS images taken over the Sudan.

As in the case of the images of the MSS and the TM, this planimetric rectification or transformation seeks to eliminate the effects of the various distortions inherent in the images of linear array systems. These include the distortions and displacements caused by the variation in the platform's velocity, attitude, and altitude in addition to those caused by the Earth's curvature and rotation. In this case, the fact that the whole scan-line is imaged simultaneously should be taken into account for the simplification of the procedures and mathematical models discussed in Chapter 4. For example, in piece-wise rectification, since all the scan line is imaged simultaneously, no subdivision across scan-lines is needed. Also since the geometric distortions introduced in each scan line are linear, a simple form of transformation such as an affine transformation may result in an accuracy which is sufficient for topographic mapping.

6.7 Three-dimensional Transformation

The formation and measurement of a three-dimensional model of the terrain from linear array scanner images is a process which is similar to the formation and exterior orientation of models and the determination of X, Y and Z coordinates of the terrain points which is carried out with frame photography. In this case, the mathematical formulae are based on the special case collinearity equations given above as equations (6.1). Linearizing equations(6.1) using Taylor's series, results in the following equations (El Hassan, 1978; Hofmann, 1985).

$$v_{x_s} = (\delta x_s / \delta w_s) dw_s + (\delta x_s / \delta \phi_s) d\phi_s + (\delta x_s / \delta k_s) dk_s + \\ (\delta x_s / \delta X_{OS}) dX_{OS} + (\delta x_s / \delta Y_{OS}) dY_{OS} + (\delta x_s / \delta Z_{OS}) dZ_{OS} + F'^0$$

$$v_{yS} = (\delta y_S / \delta w_S) dw_S + (\delta y_S / \delta \theta_S) d\theta_S + (\delta y_S / \delta k_S) dk_S +$$

$$(\delta y_S / \delta X_{OS}) dX_{OS} + (y_S / \delta Y_{OS}) dY_{OS} + (\delta y_S / \delta Z_{OS}) dZ_{OS} + F''^O$$

.....(6.3)

in which F'^O and F''^O are the discrepancies between the measured image coordinates and those computed from equation (6.1) using approximate orientation elements.

If the approximate orientation elements corresponding to one scan-line selected as the reference line are $X_{OC}, Y_{OC}, Z_{OC}, w_C, \theta_C,$ and k_C then the approximate values of $X_{OS}, Y_{OS}, Z_{OS}, w_S, \theta_S,$ and k_S corresponding to scan-line s will be given by:

$$\begin{array}{rcl} X_{CS} & & X_{CC} & & dX_O \\ Y_{OS} & & Y_{OC} & & dY_C \\ \cdot & = & \cdot & + & \cdot \\ \cdot & & \cdot & & \cdot \\ k_S & & k_C & & dk \end{array} \quad \text{.....(6.4)}$$

in which dX_O, \dots, dk are the change values in the orientation elements.

These orientation element changes are functions of the time difference t_s between the instant of exposing the reference scan-line and that of exposing the scan-line s . t_s can be considered as a linear function of x_s , the x-coordinate, in which case, the changes in orientation elements of scan-line s relative to those of the reference scan-line are given by:

$$\begin{array}{l} dX_O = a_x + b_x x_s \\ dY_C = a_y + b_y x_s \\ \cdot \\ \cdot \\ \cdot \\ dk = a_k + b_k x_s \end{array} \quad (6.5)$$

Substituting these in equations(6.3), they reduce to the following equations (El Hassan, 1978):

$$\begin{aligned}
v_{x_s} = & (\delta x_s / \delta w_s) a_w + (\delta x_s / w_s) b_w x_s + (\delta x_s / \delta \phi_s) a_o + (\delta x_s / \delta \theta_s) b_o x_s \\
& (\delta x_s / \delta k_s) a_k + (\delta x_s / \delta k_s) b_k x_s + (\delta x_s / \delta X_{OS}) a_x + (\delta x_s / X_{OS}) b_x x_s + \\
& (x_s / \delta Y_{OS}) a_y + (\delta x_s / \delta Y_{OS}) b_y x_s + (\delta x_s / \delta Z_{OS}) a_z + (x_s / \delta Z_{OS}) b_z x_s + F''^0 \\
v_{y_s} = & (\delta y_s / \delta w_s) a_w + (\delta y_s / \delta w_s) b_w x_s + (\delta y_s / \delta \phi_s) a_o + (\delta y_s / \delta \theta_s) b_o x_s + \\
& (\delta y_s / \delta k_s) a_k + (\delta y_s / \delta k_s) b_k x_s + (\delta y_s / \delta X_{OS}) a_x + (\delta y_s / X_{OS}) b_x x_s + \\
& (\delta y_s / \delta Y_{OS}) a_y + (\delta y_s / \delta Y_{OS}) b_y x_s + (\delta y_s / \delta Z_{OS}) a_z + (\delta y_s / \delta Z_{OS}) b_z x_s + F'''^0 \\
& \dots\dots\dots (6.6)
\end{aligned}$$

At least six points are needed for the determination of the 12 unknown coefficients. For a stereo pair, 24 unknown coefficients need to be determined, but since each point contributes four equations, two for each image, the six points will be necessary and sufficient for the solution.

With film transparencies, the central scan-line in the image frame can be taken as reference and the central pixel in this scan-line as the principal point. Reference marks at frame corners or mid-sides will help locating this principal point. The image can then be regarded as if it was taken by a strip camera. Equations (6.1) and (6.6) are then used with image coordinates which are measured on a comparator. Alternatively conventional collinearity equations may be used, in which case, additional adjustment parameters should be incorporated in the solutions to compensate for image distortions resulting from the difference in geometry between the conventional frame photograph and the scanner image (El Hassan, 1978; Konecny, 1987).

The 3D solution using equations (6.3) to (6.6) is planned to be used in the automatic processing and mapping procedures using stereo MQMS images proposed by Hofmann (1985 and 1986). In this solution, the satellite positional and attitude parameters are given by a satellite positioning and attitude measurement system which can provide these parameters with a satisfactory precision each time a number of scan lines is acquired (Fig. 6.11). The satellite positions at which these parameters are read are called anchor points. From the positional and attitude readings at the anchor points, the position and attitude

parameters which were present during the acquisition of the scan lines between these anchor points are computed using equations (6.4) and (6.5). These parameter values are then substituted in equations (6.1) to determine X, Y, Z coordinates of the terrain or execute any mapping process.

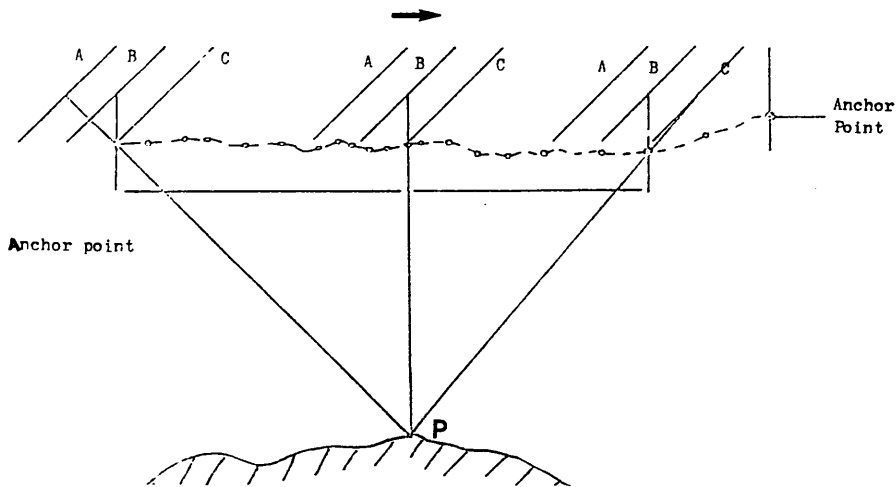


Fig. 6.11 Principle of Linear Array Automatic Mapping Operations.

With linear array systems having a configuration such as the SPOT HRV, where the reflecting steerable mirror or some other mechanism is used to reflect the solar radiation coming from the off-nadir direction into the scanner telescope, the effect of the angle to which this mirror is tilted can be added to the rotation matrix of equations (6.1).

With digital images, the image coordinates of the points required for the above planimetric and 3D transformation operations can be computed from the row and column values of each point by multiplying these values by the dimensions of the pixel at the focal plane of the sensor system and deducting the computed coordinates of the central pixel. The row and column values can be determined after displaying the digital image on the screen of the image processing system by centring the cursor on the point and taking the readings displayed. However, this may be the case when the coordinates of a limited number of points are required such as in accuracy testing, resection, triangulation, etc. In operations where the stereoscopic measuring of model coordinates of great numbers of points, such as in image rectification, is required, analytical machines using digital correlation may be used.

In general, if a fully automated rectification or 3D transformation

of images is desired in which correlation is used with either hard copy or digital images, linear array systems can offer substantial flexibility in this complex solution. In such a solution, digital correlation is utilized to determine the conjugate image points on the overlapping images and hence determine the X,Y,Z coordinates of the points from the solution of equations (6.1) and (6.3). This possible flexibility is discussed in detail by Snyder (1982) with respect to Mapsat and Stereosat proposals and by Hofmann (1981) with respect to stereo MOMS.

However, the difficulties of applying this fully automated rectification in woody areas, deserts, sandy plains and vast areas where no significant features are present still remain unsolved. These difficulties make this solution impracticable.

In general, the digital rectification of the linear array images can be carried out by both direct or indirect methods as shown in Figs. 6.12 and 6.13 (Amin, 1986; Konecny, 1987). In the direct method, the positions of the image points (pixels) in the rectified image are computed using the inverse of the collinearity equations (6.1). The brightness values of these pixels are interpolated from those in the original image.

By contrast in the indirect method, the points or pixels in the rectified image are selected first, i.e a uniform grid of pixels covering the area of the rectified image is selected. Then the positions of the corresponding pixels on the original image are computed using the collinearity equations (6.1). The brightness values are then interpolated from the pixels of the original image surrounding the computed locations of the pixels of the rectified image.

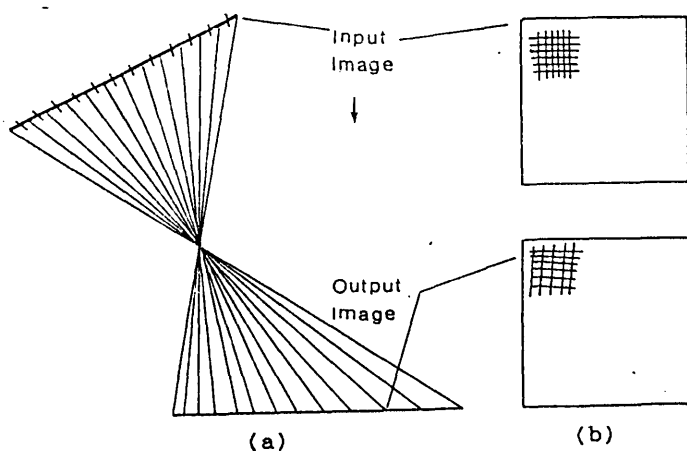


Fig. 6.12 Direct Method of Digital Image Rectification.

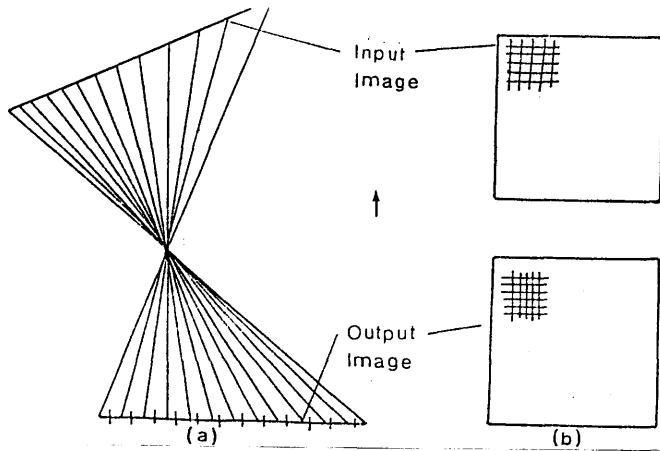


Fig. 6.13 Indirect Method of Digital Image Rectification.

However, both the direct and indirect methods involve the computation of the positions of all points using either the inverse collinearity or the collinearity equations. The computation in the indirect method, can be greatly reduced if only a small number of pixels (anchor points), which are distributed over the area of the rectified image are used. The positions on the original image of these anchor points are computed first using the collinearity equations (6.1). Then the positions on the original image of the rest of the pixels of the rectified image are interpolated using 2D polynomials based on the computed locations of the anchor points.

The computation in the direct method of rectification can also be reduced by dividing the original image into small areas. The positions on the rectified image of the pixels within each small area is computed using simple 2D polynomial transformation. This is followed by the interpolation of the brightness values.

6.8 Summary

In the above account, a short description of linear array systems in general has been given, followed by an explanation of the geometrical relations which exist in the images acquired by these systems. The various configurations of stereoscopic imaging linear array systems have also been explained. The German MOMS device has been described, followed by a description of the SPOT HRV system as an operational linear array system. This was followed by a discussion of the planimetric transformation procedures used in the accuracy tests conducted on MOMS images and a theoretical discussion of the 3D transformation of linear array images in general. In the next chapter, the accuracy and interpretation tests carried out by the author on MOMS

images over the Sudan will be reported and described. The results obtained from these tests will be presented and analyzed. The accuracy of the height determination expected to be obtained from SPOT HRV stereoscopic images is then predicted from those results and compared with those which have resulted from actual height tests carried by various investigators on SPOT HRV images which have been published recently.

CHAPTER 7

Geometric Accuracy and Interpretation Tests of MOMS Images

7.1 Introduction

As mentioned in Chapter 6, solid state array sensors represent the latest achievement in the technology of remote sensors. The first experiments using imaging array sensors from space were those conducted from the Space Shuttle utilizing the German-built sensor called the Modular Opto-electronic Multispectral Scanner (MOMS). MOMS was designed as an experimental imaging system for multimission utilization and implemented as a modular system to allow different configurations of the sensor modules to suit the requirements of individual missions. In the two experiments conducted till now, MOMS was used to acquire monoscopic images only. A stereo MOMS mission was planned to be launched in 1986/87, but unfortunately all planned missions have been halted by the loss of the American Space Shuttle Challenger and the subsequent cessation of all Shuttle flights on which MOMS experiments depend to provide the imaging platform. The two MOMS experimental flights were soon followed by the launch of the first operational space remote sensing system which is totally based on linear array sensors - the SPOT-1 HRV. The SPOT mission has been very successful, the sensors having returned several thousand scenes at the time of writing this thesis. Unfortunately it has not been possible to acquire SPOT images of the test areas in the Sudan. However, fortunately MOMS images had been taken over these areas and these have been used to carry out geometric and interpretational tests which should be representative of the results that can be obtained from linear array imaging scanners.

Thus in this chapter, the geometric accuracy and interpretation tests which have been conducted by the author on the images which were acquired by MOMS over the Red Sea Hills area are reported upon. The test procedure is explained and the results which have been obtained are presented and analyzed. The planimetric and height accuracies which might be obtained from SPOT-HRV images over the Sudan are then estimated and an analysis of the applicability of SPOT-HRV images to the topographic mapping of this area is conducted. Following this, the results of the interpretation test are presented and discussed. Finally the conclusions which may be drawn from the geometric accuracy and interpretation tests regarding the applicability of linear array sensors to the topographic mapping of the developing countries in

general and the Sudan in particular are stated.

7.2 Test Area

As noted above, one of the STS-11 orbital tracks passed over the northern part of the Red Sea Hills area described in Chapter 3 and images of the area were taken using the MOMS-1 sensor. Two MOMS images centred at latitude $19^{\circ} 27' N$ and longitude $35^{\circ} 29' E$ have been used in this investigation. These two images were taken simultaneously and therefore cover the same ground area which extends between latitudes $18^{\circ} 52' N$ & $20^{\circ} 15' N$ and longitudes $35^{\circ} 45' E$ & $36^{\circ} 42' E$. The first of these images is Scene no. 235 which was acquired by the panchromatic channel of MOMS (Channel 1) and is referred to as Scene 1 in this investigation. The other image is Scene no. 236 (Scene-2) which was acquired by the infrared channel of MOMS (Channel 2). Figs. 7.1 and 7.2 show the 1:782,000 scale paper prints of these two images. The two images were acquired simultaneously on 8th February, 1984 at 6.27 GMT (8.17 :am Sudan local time) from an altitude of 296 km. As can be seen from Figs. 7.1 and 7.2, the radiometric quality of these images is superb but the area which is covered by them is rather hilly with very few cultural features. While the superb quality of these images confirms the potential of linear array sensors in space remote sensing, the area imaged is typical of a rugged area with little development where the scarcity of detail poses a big problem in undertaking image rectification and transformation operations.

A set of 51 well defined points was selected and identified on the 1:100,000 scale maps covering the area. Since the area is that described in Chapters 3 and 5 and shown in Figs. 7.1 and 7.2, these points are mostly hill tops, ridges, and well-defined points located along dry streams with a few points situated on top of isolated rocks. The image coordinates of these points were measured on both scenes monoscopically using the Stecometer as described in Chapter 3. The along-scan axis of each image was oriented approximately parallel to the x-axis of the comparator. The corresponding ground coordinates of these points were scaled off the 1:100,000 scale topographic maps covering the area in a manner similar to that described in Chapter 3.

PLR WT-DA/BW MOMS-01 STS-11 / ABS.KORR. CCT-NR.236 / 4.04.86 A.NR.056103
630 MICROMETER
TS-11 DP-LP WT-DA 09 00 85 MITTHEIER CCT-NR. 236



Fig. 7.1 1:782,000 Scale Paper Print of MOMS Scene 2.

ALR WT-DA/BV MOMS STS-11 ABS.KORR. CCT-NR.235 29.11.85 A.NR.055344

090 PPKHTEP
STS-11 10:14:50 UT-04 04 05 WITTHEIEP CCT-HP 235

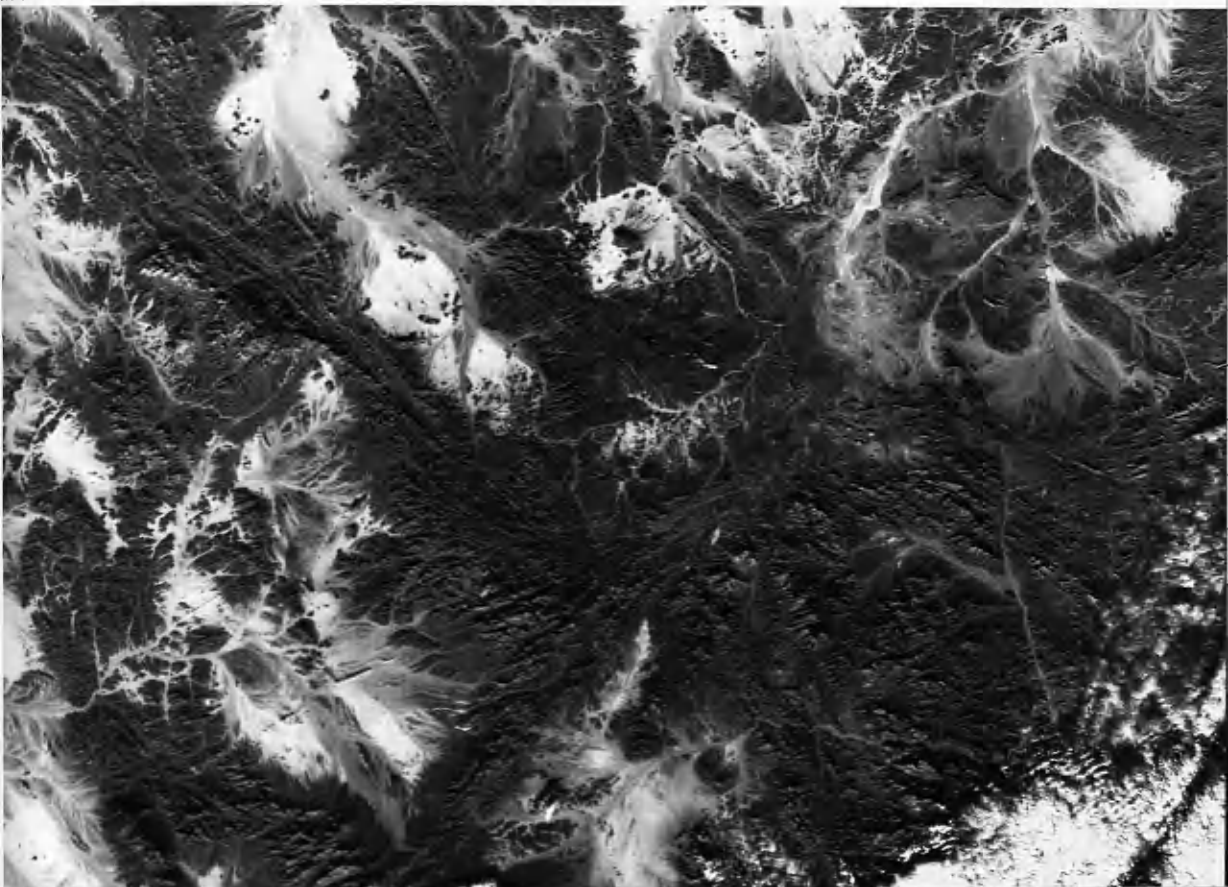


Fig. 7.2 1:782,000 Scale Paper Print of MOMS Scene 1.

7.3 Test Procedure

The same procedure as that carried out in the geometric accuracy tests of the MSS and TM images in Chapter 5 was followed in the geometric accuracy test of MOMS images over the Sudan Red Sea Hills area. As explained in Chapter 6, the geometry of the images acquired by linear array sensors is much closer to that acquired by photographic strip cameras than to that of the optical mechanical scanners. Therefore the distortions inherent in their images should be simpler in terms of pattern compared with those inherent in those images which are acquired by optical-mechanical scanners. For this reason, the use of quite simple two-dimensional (2D), i.e affine or first order, polynomial transformations might be expected to produce the required planimetric accuracy inherent in their images. This is expected to be the case with MOMS images despite the fact that the optical system of MOMS uses two lens systems to project the image of the narrow ribbon of the ground surface across the direction of flight onto the linear array of CCDs. The use of two lenses destroys the simple central projection geometry within the individual scan lines and could introduce different patterns of distortion in different parts of the image. Thus in this investigation, once again linear conformal and affine transformations were executed first and were then followed by a series of polynomial transformations of various orders, i.e polynomials from the 4-term to the full 10-term of Table 4.1 were used in the geometric accuracy test of the MOMS images.

In the first set of transformations, all 51 measured points have been used as control points to compute the transformation parameters in each individual transformation and to derive the residuals between the computed ground coordinates and the corresponding values which had been scaled off the 1:100,000 scale topographic maps. In the second set of transformations, a set of 20 well distributed points were selected and used as control points. The remaining 31 points were considered as check points.

Following the geometric accuracy test, an interpretation test was carried out on the two MOMS images covering the Red Sea Hills area. As had been done in the interpretation tests of the MSS and TM images in Chapter 5, a list of these features which are shown on the 1:100,000 scale topographic maps of the area was prepared. To this list were added those features which are not available in this part of the Red Sea Hills area but they are usually shown on this series of topographic maps. Then a thorough search for these features which are available in the area and shown on the 1:100,000 scale maps was conducted using a

mirror stereoscope and a magnifier. For those features which are not available in the area covered by the images, estimates were made about their detectability on the MOMS images judging from the radiometric quality of the two images and the experience of detecting these features on the MSS and TM images.

7.4 Accuracy Test Results

As expected, the results which have been obtained from the geometric accuracy test of MOMS images give planimetric root mean square errors (r.m.s.e.) roughly about equal to the ground pixel size of these images using an affine transformation. No significant improvement occurred with the use of high order polynomials. In more detail, the results are as follows:

7.4.1 Linear Conformal Transformation Results

The linear conformal transformation of the MOMS Scene 1 using all the 51 points as control points resulted in r.m.s.e. values of ± 547 m, ± 508 m and ± 746 m in easting (E), northing (N) and vector (V) respectively. The corresponding values which resulted from the linear conformal transformation of Scene 2 using all 51 points as control points are ± 542 m ± 510 m and ± 744 m. The residuals which have resulted from this transformation at all points in Scenes 1 and 2 have been plotted as Fig. D.1 and D.2 to see whether they have any systematic behaviour or not.

The linear conformal transformation of Scene 1 using the set of 20 well distributed points as control points on both scenes has resulted in r.m.s.e. values of ± 724 m, ± 630 m, & ± 959 m in eastings, northings, and vector respectively at the control points and corresponding values of ± 500 m, ± 353 m, and ± 612 m at the check points. The r.m.s.e. values which were obtained from the linear conformal transformation of Scene 2 using the 20 points as control points were: ± 724 m, ± 628 m, and ± 959 m in easting, northing and vector respectively at the control points and ± 502 m, ± 341 m, and ± 607 m in those at the check points. The patterns of the residuals which have resulted from this transformation are shown in Figs. D.3. and D.4. It is clear that the r.m.s.e. values which have resulted from the linear conformal transformation are much too large to be acceptable in topographic mapping at any of the small scales considered in this investigation. However, the plots of the residual errors displayed in Figs. D.1 to D.4 show quite clearly that a large proportion of these residuals result from the systematic distortions inherent in MOMS images which have not been eliminated during

processing. The major part of these systematic distortions results from a scale affinity, a feature which is very common in scanner images. Therefore one would expect an affine transformation to eliminate most of these distortions and produce much better results.

7.4.2 Affine Transformation Results

Using all the 51 measured points as control points in the affine transformation of both images has resulted in r.m.s.e. values of ± 19 m, ± 20 m and ± 27 m in easting, northing and vector respectively for Scene 1. The corresponding r.m.s.e. values for Scene 2 were ± 19 m, ± 21 m and ± 28 m. The patterns of the residuals which have resulted from this transformation are shown in Figs. D.5 and D.6. It goes virtually without comment that these figures represent a giant improvement (27 times better) over those for the original unrectified image given by the linear conformal transformation.

The r.m.s.e. values which have resulted from the affine transformation of Scene 1 using the set of 20 well distributed points as control points are ± 22 m, ± 20 m and ± 30 m in easting, northing and vector respectively at the control points. The corresponding values of ± 18 m, ± 21 m and ± 28 m have resulted in the easting, northing and vector at the check points. Again this represents a 20x improvement in the planimetric accuracy of the image over the figures obtained with the unrectified MOMS image.

The r.m.s.e. values which have resulted from the similar affine transformation of Scene 2 were ± 25 m, ± 21 m and ± 33 m in easting, northing and vector at the control points and ± 19 m, ± 21 m and ± 28 m respectively in those at the check points. The patterns of the residuals which have resulted from this transformation on Scenes 1 and 2 are shown in Figs. D.7 and D.8. As can be seen from Figs. D.5 to D.8, no obvious systematic pattern or trend in the resulting residuals can be noticed. This confirms that the largest proportion of the distortion inherent in MOMS images results from scale affinity. Moreover, from all the r.m.s.e. values which have resulted from the affine transformation, it is clear that an average vector planimetric accuracy of ± 28 m has been achieved from the MOMS images over the Red Sea Hills area. The comparison of this planimetric accuracy with the accuracy requirement values of Table 3.2 reveals that, by using a simple affine transformation, information with a planimetric accuracy which satisfies the accuracy requirements of the 1:100,000 scale topographic maps can be extracted from MOMS images.

The planimetric accuracy value of ± 28 m is quite satisfactory especially when one considers that the ground coordinates of the points used as control and check points in this test were scaled off the 1:100,000 scale topographic maps of the area with an estimated precision of about ± 14 m and that the control and check points which were used were not as well defined as they should be. Taking the accuracy of the scaled ground coordinates of the points into consideration, the planimetric accuracy which can be achieved from MOMS images over the Sudan can be taken as ± 25 m, which is about equal to the ground pixel size in MOMS images.

Despite the fact that the use of an affine transformation resulted in a satisfactory planimetric accuracy, polynomial transformations were carried out to investigate whether the residual geometric distortions inherent in the MOMS images can be compensated for more rigorously using high order polynomials than is possible using the affine transformation.

7.4.3 Polynomial Transformation Results

As mentioned above, the 4-term to 10-term polynomials of Table 4.1 were employed in the polynomial transformations of the MOMS images used in this investigation. Again these transformations were carried out in a similar way to that followed in the geometric accuracy tests of the MSS and TM images in Chapter 5, i.e. starting with the 4-term polynomial and adding a term with each iteration until the full 10-term polynomial has been reached. The r.m.s.e. values which have resulted from use of all points as control points in these polynomial transformations of Scenes 1 and 2 are listed in Table 7.1. As can be seen from Table 7.1, no significant improvement whatsoever occurred with the application of these polynomial transformations. This is confirmed by the patterns of residuals which resulted from each of the polynomial transformations and which have been plotted in Figs. D.9 to D.22. As can be seen from these figures, the patterns of the residual errors remain virtually the same as those which have resulted from the affine transformation.

The results which were obtained from each of the polynomial transformations that were carried out using the set of 20 well distributed points as control points are listed in Tables 7.2 and 7.3. The patterns of the residuals which have resulted from the application of these transformations on Scene 1 are shown in Figs. D.23 to D.29. Since the patterns of the residuals which have resulted from the various polynomial transformations of Scene 2 are virtually the same,

they are not included in this thesis. Again, as can be seen from Tables 7.2 and 7.3 and Figs. D.23 to D.29, no significant improvement has occurred through the application of any of these polynomials. This again confirms the fact that the geometrical distortions inherent in MOMS images are of a very simple pattern and can easily be compensated for using an affine transformation.

TRANSFORMATION	SCENE 1			SCENE 2				
	No. of Pts	r.m.s.e. E (m)	r.m.s.e. N (m)	r.m.s.e. V (m)	No. of Pts.	r.m.s.e. E (m)	r.m.s.e. N (m)	r.m.s.e. V (m)
LINEAR	51	547.25	507.66	746.46	51	542.20	509.56	744.06
AFFINE	"	19.45	20.50	28.26	"	19.00	19.78	27.43
POLYNOMIALS:								
4 terms $x y$	"	19.65	20.51	28.40	"	19.20	19.81	27.59
5 terms x^2	"	19.77	20.65	28.59	"	19.38	19.94	27.81
6 terms y^2	"	19.66	20.87	28.68	"	19.15	20.16	27.81
7 terms $x^2 y$	"	19.60	21.06	28.77	"	19.19	20.37	27.99
8 terms $x y^2$	"	19.82	21.17	29.00	"	19.41	20.36	28.13
9 terms x^3	"	19.56	20.81	28.56	"	19.20	20.32	27.96
10 terms y^3	"	19.12	20.87	28.31	"	18.73	20.32	27.63

Table. 7.1 Geometric Transformation Results for MOMS Images (using all control points).

TRANSFORMATION	CONTROL			CHECK				
	No. of Pts.	r.m.s.e. E (m)	r.m.s.e. N (m)	r.m.s.e. V (m)	No. of Pts.	r.m.s.e. E (m)	r.m.s.e. N (m)	r.m.s.e. V (m)
LINEAR	20	723.96	629.61	959.44	31	499.90	352.72	611.81
AFFINE	"	22.11	20.23	29.97	"	18.31	21.23	28.03
POLYNOMIALS:								
4 terms $x y$	"	22.68	19.83	30.13	"	18.47	21.61	28.42
5 terms x^2	"	23.34	20.21	30.87	"	19.24	22.84	29.87
6 terms y^2	"	23.76	20.87	31.62	"	19.32	22.85	29.92
7 terms $x^2 y$	"	23.15	21.44	31.55	"	19.63	22.57	29.91
8 terms $x y^2$	"	24.08	22.31	32.83	"	19.53	22.57	29.85
9 terms x^3	"	25.05	21.41	32.95	"	19.03	23.67	30.38
10 terms y^3	"	23.75	22.09	32.44	"	19.26	23.56	30.43

Table 7.2 Geometric Transformation Results for MOMS Scene 1.

TRANSFORMATION	CONTROL				CHECK			
	No. of Pts.	r.m.s.e. E (m)	r.m.s.e. N (m)	r.m.s.e. V (m)	No. of Pts.	r.m.s.e. E (m)	r.m.s.e. N (m)	r.m.s.e. V (m)
LINEAR	20	724.09	628.14	958.57	31	502.23	340.86	606.98
AFFINE	"	24.69	21.74	32.90	"	18.99	20.57	28.00
POLYNOMIALS:								
4 terms xy	"	25.44	21.64	33.40	"	18.94	21.14	28.38
5 terms x^2	"	26.21	22.23	34.37	"	19.59	22.04	29.49
6 terms y^2	"	26.95	22.96	35.40	"	19.63	21.97	29.46
7 terms x^2y	"	26.79	23.62	35.72	"	19.69	21.77	29.35
8 terms xy^2	"	27.88	24.57	37.16	"	19.73	21.69	29.32
9 terms x^3	"	29.11	24.13	37.81	"	19.59	23.69	30.74
10 terms y^3	"	28.30	24.94	37.72	"	19.36	23.59	30.52

Table 7.3 Geometric Transformation Results for MOMS Scene 2.

7.4.4 Analysis of the MOMS Geometric Accuracy Test Results

Obviously it has been demonstrated that no significant improvement occurs with the application of high order term polynomials and that the planimetric accuracy of well-defined detail which can be extracted from the MOMS images can be taken as ± 25 m. The comparison of this value with those given in Table 3.2 reveals that this is accurate enough to satisfy the topographic mapping standards for line maps or image maps of the Sudan at 1:100,000 scale. However, whether MOMS images could provide all or most of the information required to be shown on the 1:100,000 scale topographic maps or not still remains to be found out. This will be done in Section 7.5.

Several tests are reported to have been carried out by various investigators on MOMS images taken over various test areas. However almost^{all} the results of these published tests are interpretational in nature rather than geometric. Bodechtel (1987) reported upon tests in which a comparison of the MOMS images taken over five test areas with the TM images taken over the same areas was carried out by the AGF working group which was set up at the University of Munich in collaboration with NASA GSFC. The test areas selected were the Red Sea Hills area, the Cordillera coast in Chile, Nairobi in Kenya, the Sahel Channel in Mali and the cities of Jeddah, Mekkah and At'Taif in Saudi

Arabia. In this test, ground control points were selected and used to register TM Bands 2, 3 and 4 to MOMS images using second order polynomials and nearest neighbour resampling. The results presented by Bodechtel (1987) indicated that subsets of TM images could be registered to the MOMS images with an average r.m.s.e. of ± 10 m and that the geometry of MOMS was found to be very stable. It is interesting to note that the r.m.s.e. value of ± 10 m which was obtained is equal to the difference in the ground pixel sizes of MOMS and TM images. In terms of ground resolution and image content, the results showed that, although the MOMS has a smaller ground pixel size, it appeared to have the same feature resolving capability as the TM in these test areas.

In general, the results obtained from the geometric accuracy test which has been carried out on MOMS images over the Red Sea Hills area confirm that linear array sensors have a potentially valuable role to play in the small-scale topographic mapping of the developing countries. This is especially true when one considers that linear array sensors such as SPOT-HRV with ground pixel sizes of about half the 20 m pixel size of MOMS can be used to acquire high resolution images of the Earth's surface.

7.4.5 SPOT Geometric Accuracy Test Results

The discussion of the MOMS geometric test results leads to a discussion as to what could be expected from SPOT images in terms of planimetric and height accuracy. As mentioned in Chapter 6, the SPOT HRV sensors acquire panchromatic images with a 10 m ground pixel size as well as colour images with a 20 m ground pixel. The 10 m ground pixel size of the SPOT panchromatic channel could be expected to produce an improvement in the planimetric accuracy of the information which can be extracted from these images. Indeed the expected improvement in planimetric accuracy is now in fact being realised since published results give planimetric accuracy values which were obtained from SPOT as 3x better than those obtained by the author from the MOMS images over the Sudan Red Sea test area.

Hartley (1988) has reported the results obtained from the planimetric accuracy tests carried out by various investigators on the SPOT images taken over different test areas. These results were presented at the conference held in Paris in November 1987 to assess the capabilities of SPOT. Hartley reported that there was a definite trend in all the results presented to support the belief that SPOT images can be used to provide planimetric accuracy of ± 8 to ± 10 m. Hartley (1988) also gave the experience of the Ordnance Survey (OS) in

using SPOT images for the 1:100,000 scale mapping of the Yemen Arab Republic. In this, he reported that a planimetric accuracy of ± 12 m was obtained by the OS. This slightly poorer figure reflected the low density of control and the difficulty in finding natural detail which had not been distorted by the pixel structure to use as control points. In general, the expected improvement in planimetric accuracy is being realised since several other recently published results (e.g Picht, 1987; Kruck, 1987) give the planimetric accuracy which can be obtained from SPOT level 1A panchromatic images over certain test areas in developed countries as ± 8 m on average. These planimetric accuracy values, when compared with the values given in Table 3.2, indicate that SPOT images could be used as a source of information which is accurate enough to satisfy the planimetric accuracy requirements of 1:50,000 scale topographic maps. However, for most of the developing countries, a 1:100,000 scale series of topographic maps will often be regarded as quite enough. Therefore, in terms of purely geometric accuracy, SPOT images seem to be quite an appropriate choice for the topographic mapping of these countries. However, the cost of these images at present may be quite prohibitive for many developing countries as will be shown later.

As far as the accuracy of the height information which could be achieved from overlapping SPOT images is concerned, it depends basically on the base to height ratio (B:H). As mentioned in Chapter 6, various B:H ratio configurations can be obtained using the imaging process of SPOT HRV. However, published results of the geometric tests of the SPOT images which have been carried out by various investigators indicate that spot height accuracy of ± 4 m to ± 10 m could be obtained from these images (Hartley, 1988). Hartley reported that a spot height accuracy (m_h) of ± 4.4 m has been obtained by Denis of the IGN using the SPOT images taken over Algeria using 285 check points, while a spot height accuracy of ± 10 m has been obtained by the OS using the SPOT images taken over the Yemen Arab Republic.

With a 1:1 B:H ratio and level 1A panchromatic images, a spot height accuracy of ± 7 m is reported to have been obtained (Picht, 1987; Kruck, 1987). This was, of course, obtained over well developed areas using well defined control points such as road intersections, building corners, etc. Well defined control points of this kind are very difficult if not impossible to find in most of the developing countries. With the difficulties experienced by the author in finding suitable control points in the Red Sea Hills test area in mind, one can say that a spot height accuracy of ± 15 to ± 20 m should be obtainable in these areas using SPOT level 1A panchromatic images with 1:1 B:H ratio.

As mentioned in Chapter 3, the minimum contour interval possible for the plotting of contours photogrammetrically from any overlapping images is taken as 3.3x the value of the accuracy of the spot heights determined from the same images. Applying this to the average value of the spot height accuracy estimated above, the minimum contour interval possible with the SPOT images taken over the Sudan Red Sea should be 50 m. This contour interval value, when compared with the map requirements which were given in Table 3.2, shows that SPOT images can only be used for contouring which satisfies the requirements of the 1:500,000 scale maps. However, for some areas in the developing countries a contour interval of 50 m is quite acceptable on 1:100,000 scale maps. Table 3.1 which summarizes the most commonly used contour intervals worldwide shows the 50 m contour interval as being used in 1:100,000 scale maps. In fact, the experience of the OS in the Yemen Arab Republic, as reported by Hartley (1988), indicated that adequate 1:100,000 scale topographic maps with a contour interval of 40 m can be produced from the SPOT images despite the fact that some features which are required to be shown on these maps cannot be detected in the images. The contour interval of 40 m may be regarded as quite acceptable for the 1:100,000 scale topographic maps of the Sudan.

As far as the image content and the amount of information which can be extracted from the SPOT panchromatic image are concerned, surely a considerable improvement over the MOMS images will result from using the 10 m ground pixel size of SPOT. However this improvement is limited by the degree of development of the area under consideration. This point will be discussed further in Section 7.5 below.

7.5 Interpretation of MOMS Images

The area covered by the MOMS images in this investigation is similar to that covered by the TM image which was described in Chapter 5 in that it is a very hilly and thinly populated area. As mentioned in Chapter 5 and shown in Figs. 7.1 and 7.2, the dominant features in this area are the relief forms, including hills, ridges, isolated rocks, valleys, etc, and the natural drainage network system comprising dry streams, khors and wadis. Unfortunately cultural features are scarce since this area is thinly populated and only very small isolated villages and scattered nomadic camps are to be found in the narrow valleys between the hills and in the sandy plain to the west. The locations of some of these villages are shown on the 1:100,000 scale topographic maps of the area.

(1) Lines of Communication

Unfortunately not a single surfaced or unsurfaced road exists in this area. All the lines of communication that do exist comprise unsurfaced tracks interconnecting the scattered small villages and traversing the dry stream beds. These tracks have been plotted from 1:40,000 scale aerial photographs during the SSD and DOS photogrammetric mapping activities and are shown on the 1:100,000 scale topographic maps of the area as dotted lines. On the MOMS images, although the image radiometric quality is very good and the ground resolution is much improved over that of the MSS and TM images, these tracks still cannot be detected. In fact, the detection of these tracks may be expected to be very difficult if not impossible even on space images of still better ground resolution. This is because these tracks follow the highly reflective sandy beds of the wadis and khors. Therefore the contrast between these tracks and the background is negligible. However judging from the radiometric quality of the MOMS images and the degree of detail with which the existing relief and hydrological features are shown, one can say that surfaced roads, streets, railway lines, bridges, etc should be detectable on MOMS images, especially when the surrounding details are aligned in a regular pattern along both sides of these roads or railway lines.

(2) Cultural Features

The 1:100,000 scale topographic maps of the area show hardly any cultural features, but a number of wells are shown scattered over the plains and valleys. These wells could not be expected to be detectable on the MOMS images and indeed were not found.

(3) Built up Areas

As mentioned above, the built up areas in the area covered by the MOMS images in this investigation comprise very small villages and nomadic camps. The buildings within these small villages tend to be located widely apart from one another. Furthermore these buildings are built from bricks or mud formed from the local soil or from wood and bushes, all of which have negligible contrast with the background. The effect of all these factors is that not a single village has been detected on the MOMS images. However, one expects cities and towns of the kind which exist in the southern part of the Red Sea Hills area and in the Nile test area to be detected on the MOMS images. Judging from the radiometric quality of the images and the high resolution of these images, larger cultural features such as blocks of buildings, parks,

playgrounds, etc should be detectable on the MOMS images.

FEATURES SHOWN ON 1:100,000 SCALE MAPS	Scene 1		Scene 2	
	DETECTED	IDENTIFIED	DETECTED	IDENTIFIED
Communication:				
Hard surfaced roads	3	2	3	2
Unsurfaced roads	2	1	2	1
tracks	0	0	0	0
Footpaths	0	0	0	0
Streets	1	0	1	1
Bridges	3	2	3	3
Ferry terminals	0	0	0	0
Railways	2	1	2	1
Railway stations	0	0	0	0
Culture:				
Cultivated land	3	3	3	3
Big cities	3	2	3	3
Towns	2	1	2	2
Villages	1	0	1	0
Ruins	0	0	0	0
Electrical stations	0	0	0	0
Pipelines	0	0	0	0
Powerlines	0	0	0	0
Wells	0	0	0	0
Storage tanks	0	0	0	0
Cemeteries	1	0	1	0
Airports	3	3	3	3
Landing Grounds	2	1	2	1
Hydrology:				
Rivers	3	3	3	3
Falls	3	2	3	3
Canals	3	3	3	3
Irrigation channels	2	0	2	1
Water bodies	3	1	3	2
Dams	3	3	3	3
Reservoirs	3	2	3	3
Hydrography:				
Tidal flats	*	*	*	*
Reefs	*	*	*	*
Rocks	3	0	3	0
Near shore bathymetry	0	0	0	0
Water depth	0	0	0	0
Marsh	3	3	3	3
Harbours	3	2	3	3
Small harbours	3	1	3	2
Shore line	3	3	3	3
Islands	3	3	3	3
Relief forms:				
Sand dunes	3	0	3	0
Gravel beds	1	0	2	0
Elevated grounds	3	3	3	0
Contours	0	0	0	0
Vegetation:				
Woodlands	3	2	3	3
Scattered trees	0	0	0	0
Scrub	0	0	0	0
Orchards	2	1	3	2
Others:				
Adminstrative boundaries	0	0	0	0
Rest houses	0	0	0	0
Triangulation pillars	0	0	0	0

0 = NOT; 1 = SOMETIMES; 2= OFTEN; 3 = YES; AND * = REQUIRES REPEATED AVERAGE

Table 7.4 Interpretation Results for the MOMS Images.

(4) Hydrology

The main hydrological features in the area covered by the MOMS images in this investigation are dry streams, wadis, and khors. All these features show up quite clearly on the MOMS images and no difficulty was experienced in their detection. In fact, the degree of detail in which these features are imaged will almost certainly be difficult to show on the 1:100,000 scale maps. However, over the highly reflective sandy plain to the west of the Red Sea Hills, the detection of the small details of these features does become difficult on Scene 1 i.e the panchromatic image. This is because the high reflection of this sandy plain makes the area appear in a uniformly white tone so hiding these small details. In general, these hydrological features show up much more clearly on Scene 2 (the near infrared image) than on the panchromatic image.

(5) Vegetation

No vegetation of significance is shown on the 1:100,000 scale maps of the area. Also no cultivated areas are shown to be existing in the area. Instead a general representation of the scattered leafless trees and bushes is shown. A general indication of the existence of desert grassy vegetation on the beds of khors and wadis is also given on the maps. On the MOMS images, no vegetated or cultivated areas can be detected. However judging from the previous experience in the interpretation of MSS over the Nile test area, if vegetated or cultivated areas were present, then almost certainly they could be detected on the MOMS images.

The results of the interpretation test of the MOMS images over the Red Sea Hills area are summarized in Table 7.4. In fact, the amount of information which can be extracted from MOMS images over such a hilly area does not differ much from that which could be extracted from the TM images taken over the same area. However, one would expect this situation to improve in more developed areas. In areas such as the Nile test area, the amount of information which could be extracted from the MOMS images might be expected to reach about 60% of the total information which is required to be shown on the 1:100,000 scale topographic maps.

Alwashe et al (1986) reported the results of the interpretational and mapping tests which have been carried out on the MOMS image taken over Jeddah, Suadia Arabia. The result of this work was two city maps showing (i) the road network; and (ii) a thematic land use

classification exhibiting built up areas; dense and sparse vegetated areas; outcropping rocks; sand, gravel or clay coverage; shallow water and tidal fluctuation zone; coral reef and perennial water. These results confirm that the information which can be extracted from MOMS images taken over developed and built up areas is much greater than what has been found possible over the Red Sea Hills.

7.6 Conclusion and Summary

The results of the geometric accuracy and interpretation tests of the MOMS images show that the use of a linear array sensor in space remote sensing represents a substantial step forward towards fulfilling the requirements of small-scale photogrammetric and topographic mapping operations. These results show that linear array sensors should have an important role to play in topographic mapping and one would expect this to be fulfilled in the near future. However, as far as the topographic mapping of the Sudan is concerned, there are still many difficulties to be resolved. These difficulties arise from the fact that many of the cultural features which are required to be shown on the 1:100,000 scale topographic maps still remain very difficult to detect on these linear array images.

In this Chapter, the results of the accuracy and interpretation tests carried out by the author on MOMS images have been reported and analyzed. In the next Chapter, Landsat-3 RBV camera system will be described in some detail and the geometry of RBV images explained. This is followed by a chapter in which the results of geometric and interpretation tests of RBV images are reported upon and analysed.

CHAPTER 8

Landsat RBV Systems

8.1 Introduction

As mentioned in Chapter 2, Return Beam Vidicon (RBV) cameras which are high resolution television cameras were used as imaging devices on the first three Landsats.

As can be seen from Fig. 8.1, an RBV camera consists of an optical unit comprising a lens and a focal plane shutter which is coupled to an electronic unit comprising an RBV tube, a thermoelectric cooler, deflection and focus coils and erase lamps. The RBV tube is an evacuated glass envelope containing an electron gun facing a thin photoconductive layer coating the internal surface of the tube at the target end. The optical unit is coupled to the RBV tube so that the image of the Earth's surface formed by the lens is focused on the tube faceplate. In operation, the electron beam generated by the gun is made to scan the target to maintain its stabilization at zero voltage. The conducting transparent thin layer coating the internal surface of the tube faceplate is held at +30 v (EMI Electronics, 1973).

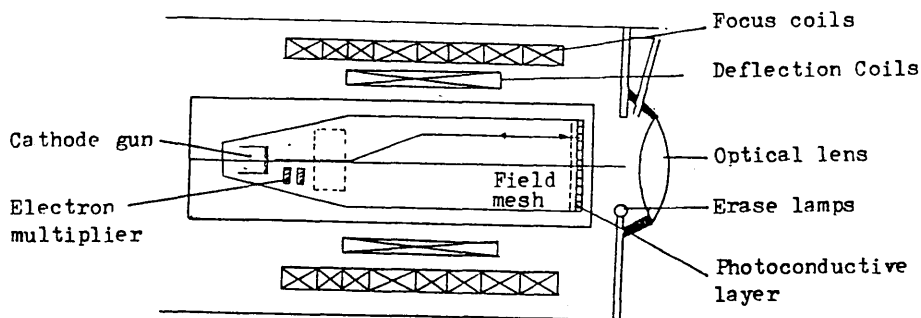


Fig. 8.1 Components of the RBV Camera.

When the image of the Earth's surface formed by the optical lens is focused on the target, the conduction characteristics of the conductive layer changes according to light intensities present in the image. This causes the stabilized surface to start drifting towards the +30 v potential of the faceplate in proportion to these light intensities. Because of the high resistivity of the target material, a

charge pattern is built up on the target surface. This charge remains until the electron beam scans the surface again to restore it to zero equilibrium potential by depositing electrons. This scanning process is achieved by the use of an axial magnetic field which overlaps the normal deflection fields and extends the full length of the camera tube. The combined effect of the axial field and the transverse deflection field is a resultant field making an angle α with the tube axis (Wong, 1969). When the electrons in the scanning beam enter the combined field area, they are forced to move in a helical path along an axis which makes the angle α with the tube axis (Fig. 8.2). When these electrons emerge from the area of the combined field, they come under the influence of the axial field only. The axial field, therefore, forces them to move in a helical path along a line parallel to the tube axis. Hence, the combined effect of the two magnetic fields is to displace the beam laterally in the direction of the transverse field. The lateral displacement is directly proportional to the transverse magnetic field. Therefore, the electron beam can be deflected and displaced by varying the transverse magnetic field to generate the scanning pattern required (Wong, 1969; Schade, 1971).

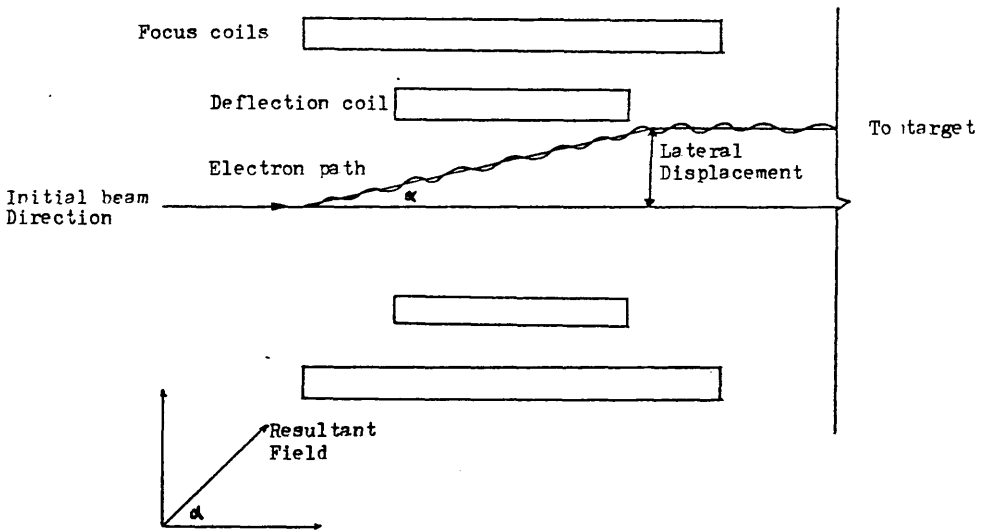


Fig. 8.2 Scan Pattern Generation in RBV Tubes.

The electrons travel at high speed until they approach the target, where they are slowed down by an electronic field, set up between the wall anode and the target, to reach the target at nearly zero speed.

Instead of using the displacement current at the faceplate to generate the video signals as in vidicon tubes, RBV tubes use the remaining electrons present in the electron beam. These remaining electrons travel back along the same path as the forward beam - hence

the name return-beam-vidicon - and the signals are then derived as a video modulated electron beam which is amplified by the electron amplifier surrounding the electron gun. After each read-out operation, the photoconductive target is cleared of any residual image charges by a high-intensity light flash provided by the erase lamps. The target is then resensitized for the new exposure by recharging it to its polarizing potential. The recharging operation is done by scanning the target in darkness by an electron beam in which the electron current density is highly increased to reduce recharging time (Schade, 1971).

Compared with the standard tubes used in TV cameras, the signal read-out system is considerably more sophisticated since it was designed to provide a performance as nearly equivalent to a photographic system as possible. To this end, the aperture of the electron gun of the RBV camera is considerably demagnified (0.7 mm. diameter) and the beam is further demagnified by the electronics surrounding the electron gun to obtain a small spot size at the target plate. The smaller electron spot size is essential to produce high resolution TV images. Furthermore, the simple focus coils of the normal tubes are replaced by four sophisticated coils to permit precise control of the magnetic field shape which is essential for the production of RBV images with little inherent distortion (Schade, 1971).

In order to achieve high resolution in RBV images, the sensor, i.e. the photoconductive layer, must have a high electron storage capacity per unit area. For this reason, the compound antimony trisulfite (ASOS) was used as the photoconductor in the Landsat RBV cameras. This photoconductor has the characteristics of high resolving power, a structure-free surface, and a high storage capacitance with good sensitivity. The relative spectral sensitivity of the ASOS photoconductive layer is shown in Fig. 8.3.

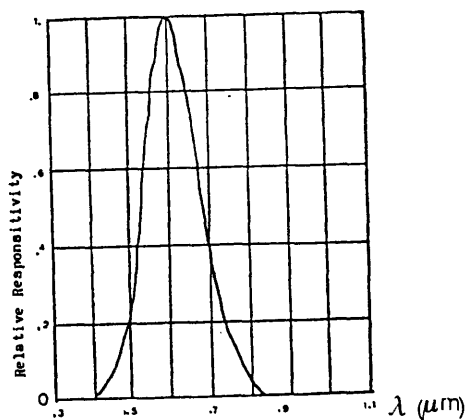


Fig. 8.3 ASOS Spectral Sensitivity.

8.2 Geometric Distortion in RBV Images

As mentioned above, the Landsat RBV cameras comprised two separate units: optical and electronic units. Therefore, the geometric distortions inherent in the RBV images are the combination of the distortions which were introduced by these optical and electronic units.

8.2.1 Geometric Distortions Introduced by the Optical Unit

As in conventional photography, the geometric distortions which are introduced by the optical unit of an RBV camera result from two main causes:

- (i) imperfect lens design and/or manufacture which results in symmetric radial lens distortions; and
- (ii) imperfect centering of the optical elements of the lens assembly which results in asymmetric tangential and radial distortions.

These lens distortions can be described by the well known expressions which are used in photogrammetry for conventional frame photography.

8.2.2 Distortions Introduced by the Electronic Unit

The scanning of the photoconductive target by the electron beam is by far the most serious source of geometric distortions in RBV cameras (Wong, 1969, 1975). In order to obtain perfect scanning geometry, the movement of the scanning electron beam must fulfil the following requirements:

- (i) the electron beam should move with a constant speed along each scan line;
- (ii) the scan lines should be straight and equally spaced from one other; and
- (iii) the beginnings and ends of all scan lines should fall on the lines forming the border of the image field.

However, because of the use of the focussing and deflecting coils (magnetic fields) to achieve and control the scanning process, problems

such as a non-uniform magnetic field, the presence of a fringe field and oscillations in the windings are present in RBV cameras. These problems give rise to a complex pattern of distortion. Wong (1969) discussed the distortions which are introduced by the electronic units of television systems and showed that, as a result of the problems associated with the use of magnetic fields in generating and controlling the scanning pattern in both the television camera and the display systems used subsequently, several geometric distortions are introduced in the image.

Firstly, the electric field, which is set up between the target and the wall anode, tends to be non-uniform at the edges of the target. Instead of being perpendicular to the target, as is the case near the tube axis, this field deviates to make a small angles with tube axis away from the target centre. Therefore, away from the centre of the target, the electric field has a radial component. This radial component deflects the electron beam radially, in which case, the beam cuts the axial magnetic field which in turn deflects it in a direction tangential to its radial motion. As a result, the path of the scanning spot will be rotated through a small angle. This angle varies from one point to another along the scan line and since the radial component of the magnetic field is larger at the edges of the target, the angular rotation increases from zero at the centre of each scan line to its maximum value at these edges. This results in scan lines having an elongated S shape as shown in Fig. 8.4.

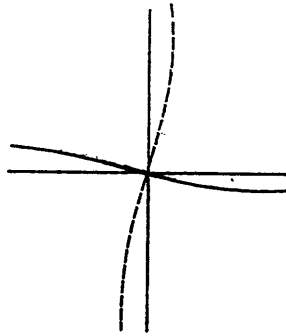


Fig. 8.4 Distorted Scan Line Pattern.

Secondly, any failure to achieve the exact synchronization of the horizontal and vertical components of the motion of the electron beam, which is required to ensure that the positions of the scan lines are

identical from frame to frame and that the beginnings and ends of the scan lines are always the same, introduces more geometric distortions. Failure in the first condition results in the rotation of each scan line about the horizontal, while failure in the second will introduce a linear shift of the scan lines relative to one another.

In general, Wong (1969) gives the mathematical model that expresses all the geometric distortions inherent in TV images as follows:

$$\Delta x = x(a_0 + a_1r^2 + a_2r^4 + a_3r^6 + \dots) - y(b_1r + b_2r^3 + b_3r^5 + \dots) - (c_1r^2 + c_2r^4 + c_3r^6 + \dots)\sin\theta_0 + (d_0 + d_1x + d_2xy + d_3y^2)$$

$$\Delta y = y(a_0 + a_1r^2 + a_2r^4 + a_3r^6 + \dots) + x(b_1r + b_2r^3 + b_3r^5 + \dots) + (c_1r^2 + c_2r^4 + c_3r^6 + \dots)\cos\theta_0 + (d_0 + d_1x + d_2xy + d_3y^2)$$

.....(8.1)

in which Δx , Δy are the distortion displacements in x and y coordinates of a point;

x, y are the image coordinates of the point;

$r = (x^2 + y^2)^{.5}$ is the radial distance;

$a_0, a_1, \dots; b_0, b_1, \dots; c_0, c_1, \dots; \text{ and } d_0, \dots$ are constant coefficients; and

θ is the angle which the axis of maximum asymmetry makes with the x-axis.

The first pair of brackets in these equations contains the polynomial which represents the radial distortion caused by the lens, the non-uniform magnetic field and the fringe field effect. The second pair of brackets contains the polynomial representing the tangential distortions caused by the interaction between the focus and deflection fields and by the deceleration field at the camera tube. The third pair of brackets contains the polynomial which represents the asymmetric tangential and radial distortions caused by the decentering of the elements of the optical lens; and the fourth contains the polynomial that represents the effects of camera orientation.

8.3 Landsats -1 and -2 RBV Systems

Landsats -1, and -2 carried identical RBV systems consisting of three cameras boresighted to image the same ground scene in three different spectral bands as given in Table 2.1. Fig. 8.5 shows the alignment of the three RBV cameras on-board Landsats -1 and -2. The cameras were operated to simultaneously image a 185km x 185 km area every 25 seconds. During this period, the satellite moved only about 165 km along its path. Therefore, an overlap of 18.5 km resulted between consecutive RBV scenes. Each RBV image consisted of 4,125 TV lines and since the scanning rate of the read-out system in these cameras was 1,250 lines per second, it took 3.3 seconds for each RBV image to be read out and converted to video signals. The images of the three cameras were read out sequentially during the last 10.5 seconds of the 25 seconds shuttering cycle. Unfortunately these two systems did not produce any significant ground coverage since the one on board Landsat-1 was shut down shortly after launch due to a circuit failure and that on board Landsat-2 was only operated for equipment testing before being shut down (NASA, 1979).

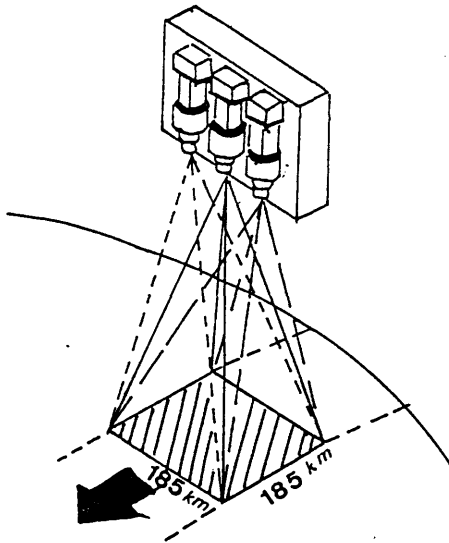


Fig. 8.5 Landsats -1 & -2 RBV Camera Systems.

8.4 Landsat-3 RBV System

Two RBV cameras were carried on board Landsat-3 to acquire panchromatic RBV images of the Earth's surface using a broad band ($\lambda=0.51$ to $0.75 \mu\text{m}$) in the visible region of the electromagnetic spectrum. The two cameras are aligned so that when their shutters were

released, two images of the Earth's surface were acquired covering laterally adjacent ground subscenes within the 185 km width of one MSS scene. As shown in Fig. 8.6, the two cameras were displaced about 2.7° in roll angle and 0.71° in pitch angle to image the two adjacent ground subscenes (Clark, 1981).

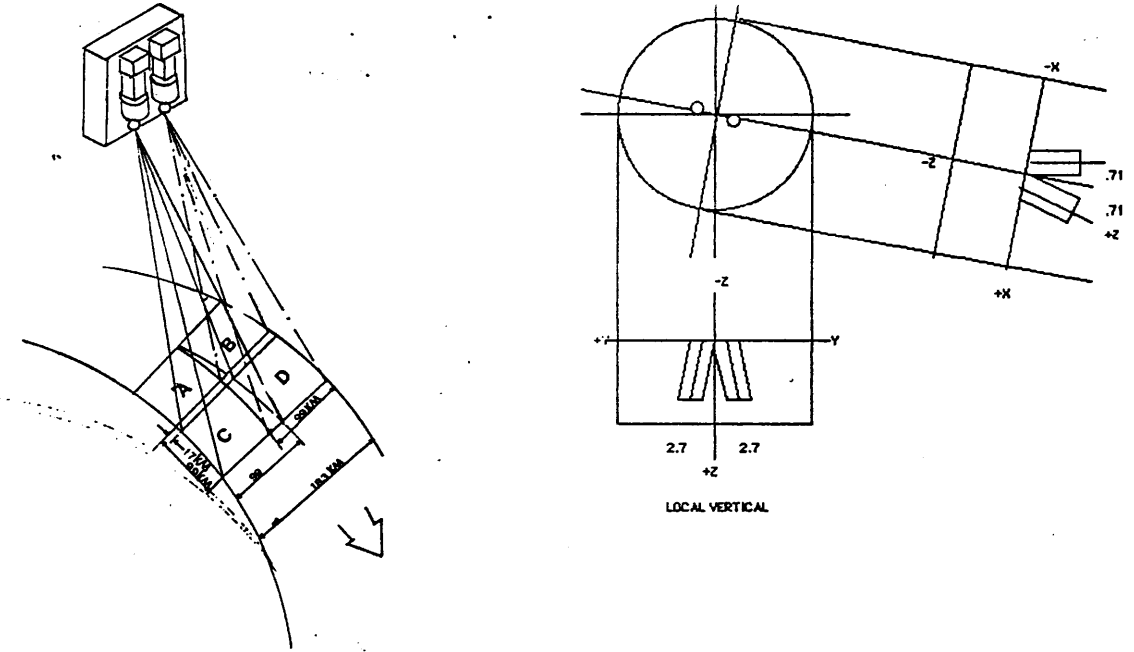


Fig. 8.6 Landsat-3 RBV System.

The shutter of the second RBV camera (Camera 2 in Fig. 8.6) was released 3 seconds later than that of Camera 1 to achieve the imaging of laterally adjacent subscenes. Each of these subscenes covers a ground area of 98 km x 98 km. A set of four subscenes cover the same 185 km ground area which is covered by one MSS image. The reduction in the area covered by one subscene is achieved by using lenses having focal lengths ($f=236$ mm) which are double those of the previous Landsat RBV optical units. With the satellite altitude of 920 km, this focal length resulted in 1:3,900,000 scale images of the Earth's surface being focused on the tube target each time the shutter is released compared to the 1:7,300,000 scale of the images focused by the optical units on the tube targets of the previous Landsat RBV cameras. As a consequence of this, the nominal ground resolution of these cameras is improved to twice that of the previous cameras. Table 8.1 lists the characteristics of the Landsat-3 RBV cameras.

To assist the monitoring and correction of the geometric distortion, each RBV camera of these systems had a 9x9 reseau of grid

crosses engraved on the tube faceplate. USGS(1979) gives the arrangement and dimensions of these reseau crosses. The positions of these crosses had been determined during the pre-flight calibration of the cameras.

Parameter	Performance
Spectral Band	$\lambda=0.505$ to 0.75 μm
Focal Length (f)	236 mm
Angular Field	8.7°
Horizontal Read rate	1,250 lines/sec.
No. of TV lines	4,125 per frame.
Read-out time	3.5 seconds
Cycle Rate	12.5 seconds.

Table 8.1 Characteristics of the Landsat-3 RBV Camera System.

The nominal resolution of the optical lens of the Landsat-3 RBV camera is 90 lp/mm. Since the faceplate is 25.4 mm x 25.4 mm, the number of line pairs which can be defined by the optical system on the faceplate is 2286 lp. (90×25.4). Any linear objects of frequency higher than this cannot be resolved. Dividing the across-track ground distance covered by the image by the number of lines which can be imaged by the optical system on the faceplate, the equivalent lens-limited ground resolution is found to be 21.5 m. In contrast to lens-limited ground resolution, the ground pixel size is determined by the sampling rate adopted at ground receiving stations. The sampling rate adopted at NASA GSFC where the RBV images in this investigation have been processed is about 3200 samples per line. This sampling rate results in ground pixel size of 30 m. However, to make a good estimation of the ground resolution of any system, the contrast of the scene must be considered. The MTF curve of the system together with a certain contrast threshold are usually used for this estimation. Although the NASA produced Landsat-3 RBV images were sampled to give a ground pixel size of 30 m, Dosiere and Justice (1983) estimated the ground resolution of these images from the theoretical MTF curve of one of Landsat-3 RBV camera to be about 45 m by taking the spatial frequency at which the image to object modulation factor is 50%.

Furthermore the ground resolution of Landsat-3 RBV images was estimated by Welch & Pannell (1982) to be worse than the theoretical 45 m estimated by Dosiere and Justice (1983). As mentioned in Chapter 4, for the estimation of the actual ground resolution, the MTF of the system is first translated vertically to a modulation of 0.23, which is

equivalent to the 1.6:1 scene contrast which prevails in the operational environment, is used (Welch,1982). For a normal observer to resolve low contrast targets at the resolution limit, a modulation of approximately 10% is required. Therefore the spatial frequency corresponding to a 10% modulation can be taken as a measure for the resolution of the system. Fig. 8.7 shows the MTF curve of one of the Landsat-3 RBV cameras. As can be seen from the figure, the spatial frequency at 10% modulation is about 14 cycles per mm. The ground resolution of a Landsat-3 RBV 1:1,000,000 scale image can, therefore, be taken as 70 m (Welch, 1982).

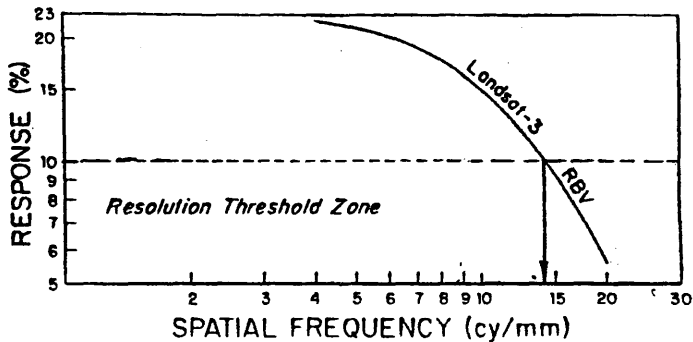


Fig. 8.7 MTF and Resolution of Landsat-3 RBV Images.

8.5 Data Reception and Processing

The RBV data were transmitted to ground receiving stations over two S-band links as a video modulated carrier signal within an RF bandwidth of 20 MHz. At the ground receiving stations, the composite video data of the RBV cameras were recorded as analogue data on video tapes, while the MSS serial bit stream is demultiplexed into the individual channels and then recorded on tape after adding line-start and line-length codes. Both data sets are then subjected to further processing.

Landsat image data processing procedures and models at each of the receiving stations might be different in the manner and the accuracy with which various processes are carried out, but the objectives are generally the same. The images which have been used in this investigation have been processed at NASA's GSFC Image Processing Facility (IPF). At this facility, RBV processing has been carried out in three steps (Forrest, 1972; NASA, 1979):

i) The assessment and annotation step, in which, first of all, the cloud cover percentage was assessed, and was followed by the attachment of the time and date of acquisition, orbit number and sun elevation to the images. Next tick marks, which were computed from the spacecraft position and attitude data, were placed on the output to define the locations of the centre and corners of the image on the surface of the Earth.

ii) The radiometric correction step, in which operations were performed to correct for shading and striping effects, gain changes and offset changes, as well as several other radiometric artefacts. Several possible radiometric artefacts in RBV images have been identified by the EROS Data Centre. These are:

- 1) shading and stairsteps;
- 2) corners being out of focus;
- 3) missing reseau crosses;
- 4) reseau and data distortion;
- 5) grain effect; and
- 6) faceplate contamination.

These artefacts may occur singly or in combination. Radiometric corrections of these artefacts was done using the pre-flight calibration data and interpolation procedures to estimate the brightness values of the missing image lines or the specific features present (or absent) from the image.

iii) The geometric correction step, in which geometric distortions caused by the electronics, satellite attitude and Earth's curvature were removed. The resulting images were then fitted to a map projection. As mentioned in Chapter 4, three classes of image products have been distinguished depending on the accuracy to which this step is carried out. These are:

(a) bulk-processed images in which the systematic distortions are corrected using calibration and satellite position and attitude data;

(b) precision-processed images in which these corrections are further refined using a number of ground control points; and

(c) intensive-processed images which are precision processed images produced in digital form.

8.6. Rectification and Transformation of RBV Images

As mentioned in Chapter 6, the rectification of digital images can either be carried out directly or indirectly. The indirect method is carried out by assuming a regular grid ^{of} points in the rectified image space and then transforming this grid to the non-rectified image space using a suitable transformation model. A resampling step is then followed to determine the brightness values at the intersection points of the transformed grid from the interpolation of the surrounding brightness values of the original non-rectified image.

If the distortion effects in RBV images can be eliminated, the geometry of the resulting images is essentially similar to that of frame photography. Therefore a pre-rectification process, in which are eliminated all the geometric distortions inherent in the images so that the resulting image can be considered as a distortion-less frame photograph, is often carried out. Following this, the rectification methods which are used with frame photographs can be utilized with RBV images. However, with the assumption of small relief variation and the consideration that these images were taken from an altitude of 920 km, system-corrected RBV images can readily be transformed planimetrically to any map projection using a suitable two-dimensional transformation in combination with a set of ground control points.

8.6.1 Pre-rectification of RBV Images

An RBV camera taken together with the data transmission and reception systems used with Landsat satellites can be considered to be similar to a television system. Thus equations (8.1) can be considered to represent closely the pattern of distortion which one might expect to be inherent in the finally produced RBV images. Therefore, two-dimensional polynomials having the same form as equations (8.1) can be used as a mathematical model for the pre-rectification process of the RBV images (Wong, 1975). These polynomials can be derived from equations (8.1) and put in the following form:

$$\begin{aligned} \Delta x = & a_0 + a_1x + a_2y + a_3xy + a_4x^2 + a_5y^2 + a_6x^2y + a_7xy^2 \\ & + a_8x^3 + a_9y^3 + a_{10}x^3y + a_{11}xy^3 + a_{12}x^4 + a_{13}y^4 + \\ & a_{14}x^2y^2 + a_{15}x^3y^2 + a_{16}x^2y^3 + a_{17}x^5 + a_{18}y^5 + a_{19}x^3y^3 \end{aligned}$$

$$\Delta y = b_0 + b_1x + b_2y + b_3xy + \dots + \dots + b_{19}x^3y^3 \dots \dots (8.2)$$

These polynomials are similar to the polynomials used in this investigation for the planimetric transformation of MSS, TM, MOMS and RBV images, but, in this case, instead of transforming the image into the ground coordinate system, the polynomials are used to recover the internal geometry of the RBV image, i.e to carry out an inner orientation. As mentioned above, this inner orientation is carried out as a pre-rectification process.

In this inner orientation or pre-rectification process, first of all, the image coordinates of the reseau crosses are measured on the images. This measurement operation can be carried out on a comparator if a hard copy image is used or on the screen of an image processing system if the image is in a digital form. The measured reseau coordinates are then compared with the calibration reseau data. The discrepancies between the two provide a measure for the image distortions at these crosses. Substituting these discrepancies and the reseau data in equations (8.2) produces two equations for each reseau cross in which the coefficients are unknown. A least squares solution may be used to determine these coefficients. The determined coefficients are then used to model the distortion at any point in the image which can then be eliminated.

Another alternative is a piecewise pre-rectification process in which each RBV subscene is subdivided into regions, each containing n reseau crosses. The computation and elimination of distortion is carried out in these individual regions using reseau crosses within the area of the region being considered. Polynomials of a much smaller order may be used for this computation, so reducing the computational effort.

Since the distortion in RBV images is highly systematic, a distortion table for a set of images acquired during the same day may be determined by taking the average distortion from selected images of that day. Then the distortion at any point in any image taken on that day is determined by linear interpolation.

8.6.2 Planimetric Transformation of RBV Images

In all three Landsat missions, RBV images were acquired with only slight overlap between adjacent images in one orbit path. This might be because height determination or topographic mapping in general was not one of the mission objectives. Therefore, only the planimetric transformation of image coordinates to the ground space can be contemplated in most areas. A preliminary step in which distortion at measured points is computed from reseau data and then corrected for, as shown above, often precedes the image transformation step especially in the case of digital images. As mentioned in Chapter 4, the planimetric transformation of satellite remote sensor images is usually done using two-dimensional polynomials.

The choice of the effective terms in these equations depends on the distortion characteristics of the system under consideration. The polynomial consisting of these effective terms should be used to transform images taken by that particular system. Simple forms of planimetric transformation are the linear conformal and affine transformations. As for the polynomial transformation of RBV images, the obvious choice is polynomials having the same terms as those of equation (8.2). In fact, these are the same two-dimensional polynomials which have been used for the planimetric accuracy tests of the MSS, TM and MOMS images in Chapters 5 and 7. Therefore in this investigation, the planimetric test procedure described in Chapter 4 and followed in the geometric accuracy tests of the MSS, TM and MOMS images has also been followed in the planimetric geometric tests of the RBV images.

8.6.3 Three Dimensional Transformation of RBV Images

The designed path of each of Landsat 3 orbits resulted in a sidelap between adjacent satellite paths which amounts to 14% at the Equator. Due to the convergence of satellite paths, this sidelap increases as one goes pole-ward away from the Equator. Since two laterally overlapping RBV subscenes from Landsat 3 cover one swath width, the percentage of the sidelap between Landsat 3 RBV subscenes taken from adjacent paths is equal to twice the percentage of the corresponding MSS scenes sidelap. Fig. 8.8 shows that, this will be the case till the RBV sidelap reaches 100% at about 54° latitude approximately. Further north (or south) of these latitudes, the sidelap starts to decrease due to the fact that the base between the images gets so small that the left part of the subscene on the left path overlaps the right part of the subscene on the right path. Table 8.2 lists the RBV sidelap against

the corresponding MSS sidelap at various latitudes.

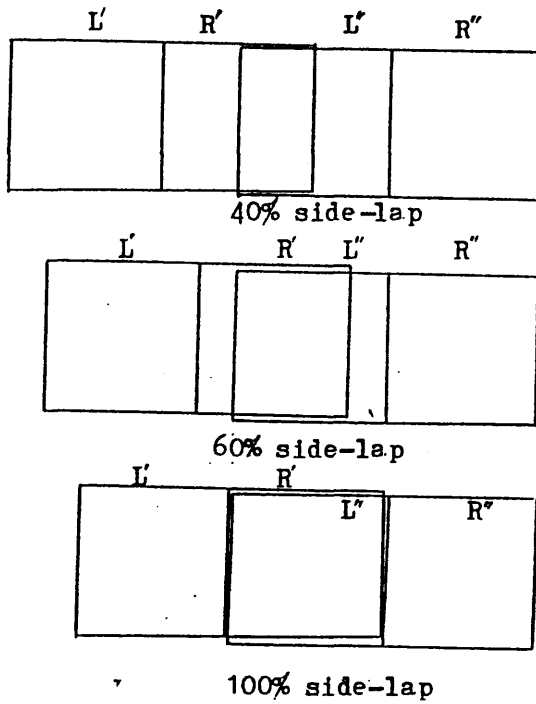


Fig 8.8 Sidelap in Landsat-3 RBV Images.

Latitude Deg.	MSS sidelap %	RBV sidelap %
0	14.0	28.0
10	15.4	30.8
20	19.1	38.2
30	25.6	51.2
40	34.1	68.2
50	44.8	89.6
60	58.0	86.0
70	70.6	58.8
80	85.0	30.0

Table 8.2 Sidelap Between MSS and RBV Images From Adjacent Orbits.

As mentioned in Chapter 3, the ability to extract accurate height information from stereomodels depends on the scale of the images and

their base:height ratio (B:H). The approximate B:H ratios corresponding to the sidelap values listed in Table 8.2 are given in the second column of Table 8.3. From Table 8.3, it is clear that when the base:height ratio is relatively big, the sidelap is not sufficient for forming a stable model. For the purpose of this investigation therefore, a compromise should be reached. If a model is formed from subscenes having 68% sidelap, the B:H ratio will be 0.134.

Taking the accuracy of x-parallax measurement on RBV images as 10 μ m, the accuracy of height information determined from RBV images can be computed using equation (3.3) for various B:H ratios listed in Table 8.3. The third column of Table 8.3 lists these height accuracy values against their corresponding B:H ratios, assuming that the height measurement is made on 1:1,000,000 scale transparencies. The fourth column of Table 8.3 lists these height errors in % of the satellite altitude. These are of course the errors due to measurement with the assumption that no residual distortion is present in the images after the elimination of all systematic distortions as shown above.

RBV Sidelap %	B:H Ratio	Terrain Height (m)	% H (H=920 km)
28.0	.174	58.0	0.063
30.4	.172	58.0	0.063
38.2	.164	61.0	0.066
51.2	.151	66.0	0.072
68.2	.134	75.0	0.082
89.6	.112	89.0	0.097
86.0	.087	115.0	0.125
58.8	.060	167.0	0.182
30.0	.030	333.0	0.362

Table 8.3 Theoretical Height Accuracy from RBV Images.

As mentioned above, after the elimination of the various distortions inherent in the RBV images, they will have the perspective geometry of conventional frame photography. This means that the mathematical models and photogrammetric operations which are usually used with conventional frame photographs can be applied in the reduction of the RBV images.

As shown in Chapter 3, the accuracy of photogrammetrically determined heights depends on the scale, image resolution, flying

height and base:height ratio (B:H). The B:H ratio determines the intersection angles between intersecting light rays from the two photographs of the stereopair to common points in model space. The greater the B:H ratio, the greater these intersection angles will be and hence a much stable model can be formed. As can be seen from Fig 8.9, the greatest angle in every model is that at the midpoint p_1 . At the edges of the model, the greatest angle will be at the point p_2 , the location of the foot of the perpendicular from p_1 . Intersection angles p_1 , p_2 , p_3 , and p_4 in a stereomodels formed from photographs having 60% overlap have been computed by Petrie (1970) for superwide, wide, normal, and narrow angle cameras. These intersection angles are given in Table 8.4 together with the intersection angles computed at the same points on RBV stereopairs under this investigation.

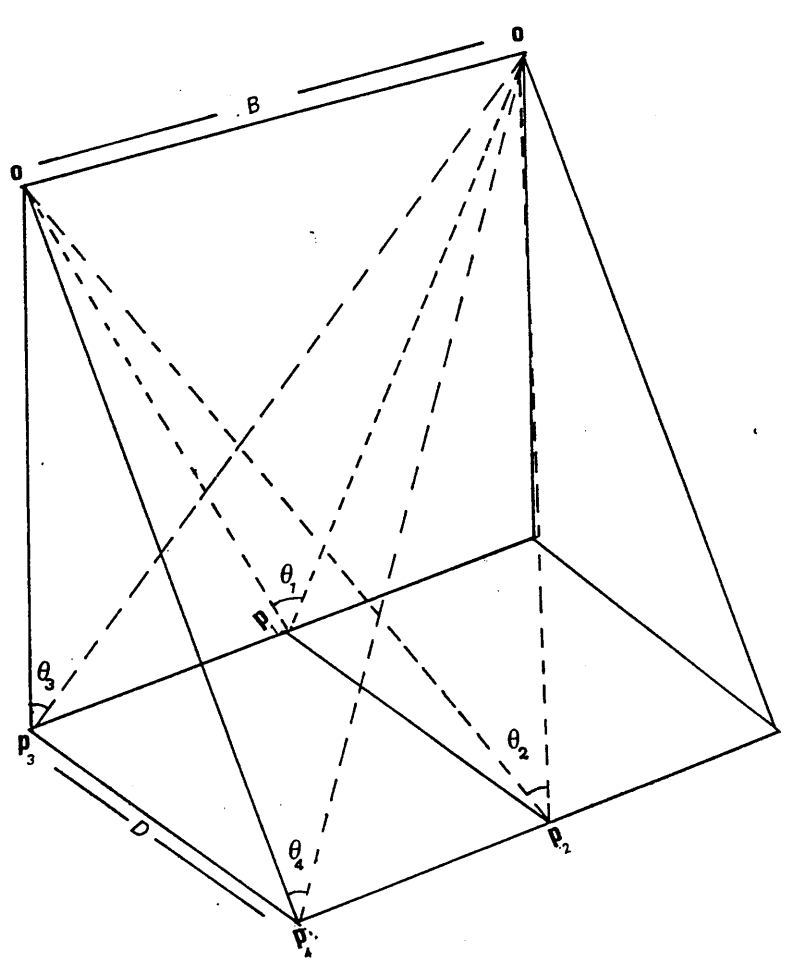


Fig. 8.9 Intersection Angles in Stereomodels.

TYPE	FRAME CAMERAS				LANDSAT3
	S.WIDE	WIDE	NORMAL	NARROW	RBV
ANGULAR COVERAGE	122°	95°	56°	30°	8.7°
B/H RATIO	1.02	0.61	0.31	0.15	0.074
INTERSECTION ANGLES: (°)					
θ1	45.9	31.5	17.1	8.7	4.232
θ2	54.1	34.1	17.4	8.8	4.218
θ3	32.2	25.5	16.0	8.5	4.217
θ4	35.0	27.3	16.2	8.6	4.211

Table 8.4 Intersection Angles with Various Field Angular Coverages.

For the height accuracy test of the RBV images conducted in this investigation, the coordinates of the reseau crosses have been measured monoscopically while the coordinates of the points which were selected as control and check points have been measured stereoscopically on the Stecometer as described above. The measured coordinates of the reseau crosses were used to transform the measured coordinates of the selected points into the nominal reseau coordinates system using equations (8.2) put in the following form:

$$x' = a_0 + a_1x + a_2y + a_3xy + a_4x^2 + a_5y^2 + a_6x^2y + \dots$$

$$y' = b_0 + b_1x + b_2y + b_3xy + b_4x^2 + b_5y^2 + b_6x^2y + \dots$$

... (8.3)

where x', y' are nominal reseau coordinates; and
 x, y are measured image coordinates of the crosses.

First, the measured reseau coordinates were used to compute the coefficients, a_0, a_1, \dots, b_19 which were then used in the equations to

determine the transformed coordinates of the selected image points.

This transformation was applied to correct for the image distortions which were introduced by the electronic parts of the RBV camera and the film writing system. However after this transformation, the distortions introduced by the optical lens of the camera and errors due to the uncertainty of the location of principal point and the value of the effective focal length are still present in the image. Since the data about these elements are not available, their effects should be compensated for in the solution. One way of doing this is by adding additional parameters expressing the errors introduced by this lack of knowledge of these inner orientation elements. This technique has been applied particularly in bundle adjustment in aerial triangulation (Bauer & Muller, 1972; Brown, 1976) and is often called a self-calibration method. In this method, no prior system calibration data is needed since the calibration is carried out by suitable procedures while forming the model itself. The specific parameters added to the projective equations act to correct the measured image coordinates. The solution for these parameters is carried out simultaneously with that for the exterior orientation carried out as explained in Appendices A and B.

In the intersection phase, these determined parameters are used first to correct the measured image coordinates which are then input to the usual space intersection procedure. The expense of using additional parameters is that more control points are required to carry out the solution.

The following error model was suggested by Brown, (1976) to be applied in the solution of reconnaissance frame photography:

$$\begin{aligned}
 dx &= a_1x + a_2y + b_1xy + b_2xy^2 + b_3x^2y + c_1xr^2 + c_2xr^5 + d_1 \\
 dy &= -a_1x + a_2y + b_1xy + b_2xy^2 + b_3x^2y + c_1yr^2 + c_2yr^5 + d_2 \\
 &\dots\dots(8.4)
 \end{aligned}$$

where dx, dy are corrections to the image coordinates x, y of a point;
 r is the radial distance ($r = (x^2 + y^2)^{.5}$);
 a_1x - corrects for image scale error i.e focal length error;
 a_2y - corrects for axes non-orthogonality;
 b terms correct for film deformation;
 c terms correct for radial lens distortion; and
 d terms correct for principal point displacement.

In this investigation, the b terms are neglected. The rest of the terms have been incorporated in the space resection phase of a space resection/intersection computer program (SPRES) written by El Hassan (1978). The program was modified by the present author, such that individual terms can be selected separately to examine their effects individually and hence determine effective terms, or as groups to compensate for the collective effects after the effective terms have been determined.

The corrected image coordinates which have been obtained from the transformation of the measured coordinates to the nominal reseau coordinate system using equations (8.3) in combination with the reseau nominal data (McEwan, 1971), are regarded as having the geometry of frame photographs. These corrected image coordinates were then input to the space resection program (SPRES).

8.7 Summary

In this chapter, the design and operation of the Landsat RBV cameras have been described and the geometry of the images acquired by them has been explained. The procedure and the mathematical models used in the elimination of the systematic distortions in the RBV images or the geometric correction carried out prior to their rectification and transformation have also been described. Finally, the procedures and mathematical formulae which have been used in the planimetric and height accuracy tests carried out in this investigation were outlined. In the next chapter, the results of these planimetric and height accuracy tests will be presented and analyzed. This will be followed by the presentation and analysis of the interpretation test carried out on the RBV images in this investigation. These results will then be compared with some published results over various test areas before the conclusions are drawn from these tests regarding the applicability of these images to topographic mapping can be given.

CHAPTER 9

Geometric Accuracy and Interpretation Tests of RBV Images

9.1 Introduction

As shown in Sections 8.1 and 8.6.1, RBV cameras have the advantage of imaging the whole scene simultaneously producing images having the perspective geometry of frame photography. At the same time, the image can be telemetered to the ground shortly after it has been recorded unlike photographs which need to be physically recovered for processing and are usually not available for some considerable time after exposure. This makes RBV images a cheap alternative for acquiring stereo imagery from long life space missions. However until now no RBV system has been launched with the objective of height determination and hence topographic mapping in mind. Nevertheless, Landsat-3 RBV system provides a means for testing the possibility of height determination from overlapping images acquired by TV cameras from space platforms. As shown in Table 8.2, RBV images with 60% to 80% lateral overlap were acquired by the Landsat-3 RBV camera system covering Earth's surface between latitudes 40° and 60° north and south of the Equator. Therefore, the geometric accuracy tests which have been carried out by the present author on Landsat-3 RBV images comprised both planimetric and height accuracy tests. Interpretation tests were also carried out on the RBV images to determine the amount of information which can be extracted from these images if they are used for topographic mapping of the test areas.

Three areas were used which were suitable for the various tests carried out using Landsat-3 RBV images. Two of these test areas were located in the Sudan. The first image used was Subscene E 30232-07184 D which was acquired on 23rd October, 1978 and covered part of the Red Sea Hills test area (Fig. 9.1). The second image was Subscene E-30234-07310 C which was acquired two days later than the first (on 25th October, 1978) and covered part of the Nile test area (Fig. 9.2). The first subscene was used for both planimetric accuracy and interpretation tests while the second was used for the interpretation test only. This was again due to the unavailability of suitable topographic maps in the Nile test area.

As described in Chapter 3, the Red Sea Hills test area extends between latitudes 18° and 22° . Therefore, the sidelap between the Landsat-3 RBV subscenes which were acquired over this area from adjacent satellite paths can be estimated from Table 8.2 to be about

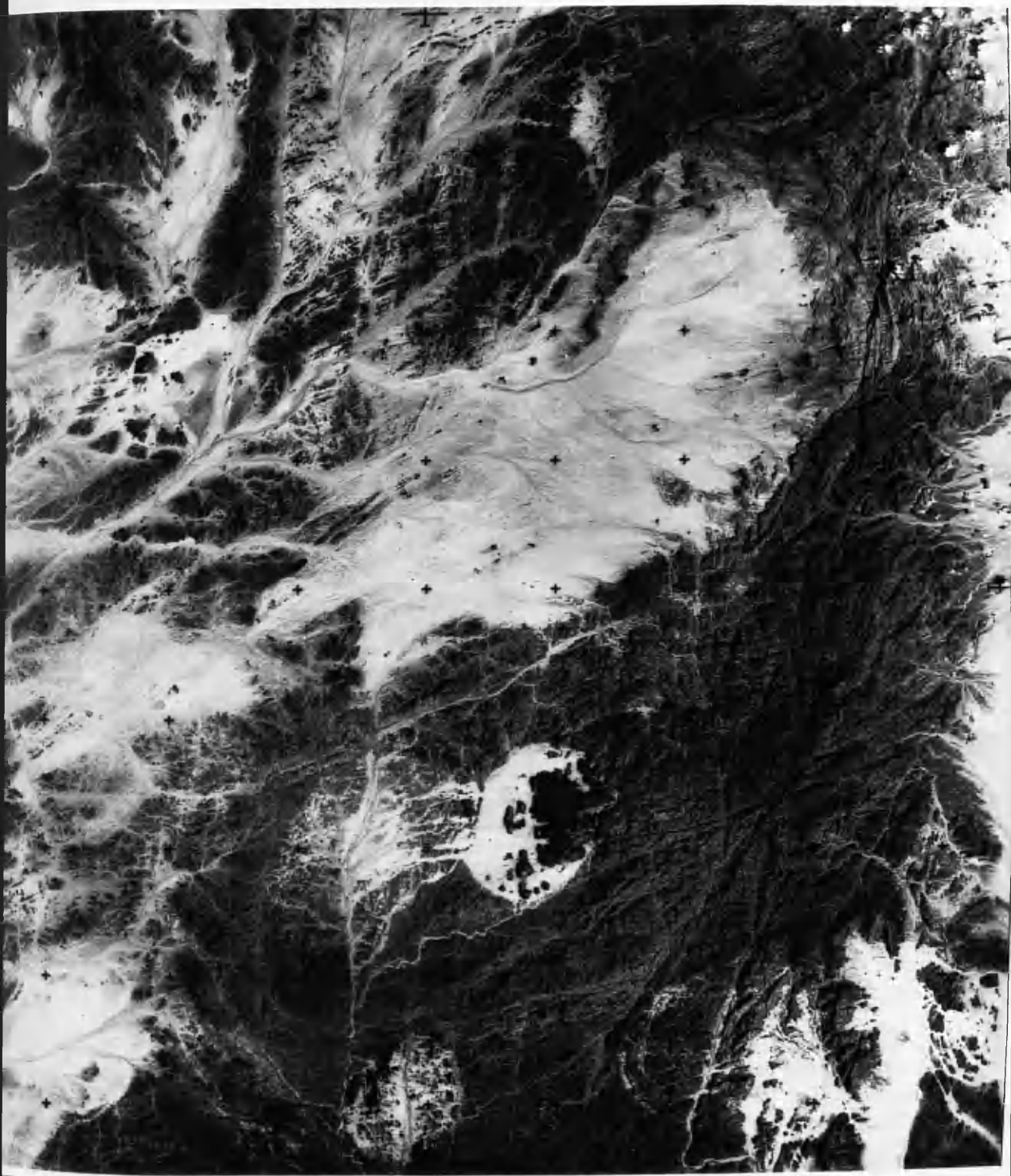


Fig. 9.1 RBV Subscene E-30232-07184 D 1:500,000 Scale Print of the Red Sea Hills Test Area.

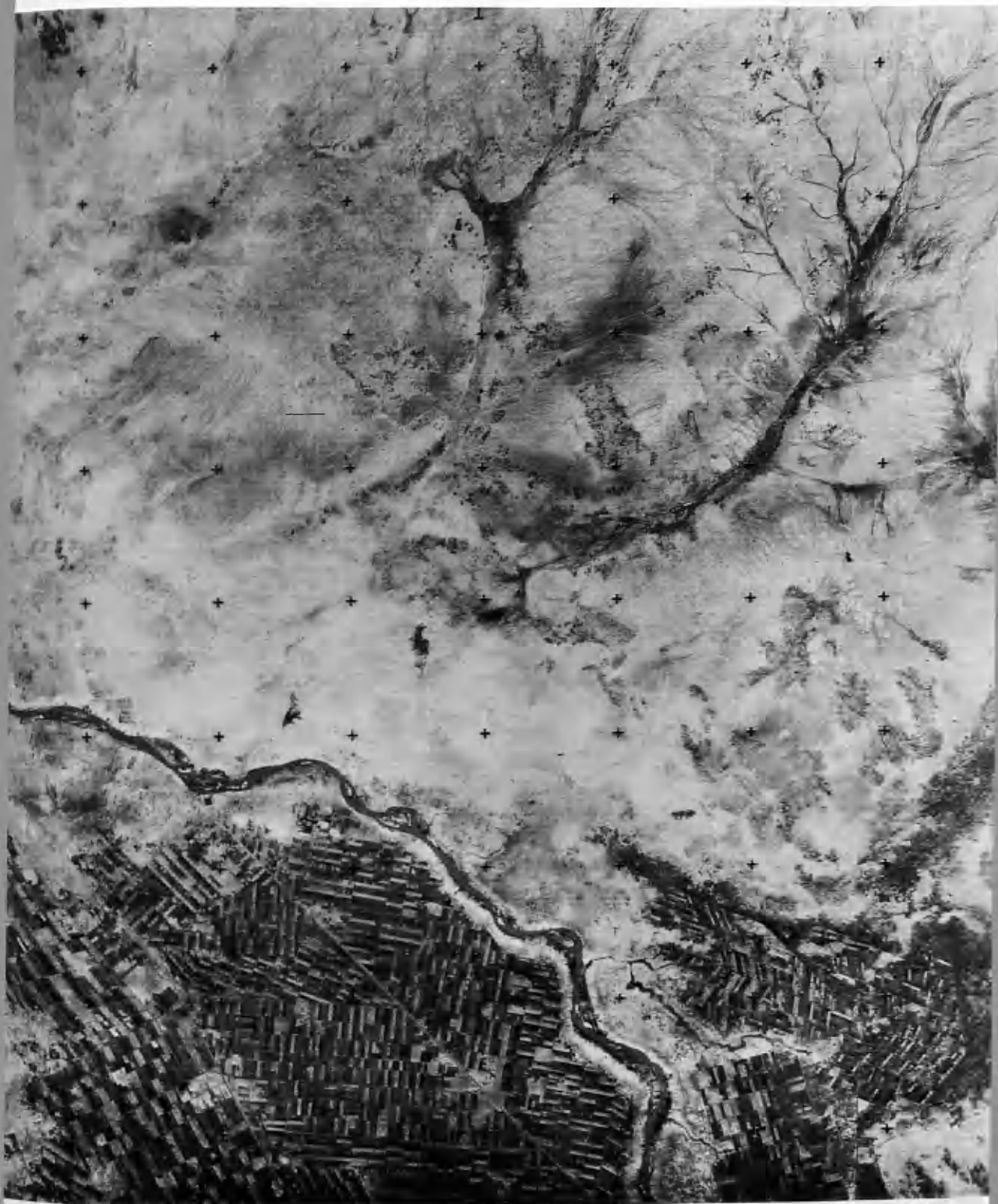


Fig. 9.2 RBV Subscene E-30234-07310 C 1:500,000 Scale Print of the Nile Test Area.



Fig. 9.3 RBV Subscene E-30159-20444 A 1:500,000 Scale Print of the Alaskan Test Area.



Fig. 9.4 RBV Subscene E-30159-20444 C 1:500,000 Scale Print of the Alaskan Test Area.



Fig. 9.5 RBV Subscene E-30160-20503 B 1:500,000 Scale Print of the Alaskan Test Area.



Fig. 9.6 RBV Subscene E-30160-20503 D 1:500,000 Scale Print of the Alaskan Test Area.

38%. Since this did not give good stereoscopic cover, it was necessary to acquire overlapping RBV images at a high latitude. Thus four Landsat-3 RBV subscenes covering part of the state of Alaska in the USA were acquired by the Department primarily for the RBV height accuracy test. These were Subscenes E-30159-20444 -A and C and E 30160-20503 B and D which were acquired on consecutive days 11th and 12th August, 1978 (Figs. 9.3 to 9.6). These subscenes cover the area extending between latitudes 64° N and 66° 15' N and longitudes 146° 30' W and 148° 50' W. In addition to the height accuracy tests, planimetric accuracy tests have also been carried out on two of the Alaska subscenes. In the following paragraphs, the results of the planimetric accuracy tests which have been obtained by the author on both the Red Sea Hills and Alaska test areas are presented and discussed. This is followed by a survey of the published results obtained by the investigators on testing RBV imagery over various test areas. The results of the height accuracy tests which have been obtained by the author are presented. Finally, the results of the interpretation tests carried out on the three test areas are discussed before the conclusions which can be drawn out of these tests regarding the applicability of the RBV images to the topographic mapping of the Sudan are stated.

9.2 Test Areas

As mentioned above, part of the Sudan Red Sea Hills test area, described in Chapter 3, is covered by RBV Subscene E 30232-07184 D centred at latitudes 18° 43' N, 36° 30' E. This area was described in Chapters 3 and 4 as very hilly and rugged. The dominant details in this area are relief forms and natural drainage streams with a very few small settlement areas scattered in the area. However a set of 87 points, most of them located on ridges, small hill tops and identifiable points on stream confluences, were identified and selected for the planimetric accuracy test. Again finding well defined points proved to be very difficult.

The other area in Sudan which has been selected for this investigation is the part of the Nile test area covered by the RBV Subscene E-30234-07310 C which is centred at latitude 15° 30' N and longitude 32° 23' E. This area was described in Chapter 3 and 4 as the most developed area in the Sudan. A wide range of features and man-made details can be found in the area. However, since only a very few topographic map sheets are available covering a very small part of this subscene, only an interpretation test was carried out on the subscene.

As mentioned above, in addition to the main test areas in the Sudan used in this investigation (the Red Sea Hills and Nile test areas), the area extending between latitudes 64° N and 66° 15' N and longitudes 146° 30' W and 148° 50' W in Alaska was selected primarily for height determination accuracy test. The selection of this area was dictated by the availability of cloud free adjacent frames and the percentage of overlap between subscenes from adjacent satellite paths. This area can be characterised as a hilly area with relief variations of 100 to 500 m. above datum. The density of detail in the area is not far greater than that in the Red Sea Hills area. Details such as road intersections, ridges, small water bodies were used as control and check points, their terrain coordinate values being obtained from 1:63,360 scale U.S.G.S maps of the area.

9.3 Coordinate Measurement

The ground coordinates of the selected points were scaled off map sheets covering the area in the same manner described in Chapter 3. As explained in Chapters 3 and 5, the precision with which the ground coordinates of the points can be scaled off the Sudan 1:100,000 scale topographic maps which cover the Red Sea Hills area is estimated to be ± 10 m. The ground coordinates of the points selected for the accuracy test of the Landsat-3 RBV images covering the Alaskan test area were scaled off the U.S.G.S 1:63,360 scale topographic maps covering this area which had been acquired by the Department for this investigation. The precision of scaling the ground coordinates using the engineering scale which has been used by the present author is ± 0.1 mm at the map scale which gives the accuracy of the scaled ground coordinates in the Alaskan test area as ± 6 m.

Film positives of 19.5x19.5 cm format were produced in the Department photographic laboratory from the 70 mm images of Subscenes E-30232-07184 D and E-30234-07310 C which were acquired from EROS Data Center. The subscenes covering the Alaskan test area were obtained as 19.5 cm x 19.5 cm diapositives from the EROS Data Center. The image coordinates for the planimetric accuracy tests were measured monoscopically while those for the height accuracy test were measured stereoscopically on the Stecometer CII stereocomparator at the N.E.L. The measuring technique adopted is as follows:

9.3.1 Monoscopic Measuring Procedure

For monoscopic measuring, the diapositive frames were aligned on the left carrier plate, one at a time, such that the comparator x-axis

passes through reseau crosses 55 and 59 (Fig. 9.7). The measuring procedure was started by loading the measuring program (STECA) in the computer memory while keeping the measuring mark of the comparator centered at reseau cross 55. This was done so that the cross 55 could act as the origin of the coordinate system. Following this preliminary operation, the selected image points were measured making three pointings at each point. The 9.6x magnification eye-piece of the Stecometer was found to be the most suitable since the use of its larger magnifications makes the granularity of the emulsion more profound.

9.3.2 Stereoscopic Measuring Procedure

In this procedure, the left and right diapositive frames were aligned on the left and right carrier plates respectively such that the comparator x-axis passes through the side anchor marks of both frames (Fig. 9.7). The measuring program was loaded while keeping the left measuring mark of the comparator on reseau cross 55 on the left image. Then the reseau crosses coordinates were measured starting at cross 11 and measuring the odd-numbered rows from left to right and the even-numbered rows from right to left till cross 99 was reached. This measurement pattern was then repeated in reverse order starting at cross 99 and ending at cross 11. The selected control and check points were then measured stereoscopically making three measurements at each point. Stereoscopic vision proved to be very difficult at the edges of the image frames. Again the 9.6x magnification eye-pieces were used for measurement.

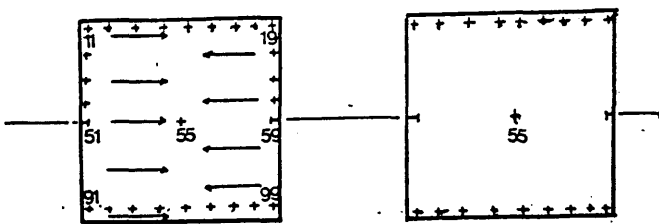


Fig. 9.7 Stereoscopic Measuring Procedure

9.4 Planimetric Accuracy Test Results

The procedure explained in Chapter 4 was again followed in the planimetric accuracy tests which have been carried out on the Landsat-3 RBV images. The results obtained from the planimetric accuracy tests of

this procedure, carried out on the Landsat-3 RBV images in this investigation, are as follows:

9.4.1 Red Sea Hills Test Area Results

The results obtained from the planimetric test of the RBV bulk-processed Subscene E-30232-07184 D over the Red Sea Hills test area after each transformation which are summarized in Tables 9.1 and 9.2 are as follows:

9.4.1.1 Linear Conformal Transformation Results

The linear conformal transformation using all measured points has resulted in r.m.s.e. values of ± 61 m, ± 65 m, and ± 89 m in easting, northing and vector respectively. The pattern of the residuals which have resulted at these points is shown in Fig. E.1. These planimetric r.m.s.e. values are almost three times the ground pixel size of 30 m. However, as can be seen from Fig. E.1, the resulting residuals have a very obvious systematic nature once again indicating that there are some systematic distortions inherent in the image.

Using a set of 40 well distributed points as control points and the remaining 47 points as check points, the linear conformal transformation has resulted in r.m.s.e. values of ± 58 m, ± 62 m and ± 85 m in easting, northing and vector respectively at the control points. The corresponding r.m.s.e. values which have resulted at the check points are ± 71 m, ± 59 m and ± 93 m. Again the planimetric r.m.s.e. values at both the control and the check points are almost three times greater than the pixel size. However the pattern of the resulting residuals, as shown in Fig. E.2, again shows that there are systematic distortions inherent in the bulk-processed RBV images.

9.4.1.2 Affine Transformation Results

The execution of an affine transformation using all measured points as control points has resulted in r.m.s.e. values of ± 35 m, ± 36 m and ± 51 m in easting, northing and vector respectively. Compared with the r.m.s.e. values which have been obtained from the linear conformal transformation above, it is clear that an improvement of 38 m in vector has occurred with the application of affine transformation. However, the pattern of the resulting residuals depicted in Fig. E.3 shows that there are still some systematic distortions inherent in the RBV image remaining to be compensated for.

The use of the 40 well-distributed points as control points to compute the transformation parameters which were used to transform the image coordinates of both the control and check points has resulted in approximately similar r.m.s.e. values. The r.m.s.e. values obtained after using an affine transformation based on 40 control points are ± 34 m, ± 40 m and ± 53 m in easting, northing and vector respectively at the control points and corresponding values of ± 37 m, ± 36 m and ± 52 m at the check points. An improvement in the planimetric r.m.s.e. value of 40 m in vector over that resulting from the linear conformal transformation has occurred. Furthermore, as can be seen from Fig. E4, the resulting pattern of residuals shows the systematic nature of the residual distortions which has been shown before by Fig. E.3. These residual distortions still remain to be compensated for by the use of higher order polynomial terms.

9.4.1.3 Polynomial Transformations Results

In the first set of polynomial transformations, the 4-term to the full 20-term polynomials of equations (4.27) and Table 4.1 have been utilized. All the measured points were used as control points to compute the transformation parameters in each of these polynomial transformations. The results which have been obtained from these transformations are listed in Table 9.1. As can be seen from Table 9.1, the r.m.s.e. values in vector continued to improve with the addition of higher polynomial terms until the 10th term was reached. With the 10-term polynomial transformation, the r.m.s.e. values have dropped to ± 27 m, ± 26 m and ± 38 m in easting, northing and vector respectively. No significant improvement in the r.m.s.e. values has occurred with the addition of polynomial terms higher than the 10th term. In general, the 10-term polynomials seem to be quite sufficient for the rectification and transformation of the bulk-processed Landsat-3 RBV images.

Since it had been found in the first set of polynomial transformations that the 10-term polynomial transformation can be quite sufficient for the bulk-processed Landsat-3 RBV images, only the 4-term to 10-term polynomials of Table 4.1 were used in this second set of transformations. Using the set of 40 well-distributed points as control points, the r.m.s.e. values at the control and check points which have resulted from each of these transformations are listed in Table 9.2. This gave best-fit r.m.s.e. values of ± 28 m, ± 29 m and ± 40 m in easting, northing and vector at the control points and corresponding values of ± 32 m, ± 26 m and ± 41 m at the check points. Figs. E.5 to E.11 show the pattern of the residuals which have resulted from each of these polynomial transformations.

These r.m.s.e. values for planimetric accuracy mean that topographic information with a planimetric accuracy of ± 40 m can be extracted from the Landsat-3 RBV images covering the Red Sea Hills area. This planimetric accuracy when compared with the values which are listed in Table 3.2 as planimetric accuracy requirements in topographic mapping, reveals that the Landsat-3 RBV images after being rectified can be used for the production of 1:150,000 or smaller scale image maps or line maps for the Sudan. However, whether or not the image content or resolution is sufficient to provide all or most of the information required to be shown on these maps is a matter which still has to be found out. This point will be discussed later in this chapter under the interpretation test results.

Transformation	No. of Pts.	r.m.s.e. E (m)	r.m.s.e. N (m)	r.m.s.e. V (m)
LINEAR CONFORMAL	87	60.90	64.90	89.00
AFFINE	"	35.50	36.20	50.70
POLYNOMIALS				
4 terms $x y$	"	33.10	35.70	48.70
5 terms x^2	"	32.00	35.80	48.00
6 terms y^2	"	30.30	30.40	42.90
7 terms $x^2 y$	"	29.60	30.60	42.60
8 terms $x y^2$	"	29.20	25.70	39.00
9 terms x^3	"	27.20	25.90	37.50
10 terms y^3	"	27.00	26.00	37.60
11 terms $x^3 y$	"	27.20	26.10	37.70
12 terms $x y^3$	"	27.30	26.00	37.70
13 terms x^4	"	27.40	26.00	37.80
14 terms y^4	"	27.50	26.00	37.80
15 terms $x^2 y^2$	"	27.60	26.10	37.90
16 terms $x^4 y$	"	27.80	26.20	38.20
17 terms $x y^4$	"	27.90	26.30	38.30
18 terms x^5	"	28.00	26.50	38.50
19 terms y^5	"	28.10	26.30	38.40
20 terms $x^3 y^3$	"	28.20	26.30	38.60

Table 9.1 Results of the Planimetric Accuracy Test of the RBV Image of the Red Sea Hill Area (using all points as control points).

Transformation	CONTROL POINTS				CHECK POINTS			
	No. of Pts.	r.m.s.e. E (m)	r.m.s.e. N (m)	r.m.s.e. V (m)	No. of Pts.	r.m.s.e. E (m)	r.m.s.e. N (m)	r.m.s.e. V (m)
LINEAR	40	58.60	62.20	85.40	47	71.60	58.90	92.70
AFFINE	"	34.50	39.80	52.70	"	37.30	35.60	51.60
POLYNOMIALS								
4 terms $x y$	"	28.00	39.30	48.20	"	35.90	35.00	50.10
5 terms x^2	"	27.30	34.20	43.70	"	33.80	29.80	45.00
6 terms y^2	"	27.60	34.00	43.80	"	32.80	31.30	45.30
7 terms $x^2 y$	"	27.70	29.50	40.40	"	31.60	25.60	40.70
8 terms $x y^2$	"	27.60	29.30	40.20	"	30.70	27.80	41.40
9 terms x^3	"	27.80	29.40	40.45	"	30.50	28.40	41.80
10 terms y^3	"	26.80	29.50	39.90	"	30.50	33.90	45.60

Table 9.2 Results of the Planimetric Accuracy Test of the RBV Image of the Red Sea Hills Area.

9.4.2 Alaskan Test Area Results

As mentioned above, planimetric accuracy tests were also carried out on Subscenes E-30159-20444 C and E-30159-20444 A of the Alaskan RBV images. These tests were carried out to provide a comparison of the planimetric accuracy which had been obtained in the Red Sea Hills area with what can be obtained in other similar areas. Topographic maps covering the whole area imaged by the two subscenes were available. For this test, 48 points were selected and measured on Subscene 1 (E-30159-20444 C) while a set of 43 points were selected and measured on Subscene 3 (E-30159-20444 A). Again two sets of transformations have been carried out in these tests. In the first set of transformations, all measured points were used as control points while, in the second set of transformations, a set of 20 well distributed points was taken as control points in each subscene, the remaining 28 points being used as check points. The results obtained in these tests are summarized in Tables 9.3, 9.4 and 9.5.

9.4.2.1 Linear Conformal Transformation Results

The linear conformal transformations which were carried out using all measured points as control points have resulted in r.m.s.e. values of ± 41 m, ± 44 m and ± 60 m in easting, northing and vector respectively at the points on Subscene 1; and corresponding r.m.s.e. values of ± 39

m, ± 41 m and ± 57 m on Subscene 3. The patterns of the resulting residuals are shown in Figs. E.12 and E.13.

The r.m.s.e. values in easting, northing and vector which have resulted from the linear conformal transformations using the more restricted set of 20 points as control points are ± 54 m, ± 53 m and ± 75 m respectively at the control points and corresponding values of ± 45 m, ± 45 m and ± 63 m at the check points on Subscene 1. The corresponding r.m.s.e. values which have resulted for Subscene 3 are ± 40 m, ± 39 m and ± 52 m at the control points and ± 42 m, ± 38 m and ± 57 m at the check points. The patterns of the resulting residuals at the points on these two subscenes after the linear conformal transformation are shown in Figs. E.14 and E.15. Again these planimetric accuracy values are rather large considering the ground pixel size of 30 m in RBV images. However, as can be seen in Figs. E.12 to E.15, the patterns of the residuals show that there are still some systematic distortions in the images which can be compensated for by using affine or high order polynomial transformations to yield much better results.

9.4.2.2 Affine Transformation Results

The execution of the affine transformation using all the measured points as control points has resulted in r.m.s.e. values of ± 35 m, ± 36 m and ± 50 m in easting, northing and vector respectively at the points on Subscene 1; and corresponding r.m.s.e. values of ± 37 m, ± 40 m and ± 54 m at the points on Subscene 3. The patterns of the resulting residuals at these points are shown in Figs. E.16 and E.17.

The use of the more restricted set of 20 control points with an affine transformation has resulted in r.m.s.e. values ± 45 m, ± 39 m, and ± 60 m in easting, northing and vector respectively at the control points; and ± 35 m, ± 35 m and ± 50 m at the check points in Subscene 1. The corresponding r.m.s.e. values which have resulted at the points in Subscene 3 are ± 36 m, ± 28 m, ± 46 m at the control points and ± 39 m, ± 41 m and ± 57 m at the check points. These planimetric accuracy values are, again, rather large considering the 30 m ground pixel size. However, the patterns of the resulting residuals which are shown in Figs. E.18 and E.19 reveal that there are still residual systematic distortions in these images.

9.4.2.3 Polynomial Transformation Results

The execution of the set of polynomial transformations using all the measured points as control points has resulted in the r.m.s.e.

values listed in Table 9.3. These give minimum planimetric r.m.s.e. values of +36 m and +32 m in vector on Scenes 1 and 2 respectively. As can be seen from Table 9.3, the 10-term polynomial transformation again proved to be quite sufficient to yield the potential planimetric accuracy in these images.

The 4-term to 10-term polynomial transformations which were carried out using the more restricted set of 20 control points have resulted in the r.m.s.e. values listed in Tables 9.4 and 9.5. These transformations give best r.m.s.e. values of +27 m, +29 m & +39 m in easting, northing and vector at the check points on Subscene 1; and +21 m, +28 m and +35 m at the check points on Subscene 3. These values give average r.m.s.e. values of +24 m, +28 m and +37 m. in easting, northing and vector respectively.

Transformation	Subscene 1			Subscene 3				
	No. of Pts.	r.m.s.e E (m)	r.m.s.e N (m)	r.m.s.e V (m)	No. of Pts.	r.m.s.e E (m)	r.m.s.e N (m)	r.m.s.e V (m)
LINEAR CONFORMAL	48	41.40	43.90	60.50	43	38.70	41.30	56.60
AFFINE	"	34.60	35.80	49.80	"	36.80	39.60	54.10
POLYNOMIALS								
4 terms x y	"	33.42	35.00	48.40	"	24.60	25.31	35.30
5 terms x ²	"	26.80	35.20	44.20	"	24.90	25.60	35.70
6 terms y ²	"	24.40	29.60	38.40	"	21.40	24.50	32.50
7 terms x ² y	"	24.60	29.90	38.70	"	21.50	24.50	32.60
8 terms x y ²	"	23.10	30.00	37.80	"	21.30	24.80	32.70
9 terms x ³	"	23.30	30.20	38.20	"	21.20	25.10	32.90
10 terms y ³	"	23.30	30.60	38.50	"	21.10	24.60	32.40
11 terms x ³ y	"	23.60	30.90	38.90	"	21.30	24.90	32.80
12 terms x y ³	"	22.90	29.20	37.10	"	21.50	25.30	32.20
13 terms x ⁴	"	22.50	29.60	37.20	"	21.54	25.30	33.30
14 terms y ⁴	"	22.60	29.80	37.30	"	21.30	23.60	31.80
15 terms x ² y ²	"	22.80	29.40	37.20	"	21.30	24.00	32.10
16 terms x ³ y ²	"	23.10	29.66	37.70	"	21.60	24.30	32.50
17 terms x ² y ³	"	23.10	28.70	36.80	"	21.40	24.40	32.50
18 terms x ⁵	"	22.90	29.20	37.10	"	21.60	24.50	32.70
19 terms y ⁵	"	23.1	29.60	37.50	"	21.30	24.80	32.70
20 terms x ³ y ³	"	22.80	28.90	36.80	"	21.70	24.20	32.50

Table 9.3 Results of the Planimetric Accuracy Test of Alaskan RBV Images.

Transformation	CONTROL POINTS				CHECK POINTS			
	No. of Pts.	r.m.s.e E (m)	r.m.s.e N (m)	r.m.s.e V (m)	No. of Pts.	r.m.s.e E (m)	r.m.s.e N (m)	r.m.s.e V (m)
LINEAR	20	53.70	52.80	75.20	28	44.60	44.70	63.10
AFFINE	"	45.47	39.07	59.95	"	35.12	35.44	49.89
POLYNOMIALS								
4 terms x y	"	44.78	39.27	59.56	"	33.41	34.87	48.29
5 terms x ²	"	34.95	34.66	49.23	"	36.21	29.11	46.46
6 terms y ²	"	33.95	35.50	49.12	"	26.90	29.03	39.58
7 terms x ² y	"	32.63	36.20	48.74	"	27.26	28.97	39.78
8 terms x y ²	"	32.63	36.20	48.74	"	27.26	28.97	39.78
9 terms x ³	"	31.91	37.53	49.26	"	26.21	28.83	38.96
10 terms y ³	"	33.12	38.58	50.85	"	26.31	33.65	42.71

Table 9.4 Results of the Planimetric Accuracy Test of Alaskan RBV Subscene 1.

Transformation	CONTROL POINTS				CHECK POINTS			
	No. of Pts.	r.m.s.e E (m)	r.m.s.e N (m)	r.m.s.e V (m)	No. of Pts.	r.m.s.e E (m)	r.m.s.e N (m)	r.m.s.e V (m)
LINEAR	20	40.02	33.81	52.39	23	42.29	38.49	57.18
AFFINE	"	36.02	28.49	45.92	"	39.05	41.78	57.19
POLYNOMIALS								
4 terms x y	"	22.98	20.11	30.54	"	23.90	27.14	36.16
5 terms x ²	"	22.85	20.68	30.82	"	21.40	28.06	35.29
6 terms y ²	"	23.37	20.77	31.27	"	21.14	28.73	35.67
7 terms x ² y	"	21.27	21.50	30.25	"	20.90	29.60	36.23
8 terms x y ²	"	19.74	19.52	27.76	"	21.00	29.84	36.50
9 terms x ³	"	19.79	19.77	27.98	"	21.05	29.43	36.20
10 terms y ³	"	19.24	20.74	28.29	"	22.97	29.50	37.40

Table 9.5 Results of the Planimetric Accuracy Test of Alaskan RBV Subscene 3.

9.5 Planimetric Accuracy Test Summary

The linear conformal transformation of RBV Subscene covering part of the Red Sea Hills area has resulted in r.m.s.e. values of ± 72 m, ± 59 m and ± 93 m in easting, northing and vector at the check points while that of the Subscenes covering the Alaskan test area has resulted in average r.m.s.e. values of ± 47 m, ± 43 m and ± 46 m in easting, northing and vector at the check points. The difference between these two sets of r.m.s.e. values may be due to the difference in rigor and precision in the system correction applied during the bulk-processing procedures. In addition to this, the fact that the Subscene E-30232-07184 D covering the Red Sea Hills area was enlarged by a factor of three from the original 70 mm transparency has probably added to the degradation of the image and in turn affected measurement accuracy.

Furthermore, the difference in the type of detail and the specific features which were selected as control and check points in the two areas has its effects on the results. While road intersections, airfields, field corners, railway lines and their sidings were easily found and selected as control and check points in the Alaskan test area, the points used in the Red Sea Hills test area were hilltops, rocks and stream confluences which were not as well defined as the points in the Alaskan test area. This highlights the problem in developing countries where details which can be selected as control points are either scarce or the contrast between the details and the background is too poor for these details to be identified on the image. In addition, the topographic maps available for control purposes in Alaska are at a larger scale (1:63,360) and allow a greater accuracy in scaling off control point coordinates than is possible with the 1:100,000 scale Sudan sheets.

However most importantly, the results of the linear conformal transformation of the RBV images show that there is no significant affinity in them compared with the MSS, TM and MOMS images. This means that the bulk-processed Landsat-3 RBV images received by the user are superior in geometric accuracy to the similarly processed MSS, TM and MOMS images.

With the higher degree transformations, the results improved in both areas but the improvement is more rapid and regular in Alaska test area. It is clear from these results that the accuracy that can be obtained in more developed areas with well-defined control points with more accurate coordinates is much better than that which can be achieved in developing areas. This means that while RBV images can be

used to produce image maps for developed areas at scales as large as 1:100,000, they can hardly satisfy map accuracy requirements at 1:200,000 scale in developing areas. This however needs more qualification since most of the developing countries lack topographic maps at scales as small as 1:250,000. Bearing in mind that few attempts have been made to develop or use such areas, therefore little man-made detail can be expected to be found. Furthermore since some kind of starting point is needed in the mapping of these areas, one can say that image maps at 1:150,000 scale can be produced from RBV images to serve as a base on which information from other sources may be added.

9.6 Published Tests and Applications

Since the RBV subsystems on board Landsat-1 and -2 had not been successful, by the time Landsat-3 was launched, the attention of investigators was concentrated on MSS imagery. This resulted in the RBV images receiving little attention. Thus in contrast to the situation with MSS, very little can be found in the literature about RBV and its possible applications to topographic mapping. Wong (1975) investigated Landsat-1 RBV images by using four scenes. Three of these were first generation 70 mm film transparencies produced at 1:3,369,000 scale and the fourth was printed on a glass plate at 1:1,000,000 scale. In this investigation, similarity (linear conformal) and affine transformations between the measured coordinates of the reseau crosses and their calibrated coordinates gave planimetric r.m.s.e. values of +58 m and +50 m respectively. Using image identified control points, the corresponding values for the linear conformal and affine transformations were found to be +131 m. and +105 m respectively.

As far as Landsat-3 RBV cameras are concerned, most of the published tests were carried out to determine the amount of information that can be extracted from their images. However, the experiments carried out as part of Landsat research conducted by the U.S Geological Survey Mapping Division for image maps, were reported by Bender and Falcone (1982) to have shown that RBV images could be used to produce planimetrically accurate 1:250,000 scale image maps. In the first group of these experiments, control points were first identified on 1:24,000 scale topographic maps of the area and visually transferred to much smaller 1:500,000 scale RBV images. In the second group, control points which had been field identified and marked on aerial photographs were used. The horizontal control points were directly transferred from the film transparencies of these aerial photos and marked on the RBV subscenes using a Kern PMG-2 zoom point transfer instrument. The RBV

image coordinates of the points in both experiments were then measured on a Kern MK-2 monocomparator, which has ± 1 μm resolution. The measured control points were transferred to the corresponding state plane coordinates using linear conformal transformation. The resulting r.m.s.e. values which were reported to have been obtained from these two experiments fall in the range of ± 43 to ± 50 m (Bender and Falcone, 1982).

In another investigation carried out by the U.S.G.S (Williams et al, 1983), the ground coordinates of the points, which have resulted from a planimetric block adjustment of RBV images, were plotted on a sheet of scribe-cote at 1:100,000 scale as control base using a Gerber 1232 flatbed plotting system. The transformation parameters obtained during the planimetric block adjustment were used to compute the precise scale factor for the enlargement of each subscene to the 1:100,000 scale. After the four subscenes were photomechanically mosaicked at 1:100,000 scale, a planimetric accuracy test was performed on the produced image map in which a vector r.m.s.e. value of ± 50 m was reported to have been achieved.

9.7 Height Accuracy Test Results

The r.m.s.e. in easting (E), northing (N), and height (H) which have resulted from the space resection and intersection procedure which was carried out on the two models formed from the four RBV subscenes covering the Alaskan test area are summarized in Table 9.6. In both stereomodels, a set of 16 points were used as control points in the resection phase. The conventional space resection/intersection without using additional parameters has resulted in r.m.s.e. values of ± 32 m, ± 33 m and ± 286 m in easting, northing and height respectively at the points on Model 1; and corresponding values of ± 35 m, ± 34 m and ± 305 m at the points on Model 2.

Adding the first term of equation (8.4) to the conventional space resection has resulted in r.m.s.e. values of ± 31 m, ± 31 m, and ± 149 m in easting, northing and height respectively at the points on Model 1; and corresponding values of ± 31 m, ± 31 m and ± 165 m at the points on Model 2. This sharp reduction in the r.m.s.e. for the height in both models is brought about by the correction for the scale error which was introduced by the lack of knowledge of the equivalent focal length of the camera.

The addition of the last term of equation (8.4) to the conventional resection solution has resulted in r.m.s.e. values of ± 30 m, ± 31 m and

± 286 m in easting, northing and height at the points on Model 1; and corresponding r.m.s.e. values of ± 30 m, ± 30 m, and ± 290 m at the points on Model 2. This slight improvement is due to the compensation for the error caused by the lack of knowledge of the principal point location.

Adding both the first and last terms of equation (8.4) together to the conventional resection has resulted in r.m.s.e. values of ± 31 m, ± 30 m, and ± 135 m in easting, northing and height respectively at the points on Model 1. The corresponding r.m.s.e. values which have resulted at the points on Model 2 are ± 32 m, ± 32 m and ± 150 m.

The addition of each of ^{the} other terms from equation (8.4) has resulted in no significant improvement in the resulting r.m.s.e. values. However, when these terms were added together the r.m.s.e. values which have resulted are found to be slightly worse than the ± 135 m and ± 150 m obtained by the addition of the first and last terms of equation (8.4) to the conventional resection. This may be due to the reduction in the redundancy in the least square solution. Therefore, the best height accuracy which may be achieved from similar overlapping RBV images can be taken as the average of these best results. This gives the accuracy of ± 145 m in the height determination using RBV images which is equivalent to 0.155% of the satellite altitude. To the author's knowledge, no other tests of stereo RBV images have been made, so no comparative figures are available.

Solution	M O D E L O N E					M O D E L T W O				
	No. of Pts	r.m.s.e E (m)	r.m.s.e N (m)	r.m.s.e V (m)	r.m.s.e H (m)	No. of Pts	r.m.s.e E (m)	r.m.s.e N (m)	r.m.s.e V (m)	r.m.s.e H (m)
Resection	30	32.00	33.00	46.00	286.00	25	35.00	34.00	48.00	305.00
" + ax	30	31.00	31.00	44.00	149.00	25	31.00	31.00	44.00	165.00
" + d	30	30.00	31.00	43.00	257.00	25	30.00	30.00	42.00	290.0
" + ax + d	30	31.00	30.00	43.00	135.00	25	32.00	31.00	44.00	150.00

Table 9.6 RBV Height Accuracy Test Results.

Although these results when compared with the values of Table 3.2 rule out Landsat-3 RBV images for height determination for topographic mapping, they do provide an insight into what could be expected from television cameras in space. An improvement in the height accuracy could be achieved by increasing the B:H ratio through convergent imaging. Increasing the B:H ratio through increasing the tube size is

not feasible at the moment since it is difficult to control the scanning beam to achieve the scan line pattern required to produce images having simple and stable geometry as discussed in Chapter 8. However it is quite possible that this difficulty may be overcome in the future, especially given the large research effort and rapid development of high definition television (HDTV) which is going on at the present time.

9.8 Results of the Interpretation Tests

Interpretation tests were carried out in this investigation on both the Sudanese test areas and the Alaskan test area. The aim of these interpretation tests is to evaluate the amount of the type of information required to be shown on 1:100,000 to 1:250,000 scale topographic maps and which can be extracted from the Landsat-3 RBV images in each of these areas.

In each of these interpretation tests, a comprehensive list of features and detail which are shown on the 1:100,000 scale topographic maps of the Sudanese test areas and the 1:63,360 scale topographic maps of the Alaskan area was first prepared. Then the detection and identification of these features was attempted using a mirror stereoscope and a reading magnifier. The result of these interpretation tests are as follows:

9.8.1 Interpretation Results of the RBV Images over Sudan

Interpretation of the Landsat-3 RBV images taken over Sudan had already been carried out in the Department as part of a previous interpretation test done in collaboration with the Sudan Survey Department to evaluate the feasibility of using Landsat images in the production of a series of topographic maps at 1:250,000 scale (Abdalla, 1980; Petrie, 1985). This work covered parts of the Red Sea Hills and the Nile test areas described in Section 3.4.1. However, further interpretation tests on these two areas were carried out by the present author with the help of the 1:100,000 scale topographic maps of these areas which had not been available to Mr. Abdalla when he carried out the first tests. The results of all interpretation tests carried out on the two Sudanese test areas are summarized in Table 9.7 and discussed below:

9.8.1.1 Interpretation of RBV Images over the Nile Test Area

Unfortunately, the contrast of the RBV image covering part of this

area is very poor. This poor contrast might be due to a presence of dust in the atmosphere above the area as a result of sand storm during the time of acquisition of this image. The probability of a sand storm taking place in October is very high in this area. The features which were looked for in this area fall in the five groups mentioned in Section 5.5.1 as follows:

(1) Lines of Communication

Lines of communication which are shown on the 1:100,000 scale topographic maps of this area include surfaced roads, unsurfaced roads and tracks, telephone lines, power lines, railway lines, etc. However, those specific features, the detection of which was attempted in this investigation, were hard surfaced roads, unsurfaced roads and tracks, bridges, ferry terminals and railway lines.

Surfaced roads can be detected on the RBV image where the contrast between these roads and the surrounding background is very sharp and the features located along both sides are aligned in regular pattern. In general, almost a complete failure was experienced in attempts to detect the full length of these roads on the image. Instead parts of these roads were detected here and there wherever the contrast and the pattern of the surrounding features made it possible. However, surfaced roads would be expected to show up much more clearly on a sharp-contrast RBV image.

As was the case with the MSS images, the detection of unsurfaced roads could be expected to be very difficult if not impossible on the RBV images since they are mostly formed by the repeated passage of lorries and trucks. As mentioned in Chapter 5, often these roads have no planned permanent locations. Although certain parts of these roads in the Gezira area, especially when they converge at villages, were detected on the RBV image, the general result is a failure.

Tracks are not expected to show up on any space image since they are extremely narrow and continuously changing in location. Even on the 1:100,000 scale topographic maps of the area, only the general approximate locations of these tracks are shown.

All bridges and dams across the Blue Nile, the White Nile and the main Nile in the area covered by the RBV image could be detected. In fact, it is even possible to guess the locations of these bridges by naked eye from the pattern of details and the roads converging towards them.

As in the case of the MSS images, the detection of railway lines in this area on the RBV image was found to be very difficult. However, long parts of the railway line in the Gezira area were detected with an ease which was not possible with the MSS images despite the fact that this RBV image is poorer in contrast than the MSS images. North of Khartoum, only short parts of the railway line where it runs through cultivated areas can be detected.

As described in Chapter 5, the locations of ferry terminals are not fixed and therefore no auxiliary features such as passenger waiting halls, docking pavements, etc. are present at these locations to assist in their detection. Therefore as expected, ferry terminals could not be detected on the RBV images.

(2) Cultural Features

The cultural features which are available and shown on the 1:100,000 scale topographic maps of the Nile test area include cultivated lands, built-up areas comprising big cities, towns and villages with associated features such as cemeteries, airfields, pipelines, parks, football grounds, etc.

A generalized picture of the cultivated areas of the Gezira, Gunied, etc. is indeed shown on the RBV image. However, these areas were found to show up more clearly on the MSS false colour mosaic covering the same area than on the RBV image. This is mainly due to the fact that cultivated areas are more absorbent to the electromagnetic radiation in the infra red region. This is in addition to the sharper contrast of the MSS image compared with the RBV image.

A generalized image of the areal extent and the pattern of the built-up areas of the three cities of the capital is also given by the RBV image. However, few internal details other than the major surfaced roads, the airports, parks, and football grounds are shown. Buildings are recorded in large blocks delineated by these major roads. Again in general, these internal features showed up more clearly on the MSS false colour mosaic than on the RBV image. The main reason for this is the poor contrast of the RBV image.

(3) Hydrology

All the three rivers in the area show up very clearly on the RBV image. The low plains along the west bank of the White Nile north of

Jebel Awlia which had been flooded by water during the autumn which had ended less than one month before the acquisition of this RBV image, also showed up quite clearly. All small islands in these three rivers also showed up quite clearly.

However, the natural drainage network of small streams which show up quite clearly on the MSS false colour mosaic of the same area cannot be detected on the RBV image despite the fact that this image was acquired less than a month after autumn ended. This is because, water and moisture in the soil is highly absorbent to infra red radiation.

(4) Relief Features

An extremely poor picture of the general form of the terrain in the area is shown on the RBV image. Again the MSS image and the MSS false colour mosaic showed this general form much more clearly than the RBV image, but here the main reason may be the poor contrast of the RBV image.

(5) Vegetation

Only large woods such as the Khartoum green belt, the Ghaba area and the Suba forests can be detected on the RBV image. Again only the general picture of the area covered by these large woods is shown.

In general, the results of the interpretation test of the RBV image over the Nile test area are quite disappointing and, judging from these results, the percentage of the information which can be extracted from this image compared with that required to be shown on the 1:100,000 scale topographic maps of the area can be estimated to be less than 30%. This means that it is not at all feasible to use Landsat-3 RBV images for the compilation of 1:100,000 to 1:250,000 scale topographic maps. However, these disappointing results are mainly due to the extremely poor contrast of the image made available for this investigation (Fig. 9.2). As shown in Chapters 4 and 8, the ground resolution of space images deteriorates very rapidly with diminishing contrast. At normal contrast (1.6:1), Welch et al. (1982) estimated the ground resolution of Landsat-3 to be about 70m. The contrast of the RBV image of the Nile area used in this investigation is much poorer than the 1.6:1 value. Hence the ground resolution must be much more coarser than the 70 m. Abdalla (1980) reported the unsuccessful attempts to enhance the contrast of this image using a dodging printer which were tried in the Department. However, as will be discussed later in this chapter, better-contrast Landsat-3 RBV images in other areas gave much

more information and detail than the MSS images.

FEATURES SHOWN ON MAPS	KHARTOUM TEST AREA		RED SEA TEST AREA		ALASKA TEST AREA	
	DETECTED	IDENTIFIED	DETECTED	IDENTIFIED	DETECTED	IDENTIFIED
Communication						
Hard surfaced roads	2	1	-	-	3	3
Unsurfaced roads	0	0	0	0	2	2
tracks	0	0	0	0	1	0
Footpaths	0	0	0	0	0	0
Streets	2	0	0	0	2	1
Bridges	2	1	0	0	3	1
ferry terminals	0	0	0	0	-	-
Railways	1	0	0	0	3	1
Railway stations	0	0	0	0	0	0
Culture						
Cultivated land	3	3	2	0	3	3
Big cities	3	1	2	1	3	2
Towns	2	0	0	0	2	2
Villages	0	0	0	0	0	0
Ruins	0	0	0	0	0	0
Electrical stations	0	0	0	0	0	0
Pipelines	0	0	0	0	0	0
Powerlines	0	0	0	0	0	0
Wells	0	0	0	0	0	0
Storage tanks	0	0	0	0	0	0
Cemeteries	1	0	0	0	1	0
Airports	3	3	0	0	3	3
Landing Grounds	0	0	0	0	2	1
Hydrology						
Rivers	3	3	-	-	3	3
Falls	3	1	-	-	3	2
Canals	3	3	-	-	3	3
Irrigation channels	1	0	-	-	-	-
Water bodies	3	3	3	3	3	3
Dams	3	3	-	-	-	-
Reservoirs	3	1	-	-	3	2
Hydrography						
Tidal flats	*	*	*	*	*	*
Reefs	*	*	*	*	*	*
Rocks	3	0	3	0	3	1
Near shore bathymetry	0	0	0	0	0	0
Water depth	1	1	1	1	0	0
Marsh	3	3	-	-	-	-
Harbours	-	-	3	3	3	3
Small harbours	3	1	3	1	3	2
Shore line	3	3	3	3	3	3
Islands	3	3	3	3	3	3
Relief forms						
Sand dunes	3	0	3	0	3	0
Gravel beds	1	0	1	0	2	0
Elevated grounds	3	3	3	2	3	3
Contours	0	0	0	0	0	0
Vegetation						
Woodlands	3	1	1	0	3	2
Scattered trees	0	0	0	0	0	0
Scrub	0	0	0	0	0	0
Orchards	2	0	0	0	0	0
Others						
Administrative boundaries	0	0	0	0	0	0
Rest houses	0	0	0	0	0	0
Triangulation pillars	0	0	0	0	0	0

0 = NOT; 1 = SOMETIMES; 2= OFTEN; 3 = YES; - = NOT AVAILABLE; AND * = REQUIRES REPEATED AVERAGE

Table 9.7 Interpretation Results of REV Images.

9.8.1.2 Interpretation of RBV Images over the Red Sea Hills Area

The part of the Red Sea Hills which is covered by the RBV image in this investigation is generally very hilly with narrow sandy valleys and plains between the hills. Being so, the area has had very little development and only very small villages scattered over the sandy plains can be found in the area. Therefore, cultural features are very scarce comprising mainly wells for the drinking water supply. Since the area is in the shadow of the very small winter rainfall which takes place on the Red Sea coast, no cultivated area as such can be found. Instead only scattered desert trees and short grassy vegetation are present in this area. Therefore, the dominant features in the area comprise the various relief forms and the dry streams forming the natural drainage network. Very narrow unsurfaced roads interconnecting the scattered villages are also present. However, nothing can be detected on the RBV image other than the hills, ridges, cliffs, isolated rocks and the natural drainage network. As expected, a complete failure was experienced in detecting the villages and the narrow unsurfaced roads interconnecting them. However, the degree of clarity with which the relief forms and the dry streams are shown confirm that the poor contrast of the RBV image covering the Nile test area is the main reason for the poor results of its interpretation.

In summary, the results of this interpretation test of the RBV image over the Red Sea Hills area simply reinforce the conclusions reached after the interpretation test of the Nile area and rule out the Landsat-3 RBV images from being a feasible source of the information required to be shown on topographic maps in the scale range 1:100,000 to 1:250,000.

9.8.2 Interpretation Results of RBV Images over Alaska

A similar interpretation test was carried out on the Alaskan subscenes by the author using a magnifier lens and mirror stereoscope together with the topographic maps covering the area. The overall interpretation results over this area are summarized in the last two columns of Table 9.7. A list of the features present in the area was first prepared from the 1:63,360 scale maps, then the lens and the stereoscope were used to detect and identify these features on the images. The results of this simple interpretation test showed a substantial improvement over the results of the same test on the Sudanese test areas, especially in and around the towns where various details could be found. For example, highways such as Richardson Highway, roads such as Chena Hot Springs Road, airfields, cities and

railway lines can easily be detected and plotted. Elsewhere however, in the undeveloped areas, a conclusion similar to that drawn from the interpretation of the RBV images covering the Nile and the Red Sea Hills test areas in the Sudan was reached. However, the results again confirm the poor contrast of the RBV image of the Nile test area as the main reason for the disappointing results of its interpretation.

9.8.3 Other Interpretational Tests of Landsat-3 RBV Imagery

A study to evaluate Landsat-3 RBV imagery for the discrimination of land cover and drainage basins, and the recognition of man-made features was carried out by Townshend et al (1980) in the regions of Basilicata and Apulia in southern Italy. First, the woodlands interpreted on the RBV images were delimited on a 1:60,000 enlargement of the image and then the boundaries were geometrically corrected and drawn on a topographic map base using an O.M.I. Stereo-Facet Plotter. This map was then compared with another map plotted from recent air photographs. The degree of correspondence between the two maps was computed by laying a grid over each map and observing the agreement at each 1/10 inch grid intersection. It was found that about 9% of the woodlands had been interpreted as non-woodland area and about 4% of non-woodland area had been interpreted as woodlands giving a total error of omission of 5%. Drainage nets detected and delimited on the Landsat-3 RBV images were found to be similar to those shown on 1:25,000 maps of the area disregarding very small streams. For man-made features, the conclusion was that principal roads are very distinct on the images and smaller routes are also well shown when they are radiating from a city. The larger internal features of cities such as airports, harbours etc. can also be identified. Elsewhere roads are less clear. The smallest detectable field was found to be about 50 m to 60 m in width, confirming Welch's (1982) estimate that RBV images have a ground resolution of about 70 m. At high contrast, the smallest detectable field was found by Townshend et al (1980) to be about 30 m to 40 m in width.

Another study was also carried out at the University of Georgia (Welch et al., 1982; Pannell and Welch, 1980) to assess the performance of Landsat-3 RBV images in terms of the land use information that can be extracted from them. Three Chinese test areas were selected, which included two of the largest Chinese cities, Beijing and Tianjin, and an important agricultural area at the confluence of the Huang and Wei rivers. Features shown on urban plans of Beijing and Tianjin and on 1:250,000 scale maps of all three test areas were identified and grouped into nine land use classes - parks, transportation features,

institutions, settlements, airfields, water area features, water line features, agriculture and land forms, which represent the details that are normally shown on 1:250,000 scale or larger topographic maps.

Within each test area, the features were identified and numbered on the base maps and assigned to the appropriate land use class. 70 mm. RBV transparencies were then viewed with a Bausch and Lomb Zoom 70 binocular system. Features were identified and assigned a rating value according to their contrast, size, shape, and the ease of their identification as follows:

i) Features which could be identified without reference to the maps, having a good contrast and their shape and size are distinct are assigned the value 3.

ii) Features which had an adequate contrast and can be identified with the aid of the maps, but their shape and size are indistinct, were assigned the value 2.

iii) Features, such as roads and railways etc., which can be detected but often their contrast is poor, are assigned the value 1. And those which cannot be detected are assigned the value 0.

The overall results of this analysis were expressed in terms of percentage completeness. The percentage scored by each class are shown in Fig. 9.7. A 100% was scored for airfields, 58% for water linear features, 76% for agriculture, and 88% for landforms.

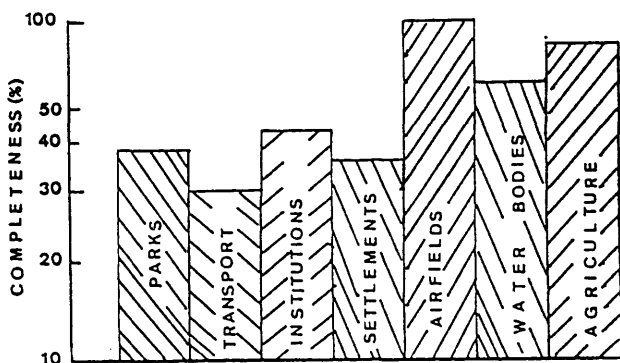


Fig. 9.7 Results of RBV Images Interpretation over China (Welch, 1983).

The good interpretation results of the RBV images over China once again confirmed the poor contrast of the Sudanese RBV images, especially that of the Nile Area, as the main cause for the poor interpretation results. This means that, with better contrast RBV images, the amount of information which can be extracted for the topographic mapping of the Sudan can be greater than what was estimated from this interpretation test. However, in all cases, this amount will be far less than what is required to be shown on the topographic maps at the scale range considered in this investigation and therefore the utilization of RBV images in this topographic mapping can hardly be justified.

9.9 Conclusion

The results of the planimetric accuracy and interpretation tests of the RBV images again show that, while the geometric accuracy of the information extracted from these images is quite satisfactory for topographic mapping at scales smaller than the 1:100,000 scale, the percentage of the information which can be extracted from these images compared with what needs to be shown on maps at these scales is very small. This small percentage rules out the RBV images as a major source of information as far as the topographic mapping of the Sudan is concerned. In general, television cameras which are capable of acquiring images with higher ground resolution are required if this type of sensor is to play a role in the topographic mapping process. The research for manufacturing this improved type of television camera (such as HDTV) is in progress. However, with the availability of alternative sensors which can be used on long-life space platforms, such as those based on linear or areal arrays of CCDs, it seems very difficult to turn back to television cameras, especially after the experience of the Landsat RBV cameras. Furthermore, with the possibility of putting high resolution photographic cameras into space to take photographs of the Earth's surface for several days before being recovered, the attention of many photogrammetrists and topographers will be concentrated on such photographic systems. Therefore, the following three chapters will cover the possibilities offered by space photographic systems.

CHAPTER 10

Space Photographic Systems

10.1 Introduction

Photography was for a long time the only method of acquiring images of the Earth's surface. From the First World War onwards, aerial photographic systems have continued to be developed and refined in many ways. During the most recent years, remarkable progress has been made in the development and manufacture of precision cameras for mapping purposes. Perhaps the most significant achievement in this development has been the capability to produce lenses of high resolving power which are free from distortion. The procedures and instrumentation used in the process of topographic mapping from aerial photographs have also been continuously developed. The application of aerial photography to topographic mapping is well established and well documented.

In general, various types of cameras having different format sizes, focal lengths and angular coverages have been developed to cope with the very varied requirements of mapping at different scales. Also in recent decades, the development of space technology, and especially the capability of launching manned space missions such as Skylab, Soyuz and the Space Shuttle which can orbit the Earth for periods ranging from several days to several months, has offered the opportunity to use these highly developed photographic systems in space to acquire photographs of the Earth's surface for mapping purposes.

As is well known, a photographic system consists mainly of two components which act together to produce the photographs. These components are the photographic camera which acts as an image-forming sensor; and the photographic film which acts as the image detecting and recording medium. As mentioned in Chapter 2, either the fixed frame/fixed lens mapping cameras or the rotating lens panoramic cameras can be used for space photography. Both types of cameras have been described in outline in Chapter 2. In this chapter, the description continues with a discussion of the special features of space photography which influence camera selection and design; the various types of photographic films which are available and suitable for the purpose; and the various configurations of multispectral photographic systems which are suitable for use from space platforms. This is followed by a discussion of the geometry of the photographs acquired by

these cameras and a general survey of past space photography experiments. Following this, recent space photography experiments are described and the analytical procedures followed by the present author in the geometric tests of space photographs are discussed.

10.2 **Considerations of Space Photography**

The motion of satellites in space is governed by the classical Keplerian laws which were originally developed to explain the motions of the planets around the Sun. According to these laws, a satellite moves around the Earth in an elliptical orbit with the Earth at one focus. Petrie (1970) gives a deep insight into the various effects which these laws have on the planning of space photographic missions. As a general rule, for space photographic missions, orbits are required to be circular to acquire photography of equal scale. This circular orbit can now be achieved with fairly good accuracy.

The period of time needed by a satellite to complete one orbit around the Earth depends very much on the satellite altitude. The higher the altitude, the longer period of time a satellite moving with a given speed takes to complete one orbit. Therefore, with the need to photograph the maximum area of the Earth's surface from a satellite moving with a given speed in a mission of short duration, the orbital altitudes should be very much more lower than the 920 km of Landsat. On the other hand, the lower the altitude, the shorter the life time of the mission because of the atmospheric drag. Therefore a compromise must be reached regarding these conflicting requirements.

As mentioned in Chapter 2, Skylab was launched in orbit having an altitude of 435 km, while both the MC and the LFC were orbited at 250 km orbital altitude. In general, orbital altitudes between 200 km to 400 km seem to be the most suitable for photographic manned space missions. However, other considerations point in the direction of keeping orbital altitudes as low as possible. As mentioned in Chapter 3, the accuracy of photogrammetrically determined spot heights is often taken as 0.15% H. Applying this to the 200 - 400 km range of orbital altitudes results in spot height accuracies ranging between ± 30 m to ± 60 m. However, with modern instruments, spot height determination to accuracies of 0.05% H, in terms of standard deviation, may be possible thus allowing spot height accuracies to lie in the range between ± 10 m to ± 25 m. This in turn will allow contour intervals of 30 m to 60 m. Obviously from the discussion already included in Chapter 3, it would be best if the smallest possible values can be achieved if the normal specifications for height and contour values on small-scale topographic

maps are to apply. This again points in the direction of having low orbital height values for space photographic systems designed for topographic mapping.

Another aspect of manned space systems is the inclination of the orbit which is the angle i that the plane of the orbit makes with the plane of the Equator (Fig. 10.1). This angle determines the maximum latitudes north and south of the Equator that the satellite can reach, i.e. the extent of the area which can be covered by the photographic camera. For global coverage, the satellite should be injected into a polar orbit ($i=90^\circ$). While this is done quite routinely with unmanned satellites, e.g Landsat and SPOT, which have near-polar orbits, quite different considerations operate with manned missions. With these, the orbit inclination is determined by other factors concerning launch and safety which in turn depend on the communication and tracking capability of the launching organization. By keeping the orbital inclination to a small value, these matters are much easier to handle. Thus the Space Shuttle being launched from NASA's Kennedy Space Centre has often been launched in quite small orbital inclinations - no greater than 30° in many cases - which means that the photographic coverage could not exceed 30° latitude north or south of the Equator. Even the highest orbital inclinations used by the Space Shuttle have not exceeded 56° , so that no MC or LFC photographs have been taken for latitudes higher than 56° N or S.

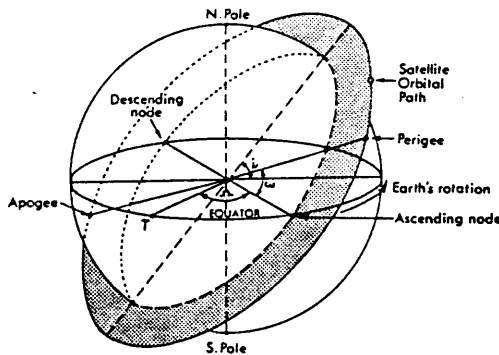


Fig. 10.1 Orbit Geometry.

From the above discussion, it is clear that low orbital altitudes are suited to space photography and that, at the present time, only coverage of relatively limited latitudinal extent can be expected. However, compared with aerial photography altitudes, these low orbital altitudes are still very high and special considerations regarding the

angular field, the photo scale and the resolution of the lens/film combination must be taken into account if the resulting photographs are to be used for mapping.

As shown in Chapter 8, the accuracy of forming a stereomodel from overlapping photographs and the subsequent measurements and plotting depends very much on the intersection angles between the rays coming from each of these photographs at the surface of the model. In turn, these angles depend on the base:height (B:H) ratio of the photographs. As is well known in photogrammetry, survey cameras can be classified into five types according to their angular fields. These are: (i) ultra-narrow angle (15°); (ii) narrow angle (30°); (iii) normal angle (56°); (iv) wide angle (93°); and (v) super-wide angle (122°). For a given photo format size, the wider the angle, the larger the area which is covered by a single frame from a given altitude and hence the bigger the B:H ratio resulting from a given overlap percentage. On the other hand, for a given format size, the wider the angular coverage, the smaller the resulting photo-scale. As discussed in Chapter 3, the influence of the photo-scale on the ground resolution of the acquired photography is very substantial, since the photo-scale, together with the resolving power of the lens/film combination, determines the smallest detail on the ground surface which can be resolved on the photographs. For high ground resolutions, the photo-scale should not be extremely small. Fig. 10.2 shows the various photo-scales of the photography acquired by each of the five types of camera resulting from various orbital altitudes.

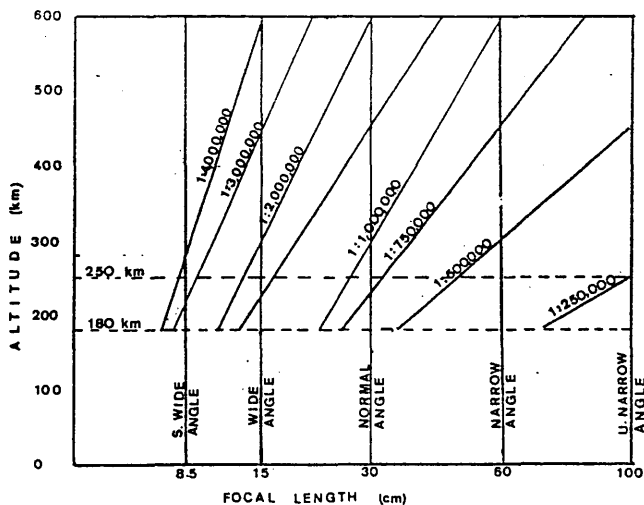


Fig. 10.2 Photo-scales for Various Cameras and Orbital Altitudes.

In general, judging by the B:H ratio, the super-wide angle camera would seem to be most suitable for space photography, but the

extremely small photo-scale will greatly reduce the amount of information which can be extracted from the photographs. On the other hand, judging from the photo-scale alone, the ultra-narrow angle camera would seem to be the most suitable camera for space photography. However, as mentioned above, the photography taken by an ultra-narrow angle camera will result in very small B:H ratios and hence very poor height and contouring accuracies.

One solution for the problems posed by these two conflicting factors is to use cameras with an increased format size in the direction of flight as was applied in the LFC. The increase of the format width in the direction of flight will ensure that the angular coverage is increased in this direction, without a reduction in the photo scale, since the camera focal length can remain fixed at a reasonably large value to give a good ground resolution. Furthermore, by acquiring photographs with 80% overlap, several B:H ratio configurations could be chosen in the mensuration process through the selection of stereopairs from the four consecutive photographs taken along the same strip. For example, the selection of the first and the third photographs from the set of four consecutive photographs will result in a stereopair having a 60% overlap area, while the selection of the first and the fourth will result in a 40% overlap area. This reduction in the overlap percentage will in turn be reflected in an increase in the B:H ratio.

Another factor to be considered in space photography is the resolving power of the lens/film combination. Resolving powers of more than 80 lp/mm are required if this photography is to be used for small scale topographic mapping. The 80 lp/mm resolving power will result in ground resolutions of 12.5 m and 7 m respectively in photographs taken by $f=300$ mm and $f=600$ mm cameras from an orbital altitude of 300 km. This order of resolving power is becoming increasingly possible using modern survey cameras and films. However light illumination can still be a problem. Therefore, either large apertures which allow a sufficient exposure with very brief exposure times or very slow fine-grained films and long exposure times need to be used.

The first option of using large aperture lenses raises problems of manufacture and weight since, for a lens of focal length $f=1.2$ m, if an $f/4$ aperture is required to achieve the necessary exposure, the diameter of these lenses will be 30 cm. This size of the lens will raise many other problems such as the difficulties in achieving the accurate centering of the lens elements and keeping the lens distortion at a minimum. In addition, the weight of a camera with a multiple-

element lens of this size will be quite heavy.

The other option of using slow fine-grained films will raise the problem of image motion. The relatively low orbital altitudes of manned photographic space satellites mean that the satellite will be moving over the ground at a speed of 8 km per second. This speed, together with long exposure times would result in considerable image motion causing the acquired photographs to be blurred and reducing their resolution drastically. However, this image motion can be compensated for by a suitable IMC mechanism as explained in Chapter 2.

At the present time, the option which is widely accepted as being the more desirable for space photography is the combination of lenses of high resolving power, slow fine-grained film, long exposure times and the implementation of an IMC mechanism.

10.3 Photographic Films

As mentioned above, photographic films serve as the image detecting and recording media in all cameras. In principle, the photographic film consists of a film base or support and one or more light sensitive layers or emulsions. The emulsion is a specially prepared gelatin containing the photo sensitive materials which are silver halide crystals and dyes held in suspension. In general, photographic films can be described by the characteristics of their emulsion materials as follows (ASP, 1968):

- i) Negative film in which the tones present in the photographed scene are reversed in the recorded image. Bright areas in the original scene, are imaged as dark areas in the film and shadows or dark areas of the scene appear light in the film.
- ii) Reversal film in which the inherent characteristics of the silver-based light-sensitive photographic material may be reversed by means of a multiple step process so that a positive image is produced on the film.

Both the negative and reversal films can be classified into low-contrast films which reproduce tone values in which the degree of separation between individual tone is less than in the original scene and high-contrast film in which the tonal separation is exaggerated in the image. Furthermore, films are also classified according to tone rendition into monochrome and colour films:

i) Black/white or monochrome films are those which produce all the values of the luminance in the original scene without respect to the colours in some shade of black, gray or white. They are usually sensitive to the radiation over the visible spectrum ($\lambda = 400$ to 700 nm) in which case, they are known as panchromatic films. A monochrome film whose spectral sensitivity is extended to cover the near infrared region ($\lambda = 700$ to 900 nm) as well, is identified as a monochrome infrared film.

ii) Colour films are those which by using separate layers of emulsions, are capable of reproducing different colours of the visible spectrum in terms of the original hue, saturation and brightness of the scene as faithfully as the process may allow. As is well known, both true-colour and false-colour aerial films are available, the former either as a negative film or as a reversal film, while the latter is normally available as a reversal film only.

Table 10.1 lists some of the available and commonly used films together with their resolutions at high and low contrast conditions.

Type	Film	Resolving Power (lp/mm) at contrast	
		1000:1	1.6:1
Monochrome	High Definition Aerial 3414	630	250
Monochrome	Panatomic X Aerocon II 3412	400	160
Monochrome	Panchromatic X 3400	160	63
Monochrome	Plus X Aerographic 2402	100	50
Monochrome	Double X Aerographic 2405	80	40
Monochrome	Infra-red Aerographic 2424	80	32
Colour	Ektachrome Infra-red Aerographic 2448	80	40
Colour	Aerochrome Infra-red 2443	63	32

Table 10.1 Characteristics of Available Photographic Films.

10.4 High Definition Films

Obviously in the light of the discussion included in Section 10.2, high-definition films are particularly suited to space photography. In these films, fine grained slow speed emulsions are used to improve the image quality. It should be noted that it is difficult to achieve high-definition in colour films because of the fact that instead of one emulsion layer, these films have three such layers with dye filters between them. This is evident from Table 10.1 which shows that colour films, at low contrast, have low resolving powers and that all available high-definition films are black/white films.

10.5 Multispectral Photographic Systems

Multispectral remote sensing has proved to be valuable in various fields, especially those concerned with image interpretation and analysis. In multispectral photography, the photographic system records a number of images of a scene through several different spectral filters. Multispectral photographic systems have been developed along three different paths. These are as follows:

(i) A multi-camera installation consisting of several identical cameras mounted on a single camera mount which are bore-sighted to photograph the same ground scenes. Using filters, each camera is made to photograph the Earth's surface in one of several different narrow spectral bands. Examples of this type of camera system are the S-190A used on Skylab and the Zeiss Jena MKF-6 used on Soyuz;

(ii) The multi-lens camera consisting of several lens assemblies, each with appropriate filters, coupled to a single camera body and a camera magazine accommodating different rolls of films. A between-the-lens shutter in each lens assembly with a single tripping pulse or a focal plane shutter with multiple slits can be used to take the exposures. The Itek nine lens multispectral camera is one example of this system; and

(iii) The beam-splitter camera in which a single-lens, together with a beam-splitter prism assembly between the lens and focal plane of each spectral image, is used to produce the several spectral images of the same scene. The incoming light passes through the single objective and is spectrally separated by the beam dispersing prism assembly which is coated with broad band

dichroic filters. Each spectral band is recorded on a separate emulsion (EMI Electronics, 1973; El Hassan, 1978).

However, all of these multi-spectral camera systems suffer from the drawbacks associated with the small format sizes of the acquired photography. Either the photographs will be deficient in scale and resolution or they will be deficient in their angular coverage and B:H ratio. Therefore, as far as stereoplotting, ground coordinate determination, etc. are concerned, space multi-spectral photographic systems are of little use. Furthermore, their usage in the interpretation of topographic detail is also limited and can hardly justify orbiting such systems for the sole purpose of interpretation.

10.6 Space Photography Experiments

Experiments involving space photography were started as early as 1965, but the objectives of the experiments conducted at that time were totally different to those of more recent ones (ASP, 1980, 1983; Konecny, 1983). However, the photographs of the Earth's surface taken by the astronauts in these early missions have demonstrated the feasibility of space photography of the Earth's surface. As mentioned in Chapter 2, the first significant step in space photography was started with the launch of Apollo-7 by NASA in 1968. Following the Apollo series, several space photographic mission were launched by both civilian and military organizations. The information and photography from the military missions has not yet been made available for the civilian user. Table 10.2 lists the known civilian space photography missions prior to the launch of the Space Shuttle mission carrying the Metric Camera (MC) and the Large Format Camera (LFC).

Mission	Year	Camera	Format Size	Scale	Ground Resolution
Gemini 4 - 7	1965	Hasselblad (C. Zeiss)	70 mm	1:3,000,000	125 m.
Gemini 10 - 12	1966	Maurer	70 mm	1:3,000,000	125 m.
Apollo 7	1968	Maurer R220	70 mm	1:2,800,000	70 m.
Apollo 9	1969	Hasselblad	70 mm	1:3,000,000	70 m.
Skylab (S190A)	1973	Itek	70 mm	1:2,850,000	50 m.
Skylab (S190B)	1973	EIC Actron	115 mm	1:945,000	20 - 30 m.
Apollo - Soyuz	1975	Hasselblad	70 mm	1:2,800,000	70 m.
Soyuz 22 - 30	1976-	Zeiss Jena MKF-6	70 mm	1:2,000,000	40 - 60 m.

Table 10.2 Past Experiments of Space Photography..

In the context of topographic mapping of the Earth's surface, the most significant of these past civilian experiment was that of the manned Skylab. This experiment was conducted by NASA to find a sensor which was capable of satisfying the requirements of the topographic mapping of the Earth soon after it was realized from Landsat-1 images that, for topographic mapping, the spatial resolution has to be far finer than the 79m pixel size of the MSS. Skylab was put into a circular orbit at 435 km above the Earth on May 14th, 1973. Three imaging remote sensing systems were carried on board forming the Earth Resources Experiment Package (EREP). Two of these were photographic systems: S-190 A and S-190 B which have been described in Chapter 2. Several research works have been carried out by various investigators on the photographs acquired by these photographic systems to assess their applicability to topographic mapping. Some of the results obtained in these research works will be given and compared with the results obtained in this investigation in the next chapter.

More recently, two space photographic experiments have been conducted. These are the Metric Camera experiment which was sponsored by the European Space Agency (ESA) and the Large Format Camera experiment which was planned and sponsored by NASA. In addition to these, four Russian photographic systems have been in operation since 1980. Photographs from these Russian cameras have only very recently been made available to users in the West.

10.6.1 **Metric Camera (MC) Experiment**

In the first Spacelab mission carried out in December 1983, a mapping camera was flown as part of the Earth observation payload. The camera was a modified Zeiss Oberkochen RMK A 30/23 aerial survey camera. The experimental hardware was developed jointly by the German Aerospace Industry and the German Aerospace Research Establishment (DFVLR), and was provided free of charge to ESA as part of the common European Experiment Facilities provided onboard Spacelab-1. It was deployed on the Space Shuttle STS-9 at a nominal orbital altitude of 250 km. The scientific objectives of the experiment can be summarized as:

- i) the compilation of topographic and thematic maps, especially over the unpopulated and less developed areas of the world;
- ii) the updating and revision of topographic and thematic maps in populated and developed regions; and

iii) the reduction in the cost of map compilation through the provision of control networks and by making photomaps.

The MC system (Fig. 10.3) consisted of: (1) the camera body with optical system; (2) two film magazines, one containing Kodak Double-X Aerographic film 2405 (black/white) and the other containing Kodak Aerochrome Infrared Film 2443 (colour); (3) two filters; (4) remote control unit (RCU); (5) camera suspension mount; and (6) stowage containers. The camera, film magazines and filters were stowed in the stowage containers in experiment racks during launch and landing to protect them from possible damage. The camera was interfaced to the optically flat high quality window via the suspension mount which was permanently mounted to the window adaptor plate. In orbit, the camera was assembled on the suspension mount, fitted with the magazine, and electrically connected to the remote control unit by the payload specialist. The characteristics of the MC are summarized in Table 10.3.

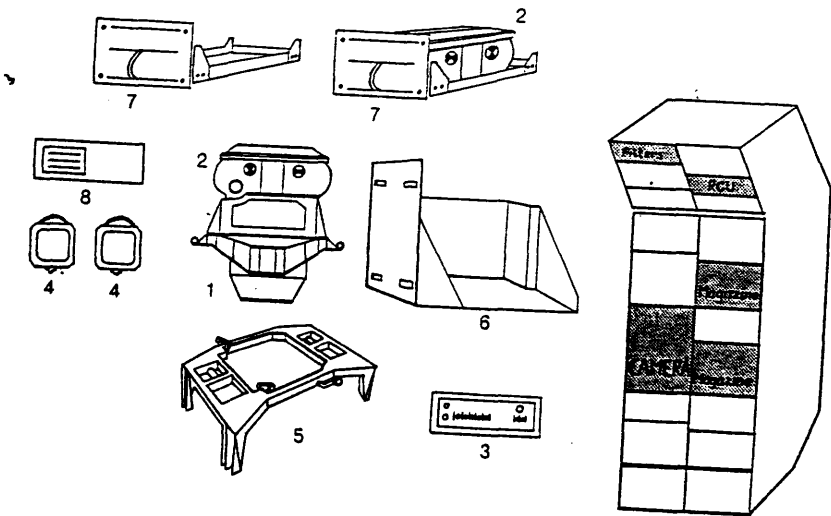


Fig. 10.3 The Metric Camera System.

Lens	Topar Al with 7 lens elements, f/5.6 to f/11.0
Calibrated Focal Length	305.128 mm.
Maximum Distortion	6 micrometres
Resolution	39 lp/mm. AWAR on Aviophot Pan 30 film.
Film Flattening	By blower motor incorporated in the camera body.
Shutter	Aerotop rotating disk shutter, 1/250 sec. to 1/1,000 sec.
Exposure Frequency	4 to 6 sec. and 8 to 12 sec.
Image Format	23 x 23 cm.

Table 10.3 Characteristics of the Metric Camera Experiment.

The camera was operated automatically by the on-board computer system. The control data for this automatic operation consist of:

- i) Number of images in one cycle.
- ii) Overlap adjustment.
- iii) F/stop adjustment for each exposure.
- iv) Exposure time for every exposure.
- v) Start and Stop time.

With the focal length of 305.128 mm, an orbital altitude of 250 km MC yields a photo scale of 1:820,000 which, with the 23 x 23 cm format, yields ground coverage of 189 x 189 sq. km. per frame. Spacelab moves in its orbit at a speed of 7.55 km./sec., so to prevent image blur, exposure times were taken between 1/500 to 1/1,000 sec.

10.6.2 Large Format Camera (LFC) Experiment

Another mapping camera experiment was conducted by NASA with the same scientific objectives as in the MC experiment. This was the Large Format Camera experiment. The LFC system consisting of the large format camera and the stellar attitude reference system, (ARS) was flown in the Space Shuttle mission STS-41G in the period 5th to 13th Oct. 1984. The camera system was built by Itek Optical Systems to a specification as to permit topographic mapping at scale of 1:50,000.

The LFC, derives its name from the size of its format, was mounted directly on an exterior pallet located in the Shuttle cargo bay, Fig. 10.4. The camera lens assembly consists of eight elements and antivignetting filter and has a maximum distortion of 15 μm over the entire format and 10 μm over the central 23x23 cm portion of the format. The lens is colour corrected for the wavelength range of $\lambda = 0.40$ to 0.90 μm , and optical filters can be inserted in the centre of the lens assembly to correct the colour balance for various films. Table 10.4 lists LFC experiment specifications which are specified to satisfy 1:50,000 scale topographic map requirements. The camera was operated by signals from ground controllers.

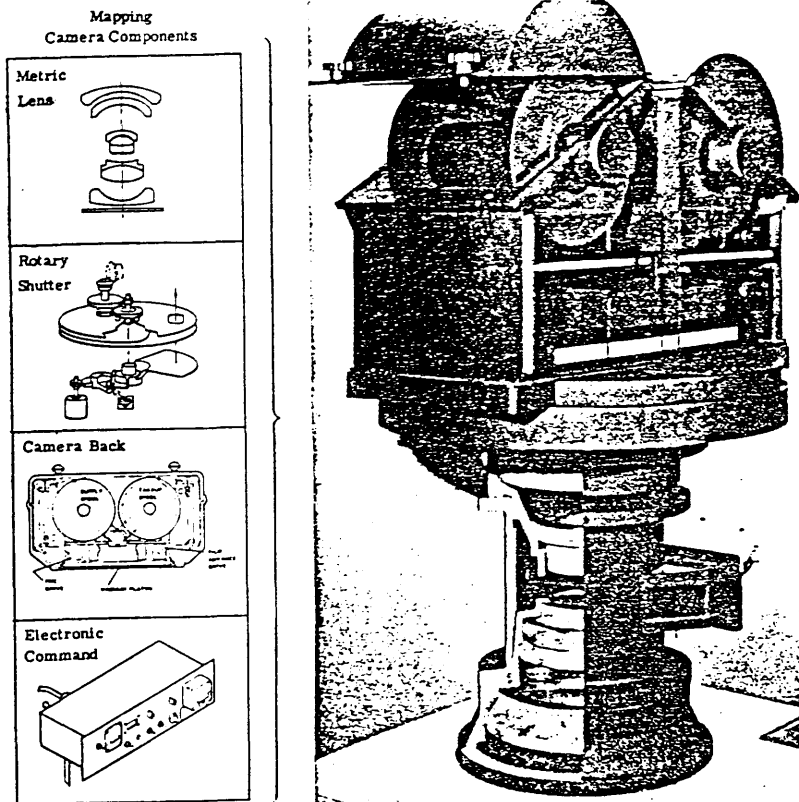


Fig. 10.4 Large Format Camera System.

The camera magazine has a maximum capacity of 1,200 m. of film sufficient for 2,400 exposures. The film spool rotates continuously during camera operation to avoid the serious vibration effects of starting and stopping. The film is held against the platen by a negative pressure differential between the lens cone and the camera back provided by a gaseous nitrogen system which also prevents static charge build-up and film brittleness.

The film platen combination is translated in the direction of flight to provide forward motion compensation in the range of 0.01 to

0.045 rad/sec. The platen contains a reseau at 5 cm holes, illuminated by light emitting diodes from the rear of the platen which can be switched on or off upon command. The arrangement of fiducial marks allows either the left, centre, or right 23x23 cm parts of each photograph to be used in standard photogrammetric instruments. The normal operation mode is 80% forward overlap, but 60% and 20% are also possible on command. Appropriate selection of frames provides stereo-models with base to height ratios from 0.3 to 1.2 from orbital altitude of 250 km.

Operation Parameters:	
Lens	f=305.0 mm. Aperture f/6.0 Spectral range =400 to 900 nm. Distortion < 10 um.
Shutter	3 disk rotary intralens with capping blade. Speed range 4 to 32 milli-sec.
Filters	Anti-vignetting front-lens. Minus haze and minus blue intralens.
Film types:	
3412	Panatomic-X Aerocon (Neg.) B/W Panchromatic having resolution of 400 and 160 lp/mm at high and low contrast respectively.
SO-131	High definition Aerochrome-IR (Pos.) CIR. Resolution 160 and 50 lp/mm.
SO-242	Aerial Color (Pos.) Colour. Resolution 200 and 100 lp/mm.

Table 10.4 Characteristics of LFC Experiment.

10.6.3 Russian Space Photographic Systems

As mentioned above, four space photographic systems have been launched by the Russians on board Salyut, Soyuz, Resurs and MIR satellites since 1980. These are:

(i) The KATE-140 camera operating in the visible spectral band ($\lambda = 0.5 \text{ } \mu\text{m}$ to $0.7 \text{ } \mu\text{m}$). Having a focal length of $f=140 \text{ mm}$ and a format size of $180 \text{ mm} \times 180 \text{ mm}$, the camera gives a ground coverage of $270 \text{ km} \times 270 \text{ km}$ per frame from Salyut's orbital altitude of 250 km . The ground resolution of the photographs acquired by this camera is estimated to be about 60 m .

(ii) The MKF-6 multispectral camera which was described in Chapter 2. This camera system consists of six photographic cameras, each having an $f=125 \text{ mm}$ lens, coupled together to photograph the same ground scene of $116 \text{ km} \times 162 \text{ km}$, from the orbital altitude of 250 km of Soyuz 22, in 6 narrow spectral bands. The ground resolution of the photographs acquired by this camera system is estimated to be about 40 to 60 m .

(iii) The KATE-200 multispectral camera which consists of three cameras coupled together and operated simultaneously to photograph the same ground scene in three spectral bands ($\lambda = 0.5 - 0.6 \text{ } \mu\text{m}$; $\lambda = 0.6 - 0.7 \text{ } \mu\text{m}$; and $\lambda = 0.7 - 0.9 \text{ } \mu\text{m}$). The focal length $f=200 \text{ mm}$ of the camera and the frame format of $180 \text{ mm} \times 180 \text{ mm}$ give a ground coverage of $225 \text{ km} \times 225 \text{ km}$ from the orbital altitude of 250 km . The ground resolution of the photographs acquired by this camera system is estimated to be 25 m , i.e. about equal to the ground resolution of the MC photographs. In addition, this camera gives overlapping photographs having a base:height (B:H) ratio of $1:0.38$ which is again equal to the base:height of the MC photographs. As far as this investigation is concerned, this base:height ratio, together with the ground resolution, makes the results which can be obtained from the geometric accuracy testing of the photographs acquired by the MC approximately similar to these which could be obtained from the KATE-200 photography.

(iv) The KFA-1000 camera which has a focal length of $1,000 \text{ mm}$. The KFA-1000 operates in the spectral band $\lambda = 0.57 - 0.8 \text{ } \mu\text{m}$ to photograph a ground scene of $80 \text{ km} \times 80 \text{ km}$ from an orbital altitude of 250 km on a format size of $300 \text{ mm} \times 300 \text{ mm}$. The

ground resolution of the photographs acquired by this camera is estimated to be about 5 m. This high ground resolution is achieved through the use of very long focal length i.e larger photo-scale. However, the base:height (B:H) ratio of the adjacent overlapping photographs of this camera is too small (1:0.125) for these photographs to be considered for height determination.

In the context of this investigation, the MC, the LFC and the last two Russian cameras are of prime interest. Since the photography which was acquired by the two Russian cameras was not available to the author, only the MC and the LFC were considered in this investigation. Several tests have been carried out by the present author on photographs acquired by the MC and the LFC covering parts of the two Sudanese test areas and the Georgia test area. These tests were carried out to determine the degree of contribution to the topographic mapping process of the Sudan and other developing countries which these two cameras in particular and space photography in general can offer. The tests comprise geometric accuracy tests to determine the accuracy of the information which can be extracted from these photographs; interpretation tests to determine the amount of this information and hence the scale of the topographic mapping in which these photographs can be used; and an orthophotography experiment which included an accuracy test of the produced orthophotograph and the DTM created from the height data gathered during the profiling operation which preceded the orthophoto production. The results of the geometric accuracy and interpretation tests of the photographs and their analysis, as well as those of other tests conducted by other investigators over various test areas, will be presented and discussed in the next chapter. The discussion of the orthophotography experiment and the results of the accuracy tests carried out on the produced orthophoto and DTM will be given in Chapter 12. In the following paragraphs, the geometrical aspects of frame photography are discussed briefly and the test procedures followed by the author in the geometric tests of the above mentioned space photographs are explained and discussed.

10.7 **Geometry of Frame Photographs**

The geometry of frame photographs is well known to photogrammetrists and well documented in the literature (ASP, 1944, 1966, 1980). Therefore, only a brief account of this basic geometry seems to be appropriate. If no image distortion has taken place, frame photographs will have the ideal geometry of the central projection where the nodal point of the camera lens is the perspective centre. Thus it is the point through which each of the image forming rays

passes to be recorded as a point image on the camera focal plane. In this ideal central projection geometry, the ground point, its image point and the lens nodal point are collinear. This collinearity condition represents one of the basic two conditions which are applied in photogrammetry for the operations carried out in the process of topographic mapping. The other condition which is applied in photogrammetry is the coplanarity condition. This condition states that the exposure stations of two overlapping photographs, the images of an object point on the two photographs and the point of intersection of the lines passing through the exposure station and the image point in each photograph all lie on the same plane. Figs. 10.6 show the the coplanarity conditions in frame photographs.

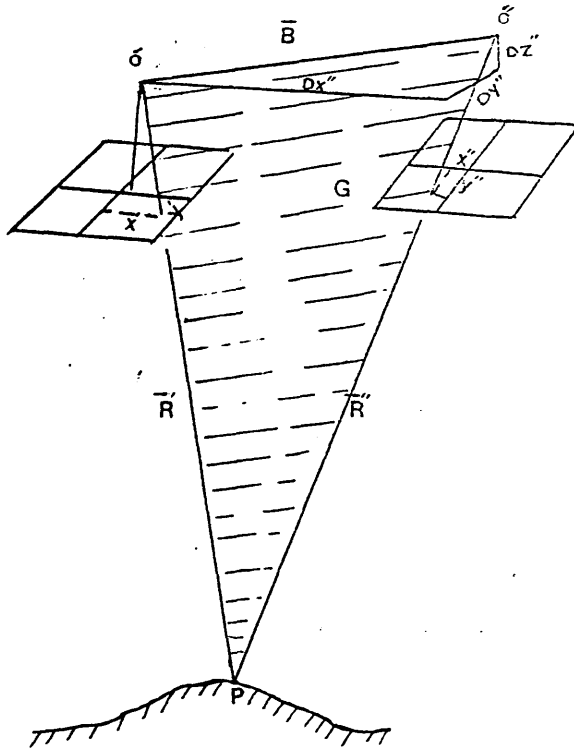


Fig. 10.6 Coplanarity Condition in Frame Photographs.

In general, the basic projective transformation describing the relationship between two mutually associated three-dimensional systems, xyz and XYZ, is that known as similarity projective transformation and is expressed as:

$$\begin{pmatrix} x \\ y \\ z \end{pmatrix} = SM \begin{pmatrix} X - X_0 \\ Y - Y_0 \\ Z - Z_0 \end{pmatrix} \dots\dots\dots (10.1)$$

where:

- x, y, z are the transformed coordinates of a point;
- X_0, Y_0, Z_0 are the coordinates of the origin in an X, Y, Z system;
- X, Y, Z are the coordinates of the point in the original coordinate system;
- S is a scale factor; and
- M is a 3×3 orthogonal rotation matrix made up of three independent rotations around the three axes $x, y,$ & z .

Applying this similarity projective transformation to the points imaged on a frame photograph and their respective ground coordinates leads to the collinearity condition equations which express mathematically the collinearity condition stated above. In more detail, these collinearity condition equations can be derived from equation (10.1) as follows:

$$\begin{pmatrix} x_p - x_o \\ y_p - y_o \\ -f \end{pmatrix} = SM \begin{pmatrix} X_p - X_o \\ Y_p - Y_o \\ Z_p - Z_o \end{pmatrix} \quad \dots\dots\dots(10.2)$$

Where:

- x_p, y_p are the image coordinates of point p ;
- x_o, y_o are the image coordinates of the principal point of the photograph;
- X_p, Y_p, Z_p are the ground coordinates of point p ;
- X_o, Y_o, Z_o are the ground coordinates of the exposure station;
- f is the focal length of the camera;
- S is a scale factor; and

$$M = \begin{pmatrix} m_{11} & m_{12} & m_{13} \\ m_{21} & m_{22} & m_{23} \\ m_{31} & m_{32} & m_{33} \end{pmatrix} \quad \text{is the rotational matrix.}$$

Dividing the first and second rows by the third row and then multiplying by $-f$, gives the collinearity equations for frame photography as follows:

$$x'_p = -f \frac{m_{11}(X_p - X_o) + m_{12}(Y_p - Y_o) + m_{13}(Z_p - Z_o)}{m_{31}(X_p - X_o) + m_{32}(Y_p - Y_o) + m_{33}(Z_p - Z_o)}$$

$$y'_p = -f \frac{m_{21}(X_p - X_o) + m_{22}(Y_p - Y_o) + m_{23}(Z_p - Z_o)}{m_{31}(X_p - X_o) + m_{32}(Y_p - Y_o) + m_{33}(Z_p - Z_o)}$$

.....(10.3)

where x'_p , y'_p are equal to $(x_p - x_o)$ and $(y_p - y_o)$ respectively.

Since equations (10.3) are non-linear functions of the orientation elements and object space coordinates, they are linearized using Taylor's series expansions. Their use in the various analytical photogrammetric operations involves an iterative solution. The linearized form of the collinearity condition equations taking the first order terms of the Taylor's series expansion may be written as (Ghosh, 1979, Baz, 1984):

$$(p_{12} \cdot dw + p_{13} \cdot d\phi + p_{14} \cdot dk - p_{15} \cdot dx_o - p_{16} \cdot dy_o - p_{17} \cdot dz_o + p_{15} \cdot dx + p_{16} \cdot dy + p_{17} \cdot dz) / q = - p_{11} / q$$

$$(p_{22} \cdot dw + p_{23} \cdot d\phi + p_{24} \cdot dk - p_{25} \cdot dx_o - p_{26} \cdot dy_o - p_{27} \cdot dz_o + p_{25} \cdot dx + p_{26} \cdot dy + p_{27} \cdot dz) / q = - p_{21} / q$$

....(10.4)

in which dw , $d\phi$, dk , dz are the corrections to the initial approximate values and:

$p_{11} = x \cdot M_3 \cdot B + f \cdot M_1 \cdot B$	$p_{21} = y \cdot M_3 \cdot B + f \cdot M_2 \cdot B$
$p_{12} = x(\delta M_3 / \delta w) B + f(\delta M_1 / \delta w) B$	$p_{22} = y(\delta M_3 / \delta w) B + f(\delta M_2 / \delta w) B$
$p_{13} = x(\delta M_3 / \delta \phi) B + f(\delta M_1 / \delta \phi) B$	$p_{23} = y(\delta M_3 / \delta \phi) B + f(\delta M_2 / \delta \phi) B$
$p_{14} = x(\delta M_3 / \delta k) B + f(\delta M_1 / \delta k) B$	$p_{24} = y(\delta M_3 / \delta k) B + f(\delta M_2 / \delta k) B$
$p_{15} = -x \cdot m_{31} - f \cdot m_{11}$	$p_{25} = -y \cdot m_{31} - f \cdot m_{21}$
$p_{16} = -x \cdot m_{32} - f \cdot m_{12}$	$p_{26} = -y \cdot m_{32} - f \cdot m_{22}$

$$P_{17} = -x \cdot m_{33} - f \cdot m_{13}$$

$$P_{27} = -y \cdot m_{33} - f \cdot m_{23}$$

$$q = M_3 B$$

$$\text{where } B = \begin{pmatrix} X_p - X_o \\ Y_p - Y_o \\ Z_p - Z_o \end{pmatrix}$$

M_1 , M_2 and M_3 are the first, second and third rows of the rotational matrix M .

Equations (10.4) may be written for any observed point i and put in the general form for a least squares solution.

$$(V_i) + (B_i) (\Delta) = (F^O_i) \dots\dots\dots (10.5)$$

in which:

$V_i = (vx_i \quad vy_i)$ are remaining residuals in the observations.

$$(B_i) = \begin{pmatrix} P_{15} & P_{16} & P_{17} & P_{12} & P_{13} & P_{14} & -P_{15} & -P_{16} & -P_{17} \\ P_{25} & P_{26} & P_{27} & P_{22} & P_{23} & P_{24} & -P_{25} & -P_{26} & -P_{27} \end{pmatrix}_i$$

$$\Delta = (dx \quad dy \quad dz \quad dw \quad dO \quad dk \quad dx_o \quad dy_o \quad dz_o)_i$$

$$(F^O_i) = (-P_{11}/q \quad -P_{21}/q)_i$$

The above mathematical formulae represent the basis of almost all analytical photogrammetric solutions. Equations (10.4) take various forms depending on the analytical photogrammetric solution intended to be carried out. As will be seen later, various forms of equations (10.4) have been used in this investigation.

10.8 Test Procedures with Space Photographs

As in the previous tests, the tests which were carried out in this

investigation on space photography comprise both interpretational and geometric accuracy tests, including both planimetric and height accuracy tests. The procedure followed in the interpretational tests was similar to that applied in the previous tests. However, in this case, the advantage of the stereoscopic viewing was utilized to detect the features present on the space photographs.

In the geometric accuracy tests, which were carried out in this investigation on the space photography, three analytical photogrammetric solutions were executed. These were:

- (1) Conventional relative and absolute orientation which was carried out on each stereo-model;
- (2) Conventional space resection and intersection which was carried out in the form of a bundle adjustment of three consecutive photographs; and
- (3) A stereo-model solution based on the use of of a combination of the collinearity and coplanarity condition equations.

Before these three solutions were carried out, a preparatory step was executed to transform the measured comparator coordinates into the image coordinate system and to refine the image coordinates by applying corrections for lens distortions and Earth's curvature. The preparatory step was executed using a computer program (REFOTO) written for this purpose. A detailed description of REFOTO is given in Appendix B.4. In this step, the transformation of the ground coordinates of the control and check points (which fall within two different UTM zones), into a common system (zone) was carried out as well as that of all points into a tangential plane projection.

10.8.1 **Relative and Absolute Orientation**

The relative orientation of a stereopair of photographs is the process of establishing the correct position and orientation of one of these photographs relative to the other. This is achieved by enforcing the condition that corresponding (conjugate) light rays intersect at a minimum of five common points. One or other of two analytical solutions is usually followed in carrying out the relative orientation. The first is based on the coplanarity condition equation, while the other is based on the collinearity equations. Since, in this investigation, the latter solution has been used, it will be explained in detail.

If an arbitrary orientation is assumed for one photograph of the stereo-pair, then a set of six unknown parameters need to be computed to determine the position and orientation of the second photograph relative to it (Fig. 10.6). If X' , Y' , Z' and w' , ϕ' and K' of the left photo are all taken to be equal to zero, the right photo can be oriented relative to the left one by the rotational elements Dw'' , $D\phi''$ and Dk'' ; and the base shifts DX'' , DY'' and DZ'' . DX'' can be selected as a fixed value since it only determines the model scale. Thus only five unknown parameters - dw'' , $d\phi''$, dk'' , dY'' and dZ'' need to be determined.

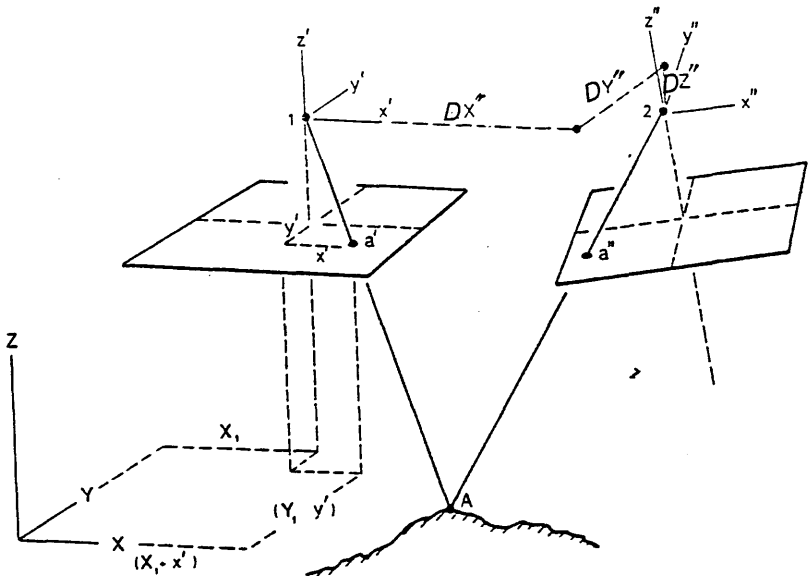


Fig. 10.6 Relative Orientation by Collinearity Equations.

Using the collinearity equation for the relative orientation solution will bring the model coordinates of the points into the equation. Since these are unknown too, approximate values have to be used. Therefore, three more unknowns, dX , dY and dZ , associated with the model coordinates of each point will also need to be found.

From Fig.10.6, the following four equations may be written for each point observed in the overlapping area of the stereo-pair.

$$\begin{aligned}
 v_{x'} &= p_{15}dX + p_{16}dY + p_{17}dZ + A' \\
 v_{y'} &= p_{25}dX + p_{26}dY + p_{27}dZ + B' \\
 v_{x''} &= p_{12}dw'' + p_{13}d\phi'' + p_{14}dk'' + p_{16}dY'' + p_{17}dZ'' + p_{15}dX + \\
 &\quad p_{16}dY + p_{17}dZ + A'' \\
 v_{y''} &= p_{22}dw'' + p_{23}d\phi'' + p_{24}dk'' + p_{26}dY'' + p_{17}dZ'' + p_{25}dX + \\
 &\quad p_{26}dY + p_{27}dZ + B''
 \end{aligned}$$

..... (10.6)

where $v_{x'}$, $v_{y'}$, $v_{x''}$ and $v_{y''}$ are the residual discrepancies in the measured photo coordinates;

dy'' , dz'' , dw'' , $d\phi''$ and dk'' are the five corrections to be made to the approximate values of DY'' , DZ'' , Dw'' , $D\phi''$ and Dk'' ;

dx , dy and dz are the corrections to be made to the approximate values of the model coordinates of a point;

P_{12} , P_{13} P_{27} are as in equations (10.5) and are evaluated using the assumed orientation values of the left photo for the first two equations and the approximate orientation values of the right photo for the second set of equations;

$A' = -p_{11}$, $B' = -p_{21}$ calculated for the left photo; and

$A'' = -p_{11}$, $B'' = -p_{21}$ calculated for the right photo.

Since, for each point that is observed, 4 equations can be written and 3 more unknowns have to be determined, a set of five points represent the minimum requirement for the solution (the five points give rise to 15 unknown values of the model coordinates; plus the unknown values of the 5 elements of orientation, making a total of 20 unknowns).

Absolute orientation was carried out to transform the model formed by the relative orientation into the object (ground) space coordinate system. The absolute orientation was carried out using the 3D similarity transformation. As shown in equation (10.1), the 3D similarity transformation involves 7 parameters - namely, 3 rotations and 3 translations of the model as a whole and a scale factor - as unknowns.

In this investigation, a set of well-distributed points were selected over the overlapping area and their coordinates measured on the Stecometer CII. These were used as control points to determine the unknown absolute orientation parameters of the 3D similarity transformation. Once they had been determined, these absolute orientation parameters were used, together with the model coordinates of another set of points, considered as check points, to compute the ground coordinates of these points. The computed ground coordinates of the points were then compared with the corresponding ones which were scaled off the topographic maps of the area to compute the residuals at each individual point. The root mean square errors (r.m.s.e.) in Easting, Northing and Height were computed as a measure of accuracy. The computer programs which were written to carry out the relative orientation (RELOR) and the absolute orientation solution (ABSTEST) are described in Appendix B.5.

10.8.2 Bundle Adjustment

Bundle adjustment is a form of space resection and intersection solution. However, instead of carrying out the resection and intersection computations on each pair of photographs forming a stereo-model in a separate step as is described in Appendix A, the resection of all photographs in a block and the subsequent intersection operation are carried out simultaneously. Therefore, the bundle adjustment procedure essentially consists of:

- i) A space resection of each individual photo using the provisional terrain coordinates to provide the initial approximate values of orientation parameters for each photograph.
- ii) Simultaneous exterior orientation of all the photographs in the block to obtain more accurate values for the orientation parameters of each photograph and intersection operations to determine the required ground coordinates of the measured points. In this way, the ground coordinates of the points which fall on the common overlap areas will be determined from more than two photographs, hence more accurate results will be obtained.

For the bundle adjustment solution, equations (10.4) may be written for all points in each photograph of the block as follows:

$$\begin{aligned}
 & v_{x_{ij}} + (p_{11ij} + p_{15ij} dx_i + p_{16ij} dy_i + p_{17ij} dz_{ij} + p_{12ij} dw_j + p_{13ij} d\theta_j + \\
 & p_{14j} dk_j - p_{15ij} dx_{oj} - p_{16ij} dy_{oj} - p_{17ij} dz_{oj}) = 0 \\
 & v_{y_{ij}} + (p_{21ij} + p_{25ij} dx_i + \dots - p_{27ij} dz_{oj}) = 0
 \end{aligned}
 \dots (10.7)$$

in which i, j denote the point and photograph numbers respectively.

For the control points, dx, dy and dz are equal to zero. Rearranging the corrections to the ground coordinates of the points as a separate group, equation (10.5) becomes:

$$(V) + (\dot{B})(\dot{\Delta}) + (\ddot{B})(\ddot{\Delta}) = F^0$$

in which:

- $\dot{\Delta}$ = corrections to the ground coordinates estimates.
- $\ddot{\Delta}$ = correction to the orientation parameters of each photograph in the block.

Utilizing matrix partition principles, the normal equations are then given by:

$$\begin{pmatrix} \dot{N} & N \\ N^T & \ddot{N} \end{pmatrix} \Delta = \begin{pmatrix} c' \\ c'' \end{pmatrix}$$

in which:

$$\begin{aligned} \dot{N} &= \dot{B}^T W \dot{B} & c' &= \dot{B}^T W F^O \\ \ddot{N} &= \ddot{B}^T W \ddot{B} & c'' &= \ddot{B}^T W F^O \\ N &= \dot{B}^T W \ddot{B} \end{aligned}$$

In this investigation, the ground coordinates of a set of the control points, which were scaled off the topographic maps, were considered fixed, while those of the check points were considered approximate values for which corrections were computed through the solution. These computed enhancements (corrections) in each iteration were added to the approximate coordinates to give better approximations for the next iteration. When the change in these corrections reached a lower limit of 0.5 m, the iteration was stopped and the enhanced ground coordinates of the check points were computed.

The computed ground coordinates were again compared with those scaled off the topographic maps and the discrepancies and the root mean square errors of the computed coordinates were computed. The computer program (BUNFIX) which carries out this solution is described in Appendix B.6.

10.8.3 **Resection/Intersection Solution Based on the Use of Combined Collinearity and Coplanarity Conditions**

Instead of carrying out the resection of each photograph separately, as is explained in Appendix A, this solution considers and treats both photos in the stereo-pair simultaneously as a unit instead of carrying out the resection of each photograph separately. The mathematical model which has been used for this solution is based on a combination of the coplanarity and collinearity condition equations and is explained in detail by Shortis (1980).

This combined coplanarity-collinearity condition solution is that adopted by the Photogrammetric Unit of N.E.L, East Kilbride in its

reduction program used with measurements made on its stereocomparator. The same program was transferred and modified by the author to run on the ICL mainframe machine of the University Computing Service for the purpose of carrying out the geometric accuracy test as well as for the reduction of the comparator measurements. A full description of the program is given in Appendix B.7.

10.9 **Summary**

In this chapter, the description of the photographic systems which was presented in Chapter 2, continued with the explanation of the main considerations which apply to the taking of space photography for the purposes of topographic mapping and the description of the various types of aerial films which are available and suitable for this specific purpose. This was followed by a survey of past space photography experiments. The Metric Camera and Large Format Camera which are the main interest in this investigation have been described in detail followed by a short description of the principal Russian space photographic systems. Following this, the geometry of frame photographs has been discussed in relation to analytical photogrammetry. Finally, the mathematical models used in this investigation for the test of space photography have been outlined. In the following chapter, the procedure followed and the operations carried out by the author in each of the accuracy and interpretation tests of the space photographs will be explained in some detail and the results of these tests will be reported and analyzed.

CHAPTER 11

Geometric Accuracy and Interpretation Tests of M.C and L.F.C Photographs

11.1 Introduction

In this chapter, a summary of the results obtained from the geometric tests carried out by several investigators on Skylab photographs is given first to show what was possible from space photography before the recent experiments. Next the test areas and the photographs which have been used in this investigation are described followed by the presentation and analysis of the results obtained from each part of the geometric test procedure described in the previous chapter. The results obtained from the accuracy tests of the MC photographs are presented and analyzed first followed by those obtained from the accuracy tests of the LFC photographs. Finally the results of the interpretation tests are presented before the conclusions which have been drawn from these tests are stated.

11.2 Skylab Photography Geometric Accuracy Results

As mentioned in Chapters 2 and 10, two photographic camera systems were flown onboard Skylab. These are the (i) S-190A multispectral metric camera which gave 1:2,850,000 scale photographs; and (ii) the S-190B long focal length camera having a focal plane shutter. Geometrical accuracy tests have been carried out by several investigators on these two types of photography. The results of some of these tests are as follows:

(i) S-190A Accuracy Tests

The photography acquired by the S-190A camera has very small scale and low ground resolution (40 to 100 m), but has a wider angle of coverage and better base:height ratio (0.19) compared with that acquired by the S-190B. Stewart (1975) reported that planimetric accuracy (m_{p1}) of ± 85 m to ± 133 m, (equivalent to 30 μ m and 44 μ m at image scale) can be obtained from the S-190A photography. However when measurement was carried out on 4x enlarged diapositives, an $m_{p1} = \pm 26$ m had been obtained. As for the height accuracy, Stewart (1975) also reported that an r.m.s.e. value in height (m_h) of ± 72 m had been obtained from the

S-190A photography. Mott (1975) adjusted a strip of S-190A to a set of 16 height control points obtaining an r.m.s.e. value (m_h) of ± 117 m in height (0.25%oH).

(ii) S-190B Accuracy Tests

The S-190B photography has special importance in the context of this investigation since its scale (1:950,000) and ground resolution (15 to 30 m) are approximately similar to those of the MC and LFC photography. Accuracy tests carried by Keller (1976) on the S-190B photography had resulted in a planimetric accuracy (m_{pl}) of ± 17 m. and a height accuracy (m_h) of ± 115 m. More extensive accuracy tests were carried out by El Hassan (1978) on the S-190B photographs. El Hassan (1978) reported that a planimetric accuracy of the order of ± 20 to ± 25 m and a height accuracy of ± 60 to ± 90 m had been obtained from these tests.

In general, although they couldn't deliver the height accuracy and amount of information required for topographic mapping at 1:50,000 to 1:100,000 scales, the Skylab camera systems demonstrated the possibilities of space photography quite well. However, some ten years had to elapse before suitable photogrammetric cameras were orbited in the shape of the Metric Camera (MC) and the Large Format Camera (LFC).

11.3 MC Photographs and Test Areas

As mentioned in Chapter 10, accuracy and interpretation tests have been carried out on the MC photographs to determine the degree to which this type of photographs can contribute to the topographic mapping of developing countries in general and of the Sudan in particular. For these tests, a set of six photographs were selected from the strip of photography acquired by the MC during orbit track No. 3. This strip was acquired on 2nd December, 1983 and recorded on the Kodak Aerochrome Infrared Film 2443. The photographs selected from this strip were: Photos. nos. 110, 111 and 112 covering part of the Red Sea Hills test area and Photos. nos. 104, 105 and 106 covering part of the Nile test area. Figs. 11.1 and 11.2 shows Photo. no. 111 and Photo. no. 104 respectively.

For the same reason stated in the previous chapters, while both accuracy and interpretation tests have been carried out on the photographs covering the Red Sea Hills test area, only an interpretation test has been carried out on those covering the Nile test area.



Fig. 11.1 1:820,000 Scale Contact Print of MC Photo. No. 111.



Fig. 11.2 1:820,000 Scale Contact Print of MC Photo. No. 104.



Fig. 11.3, 1:820,000 Scale Contact Print of MC Photo. No. 986.

To provide a comparison between the results obtained over Sudan with those obtainable over more developed areas of the world, another test area was selected. This was part of the state of Georgia, U.S.A, extending between latitudes 31° N and $32^{\circ} 30'$ N and longitudes $81^{\circ} 15'$ W and $82^{\circ} 40'$ W. As described in Chapter 3, this area can be considered as a good example of a developed area since it contains the variety and density of details that are associated with such areas. Three overlapping MC photographs acquired during orbit track no. 34 on 7th December, 1983 and recorded on the Double-X Aerographic 2405 black and white film cover this particular area. These are Photos. nos. 985, 986 and 987. The contact print of Photo. no. 986 covering the overlap area is shown in Fig. 11.3.

For the geometrical test, a set of image coordinates were used together with their corresponding ground coordinates to carry out all of the analytical photogrammetric operations described in Chapter 10. In each of these operations, the image coordinates of a set of control points were measured and, in combination with the corresponding set of terrain coordinates, were used to solve for the exterior orientation parameters of the photographs. These were then used to compute the ground coordinates of another set of measured points which were regarded as check points. The computed ground coordinates of the check points were compared with those derived from the topographic maps and the individual residual errors were computed. The root mean square errors were then computed to determine the accuracy of the positional and height information which could be extracted from these photographs.

The data needed for the geometrical test, therefore, comprise the ground and image coordinates of well defined and identified image points together with the inner orientation data of the camera. The inner orientation data were obtained from the calibration certificate of the camera. Well defined image points were identified on medium-scale topographic map sheets and their Universal Transverse Mercator (UTM) coordinates were carefully scaled using an engineering scale, in which the scale divisions were read through a magnifying lens, as described in Chapter 2.

The image coordinates of all the selected points were measured stereoscopically on the Zeiss Stecometer CII owned by the National Engineering Laboratories (N.E.L) at East Kilbride. The technique followed in measuring the image coordinates was as follows:

- (i) The diapositives were mounted on the carrier plates so that fiducial marks 1 and 3, located at the middle of left & right

sides of each photograph, were made collinear in both the left and right photos. Several pointings were made at various points using different eyepieces of different magnifications to determine the most suitable magnification for measurement. This was found to be 9.6x.

(ii) All the fiducial marks were measured four times, once on each round.

(iii) The image points were then measured three times, i.e. three pointings were made at each control point and check point. The mean of these three pointings is taken as the image coordinates of the point. Any pointing whose deviation from the mean was greater than 10 μm was rejected and the point was remeasured.

(iv) The image coordinate data were recorded on the Cromemco microcomputer attached to the stereocomparator and transferred to the University ICL/VME mainframe computers on which the computations were carried out.

11.4 Accuracy Test Results of MC Photographs of the Sudan

As mentioned above, accuracy tests have been carried out on MC Photos. nos. 110, 111 and 112 which cover part of the Red Sea Hills test area. The selection of these particular photographs was dictated by the availability of the topographic maps of the Red Sea Hills area. Two adjacent stereo-pairs were formed from these photographs - Photos. no. 110 and 111 as Stereopair 1 and Photos. nos. 111 and 112 as Stereopair 2.

Well defined points were selected on the central photograph (Photo no. 111) bearing in mind that they should be well distributed over the area. These points were then identified on the 1:100,000 scale topographic map sheets. Eighty eight of these points fall in the overlapping area of Stereopair 1 and fifty points on that of Stereopair 2. The image (x,y) coordinates of these points were measured on the Stecometer CII. The ground coordinates (as eastings and northings in the UTM coordinate system) were scaled off the 1:100,000 scale maps as explained in Chapter 3.

11.4.1 Results Using Space Resection/Intersection

Twenty nine well distributed points were selected as control points on Stereopair 1 while 25 points were selected on Stereopair 2. The rest

of the points in each stereopair were considered as check points. The space resection/intersection program (REDUCT) was run twice on each stereopair. In the first run, image coordinates were corrected for Earth's curvature before input to the program and ground coordinates of the points in U.T.M coordinate system were used. The root mean square errors (r.m.s.e.) in Eastings, Northings and Height were computed for both the control and check points. On Stereopair 1, the r.m.s.e. values which were obtained were ± 19 m, ± 16 m and ± 30 m in easting, northing and height respectively at the control points and corresponding values of ± 21 m, ± 20 m and ± 35 m at the check points. The r.m.s.e. values which resulted at the measured points on Stereopair 2 were ± 17 m, ± 19 m and ± 32 m at the control points and ± 21 m, ± 22 m and ± 31 m at the check points. The pattern of residuals in ground coordinates of all points in Stereopair 1 is shown in Fig. F.1 and those occurring in Stereopair 2 are given in Fig. F.2.

In the second run, the same control points used in the first run were used again but no attempt was made to correct image coordinates for the Earth's curvature. Instead, the UTM coordinates of the points were transformed into the geocentric coordinate system and then to the tangential plane centred at the exposure station of Photo. No. 110. The tangential plane coordinates were then used, catering for the image distortions introduced by the Earth's curvature, in the REDUCT program. The r.m.s.e. values which were obtained were ± 16 m, ± 16 m and ± 32 m in easting, northing and height respectively at the control points on Stereopair 1. The corresponding r.m.s.e. values which have resulted at the check points on the same stereopair are ± 15 m, ± 16 m and ± 30 m. The r.m.s.e. values which have resulted in easting, northing and height at the control on Stereopair 2 are ± 14 m, ± 17 m, and ± 30 m respectively. The corresponding r.m.s.e. values at the check points on this stereopair are ± 14 m, ± 16 m and ± 30 m respectively. The pattern of the resulting residuals in the ground coordinates of all points in the two stereopairs are shown in Fig. F.3 and Fig. F.4.

11.4.2 Results Using Relative/Absolute Orientation

A relative orientation was computed using 14 points well distributed over the area of each model. In both stereopairs, 4 iterations were enough to obtain convergence and to achieve y-parallax values less than 10 μ m. The same control points which were used for each stereopair in the space resection were used again for the absolute orientation. The r.m.s.e. values in easting, northing and height which have been obtained at the control points on Stereopair 1 were ± 18 m, ± 18 m and ± 30 m respectively. The corresponding r.m.s.e. values which have

resulted at the check points on the same stereopair were ± 21 m, ± 21 m and ± 36 m. For the points on Stereopair 2, the r.m.s.e. values which have resulted in easting, northing and height were ± 20 m, ± 23 m and ± 35 m at the control points and ± 20 m, ± 17 m and ± 39 m at the check points. The pattern of residuals which have resulted in the ground coordinates of the points on Stereopairs 1 and 2 are shown in Fig. F.5 and F.6.

11.4.3 Results Using Bundle Adjustment

In the BUNFIX bundle adjustment program, all the control points which were used in the previous two operations have been used again, but on this occasion, they have been used for the transformation of the three photos as a single unit. In this solution, instead of using the control points to compute the exterior orientation and then using the computed orientation parameters to transform the image coordinates of the check points into the ground coordinate system, the transformation of check points to ground coordinate system has been carried out simultaneously with the solution of the orientation as described in Appendix A. As explained in Appendix B-7, the control points were considered as fixed and no residuals or r.m.s.e. values were computed at them. R.m.s.e. values in easting, northing and height which have resulted at the check points from this adjustment are ± 20 m, ± 21 m and ± 33 m respectively.

11.4.4 Summary of Accuracy Results for the Red Sea Hills Test Area

From all these results, it is clear that coordinate determination with an accuracy (r.m.s.e.) of ± 28 m (vector) in planimetry and ± 30 m. in height can be achieved from MC photographs over the Sudan and similar areas. In fact, if the planimetric accuracy of scaling the ground coordinates off the 1:100,000 scale topographic maps, as shown in Chapter 3, is $m_{p1} = \pm 14$ m. (± 10 m in each direction), then the planimetric accuracy obtainable from these photographs will be ± 24 m. Similarly if the accuracy of interpolating height information from contours is taken as 0.3 of the contour interval (CI), as shown in Chapter 3, then the accuracy of height information interpolated from the 40 m CI for this test can be taken as ± 12 m (0.3×40). Taking this value into consideration, the accuracy of spot height information (m_h) derived from MC photographs over the Sudan will be ± 27 m ($(30^2 - 12^2)^{0.5}$). Checking the planimetric accuracy of ± 24 m against Table 3.2 shows that MC photographs can be used in the production of 1:100,000 and smaller scales maps of the Sudan. But if the value $3 \times m_h$ specified in Chapter 3 for the possible minimum contour interval is strictly applied, then the ± 27 m obtained for the spot height height accuracy

leads to the conclusion that contours can only be plotted at a contour interval of 80 m or larger - which is much larger than the 40 m or even 20 m CI often required at those scales.

11.5 Accuracy Test Results of MC Photographs of Georgia

As mentioned above, geometric accuracy tests have also been carried out on the MC photographs covering the Georgia test area. In this discussion, the stereopair formed from Photos. nos. 985 and 986 is referred to as Stereopair 3 and that formed from Photos. nos. 986 and 987 is denoted as Stereopair 4. A set of 97 well-distributed points were selected on Stereopair 3, while 88 points were selected in Stereopair 4. The state plane coordinates of these points were scaled off the 1:24,000 scale topographic maps of the area in the manner explained in Chapter 3. The planimetric accuracy of these scaled coordinates is estimated to be ± 7 m in vector. Spot height values were interpolated linearly from the 10 ft (3 m) CI contours shown on these maps to an estimated accuracy of ± 1 m (0.3x3). Image coordinates were then measured following the measuring technique stated above. Space resection/intersection, relative/absolute orientation and bundle adjustment operations were carried out on these data following the test procedure which had already been applied to the MC photographs of the Red Sea Hills test area.

11.5.1 Results Using Space Resection/Intersection

The r.m.s.e. values which have resulted for Stereopair 3 from the resection/intersection operation were ± 17 m, ± 18 m and ± 24 m in easting, northing and height respectively at the control points and of ± 18 m, ± 15 m and ± 21 m at the check points. The r.m.s.e. values which have resulted from the same operation for Stereopair 4 were ± 18 m, ± 18 m, and ± 25 m in easting, northing and height respectively at the control points and corresponding values of ± 17 m, ± 16 m and ± 22 m at the check points. The patterns of the resulting residuals in planimetric and height at each point in Stereopair 3 are shown in Fig. F.7, while those of the resulting residuals at each point in Stereopair 4 are shown in Fig. F.8. These figures show no sign of systematic errors in either of the stereopairs.

11.5.2 Results Using Relative/Absolute Orientation

The r.m.s.e. values which have resulted in this area from the relative/absolute orientation operation were ± 21 m, ± 20 m and ± 29 m in easting, northing and height respectively at the control points and ± 21

m, ± 17 m and ± 28 m at the check points on Stereopair 3. On Stereopair 4, the r.m.s.e. values of ± 20 m, ± 20 m and ± 29 m at the control points and ± 21 m, ± 19 m and ± 28 m at the check. The patterns of the resulting residuals at each point on these stereopairs are shown in Figs. F.9 and F.10. Again there is no pattern of systematic errors to be seen in these figures.

11.5.3 Results Using Bundle Adjustment

As was done with the MC photographs covering the Red Sea Hills test area, the bundle adjustment was carried out using the control points which were used for the space resection and absolute orientation. As mentioned above, no residuals or r.m.s.e. values were computed at the control points. The corresponding r.m.s.e. values which have been obtained from the bundle adjustment were ± 18 m, ± 17 m, and ± 23 m in easting, northing and height at the check points on the overlapping area.

11.5.4 Summary of MC Accuracy Results for the Georgia Test Area

Taking the average of all three sets of r.m.s.e. values gives an average accuracy of ± 26 m in planimetry and of ± 24 m in height. Considering the accuracy of planimetric information scaled off the maps as ± 4 m (2.6 m in each axis) and that of the interpolated height information as ± 1.0 m, the resulting accuracy in the determination of these values from MC photographs over Georgia still remains as ± 25 m in planimetry and ± 24 m in height.

Comparing these values with those obtained in Stereopairs 1 & 2, it is clear that the planimetric accuracies obtained in both test areas are almost the same while a sharp shortfall in height accuracy occurs in Red Sea Hills test area. This shortfall is partly due to the difference in the types of points selected for measurement in the two test areas. While hill tops, ridges, and defined points along the paths of dry streams were selected in the Red Sea Hills test area due to the lack of well defined man-made detail in the area, in the Georgia test area, road intersections, runways, railway line intersections, bridges, and field corners were easily found and selected. Although the type of control and check points selected in the Georgia test area should also result in better planimetric accuracy, values were obtained which are approximately equal to those obtained over the Red Sea Hills test area after taking the precision of scaling the terrain coordinates from the 1:100,000 scale topographic maps of this area into consideration. However, the advantages of having well-defined image

points was much more felt during the image coordinate measurement.

Tables 11.1 and 11.2 list the r.m.s.e. values at the control and check points which have been obtained from the above discussed solutions for the four stereopairs.

System of Coords.	Model No.	C O N T R O L P O I N T S				C H E C K P O I N T S					
		No. of Pts.	r.m.s.e. E	r.m.s.e. N	r.m.s.e. V	r.m.s.e. H	No. of Pts.	r.m.s.e. E	r.m.s.e. N	r.m.s.e. V	r.m.s.e. H
UTM	110/111	30	18.60	15.50	24.14	29.80	55	20.70	20.20	28.90	34.60
TAN	110/111	30	15.70	16.00	22.40	30.00	55	14.50	15.60	21.30	29.70
UTM	111/112	25	17.00	19.30	25.72	31.80	31	20.90	22.40	30.60	30.70
TAN	111/112	25	14.10	17.70	22.63	30.40	31	14.00	15.70	21.04	30.00
UTM	985/986	30	17.20	18.00	24.90	23.90	67	17.50	15.30	23.24	21.30
UTM	986/987	30	17.80	17.60	25.03	22.50	58	17.00	15.80	23.20	21.80

Table 11.1 MC Space Resection/Intersection Results.

System of Coords.	Model No.	C O N T R O L P O I N T S				C H E C K P O I N T S					
		No. of Pts.	r.m.s.e. E	r.m.s.e. N	r.m.s.e. V	r.m.s.e. H	No. of Pts.	r.m.s.e. E	r.m.s.e. N	r.m.s.e. V	r.m.s.e. H
UTM	110/111	30	17.50	18.64	25.57	29.56	55	20.86	20.95	29.56	36.00
UTM	111/112	25	20.20	22.80	30.46	34.80	31	20.60	16.80	26.60	39.00
UTM	985/986	30	21.72	20.40	29.80	38.64	67	20.60	16.83	26.60	28.00
UTM	986/987	30	20.20	14.00	24.60	29.96	58	20.50	19.20	28.10	27.64

Table 11.2 MC Relative/Absolute Orientation Results.

In general, the MC photography has proved to be more than a step forward towards fulfilling the requirements of topographic mapping, in terms of geometric accuracy, compared with the photography of the Skylab missions.

11.5.5 Summary of Other MC Accuracy Tests Results and Analysis

Numerous investigators have tested the MC photography over various test areas. Early results of testing MC photography were presented at the Metric Camera Workshop held at Oberpfaffenhofen in February, 1985. Ackermann and Stark (1985) reported their experience in forming

stereomodels from MC photographs of southern Bavaria using a Zeiss Planicomp analytical plotter. The relative orientation of these models was computed using 15 points. The mean y-parallax after this relative orientation was reported to be 7 to 10 μm at photo-scale. Using 10 control points, for which the ground coordinates were scaled off the 1:25,000 scale German topographic maps, they computed the absolute orientation to result in r.m.s.e. values of ± 12 m and ± 16 in planimetry and height respectively.

Downman et al. (1985) also reported their experience in testing MC photography. In this, two stereopairs of MC photographs were used, the one covering a test area in Libya and the other taken over Marseilles. The ground coordinates of the control points used in this test were scaled off existing maps. In the Libyan area, the ground coordinates were scaled off 1:50,000 scale maps, while in Marseilles, the 1:25,000 scale maps were used. For this test, a Kern DSR-1 analytical plotter was used as the measuring instrument. The results of the relative orientation which was computed from 31 to 38 measured points yielded a maximum y-parallax of 10 μm . The space resection which was computed using 16 control points on two MC photographs taken over Libya resulted in a planimetric r.m.s.e. values of ± 46.7 m and ± 43.5 m, while the space resection of the Marseillies photographs which was computed using 35 control points resulted in planimetric r.m.s.e. values of ± 32.8 m and ± 34.4 m. Using 8 and 13 control points in the absolute orientation of the model formed from the MC photographs taken over Libya, r.m.s.e. values of ± 13.7 to ± 27.6 in easting and northing and ± 22.2 to ± 25.1 m in height at the control points were achieved. Similarly, using 24 and 26 control points for the absolute orientation of the model formed from the MC photographs taken over Marseilles, r.m.s.e. values of ± 19.1 to ± 30.6 m in easting and northing and ± 33.8 to ± 38.3 m in height at the control points were achieved. In both of these two experiments, the r.m.s.e. values are computed at the control points to show the accuracy with which these analytical photogrammetric operations can be carried out with the MC photographs and no check points were used.

Engel et al. (1986) carried out a bundle adjustment of each of three individual strips of MC photographs taken over different types of terrain. These are (i) a strip of 6 photographs recorded on the colour IR film and covering part of China; (ii) a strip of 5 black-and-white photographs taken over the Alps; and (iii) a strip of 4 black-and-white photographs over the northern part of Germany. The measurements and computations for these bundle adjustment tests were made using the Planicomp C-100 analytical plotter. The ground coordinates of the control points for the Chinese area were digitized from 1:100,000

topographic maps. The ground coordinates of the control points in the Alps area were obtained from Austrian, Swiss and Italian 1:50,000 scale topographic maps, while the ground coordinates of the control points in the German area were digitized from 1:5,000 scale German topographic maps. The r.m.s.e. values reported to have been obtained from the adjustment of the first strip over China were ± 45.1 m, ± 48.6 m and ± 47 m in easting, northing and height respectively. The results obtained from the adjustment of the second strip over the Alps gave r.m.s.e. values ± 16 to ± 18.5 m, ± 16 to ± 22 m and ± 27 to ± 36 m in easting, northing and height respectively. The adjustment of the third strip over West Germany resulted in average r.m.s.e. values of ± 10 m, ± 11 m and ± 32 m in easting, northing and height respectively.

The OSD (OSD Report Y01AAD, 1986) has formed a model from Photos nos. 110 and 111 taken over the Sudan. In this, a Kern DSR-1 was used for the measurement and the subsequent analytical operations. The relative orientation of this model was reported to have been carried out to yield a maximum y-parallax of 6 μ m. Using 4 points at the corners of the model as control points and 31 as check points, it was reported that planimetric and height accuracies of ± 28 m and ± 22 m respectively had been achieved at the check points. The results of the OSD test show that, while the planimetric accuracy obtained from this model is similar to that obtained in this investigation, the height accuracy is better by 5 m than the height accuracy obtained by the author. This is mainly due to the accuracy of the control points used. While in this investigation, the control and check points have been selected on the MC photographs and scaled off the 1:100,000 scale topographic maps, the OSD has used the control points which they had already utilized in the photogrammetric operations carried out for the production of the 1:100,000 scale maps. These control points were marked on the aerial photography and identified on the MC photographs.

Table 11.3 summarizes the results of some of the published tests carried out on the MC photography. In general, these results indicate that planimetric accuracies of ± 15 to ± 25 m and height accuracies of ± 20 to ± 25 m can be achieved using the MC photography over developed areas with good quality control points. In developing areas, the planimetric and height accuracy values which can be achieved with the MC photographs range from ± 28 to ± 60 m and ± 30 to ± 48 m respectively. From this account, it appears that the results obtained in this investigation are not only better than the results obtained over Libya and China, but are similar to the results obtained over much more highly developed areas.

Investigator	Instrument	Area	r.m.s.e E (m)	r.m.s.e N (m)	r.m.s.e H (m)
MC: Ackerman and Stark (1985)	Planicom	Germany	12	12	16
Bahr (1985)	Zeiss Jena Topocart B	Germany	20 - 50	20 - 50	20
Downman et al. (1985)	Kern DSR-1	France Libya	20 - 30	20 - 30	25
Togliatti (1984)	Planicom	Italy	12	12	22 - 24
Ducher (1985)	Matra Traster	France	15 - 20	15 - 20	30
Engel, et al. (1986)	Planicom	China	45	48	47
"	"	Alps	16	16	27
"	"	Germany	5	6	20
Jacobsen (1985)	Planicom	Germany	8	8	20
"	"	Alps	16	13	32

Table 11.3 Summary of the Results Obtained by Other Investigators.

11.6 Geometric Accuracy Tests of LFC Photographs

Three strips of LFC photography have been acquired over the Sudan during the Space Shuttle Mission STS-41G. The three strips were acquired during the Shuttle orbit tracks 2, 65 and 97. However, the selection of the specific photographs from these three strips which were used for the geometric accuracy test in this investigation is dictated by the availability of the topographic maps and the desire to test LFC photographs covering the area which was covered by the MC photographs to provide grounds for comparison between the two cameras.

Three LFC photographs covering part of the Red Sea Hills test area were selected for the accuracy tests. These are Photos. nos. 1319, 1320 and 1321 which have been acquired during the Shuttle's orbit track

no. 65 at 11.32 GMT (14.32 Sudan local time) on the 9th of October, 1984. The overlap between each two adjacent photographs acquired during this orbit track is 70%. Fig. 11.4 shows Photo. no. 1320 showing the area of the overlap.

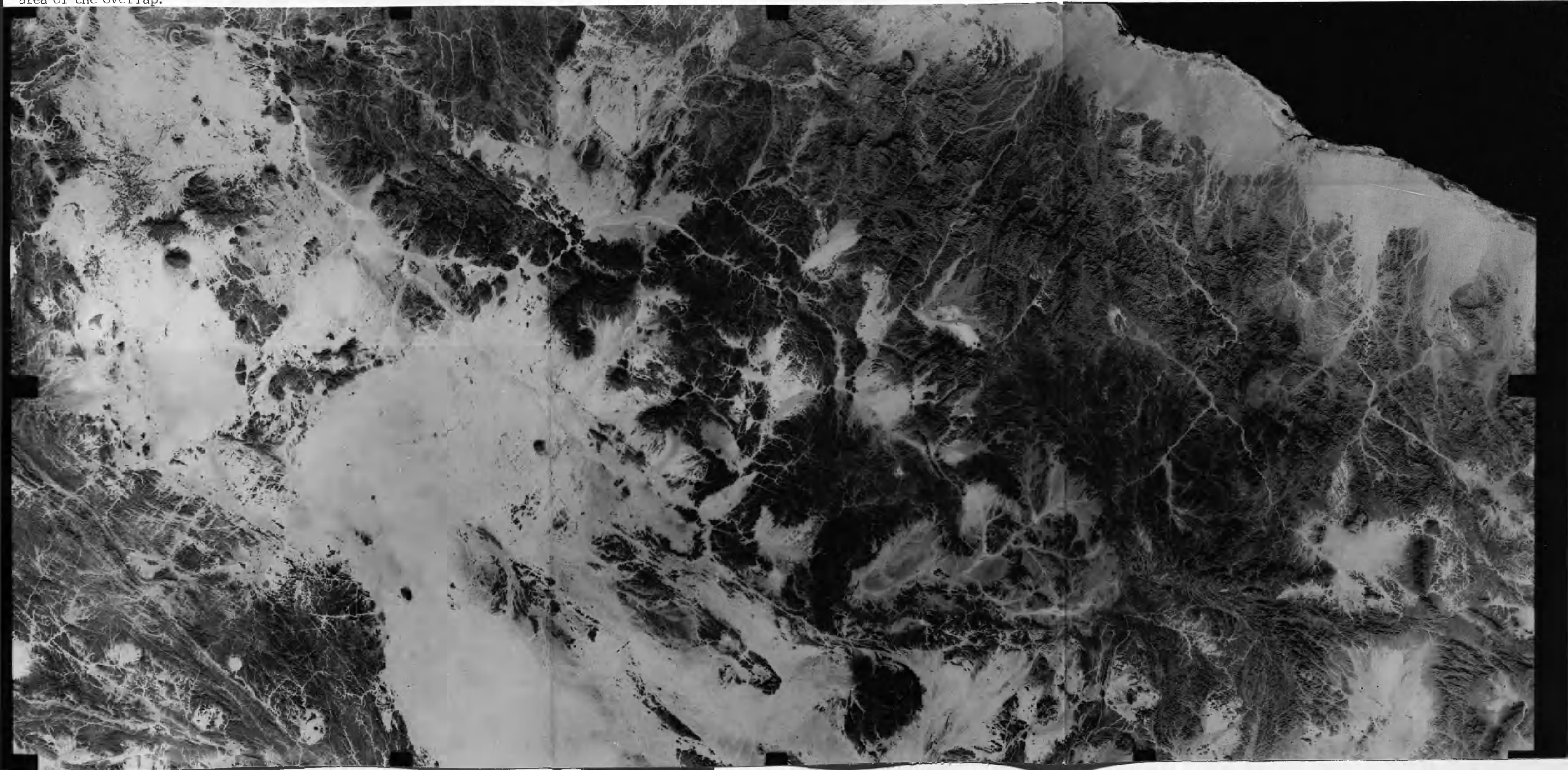


Fig. 11.4 1:754,000 Scale Contact Print of LFC Photo. No. 1320.

As mentioned in Chapter 10, with the 23cm x 46cm format of the LFC photographs, various configurations of the 23 cm x 23 cm portions of these photographs can be taken to form a stereopair. However, during the test carried out by the author on the above mentioned LFC photographs, no attempt was made to select a specific configuration. Instead, points were selected and marked on the print of the central photograph (Photo. no. 1320). Then the full size (23x46) film transparencies were mounted on the carrier plates of the stereocomparator. Since the carrier plates can only accommodate the 23x23 cm format, the transparencies were positioned such that a 23x23 cm overlapping part is located over the plate area. Measurement again starts with the six fiducial marks of this part in each photograph of the stereopair as described in the measurement of MC photographs above. After all the points in that part of the stereo-pair had been measured, the transparencies were shifted to position the remaining 23x23 cm part of the stereo-pair that includes the rest of the overlapping area on the plates. The points in this part were also measured, starting once again with the measurement of the six fiducial marks. This procedure is explained in Fig. 11.5.

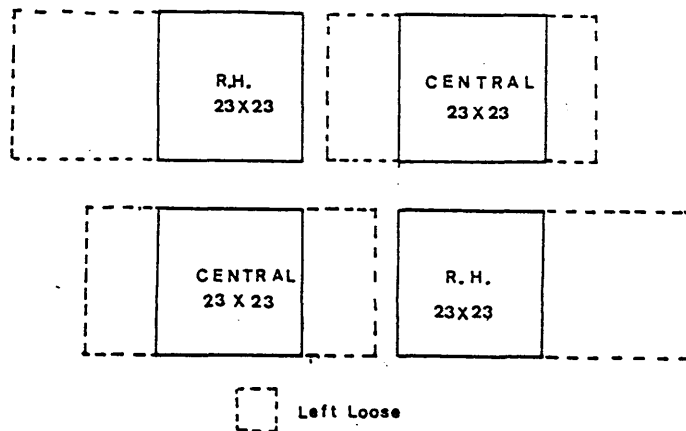


Fig. 11.5 Measurement Procedure of LFC Photographs.

In the measurement of Stereopair 5 (1319/1320), the right-hand 23 cm x 23 cm part of Photo 1319 was used together with the central 23 cm x 23 cm part of Photo. no. 1320 for the measurement of the image coordinates of points located in this part of the stereo-pair. Then both photos were shifted such that the central 23 cm x 23 cm part of Photo 1319 was used with the left-hand 23 cm x 23 cm part of Photo. no. 1320 and the image coordinates of the points on this part were

measured. In the preparation step of the test procedure described in Chapter 10, the two parts are brought to a common image coordinate system (in this case, the fiducial coordinate system) using REFOTO program, before proceeding to the space resection/intersection and relative/absolute orientation steps of the procedure. The same measurement procedure was followed in the measurement of the image coordinates of the points on Stereopair 6 (1320/1321) with Photo. no. 1320 being the left photograph.

11.6.1 Accuracy Test Results of LFC Photographs

A set of 30 well-distributed points were selected as control points in each stereopair for the whole of the overlapping area to enable these various photogrammetric operations to be carried out. The results obtained are summarized in Tables 11.4 and 11.5 and the patterns of the residuals which have resulted at all the points in each stereopair are shown in Figs. F.11 to F.12.

System of Coords.	Model No.	C O N T R O L P O I N T S				C H E C K P O I N T S					
		No. of Pts.	r.m.s.e. E	r.m.s.e. N	r.m.s.e. V	r.m.s.e. H	No. of Pts.	r.m.s.e. E	r.m.s.e. N	r.m.s.e. V	r.m.s.e. H
UTM	1319/1320	30	17.23	11.99	20.99	17.47	53	14.52	14.16	20.28	19.91
UTM	1320/1321	30	13.59	11.81	18.00	20.36	57	14.10	12.68	18.97	17.26
TAN	1319/1320	30	13.72	14.00	19.60	19.20	53	13.82	12.09	17.35	17.35
TAN	1320/1321	30	15.97	16.00	22.61	18.70	57	12.40	12.87	17.87	17.76

Table 11.4 LFC Space Resection/Intersection Results.

System of Coords.	Model No.	C O N T R O L P O I N T S				C H E C K P O I N T S					
		No. of Pts.	r.m.s.e. E	r.m.s.e. N	r.m.s.e. V	r.m.s.e. H	No. of Pts.	r.m.s.e. E	r.m.s.e. N	r.m.s.e. V	r.m.s.e. H
UTM	1319/1320	30	17.53	13.99	20.99	18.57	53	15.22	14.56	20.28	21.51
UTM	1320/1321	30	14.92	14.72	20.96	20.36	57	16.10	15.68	22.47	20.46

Table 11.5 LFC Relative/Absolute Orientation Results.

From Tables 11.4 and 11.5, it is clear that a planimetric accuracy (in terms of r.m.s.e.) of ± 19 m and a height accuracy of ± 18 m can be achieved from the LFC photographs taken over the Red Sea Hills area. Checking these values against Table 3.2, shows that, in purely geometrical accuracy terms, LFC photographs can be used for the topographic mapping of Sudan at scales as large as 1:80,000. This statement, however, needs more qualification to determine the amount of information which has to be shown on maps at this scale and the extent to which it could be extracted from these photographs.

Comparing these results with those obtained from the test of the MC photographs, shows that a substantial improvement in both the planimetric accuracy and the height accuracy has occurred in the LFC test. This is despite the fact that the two cameras have equal focal length and were flown at almost equal altitude. But while the 60% overlap MC photography resulted in a B:H ratio of 0.3, the 70% overlapping LFC photography has resulted in B:H ratio of 0.5 from adjacent photos. Obviously this greater B:H ratio has had its impact in improving the height accuracy. Theoretically the r.m.s.e. values in height which can be determined photogrammetrically from these LFC photographs should be about 60% (0.3/0.5) of those resulted from the MC photographs. Since the spot height accuracy obtained in the MC photographs test was about ± 30 m, the corresponding theoretical value for the LFC should be about ± 18 m. This is about the actual value obtained in this test.

In addition to this, it was noticed that the selection and pointing to the control and check points made during the measurement of image coordinates was much easier in the case of the LFC photographs. This is of course a result of the much improved resolution of these photographs which in turn improves the degree of certainty with which each point can be pointed to and hence the measurement accuracy is also improved. The very good quality of these photographs is partially due to the better resolution of the lens used in the LFC.

Furthermore, the LFC photographs covering the Red Sea Hills area were recorded on the high-definition 3414 film which has a higher resolving power compared with the Aerochrome Infrared film used for the MC photographs. This, together with the time of acquisition, surely has its impact on the difference in image quality. As to the actual time of acquisition, the MC photographs were acquired at about 9 am Sudan local time in December, at which time and season, light fog often covers the area of the Red Sea Hills and the solar elevation is very small. By contrast, the LFC photographs were acquired on a sunny, bright late

summer afternoon.

However, the most important single factor in the good image quality of the LFC photography does seem to be the use of FMC (or IMC) in the LFC. The lack of this specific feature in the MC has been pointed at as the main cause of its poorer image quality and poorer positional and height accuracy by more than one investigator (Snowsill, 1985, Downman, 1985, OSD Report Y01AAD, 1986). As mentioned in Chapter 3, the image displacement due to image motion amounts to 18 μm for 1/500 sec. exposure. This amounts to 14 m on the ground. The displacement is of course occurring in the x- direction and, in turn, this affects the accuracy of x- parallax measurement which in turn affects the accuracy of height determination.

11.6.2 **Summary of Other LFC Tests Results and Analysis**

Several tests have been carried out by other investigators using the LFC photography over various test areas. Derenyi and Newton (1986) have reported the experience of testing the LFC photography at the University of New Brunswick. In this test, an OMI AP-2C analytical plotter was used to measure a test field covering the area of Empress to Rockglen in Canada. It was reported that, using a set of points (most of which were road intersections) occurring on 9 LFC photographs and processing the measured coordinates in a block adjustment by independent models, r.m.s.e. values of ± 9.9 to 12.1 m; ± 9.1 to ± 10.8 m; and ± 15.5 to ± 24.4 m were obtained in easting, northing and height respectively. Derenyi and Newton (1987) also reported that r.m.s.e. values of ± 9.5 to ± 10.9 m; ± 8.1 to ± 10.8 m; and ± 13.1 to ± 16.4 m in easting, northing and height respectively have resulted from single model formation. They concluded that map compilation at 1:50,000 scale maps with a contour interval of 75 m (using analogue means) or 50 m (using digital means) should be possible from LFC photographs.

More recent results were published by Jacobsen (1987) which reported his experience in testing LFC photography. LFC photographs taken over the northern part of Germany and the Zeiss Planicom analytical plotter were used in this test. The r.m.s.e. values obtained from the bundle adjustment of these photographs were reported to be ± 7.3 m, ± 9.5 m and ± 8.5 m in easting, northing and height respectively. These results seem to be almost too good compared with the results obtained by the present author and all other published results. The reason for these too good results may be the procedure followed in the measurement of the photo coordinates. In this procedure, only a small

number of points were measured first. Using these measured points, each model was formed and absolutely oriented. Then based on the ground coordinates of the rest of the points, the plotter was made to move to each point in turn. The operator then carried out the fine pointing at each point before the photo coordinates of that point were recorded. In this way, although the pointing precision was increased and the measuring operation was speeded up, the resulting measurements were not as independent as they should be, since the decision of the operator was influenced by the computer. Comparable figures cannot be obtained in a normal direct measuring operation.

Togliatti (1987) reported the results obtained from testing a stereopair of LFC photographs taken over the Po Valley. In this test, control and check points comprising road crossings, road intersections, field corners and the centres of curves were used. The ground coordinates of these points were digitized from 1:5,000 scale maps. A Zeiss Planicomp C-100 was used for the measurement of photo coordinates and for the processing of the measured data. Using a set of 24 points for the absolute orientation, she reported that r.m.s.e. values of +5 m, +5 m and +5.1 m, in easting, northing and height respectively, have resulted for the 364 check points used in the test. These results also seem to be incredibly good, but again they do not reflect the accuracy with which information can be extracted from the LFC photographs since only those points which are rated as highly identifiable were used in this test and all points which had large residuals were rejected.

Hartley (1987) reported the results of the geometric and interpretation tests which have been coordinated by the OS in collaboration with several mapping organizations in Western Europe. The test was conducted on the LFC infra-red photographs of the north-east of the Sudan. The control and check points were supplied by the OS to these mapping organizations. The results of the geometric tests carried out by these organizations gave r.m.s.e. values at the control points ranging between +10.9 to +148 m in planimetry and +7.4 to +57.4 m in height. All investigators in this test have reported difficulties in identifying and transferring control points. The r.m.s.e. values in planimetry at the check points obtained by these investigators are rather poor. However, since no information was given about the instrument used by each investigator, no meaningful comparison can be made. Nevertheless, the diversity and variation in the quality of these results highlight the difficulty of testing space imagery in developing areas.

In general, the results obtained from the geometric test of the LFC

photographs in this investigation are quite comparable with the results obtained by most investigators over much more developed areas. In fact, if the quality of control and check points used by the author is considered, the results obtained in this investigation can be rated as very good.

11.7 Interpretation Tests

Interpretation tests have been carried out by the author on both the MC and LFC photographs. As mentioned in the previous interpretation tests, this was done by first making a comprehensive list of the features and detail that are shown on the 1:100,000 scale topographic maps covering each test area, then, using a mirror stereoscope, the detection and identification of these features was attempted. Features which were not detected using the stereoscope despite the expectation were searched for again under the Stecometer. The results of these interpretation tests are summarized in Table 11.6.

11.7.1 Interpretation of MC Photographs over the Nile Test Area

As was done in the previous interpretation tests in Chapters 5, 7 and 8, the features which exist and are shown on the 1:100,000 scale topographic maps were grouped into and discussed under the following 5 groups - lines of communication; cultural features; hydrology; relief features and vegetation.

1) Lines of Communication:

As mentioned in the previous chapters, the lines of communication that are usually shown on 1:100,000 scale maps include roads, streets, tracks, telephone lines, power lines, pipelines, railroads, etc. Telephone and power lines cannot be expected to appear on space photographs. Lines of communications considered in the Nile test area include hard surfaced roads, unsurfaced roads, tracks, bridges, ferry terminals, and railway lines.

i) Surfaced Roads:

The Khartoum - Elgiali surfaced road which serves the villages and towns located on the strip of fertile land along the eastern bank of the Nile, which is densely populated and heavily cultivated, can easily be detected on the photograph. Along the edge of the strip of fertile land which extends along the western bank of the Nile and separates the fertile land from the semi-

desert away from the Nile runs a short surfaced road. Again this road was easily detected on the MC photograph, although the surrounding area is bare open land. This is because the contrast between the road and the background sandy soil is sharp enough to make the road appear as a sharp black line against the light tone of the high reflective sandy soil.

As mentioned in Chapter 5, details in the area between the Blue and White Nile Rivers south of Khartoum are very dense. The Khartoum - Wad Medani road was easily detected and no interruption in its detection was experienced. This is due mainly to the occurrence of the cultivated plots of land which are very regular in pattern and the sharp contrast between the road and this cultivated land.

The surfaced road which runs almost parallel to the eastern bank of the White Nile between Khartoum and Jebel Awlia can also be detected where it runs through stretches of cultivated areas. Elsewhere detection of this road is very difficult since the contrast between the road and the light black clay soil is very poor. In general, one can say that surfaced roads can be detected on the MC photographs.

ii) Unsurfaced Roads and Tracks:

As mentioned in Chapter 5, unsurfaced roads are usually very difficult to detect since they are nothing but a trace of a repeated passage of lorries and trucks along a route which is selected by drivers and therefore they have no exact planned location with respect to the other detail present in the area. In spite of this, some of these roads can be detected on the MC photographs, especially those in the Gezira area where the fact that these roads run in the strip between two large cultivated blocks assists in their detection. Unsurfaced roads can also be detected where they run alongside canals and irrigation channels, in which case, the prominence of the canals and the fact that the vehicles are constrained in the area along which they can travel makes it possible to do so. No space imagery can be expected to show those tracks which are extremely narrow and are continuously changing in location. In general, unsurfaced roads were detected more easily on the MC photographs than on any of the MSS, TM and RBV images used in this investigation. But still it is not possible to detect all unsurfaced roads in the area. Instead,

parts of these roads were detected where the contrast and pattern of the surrounding details helps to make it possible.

iii) Bridges:

All five bridges which exist in this area (already mentioned in Chapter 5) were clearly shown on the MC photographs.

iv) Railway Lines:

Again as mentioned in Chapter 5, railway lines in Sudan are narrow gauge, single track lines, in this case, running through the fairly flat plains of the test area. Very few embankments, cuttings, or bridges can, therefore, be found along their course. These lines exhibit only a very slight contrast with the surrounding environment since they are laid on a very slightly elevated railbed made from the local soil. Although this very low contrast should make it very difficult for these lines to be detected, in fact, the Khartoum - Wad Medani railway, which runs through the cultivated land of the Gezira, can easily be detected and followed. The other railway line goes north from Khartoum to Atbara where it splits into the northern and eastern lines mentioned in Chapter 5. The part of this line that stretches between Khartoum and Atbara can easily be detected on the MC photographs. This is due to the fact that this line also runs through the narrow cultivated fertile strip of land along the eastern bank of the Nile. The location of the part that stretches between Atbara and Port Sudan can only be guessed at from the pattern of details such as the form of the individual villages which are stretched-out alongside the line. These villages are in fact settlements grouped around the railway stations since this area is barely inhabited. These stations are meant to act as meeting and passing points for trains that are travelling in opposite directions since the line is single track, rather than primarily for passengers to board or leave the trains.

In general, railway lines can be detected on the MC photographs where the contrast and patterns of the surrounding detail allow. In other areas, such as the bare sandy soil ground north-east of Atbara, detection is very difficult if not impossible. In fact, one can say in areas like this, narrow railway lines are unlikely ever to be detected on space imagery.

2) Cultural Features:

Cultural features that are usually shown on 1:100,000 and smaller scale topographic maps and which are present in the Nile test area include cultivated land, big cities, towns and villages, cemeteries, airfields, pipelines, parks and recreation areas, wells, fountains, etc.

i) Cultivated Areas:

In this test area, cultivated areas include large irrigated schemes such as the Gezira Irrigated Scheme, the Gunied Sugar Cane Scheme, and the White Nile Pump Schemes, as well as several smaller ones. As mentioned in Chapter 5, these schemes are well planned such that the area of each scheme is divided into smaller units supplied with water from the main canal by 2 to 4 m. wide water channels. All these well planned schemes show up quite clearly as patterned areas on the MC photographs. Indeed this could be expected since vegetation appears as dark reddish areas on IR colour films. As already noted above, the regular pattern of the cultivated plots makes it possible to detect narrow unsurfaced roads and tracks that traverse them. Small villages located beside irrigation canals within such a scheme appear as uncultivated areas where the pattern of cultivated plots is suddenly broken. These villages are often the sites of administrative centres and irrigation monitoring stations which have been established by the scheme authorities. Other smaller cultivated areas located along the banks of the White and Blue Niles, which are mostly private farms, can also be detected. The green belt sheltering Khartoum, Soba Agricultural Research Farm and the SMA oil & soap factories can also be detected and mapped.

Further north of Khartoum, cultivated areas are mainly restricted to the narrow strips of fertile land located along the Nile banks with the exception of three small irrigated schemes. These show up on the MC photographs as a continuous reddish strip with the river running in the middle. Some sparse cultivated farms were also detected on dry stream beds such as Wadi Alhawad. In general, cultivated lands can easily be detected and delineated with a degree of confidence which was not possible with the MSS infrared images. This was the case everywhere with the exception of the narrow clay strips located immediately along the river shores which are usually submerged during the flooding season. Again delineation of these cultivated lands was found to

be very difficult. This is because the vegetation on these shores extends right to the water line and with these shores being saturated with water, the deep red colour of vegetation is difficult to separate from the black colour of water.

ii) Built-up Areas & Settlements:

As mentioned in Chapter 5, built up areas in the Nile test area comprise big cities as the three cities of the capital triangle, Wad Medani and Atbara; smaller towns such as Hasaheisa, Kamleen, Maseed, Jebel Awlia, and Shendi; and villages which are scattered throughout the area. All the big cities and towns can be detected easily on the MC photographs. But, as mentioned above, villages can only be detected where they are surrounded by cultivated land or the roads that converge towards them are detected. The internal detail of cities and towns can be detected where they are regular in pattern. In Khartoum, Khartoum North and Wad Medani, these internal details show up quite clearly, especially the industrial centre in Khartoum North. Detection of the main internal streets and roads was also found to be relatively easy. Since the main blocks of buildings are delineated by these streets, they can also be detected. In Omdurman and Atbara, detection of internal details was found to be very difficult, since the streets are narrow and the buildings small and irregular in size and shape, but it was still possible to detect main roads, recreation areas, factories, and other big buildings.

iii) Cemeteries:

Big cemeteries in Khartoum, Omdurman, Khartoum North, and Wad Medani can be detected as areas of bare ground having irregular shapes surrounded by building blocks. In all cases, detection of cemeteries requires collateral information to be able to identify these bare grounds as cemeteries. Cemeteries which are located at city outskirts cannot be identified.

iv) Airfields:

The Khartoum International Airport and the Wadi Saidna Military Airport in which the runways are long and wide and are surfaced either by a concrete layer or tar macadam showed up very clearly on the MC photographs as did the details of parking areas and passenger halls. Other smaller airports in cities such

as Wad Medani and Atbara have no surfaced runways since the runways are just long wide strips of bare ground which have been flattened and are used for domestic flights. These could in fact be detected but required collateral information for them to be identified as airports.

Cultural features occupying a very small area such as wells, springs, tanks and towers could not be expected to show up on these photographs although they are required to be shown on the 1:100,000 scale topographic maps.

3) Hydrology

The hydrological features in the Nile test area include rivers, falls, canals, irrigation channels, water bodies, dams, islands and dry streams.

i) Rivers:

As expected, rivers appear quite clear and sharp on the MC photographs. The land/water boundary was very well defined and no difficulty was experienced in detecting and delineating the rivers. In addition to the Blue, the White and the Nile rivers which represent the major life vein of the area, there are the Rivers Rahad and Dinder which join the Blue Nile at Wad Medani in the south of the area and the River Atbara which joins the Nile at Atbara. Although these three rivers are seasonal and nearly dry out in the summer leaving small water pools here and there, they showed up quite clearly on the MC photographs and again the water/land boundary defining their actual width can easily be delineated. This resulted from the fact that the MC photographs were acquired just after the rainy season, during which period, these rivers are filled with rain water from the high mountains in Ethiopia.

ii) Water Bodies:

Water bodies exist mainly along the White Nile and the course of the main River Nile. A wide area along the White Nile banks is submerged when the river floods, but when the flood season ends, water pools will be created scattered over this previously submerged area. These water pools usually don't last long but since the MC photographs were taken immediately after the flood season, they appear as sharp black spots with a reddish

tone surrounding them. This reddish tone could indicate a cultivated area since all of these areas surrounding such pools are seasonally cultivated.

iii) Dry Streams

Dry streams are the natural drainage system which drains the occasional or seasonal rain water to the rivers. Since the terrain in the Nile test area is mainly made up of a series of very flat plains, these dry streams are very complex. They include 1 m wide streams which drain the water into bigger streams which in turn drain into still bigger streams up to 10 m wide. In fact, the vast majority of these dry streams appear very sharp with a complexity which could not be possibly be shown on line maps. This is again due to the fact that the photos were taken immediately after the rainy season in Sudan.

4) Relief Features:

As mentioned in Chapters 3 and 5, the Nile test area is mainly very flat with a few scattered low hills such as Jebel Awlia, Karrari and Markhiat, north of Omdurman and a series of hills in the north of the test area such as Jebal Um Ali, Nagaa and Musawarat. Sand dunes dominate the semi-desert area with gravel beds appearing on the floor of the wadis in this area. All these relief features can easily be detected since the stereoscopic viewing greatly facilitates the detection and interpretation of each form in a way which would not be possible with the monoscopic viewing of images acquired by systems which do not have the stereo-acquisition facility of a mapping camera or a stereo-scanner system.

5) Vegetation

This includes scattered trees, scrub, orchards and woodlands. Interpretation of these elements is generally affected by the season in which the photographs were acquired. At the time that the MC photographs were acquired, tree leaves start to fall but, despite that, the woodlands show up quite clearly and can easily be detected and delineated. Delineation of woodlands is noticeably easier in the Elghaba area and in the Khartoum green belt where these woods have more or less a regular shape with buildings constructed right at their edges. Scattered trees cannot be expected to be detected and scrub areas can only be detected where they occur on dry stream beds with the ground underneath saturated with water. Orchards exist along the

Nile banks, but they cannot be differentiated from cultivated lands.

In summary, the results of the interpretation test which has been carried out on the MC photographs over the Nile test area show a very significant improvement over those obtained from the interpretation tests which were carried out on the Landsat MSS, TM and RBV images of the same area. From this, the amount of the topographic information required for 1:100,000 scale mapping which can be extracted from the MC photographs of the Nile test area can be estimated to be in the range 55% to 60%. This amount, although it represents a significant improvement, still stops short of the limit set in Chapter 3 as a feasibility factor for using space imagery for topographic mapping. This result does tend to generate doubts that this minimum feasibility factor will be fulfilled by the current space imagery of the Sudan where the low contrast between the existing features and the background is the main problem. However, only the advent of substantially better resolution space photography leaves this as an open question at the present time; the answer can only be forthcoming in the future.

11.7.2 Interpretation of MC Photographs over the Red Sea Hills Area

The part of the Red Sea Hills test area covered by MC photos is generally semi-desert in the west and hilly in the east with little population and hence a small number of cultural features. Therefore the dominant information which will appear on a topographic map will be relief forms, dry streams, surface materials, the coast line and islands.

Lines of communication present in the Red Sea Hills area at the time of acquisition of the MC photographs include a two-lane surfaced road that connects Port Sudan, Kassala and Wad Medani to Khartoum; several smaller internal surfaced and unsurfaced roads in Port Sudan city; and a single narrow gauge railway line.

Unfortunately Port Sudan, which is the biggest city in this area, is just off the area covered by the MC photographs. Furthermore the part over the coastal plain area which was covered by the MC camera track cannot be seen due to thick cloud. Hence there was no possibility of detecting these parts of the surfaced road and the railway line that traverse the coastal plain before entering and crossing the hills at Summed (Summit). Almost certainly, these features would have been detected had there been no clouds, since the contrast between them and their surroundings would have made them show up very clearly. Through

the semi-desert area on the other (western) side of the Red Sea Hills, only the part of the railway line and the surfaced road can be detected in the Haya area. As they traverse the dry wadis before reaching the Red Sea Hills, substantial interruptions in the detection of these lines were experienced and the location of the road and the railway line can only be guessed at by the alignment of features along their paths.

Unsurfaced roads and tracks cannot be detected since these follow the dry stream courses and wadis which have mainly sandy beds. The resulting contrast between the roads and the highly reflective sands is extremely poor.

Unfortunately all the larger settlements in the Red Sea Hills test area are located outside the area covered by these photographs. The exceptions are the villages of Sinkat and Summed located on the railway which can be detected with the aid of the topographic maps of the area, but as small settlements; their internal detail cannot be recognized.

In summary, the results and the conclusion reached from the interpretation test of the MC photographs of the Red Sea Hills test area do not differ greatly from those resulting from the similar test carried out over the Nile test area given above. Although the MC photographs represent a significant step forward in achieving the objective of fulfilling the requirements of 1:100,000 scale topographic mapping of the Sudan, they still cannot deliver the information that is needed. One obvious reason for this is that the lack of an IMC mechanism in the MC has greatly affected the quality, in particular the resolution of the acquired photographs. This lack of an IMC mechanism has been singled out by many investigators in other recent tests of the MC photography as being a main cause of the shortfall in the image resolution expected from this camera.

11.7.3 The Results from Other Interpretational Tests of MC Photography

The interpretation of the MC photographs of Georgia has resulted in better percentage for the information which can be extracted from them. This can be seen from Table 11.6 which lists the results of the MC interpretation tests over the three test areas. The better result obtained over Georgia test area is due partially to the improved contrast in the objects which have to be detected and mapped in the Georgia test area and partially to the fact that the Sudanese MC photographs were recorded on the Aerochrome Infrared 2443 film which

has a lower resolving power compared with the Double X Aerographic film which was used to record the photographs of Georgia.

: Feature shown on 1:100,000	METRIC		CAMERA		PHOTOS		LFC	PHOTOS
	NILE AREA: RED SEA AREA:		GEORGIA AREA:		RED SEA AREA			
	D	I	D	I	D	I	D	I
Communication:								
Hard surfaced roads	3	2	2	0	3	2	3	3
Unsurfaced roads	3	0	0	0	2	2	2	0
Tracks	0	0	0	0	1	0	0	0
Footpaths	0	0	0	0	0	0	0	0
Streets	3	2	0	0	2	2	3	0
Bridges	3	3	*	*	3	3	3	3
Ferry terminals	0	0	*	*	*	*	*	*
Railways	3	0	2	0	3	2	3	3
Railway stations	0	0	0	0	2	1	0	0
Culture:								
Cultivated land	3	3	*	*	3	3	3	3
Big cities	3	2	2	0	3	3	3	3
Towns	2	1	2	0	3	2	3	2
Villages	1	0	0	0	2	0	1	0
Ruins	0	0	0	0	0	0	1	0
Electrical stations	0	0	0	0	0	0	0	0
Pipelines	0	0	0	0	0	0	0	0
Powerlines	0	0	0	0	2	1	0	0
Wells	0	0	0	0	*	*	0	0
Storage tanks	0	0	0	0	0	0	0	0
Cemeteries	3	1	0	0	2	1	2	0
Airports	3	3	*	*	3	3	3	3
Landing Grounds	3	2	*	*	3	3	3	3
Hydrology:								
Rivers	3	3	*	*	3	3	*	*
Falls	3	3	*	*	*	*	*	*
Canals	3	2	*	*	3	3	*	*
Irrigation channels	2	0	*	*	2	2	*	*
Water bodies	3	3	3	3	3	3	3	3
Dams	3	3	*	*	3	3	*	*
Reservoirs	3	3	*	*	3	3	*	*
Hydrography:								
Tidal flats	*	*	*	*	0	0	0	0
Reefs	*	*	*	*	*	*	*	*
Rocks	*	*	3	0	*	*	3	0
Near shore bathymetry	*	*	0	0	0	0	0	0
Water depth	*	*	0	0	0	0	0	0
Marsh	*	*	*	*	*	*	*	*
Harbours	*	*	*	*	3	3	3	3
Small harbours	2	0	*	*	3	3	3	3
Shore line	*	*	3	3	3	3	3	3
Islands	3	3	3	3	3	3	3	3
Relief forms:								
Sand dunes	3	3	3	3	*	*	3	3
Gravel beds	2	0	2	0	*	*	2	0
Elevated grounds	3	3	3	3	3	3	3	3
Contours	0	0	0	0	0	0	0	0
Vegetation:								
Woodlands	3	2	*	*	3	3	*	*
Scattered trees	0	0	0	0	0	0	0	0
Scrub	0	0	0	0	0	0	0	0
Orchards	0	0	0	0	0	0	0	0
Others:								
Administrative boundaries	0	0	0	0	0	0	0	0
Rest houses	0	0	0	0	0	0	0	0
Triangulation pillars	0	0	0	0	0	0	0	0

D= Detected, I= Identified, 0= not, 1=Sometimes, 2= Often, 3= Yes, and *= Not available.

Table 11.6 Interpretation Results of MC and LFC Photographs.

The experience of the OSD in plotting detail from the MC photographs of the Red Sea Hills also showed that identification of features proved difficult because of the combination of poor resolution and poor contrast. Settlements could not be identified without reference to the map and then only with considerable difficulty (OSD Report YG1AAD, 1986). The narrow gauge railway line was not identified by the operator who misidentified part of it as a road. Even with the help of the maps, it was not possible to identify the railway throughout its length.

No problem was experienced in identifying and plotting water courses; subsequent comparison with the map showed that the positions and shapes of the plotted streams were good. Relief features such as jebels as well as wadis were readily identified and their plotted position compared well with the map.

Ducher (1985) reported the experience of the IGN in testing the MC photography. In this test, MC photographs taken over the European standard test field of Marseilles were used. A line map at 1:100,000 scale and with 50 and 100 m contour intervals was prepared using the Matra Traster analytical plotter. The comparison of this line map with the topographic data base revealed that agreement in height within 30 m in flat areas and 50 m in steep slope areas can be achieved. Also a comprehensive interpretation test was carried out on these photographs. Ducher gives the percentages of features identified on the MC photographs as follows:

100%	for roads of 25 - 35 m width, railways of 25 m width, hedges of 25 m width, piers, dams of 18 m width, rivers of 25 - 35 m width and canals of 25 m width.
80%	for roads and hedges of 18 m width.
65%	for hedges of 12 m width.
60%	for rivers of 18 m width.
50%	for dams of 12 m width.

For features of widths less than 12 m width, the percentages are as low as 25%. As a result of this interpretational test, he concluded that the minimum width for linear features to be identified with certainty on the MC photographs is about 18 m.

Engel et al. (1986) conducted a mapping experiment using the MC photographs covering part of the northern part of West Germany. A Kern DSR-11 was used for the stereocompilation. The completeness of the

stereocompilation and the frequency of incorrect classification was checked by measuring the length of the road, the railways and the drainage networks both on the map and the plotted manuscript. The results of this mapping experiment can be summarized as follows:

(i) 100% of the highways were plotted correctly with no misidentification.

(ii) 81% of the roads were plotted correctly and 2.5% were misidentified as roads, while 2.5% were plotted incorrectly and 14% were not recognized.

(iii) 38.7% of minor roads were plotted and identified correctly and 42.3% were not recognized. Only 7% of the field paths can be plotted and identified.

(iv) 90% of the railways were plotted correctly and 28% of the drainage consisting of rivers and creeks of widths greater than 3 m were plotted.

Jacobsen (1987) reported on a mapping experiment carried out at 1:50,000 scale on the MC photographs of East Germany. He concluded that the main problem of mapping from these photographs is the identification of the objects present in the terrain. Put into percentages, he reported that 100% of highways, 81% of roads, 91% of railway lines and 25% of field paths can be identified on the MC photographs of the test area.

In general, all these interpretational and mapping experiments confirm the conclusion drawn from the interpretational tests carried out in this investigation that, while features such as highways, roads, railway lines and rivers can be identified and plotted easily in areas of good contrast, and with some difficulty in areas with poor contrast, small man-made features cannot be detected on the MC photographs.

11.7.4 Interpretation of the LFC Photos over the Red Sea Hills Test Area

The details and feature which exist in the area covered by the LFC photographs and the result of their interpretation are as follows:

1) Lines of Communication:

The photographed area includes the two cities of Port Sudan and

Suakin on the coast of the Red Sea and the part of the coastal plain that extends from about 45 km north of, to 60 km south of Port Sudan. Lines of communication existing in this area include the Port Sudan-Khartoum surfaced road and the Port Sudan-Khartoum railway already mentioned above, and the several surfaced and unsurfaced internal roads and streets in Port Sudan and Suakin. All of these appear very clear and sharp on the LFC photography.

The part of the main Port Sudan-Khartoum road located in the area covered by these photographs appears as a very sharp black string against the light white tone of the coastal plain. Surprisingly the part of the Port Sudan-Khartoum railway line located in the area covered by the LFC photographs also appears as a very clear and sharp black thin string traversing the coastal plain and crossing the hills at Summed. This is because the slightly elevated bed on which the rails are laid is constructed from dark grey rocks and gravels taken from the adjacent hilly area and it is this slightly elevated ground strip which helps to make the railway line stand out as a sharp black string against the white tone of the coastal plain.

Interpretation of the main internal roads and streets in the towns is aided by the fact that there are no trees along their pavements. This has made the roads appear very sharp and they can easily be picked out and delineated. Since these internal streets define the pattern of the blocks of buildings, these blocks appear very clear and the various parts of Port Sudan appear as a large chequerboard pattern. In the hilly area, lines of communication are mainly tracks which follow the dry streams and valleys. Interpretation of these tracks is very difficult and collateral information is needed to confirm their existence and establish their exact location in the area.

2) Cultural Features:

Cultural features in this area include the built-up areas of large towns, smaller towns, villages, ruins, cemeteries, quarries, an airfield, a pipeline and sea ports.

As mentioned above, built-up areas include the two coastal cities (Port Sudan and Suakin), and the small town of Summed. All three showed up quite clearly. The major internal structure of the cities can be identified. Buildings in these two cities are in fact mostly made of wood since it is durable in the damp and high salinity coastal area compared with any other affordable building materials. The governmental buildings are mostly made of steel frames with metal

sheets acting as walls and roofs. The outer sides of these buildings are usually painted in various colours. Therefore the contrast between these buildings and their background is enough for them to show up very clearly on the photography. Fig. 11.6 shows an enlarged part of the LFC photograph taken over Port Sudan. As expected, the city's airport shows up clearly. The seaport with its buildings, docks, and loading and unloading yards appears quite clearly. The scene of the docking ships and those waiting to be guided into the docking area is quite striking. In general, the amount of internal detail detectable is far greater than might be expected.

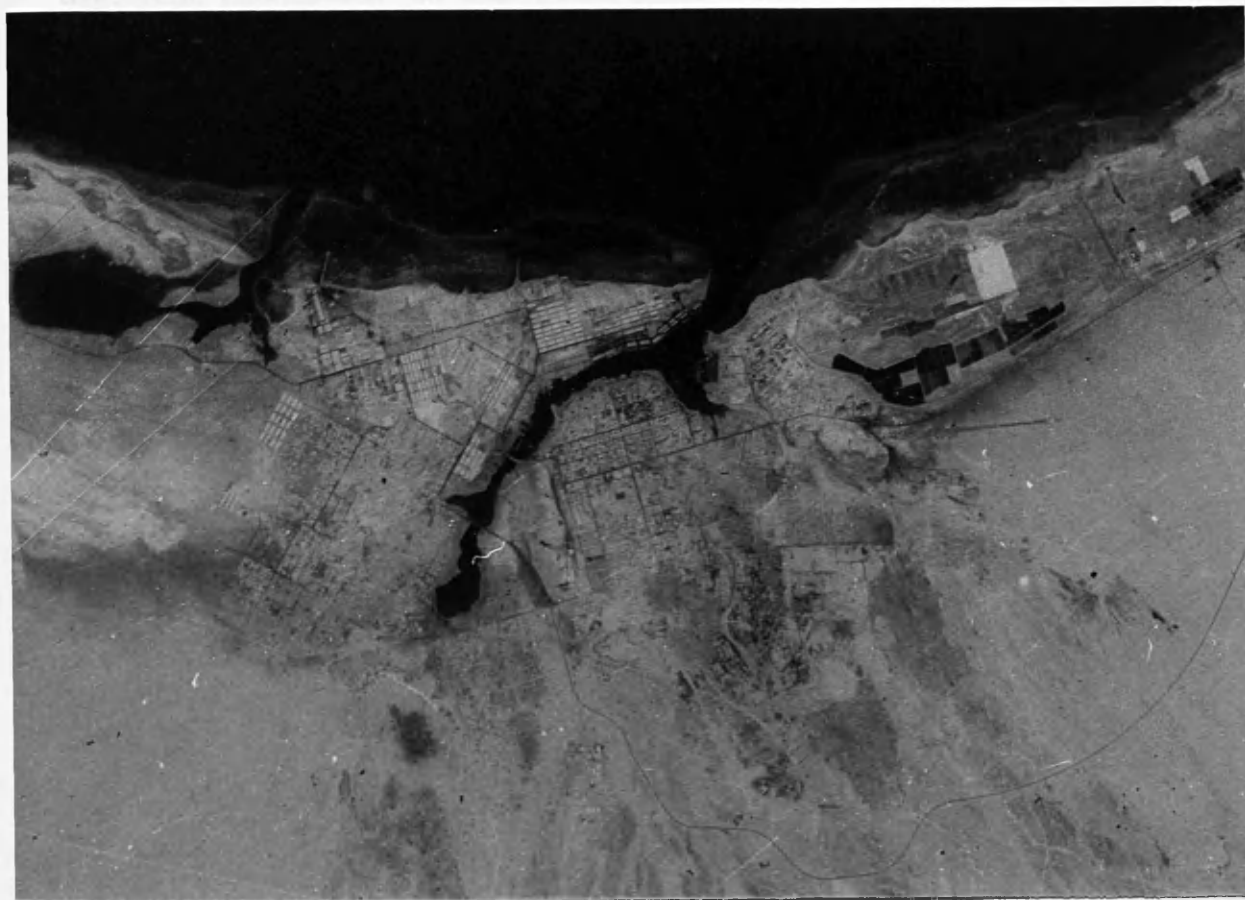


Fig. 11.6 An 8x Enlarged Part of the LFC Photographs Showing Port Sudan City and its Vicinity.

Interpretation of villages in the semi-desert plains beyond the hill range is very difficult since these villages are small nomadic camps rather than villages. Smaller cultural details need collateral information in order to be identified, which is not available to the author. The result of this interpretation is summarized in Table 10.6.

In summary, the amount of information which can be extracted from the LFC photographs is far larger than that which is estimated to be possible with the MC photographs. Judging from the degree of detail visible in the Port Sudan area, the percentage of the information which can be extracted from the LFC photographs over Sudan can be estimated to be as large as 75%. This large percentage confirms on the one hand the lack of IMC in the MC as the cause of the poor quality and resolution of the MC photographs and the lower-than-expected results of all the accuracy and interpretation tests carried out on them in different countries. On the other hand, these results confirm the combination of slow high-definition films and long exposures with IMC as one giving the best results with space photography.

11.7.5 The Results from Other Interpretational Tests of the LFC Photography

Other interpretational and mapping experiments carried out by several investigators confirm the results of the LFC interpretational test in this investigation. Jacobsen (1987) carried out a mapping experiment using the LFC photographs covering part of East Germany as part of a comparative test on the MC and the LFC photography. From this experiment, he concluded that 100% of the highways have been detected and plotted as in the case of the MC photography; 93% of the roads were plotted compared with 81% from the MC photography; and 90% of the field paths were plotted from the LFC photographs against 25% from the MC ones. This comparative test shows the superiority of LFC photography in showing smaller and poor contrast detail, confirming the results which were experienced in this investigation.

Togliatti (1987) also reported the results of the interpretational test carried out on the LFC photography taken over the Po valley and the Italian coast on the Adriatic Sea, an area which has been equipped with a planned test field. In this test, the features were divided into 4 categories according to their contrast with the background - no-contrast features; poor-contrast ones; medium-contrast ones; and good-contrast features. The result of identifying these features on the LFC photographs is as follows:

- (i) No individual no-contrast feature has been identified.
- (ii) Identification of poor-contrast features was very difficult and poor.

- (iii) Out of 70 medium-contrast features, 7 were poorly identified, 57 features were identified with medium identification and ease and 6 features were easily identified with good certainty.
- (iv) Out of 70 good-contrast features, 7 features were identified with medium identification and 63 were easily identified with good identification certainty.

11.8 Conclusion

The results of the geometric accuracy and interpretation tests carried out in this investigation confirm the superiority of photographic cameras in space as far as topographic mapping is concerned. This superiority will remain until a different type of sensor can be devised which improves upon the photographic systems in both geometry and resolution. The results of height accuracy obtained from the LFC photographs confirms the success of the solution adopted by the Americans to solve the problems of the small B:H ratio which are encountered with the standard format long focal length cameras. Therefore, despite all the shortcomings attributed to the space photographic systems by the remote sensing community, the solution of the problems associated with small-scale topographic mapping in developing countries of large areal extent still remains dependent on the development and implementation of space photographic systems on a systematic operational basis. This conclusion leads to the discussion of rapid methods of topographic mapping from space photographs. One of these methods is the production of orthophotos and orthophotomaps. This will be the subject of the next chapter.

CHAPTER 12

Space Orthophotography

12.1 Introduction

In this chapter, the processes involved in the experiments which have been carried out for the production of an orthophotograph from the MC photographs of the Red Sea Hills test area will be explained. The results of the planimetric accuracy test which has been carried out on the produced orthophotograph will be reported on and analyzed. This will be followed by the results of the test which has been carried out on the DTM generated from the profile data which have been collected for the production of the orthophotograph.

It must be clear that the instruments which have been used for the production of this orthophotograph are not of the type which can be afforded by the developing countries. This may seem to be contradicting the stated condition in this investigation. However, since the results of the geometric accuracy and interpretation tests of the MC and LFC photographs have shown the possibility of fulfilling the requirements of topographic mapping in these countries, it is appropriate to test quick methods of utilizing space photographs for this purpose. As for the question whether the developing countries will afford these methods or not, it will be dealt with after the assessment of the results of this experiment.

12.2 Development of Orthophotography

In addition to the tilt displacements in a frame photograph which can be removed using an optical rectifier, there are also displacements due to relief which cause local scale variations across the photograph. Since relief displacements increase with the radial distance, a simple approach to minimize their effects is to consider only the central part of the photograph, ie. the area where there are small radial distances. This solution is usually adopted in the construction of controlled mosaics. However since, in most cases, the photomaps produced by this process are enlarged 5 to 8 times in the rectifier to arrive at the desired map scale, this solution stops short of offering the accuracy required in topographic mapping. The alternative and most effective way is to correct for the local scale variations across the photograph. The process of carrying out this correction is termed differential rectification and the resulting product is an orthophotograph. In the orthophotograph, all points in the rectified photographic image will

lie in their correct map locations. The basic principle of differential rectification is shown in Fig. 12.1 in which two overlapping photographs are set up in the same way as is done in stereoplotting machines but the measuring mark used to locate points in the plotting machine is replaced by a narrow slit through which light rays from only one of the photos are admitted to be recorded on a film located on the reference surface.

Fig. 12.1

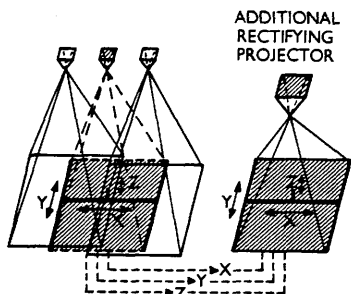


Fig. 12.1 Principle of Differential Rectification.

Instead of following individual features which is done in plotting, the slit is made to scan the stereomodel systematically in a series of parallel traces. During this scanning process, the operator keeps the slit continuously at the surface of the model, so that all the detail present in the stereo-model is recorded orthogonally on the film below. Also during the systematic scanning of the model, the height information at each point may be recorded for later use.

Instruments which were based on this principle were first manufactured and used solely for the production of orthophotographs. In another development, add-on orthoprojectors were produced to be attached to the existing plotting machines. With the development of digital processors and analytical plotters, a new generation of orthophoto instruments emerged. In this latest generation, the orthophoto-instrument is simply a film-writer which operates under direct control of a digital computer and is not tied to the stereoplotting machine in any way. The height information used with this film writer may be gathered on a plotting machine in a separate step or taken from an existing Digital Terrain Model (DTM) data base. DTMs have gained a wide attention during the recent years and several

surveying and mapping organizations have started generating them in a systematic manner and making them available to users.

A quick survey of the landmarks in the development of orthophoto production instruments may serve to demonstrate the various possibilities of this type of operation. Orthophoto instruments can be classified into instruments based on the optical projection principle; those which use optical transfer devices; and those which use electronic transfer devices.

12.2.1 Instruments Based on Optical Projection

Attempts to design instruments for orthophoto production began as early as 1930 s, but orthophotography started to be considered seriously much later when the U.S.G.S began experimenting with orthophoto production. As a result of this, the T-64 was produced by Kelsh after a series of prototype or development machines known as orthophotoscopes. The T-64 uses the principle and operational procedures which are shown in Fig. 12.1. This principle was also employed in the Kelsh K 320 Orthoscan and the SFOM 693 built by the French Matra-SFOM organization. In another development, started in Russia, a three-projector Multiplex instrument was used. To this Multiplex, an additional projector was added in which a full-size diapositive corresponding to the central projector of the Multiplex could be mounted was added. This additional projector was equipped with rotation movements which allowed it to be oriented to the same values as those in the central projector of the Multiplex. Systematic scanning by a series of parallel profiles took place in the Multiplex as before but exposure of the orthophotograph was made with the additional projector in which all movements in X, Y and Z made in the Multiplex were duplicated by the scanning slit (Petrie, 1977). This idea of an additional rectifying orthoprojector to be added to an existing stereo-plotting machines has been adopted widely. In particular, Zeiss Oberkochen introduced the GZ-1 Orthoprojector as an additional projector designed for attachment to Zeiss Oberkochen high precision stereoplotters (Stereoplanigraph and Planimat) and some other instruments (Hobbie,1970).

This arrangement of an additional projector introduced the possibility of off-line production of orthophotographs. This, of course, involved the use of a storage device on which the measured profiles can be recorded. The recorded profiles are later used to control the operation of the orthoprojector in producing the

orthophotograph. The off-line mode of operation offers considerable advantages since erroneous measurement can be eliminated and the profile remeasured, whereas in the on-line mode of operation, elimination of errors is impossible unless the whole operation is repeated again with a new sheet of film. Also during on-line operation, the orthoprojector is idle 50% of the time, while diapositives are being changed, set up and oriented, whereas the off-line mode allows the orthoprojector to be used with more than one plotter and hence ensures 100% time use (Kraus, 1970).

However, orthoprojectors based on optical projection inherit the limitations of all optical projection stereo-plotting machines. Most serious is the lack of flexibility in handling different types of photography and the need to change projectors every time a new type of photograph with a different focal length is encountered. The desire to overcome these limitations led to the development of optical transfer devices.

12.2.2 Optical Transfer Devices

These were developed as attachments to the great number of mechanical stereoplotting machines which otherwise would not lend themselves to on-line orthophoto production unless an additional optical-projection-type orthoprojector is purchased. In these machines, the rays forming the image are reprojected as mechanical space rods. Coupled to the rods are microscopes which view or scan the actual photographs and transmit the image via a separate optical train to the observer's eyes. As shown in Fig. 12.2, somewhere in these trains the image can be transferred optically via a semi-reflecting mirror to produce the orthophotograph. However, since there is no optical reprojected of rays with a variation in the projected distance corresponding to the variation in the terrain heights, the transferred image has to be continuously changed in scale. Also, because of the frontal viewing instead of projected viewing, the effects of tilts are also not rectified. The scale rectification is performed using a pair of prisms which shorten or lengthen the image path, while the image rotation to correct for the convergence imparted by the tilts is produced by a Dove prism. The image is recorded on a sheet of film wrapped around a drum which can be rotated in synchronization according to the scanning movement in the model. The stereomodel is scanned in a manner similar to that used in optical projection devices.

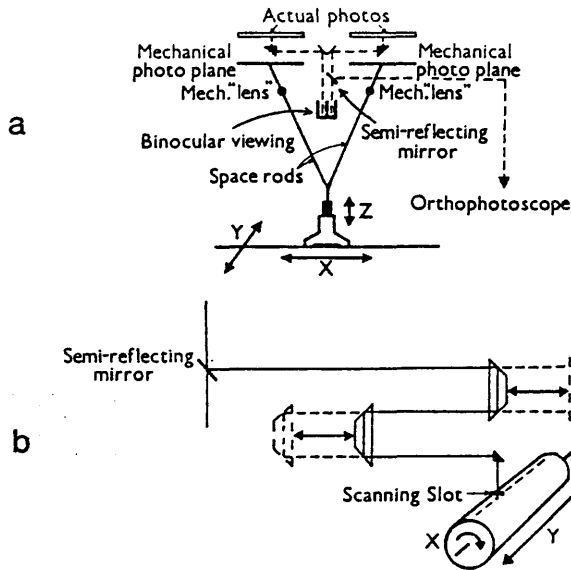


Fig. 12.2 Principle of Optical Transfer Devices.

This basic concept has been adopted widely in the last 20 years, e.g. in the Orthophot which can be linked to the Zeiss Jena Topocart; the Wild PPO-8 for attachment to the A8 Autograph; the Orthosimplex which attaches to Galileo Stereosimplex; and the OP-C which can be attached to the OMI AP-C analytical plotters.

Again this development led to the development of optical transfer orthoprojectors to combine the advantages of off-line mode of operation with those offered by optical transfer. Examples of these are the Wild Avioplan OR-1, which was described in Chapter 3, and the OMI OP-C2. In both of these instruments, rectification is carried out under control of a digital computer. As mentioned in Chapter 3, the Wild Avioplan OR-1 has been used for the production of the orthophotograph in this investigation.

12.2.3 Electronic Transfer Devices

Electronic transfer involves the scanning of a pair of overlapping photographs followed by rectification using electronic digital or analogue means before finally printing the orthophotograph using a CRT or laser-based film writer. Electronic transfer has been developed to be applied in conjunction with automated methods of scanning and measuring a stereomodel where electronic correlators are used for these

tasks.

When applied to the Wild B8 - Stereomat, since the mechanical projection system of the Wild B8 stereoplotter is used, a separate CRT is necessary for the scanning of each photo. Each CRT gives a signal to the correlator which allows measurement of parallaxes to allow the correct height to be set in the machine. For the production of the orthophotograph, profiling is carried out in the same way as with optical projection and optical transfer devices. A series of parallel scans is made in the y-direction with a step over of a pre-determined amount in the x-direction until the whole model is scanned. The orthophotograph is finally printed by taking the signal from one of the photoelectric cells and applying it to control the light output on the face of a third CRT. The coils of this CRT generate the same pattern as that on the scanning CRT, but the pattern can be modified slightly so as to provide the corrections necessary for scale, terrain slope and tilt. The printing CRT on the B8-Stereomat is mounted on a cross slide system in a light tight box located behind the B8. The CRT image is projected through a lens to be imaged on a sheet of film. A fourth CRT may be mounted alongside the third to produce a contour segment plot. The film which is placed in the light tight box therefore may have two emulsion layers; the one blue-sensitive is used to record the orthophoto image and the red-sensitive to record the contour.

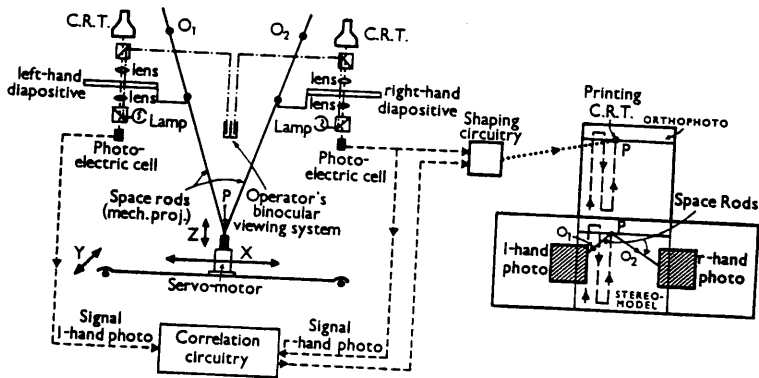


Fig. 12.3 Principle of Electronic Transfer Devices.

Besides the B8-Stereomat, two large American automated systems, the Bunker Ramo UNAMACE and the OMI-Bendix AS-II B/C, representing the first generation of another development, were developed for use in the Topographic and Aeronautical Charting Branches of the US Defense Mapping Agency (DMA). In these machines, the mechanical projection system of the B8 has been replaced in each case by a digital computer which resulted in more flexibility in the type of photography which can be accommodated and speed of the operation. More recently, the Northway-Gestalt GPM II has continued this development path. The pros and cons of these automated systems were discussed in detail by Petrie (1984).

Higher up the "automation ladder", all-digital instruments are being developed for the production of orthophotographs from digital images. This development has been brought about by the development of fast digital processors and boosted by the advances in image digitization systems such as these produced by Hell, SysScan and Optronics. The recent development of linear array cameras should boost the development of all-digital orthophoto instruments still further. Digital correlation methods are used with these digital images to carry out the photogrammetric scanning and measuring operations. In these instruments, for each node of the fine grid assumed to exist in the model covering the area of the orthophotograph, an image coordinate pair x,y is computed using the parameters determined in the orientation phase. Then the brightness values at each of these points are computed from the neighbouring pixels in the original image. Packages for digital orthophoto production have already begun to appear (Forstner, 1982; Mikhail, 1983; Wiesel, 1985; Wiesel and Behr, 1987; Petrie, 1987a).

12.3 Digital Terrain Models (DTMs)

As mentioned above, the off-line technique used in modern orthophoto production instruments requires digital terrain data to be available for the area in question together with the orientation data of the photographs from which orthophotographs are to be produced. The digital terrain data may not necessarily be profiles gathered from the same photos that are going to be used in the production. They can be taken from an existing terrain height data base usually described as a Digital Terrain Model (DTM). Generation of DTMs involves the following:

- a) Digital Terrain Data Acquisition; and
- b) Data Processing and Interpolation of the DTM.

12.4 Digital Terrain Data Acquisition

The basic digital terrain data can be acquired by carrying out direct field measurements using land surveying methods and equipment, by digitizing contours on existing maps using digitizers, or by photogrammetric methods using stereomeasuring machines. Each of these methods is suitable for a certain type of application and scale.

12.4.1 Land Surveying Methods of DTM Data Acquisition

These are mainly suited for site planning and large-scale engineering and mining projects. Although techniques such as grid levelling and stadia tacheometry may be used for data collection, their use has become much less common since the introduction of the total station types of electronic tacheometer which is able to measure both angles and distances electronically and to perform some limited computational tasks such as the reduction of the measured slope distances to horizontal distances and the calculation of coordinates from bearings and distances. A wide range of instruments are currently available for field gathering of terrain data ranging from integrated measurement and recording devices such as Sokkisha SET 2 and 3 and Geodimeter 440 to modular systems based on several individual units such as Wild T-1000/DI-1000, T-2000/DI-5 and Kern EI/DM 550, E2/503 (Kennie, 1987). However, since the acquisition of digital elevation data by land survey methods is not feasible and economic over large areas such as those encountered in the Sudan, essentially the remaining two methods are of main concern to topographic mapping and photogrammetrists in general.

12.4.2 DTM Data Acquisition Based on Contour Digitization

In this method, the height (DTM) data are acquired by first measuring (digitizing) the contours present on an existing map and then processing the digitized data to produce a DTM on either a grid or a triangular basis. A comprehensive review of the instrumentation and processing used in this approach is given by Petrie (1987a). However, contour digitizing assumes the existence of topographic maps with good quality contours, which, as will now be plain from the previous chapters, is one of the major problems which has to be solved in developing countries. Therefore, the only alternative left as far as orthophoto production in these countries is concerned is the generation of digital terrain data photogrammetrically. As will be seen, it is possible to do this using space photography.

12.4.3 Photogrammetric Methods of DTM Data Acquisition

In general, all photogrammetric methods of digital terrain data acquisition with conventional machines are based on the basic principle of stereo-measurement; therefore many possibilities of measurement are available. For the purpose of acquiring digital 3-D data in an analogue stereo-plotting machine, the measuring mark is mounted on a cross-slide system and linear or rotary encoders are used to encode each of the axes individually. A variety of digitizing units can be attached to these stereo-plotting machines. These can be either hardware-based, firmware-based or software-based units (Petrie, 1981). The hardware- and firmware-based units are essentially stand-alone electronic boxes which decode and count the signals coming from the linear or rotary encoders and convert them to digital values of the X,Y,Z coordinates which are displayed and recorded on magnetic tapes, disks, cassettes or cartridges. The software-based units are based on the use of a dedicated or time-shared on-line computer which can assist and guide the operator through prompts during setting-up of the stereomodel and carry out checks on the measurement as well as recording the data.

At present, the trend is the attachment of graphics work-stations to the stereo-plotting machines to allow instant checking and interactive editing of the measured data. Several photogrammetric equipment manufacturers have picked up the idea and developed their own integrated systems such as Kern's MAPS 200 and 300 systems based on the PDP-11 series of computers and Imlac or Tektronix screens which have been developed to allow their attachment to their FG-2 stereo-plotting machines, and the Zeiss Oberkochen/Intergraph system which has the advantage of displaying the plotted contours on a graphics display mounted on the side of the machine. The graphical image of the measured information is then injected via a semi-reflecting mirror into the optical channel of the plotting machine so that the operator can see what has been measured without the need to lift his eyes from the eyepieces.

The terrain heights are measured at sample points covering the model area. Sampling may be in several patterns as follows:

(i) Systematic (Grid-based) Sampling. In this method, spot heights may be measured in a regular geometric pattern (square, rectangular, triangular) as shown in Fig. 12.4. Such sampling is favoured in partially or fully automated photogrammetric operations where the location of the required grid nodes can be pre-programmed and driven to under computer control. This allow

pre-setting of the grid to a specific interval that ensures accurate terrain representation.

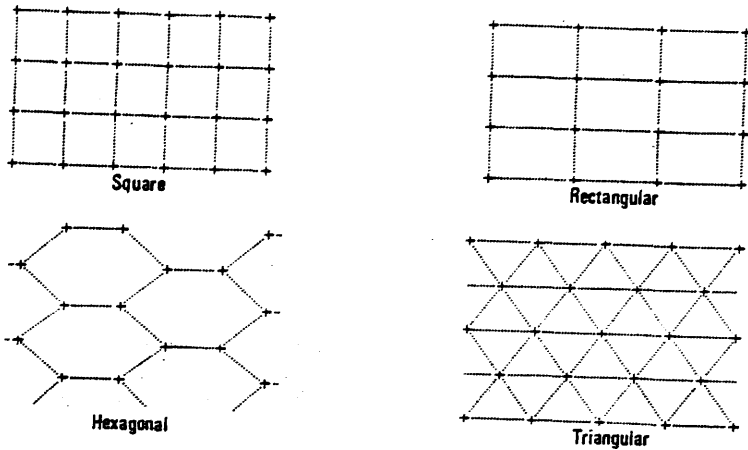


Fig. 12.4 Systematic Grid-based Sampling.

(ii) Profiling. The photogrammetric acquisition of digital terrain data for the purpose of orthophotography is often done in profiles. In the same manner as has been described for direct production of orthophotos, after the stereo-model is formed, a series of parallel profiles are scanned and measured with the operator keeping the measuring mark on surface while the digital data are recorded on a storage device.

(iii) Random (Specifically Located) Sampling. In this method, the photogrammetrist measures heights selectively at significant points only, i.e. at hill tops, in hollows and along breaks of slope, ridge lines and streams, as is done in field methods with small areas. Therefore the measured points will be randomly located in a sense that no regular pattern governs their locations relative to one another.

(iv) Composite Sampling. This combines the elements of both above sampling approaches and is one which is often followed by photogrammetrists, especially when non-automated machines are used for height measurement. A relatively coarse grid is measured first then measurements are made at significant points in terms of terrain representation. Also profiles may be measured depending on the particular application under consideration.

(v) Contour Measurement. In this method, heights are measured in terms of contours. The photogrammetrist selects the required contour value and, keeping the measuring mark on the surface of the stereo-model at that height, he traverses the contour lines of that specific value over the whole model. This operation is repeated for all other contour values. Again this may be supplemented by spot heights measured along break lines.

Although analogue stereo-plotters can be used for the above DTM data collection operations, analytical and all-digital stereo-plotters are best suited for this job, since they can be programmed and back-driven to any required position. In particular, they allow an easy implementation of the grid-based or profiling modes of measurement described above. Petrie (1987b) gives a detailed account of the state-of-the-art in this field.

12.5 Space Orthophotography Over the Sudan

An orthophotograph covering part of the Red Sea Hills test area described in Chapter 3, was produced from the MC photographs 111/112 forming Stereopair-1 described in Chapter 11. As mentioned in Chapter 3, for the production of this orthophotograph, terrain height data were collected as a series of profiles from the same stereomodel using a Kern DSR-1 analytical plotter. These profiles were then input to the SCOP program at the Institute of Photogrammetry at the Technical University of Vienna to produce the denser grid-based DTM necessary for the production of the orthophoto. An analytically-controlled Wild OR-1 Avioplan instrument was used to produce the final orthophotograph. In the following paragraphs, the processes of profiling, DTM generation and the results of the geometrical tests of the produced orthophotograph and the generated DTM are discussed.

12.5.1 CRISP Package

As mentioned in Chapter 3, a suite of computer programs called CRISP were used to implement the various photogrammetric operations carried out with the Kern DSR-1 analytical plotter. The block diagram (Fig. 12.5) shows the various modules available within the CRISP package and the operations that can be executed in terms of menus and submenus accessible to the operator from the main menu displayed when starting up the program.

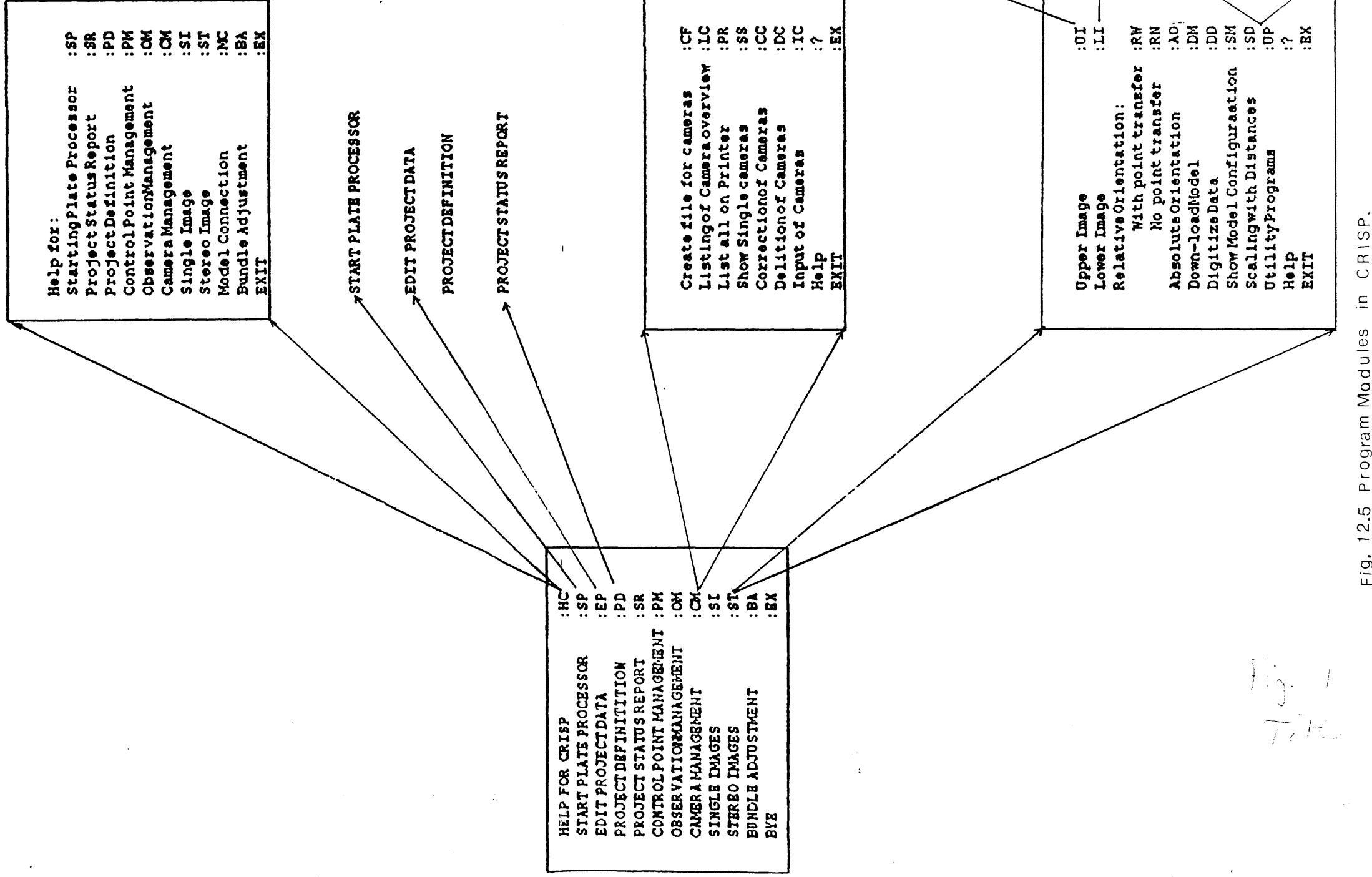


Fig. 12.5 Program Modules in CRISP.

An initial series of steps are executed, in which the basic information that is used by the various modules is input. These initial steps are called from the main menu. In this, the following steps are carried out:

a) Initialization: This is executed for entering the basic information about the project such as its name, the area covered, data, operator name, dimensions used (Metric or Imperial) and model configuration.

b) Control Point Management: for entering the coordinate data for the control points into a file (Control) which is later called by other modules.

c) Starting the Plate Processor: This is done by selecting the acronym SP from the main menu. This then loads and initializes the plate processor program P2PPERS.SAV. A request to switch on the DSR will be displayed on the screen. If the DSR is already on, then by switching it off and then on again, the process of downloading the plate processor programs from the controlling computer is started. When downloading is complete, the operator can then move the plates individually or together.

After the initial steps, various paths through these menus may be followed depending on what needs to be done in the particular project being executed. Only those specific operations that have been carried out in the acquisition of digital terrain data for this investigation are explained here. These are as follows:

Since stereoscopic measurement would take place, the command ST (Stereo Images) was selected from the main menu. Upon selecting this, a submenu of various operations that can be carried out on stereo-pairs was presented to the operator. The initial operations which were executed by this module were to mount the photographs on the plate carriers and to carry out the inner orientation. Mounting the photos was done by first selecting the upper image (UI) and then selecting "Mount Photo" (MP) from the submenu that was displayed. This moved the upper plate to a convenient position for the operator to mount the diapositive. Then by selecting the Go TO lower command and MP again, the upper plate was moved away and the lower one moved near to the operator in order to mount the other diapositive. After the mounting of the photos had been completed, the command Image Definition (ID) was called to input image calibration data for each diapositive and to define which diapositive (left/right) was on each plate. After this had

been accomplished, the Inner Orientation (IO) module was called. This moved the plates to the vicinity of the fiducial marks in the order in which their calibration values had been entered during the execution of the ID module. The operator then centred the measuring mark on each fiducial mark and pressed the right foot pedal to record the plate coordinates of that mark. After all the fiducial marks specified in ID had been measured, an inner orientation was carried out using the specified transformation (linear, affine or deformational). The r.m.s.e. values for the inner orientation was then computed and displayed and, if unsatisfactory, the process was repeated. On completing the inner orientation, the results were recorded in a file (INNER.ORI). Next the module was exited and the operator transferred back to the calling module ST by pressing the exit key (X).

From ST, the submodule to be selected after the inner orientation had been completed depended on the particular project being executed. For the purpose of this investigation, Relative Orientation (RO) was selected. The plates were then moved automatically to the vicinity of the standard relative orientation point positions. The operator then eliminated the parallaxes in each point and pressed the right foot pedal to digitize that point. When all points had been digitized, a relative orientation was carried out and residual y-parallax at each point displayed. If this was not satisfactory, the operator repeated the process again by again calling RO. On completion of the relative orientation, the results were then recorded in a file (RELATIVE.ORI) and the Absolute Orientation (AO) module was called. In this, the operator moved the measuring mark to the locations of each of the 3 well distributed control points whose ground coordinates had been stored in the control file created in the initial step. After centring the mark on each of these points, the right foot pedal was pressed to digitize the model coordinates of that point. After all three points had been measured, a quick absolute orientation was computed to establish the approximate model positions of the rest of the control points. The plates were then driven automatically to each of these positions in turn and the operator could then centre the measuring mark on each point and press the foot pedal to read its model coordinates. After all points in the control file had been measured, absolute orientation was computed using all these points in a least squares solution. The results of the absolute orientation together with the residuals at each point were displayed and the operator could then judge whether to accept, re-measure some points and/or reject others and recompute the absolute orientation. When accepted, the absolute orientation parameters and results were stored in a file (ABSOLUTE.ORI).

With all the orientation data recorded, they can be recalled every time the machine is switched on to resume the execution of the project with only the inner orientation needing to be updated.

After the model had been absolutely oriented, the plate processor maintained the position of the plates and computed the positions of the points measured in the ground space in real time. From the ST menu various Utility Programs could be executed by selecting submenu UP. In this case, profiling was selected from UP. In the profiling program, the profile is defined by the start and end points given in XYZ coordinates. The start and end points of all profiles may be specified and stored in a file. This file can be called later and the profiles are read and executed one after the other. In this investigation, the profiles were specified by moving to the start point, defining its position and then moving to and defining the end point. When the end point had been defined, the measuring mark was moved automatically to the start point and the measurement of that profile could then start. With the operator pressing the right-hand wheel to the right, the measuring mark moved from the start point towards the end point of the profile and, using the foot disk, the measuring mark was kept continuously on the surface of the model.

The coordinates of the points were recorded continuously at the specified interval while the measuring mark was moving. Recording was activated by pressing the left foot pedal. The interval between recorded points along a profile is determined by two factors. One is the specified limit of the coordinate readings; below that limit, no recording will take place, i.e. if 20 μm was specified, then more than 20 μm will have to be travelled by the measuring mark before a point can be recorded. The selection of this lower limit depends on the scale factor between model and ground systems of coordinates. The other factor which has to be considered is the selection of either the speed of the moving measuring mark along the profile in a speed-controlled profiling or the elapsed distance in distance-controlled profiling. This determines the the maximum distance which could be moved before a recording is made. In speed-controlled profiling, if the speed is high, this maximum distance will be longer than in low speed profiling. Therefore, the resulting intervals between the points will differ according to the ruggedness of the terrain and the ability of the operator. On the other hand, much more regular intervals will result from the distance controlled-profiling. Since keeping the measuring mark on the surface of the model formed from space photographs is much more difficult than on models formed from aerial photographs, due to

the small scale of the former, the measuring mark had to be driven with low speeds. Therefore, if speed-controlled profiling was selected, very dense points would result. Therefore, for the purpose of this investigation, distance-controlled profiling was selected.

As mentioned in Chapter 3, the interpolation of the grid based DTM needed for the production of the orthophotograph was carried out using the Stuttgart Contour Program (SCOP), while the determination of image positions of the grid nodes of this DTM and the computation of the line elements forming the orthophotograph was done using the SORA-CP (Software for Off-line Rectification with the Avioplan - Orthophoto and Stereo orthophoto).

12.5.2 SCOP Package

SCOP is a collection of computer programs for maintaining, manipulating and utilizing digital terrain data and for the generation of grid-based DTMs. Such digital data are structured in SCOP in one or other of two major output formats (Institute of Photogrammetry, Vienna, 1986):

a) The DATAFILE structure (DAF), suitable for maintaining the set of data required for a single task. The data input, coordinate transformation, data plotting, automatic checking, data editing, and data conversion operations may be carried out using this DAF structure. Data input is handled by two submodules: WINPUT which accepts the data acquired by photogrammetric methods and contour digitizing; and KA001 for reading data acquired by land survey methods. In WINPUT, the input format is user-defined. Points may be defined by just X,Y,Z coordinates or by including a code such as the number of the point or its classification with these coordinates, i.e. CODE,X,Y,Z. The order of the XYZ coordinates is also user-defined. The WINPUT data header may be used to describe the form and order of the data in the file.

b) The structure of the derived grid-based DTM. This is a special structure maintained by the package and used by various modules as for contour derivation, cross sectioning, orthophotography control, etc.

Fig. 12.6 shows the general architecture of SCOP, of which the main following modules are of interest in orthophotography:

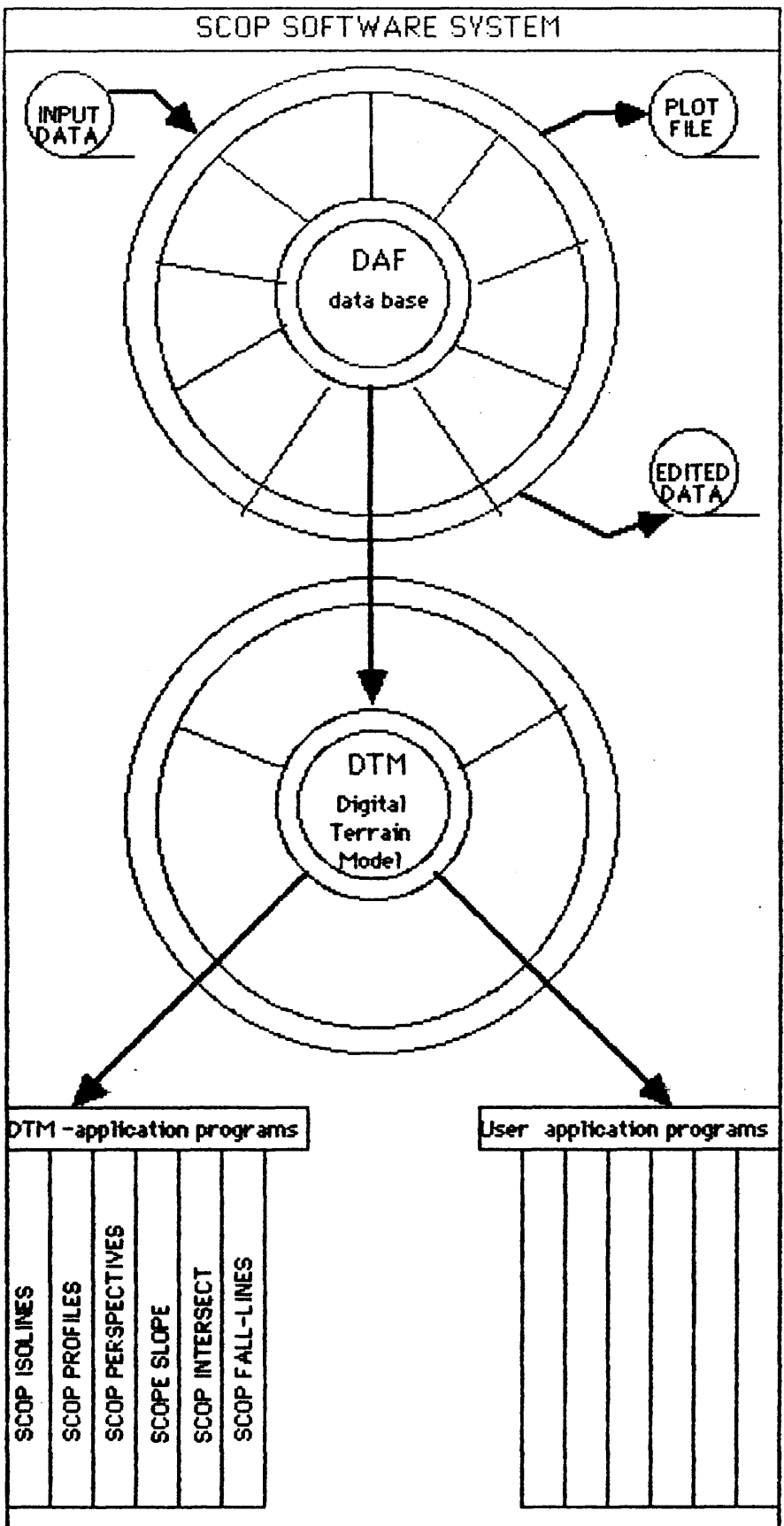


Fig. 12.6 The General Structure of SCOP.

1) SCOP.DMS which is a collection of computer programs for data input and output manipulation. It contains those tools which are associated with or operating on the datafile (DAF) structure. These include the reading in of the digital data in various formats; performing any of the operations mentioned above and writing the result in any of the input formats required by other programs such as SORA.

2) SCOP.DTM which is a collection of computer programs for the generation of grid-based DTMs of various structures. It interpolates the DTM either as requested by the operator or automatically as is found reasonable based on the density and distribution of data. Three methods of interpolation are provided:

(a) Surface modelling using biquadratic functions over local patches and using covariance functions varying according to local terrain conditions with the parameters determined for each patch for smoothing;

(b) a moving tilted plane over regions surrounded by 4 or 8 points (normally used in the preliminary steps of the modelling to detect data problems); and

(c) moving average, which is a form of pointwise interpolation, for quick blunder detection.

With the DTM interpolated, contour lines can be derived and plotted within SCOP.DTM.

3) SCOP.DTM-application which consists of a series of modules for the computation or production of contours (SCOP.ISOLINES), profiles (SCOP.PROFILES), slope maps (SCOP.SLOPE), perspective views (SCOP.PERSPECT), volumes, etc. Each of these modules can access one or more DTM files created by SCOP.DTM. Of these application modules, SCOP.PROFILES and SCOP.ISOLINES are of most interest in orthophotography.

a) SCOP.PROFILES interpolates elevations along specified lines, curves or polygons, but most importantly, as far as orthophotography is concerned, is the grid-to-grid interpolation, the output of which is a series of parallel profiles at the density required over the area specified. As mentioned above, these profiles represent the input to the SORA program used to produce orthophotographs in the OR-1 Avioplan.

b) SCOP.ISOLINES interpolates contours at specific levels, at regular intervals or at intermediate levels, depending on a user specified threshold. The interpolated contours may then be plotted on vector plotters, displayed on graphics screens, or stored in a metafile for use with independent devices. The suppression of contours in exclusion areas such as buildings, roads, etc. is also possible. This module is therefore used for derivation of contours which may be plotted and overlaid on the orthophoto.

12.5.3 SORA-OP Package

SORA (Software for Offline Rectification by the Avioplan) is a multimodule computer program developed by the Institute of Photogrammetry, Technical University of Vienna originally under contract to Wild for the control of the Avioplan OR-1. It consists of the following modules:

- 1) SORA-OPS for Orthophoto and Stereomate production.
- 2) SORA-MS for MSS image rectification.
- 3) SORA-DS for Developable Surfaces.

SORA-OPS is the module of main interest in this discussion. It is the computer program that carries out the transformation of terrain profiles from the ground (or model) coordinate system to the image coordinate system and performs the interpolation of scans and controls the operation of the OR-1 Avioplan -as mentioned previously in the discussion of the principle of operation of the OR-1 in Section 3.5. SORA-OPS consists of three sub-modules:

- (a) Sub-module 1 for the DTM profile interpolation;
- (b) Sub-module 2 carries out the terrain-to-image transformation mentioned above; and
- (c) Sub-module 3 for the control of OR-1 operations.

Since in principle, interpolation of the DTM profiles may be carried out by any DTM package, Sub-module 2 of SORA-OPS can accept these profiles from any package - provided that they are stored in the format required. This was the case in this investigation where the profile interpolation was carried out as a preliminary operation using SCOP. Therefore, only Sub-modules 2 and 3 are considered here.

The input data for Sub-module 2 were read from two separate files: one containing the DTM profiles as determined by SCOP, and the other containing the set of control data. The control data may consist of inner and outer orientation elements or the inner orientation elements and coordinates of a set of control points whose coordinates are also known in the ground (or model) coordinate system. However, both sets of data were sent to Vienna, as requested, for the purpose of checking and to ensure that the process was carried out accurately.

Sub-module 2 reads the control data from the control file and checks for the presence of the elements of orientation. If they are present, then it next checks the presence of the control point data. If this is also present, the program computes the corresponding image coordinates of these points using the given orientation elements and the coordinate data of the terrain points. Then it compares the computed image coordinates with the given ones. If the difference between the two at any point is more than 0.2mm at the orthophoto scale, a space resection is carried out with a view to discarding that point and deriving a new set of orientation elements. If no outer orientation elements are given in the control file, the program computes them using the control point data.

The control data needed for the operation of OR-1 are then computed. Then the profile data are read in and transformed into the image plane. The control data, together with the transformed profiles, are then stored on a magnetic tape to control the operation of the Avioflan later. The first block on this tape contains the control data consisting of an 8-digit identification number; the scan length and scan width in mm on the orthophoto; and the x,y coordinates of three points to serve as orientation points.

In the operation carried out after preliminary steps of illumination setting for the exposure, magnification setting and orientation, the profile data of the first two profiles are read by Sub-module 3. The first point in scan 1 is computed and, with the shutter closed, the photo carriage moves to this point. The computer first computes the quantities of equations (3.5) for the first two line elements. Then the computer executes a loop in which the values x_0 , y_0 , θ and v (image coordinates, rotation angle and magnification of equations (3.5)) for 99 line elements are linearly interpolated between the end values first computed. The computed and interpolated values of x_0 and y_0 are then sent to the x- and y- servos of the carriage, while the computed and interpolated values of θ and v are transmitted via digital/analogue convertors to the servos of the Dove

prism, which applies the small individual rotation for each line element, and the terrain zoom lens which applies the differential magnification for this line element. As soon as the scan has reached the centre point of line element 2, the process is repeated for line elements 2 and 3, and so on for the rest of the scan. At the end of each scan, the drum step is automatically generated. Simultaneously, profile 3 is read, over-writing profile 1. The first point of the scan is computed and the photo carriage moves to it and scan 2 begins. This procedure is repeated for the rest of the scans.

Two complete consecutive image profiles are always held at any one time in the computer memory. The real-time program computes and interpolates the coordinates of the points (x_{on}, y_{on}) of the image profiles between and the required rotations and magnifications. Thus the photo carriage always moves along interpolated scans between consecutive recorded profiles. The rotated and scaled (rectified) image is finally projected through a narrow slit onto the film.

12.6 Space Orthophotography Experiments

Metric Camera (MC) photographs no. 111 and 112 covering part of the Red Sea Hills test area and forming model no.1 described in Section 5.7, were mounted on the plate carriers of the Kern DSR-11 analytical plotter with their emulsion side down. The right hand photo No. 112 was mounted on the upper plate. Inner orientation was carried out using the affine transformation option. The largest residuals in the x and y coordinates of the fiducial marks after this transformation were 4 μ m. Relative orientation followed as described previously. The largest residual y-parallax resulted from the relative orientation was 12 μ m. and the r.m.s.e. of all parallaxes was ± 8 μ m after relative orientation. Absolute orientation was carried out using 14 control points, well distributed over the model area. The absolute orientation resulted in r.m.s.e. values of ± 21 m. in planimetric position and ± 30 m. in height.

The model formed by these photos covers ground area of 100 km. x 180 km. Recording points at intervals of 400 m along each profile and making profiles 400 m apart will result in a minimum of 117,000 points. The interval of 400 m selected represents the maximum distance in the object space (slope distance) that the measuring mark can move before the recording of a point takes place. Therefore points were chosen along the profile which would be much closer than 400 m in hilly areas, while in flat terrain, the intervals between points will be approaching the 400 m limit. On this model, 182,000 points were recorded in 252

profiles. This took 40 solid hours to be completed. The profile data recorded on the PDP-11 control computer of the DSR-1 were then transferred to the DEC Rainbow 100 linked to the PDP-11 through its serial port. This was done so that the data could be recorded into floppy disks which are readable by the "Magic Machine" available in the Data Transfer Section of the Glasgow University Computing Service. This was used to transfer the data to the ICL 2988 which was the mainframe computer available in the University Computing Service at that time. Transferring this amount of data proved to be very tedious and time consuming.

On the ICL 2988, any text coding and labelling were stripped from the data which were transformed into the format required by SCOP package which is described in Section 12.5.2. Handling and editing this huge data set using the normal simple file handling on the ICL machine proved to be very difficult. Therefore, the data were divided into several files and each file was edited separately. After the edition was complete, the individual files were appended again to form the file containing the data to be sent to Vienna. When the transformation was complete, the data were transferred to a VAX 11/750 mini-computer in the Mechanical Engineering Department to be put into a suitable VAX tape format since SCOP is mounted on a VAX mini-computer at the Technical University of Vienna. The tape was then sent to Vienna where the data were processed and used to produce a 1:250,000 scale orthophoto of the Red Sea Hills Test area on the OR-1 Avioplan using the procedures described above. The scale of the orthophoto is determined by the length of the film sheet which can be accommodated by the OR-1 Avioplan. The maximum length which can be accommodated is about 780 mm. Since the length of the ground area covered by the stereo-model formed from Photos. nos. 111 & 112 is about 180 km, the largest possible scale of the orthophoto is about 1:230,000. Therefore, the largest possible standard scale (1:250,000) was selected for the produced orthophoto. In general, the quality of the produced orthophoto is quite good and the contrast of the details was considerably improved over the original MC colour IR photographs (Fig 12.12).

12.6.1 Planimetric Accuracy Test of the Produced Orthophotograph

First of all, planimetric tests were carried out on the produced orthophoto to determine its geometrical accuracy. These tests comprise measuring the coordinates of identified points on the orthophoto in an arbitrary coordinate system and transforming these measured coordinates to the map projection coordinate system (UTM). The residuals between the computed coordinates and the corresponding ones scaled off the maps

were computed. The r.m.s.e. values in eastings (E), northings (N), and vector (V) were then computed.

A set of 75 of the identified points originally selected for the geometric test of the MC photographs no. 111 & 112 were measured on the Map Data digitizing system which consists of a GTCO digitizer connected to an Apricot Xi microcomputer. In this digitizing system, the coordinate system of the digitizer is mapped onto an internal memory space on the Apricot computer. This limits the range of coordinates to -32,768 to +32,768 units (total 65,535 square units). This range determines the accuracy to which point coordinates can be measured. With this range, it is clear that the resolution of digitizing carried out on small-scale maps will be coarse if a mapping of the ground coordinate system to this internal space is attempted. For this reason, point coordinates are measured in an arbitrary coordinate system. This was selected by measuring the length of the orthophoto transparency in mm and mapping this range to the internal range of the digitizer system. The lower left corner of the orthophoto was taken as the origin. The length of the orthophoto transparency is 780 mm which, when mapped to the digitizer unit range, gives a measurement resolution of 0.012 mm. A 0.015 value was actually taken to make sure that the whole of the orthophoto will lie within that space. This value represents the precision of coordinate measurement in this arbitrary coordinate system. In ground terms, this represents ± 3.75 m since the scale of the orthophoto is 1:250,000.

The digitizer coordinates of the measured points were then transferred to the ICL mainframe machine for further processing, using the terminal emulation program of the Apricot Xi. On the main frame machine, the two planimetric transformation computer programs LINCCN and POLY20 from the Department's software library were again used. Thirty well distributed points were used as control points in a least squares solution of the linear conformal and affine transformations. The rest of the points were taken as check points for which the residuals in Easting and Northing and the r.m.s.e. values were computed to assess the planimetric accuracy of the tested orthophoto. Table 12.1 lists the results obtained with these two transformations.

The r.m.s.e. values which have resulted are: ± 36 m in vector at the check points using the linear conformal transformation and ± 39 m in vector using the affine transformation. These values represent ± 0.14 and ± 0.16 mm respectively on the orthophotograph. This includes the ± 5.3 m. (± 3.75 m on each axis) contributed by coordinate measurement. These results show that no affinity in scale is present in the finally

produced orthophoto. Considering that the accuracy of plotting line maps is often taken as ± 0.2 mm, it is clear that orthophotos at scales of 1:250,000 and smaller can be produced with high planimetric accuracy. Actually by adjusting the 36 m to represent just 0.2 mm. on orthophoto leads to orthophoto scale of 1:180,000. In the case of developing areas, this factor could be relaxed still more, in which case, acceptable orthophotos at scales as large as 1:100,000 can be produced from MC photos. In fact, Table 3.2 gives ± 30 m as the r.m.s.e. in 1:100,000 photomaps. This shows that by slightly relaxing this specification, it will be possible to accept an r.m.s.e. value of ± 36 m on photomaps at this scale. However, the conclusion which was drawn from the interpretation test of these photographs in Chapter 11 about image content will also apply to the orthophoto which has been produced in this test and represents the limiting factor in its use as a topographic/cartographic document.

Transformation	Control Points			Check Points				
	No. of Pts.	r.m.s.e. E (m)	r.m.s.e. N (m)	r.m.s.e. V (m)	No. of Pts.	r.m.s.e. E (m)	r.m.s.e. N (m)	r.m.s.e. V (m)
Linear Conformal	30	34.4	34.4	48.6	45	28.3	22.9	36.4
Affine	30	33.7	33.8	47.7	45	30.9	23.5	39.0

Table 12.1 Results of the Planimetric Test of the MC Orthophoto.

12.6.2 Accuracy of the Generated DTM and Contours

A grid-based DTM generated from the profile data measured on the MC photographs and a contour map derived from the grid DTM were also produced by the author using a computer program suite called PANACEA installed on the ICL 3980 mainframe machine of the University Computing Service. In the following paragraphs, the operation carried out for the contour generation and results of its accuracy test will be reported.

12.6.2.1 PANACEA Package

PANACEA is a triangular-based DTM package devised by Dr. McCullagh of the University of Nottingham (McCullagh, 1983). The initial input data to this package consists of height values associated

with their plan positions. These can be a series of points defining a line such as a contour line or break-line, etc. or discrete points such as spot heights or points gathered by photogrammetric profiling as described above.

The package consists of various modules and the selection of modules depends on the particular application needed (Fig. 12.7). In DTM generation, the package can convert the profile data, which are considered as randomly located points, into a rectangular grid DTM. First, using the Delaunay triangulation algorithm, all the points are connected to form a triangular network, then a regular grid DTM is fitted on top of the triangulation network with the height value at each grid node being interpolated from the values at the vertices of the triangle in which it falls. The resolution of the grid is selected by the user according to a combination of factors such as the density of the initial data, the expected accuracy and the storage capacity which is available. This happens because the triangulation is adjusted exactly to the data distribution with no redundancy in areas of densely distributed data and no lack of information where points are more widely dispersed.

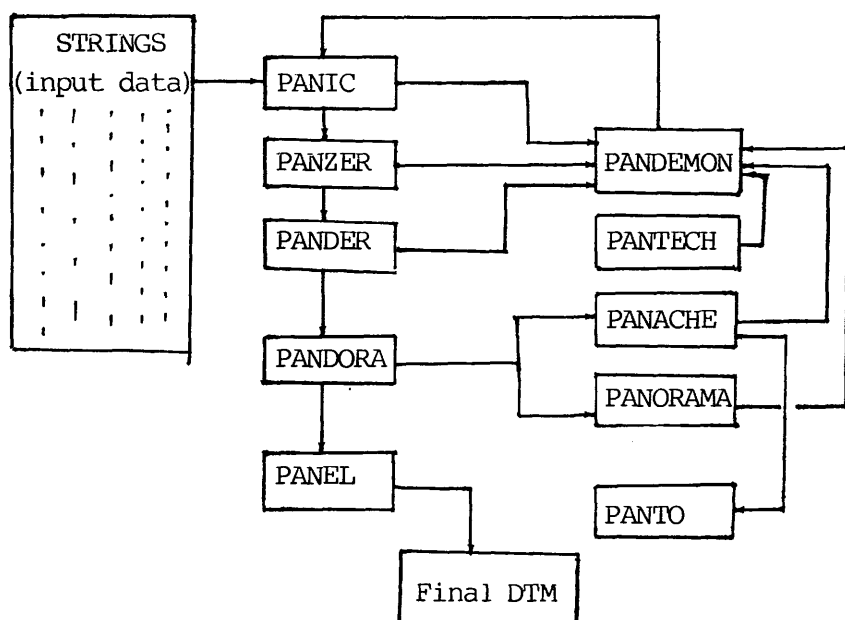


Fig. 12.7 Flow of the Interactions Between PANACEA Modules.

The contours can be generated directly from the triangular network using the module PANTECH. However, this particular module was not installed on the mainframe machine of the University Computing Service. Therefore, the triangular DTM was used to generate a rectangular grid-based DTM which could then be used to generate contours, isometric

views, etc. as will be explained later in this chapter. For editing and checking purposes, the digital terrain model can then be displayed either by means of contours, which are interpolated either from the previously calculated grid or directly from the triangulated data, or by means of an isometric view. Interactive editing and the addition of special purpose strings can also be carried out.

The version of the PANACEA package which is installed on the ICL 3980 of the University Computing Service comprises the following modules: (i) PANIC; (ii) PANDEMON (which is a combination of the PANDEMON & PANZER shown in Fig. 12.7); (iii) PANDORA (which is a combination of PANDER & PANDORA of Fig. 12.7); (iv) PANACHE; (v) PANORAMA; and (vi) PANEL. Recently, the module PANTECH has been installed as well. This version of PANACEA calls GINO subroutines, which were installed on the ICL 3980, to produce the graphical output. In the context of this investigation, only 4 modules have been used. These are: (i) PANIC; (ii) PANDORA; (iii) PANACHE; and (iv) PANORAMA.

(1) **PANIC**

PANIC reads in the initial input data and carries out the triangulation process. At the end of execution, two output meta-files are created by PANIC. One stores the node data and the other stores the Thiessen neighbours associated with each node of the first file. These are internal files specially structured to speed up data access by the next module. PANIC on the ICL 3980 was configured to accept up to 12,000 points. Since the number of points measured on the DSR-1 is much greater than this limit (185,000), the area of the model is divided into smaller areas. The resulting triangulation network, when plotted, appeared very dense. Figs. 12.8a & b show samples of the triangulation networks.

(2) **PANDORA**

This module carried out the interpolation of the grid-based DTMs for each one of the smaller areas. Each grid-based DTM is derived from the triangular structure created by PANIC using the derived slope derivatives. For this investigation, the resolution of the grid is defined as 200 m. The selection of this grid interval is restricted by the storage capacity handled by the package. The 200 m grid interval seems reasonable since the original profiling is carried out at 400 m interval.

In PANDORA, all the grid nodes which fall within a triangle are

assigned height values interpolated on the basis of the height values and estimated slope derivatives at the vertices of the triangles which have been derived before by PANIC. Two methods of interpolation can be used: (i) interpolation based on a linear triangular facet; and (ii) interpolation using a smooth curved surface patch fitted to the triangle vertices. In this investigation, two experiments were carried out first of all using both interpolation methods. It was found that, after contour threading, while both methods gave nearly similar contours on hilly areas, the shape of the contours resulting from the grid interpolated using a smooth curve patch on flat areas is unrealistic compared with that resulting with linear interpolated grid. Therefore, for all other parts, interpolation based on a linear triangular facet was used.

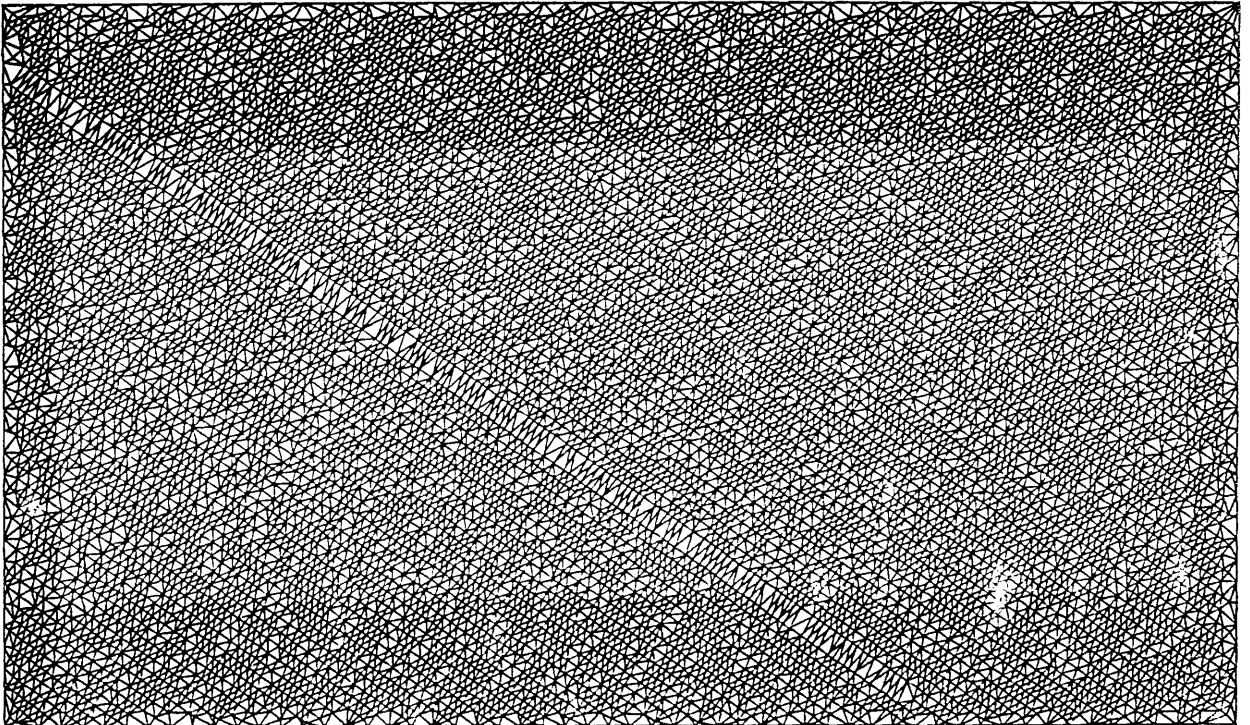


Fig. 12.8a A Sample of The Resulting Tranguation Network.

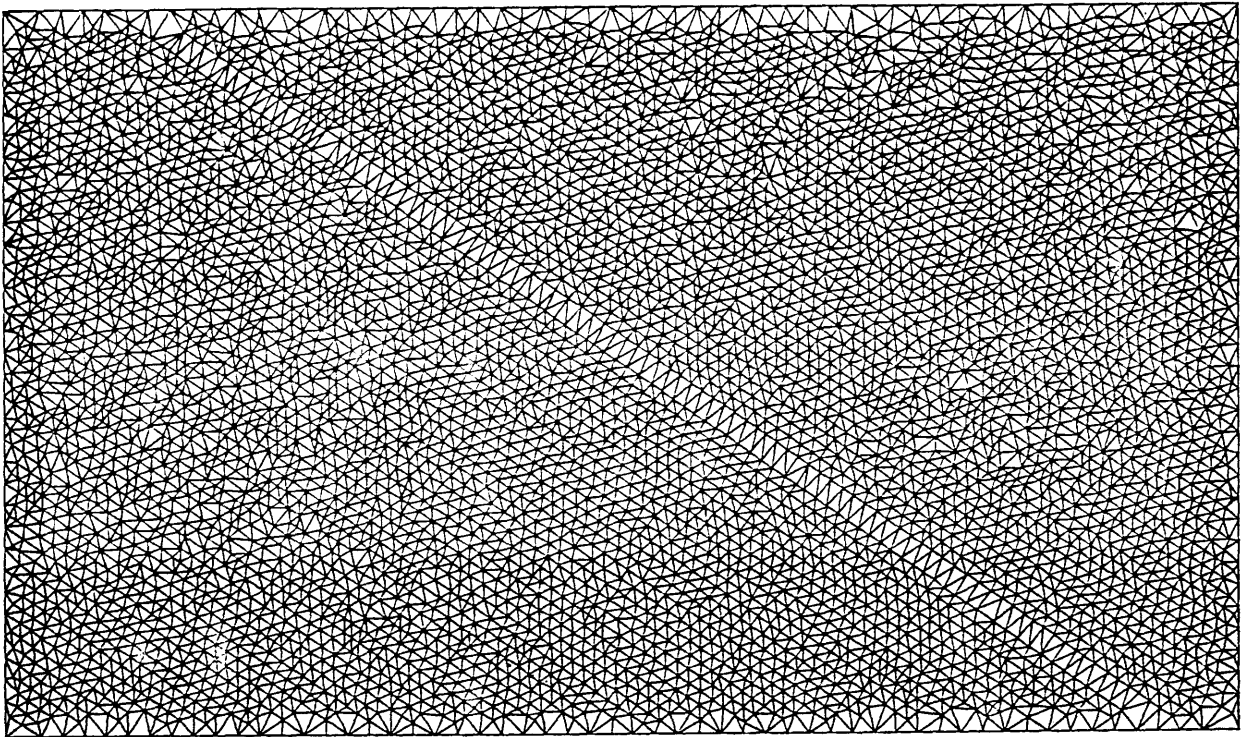


Fig.12.8b Another Sample of the Resulting Triangulation Network.

3) PANACHE

This is the grid contouring program, the input being the binary code output file from PANDORA. Linear interpolation has been used within a grid cell to determine the path of a contour. Thus the finer the resolution of the grid, the smoother will be the resulting contours. The main purpose of this module is to contour and display the contours to check for errors in the resulting DTM. The errors which can be detected by PANACHE are naturally related to the incorrect positions of contours on the surface. If the original input data were in the form of contour strings, then the output from PANACHE can be compared directly (visually) with the original map and areas of significant departure can be detected. Problematical flat spots can also be detected through the presence of angular contour segments giving a "staircase" pattern on the map. To a certain extent, this phenomenon is unavoidable but it is a function of the grid resolution and its

relation to the distribution of the original data and the contouring process. In flat areas, a number of grid nodes may have the same height value so they will belong to the same contour. Hence, during the contour threading, such contours will pass through all these grid nodes, ending up with the characteristic "staircase" shape. This effect is worse if the resolution of the grid is low. Running this module with the various grid-based DTMs created on the model area emphasized this fact by giving rather unsatisfactory contours in flat areas. The contours in these areas appear as elongated ellipses stretching along the profiling direction. Being systematically elongated in the direction of profiling, these contours suggest that this might be due to the fact that profiles are sampled in a dynamic mode, as described above, which has introduced a constant error along each profile. With the adjacent profiles sampled in opposite directions, the introduced error in one profile will be positive while that in the other profile will be negative. This is the possible cause of the pattern of contours shown in Fig. 12.9. Over hilly terrain, the results of contouring show the same pattern and complexity as the contour lines shown on the topographic maps of the area.



Fig. 12.9 A Sample of the Generated Contour Lines.

4) PANORAMA

This module creates isometric profile plots of the gridded DTM. Again a number of options regarding how the isometric view is to be displayed are offered. The isometric view can be drawn with the lines parallel to the X axis only or to the Y axis only or in both X and Y directions. An exaggeration factor can be applied to the Z axis to improve the appearance of the model. There is also an option for rotation of the DTM giving views from any corner at a constant elevation angle. The result of running this module on the data used for the generation of the contours in Fig. 12.9 is shown in Fig. 12.10. Fig. 12.10 emphasizes the problem experienced with contouring in flat areas.

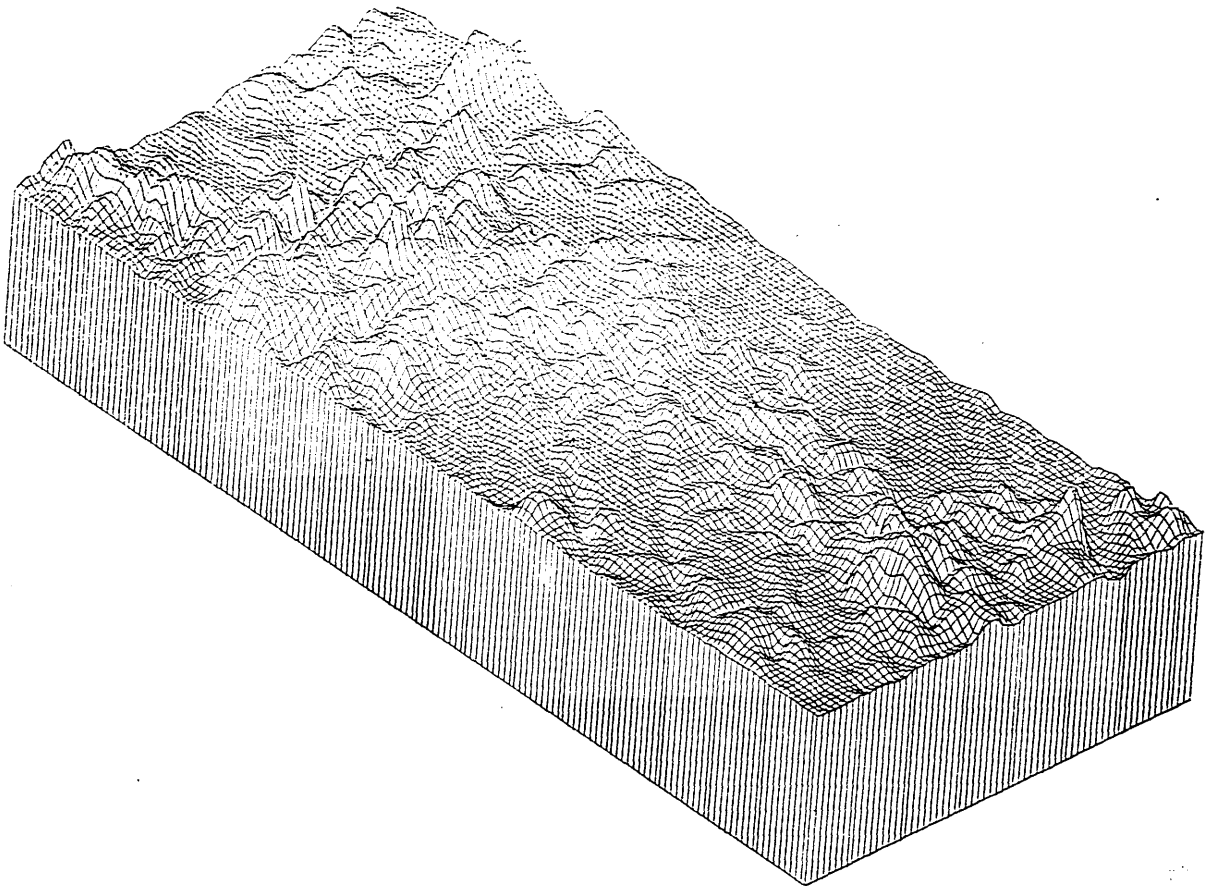


Fig. 12.10 Isometric View of the Contoured area in Fig. 12.9.

12.6.2.2 Accuracy of the Interpolated DTM

The area covered by three 1:100,000 scale topographic map sheets were used for this test. This area was divided into 12 sub-areas according to the relief and ruggedness of the terrain. The heights of a set of 1300 check points selected for the test were interpolated from the contour lines in the 1:100,000 scale topographic maps covering the area. Fig. 12.11 shows the distribution of these points. The corresponding heights of these points were interpolated from the triangulated network using the PANIC module and applying linear interpolation. The discrepancies between the two height values were computed for each point. The r.m.s.e. values were then computed as a measure of the absolute accuracy of the DTM. The results obtained are summarized in Table 12.2.

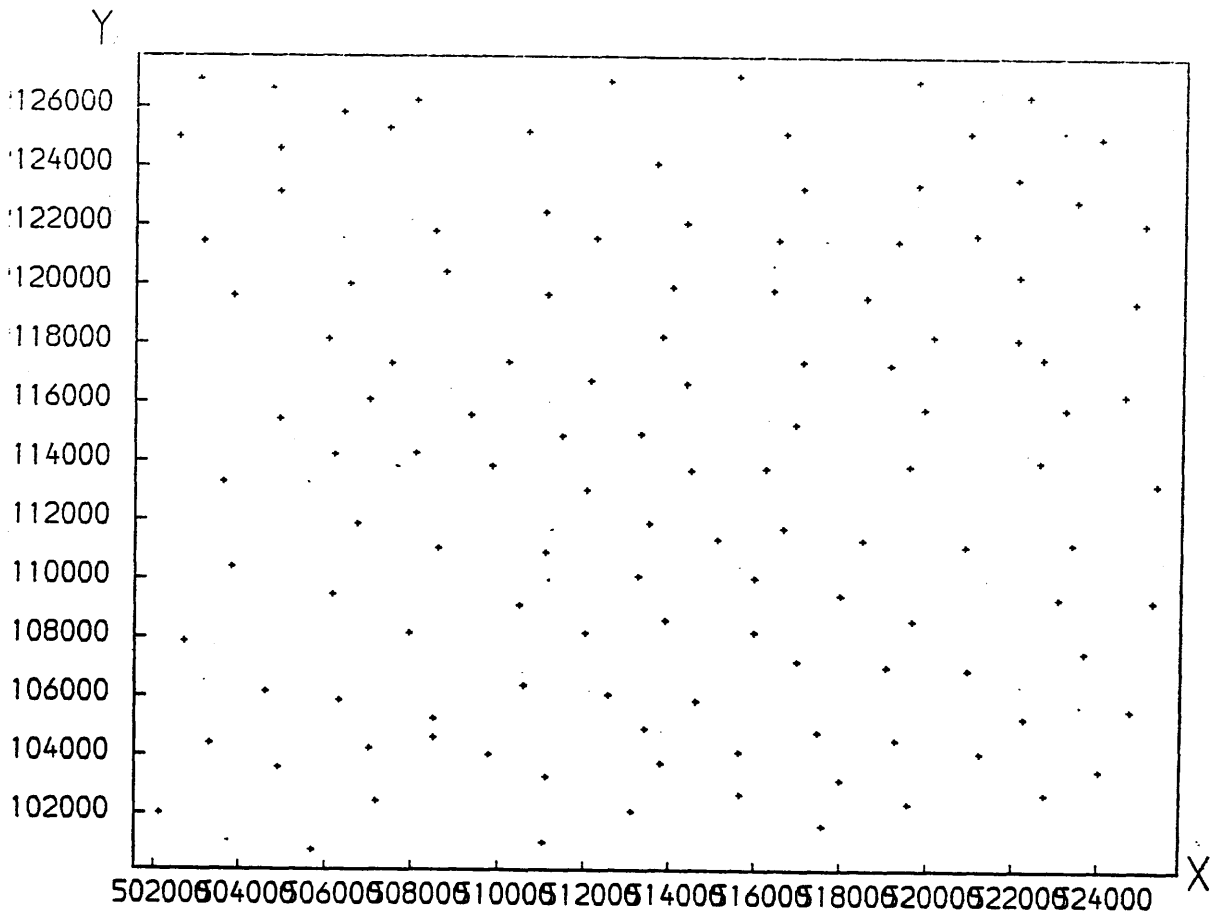


Fig. 12.11 Distribution of Height Check Points.

Area	No. of Pts.	r.m.s.e. in H (m)
A136	82	+16.1
C136	94	+25.6
D136	129	+25.1
D36B63	117	+25.9
A163	105	+18.6
B163	126	+28.3
C163	100	+45.1
D163	165	+42.0
A164	113	+35.4
B164	105	+37.2
C164	120	+38.0
D164	125	+47.2

Table 12.2 DTM Accuracy Test Results.

In general, the accuracy of the DTM generated from the profile data which were gathered from the MC photographs can be in the range of +20 m to +40 m depending on the type of the terrain and the quality of control points used for the orientation of the model.

12.7 Conclusions

The conclusion which can be drawn from both the orthophotography experiment and the DTM accuracy test is that it is quite feasible to use space photography for topographic mapping at the scale range considered in this investigation. In fact, with better resolution and a large base:height ratio, the possibility of fulfilling the requirements of topographic mapping at these scales through the space orthophotography is quite high. However, as mentioned above, the instruments required for carrying out this orthophotography are too expensive for the developing countries to acquire. Therefore, unless substantial aids are granted by international organizations such as the United Nations or governments of the developed countries, there is extremely little chance for the developing countries to afford the production of photomaps of significant coverage. Furthermore, even if these aids are granted, the acquisition of such instruments is quite unfeasible since the cost of maintenance and training will be prohibitive. This is in addition to the difficulties associated with the frequently interrupted power supply in many of the developing countries, particularly the Sudan. The solution to these difficulties

may be in the reliance on the large mapping organizations of the developed world. These organizations, paid from the aids granted, can carry out large mapping projects for the developing countries. However, this contradicts the trend of assigning the task of mapping to the national mapping agencies in the developing countries - which has been prevailing in the last two decades.

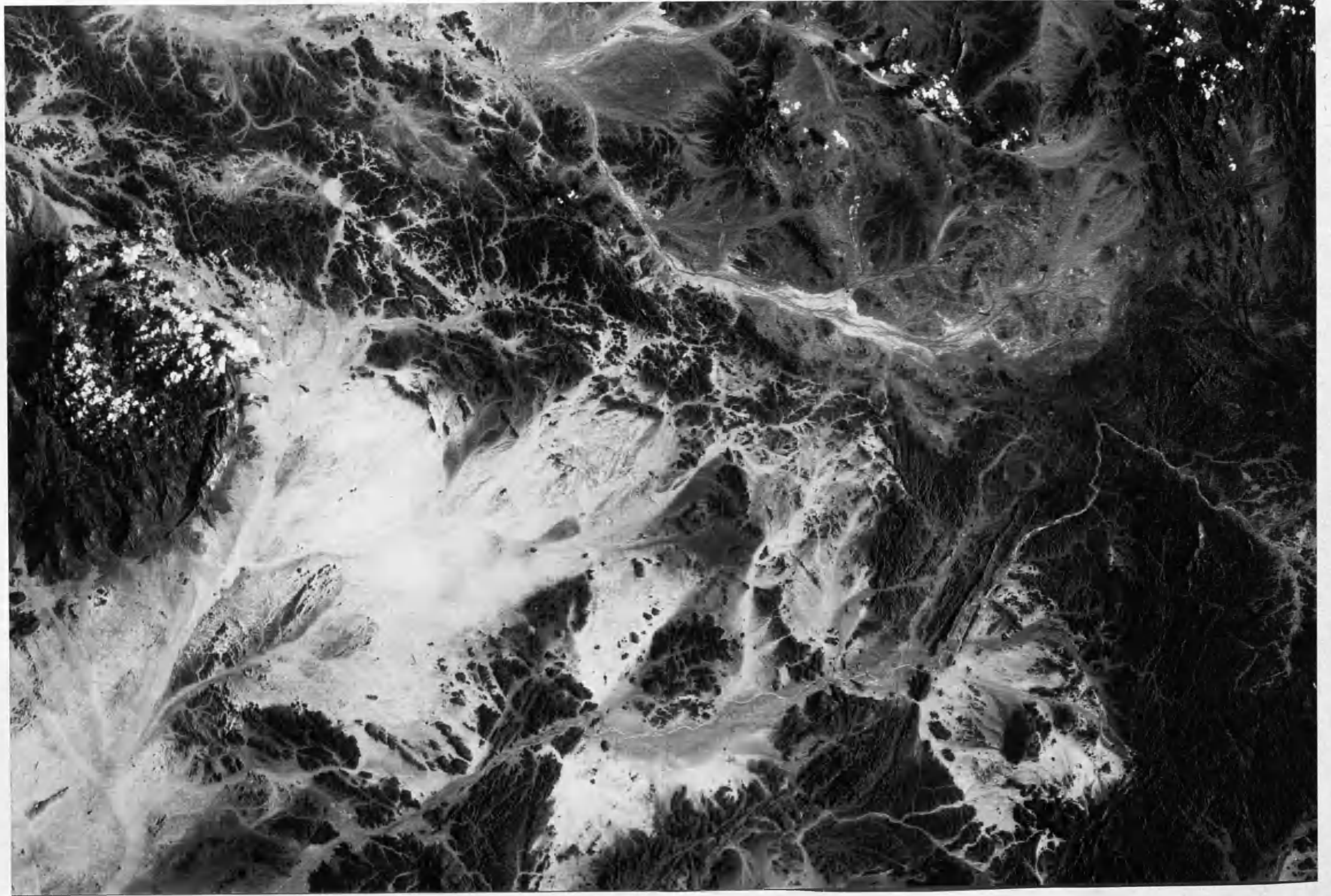


Fig 12 12 part of the produced Orthophoto
345

CHAPTER 13

Conclusions and Recommendations

13.1 General

Since the results of the geometric accuracy and interpretation tests of space images, which were acquired by various space sensors, have been reported and analyzed in the relevant chapters, it is not necessary to repeat them in this concluding chapter. However, from these results, it is clear that three specific sensor systems can be considered in the topographic mapping of the Sudan at the scale range 1:100,000 - 1:250,000. These are: (i) the Landsat Thematic Mapper (TM); (ii) the linear array sensor systems in the form of the MOMS and SPOT HRV; and (iii) space photographic systems such as the MC and LFC. Therefore, the conclusions drawn from the geometric accuracy and interpretation tests of the images acquired by these systems will be broadened and the possible contribution by each of these systems to the topographic mapping of the Sudan will be assessed.

13.2 The Potential Contribution of the TM

As shown in Chapter 5, topographic details with a planimetric accuracy of ± 42 m can be extracted from the TM images of the Sudan (Table 13.1). This satisfies the planimetric accuracy requirements of the 1:100,000 scale topographic mapping. However, the amount of topographic information which can be extracted from these images stops short of fulfilling the requirements of the map information content of topographic mapping at this scale (Table 13.2). Therefore, it can be concluded that TM images can best be utilized in the topographic mapping of areas where small man-made features are scarce. Alternatively, the images can be used as the basis of a 1:100,000 scale map series for the whole country, but without meeting the full specification of the present 1:100,000 scale line map series. Given the huge areas of the country without any proper topographic map coverage, this could still be very useful.

13.3 The Potential Contribution of the MOMS and SPOT

It can be said that the tests of MOMS and SPOT images have proved that potentially these sensors are capable of acquiring images from which 1:100,000 scale topographic maps can be produced to a reasonable

standard of accuracy and completeness. The results of the planimetric accuracy tests of MOMS images of the Sudan Red Sea Hills test area clearly demonstrated that topographic details with a planimetric accuracy of ± 25 m can be extracted from these images (Table 13.1). The interpretational tests of MOMS images (Table 13.2) have led to the conclusion that 60% of the topographic information required to be shown on the topographic maps at this scale can be extracted from these images. Furthermore, the predicted planimetric and height accuracies of the information extracted from SPOT images of the Sudan indicate that these images can be used in the production of 1:100,000 scale topographic maps. The amount of topographic detail which can be extracted from these images is relatively high. However as repeatedly mentioned in the previous chapters, many of the man-made features, although they are required to be shown on the 1:100,000 scale maps, cannot be expected to show up on any space images. Therefore, a substantial supplementary field survey completion will still be required to include the small man-made features specified to be included on maps produced at that scale. Alternatively, as in the case of the TM images, a series of image maps of the Sudan could be produced from the MOMS or SPOT images to a reduced or sub-standard specification which would still be of great value or utility to the country given the present situation.

TRANSFORMATION	TM				MOMS			
	No. of Pts.	r.m.s.e. E (m)	r.m.s.e. N (m)	r.m.s.e. V (m)	No. of Pts.	r.m.s.e. E (m)	r.m.s.e. N (m)	r.m.s.e. V (m)
LINEAR	58	41.29	54.55	68.41	31	502.23	340.86	606.98
AFFINE	"	31.87	41.69	52.48	"	18.99	20.57	28.00
POLYNOMIALS:								
4 terms $x y$	"	31.15	41.31	51.74	"	18.94	21.14	28.38
5 terms x^2	"	28.16	39.57	48.56	"	19.59	22.04	29.49
6 terms y^2	"	28.34	38.74	48.00	"	19.63	21.97	29.46
7 terms $x^2 y$	"	29.82	38.53	48.73	"	19.69	21.77	29.35
8 terms $x y^2$	"	26.99	31.67	41.61	"	19.73	21.69	29.32
9 terms x^3	"	29.00	38.00	47.80	"	19.59	23.69	30.74
10 terms y^3	"	29.96	38.05	48.43	"	19.36	23.59	30.52

Table 13.1 Geometric Accuracy Results of the TM and MOMS Images.

FEATURES SHOWN ON 1:100,000 MAPS	TM		MOMS	
	DETECTED	IDENTIFIED	DETECTED	IDENTIFIED
Communication				
Hard surfaced roads	2	2	3	2
Unsurfaced roads	0	0	2	1
tracks	0	0	0	0
Footpaths	0	0	0	0
Streets	2	1	2	2
Bridges	3	2	3	2
Ferry terminals	0	0	0	0
Railways	2	0	2	2
Railway stations	1	0	2	1
Culture				
Cultivated land	3	3	3	3
Big cities	3	2	3	3
Towns	2	1	2	2
Villages	1	0	2	0
Ruins	0	0	0	0
Electrical stations	0	0	0	0
Pipelines	0	0	0	0
Powerlines	0	0	0	0
Wells	0	0	0	0
Storage tanks	0	0	0	0
Cemeteries	2	0	2	1
Airports	3	3	3	3
Landing Grounds	2	2	3	2
Hydrology				
Rivers	3	3	3	3
Falls	3	2	3	2
Canals	3	3	3	3
Irrigation channels	2	2	2	2
Water bodies	3	2	3	3
Dams	3	3	3	3
Reservoirs	3	2	3	2
Hydrography				
Tidal flats	0	0	0	0
Reefs	*	*	*	*
Rocks	3	1	3	1
Near shore bathymetry	0	0	0	0
Water depth	0	0	0	0
Marsh	3	3	3	3
Harbours	3	3	3	3
Small harbours	3	2	3	3
Shore line	3	3	3	3
Islands	3	3	3	3
Relief forms				
Sand dunes	3	1	3	1
Gravel beds	2	0	2	0
Elevated grounds	3	3	3	2
Contours	0	0	0	0
Vegetation				
Woodlands	3	2	3	2
Scattered trees	0	0	0	0
Scrub	0	0	0	0
Orchards	3	1	3	2
Others				
Administrative boundaries	0	0	0	0
Rest houses	0	0	0	0
Triangulation pillars	0	0	0	0

0 = NOT; 1 = SOMETIMES; 2= OFTEN; 3 = YES; * = NOT AVAILABLE;

Table 13.2 Interpretation Results of the TM & MOMS

13.4 Assessment of TM, MOMS and SPOT Images

For the topographic mapping of countries having a vast area extent, such as the Sudan, a large number of space images are required to produce the complete coverage of topographic maps. On the one hand, this large number of images calls for a long-life operational space sensor system producing a worldwide coverage in a manner similar to that of the Landsat and SPOT satellite systems or a space sensor system which is planned to produce the total coverage of a specific country as part of its objectives on the basis of an agreement between that country and the launching space agency. On the other hand, in some cases, the acquisition of a complete coverage of such vast areas and the processing of the acquired images requires a large financial funding which is a real difficulty in many developing countries.

At present, the call for an operational sensor system which can acquire the images of the whole country over a substantial period of time points to the use of the TM and SPOT sensors. Although both of these operational systems can provide the complete coverage needed, there are some difficulties and drawbacks associated with the utilization of their images.

Regarding the TM images, the following drawbacks can be pointed out:

(i) Since the TM has no stereoscopic image acquisition capability, its images can only be utilized for the production of planimetric maps or image maps.

(ii) As shown by the results of the interpretational test which have been carried out on the TM image of the Red Sea Hills test area, these images will not provide all the detail required to be shown on the produced topographic maps. Given the size of the area to be covered, the supplementary work required to compensate for this shortfall in the amount of detail is huge. This may result in the utilization of the TM images for the production of planimetric maps in relatively developed areas to be impractical. In addition, topographic maps showing height information in the form of contours and spot heights are usually required in such relatively developed areas.

(iii) The complete coverage of the Sudan requires about 120 TM images. With each of these images costing around \$1,000, the total cost of the images required for the complete coverage is about \$120,000 which is not too large. However, in addition to

this, an additional large cost for the acquisition of equipment to carry out the required processing and the cartographic treatment to produce the image maps would have to be met. The alternative to this is to have all this work done abroad as in fact was done for the whole of Libya by the Earthsat Corporation. Although this might not involve too large a sum, given the benefits which will result, and will be much less than the cost of acquiring and processing SPOT images, with the crippled economy of the Sudan, it is very difficult for any politician to comprehend the necessity of producing these image maps for vast areas in the Sudan. This cost leads to the necessity of securing international aid as will be stressed later.

On the other hand, the difficulties which are associated with the utilization of SPOT images are mainly due to the even higher cost of acquiring, processing and outputting the images and the cost of establishing the required control. The ground coverage of a single frame of SPOT images is 80 km x 80 km. Therefore, 1,112 image frames (almost ten times the number of TM frames) are needed if only planimetric image maps of the complete coverage are to be derived. At present the cost of acquiring a single frame is about £1,800. A simple calculation will reveal that, for the complete coverage of planimetric maps of the Sudan from SPOT images, an even larger amount of money has to be secured. This is in addition to the fact that, for the efficient utilization of these images, contracts will almost certainly have to be signed with large foreign organizations to supply the systems needed to process the data or, more likely, to carry out the mapping process.

13.5 The Potential Contribution of Space Photographic Systems

The results of the geometric accuracy and interpretation tests which have been carried out on the MC and LFC photographs clearly indicate that conventional photography is still superior, in terms of geometric accuracy and ground resolution (Tables 13.3 and 13.4), to the TM and SPOT systems discussed above. The results of the geometric tests of these photographs (Table 13.3) show that it is quite possible to derive 1:100,000 scale topographic maps or photomaps for the Sudan from similar photography - fulfilling the accuracy requirements and a relatively large proportion of the map content requirements of this map scale. In addition, the very recently published results of the geometric tests carried out by other investigators (Dowman, 1988; Kraemer, 1988) on the photography acquired by the Russian cameras covering various test areas reinforce or confirm the superiority of

space photography.

The drawbacks which are associated with the use of space photography for mapping arise mainly from the difficulties in securing the acquisition of photographs that cover the complete area of the Sudan. All the photographic systems which have been launched up to date have been experimental systems mounted in short-duration manned satellites. The photography acquired during these experiments represents a tiny proportion of the total coverage. Till now, no attempts have been made to plan or implement systematic space photographic coverage of a country such as the Sudan. Undoubtedly, this will not be easy - the length of flight required and the difficulties in providing sufficient film and in transporting the exposed photographs back to Earth are considerable. However, in this respect, it is worth noting the very long duration manned space flights carried out by the Russians in the last few years which are regularly resupplied and have crew changes. These would seem to point to a way in which the required photography can be taken.

CAMERA	Model	C O N T R O L P O I N T S				C H E C K P O I N T S					
		No. of Pts.	r.m.s.e E	r.m.s.e N	r.m.s.e V	r.m.s.e H	No. of Pts.	r.m.s.e E	r.m.s.e N	r.m.s.e V	r.m.s.e H
MC	110/111	30	18.60	15.50	24.14	29.80	55	20.70	20.20	28.90	34.60
	111/112	25	17.00	19.30	25.72	31.80	31	20.90	22.40	30.60	30.70
LFC	1319/1320	30	17.23	11.99	20.99	17.47	53	14.52	14.16	20.28	19.91
	1320/1321	30	13.59	11.81	18.00	20.36	57	14.10	12.68	18.97	17.26

Table 13.3 Results of the Geometric Accuracy Tests of the MC and LFC.

: Feature shown on 1:100,000	MC	PHOTOS	LFC	PHOTOS
	Detected	Identified	Detected	Identified
Communication:				
Hard surfaced roads	3	2	3	3
Unsurfaced roads	3	1	3	2
Tracks	0	0	1	0
Footpaths	0	0	0	0
Streets	3	2	3	2
Bridges	3	3	3	3
Ferry terminals	0	0	0	0
Railways	3	0	3	2
Railway stations	0	0	2	0
Culture:				
Cultivated land	3	3	3	3
Big cities	3	2	3	3
Towns	2	1	3	2
Villages	1	0	2	0
Ruins	0	0	0	0
Electrical stations	0	0	0	0
Pipelines	0	0	0	0
Powerlines	2	1	2	1
Wells	0	0	0	0
Storage tanks	0	0	0	0
Cemeteries	3	1	3	2
Airports	3	3	3	3
Landing Grounds	3	2	3	3
Hydrology:				
Rivers	3	3	3	3
Falls	3	3	3	3
Canals	3	2	3	3
Irrigation channels	2	0	3	2
Water bodies	3	3	3	3
Dams	3	3	3	3
Reservoirs	3	3	3	3
Hydrography:				
Tidal flats	0	0	0	0
Reefs	*	*	*	*
Rocks	3	0	3	0
Near shore bathymetry	0	0	0	0
Water depth	0	0	0	0
Marsh	*	*	*	*
Harbours	3	3	3	3
Small harbours	3	2	3	3
Shore line	3	3	3	3
Islands	3	3	3	3
Relief forms:				
Sand dunes	3	2	3	3
Gravel beds	2	2	3	2
Elevated grounds	3	3	3	3
Contours	0	0	0	0
Vegetation:				
Woodlands	3	2	3	3
Scattered trees	0	0	0	0
Scrub	0	0	0	0
Orchards	0	0	0	0
Others:				
Adminstrative boundaries	0	0	0	0
Rest houses	0	0	0	0
Triangulation pillars	0	0	0	0

D= Detected, I= Identified, 0= not, 1=Sometimes, 2= Often, 3= Yes, and *= Not available.

Table 13.4 Interpretation Results of MC and LFC Photographs.

However to be realistic, although the results obtained from the geometric accuracy and interpretation tests which have been carried out on the MC and LFC photography have shown that space photography is superior to other systems in providing accurate and sufficient topographic detail, it will be very difficult to achieve the complete coverage of the Sudan and similar large developing countries in the near future. This will certainly be the case so, unless an agreement is reached between the Sudan and one of the space agencies of the developed world to provide a complete systematic photographic coverage of the country.

As mentioned in Chapter 12, even if the complete coverage is achieved, the process of deriving topographic maps from space photography for these large developing countries will take many years. Although quick methods such as orthophotography can cut this period significantly, the equipment needed to carry out this orthophotography may still be too expensive for a developing country to acquire which again means that it is likely that the work will have to be carried out abroad.

13.6 Near-future Space Imaging Systems

Having discussed the potential contribution of the current TM, SPOT and space photographic systems to the small-scale topographic mapping of the Sudan, it seems appropriate to look ahead to the space imaging systems planned for the near-future to assess the possibilities of these improved systems. As far as existing scanner systems are concerned, it is certain that the acquisition of SPOT HRV and TM images will continue. But more important is the launch of the Enhanced Thematic Mapper (ETM) by Eosat which is scheduled for June 1991. This will be launched in an orbit having orbital characteristics similar to those of Landsats 4 and 5 to provide continuity of the present TM data. In addition to these data, the ETM will provide panchromatic image data with a 15 m pixel size. This will result in images with a much improved ground resolution and, therefore, it will be possible to extract much more topographic detail from these images. Since the 15 m pixel size TM images are expected to be made available at a lower cost than the present price of the SPOT images, one can expect them to have a more prominent role in the process of small-scale topographic mapping of the Sudan than the SPOT images. This is despite the fact that the ETM images can only be used for planimetric mapping.

As for the space photographic systems, unfortunately it was announced recently by NASA that the LFC will not be put in orbit in the

foreseeable future. However, ESA is still going ahead with its plan to place the MC into orbit again. The plan is that on this next flight, the MC will include an FMC mechanism to compensate for the forward motion of the platform and so avoid the deterioration in the resolution of the resulting photography which was evident on its first flight. In addition, it seems that the Russian space photographic systems will continue acquiring space photography. Since the Russian cameras have been used in long-duration manned space missions, the use of these systems may well offer the best way of achieving the complete photographic coverage of the Sudan which is required.

From the above discussion, one can reach the conclusion that from a technical point of view it is quite possible to carry out the 1:100,000 to 1:250,000 scale topographic mapping of the Sudan using space images acquired by the TM, SPOT and space photographic systems. But if this is to be achieved there are many non-technical difficulties to be overcome to ensure the practical utilization of these images. In general, the following concluding points can be drawn from this investigation concerning the practical use of space images in the topographic mapping of the Sudan.

(i) Substantial financial help from international aid organizations is essential for achieving a significant coverage of topographic mapping in the Sudan.

(ii) If space photography is to make a significant contribution to the process of topographic mapping of the Sudan, an agreement with one of the space agencies should be secured in order to provide a consistent coverage of the Sudan.

(iii) Vast areas of the Sudan are desert in which few details are present other than the desert land forms and the pace of development is very slow. Bearing in mind also the fact that these areas are relatively flat, planimetric image maps derived from the existing TM images should be quite acceptable to most users in the absence of the complete systematic coverage of space photography. The 15 m pixel size ETM images which will be acquired in the 1990s will of course be even more suitable for this planimetric map series than the existing TM images.

(iv) In the absence of complete systematic coverage of the Sudan by space photography, SPOT stereo images can be utilized for the production of topographic maps for selected areas. These areas can be selected according to the development plans of the

country. However, as mentioned above, almost certainly this will require contracts to be signed with foreign agencies to carry out the mapping process efficiently using modern equipment.

(v) An alternative to the utilization of SPOT images mentioned in (iv), is to plan and execute systematic small-scale aerial photography to give coverage of the whole country. In this respect, high altitude aerial photography could well be the answer to the problem of mapping in areas where the pace of development is relatively fast. This can be achieved by signing contracts with foreign mapping organizations and companies, such as the very successful one with the Directorate of Overseas Surveys (DOS) by which the 1:100,000 scale topographic maps of the Red Sea Hills area were produced. However, this might be affected by the lack of availability of airports in certain areas.

13.7 Recommendations

In the light of the above concluding points the following research topics can be recommended:

(i) Since it has been concluded that TM images can be used for the planimetric mapping for the vast desert areas, one may recommend the investigation of the accuracy with which planimetric triangulation can be carried out using these images. This is essential for the establishment of the control points needed for the rectification of each individual image frame and hence the production of the planimetric maps. The triangulation can be implemented by utilizing the satellite positional parameters to derive the positional coordinates of well defined points in these images and also by bridging using the known ground coordinates of points in relatively developed areas bordering the desert. In this respect, the possibilities offered by modern satellite-based position fixing methods such as GPS need to be explored.

(ii) An investigation of the possibilities of topographic map production over relatively developed areas in the Sudan utilizing SPOT stereo-images using conventional photogrammetric methods based on analytical plotters should be carried out as well as methods based on image processing and digital mapping.

As for the Sudanese mapping authorities, one may also suggest the following:

(i) An investigation of the possibilities of carrying out the topographic mapping of the Sudan by the US or the British military mapping organizations using military sensors.

(ii) An investigation of the possible contribution which can be offered by the Russian sensor systems and the possibilities of achieving the complete coverage of photography for the Sudan using the Russian cameras.

13.8 **Final Note:**

Before ending this thesis, one must mention that the author has greatly benefited from undertaking this research work in various ways:

(i) This has included the acquisition of a fair experience in computer programming in Algol and Fortran and in the planning and execution of large computational work efficiently.

(ii) Experience has been acquired in dealing with the various problems of topographic mapping utilizing remote sensing images. Working on the Sudan as a test area has revealed the problems and difficulties with which the author will have to deal in his future career and has provided an insight into the possible solutions which can be adopted in each situation.

(iii) The author has greatly reinforced his knowledge in the fields of remote sensing, analytical photogrammetry and topographic mapping. Working with all types of sensors has provided the author with a good understanding of the geometry and merits of each type.

(iv) Finally and most importantly, the ability to analyze the results, derive the conclusions, and communicate the findings has also been gained together with the ability to look at the many problems which arise during the research work from various angles of view. This has been, particularly, of great benefit to the author's future career as a lecturer and researcher.

BIBLIOGRAPHY

- Abdalla, A.E., 1980. The Potential of Remotely Sensed Satellite Data for the Topographic Mapping of Sudan at Small Scales. M. App. Sci. Dissertation, University of Glasgow, 116 pages.
- Abdelaziz, Y., 1974. Expected Accuracy of Convergent Photographs. Photogrammetric Engineering, 40(11):1341 - 1346.
- Ackermann, F., Ebner, H. and Klein, H. 1973. Block Triangulation with Independent Models. Photogrammetric Engineering, 39(9):967 - 981.
- Ackermann, F., 1978. Experimental Investigation into the Accuracy of Contouring from DTM. Photogrammetric Engineering, 44(12):1537 - 1548.
- Ackermann, F., 1980. Block Adjustment with Additional Parameters. Invited Paper: Proceedings of the 14th International Congress of Photogrammetry, ISP, Commission III, Hamburg. International Archives of Photogrammetry and Remote Sensing, 23(B3):1 - 10.
- Ackermann, F., 1983. High Precision Digital Image Correlation. Proceedings of the 39th Photogrammetric Week, University of Stuttgart, 39(1):231 - 243.
- Ackermann, F. and Stark, E., 1985. Digital Elevation Model from Spacelab Metric Camera Photographs. Metric Camera Workshop, Proceedings of a Joint DFVLR-ESA Workshop, Oberpfaffenhofen, 1: 9 -12.
- Ackermann, F. and Schneider, W., 1986. High Precision Aerial Triangulation with Point Transfer by Digital Correlation. Proceedings of the Symposium From Analytical to Digital, ISPRS, Commission III, Rovaniemi. International Archives of Photogrammetry, 26(3):18 - 27.
- Ali, A.E., 1982. Investigation of Seasat-A Synthetic Aperture Radar (SAR) for Topographic Mapping Applications. Ph.D. Thesis, University of Glasgow, Two Volumes, 460 pages.
- Ali, M.E.O., 1982. Analytical Triangulation of Space Photography. Photogrammetric Engineering and Remote Sensing, 48(1):55 - 65.
- Allam, M.M., 1978. DTM's Application in Topographic Mapping. Photogrammetric Engineering and Remote Sensing, 44(12):1513 -

- Alwashe, M., Bodechtel, J. and Zigler, J., 1986. The Application of High Resolution MOMS-01 and Thematic Mapper Satellite Data for Urban Planning Purposes - Example Jeddah, Saudi Arabia. Proceedings of the Symposium: Mapping from Modern Imagery, ISPRS, Commission IV, Edinburgh. International Archives of Photogrammetry and Remote Sensing, 26(4):565 - 574.

- Amin, A.M., 1986. Geometrical Analysis and Rectification of Thermal Infrared Video Frame Scanner Imagery and its Potential Applications to Topographic Mapping. Ph.D. Thesis, University of Glasgow, 334 pages.

Anderson, J., 1964. Analytic Aerotriangulation Using Triplets. Presented Paper: Proceedings of the 10th International Congress of Photogrammetry, ISP, Commission III, Lisbon. International Archives of Photogrammetry, 15(5):29 pags.

- ASP, 1966. Manual of Photogrammetry, 3rd Edition, 6269 Lessburg Pike, Falls Church, Va. 22044, Two Volumes, 1199 pages.
- ASP, 1968. Manual of Colour Photography, 1st Edition, 62569 Lessburg Pike, Falls Church, Va. 22044.
- ASP, 1980. Manual of Photogrammetry, 4th Edition, 105 Virginia Avenue, Falls Church, Va. 22046, 1056 pages.
- ASP, 1983. Manual of Remote Sensing, 2nd Edition, 105 Virginia Avenue, Falls Church, Va. 22046, Two Volumes, 2440 pages.

Bahr, H.P., 1976. Geometrical Models for Satellite Scanner Imagery. Presented Paper: Proceedings of the 13th International Congress of Photogrammetry, ISP Commission III, Helsinki. International Archives of Photogrammetry, 21(3):11 pages.

- Bahr, H.P., 1985. Restitution of Spacelab Photography by Analog Stereoplotter. Metric Camera Workshop, Proceedings of a Joint DFVLR-ESA Workshop, Oberpfaffenhofen:25 - 28.
- Baker, J.R. and Mikhail, E., 1975. Geometric Analysis and Restitution of Digital Multispectral Scanner Data Arrays. LARS Information Note 05287, Purdue University: 297 pages.

Baudoin, A. and Brossier, R. 1982. The SPOT Programme at the IGN-F. Proceedings of the Symposium on Primary Data Acquisition, ISPRS, Commission I, Canberra. International Archives of

- Baudoin, A., 1984. Application of SPOT and DTM to Cartography. Presented Paper: Proceedings of the 18th International Symposium on Remote Sensing of the Environment, Paris, 18(1):61 - 74.

- Bauer, H. and Muller, J., 1972. Height Accuracy of Blocks and Bundle Adjustment with Additional Parameters. Presented Paper: Proceedings of the 12th International Congress of Photogrammetry, ISP Commission III, Ottawa. International Archives of Photogrammetry, 19(3):13 pages.

Bauer, H., 1974. Bundle Adjustment with Additional Parameters - Practical Experiences. Proceedings of the ISP Symposium of Photogrammetry, ISP, Commission III, Stuttgart. Deutsche Geodatische Kommission, Munchen, (1):83 - 89.

- Baz, I. 1984. The Solution of Aerial Triangulation on Vector and Parallel Array Processors. Ph.D. Thesis, University of Glasgow, Two Volumes, 400 pages.

Beyer, E.P., 1985. An Overview of the Thematic Mapper Geometric Correction System. Landsat-4 Science Characterization Early Results, NASA Conference Publication 2355, 2:87 - 145.

Bodechtel, J., 1984. The Information Network for a Real-time Control Data Acquisition of MOMS. Proceedings of IGARSS 84 Symposium, Strasbourg, ESA SP-215:33 - 36.

- Bodechtel, J. et al., 1985. MOMS Missions and Geoscientific Results. Proceedings of EARSeL/ESA Symposium, ESA-233:87 - 90.

- Bodechtel, J., 1987. Comparison of MOMS and Thematic Mapper, Data for Geoscientific Application and Aspects for Future Development of Multispectral Sensors. Remote Sensing for Resources Development and Environmental Management, A.A. Balkema, Rotterdam, 3:5 pages.

- Brock, G.C., 1976. The Possibilities for Higher Resolution in Air Survey Photography. Photogrammetric Record, 8(47):589 - 609.

Brown, D.C., 1974. Bundle Adjustment with Strip- and Block-Invariant Parameters. Proceedings of the ISP Symposium of Photogrammetry, ISP, Commission III, Stuttgart. Deutsche Geodatische Kommission, Munchen, (1):54 - 65.

- Brown, D.C., 1976. The Bundle Adjustment - Progress and Prospects. Invited Paper: Proceedings of the 13th International Congress of

Photogrammetry, ISP, Commission III, Helsinki. International Archives of Photogrammetry,

- Brown, W.M and Porcello, L.J., 1969. An Introduction to Synthetic Aperture Radar. IEEE Spectrum, 6(9):52 - 62.

Butlin, T.J., 1978. The CCRS Digital Image Correction System. Proceedings of the 5th Canadian Symposium on Remote Sensing, Victoria, 1: 271 - 283.

Case, J.B., 1966. The Analytical Reduction of Panoramic and Strip Photography. Photogrammetria, 22(4):124 - 141.

Carter, L.D. and R.C., 1974. Interpretation of Orbital Photographs. Photogrammetric Engineering, 40(2):193 - 197.

- Campbell, J. B., 1987. Introduction to Remote Sensing. Guildford Press, New York, 218 Pages.

- Chen, H.S., 1985. Space Remote Sensing Systems - an Introduction Academic Press, Orlando and London, 200 pages.

- Clark, B.P., 1981. Landsat 3 Return Beam Vidicon Response Artifacts. A Report on RBV Photographic Product Characteristics and Quality Coding System, EROS Data Center, U.S. Geological Survey, Sioux Falls, :13 pages.

Cochrane, G.R. and Browne,, G.H., 1981. Geometric Mapping from Landsat 3 Return Beam Vidicon (RBV) Imagery. Photogrammetric Engineering and Remote Sensing, 47(8):1205 - 1213.

Colvocoresses, A., 1970. ERTS-A Satellite Imagery. Photogrammetric Engineering, 36(6):1303 - 1309.

Colvocoresses, A., 1974. Space Oblique Mercator - A New Map Projection of the Earth. Proceedings of the ISP Symposium of Photogrammetry, ISP, Commission III, Stuttgart. Deutsche Geodatische Kommission, Munchen, (1):259 - 265.

Colvocoresses, A., 1976. The Status and Future of Satellite Image Mapping (Based on Experience of the U.S. Geological Survey) Proceedings of the ISP International Congress, ISPRS, Commission I. International Archives of Photogrammetry, 21(1):6 pages.

- Colvocoresses, A., 1979. Landsat Mapping and Charting by the United States of America. Conference of the Commonwealth Survey Officers. Paper No. D2, 16 pages.

- Colvocoresses, A., 1979. Proposed Parameters for Mapsat. Photogrammetric Engineering and Remote Sensing, 45(4):501 - 506.

- Colvocoresses, A., 1980. Geometric Considerations for an Automated Mapping Satellite (MAPSAT). Presented Paper: Proceedings of the 39th Annual Meeting of the American Congress on Surveying and Mapping (ASP-ASCM), Washington D.C., 10 pages.

- Colvocoresses, A., 1984. Mapping of Washington, D.C. and Vicinity with the Landsat 4 Thematic Mapper. Proceedings of the 50th Annual Meeting of the American Congress on Surveying and Mapping (ASP-ASCM), Washington, D.C., (1) 125 - 133.

- Colvocoresses, A., 1986. Image Mapping with the Thematic Mapper. Photogrammetric Engineering and Remote Sensing, 52(9):1499 - 1505.

- Colwell, N. and Poulton, E., 1984. SPOT Simulation Imagery for Urban Monitoring - A Comparison with Landsat TM, and MSS Imagery and with High Altitude Colour Photography. SPOT Simulation Applications Handbook, Proceedings of the 1984 SPOT Symposium, ASP: 139 - 147.

- Corlay, G., Henry, C. and Paul, J.B. 1984. HRV SPOT Camera Detection Unit: Optical and Radiometric Characteristics. SPOT Simulation Applications Handbook, Proceedings of the 1984 SPOT Symposium, ASP:148 - 156.

- Curran, P.J., 1985. Principles of Remote Sensing, Longman, New York, London, 200 pages.

- Derenyi, E.E. and Konecny, G., 1964. Geometry of Infrared Imagery. The Canadian Surveyor, 18(3):279 - 290.

- Derenyi, E.E., 1966. Infrared Scan Geometry. Photogrammetric Engineering, 32(5):773 - 778.

- Derenyi, E.E., 1972. Geometric Considerations in Remote Sensing. Proceedings of 1st Canadian Symposium on Remote Sensing, Ottawa, 1:547 - 550.

- Derenyi, E.E., 1974. Planimetric Accuracy of Infrared Line Scan Imagery. The Canadian Surveyor, 28(3):247 - 254.

- Derenyi, E.E., 1974. Topographic Accuracy of Side-looking Radar Imagery. Proceedings of the ISP International Symposium of Photogrammetry, ISP Commission III, Stuttgart. Deutsche

Geodatische Kommission, Munchen, (1):244 -250.

Derenyi, E.E. and Szabo L., 1980. Planimetric Transformation of Synthetic Aperture Radar Imagery. Proceedings of the 14th International Congress of Photogrammetry, ISP Commission III, Hamburg. International Archives of Photogrammetry and Remote Sensing, 23(B3):142 - 148.

Derenyi, E.E., 1986. Accuracy of Three Dimensional Coordinate Determination Using Large Format Camera Photography. Proceedings of the Symposium: Mapping from Modern Imagery, ISPRS, Commission IV, Edinburgh. International Archives of Photogrammetry and Remote Sensing, 26(4):14 - 22.

- Derenyi, E.E. and Newton, L., 1987. Control Extension Utilizing Large Format Camera Photography. Photogrammetric Engineering and Remote Sensing, 53(5):495 - 499.

DFVLR, 1980. Spacelab Metric Camera Calibration Certificate. 6 pages.

Downman, I.J., 1978. Topographic Mapping from Space Photography: Further Developments. Photogrammetric Record, 9(52):513 - 522.

- Downman, I.J., Coyle J. and Ward N., 1984. Geometric Correction of Airborne MSS Data. Department of Photogrammetry and Surveying, University of London Report. 85 pages.

- Downman, I.J., Meneguette, A. and Allan, J.A., 1985. Evaluation of Metric Camera Images at the University of London. Metric Camera Workshop, Proceedings of a Joint DFVLR-ESA Workshop, Oberpfaffenhofen, (1):59 - 63.

- Downman, I.J., ¹⁹⁸⁸ The Restitution of Metric Photography Taken from Space. Proceedings of the 16th International Congress of Photogrammetry, ISPRS Commission II/I, Kyoto. International Archives of Photogrammetry and Remote Sensing, 27(2):491 -500.

- Doyle, F.J., 1970. Photographic Systems for Apollo. Photogrammetric Engineering, 36(1):1039 - 1044.

Doyle, F.J., 1971. The Orthographic View from Space. Presented Paper: International Symposium on Orthophotomapping, ISP Commission II, International Archives of Photogrammetry, 19(3):8 pages.

- Doyle, F.J., 1975. Cartographic Application of Satellite

- Imagery. Proceedings of the Commonwealth Survey Officers Conference. Paper No. K.1, 10 pages.
- Doyle, F.J., 1979. A Large Format Camera for Shuttle. Photogrammetric Engineering and Remote Sensing, 45(1):73 - 78.
- Doyle, F.J., 1982. Satellite Systems for Cartography. Proceedings of the Symposium: Advances in the Quality of Image Data, ISP, Commission I, Canberra. International Archives of Photogrammetry and Remote Sensing, 24(1):180 - 186.
- Doyle, F.J., 1984. Surveying and Mapping with Space Data. ITC Publication, Series A, (4):314 - 321.
- Ducher, G., 1980. Cartographic Possibilities of the SPOI and Spacelab Projects. Photogrammetric Record, 10(56):167 - 180.
- Ebner, H., 1976. A Mathematical Model for Digital Rectification of Remote Sensing Data. Presented Paper: Proceedings of the 13th International Congress of Photogrammetry, ISP, Commission III, Helsinki. International Archives of Photogrammetry, 21(3):i2 pages.
- El-Baz, F., 1977. The Meaning of Desert Colour in Earth Orbital Photographs. Photogrammetric Engineering, 44(7):69 - 75.
- El-Baz, F. and Ondrejka, R.J., 1984. Earth Orbital Photography by the Large Format Camera. Proceedings of the International Symposium on Remote Sensing of the Environment, Ann Arbor, Michigan, (2) 1050 - 1066.
- E.M.I. Electronics, 1973. Handbook of Remote Sensing Techniques, The Technology Report Centre, St. Mary Cray, Orpington, 419 pages.
- Engel, H. and Konecny, G., 1985. Orthophotomapping from Metric Camera Imagery. Metric Camera Workshop, Proceedings of a Joint DFVLR-ESA Workshop, Oberpfaffenhofen, (1):13 - 18.
- Engel, H., Muller, W., and Konecny, G., 1986. Application of Spacelab "Metric Camera" Imagery for Map Production. Proceedings of the Symposium: Mapping from Modern Imagery, ISPRS, Commission IV, Edinburgh. International Archives of Photogrammetry and Remote Sensing, 26(4):170 - 182.
- Engel, H. and Muller, W., 1987. Orthocomp Operation of SPOT Imagery. Proceedings of the Seminar on Photogrammetric Mapping

from SPOT Imagery, Hannover, 1:15 pages.

Falcone, N.L., 1982. Landsat-3 RBV Imagery for Topographic Mapping. Proceedings of the Symposium: Environmental Assessment and Resource Management, ISPRS, Commission IV. International Archives of Photogrammetry and Remote Sensing, 24(4):45 - 54.

Faust, H.W., 1980. Orthocomp Z2, The Analytical Orthoprojector from Carl Zeiss. Carl Zeiss, D7082.

- Fleming, E.A., 1976. The Use of Satellite Photography in the National Mapping Program of Canada. Presented Paper: Proceedings of the 13th International Congress of Photogrammetry, ISP, Commission IV, Helsinki. International Archives of Photogrammetry, 21(3):13 pages.

Fleming, E.A., 1985. Some Results of Photogrammetric Compilation and Orthophoto Production Using Space Photography. Proceedings of the ACSM-ASPRS Fall Convention, Technical Papers, (1):51 - 64.

- Forrest, R.B., 1971. Geometric Processing of ERTS Images. Presented Paper: Proceedings of the Fall Convention of the American Society of Photogrammetry, San Francisco: 22 pages.

Forrest, R.B., 1974. Geometric Correction of ERTS-1 Images. Proceedings of the ISP Symposium of Photogrammetry, ISP Commission III, Stuttgart. Deutsche Geodatische Kommission, Munchen, (1):340 - 357.

- Forstner, H., 1982. On the Geometric Precision of Digital Correlation. Proceedings of the Symposium: Mathematical Models, Accuracy Aspects and Quality Control, ISP, Commission III, Helsinki. International Archives of Photogrammetry and Remote Sensing, 24(3):176 - 189.

- Fusco, L., Frei, U. and Hsu A., 1985. Thematic Mapper: Operational Activities and Sensor Performance at ESA/Earthnet. Photogrammetric Engineering and Remote Sensing, 51(9):1299 - 1314.

Fusco, L. and Hsu, A., 1986. Different Scanning Instruments Comparison: MOMS and TM. Earth Remote Sensing Using Landsat Thematic Mapper and SPOT Sensor System, SPIE, 660:159 - 164.

Gambino, A. and Crombie, A., 1974. Digital Mapping and Digital Image Processing. Photogrammetric Engineering, 40(11):1295 - 1302.

Gibson, J.R., 1984. Processing Stereo Imagery from Line Imagers.

Proceedings of the 9th Canadian Symposium on Remote Sensing, 1:471 - 487.

Gierloff-Emden, H.G., 1984. MOMS, Interpretation and Evaluation of the MOMS-image ARICA, West Coast of South America. Proceedings of IGARSS 84 Symposium, Strasbourg, ESA SP-215.

○ Ghosh, S.K., 1979. Analytical Photogrammetry. Pergamon Press, Oxford, 203 pages.

○ Ghosh, S.K., 1987. Photo-Scale, Map-Scale and Contour Interval in Topographic Mapping. Photogrammetria, 42(2):34 - 50.

Goodenough, D.G. and Teillet, P.M., 1979. Correction of Synthetic Aperture Radar and Multispectral Scanner Data Sets. Proceedings of the 13th International Symposium on Remote Sensing of the Environment, Ann Arbor, Michigan, 1:259 - 266.

Goodenough, D.G., 1988. Thematic Mapper and SPOT Integration with a Geographic Information System. Photogrammetric Engineering and Remote Sensing, 54(2):167 - 176.

○ Gorani, M.A., 1980. The Map of the Greater Khartoum. M. App. Sci. Dissertation, University of Glasgow, 92 pages.

Grove, A.T., 1977. Africa. Oxford University Press, London, 337 pages.

Gustafson, G.F. and Loon, J., 1958. Contour Accuracy and the National Map Accuracy Standards. Surveying and Mapping, 42(4):120 - 129.

Gut, D. and Hohle J., 1977. High Altitude Photography: Aspects and Results. Photogrammetric Engineering and Remote Sensing, 43(10):1245 - 1255.

○ Hailey, L., 1957. An African Survey Revised 1956. Oxford University Press, London, 1676 pages.

○ Hardy, J.P., 1985. Geometric Quality of a Thematic Mapper Image of the United Kingdom. Technical Papers, ACSM/ASPRS Fall Convention, Indianapolis: 937 - 948. Also in Earth Remote Sensing Using the Landsat Thematic Mapper and SPOT Sensor Systems, SPIE 660:18 - 24.

○ Hartley, G., 1988. SPOT 1 Image Utilization, Assessment and Results. Photogrammetric Record, 12(71):673 - 677.

Helava U.V., 1978. Instruments and Methods for Digital Terrain Model Data Collection. Proceedings of the Digital Terrain Models (DTM) Symposium, St. Louis, Missouri:61 - 71.

- Herda, K., 1978. Application of Multispectral Photography Using MKF-6 and MSP-4. Proceedings of the International Symposium on Remote Sensing for Observation and Inventory of Earth Resources, ISP, Commission VII, Freiburg. International Archives of Photogrammetry and Remote Sensing, 22(7):12 pages.

Hiller, J. et al., 1984. MOMS-01 Data Catalogue. DFVLR, 59 pages.

Hobbie, D., 1970. Possibilities and Methods of Orthophoto Production. 6th U.N. Regional Cartographic Conference for Asia and the Far East, Teheran: 13 pages.

- Hobbie, D., 1971. Contour Plotting in Orthoprojection Instruments Translation of a Paper Published in Bildmessung und Luftbildwesen.

- Hofmann, O., 1981. DPS - A Digital Photogrammetric System for Producing Digital Elevation Models and Orthophotos by Means of Linear Array Scanner Imagery. Proceedings of the Symposium: Mathematical Models, Accuracy Aspects and Quality Control, ISPRS, Commission III, Helsinki. International Archives of Photogrammetry and Remote Sensing, 24(3):216 -227.

Hofmann, O., 1984. Applications of the Digital Photogrammetric System DPS, A Rigorous Three Dimensional Compilation Process for Push Broom Imagery. International Archives of Photogrammetry and Remote Sensing, 25(A4):10 pages.

- Hofmann, O., 1985. The Influence of The Three Line Stereo Push-Broom Scanner and Flight Parameters on the Accuracy of the DPS-Compilation Process. Proceedings of the ACSM-ASPRS Fall Convention Technical Papers, 1:82 - 90.

- Hofmann, O., 1986. The Stereo-Push-Broom Scanner System DPS and its Accuracy. Proceedings of the Symposium: From Analytical To Digital, ISPRS, Commission III, Rovaniemi. International Archives of Photogrammetry and Remote Sensing, 26 (3):345 - 365.

Hossler, R., 1980. Differential Rectification of Digital or Digitized Imageries. Proceedings of the 14th International Congress of Photogrammetry, ISP Commission III, Hamburg. International Archives of Photogrammetry and Remote Sensing,

Hovanesian, S.A., 1980. Introduction to Synthetic Array and Imaging Radars, Artech House Inc., Washington. 156 pages.

○ Themadu, O., 1985. Satellite Remote Sensing as a Mapping Tool. ITC Journal, 3:187 - 191.

○ Imhof, E., 1965. Kartographische Gelände-Darstellung. Walter De Gruyter and Co., Berlin.

Irons, J.R., 1985. An Overview of Landsat-4 and the Thematic Mapper. NASA Conference Publications 2355, 2:15 - 46.

○ Isong, M., 1987. An Investigation of the Geometric Fidelity of Spaceborne and Airborne Thematic Mapper Imagery and its Potential Application to Topographic Mapping. M. App. Sci. Dissertation, University of Glasgow, 257 pages.

ISP, 1977. Proceedings of the Fifth Biennial Workshop on Color Aerial Photography and Related Fields, EROS Data Centre, Sioux Falls.

○ Jacobsen, K., 1987. Experiences with Space Photographs for Mapping. Proceedings of the International Scientific Colloquium "Use of Space Photographic Data for Mapping of Earth-surface" ISPRS Working Group I/II, Leipzig, 1:137 - 143.

○ Jacobsen, K. and Engel H., 1987. Aerotriangulation with Spacelab Metric Camera Images. Proceedings of EARSeL/ESA Symposium, ESA SP-233.

○ Jacobsen, K. et al., 1988. Geometric Potential of Space Images. Presented Paper: Proceedings of the 16th International Congress, ISPRS, Commission III, Kyoto, International Archives of Photogrammetry and Remote Sensing, 27(3B):12 pages.

Kaufmann, H., Bodechtel J. and Haydn, R., 1984. Spectral Significance of MOMS versus Landsat Data and Future Aspects Preliminary Results. Proceedings of IGARSS 84 Symposium, Strasbourg, ESA SP-215:39 - 44.

○ Keller, M., 1976. Analytic Aerotriangulation Utilizing Skylab Earth Terrain Camera (S-190B) Photography. Photogrammetric Engineering and Remote Sensing, 42(11):1375 - 1383.

Kennie, T.J.M. and Matthew, M.C., 1985. Remote Sensing in Civil

Engineering. Surrey University Press, Glasgow and London, 357 pages.

- Konecny, G. and Derenyi, E.E., 1966. Geometrical Considerations for Mapping from Scan Imagery. Proceedings of the 4th International Symposium of Remote Sensing of the Environment, Ann Arbor, Michigan, 1:327 - 338.
- Konecny, G., 1970. Metric Problems in Remote Sensing. ITC Publications, Series A, (50):152 - 177.
- Konecny, G., 1972. Geometric Aspects of Remote Sensing. Proceedings of the 12th International Congress of Photogrammetry, ISP, Commission III, Ottawa. International Archives of Photogrammetry: 19(4):47 pages.
- Konecny, G., 1974. Approach and Status of Geometric Restitution for Remote Sensing Imagery. Proceedings of the ISP Symposium of Photogrammetry, ISP, Commission III, Stuttgart. Deutsche Geodatische Kommission, Munchen, (1):188 - 198.
- Konecny, G., 1976. Mathematical Models and Procedures for the Geometric Restitution of Remote Sensing. Proceedings of the 13th International Congress of Photogrammetry, ISP, Helsinki. International Archives of Photogrammetry, 21(3):11 pages.
- Konecny, G. et al., 1979. Status of World Cartography. Report by Institut fur Photogrammetric und Ingenieurvermessungen, Universitat Hannover. 57 pages.
- Konecny, G., 1979. Methods and Possibilities for Digital Differential Rectification. Photogrammetric Engineering and Remote Sensing, 45(6):727 - 734.
- Konecny, G., 1980. The Potential of Space Imagery to Solve Cartographic Problems. Paper Presented to the 4th United Nations Regional Cartographic Conference for Africa and East Asia, Abidjan, 4:188 - 198.
- Konecny, G., Schuhr W. and Wu J., 1982. Investigations of the Interpretability of Images by Different Sensors and Platforms for Small Scale Mapping. Proceedings of the International Symposium: Advances in the Quality of Image Data, Canberra. International Archives of Photogrammetry and Remote Sensing, 24(1):11 - 22.
- Konecny, G., 1983. Trends in Digital Photogrammetry. EDIS 83, Earth Data Information Systems Symposium, Pretoria. 17 pages.

- Konecny, G. et al., 1984. Investigation of Metric Camera Data Quality. Proceedings of the 15th Congress of Photogrammetry, ISPRS, Commission III, Rio De Janeiro. International Archives of Photogrammetry and Remote Sensing, 25(A8a):10 pages.
- Konecny, G., 1987. Geometric Evaluation of SPOT Imagery. Seminar on Photogrammetric Mapping from SPOT Imagery, University of Hannover: 36 pages.
- Konecny, G. et al., 1987. Evaluation of SPOT Imagery on Analytical Photogrammetric Instruments. Seminar on Photogrammetric Mapping from SPOT Imagery, University of Hannover. 11 pages. Also in Photogrammetric Engineering and Remote Sensing, 53(9):1219 - 1230.
- Kraemer, J., 1988. Map Production and Revision with Satellite Photographs Taken by the MKF-6 Camera and by the Cameras KATE-140, KATE-200 and KFA-1000. Proceedings of the 17th International Congress of Photogrammetry, ISPRS, Commission II/I, Kyoto. International Archives of Photogrammetry and Remote Sensing, 27(2):506 - 512.
- Kratky, V., 1971. Precision Processing of ERTS Imagery. Proceedings of the ASP Fall Convention, Technical Papers:481 - 489.
- Kratky, V., 1972a. Photogrammetric Aspects of Precision Processing of ERTS Imagery. Proceedings of the 1st Canadian Symposium on Remote Sensing, Ottawa, 19(4/1):505 - 525.
- Kratky, V., 1972b. Photogrammetric Solution for Precision Processing of ERTS Images. Presented Paper: Proceedings of the 12th International Congress of Photogrammetry, ISP, Commission III, Ottawa. International Archives of Photogrammetry, 19(4/2):13 pages.
- Kratky, V., 1974. Cartographic Accuracy of ERTS. Photogrammetric Engineering, 40(2):203 - 212.
- Kraus, K., et al., 1979. Digitally Controlled Production of Orthophoto and Stereo-orthophoto. Photogrammetric Engineering and Remote Sensing, 45(10): 1353 - 1362.
- Kruck, E., 1987. BINGO - Bundle Block Adjustment Program for SPOT Data. Proceedings of the Seminar on Photogrammetric Mapping from SPOT Imagery, Hannover. 12 pages.

- Kubik, K., 1987. A Note on Photogrammetric Block Adjustment with Additional Parameters. Photogrammetric Engineering and Remote Sensing, 53(11):1531 - 1532.
- Larsson, J., 1980. The Use of a DTM in a Digital Multispectral Analysis. Proceedings of the 14th International Congress of Photogrammetry, ISP Commission VII, Hamburg. International Archives of Photogrammetry and Remote Sensing, 21(7):530 - 537.
- Leatherdale, J.D., 1978. The Practical Contribution of Space Imagery to Topographic Mapping. Proceedings of the Inter - Congress Symposium, ISP, Commission IV, Ottawa. International Archives of Photogrammetry, 22(4):425 - 444.
- Leckie, D.G., 1980. Use of Polynomial Transformations for Registration of Airborne Digital Line Scan Images. Proceedings of the 6th Canadian Symposium on Remote Sensing, Halifax, Nova Scotia, 2:635 - 641.
- Letts, P.J., and Rochon, G. 1980. Generation and Use of Digital Terrain Elevation Data for Large Areas. Proceedings of the 6th Canadian Symposium on Remote Sensing, Halifax, Nova Scotia, 1:642 - 654.
- Lillesand, T.M., 1976. Fundamentals of Electromagnetic Remote Sensing, Syracuse, New York. 400 pages
- Lillesand, T.M. and Kiefer, R., 1979. Remote Sensing and Image Interpretation. 1st Edition, John Wiley and Sons, New York. 660 pages.
- Lillesand, T.M., and Kiefer R. 1987. Remote Sensing and Image Interpretation. 2nd Edition, John Wiley and Sons, New York. 721 pages.
- Lo, C.P., 1986, Applied Remote Sensing. Longman Scientific Technical, New York. 393 pages.
- Lowman, 1969. Apollo 9 Multispectral Photography; Geological Analysis. Goddard Space Flight Centre X-644-69-423.
- Makarovic, B., 1973. Progressive Sampling for Digital Terrain Models. ITC Journal, (3):397 - 415.
- Makarovic, B., 1977 Composite Sampling for Digital Terrain Models. ITC Journal, (3):406 - 431.

- Makarovic, B., 1984. Selective Sampling for Digital Terrain Modelling. Proceedings of the 15th International Congress of Photogrammetry, ISPRS, Commission IV, Rio De Janeiro. International Archives of Photogrammetry and Remote Sensing, 25(A4): 12 pages.
- Markarian, H., 1973. Digital Correction for High Resolution Images. Photogrammetric Engineering, 39(12):1311 - 1320.
- Marsden, L.E., 1960. How the National Map Accuracy Standards were Developed. Surveying and Mapping, 20(4):427 - 439.
- Masry, S., 1969. Analytical Treatment of Strip Photographs. Photogrammetric Engineering, 35(12):1325 - 1262.
- Masry, S. and Gibbons, J., 1973. Distortion and Rectification of IR-Imagery. Photogrammetric Engineering, 39(8):845 - 849.
- M.B.B, 1984. MOMS-01 Announcement of Opportunity. University of Munich Press.
- McCullagh, M.J., 1979. Triangular Systems in Surface Representation. Proceedings of the International Symposium on Cartography and Computing, U.S.A (1):146 - 153.
- McCullagh, M.J., 1983. 'If You're all sitting comfortably then we'll begin'. Workshop Notes on Terrain Modelling, Australian Computing Society, Siren Systems. 158 pages.
- McEwan, R., 1971. Geometric Calibration of the RBV System for ERTS. Proceedings of the 7th International Symposium on Remote Sensing of the Environment, Michigan, 2:791 - 807.
- McEwan, R. and Schoonmaker, W., 1974. ERTS Colour Image Maps. Presented Paper: Proceedings of the ACSM-ASP Fall Convention, Washington D.C., 2 pages.
- Methley, B.D.F., 1986. Computational Models in Surveying and Photogrammetry. Blackie, Glasgow and London. 346 pages.
- Mikhail, E.M. and Baker, J.R., 1973. Geometric Aspects in Digital Analysis of Multi-Spectral Scanner (MSS) Data. Presented Paper: Proceedings of the ASP Annual Meeting, ASP, Washington D.C., 34 pages.
- Mikhail, E.M., 1983. Investigation of Generation and Analysis of

Digital Terrain Model (DTM) Data. Surveying, Mapping and Photogrammetry, CE - PH - 82, (3):1 - 93.

- Mills, D.L., 1955. The African Arc of the 30th Meridian: Completion of the Triangulation. Proceedings of the Commonwealth Survey Officers Conference:399 - 412.
- Mott, P.G. and Chismon, H.J., 1975. The Use of Satellite Imagery for Very Small Scale Mapping. Photogrammetric Record, 8(46):458 - 475.
- Murai, S. and Shibasaki, R., 1982. Automated Mapping from Linear Array Sensor Data. Proceedings of the International Symposium of Photogrammetry, ISPRS, Commission IV Symposium, Virginia. International Archives of Photogrammetry and Remote Sensing, 24(4):483 - 492 .
- Murai, S. and Matsuoka, R., 1985. Accuracy of Three Dimensional Measurement Using Stereo Space Photographs Taken by Zeiss Metric Camera of SpaceLab 1. Proceedings of the 51st ASPRS Annual Meeting, ASP, Washington D.C., 1:177 -184.
- NASA, 1967a. Earth Photographs from Gemini 3, 4, 5: NASA SP-129.
- NASA, 1967b. Terrain Photography on the Gemini IV Mission: Preliminary Report: NASA TND-3982.
- NASA, 1974. Skylab Earth Resources Data Catalogue.
- NASA, 1978. Skylab EREP Investigation: Summary Prepared by NASA Lyndon Johnson Space Centre, NASA SP-399.
- NASA, 1979. Apollo Soyuz Test Project NASA SP-412.
- Petrie, G., 1970. Some Considerations Regarding Mapping from Earth Satellites. Photogrammetric Record, 6(36):590 - 624.
- Petrie, G., 1974. Mapping from Earth Satellites. Proceedings of PTRC Summer Annual Meeting, University of Warwick. Paper No. 9:20 pages.
- Petrie, G., 1977. Orthophotomaps. Transactions, Institute of British Geographers, 1977, (1):49 - 68.
- Petrie, G., 1978. The Status of Topographic Mapping from Space Imagery. Remote Sensing and National Mapping, Proceedings of the 5th Annual Conference of the Remote Sensing Society, University of

Durham. 16 pages.

Petrie, G., 1976. Geometric Aspects and Cartographic Applications of Side-looking Radar. Presented Paper, 5th Annual Conference of the Remote Sensing Society, University of Durham, 21 pages.

- Petrie, G., 1981. Hardware Aspects of Digital Mapping. Photogrammetric Engineering and Remote Sensing, 47(3):307 - 320.

Petrie, G., 1984. The Philosophy of Digital and Analytical Photogrammetric Systems. Proceedings of the 39th Photogrammetric Week, Stuttgart University 39(1):53 - 67.

- Petrie, G., 1985. Remote Sensing and Topographic Mapping. A Chapter in Kennie and Matthew - Remote Sensing in Civil Engineering. Surrey University Press, London.

- Petrie, G. and Kennie, T.J.M, 1986. Terrain Modelling in Surveying and Civil Engineering. Paper Presented at the Conference on 'State of the Art in Stereo and Terrain Modelling', British Computer Society. 32 pages.

- Petrie, G., 1987a. Photogrammetric Methods of Data acquisition for Terrain models. Terrain Modelling in Civil Engineering, Proceedings of a Short Course held at the University of Surrey/University of Glasgow. 20 pages.

- Petrie, G., 1987b. Terrain Data Acquisition from Existing Maps. Terrain Modelling in Civil Engineering, Proceedings of a Short Course held at the University of Surrey/University of Glasgow. 26 pages.

- Petrie, G., 1987c. Data Interpolation and Contouring Methods. Terrain Modelling in Civil Engineering, Proceedings of a Short Course held at the University of Surrey/University of Glasgow. 15 pages.

- Picht, G., 1987a. Processing of SPOT Images with BINGO. Proceedings of the Seminar on Photogrammetric Mapping from SPOT Imagery, Hannover. 15 pages.

Picht, G., 1987b. Planicomp Operation with SPOT Imagery. Proceedings of the Seminar on Photogrammetric Mapping from SPOT Imagery, Hannover. 18 pages.

- OSD, 1986. An Evaluation of Spacelab Metric Camera Imagery of Sudan. Report Y01AAD by the Overseas Surveys Directorate (OS) of

Great Britain. 13 pages.

- Read, D. and Lane, C.J.B., 1976. Two Slanted Views of Antarctica. Photogrammetric Record, 8(48):726 - 747.

Roberts, P.A., 1981. The Use of Terrain Height Information with Satellite Imagery. Paper Presented: Conference on Matching Remote Sensing Technologies and Their Applications, London. 14 pages.

Rosenholm, D., 1986. Accuracy Improvement of Digital Matching for Evaluation of Digital Terrain Models. Proceedings of the Symposium: From Analytical to Digital, ISP Commission III, Rovaniemi. International Archives of Photogrammetry and Remote Sensing, 26(3):573 - 587.

Sabins, F.F., 1978. Remote Sensing Principles and Interpretation, Freeman Press, San Francisco. 426 pages.

Salomonson, V.V., 1978. Landsat-4 Systems Overview. Proceedings of the 12th International Symposium on Remote Sensing of the Environment, Ann Arbor, Michigan, 12(1):371 - 377.

Sawada, N. et al, 1981. An Analytical Correction Method for Satellite MSS Geometric Distortions. Photogrammetric Engineering and Remote Sensing, 47(8):1195 - 1203.

- Schade, O., 1971. Television Cameras. International Workshop on Earth Resources Survey Systems, NASA SP-283:245 - 261.

Schroeder, M., 1983. The Metric Camera Experiment on the First Spacelab Flight. Earth Observations and Remote Sensing by Satellites, Acta Astronomica 2(1):73 - 80.

- Simmons, J.W., 1976. Instruction Manual for the Preparation of a Topographical Map at the Scale 1:100,000, UNDP SUD - 70/542, 2.

- Singels C., 1968. Accuracy Specifications in Mapping. South African Survey Journal, 3:19 - 26.

- Sherwin, S.W., Ruina, J.P and Rawcliffe, R.D., 1962. Some Early Developments in Synthetic Aperture Radar Systems. IRE Transactions on Military Electronics, Vol. MIL-5:111 - 115.

- Shortis, M.R., 1980. Sequential Adjustments of Photogrammetric Models. Ph.D. Thesis, The City University, London. 247 pages.

Slater, P.N., 1980. Remote Sensing Optics and Optical Systems.

Addison-Wesley, London, 212 pages.

Smith, J.W., 1957. The Effects of Earth's Curvature and Refraction on the Mensuration of Vertical Photographs. Photogrammetric Engineering, 23(4):595 -599.

○ Snowsill, D.M., 1985. Ordnance Survey Experience With Photography from Space. Photogrammetric Record, 11(66):1593 - 1602.

○ Snyder, J.P., 1982. Geometry of a Mapping Satellite. Photogrammetric Engineering and Remote Sensing, 48(10):1593 - 1603.

Stewardson, P.B., 1976. The Wild Avioplan OR-1 Orthophoto System. Presented Paper: Proceedings of the 13th International Congress of Photogrammetry, ISP Commission III, Helsinki. International Archives of Photogrammetry, 21(3):33 pages.

○ Stone, C., 1982. The District Map: An Episode in British Colonial Cartography in Africa, with Particular Reference to Northern Rhodesia. The Cartographic Journal, 19(2):104 - 112.

Swain, P.H. and Davis S.M., 1978. Remote Sensing the Quantitative Approach, McGraw-Hill, New York. 396 pages.

○ Swithinbank, C. and Lane C., 1975. Antarctic Mapping from Satellite Imagery. Proceedings of the Commonwealth Survey Officers Conference, K3: 11 pages.

○ Taranik, J.V. and Thome P.G., 1980. Development of Space Technology for Resource Applications. Presented Paper: Proceedings of the 14th International Congress of Photogrammetry, ISP Commission II, Hamburg. International Archives of Photogrammetry and Remote Sensing, 23(B3):539 - 554.

○ Taylor, J.I, 1971. Rectification Equations for Infrared Line-Scan Imagery. ITC Publications Series A, (50):178 - 193.

○ Tham, P., 1968. Aerial Map Accuracy in Photogrammetry - European Standard Error V. American C-Factor. Svensk Landmateritidskrift, (2):12 pages.

○ Thompson, M.M., 1960. A Current View of the National Map Accuracy Standards. Surveying and Mapping, 20(4):449 - 457.

Thompson, M.M., 1979. Maps for America - Cartographic Products of the U.S. Geological Survey and Others. U.S. Department of the

Interior, Geological Survey National Centre, Virginia, 265 pages.

- Thrower, J.W., 1970. Satellite Photography as a Geographic Tool for Land-use Mapping of the South Western U.S. U.S.G.S. Technical Report, 69 - 3.

Togliatti, G. and Moricndo, A., 1985. Evaluation of the Accuracy of the Metric Camera Images for the Production of Line Maps and Orthophotos. Metric Camera Workshop, Proceedings of a Joint DFVLR-ESA Workshop, Oberpfaffenhofen (1):29 - 34.

- Townshend, J.R.G., Williams, D.F. and Justice, C.O., 1980. An Evaluation of Landsat 3 REV Imagery for an Areaa of Complex Terrain in Southern Italy. Proceedings of the 6th Canadian Symposium on Remote Sensing, Halifax, Nova Scotia, 3:1839 - 1852.

- Trinder, J.C. and Nasca, S.U., 1976. Tests on the Mapping Application of Landsat Imagery. Presented Paper: Proceedings of the 13th International Congress of Photogrammetry, ISP Commission III, Helsinki. International Archives of Photogrammetry, 21(3): 8 pages.

- U.N., 1976. World Cartography, Department of Economic and Social Affairs. United Nations, New York, Study no. ST/ESA/SER.L/14.

- U.N., 1983. World Cartography, New York, 17.

- U.S.G.S., 1979. Landsat Data Users Handbook.

- U.S.G.S. and NOAA, 1984. Landsat-4 Data Users Handbook.

Welch, R., 1974. Image Evaluation Techniques. Proceedings of the Symposium on Remote Sensing and Aerial Photography, ISP, Commission I, Stockholm. International Archives of Photogrammetry, 20(1):20 pages.

Welch, R. and Lo, C.P., 1977. Height Measurements from Satellite Images. Photogrammetric Engineering and Remote Sensing, 43(10):1233 - 1242.

- Welch, R., 1981. Cartographic Potential of Spacecraft Line-Array Camera System: Stereosat. Photogrammetric Engineering and Remote Sensing, 47(8):1173 - 1185.

- Welch, R., 1982. Image Quality Requirements for Mapping from Satellite Data. Proceedings of the Symposium: Advances in the Quality of Image Data, ISPRS, Commission I, Canberra.

International Archives of Photogrammetry and Remote Sensing, 24(1):50 - 54.

- Welch, R. and Pannell, C.W., 1982. Comparative Resolution of Landsat-3 MSS and RBV Image Data of China. Photogrammetric Record, 10(59):575 - 586.

- Welch, R., 1983. Impact of Geometry on Height Measurements from MLA Digital Image Data. Photogrammetric Engineering and Remote Sensing, 49(10):1437 - 1441.

Welch, R., Jordon, T.R. and Ehler, M., 1985. Comparative Evaluations of the Geodetic Accuracy and Cartographic Potential of Landsat-4 and Landsat-5 Thematic Mapper Image Data. Photogrammetric Engineering and Remote Sensing, 51(9):1231 - 1237.

- Wiesel, W., and Behr, F.J., 1987. Digital Orthophoto Generation Using the Kern DSR-11 Analytical Stereo Restitution Instrument. Proceedings of the ASPRS-ACSM Annual Convention, 2:216 - 224.

- Williams, S. et al., 1983. New Bedford Quadrangle, Massachusetts, A Prototype 1:100,000 scale Landsat-3 Return Beam Vidicon (RBV) Image Map. Presented Paper: Proceedings of the 17th International Symposium on Remote Sensing of the Environment, Michigan, 2:715 - 729.

- Wise, P.J. and Trinder, J.C., 1987. Assessment of SIR-B for Topographic Mapping. Photogrammetric Engineering and Remote Sensing, 53(11):1539 - 1544.

- Wobber, F.J., 1970. Orbital Photos Applied to the Environment. Photogrammetric Engineering, 36(8):852 - 864.

Wolf, P., 1983. Elements of Photogrammetry. 2nd Edition, McGraw-Hill International Book Company. 628 pages.

- Wong, K.W., 1968. Geometric Calibration of Television Systems for Photogrammetric Applications. Proceedings of the 11th International Congress of Photogrammetry, ISP, Commission V, Lausanne. International Archives of Photogrammetry, 17(5) 40 pages.

- Wong, K.W., 1969. Geometric Distortions in Television Imageries. Photogrammetric Engineering, 35(5):493 - 500.

- Wong, K.W., Gamble, E.F. and Riggins, R.E., 1972. Analysis of RBV Television System. Proceedings of the ASP Annual Convention, Washington D.C. Also in Photogrammetric Engineering, 39(8):851 -

- Wong, K.W., 1975. Geometric and Cartographic Accuracy of ERTS-1 Imagery. Photogrammetric Engineering and Remote Sensing, 41(5):621 - 635.
- Wright, J.W., 1951. Reconnaissance Mapping from Trimetrogon Air Photographs in Anglo-Egyptian Sudan. Empire Survey Review, 11(79):2 - 16.
- Wright, J.W., 1967. Three Types of Reconnaissance Mapping. Cartographic Journal, 2(1):16 - 22.
- Yater, R.R., 1970. 12th Parallel Survey. Proceedings of the Commonwealth Survey Officers Conference, K2:7 pages.
- Zickler, D.A., 1978. Design and Technical Parameters of the MKF-6 Multispectral Camera and the MSP-4 Multispectral Projector. International Symposium on Remote Sensing of the Environment, Manila. 26 pages.
- ASP, 1944. Manual of Photogrammetry, 1st Edition, Pitman Publishing Corporation, New York, 839 pages.
- Bahr, H.P. and Schuhr, W., 1974. Versuche Zur Ermittlung der Geometrischen Genauigkeit von ERTS Multispectralbildern. Bildmessung und Luftbildwesen.
- Bender, L.U. and Falcone, N.L., 1982. Landsat-3 RBV Imagery for Topographic Mapping. Proceedings of the 5th International Symposium on Computer-Assisted Cartography (Auto-Carto 5), 10 pages.
- Colvocoresses, A., 1973. EROS Cartographic Progress. Photogrammetric Engineering, 40(12):1303 - 1309.
- Dosiere, P. and Justice, C., 1983. Spatial and Radiometric Resolution of the Landsat-3 RBV System. International Journal of Remote Sensing, 4(2):447 - 455.
- Ducher, G., 1985. Metric Camera Data: Assessment and Potential Use at L' Institut Geographique National. Photogrammetric Record, 11(66):671 - 689.
- El Hassan, I.M., 1978. Metric Aspects of Reconnaissance Frame Photography, Ph.D. Thesis, University of Glasgow, 403 Pages.

- Goodenough, D.G. et al., 1983. A Preliminary Assessment of Landsat-4 Thematic Mapper Data. Proceedings of the Landsat-4 Scientific Characterization Early Results Symposium, NASA Goddard Space Flight Centre, Greenbelt, Maryland, 3:257 - 272.
- Institute of Photogrammetry, Vienna, 1986. Program System SCOP to Create, Maintain and Apply Digital Terrain Models. Technical University of Vienna, 13 pages.
- Jacobsen, K., 1985. Geometric Aspects of the Use of Space Photographs, Proceedings of EARSel/ESA Symposium, ESA SP-252.
- Kennie, T.J.M., 1987. Field Data Collection for Terrain Modelling. Proceedings of a Short Course held at the University of Surrey/University of Glasgow, 10 pages.
- Konecny, G., 1975. Analytical Relations for the Restitution of Dynamic Remote Sensing Imagery. A Report Submitted to E.R.D. - E.T.L. Conference, University of Glasgow.
- Kraus, K., 1970. The Production of Photomaps. Bildmessung und Luftbildwesen, 38:209 - 216.
- Markarian, H. et al., 1971. Implementation of Digital Techniques for Correcting High Resolution Images. Proceedings of the ASP Fall Meeting, 13 pages.
- Mott, P.G., 1975. Application of Satellite Imagery to Small Scale Mapping. Proceedings of the ASP-ACSM Semi-Annual Convention, Phoenix, (2):320 - 327.
- NASA, 1968. Applications of Gemini IV Photography, NASA TND-3985.
- NASA, 1973. Advanced Scanners and Imaging Systems for Earth Observations, NASA SP-335.
- Pannell, C.W. and Welch, R., 1980. Recent Growth and Structural Change in Chinese Cities. Urban Geography, 1(1):68 - 80.
- Steiner D. and Kirby M.E., 1977. Geometrical Referencing of Landsat Images by Affine Transformation and Overlaying of Map Data. Photogrammetria, 33:41 - 75.
- Stewart, R.B., 1975. Mapping from Satellite Photography. Proceedings of the Commonwealth Survey Officers Conference, K2.
- Thormodsgard, J.M., 1983. Geodetic Accuracy of Landsat-4

Multispectral Scanner and Thematic Mapper Data. Proceedings of the Landsat-4 Scientific Characterization Early Results Symposium, NASA Goddard Space Flight Centre, Greenbelt Maryland, 3:273 - 285.

- Togliatti, G., 1987. Topographic Mapping by Space Borne Cameras. Proceedings of the International Scientific Colloquium, ISPRS, Leipsig, :131 - 136.

- Wiesel, J., 1985. Digital Image Processing for Orthophoto Generation. Photogrammetria, 40:69 - 76.



GEOMETRIC ACCURACY TESTING, EVALUATION AND APPLICABILITY

OF

SPACE IMAGERY

TO

THE SMALL SCALE TOPOGRAPHIC MAPPING OF THE SUDAN

BY

ABDELAZIM ELNIWEIRI HASSAN ELNIWEIRI

B.Sc. Eng. (Honours)

Thesis Submitted for the Ph.D. Degree
in Photogrammetry and Remote Sensing
to the
University of Glasgow.

Volume II

Department of Geography and Topographic Science.
October, 1988.

APPENDICES

- APPENDIX A: Space Resection and Intersection.
- APPENDIX B: Computer Programs.
- APPENDIX C: Plots of Residuals for the MSS and TM Images.
- APPENDIX D: Plots of Residuals for the MOMS Images.
- APPENDIX E: Plots of Residuals for the RBV Images.
- APPENDIX F: Plots of Residuals for the MC and LFC Photographs.

APPENDIX A

SPACE RESECTION AND INTERSECTION

A.1 SPACE RESECTION

The problem of space resection in photogrammetry is concerned with the recovery of the exterior orientation elements of the camera at the instant of exposure based on known ground coordinates of at least three points. Collinearity condition equations are usually utilized for this purpose. Since the ground coordinates of the points are known, equations (10.4) reduce to the following:

$$\begin{aligned} (p_{12} \cdot dw + p_{13} \cdot d\phi + p_{14} \cdot dk - p_{15} \cdot dx_o - p_{16} \cdot dy_o - p_{17} \cdot dz_o) / q &= - p_{11} / q \\ (p_{22} \cdot dw + p_{23} \cdot d\phi + p_{24} \cdot dk - p_{25} \cdot dx_o - p_{26} \cdot dy_o - p_{27} \cdot dz_o) / q &= - p_{21} / q \\ &\dots\dots (A.1) \end{aligned}$$

If more than three control points are available, then a least squares solution is used. For this solution, equations (A.1) are put in the form:

$$(V_i) + (B_i) (\Delta) = (F_i^o) \quad \dots\dots (A.2)$$

in which:

$$(B_i) = \begin{pmatrix} p_{12} & p_{13} & p_{14} & -p_{15} & -p_{16} & -p_{17} \\ p_{22} & p_{23} & p_{24} & -p_{25} & -p_{26} & -p_{27} \end{pmatrix}_i$$

Δ = corrections to the initial estimates of the orientation parameters.

(V_i) and (F_i^o) are the residuals in the image coordinates; and the values $-p_{11}/q$, $-p_{21}/q$ of F of equation 10.4 evaluated using the approximate values the parameters, respectively.

Approximate initial values are assumed for the exterior orientation elements. These initial values are substituted in equations (A.1) to evaluate F^0 and in the partial derivative equations to evaluate $p_{12}, p_{13}, \dots, p_{17}$. The solution of equations (A.2) gives corrections to the approximate initial values. These corrections are added to give a better approximation for the elements of exterior orientation which are then substituted and the process is repeated. The solution is iterated until the corrections for the exterior orientation elements reach a certain pre-defined limit.

A.2 SPACE INTERSECTION

Space intersection is the reverse of space resection in that the orientation parameters are now known and the object coordinates of points have to be determined. For the intersection operation, equations (10.2) are written as:

$$\begin{pmatrix} X_i - X'_0 \\ Y_i - Y'_0 \\ Z_i - Z'_0 \end{pmatrix} = S'.M'^T \begin{pmatrix} x'_i \\ y'_i \\ -f \end{pmatrix} \dots\dots\dots (A.3a)$$

and

$$\begin{pmatrix} X_i - X''_0 \\ Y_i - Y''_0 \\ Z_i - Z''_0 \end{pmatrix} = S''.M''^T \begin{pmatrix} x''_i \\ y''_i \\ -f \end{pmatrix} \dots\dots\dots (A.3b)$$

in which the single and double primes refer to the left and right photos respectively. For each object point, six equations can be formed in which five unknowns are to be determined, namely S', S'', X_i, Y_i and Z_i . S' and S'' may be determined first in terms of the other three as follows:

$$S' = \frac{(X''_0 - X'_0) \cdot W''_i - (Z''_0 - Z'_0) \cdot U''_i}{U'_i W''_i - U''_i W'_i} \dots\dots (A.4)$$

$$S'' = \frac{(Z''_0 - Z'_0) \cdot U'_i - (X''_0 - X'_0) \cdot W''_i}{U'_i W''_i - U''_i W'_i}$$

where:

$$\begin{pmatrix} U'_i \\ Y'_i \\ W'_i \end{pmatrix} = M'^T \begin{pmatrix} x'_i \\ y'_i \\ -f \end{pmatrix}$$

$$\begin{pmatrix} U''_i \\ Y''_i \\ W''_i \end{pmatrix} = M''^T \begin{pmatrix} x''_i \\ y''_i \\ -f \end{pmatrix}$$

These values can then be substituted in equations (A.3) to give the ground coordinates X_i , Y_i and Z_i .

APPENDIX B

COMPUTER PROGRAMS

In this Appendix, the computer programs used in this investigation are described. Detailed descriptions and listings of programs which have been written or substantially modified by the author to suit the purpose of the geometric test are given where it is felt appropriate. The listed programs are extensively commented to aid the explanation of each step. Samples of input and output files are also given and explained.

B.1 PROGRAM LINCON

This program was originally written by Dr. A. Hsu and is available in the Departmental program library. The program carries out the linear conformal transformation using a set of control points to compute the transformation parameters. These are then used to compute the ground coordinates of a set of check points and to compare the result with the ground coordinates of these points which could be provided by survey methods or scaled from existing maps. The r.m.s.e. values in easting, northing and vector are computed for both the check and control points individually.

B.2 PROGRAM POLY20

As mentioned in Chapter 4, this program is available in the Departmental program library being written originally by Dr. A. Hsu to carry out polynomial transformations of radar imagery. The modification introduced by the present author comprises the incorporation of the 20 term polynomials of equation (8.3) which were originally developed by Wong (1975). The program carries out the required polynomial transformation using a set of control points to compute the transformation parameters which are then used to compute the ground coordinates of a set of check points. The program operates in such an interactive manner that the operator can specify any number of terms between 3 to 20 to be used in each individual run.

B.3 PROGRAM SPRES

As mentioned in Chapter 8, this program was originally written

by Dr. El Hassan and a complete description of it is given in El Hassan (1978). The modifications which have been made by the present author to the program are discussed below:

B.3.1 Space Resection with Additional Parameters:

For the conventional space resection case, the linearized collinearity equations can be written as in equations 10.4 and 10.5. The least squares solution of equation 10.5 is given as:

$$X = (B^T B)^{-1} \cdot B^T \cdot L \quad \text{.....B.2}$$

However, when the parameters of equation (8.5) are added to the observation equations, the resulting equation can be written in the form:

$$V = B_1 X + B_2 X_2 - L \quad \text{.....B.3}$$

in which $B_2 \cdot X_2$ represents the additional parameters of equation (8.5).

where:

$$B_2 = \begin{pmatrix} x & y & x \cdot r^2 & x r^5 & 1 \\ -x & y & y \cdot r^2 & y^5 & 1 \end{pmatrix}; \text{ and}$$

$$X_2 = \begin{pmatrix} a_1 & a_2 & c_1 & c_2 & d_1 \\ a_1 & a_2 & c_1 & c_2 & d_2 \end{pmatrix}$$

The intersection phase in this program is carried out as explained in Chapter 10.

B.4 PROGRAM REFOTO

REFOTO carries out the interior orientation and measured image coordinates refinement. It also transforms the comparator coordinates of points measured in different comparator reference systems into a common coordinate system. This is extremely useful when, for any reason, the operator is not able to complete the measurements on a model in one measuring session. If the calibration data of the taking camera, giving the fiducial marks coordinates, are available, then the common coordinate system may

be that of the fiducial marks. The program also carries out image coordinate refinement by applying corrections for radial lens distortion and Earth's curvature. The output can be selected to be in the format of the input files to the RELOR and REDUCT computer programs which will be described in B.5 and B.7 respectively. The listing of the program is given in B.4.2. As can be seen from this listing, the program is broken up into blocks, each carrying a specific function to assist the explanation of the operations executed by the program.

- Block 1: Displays the title of the program and reads in the calibration data such as the focal length, the fiducial marks' coordinates and the radial lens distortion values.

- Block 2: Reads in the observation data for the fiducial marks and computes the mean and standard deviation at each fiducial mark.

- Block 3: Transforms the measured comparator coordinates of the fiducial marks to the calibrated coordinate system using either the linear conformal transformation, the affine or the deformational transformation as described in Appendix A, and computes the transformation coefficients.

- Block 4: Computes the rotation and translation parameters from the measured fiducial marks' coordinates. These are necessary to reduce the measured coordinates to the image coordinate system in the case where no calibrated coordinates are available.

- Block 5: Using the computed transformation coefficients computed in Block 3, it transforms the measured coordinates of the points to the image coordinate system. It also carries out the corrections for radial lens distortion and Earth's curvature by calling the subroutines RADIS AND ERTCRV respectively to output refined image coordinates.

- Block 6: Handles the output of the refined image coordinates. Two options are offered: (i) in the format of the observation file read in by REDUCT program; and (ii) in the format of the input file to RELOR program.

B.4.2 PROGRAM LISTING

PROGRAM REFOTO

```
C*****
C*READS INPUT PARAMETERS FOR AND PERFORMS INTERIOR ORIENTATION. *
C*RADIAL LENS DISTORTION AND EARTH'S CURVATURE CORRECTIONS ARE *
C*CARRIED OUT AND THE OUTPUT FILE CAN BE SELECTED TO BE IN THE *
C*FORM OF AN INPUT FILE TO REDUCT AND RELOR PROGRAMS. *
C* *
C*****
      IMPLICIT DOUBLE PRECISION(A-H,O-Z)
      CHARACTER*20 CONFIL,OBSFIL,ANS1,ANS2
      LOGICAL ICON,IOBS,ITITLE(70)
C
      DOUBLE PRECISION A(3),O(3),F(3),V(4,4),AR(3),RIS(200,3),
1RIST(200,4),TX(30,4),KA(2),P(2),W(2),
      INTEGER FC
      COMMON /BO/C(30,4),NC(30),U(2,30,3),AC(4,30),AL(36),AY(12),
1Q(12),AV(30,4),SQ(4),AQ(30,4),SX(30,4),VL(12),NF,FC
2FL1,FL2,FH,TH
      COMMON /B1/PV(21),XS,YS,NR,ID,SP/B2/AN(2,8)/B3/CO,D1,D2
      DATA GR,IM,LU,IC,/63.66198,3*0/
C
C      _____ BLOCK 1: READS IN CALIBRATION DATA _____
C
C      OPEN CONTROL FILE.
C
C      WRITE(6,20)
20  FORMAT(/' TYPE CONTROL FILE NAME  >')
      READ(5,30) CONFIL
30  FORMAT(A20)
      OPEN(2,FILE= CONFIL ,STATUS='OLD',FORM='FORMATTED')
C
C      CHECK IF DATA FILE APPROPRIATE - ERROR OUT IF NOT.
C
C      READ(2,70) INDIC
      IF(INDIC.NE.1) STOP
C
C      READ AND WRITE TITLE.
C
C      READ(2,50) ITITLE
50  FORMAT(70A1)
      WRITE(6,60) ITITLE
60  FORMAT(/'*****
1*****'/,'*',62A1,'*',/'*****
2*****')
C
C      INPUT INTERIOR ORIENTATION PARAMETERS.
C
C      CHECK IF DATA FILE APPROPRIATE - ERROR OUT IF NOT.
C
C      INPUT INTERIOR ORIENTATION PARAMETERS.
C
C      READ(2,70) NF, D,E
      FL1=D
      FL2=E
70  FORMAT(I5,2F10.3)
```

```

71 FORMAT (A1)
   WRITE(6,80) D,E
80 FORMAT(/'THE FOCAL LENGTHS OF LEFT & RIGHT CAMERAS ARE',/,
11X,F10.3, 'AND',F10.3,'RESPECTIVELY.')
   U(1,1,3)=-D/1000.
   U(2,1,3)=-E/1000.
   READ(2,90) A(1),A(2),A(3),W(1),P(1),K(1)
   READ(2,90) O(1),O(2),O(3),W(2),P(2),K(2)
C
C   IF FIDUCIAL COORDS ARE INCLUDED IN CONTROL FILE FC=1 AND
C   IF NOT FC=0
C
C   READ(2,70) FC
C
C   PRESET FIDUCIAL IDENTIFIERS TO 1,2,3 & 4.
C
C   DO 120 I=1,4
C   NC(I)=I
120 CONTINUE
   IM=1
   IF(FC.EQ.0)GO TO 160
C
C   CONTROL FILE WITH FIDUCIAL COORDINATES.
C
C   WRITE(6,130)
130 FORMAT(/' FIDUCIAL MARK COORDINATES'//'      PT',6X,'X',9X,'Y'/)
   DO 150 I=1,NF
   READ(2,360) NC(I),C(I,1),C(I,2),C(I,3),C(I,4)
360 FORMAT(I5,4F10.3)
   WRITE(6,140)NC(I),C(I,1),C(I,2),C(I,3),C(I,4)
140 FORMAT(I6,4F10.3)
150 CONTINUE
C
C   READ RADIAL LENS DISTORTION CORRECTION PARAMETERS.
C
150 READ(2,210) PV
210 FORMAT(7F10.3)
   READ(2,220)XS,YS
220 FORMAT(2F10.3)
   READ(2,239)NR,ID
239 FORMAT(2I5)
   READ(2,220)SP
C
C   _____ END OF BLOCK 1 _____
C
C   ZERO WORKING ARRAYS
C
C   DO 170 I=1,80
C   AL(I)=0.
170 CONTINUE
   DO 180 I=1,30
   DO 180 J=1,4
   AV(I,J)=0.
180 AC(J,I)=0.
C
C   _____ BLOCK 2: READS IN FIDUCIAL OBSERVATIONS _____
C
C   OPEN OBSERVATION FILE.

```

```

WRITE(6,190)
190 FORMAT('/' TYPE OBSERVATION FILE NAME >')
READ(5,30) OBSFIL
OPEN(3,FILE=OBSFIL ,STATUS='OLD',FORM='FORMATTED')
LU=1
LV=0
JJ=0

C
C   READ COMPARATOR COORDS OF FIDUCIALS **TERMINATE AT 9999**
C
800 READ(3,240,END=801)K,G,H,S,T
240 FORMAT(I5,4F10.3)
IF(K.EQ.9999)GOTO 804
DO 801 J=1,NF
IF(K.EQ.NC(J))JJ=J
801 CONTINUE
IF(JJ.EQ.LV)WRITE(6,241)
241 FORMAT('/'POINT IS A DUPLICATE OR IS NOT RECOGNIZED::IGNORED!'/
1)
IF(JJ.EQ.LV) GOTO 803
VL(1)=G
VL(2)=H+T
VL(3)=G+S
VL(4)=H
DO 802 J=1,4
IF(AL(JJ).EQ.0)AQ(JJ,J)=VL(J)
VL(J)=VL(J)-AQ(JJ,J)
AV(JJ,J)=AV(JJ,J)+VL(J)
802 AC(J,JJ)=AC(J,JJ)+VL(J)**2
AL(JJ)=AL(JJ)+1
803 LV=JJ
GOTO 800

C
C   OUTPUT MEAN OBSERVATIONS & STD. DEVIATION OF FIDUCIALS COORDS.
C
804 WRITE(6,805)
805 FORMAT('/' MEAN MEASUREMENTS WITH S.D'//' PT X1',8X,'Y1',
18X,'X2',8X,'Y2 MEAS'/11X,'SX1',7X,'SY1',7X,'SX2',7X,'SY2'//)
JK=0
DO 809 I=1,NF
IF(AL(I).EQ.0)GOTO 809
JK=JK+1
DO 806 J=1,4
AV(I,J)=AV(I,J)/AL(I)
VL(J)=.005
IF(AL(I).GT.1.0)VL(J)=((AC(J,I)/AL(I)-AV(I,J)**2)/(AL(I)-1))**
IF(VL(J).LE.0)VL(J)=.001
806 AV(I,J)=AV(I,J)+AQ(I,J)
WRITE(6,807)NC(I),(AV(I,J),J=1,4),AL(I),(VL(L),L=1,4)
807 FORMAT(I6,4F10.3,F5.0,/6X,4F10.3)
DO 808 J=1,2
DO 808 K=1,2
N=2*J+K-2
IF(JK.EQ.1.AND.FC.EQ.1)AN(J,K)=AV(I,N)-C(I,K)
808 U(J,I,K) =2.5E-5/VL(N)**2
IF (AL(I).EQ.0)NC(I)=-999
IF (FC.EQ.0) GOTO 810

C
C   _____ END OF BLOCK 2 _____

```



```

AL(9)=AL(19)-AL(13)
AL(10)=AL(10)+AL(15)
GOTO 816
815 AL(22)=AL(15)
AL(23)=-AL(19)
AL(29)=-AL(13)
AL(30)=AL(10)
AL(33)=-AL(24)
AL(34)=-AL(25)
816 CALL SINV(AL , N)
IF(N.EQ.0)GOTO 836
817 II=II+1
IF(IT.EQ.1)AN(I,5)=-AN(I,4)
IF(IT.EQ.1)AN(I,6)=AN(I,3)
DO 818 J=1,8
818 AY(J)=0.
DO 819 J=1,NF
IF(NC(J).EQ.-999)GOTO 819
X=AV(J,IX)
Y=AV(J,IY)
D=X
E=Y
IF(I.EQ.1) GOTO 7350
CFR=C(J,1)
CFS=C(J,2)
C(J,1)=C(J,3)
C(J,2)=C(J,4)
7350 CALL TRANSF(D,E,NS)
IF(I.NE.2) GOTO 7450
DX=C(J,3)-D
DY=C(J,4)-E
GOTO 7451
7450 DX=C(J,1)-D
DY=C(J,2)-E
7451 AY(1)=AY(1)+U(I,J,1)*DX
AY(2)=AY(2)+U(I,J,2)*DY
AY(3)=AY(3)+U(I,J,1)*X*DX
AY(4)=AY(4)+U(I,J,2)*X*DY
AY(5)=AY(5)+U(I,J,1)*Y*DX
AY(6)=AY(6)+U(I,J,2)*Y*DY
AY(7)=AY(7)+DX*U(I,J,1)*Y*Y-DY*U(I,J,2)*X*Y
AY(8)=AY(8)-DX*U(I,J,1)*X*Y+DY*U(I,J,2)*X*X
819 CONTINUE
IF(IT.EQ.1)AY(3)=AY(3)+AY(6)
IF(IT.EQ.1)AY(4)=AY(4)-AY(5)
JK=0
DO 821 J=1,N
Q(J)=0.
DO 820 K=1,N
IJ=J+(K*K-K)/2
IF( J.GT.K)IJ=K+(J*J-J)/2
820 Q(J)=Q(J)+AL(IJ)*AY(K)
AN(I,J)=AN(I,J)+Q(J)
B=DABS(Q(J))
IF(J.GT.2.AND.J.LT.7.AND.B.GT.4E-6)JK=1
821 IF(J.LT.3.AND.B.GT.4E-4.OR.J.GT.6.AND.B.GT.4E-8)JK=1
IF(JK.NE.0.AND.II.LT.10)GOTO 817
IF(JK.NE.0.AND.II.EQ.10)WRITE(6,245)
245 FORMAT(//'NO CONVERGENCE AFTER 10 ITERATIONS!????'//)

```

```

WRITE(6,246)II,N,I,(AN(I,J),J=1,N)
246 FORMAT(//' AFTER',I3,'ITERATIONS THE',I2,'PARAMETERS FOR
1PHOTOGRAPH NO',I2,'ARE:'///,4(E15.6,/))
B=0.
D=0.
E=0.
WRITE(6,247)
247 FORMAT(//'RESIDUALS AT FIDUCIAL MARKS'//' PT X',9X,
1'Y'/)
DO 822 J=1,NF
IF(NC(J).EQ.-999)GOTO 822
X1=AV(J,IX)
Y1=AV(J,IY)
CALL TRANSF(X1,Y1,NS)
AV(J,IX)=X1
AV(J,IY)=Y1
IF(I.EQ.2) GOTO 7540
DX=C(J,1)-AV(J,IX)
DY=C(J,2)-AV(J,IY)
GOTO 7541
7540 DX=C(J,3)-AV(J,IX)
DY=C(J,4)-AV(J,IY)
7541 D=D+DX*DX
E=E+DY*DY
WRITE(6,248)NC(J),DX,DY
248 FORMAT(I6,6F10.3)
822 IF(NC(J).EQ.-999)B=B+1.
D=(D/(NF-B))**.5
E=(E/(NF-B))**.5
WRITE(6,249) D,E
249 FORMAT(/' RMSE',2F10.3/)
GOTO 825

```

C
C
C
C
C

———— BLOCK 4: TRANSLATION AND ROTATION COEFFICIENTS ————

TRANSLATION ROTATION ONLY

```

823 D=AV(2,IX)-AV(1,IX)
E=AV(2,IY)-AV(1,IY)
DX=AV(4,IX)-AV(3,IX)
DY=AV(4,IY)-AV(3,IY)
T=.5*(ATAN(D/E)-ATAN(DY/DX))
AN(I,3)=DCOS(T)
AN(I,6)=AN(I,3)
AN(I,4)=DSIN(T)
AN(I,5)=-AN(I,4)
S=D*DY-DX*E
G=AV(2,IX)*AV(1,IY)-AV(1,IX)*AV(2,IY)
H=AV(4,IX)*AV(3,IY)-AV(3,IX)*AV(4,IY)
X=(DX*G-D*H)/S
Y=(DY*G-E*H)/S
AN(I,1)=Y*AN(I,4)-X*AN(I,3)
AN(I,2)=-X*AN(I,4)-Y*AN(I,3)
WRITE(6,250) I
250 FORMAT(' TRANSFORMED COORDS FOR PHOTO',I2,/' PT
1 X',9X,'Y'/)
DO 824 J=1,4
X=AV(J,IX)
Y=AV(J,IY)

```

```
CALL TRANSF(X,Y,NS)
824 WRITE(6,247) NC(J),X,Y
WRITE(6,242)
825 PAUSE
826 CONTINUE
```

C _____ END OF BLOCK 4 _____

```
DO 728 I=1,200
NRIS(I)=0
DO 728 J=1,4
RIST(I,J)=0.
728 CONTINUE
```

C ----- BLOCK 5: TRANSFORMATION OF MEASURED COORDINATES -----

```
INM=1
PRINT*, 'DO YOU WANT TO CORRECT FOR EARTH'S CURVATURE?'
READ(5,71)ANS2
IF(ANS2.EQ.'Y') PRINT*, 'INPUT FLYING ALTITUDE AND AVERAGE
1TERRAIN HEIGHT'
IF(ANS2.EQ.'Y') READ*,FH,TH
827 READ(3,240,END=829) K,G,H,S,T
IF(K.EQ.9999) GOTO 829
X1=G
Y1=H+T
X2=G+S
Y2=H
CALL TRANSF(X1,Y1,1)
CALL TRANSF(X2,Y2,2)
CALL RADIS(X1,Y1)
CALL RADIS(X2,Y2)

IF(ANS2.EQ.'N') GOTO 828
CALL ERTCRV(X1,Y1)
CALL ERTCRV(X2,Y2)
```

```
828 NRIS(INM)=K
RIST(INM,1)=X1
RIST(INM,2)=Y1
RIST(INM,3)=X2
RIST(INM,4)=Y2
INM=INM+1
GOTO 827
```

C _____ END OF BLOCK 5 AND START OF BLOCK 6 _____

```
829 WRITE(5,251)
251 FORMAT(//'
1'1/ OUTPUT FILE FOR RESECT PROGRAM'//
2'2/ OUTPUT FILE FOR RELOR PROGRAM'////)
PRINT*, 'SELECT 1, 2, OR 3'
READ(5,71) ANS1
IF(ANS1.EQ.'1') GOTO 831
IF(ANS1.EQ.'2') GOTO 833
CALL KEYFIL
DO 830 J=1,2
KJ=J*2
IJ=KJ-1
DO 830 I=1,INM
```

```

WRITE(4,252) NRIS(I),J,RIST(I,IJ),RIST(I,KJ)
830 CONTINUE
PRINT*, 'DO YOU WANT ANOTHER SELECTION?'
READ(5,71) ANS1
IF(ANS1.EQ.'Y') GOTO 829
GOTO 836
831 CALL KEYFIL
DO 832 I=1,INM
K=NRIS(I)
G=RIST(I,1)
H=RIST(I,4)
S=RIST(I,3)-RIST(I,1)
T=RIST(I,2)-RIST(I,4)
WRITE(4,240) K,G,H,S,T
832 CONTINUE
PRINT*, 'DO YOU WANT ANOTHER SELECTION?'
READ(5,71) ANS1
IF(ANS1.EQ.'Y') GOTO 829
GOTO 836
833 CALL KEYFIL
KSTRP=1
KFOT=0
DO 835 K=1,3,2
KFOT=KFOT+1
DO 834 I=1,INM
J=K+1
WRITE(4,253) KFOT,KSTRP,NRIS(I),RIST(I,K),RIST(I,J)
834 CONTINUE
835 CONTINUE
PRINT*, 'DO YOU WANT ANOTHER SELECTION ?'
READ(5,71) ANS1
IF(ANS1.EQ.'Y') GOTO 829

```

C _____ END OF BLOCK 6 _____

```

C CLOSE OPEN FILE UNITS.
C
836 CLOSE(UNIT=2)
CLOSE(UNIT=3)
CLOSE(UNIT=4)
252 FORMAT(I5,I3,2F10.3)
253 FORMAT(2I3,I5,2F10.3)
STOP
END

```

C _____ SUBROUTINES _____

```

C SUBROUTINE KEYFIL
C *****
C THIS OPENS A FILE INTO WHICH TRANSFORMED COORDINATES ARE
C TO BE STORED. FILE MUST ALREADY HAVE BEEN CREATED.
C *****
C CHARACTER* 20 OFILE
C
PRINT*, 'TYPE OUTPUT FILE NAME..>'
READ(5,70) OFILE
OPEN(4,FILE=OFILE,STATUS='OLD',FORM='FORMATTED')
70 FORMAT(A20)
RETURN
END
C *****

```

```

SUBROUTINE ERTCRV(X,Y)
C *EARTH'S CURVATURE COMPENSATION USING APPROXIMATE FLYING *
C *ALTITUDE AND AVERAGE TERRAIN HEIGHT ABOVE MEAN SEA LEVEL*
C *****
IMPLICIT DOUBLE PRECISION (A-H,O-Z)
COMMON /B0/ FL1,FH,TH
R=X*X+Y*Y
DK=12740.*FL1**2
50 X=X*(1+(FH-TH)*R/DK)
Y=Y*(1+(FH-TH)*R/DK)
RETURN
END

```

INPUT to the program REFOTO consists of two files. One is control file in which the calibration data are stored; and the other is the observation file containing the comparator or image coordinates of the fiducial marks followed by those of the measured points.

B.4.3.1 SAMPLE OF CONTROL FILE

```

(1)      1
CONTROL FILE FOR RMK A 30/23 MC IN SPACE MAPPING EXPERIMENT
(2)      4      305.128      305.128
(3)      1
1      -112.996      .046      -113.035      .034
(4)      2      .035      -112.958      -.046      -112.966
3      113.033      .045      112.958      .035
4      .034      113.035      -.045      113.033
0.000      -.210      -1.690      -5.690      -13.490      -26.350      -45.530
(5)     -72.290     -107.914     -153.650     -210.770     -280.530     -364.210     -463.060
-578.350     -711.350      0.000      0.000      0.000      0.000      0.000
(6)      0.000      -0.000
(7)      16      2
(8)      10.000

```

(1) TAG to check whether the file being read is a control file or not and to indicate which type of control file.

TAG = 1 - Control file for REFOTO.
TAG = 2 - " " " REDUCT.

(2) No. of fiducial marks; and the focal lengths of the taking cameras.

(3) TAG to indicate the availability of calibrated fiducial marks coordinates (1= available, 0= not available).

(4) Calibrated coordinates of fiducial marks. This data wouldn't be in the file if the TAG in (3) is zero.

(5) Radial distortion data.

(6) Calibrated coordinates of the principal point.

(7) (i) No. of values in the radial distortion data above.
(ii) TAG to indicate the nature of the distortion correction:

TAG = 0 to interpolate distortion correction at each point using the distortion values at the two radial distances, one less and the other greater than the radial distance to the point.

TAG = 1 means that the values in (6) represent distortion polynomial parameters which are used to compute the distortion correction at each point.

(8) The meaning of this constant depends on the value of the TAG in (7). If TAG = 0 then this constant is the radial interval of distortion values in (5). If TAG = 1 this constant has no meaning can be assigned a dummy value.

B.4.3.2 SAMPLE OF OBSERVATION FILE

1	-113.344	0.041	0.019	-0.006
2	-0.046	-113.289	0.002	-0.016
3	113.263	0.041	-0.001	-0.007
4	-0.045	113.337	-0.000	0.006
1	-113.355	0.040	0.015	-0.012
2	-0.045	-113.281	0.001	0.013
3	113.263	0.042	-0.001	-0.008
4	-0.045	113.339	-0.003	-0.005
9999				
12	47.372	111.347	-90.524	4.598
13	75.255	106.344	-90.525	4.545
14	110.549	106.049	-90.413	4.227
24	101.405	36.857	-90.558	4.514
23	31.444	42.442	-90.501	4.501
.				
.				
.				
.				
.				
9999				

B.4.4 SAMPLE OF OUTPUT

```

:
:          SPACE PHOTOGRAPHY - IMAGE COORDINATES' REFINEMENT   :
: IMAGE COORDINATES ARE IN MMS. AND ARE READ FROM  OBS. FILE:
:

```

TYPE CONTROL FILE NAME > SUDCON

```

*****
*CONTROL FILE FOR RMK A 30/23 MC IN SPACE MAPPING  EXPERIMENT*
*****

```

THE FOCAL LENGTHS OF THE LEFT AND RIGHT CAMERAS ARE
305.128 AND 305.128 RESPECTIVELY.

FIDUCIAL MARK COORDINATES

PT	X	Y		
1	-112.996	0.046	-113.035	0.034
2	0.035	-112.958	-0.046	-112.966
3	113.033	0.045	112.958	0.035
4	0.034	113.035	-0.045	113.033

TYPE OBSERVATION FILE NAME > SUDTEMP

MEAN MEASUREMENTS WITH STANDARD DEVIATIONS

PT	X1	Y1	X2	Y2	MEAS
	SX1	SY1	SX2	SY2	
1	-0.004	0.000	0.000	0.002	3.
	0.003	0.001	0.001	0.003	
2	112.962	-112.984	112.961	-112.969	3.
	0.002	0.003	0.001	0.001	
3	225.943	-0.020	225.937	0.005	3.
	0.000	0.002	0.001	0.001	
4	112.989	112.981	112.983	112.982	3.
	0.001	0.003	0.000	0.002	

COMPARATOR COORDS ARE REDUCED TO IMAGE COORDS USING:
1- RECTILINEAR, 2- AFFINE, OR 3-DEFORMATIONAL TRANSFORMATION

SELECT 1, 2 OR 3 ? 3

AFTER 2 ITERATIONS, THE 8 PARAMETERS FOR PHOTOGRAPH NO. 1 ARE:

```

=0.112992E+03
 0.459992E-01
 0.100036E+01
-0.197666E-03

```

0.176706E-04
 0.100021E+01
 0.770507E-06
 0.125359E-05

RESIDUALS AT FIDUCIAL MARKS

PT	X	Y
1	0.000	0.000
2	0.000	0.000
3	0.000	0.000
4	0.000	0.000
RMSE	0.000	0.000

AFTER 2 ITERATIONS, THE 8 PARAMETERS FOR PHOTOGRAPH NO. 2 ARE:

-0.113035E+03
 0.319998E-01
 0.100025E+01
 -0.811756E-04

 -0.545805E-04
 0.100012E+01
 -0.809617E-06
 0.326612E-06

RESIDUALS AT FIDUCIAL MARKS

PT	X	Y
1	0.000	0.000
2	0.000	0.000
3	0.000	0.000
4	0.000	0.000
RMSE	0.000	0.000

12	47.450	111.350	-90.528	4.601
13	75.332	106.347	-90.528	4.549
14	110.601	106.126	-90.519	4.576
24	101.481	36.864	-90.559	4.516
23	31.522	42.449	-90.506	4.518
21	-20.196	52.548	-90.350	4.501
31	-16.340	-1.363	-90.403	4.509
32	31.365	-2.517	-90.479	4.533
33	102.692	-3.630	-90.596	4.493
43	83.608	-39.979	-90.565	4.438
42	30.453	-38.518	-90.465	4.503

B.5.1 PROGRAM RELOR

This program carries out relative orientation, model formation and strip connection. The program is written by the present author based on the relative orientation program given by Wolf (1983). The relative orientation is carried out using the collinearity condition equations. This method was explained in Chapter 10. Equation 10.7 can be written in the least squares form as:

$$V = A \Delta + l \quad \text{.....(B.5.1)}$$

where V are the residuals in coordinate observations;

A is a matrix containing p_{12} , p_{13} , p_{27} of equation (10.7); and

l is a vector array containing A', B', A" and B" of equation (10.7).

Δ is the vector array containing corrections for the approximate values of orientaticn.

The various variables used in the program are defined in the comment statements in the listing of the program.

B.5.1.1 Explanation of the Program

The listing of the program is broken into several blocks to assist the explanation of the various operations which are carried out. These are as follows:

BLOCK 1: Initialization: in which the program interacts with the user to input the data file name. The data sets are then read and stored in their respective arrays.

BLOCK 2: Determination of the Pass Points. In this block, the program searches the input data for the points which are common to both photographs. The first 5 to 14 such common points found will be used for the relative orientation. The approximate values of the model coordinates of these points are then computed.

BLOCK 3: Rotation Matrix: This marks the start of the iteration by the computation of the rotation matrices from the initial approximation.

- BLOCK 4: Computation of dX , dY and dZ of equations A.13.
- BLOCK 5: Computation of array A.
- BLOCK 6: Computation of array L.
- BLOCK 7: In this block, the least squares solution of equation (B.5.1) takes place.
- BLOCK 8: Displays the increment and carries out the check for the convergence against the limits set for db_y , db_z , dw , $d\theta$ and dk . The residuals of the image coordinates of the pass points are also computed and displayed.
- BLOCK 9: Computation and display of the final model coordinates of all points measured in the overlapping area.
- BLOCK 10: Initializes the program for the second model of a strip by transferring the computed orientation elements of the second photo in the first model to the array storing those for the first photo and loading in the data of the third.

B.5.1.2 PROGRAM LISTING

```

C          PROGRAM RELOR
C          *****
C          *THIS PROGRAM FINDS THE FIRST 9 TO 14 COMM-*
C          *ON (PASS POINTS)-POINTS BETWEEN TWO PHOTOGRAPHS THAT*
C          *FORM A MODEL AND USES THEM TO COMPUTE THE RELATIVE *
C          *ORIENTATION PARAMETERS (OMEGA,PHI,KAPPA,YO(2),ZO(2).*
C          *IT THEN PRINTS THE PHOTO COORDS OF THE PASS POINTS *
C          *THE R.O PARAMETERS,THE MODEL COORDINATES OF THE PASS*
C          *POINTS AND THEIR STANDARD DEVIATIONS AND THE MODEL *
C          *COORDINATES OF ALL POINTS AND THEIR Y-PARALLAXES. *
C          *IT CAN GIVE THE INCREMENTS DURING SUCCESSIVE ITERAT-*
C          *IONS TO SHOW THE PROGRESS OF THE SOLUTION. *
C          *****
C
C NPL,XPL,YPL CONTAIN DATA FOR FIRST 200 POINTS FOR LEFT PHOTO.
C NPR,XPR,YPR CONTAIN DATA FOR FIRST 200 POINTS FOR RIGHT PHOTO.
C NPOINT,XP1,YP1,XP2,YP2 CONTAIN DATA FOR FIRST 10 COMMON POINTS.
C LIMIT1 - OMEGA,PHI,KAPPA FOR RIGHT PHOTO.
C LIMIT2 - YC2, THE Y COORD OF THE RIGHT EXPOSURE STATION.
C LIMIT3 - ZC2, THE Z COORD OF THE RIGHT EXPOSURE STATION.
C LIMIT4 - XP & YP, GROUND COORDS OF OBJECT POINTS.
C LIMIT5 - ZP, GROUND COORDS OF OBJECT POINTS.
C ALL ANGLES ARE INPUT AND OUTPUT IN GRADS.
C
      IMPLICIT DOUBLE PRECISION (A-H,O-Z)
      INTEGER STRIPN,FOTON1,FOTON2
      REAL LIMIT1,LIMIT2,LIMIT3,LIMIT4,LIMIT5
      DOUBLE PRECISION XPL(200),YPL(200),XPR(200),
1 YPR(200),XP1(14),YP1(14),XP2(14),YP2(14),
2 XP(14),YP(14),ZP(14),XC(2),YC(2),ZC(2),
3 SD(47),M(3,3,2),DX(14,2),DY(14,2),DZ(14,2),Q(14,2),R(14,2),
4 S(14,2),A(56,47),EL(56,1),AT(47,56),ATA(47,47),ATL(47,1),
5 X(47,1),AX(56,1),V(56,1),VT(1,56),SO(1,1),
6 OMEGA(2),PHI(2),KAPPA(2),TITLE(18)
      DIMENSION NPOINT(14),NPR(200),NPL(200)
      CHARACTER* 32 IFILE,OUTGIV
      CHARACTER*1 ANS1,ANS2
C          EVALUATE RADIAN TO GRADS CONVERSION FACTOR.
C
      RTOG=200.0/3.14159
C
C -----BLOCK 1: INITIALIZATION.-----
      WRITE(6,1)
1 FORMAT(//,' ANALYTICAL RELATIVE ORIENTATION',/,
1 ' =====',/

```

```

2          '          =====',///)
WRITE(6,2)
2 FORMAT('DO YOU WANT TO MONITOR THE ITERATIONS? Y OR N')
READ(5,3) ANS1
3 FORMAT(A1)
WRITE(6,4)
4 FORMAT('INPUT NAME OF DATA FILE>')
READ(5,5) IFILE
5 FORMAT(A30)
OPEN(3,FILE=IFILE,STATUS='OLD',FORM='FORMATTED')
WRITE(6,101)
101 FORMAT('DO YOU WANT TO OUTPUT TO FILE? Y OR N')
READ(5,3)ANS2
IF(ANS2.EQ.'N')GOTO 15
PRINT*, 'TYPE OUTPUT FILE NAME ..>'
READ(5,5) OUTGIV
C
OPEN(4,FILE=OUTGIV,STATUS='OLD',FORM='FORMATTED')
C
C
C READ TITLE FROM FILE.
C
15 READ(3,7) TITLE
7 FORMAT(18A4)
WRITE(6,8) TITLE
8 FORMAT(18A4)
C
C LEFT PHOTO DATA INPUT.
C
READ(3,9) NSTRIP
9 FORMAT(I5)
10 READ(3,9)NMODEL
READ(3,12)LIMIT1,LIMIT2,LIMIT3,LIMIT4,LIMIT5
12 FORMAT(5F9.6)
READ(3,13)F
13 FORMAT(F10.6)
READ(3,14)XC(1),YC(1),ZC(1),OMEGA(1),PHI(1),KAPPA(1)
14 FORMAT(6F10.4)
READ(3,9)M1
DO 20 I=1,M1
READ(3,19)FOTNO1,STRIPN,NPL(I),XPL(I),YPL(I)
19 FORMAT(2I3,I5,2F10.3)
20 CONTINUE
C
C RIGHT PHOTO DATA INPUT
C
30 READ(3,14) XC(2),YC(2),ZC(2),OMEGA(2),PHI(2),KAPPA(2)
WRITE(6,480)F,YC(2),XC(1),ZC(2),YC(1),OMEGA(2), ZC(1),
1 PHI(2),OMEGA(1),KAPPA(2),PHI(1),KAPPA(1),XC(2)
READ(3,9) M2
35 DO 40 I=1,M2
READ(3,19) FOTON2,STRIPN,NPR(I),XPR(I),YPR(I)
40 CONTINUE
C
C -----END OF BLOCK 1.-----
C
C OUTPUT STRIP AND PHOTO NUMBERS.
C
50 WRITE(6,52) STRIPN,FOTON1,FOTON2
52 FORMAT(//,'STRIP',I3,' PHOTOS',I3,'AND',I3,'.')
```

C
C
C

————BLOCK 2: EXTRACT FIRST 14 COMMON POINTS.————

```
N=0
DO 65 I=1,M1
DO 60 J=1,M2
IF(NPL(I).NE.NPR(J)) GO TO 55
N=N+1
NPOINT(N)=NPL(I)
XP1(N)=XPL(I)
YP1(N)=YPL(I)
XP2(N)=XPR(J)
YP2(N)=YPR(J)
IF(N.GE.14) GOTO 67
55 CONTINUE
60 CONTINUE
65 CONTINUE
67 IF(N.GT.4) GO TO 70
WRITE(6,68)
68 FORMAT('*** INSUFFICIENT PASS POINTS FOR SOLUTION-5 REQD ***')
GO TO 365
```

C
C
C

CONVERT ROTATIONS TO RADIANS.

```
70 DO 75 I=1,2
OMEGA(I)=OMEGA(I)/RTOG
PHI(I)=PHI(I)/RTOG
KAPPA(I)=KAPPA(I)/RTOG
75 CONTINUE
80 III=0
DO 100 I=1,N
IF(XP1(I).EQ.0) GO TO 90
XP(I)=XC(2)/(1.0-XP2(I)/XP1(I))
ZP(I)=ZC(1)-XP(I)*F/XP1(I)
GO TO 95
90 ZP(I)=ZC(1)-XP(I)*F/XP2(I)+XC(2)*F/XP2(I)
95 CONTINUE
YP(I)=(ZC(1)-ZP(I))*YP1(I)/F
100 CONTINUE
WRITE(6,110)
110 FORMAT('/', '          PASS POINT COORDINATES', '/',
1      '          ', '-----', '/',
2      ' ID          X          Y          Z')
DO 130 I=1,N
WRITE(6,120) NPOINT(I),XP(I),YP(I),ZP(I)
120 FORMAT(I5,3F17.3)
130 CONTINUE
```

———— END OF BLOCK 2. ————

IHAND=1

C
C
C
C
C
C

START OF ITERATION LOOP.

———— BLOCK 3: SET UP M ARRAY & SIN/COS VALUES FOR PHOTOS. ————

```
140 SM=DSIN(OMEGA(IHAND))
CO=DCOS(OMEGA(IHAND))
SP=DSIN(PHI(IHAND))
CP=DCOS(PHI(IHAND))
```

```

SK=DSIN(KAPPA(IHAND))
CK=DCOS(KAPPA(IHAND))
M(1,1,IHAND)=CP*CK
M(1,2,IHAND)=SM*SP*CK+CO*SK
M(1,3,IHAND)=SM*SK-CO*SP*CK
M(2,1,IHAND)=-CP*SK
M(2,2,IHAND)=CO*CK-SM*SP*SK
M(2,3,IHAND)=CO*SP*SK+SM*CK
M(3,1,IHAND)=SP
M(3,2,IHAND)=-SM*CP
M(3,3,IHAND)=CO*CP
IF(IHAND.EQ.2) GO TO 150
IHAND=2
GO TO 140

```

C _____ END OF BLOCK 3 _____

C _____ BLOCK 4: COMPUTATION OF dX, dY and dZ _____

```

150 DO 160 I=1,2
    DO 160 J=1,N
    DX(J,I)=XP(J)-XC(I)
    DY(J,I)=YP(J)-YC(I)
160 DZ(J,I)=ZP(J)-ZC(I)

```

_____ END OF BLOCK 4 _____

```

DO 170 I=1,2
DO 170 J=1,N
Q(J,I)=(M(3,1,I)*DX(J,I))+(M(3,2,I)*DY(J,I))+(M(3,3,I)*DZ(J,I))
R(J,I)=(M(1,1,I)*DX(J,I))+(M(1,2,I)*DY(J,I))+(M(1,3,I)*DZ(J,I))
170 S(J,I)=(M(2,1,I)*DX(J,I))+(M(2,2,I)*DY(J,I))+(M(2,3,I)*DZ(J,I))
MM=4*N
NN=3*N+5

```

C
C *** LOAD A MATRIX.

```

C ZERO(A,MM,NN,120,95)
C DO 175 I=1,MM
DO 173 J=1,NN
A(I,J)=0.0
173 CONTINUE
175 CONTINUE

```

C _____ BLOCK 5: COMPUTATION OF A MATRIX _____

```

DO 185 I=1,N
II=2*I-1
III=II+1
K=3*I+3
XP1DQ=XP1(I)/Q(I,1)
YP1DQ=YP1(I)/Q(I,1)
DO 180 L=1,3
KPLM1=K+L-1
A(II,KPLM1)=XP1DQ*M(3,L,1)+(F/Q(I,1))*M(1,L,1)
A(III,KPLM1)=YP1DQ*M(3,L,1)+(F/Q(I,1))*M(2,L,1)
180 CONTINUE
185 CONTINUE
DO 195 I=1,N
II=2*(I+N)-1
K=3*I+3
III=II+1
XP2DQ=XP2(I)/Q(I,2)
YP2DQ=YP2(I)/Q(I,2)
FDQ=F/Q(I,2)

```



```

203 CONTINUE
204 CONTINUE
   ATA(K,K)=1.0/ATA(K,K)
   DO 209 I=1,NN
   IF(I-K) 205,209,205
205 DO 208 J=1,NN
   IF(J-K) 206,207,206
206 ATA(I,J)=ATA(I,J)-ATA(I,K)*ATA(K,J)
207 CONTINUE
208 CONTINUE
   ATA(I,K)=-ATA(I,K)*ATA(K,K)
209 CONTINUE
C   MATMUL(AT,EL,ATL,NN,MM,1,95,120,1)
   DO 212 I=1,NN
   ATL(I,1)=0.0
   DO 212 K=1,MM
   ATL(I,1)=ATL(I,1)+AT(I,K)*EL(K,1)
212 CONTINUE
C   MATMUL(ATA,ATL,X,NN,NN,1,95,95,1)
   DO 213 I=1,NN
   X(I,1)=0.0
   DO 213 K=1,NN
   X(I,1)=X(I,1)+ATA(I,K)*ATL(K,1)
213 CONTINUE
C   _____END OF BLOCK 7 _____
C
C   -BLOCK 8: INCREMENT APPROXIMATIONS AND CHECK CONVERGENCE.---
C
   IF(ANS1.EQ.'N') GO TO 2010
   IF(III.EQ.0) WRITE(6,410)
410 FORMAT(1H1)
   WRITE(6,2008)
2008 FORMAT('                                MONITOR DATA')
   WRITE(6,2007)
2007 FORMAT('                                -----')
   WRITE(6,2009) III,(X(I,1),I=1,11)
2009 FORMAT(15X,'AFTER ITERATION ',I3,' THE INCREMENTS ARE:-'//
1 ' OMEGA = ',F12.6,'   PHI   = ',F12.6,'   KAPPA = ',F12.6,/
2 ' YC    = ',F12.6,'   '      = ',10X,'   ZC    = ',F12.6,/
3 ' XP1   = ',F12.6,'   YP1   = ',F12.6,'   ZP1   = ',F12.6,/
4 ' XP2   = ',F12.6,'   YP2   = ',F12.6,'   ZP2   = ',F12.6/)
2010 OMEGA(2)=OMEGA(2)+X(1,1)
   PHI(2)=PHI(2)+X(2,1)
   KAPPA(2)=KAPPA(2)+X(3,1)
   YC(2)=YC(2)+X(4,1)
   ZC(2)=ZC(2)+X(5,1)
   DO 210 I=1,N
   J=3*I+3
   XP(I)=XP(I)+X(J,1)
   YP(I)=YP(I)+X(J+1,1)
210 ZP(I)=ZP(I)+X(J+2,1)
   III=III+1
   IF(III.GT.10) GO TO 240
   DO 220 I=1,3
   IF(DABS(X(I,1)).GT.LIMIT1) GO TO 140
220 CONTINUE
   IF(DABS(X(4,1)).GT.LIMIT2) GO TO 140
   IF(DABS(X(5,1)).GT.LIMIT3) GO TO 140
   DO 230 I=1,N

```

```

II=3*I+3
IF(DABS(X(II,1)).GT.LIMIT4) GO TO 140
IF(DABS(X(II+1,1)).GT.LIMIT4) GO TO 140
IF(DABS(X(II+2,1)).GT.LIMIT5) GO TO 140
C *****
C                               END OF ITERATION LOOP.
C *****
230 CONTINUE
240 CONTINUE
C
C   SOLVE FOR V MATRIX USING ALGORITHM V=AX-L
C
C   MATMUL(A,X,AX,MM,NN,1,120,95,1)
DO 241 I=1,MM
AX(I,1)=0.0
DO 241 K=1,NN
AX(I,1)=AX(I,1)+A(I,K)*X(K,1)
241 CONTINUE
C   MATSUB(AX,EL,V,MM,1,120,1)
DO 242 I=1,MM
242 V(I,1)=AX(I,1)-EL(I,1)
C
C *** CALCULATE SO=VTV/M-N
C
C   MATRAN(V,VT,MM,1,120,1)
DO 243 I=1,MM
243 VT(1,I)=V(I,1)
C   MATMUL(VT,V,SO,1,MM,1,1,120,1)
SO(1,1)=0.0
DO 244 K=1,MM
244 SO(1,1)=SO(1,1)+VT(1,K)*V(K,1)
IF(MM.EQ.NN) GO TO 250
SO(1,1)=DSQRT(SO(1,1))/(MM-NN)
GO TO 260
250 SO(1,1)=0.0
260 CONTINUE
DO 270 I=1,NN
270 SD(I)=DSQRT(ATA(I,I))*SO(1,1)/304.8
DO 280 I=1,3
280 SD(I)=SD(I)*RTOG
WRITE(6,410)
WRITE(6,540)
WRITE(6,550)
DO 290 I=1,N
J=4*I-3
290 WRITE(6,560) NPOINT(I),XP1(I),V(J,1),YP1(I),V(J+1,1),XP2(I),V
1(J+2,1),YP2(I),V(J+3,1)
IF(III.LT.10) GO TO 300
WRITE(6,570)
300 WRITE(6,580) III
WRITE(6,590)
OMEGA(1)=OMEGA(1)*RTOG
OMEGA(2)=OMEGA(2)*RTOG
PHI(1)=PHI(1)*RTOG
PHI(2)=PHI(2)*RTOG
KAPPA(1)=KAPPA(1)*RTOG
KAPPA(2)=KAPPA(2)*RTOG
WRITE(6,600) OMEGA(2),SD(1)
WRITE(6,610) PHI(2),SD(2)

```

```

WRITE(6,620) KAPPA(2),SD(3)
WRITE(6,630) YC(2),SD(4),ZC(2),SD(5)
WRITE(6,640)
DO 310 I=1,N
  J=3*I+3
310 WRITE(6,650)NPOINT(I),XP(I),SD(J),YP(I),SD(J+1),ZP(I),SD(J+2)
WRITE(6,1000)

```

C _____ END OF BLOCK 8 _____

C — BLOCK 9: COMPUTATION AND DISPLAY OF MODEL COORDINATES —

```

DO 1111 I=1,M1
X1=XPL(I)
Y1=YPL(I)
X2=XPR(I)
Y2=YPR(I)
X1=X1*M(1,1,1)+Y1*M(2,1,1)-F*M(3,1,1)
Y1=X1*M(1,2,1)+Y1*M(2,2,1)-F*M(3,2,1)
Z1=X1*M(1,3,1)+Y1*M(2,3,1)-F*M(3,3,1)
X2=X2*M(1,1,2)+Y2*M(2,1,2)-F*M(3,1,2)
Y2=X2*M(1,2,2)+Y2*M(2,2,2)-F*M(3,2,2)
Z2=X2*M(1,3,2)+Y2*M(2,3,2)-F*M(3,3,2)
BX=XC(2)-XC(1)
BY=YC(2)-YC(1)
BZ=ZC(2)-ZC(1)
W=Z2*BX-X2*BZ
  RC=X1*Z2-Z1*X2
X3=X1*W/RC+XC(1)
Z=Z1*W/RC+ZC(1)
Y1=Y1*W/RC
Y2=Y2*(Z1*BX-X1*BZ)/RC+BY
Y=(Y1+Y2)/2.0+YC(1)
Y2=Y2-Y1
IF(ANS2.EQ.'Y')WRITE(4,4321)NPL(I),X3,Y,Z,Y2
WRITE(6,4321) NPL(I),X3,Y,Z,Y2
1000 FORMAT(//,'          MODEL COORDINATES ',/,
1'          =====',/,
2'          %%%%%%%%%%%',//)
1111 CONTINUE
4321 FORMAT(I5,2X,4F10.3)
NMODEL=NMODEL-1
IF(NMODEL.LE.0) GO TO 360

```

C _____ BLOCK 10: INITIALIZATION OF NEXT MODEL _____

C IF ANOTHER MODEL, TRANSFER RIGHT PHOTO PARAMETERS TO LEFT PHOTO

```

M1=M2-M1
DO 340 I=1,M1
  J=M2-M1+I
  NPL(I)=NPR(J)
  XPL(I)=XPR(J)
  YPL(I)=YPR(J)
340 CONTINUE
XC(1)=XC(2)
YC(1)=YC(2)
ZC(1)=ZC(2)
OMEGA(1)=OMEGA(2)
PHI(1)=PHI(2)

```

```

      KAPPA(1)=KAPPA(2)
C     ZERO(A,MM,NN,120,95)
      DO 353 I=1,MM
      DO 353 J=1,NN
353   A(I,J)=0.0
C     ZERO(AT,NN,MM,95,120)
      DO 356 I=1,NN
      DO 356 J=1,MM
356   AT(I,J)=0.0
      FOTON1=FOTON2
      GO TO 30
360   NSTRIP=NSTRIP-1
      IF(NSTRIP.GT.0) GO TO 10
365   CONTINUE
      CLOSE(UNIT=3)
      IF(ANS1.EQ.'Y')CLOSE(UNIT=4)
      WRITE(6,375)
375   FORMAT( )
      STOP
C     _____ END OF BLOCK 10. _____
480   FORMAT(9X,'FIXED CONDITIONS',22X,'INITIAL APPROXIMATIONS',/,
1      10X,'-----',22X,'-----',/,
2      'CAMERA FOCAL LENGTH =',F12.5,6X,'RIGHT PHOTO YC2 =',F12.5,/,
3      ' LEFT PHOTO      XC1 =',F12.5,20X,'ZC2 =',F12.5,/,
4      ,17X,'YC1 =',F12.5,17X,'OMEGA2 =',F12.5,/,
5      ,17X,'ZC1 =',F12.5,19X,'PHI2 =',F12.5,/,
6      ,14X,'OMEGA1 =',F12.5,17X,'KAPPA2 =',F12.5,/,
7      ,16X,'PHI1 =',F12.5,/,
8      ,14X,'KAPPA1 =',F12.5,/,
9      ' RIGHT PHOTO      XC2 =',F12.5)
540   FORMAT(//,19X,'PHOTO COORDINATES AND RESIDUALS',/,20X,'---
1      1-----')
550   FORMAT(19X,'LEFT PHOTO',22X,'RIGHT PHOTO',//,4X,'POINT
1X(MM)', ' VX(MM)  Y(MM) VY(MM)  X(MM) VX(MM)  Y(MM)
2VY(MM)')
560   FORMAT(1X,I8,1X,F8.3,1X,F5.3,1X,F8.3,1X,F5.3,1X,F8.3,1X,
1,F5.3,1X,F8.3,1X,F5.3)
570   FORMAT(1X,'WARNING.....SOLUTION HAS NOT CONVERGED AFTER 10
1ITERATIONS',/,1X,'CHECK DATA',///)
580   FORMAT(///,20X,'SOLUTION IN ARBITRARY MODEL SPACE',/,20X,'-
1-----',///,1X,'NUMBER OF ITERATIONS REQUIRED
2FOR CONVERGENCE TO SPECIFIED LIMITS = ',I2,///)
590   FORMAT(1X,'RIGHT PHOTO ORIENTATION PARAMETERS AND STANDARD
1DEVIATIONS'//,13X,'ANGLE (GRADS)          SD(GRADS)',/)
600   FORMAT(9X,'OMEGA = ',F12.6,10X,F12.6)
610   FORMAT(9X,'PHI   = ',F12.6,10X,F12.6)
620   FORMAT(9X,'KAPPA = ',F12.6,10X,F12.6,///)
630   FORMAT('COORDINATE  VALUE      SD',//,1X,'YC2',6X,F12.3,2X
1,F7.3,/,1X,'ZC2',6X,F12.3,2X,F7.3//)
640   FORMAT(12X,'MODEL COORDINATES AND STANDARD DEVIATIONS',//,
1POINT  X      SX      Y      SY      Z      SZ',/)
650   FORMAT(I6,3(2X,F10.3,1X,F6.3))
660   FORMAT(2X,'EXP',I3,5X,3F13.2)
      END

```

B.5.1.3 SAMPLE OF INPUT

RELATIVE ORIENTATION FILE MODEL 1 SUDAN TEST AREA

```

1      (Number of strips)
1      (Number of photos)
0.0050  0.0050  0.0005  0.0005  0.0005  (Limits)
305.128 (Focal length of the camera).
0.0000  0.0000  250.0000  0.0000  0.0000  0.0000
(Approximate values for Xol, Yol, Zol, w', Ø' and k')
88      (No. of points)
1 1 12  47.450  115.954 (Points data given as Strip no.,
1 1 13  75.332  110.898 Photo no., Point no., x,y)
1 1 14  110.601  110.713
1 1 24  101.481  41.382
1 1 23  31.522  46.969
1 1 21  -20.196  57.051
1 1 31  -16.340  3.147
1 1 32  31.365  2.017
1 1 33  102.692  0.864
1 1 43  83.608  -35.541
1 1 42  30.453  -34.015
1 1 41  -16.302  -48.476
1 1 51  -8.209  -105.848
1 1 52  54.635  -103.253
1 1 53  73.094  -100.739
1 1 54  113.069  -107.494
1 1 55  109.385  -106.442
1 1 3514  19.437  98.087
1 1 3515  19.575  100.596
1 1 1354  32.414  113.004
1 1 1355  31.750  114.664
1 1 1358  47.438  114.709
.
.
.
100.000  0.0000  250.0000  0.0000  0.0000  0.0000
(model base, Yo2, Zo2, w'', Ø'', k'')
88
2 1 12  -43.078  111.352
2 1 13  -15.196  106.349
2 1 14  20.082  106.137
2 1 24  10.922  36.866
2 1 23  -58.984  42.451
2 1 21  -110.546  52.550
2 1 31  -106.743  -1.363
2 1 32  -59.114  -2.517
2 1 33  12.096  -3.630
2 1 43  -6.957  -39.979
2 1 42  -60.012  -38.518
2 1 41  -106.682  -52.978
2 1 51  -98.592  -110.353
2 1 52  -35.955  -107.707
2 1 53  -17.510  -105.116
2 1 54  22.735  -111.873
2 1 55  18.913  -110.942
2 1 3514  -70.989  93.509
2 1 3515  -70.822  96.017
2 1 1354  -58.015  108.437
2 1 1355  -58.660  110.107

```

2 1 1358 -43.022 110.157
 .
 .
 .

Note: Text beteen brackets is not part of the input file.

B.5.1.4 SAMPLE OF OUTPUT

ANALYTICAL RELATIVE ORIENTATION
 =====

DO YOU WANT TO MONITOR THE ITERATION? Y OR N Y
 INPUT NAME OF DATA FILE> SUDROR1
 DO YOU WANT TO OUTPUT TO FILE? Y OR N N

FIXED CONDITIONS		INITIAL APPROXIMATION	
FOCAL LENGTH	= 305.1280	R.H. PHOTO YC2	= 0.0000
L.H. PHOTO XC1	= 0.0000	ZC2	= 250.0000
YC1	= 0.0000	XC2	= 100.0000
ZC1	= 250.0000	OM2	= 0.0000
OM1	= 0.0000	PH2	= 0.0000
KA1	= 0.0000	KA2	= 0.0000

PASS POINTS

ID	X	Y	Z
12	52.415	128.086	-87.054
13	83.214	122.501	-87.054
14	122.185	122.309	-87.087
24	112.061	45.696	-86.938
23	34.829	51.896	-87.136
21	-22.353	63.144	-87.718
31	-18.075	3.481	-87.520
.			
.			
.			
.			

MONITOR DATA

OMEGA = 0.000286	PHI = -0.001814	KAPPA = -0.001033
YC = 4.890075	YP1 = 1.775477	ZC = -4.618782
XP1 = 0.735325	YP2 = 1.200523	ZP1 = -4.722286
XP2 = 0.805884		ZP2 = -3.266872

MONITOR DATA

.
 .
 .
 .

MONITOR DATA

.
 .

PHOTO COORDINATES' RESIDUALS

	LEFT PHOTO				RIGHT PHOTO			
ID	X	VX	Y	VY	X	VX	Y	VY
12	47.450	-0.001	115.954	0.008	-43.078	0.001	111.352	0.007
.								
.								
.								
.								

NUMBER OF ITERATION = 4

RIGHT PHOTO ORIENTATION PARAMETERS

ANGLE (GRADS)

OMEGA = 0.017838
PHI = -0.115193
KAPPA = -0.019748

COORD

YC2 = 4.891000
ZC2 = 250.260000

MODEL COORDINATES AND Y-PARALLAXES

ID	X	Y	Z	PY
12	52.741	128.865	-89.153	0.001
.				
.				
.				

AS SHOWN IN THE INPUT FILE FOR THE PROGRAM ABSTEST.

B.5.2 PROGRAM ABSTEST

This program carries out the 3D transformation of points from one model space to another. The transformation adopted is the similarity transformation with 7 parameters, namely three rotations, three translations and a scale factor. The formulation of this transformation can be found in Methley (1986). However, the linearized equations of this transformation are as follows:

$$\begin{aligned}v_x &= b_{11}d\lambda + b_{12}d\psi + b_{13}d\phi + b_{14}dk + b_{15}dX_t + C \\v_y &= b_{21}d\lambda + b_{22}d\psi + b_{23}d\phi + b_{24}dk + b_{25}dY_t + D \quad \dots (B.5.2) \\v_z &= b_{31}d\lambda + b_{32}d\psi + b_{33}d\phi + b_{34}dk + b_{35}dZ_t + E\end{aligned}$$

where v_x , v_y , and v_z are unknown residuals;
 $d\lambda$, $d\psi$, $d\phi$, \dots , dZ_t are unknown corrections to approximate values for the 7 parameters of the transformation; and
 b_{11} , b_{12} , \dots , b_{35} are unknown coefficients evaluated using approximate values of the parameters.

Equation (B.5.2) can be written in the least squares solution form as follows:

$$V = A \Delta + l \quad \dots (B.5.3)$$

where V is a vector of unknown residuals;
 A is the array containing the coefficients b_{11} , \dots , b_{35} ; and
 l is a vector array containing C , D , and E values.

Δ is a vector array containing corrections for the approximate values of the 7 transformation parameters.

B.5.2.1 Definition of Arrays and Explanation of the Program:

ID1, XP1, YP1 and ZP1 are arrays storing identification numbers, X , Y , Z respectively of the points in model 1.

ID2, XP2, YP2 and ZP2 are arrays storing identification numbers,

X, Y,Z respectively of the points in model 2.

ID3, XP3, YP3, and ZP3 are working arrays for the control points.

The program listing is broken up into four blocks to assist the explanation of the varicus operations which are carried out. These are as fcllows:

- BLOCK 1: Initialization: in which the program interacts with the user to input the data file name. The data ~~are~~ then read and displayed for the user to check. Finally the control points are extracted from tne data and stored into the arrays ID3, XP3, YP3, and ZP3.
- BLOCK 2: Computaion of Rotation and Coefficients: in which the elements of the rotation matrix; the coefficients b_{11} , b_{12} ,, b_{35} ; and the elements of the vector array 1 are computed.
- BLOCK 3: Least Squares Solution: in which the least squares solution of equation (B.5.3) is carried out as explained in the comment statements preceding each step. The check against the limits set for the corrections to the approximate values of the rotation, translation and scale factor parameters is made.
- BLOCK 4: Computation of the Transformed Coordinates: in which the transformed coordinates are computed using the rotation, translation and scale factor parameters computed in Elock 3. The check against the given cordinates is made and the residuals and the r.m.s.e values in X, Y, and Z are computed and displayed.

B.5.2.3 PROGRAM LISTING

C *** 3-DIMENSIONAL COORDINATE TRANSFORMATION PROGRAM.

```

C
  IMPLICIT DOUBLE PRECISION (A-H,O-Z)
  DIMENSION ID1(300),ID2(300),ID3(300),L(150,1),TITLE(18)
  DOUBLE PRECISION XP1(300),YP1(300),ZP1(300),
1      XP2(150),YP2(150),ZP2(300),A(150,7),AT(7,150),
2      ATA(7,7),ATAAT(7,150),D(7,1),VT(1,150),
3      PY(150),VTV(1,1),XP3(150),YP3(150),ZP3(150),
4      XT(150),YT(150),ZT(150),Q(2,3),KAPPA
  REAL M11,M12,M13,M21,M22,M23,M31,M32,M33,L
C
  CHARACTER* 32 IFILE,ANS
C
  _____ BLOCK 1: INITIALIZATION _____
  WRITE(6,1)
1  FORMAT( 'TYPE INPUT DATA FILE NAME >' )
  READ(5,2) IFILE
2  FORMAT(A30)
  OPEN(3,FILE=IFILE,STATUS='OLD',FORM='FORMATTED')
  WRITE(6,5)
4  FORMAT(A1)
5  FORMAT( 'DO YOU WANT TO OUTPUT TO A FILE? Y OR N' )
  READ(5,4) ANS
  IF(ANS.EQ.'N') GO TO 9
  WRITE(6,1)
  READ(5,2) IFILE
  OPEN(4,FILE=IFILE,STATUS='OLD',FORM='FORMATTED')
9  READ(3,10) TITLE
10 FORMAT(18A4)
20 FORMAT(2I5)
  READ(3,20) M0,M1
  M1=M0+M1
  DO 30 I=1,M1
  READ(3,190) ID1(I),XP1(I),YP1(I),ZP1(I)
30 CONTINUE
  READ(3,40) S
40 FORMAT(F6.2)
  READ(3,60) OMEGA,PHI,KAPPA,TX,TY,TZ
60 FORMAT(6F10.3)
  NI=0
  J=1
  N=0
  LL=0
  K=0
  WRITE(6,80)
80 FORMAT( 'THREE DIMENSIONAL COORDINATE TRANSFORMATION',/,1X,'-
1-----' )
  WRITE(6,85) TITLE
85 FORMAT(18A4)
  WRITE(6,100)
100 FORMAT( '1. INPUT DATA',/, ' -----' )
  WRITE(6,330) S
  WRITE(6,120) OMEGA,PHI,KAPPA
120 FORMAT (4X,'OMEGA=',F10.6,' PHI=',F10.6,' KAPPA=',F10.6)
  WRITE(6,370) TX,TY,TZ
  GTOR=3.14159 /200.0
  OMEGA=OMEGA*GTOR
  PHI=PHI*GTOR

```

```

KAPPA=KAPPA*GTOR
WRITE(6,150)
150 FORMAT(' POINTS IN MODEL 1 COORDINATE SYSTEM')
WRITE(6,155)
155 FORMAT(1H,'-----')
WRITE(6,160)
160 FORMAT(4X,'POINT',8X,'X',11X,'Y',11X,'Z')
DO 170 I=1,M1
WRITE(6,180) ID1(I),XP1(I),YP1(I),ZP1(I)
170 CONTINUE
180 FORMAT(I6,2X,3F13.3)
190 FORMAT(I5,2X,3F13.4)
M1=M1-M0
READ(3,20) M2
WRITE(6,200)
200 FORMAT(' POINTS IN MODEL 2 COORDINATE SYSTEM')
WRITE(6,205)
205 FORMAT(1H,'-----')
WRITE(6,160)
DO 250 I=1,M2
K=K+1
READ(3,190) ID2(K),XP2(K),YP2(K),ZP2(K)
191 FORMAT(I6,3F12.3)
WRITE(6,180) ID2(K),XP2(K),YP2(K),ZP2(K)
IF(K.GT.M1) GO TO 220
DO 210 J=K,M1
IF(ID1(J).EQ.ID2(K)) GO TO 230
210 CONTINUE
220 LL=LL+1
ID3(LL)=ID2(K)
XP3(LL)=XP2(K)
YP3(LL)=YP2(K)
ZP3(LL)=ZP2(K)
N=N+1
K=K-1
GO TO 240
230 IF(J.EQ.K) GO TO 240
NTEMP1=ID1(J)
TEMPX=XP1(J)
TEMPY=YP1(J)
TEMPZ=ZP1(J)
ID1(J)=ID1(K)
XP1(J)=XP1(K)
YP1(J)=YP1(K)
ZP1(J)=ZP1(K)
ID1(K)=NTEMP1
XP1(K)=TEMPX
YP1(K)=TEMPY
ZP1(K)=TEMPZ
240 IF(K.GE.(M2-N)) GO TO 260
250 CONTINUE
260 CLOSE(UNIT=3)
N=K
IF(K.NE.1.AND.J.NE.1.AND.I.NE.1) GO TO 270
IF(N.GE.M1) GO TO 270
NNN=N+1
270 CONTINUE
----- END OF BLOCK 1 -----
MM=N*3

```

C


```

      ATA(I,J)=ATA(I,J)+AT(I,K)*A(K,J)
292 CONTINUE
C     MATINV(ATA,7,7)
      DO 308 K=1,7
      DO 303 J=1,7
      IF(J-K) 301,302,301
301  ATA(K,J)=ATA(K,J)/ATA(K,K)
302 CONTINUE
303 CONTINUE
      ATA(K,K)=1.0/ATA(K,K)
      DO 308 I=1,7
      IF(I-K) 304,308,304
304  DO 307 J=1,7
      IF(J-K) 305,306,305
305  ATA(I,J)=ATA(I,J)-ATA(I,K)*ATA(K,J)
306 CONTINUE
307 CONTINUE
      ATA(I,K)=-ATA(I,K)*ATA(K,K)
308 CONTINUE
C     MATMUL(ATA,AT,ATAAT,7,7,MM,7,7,200)
      DO 293 I=1,7
      DO 293 J=1,MM
      ATAAT(I,J)=0.
      DO 293 K=1,7
      ATAAT(I,J)=ATAAT(I,J)+ATA(I,K)*AT(K,J)
293 CONTINUE
C     MATMUL(ATAAT,L,D,7,MM,1,7,200,1)
      DO 294 I=1,7
      D(I,1)=0.
      DO 294 K=1,MM
      D(I,1)=D(I,1)+ATAAT(I,K)*L(K,1)
294 CONTINUE
      S=S+D(1,1)
      OMEGA=OMEGA+D(2,1)
      PHI=PHI+D(3,1)
      KAPPA=KAPPA+D(4,1)
      TX=TX+D(5,1)
      TY=TY+D(6,1)
      TZ=TZ+D(7,1)
      IF(NI.GE.5) GO TO 300
      IF(DABS(D(1,1)).GE..000001) GO TO 280
      IF(DABS(D(2,1)).GE..000002) GO TO 280
      IF(DABS(D(3,1)).GE..000002) GO TO 280
      IF(DABS(D(4,1)).GE..000002) GO TO 280
      IF(DABS(D(5,1)).GE..0005) GO TO 280
      IF(DABS(D(6,1)).GE..0005) GO TO 280
      IF(DABS(D(7,1)).GE..0005) GO TO 280
300 CONTINUE
C     ----- END OF BLOCK 3 -----
      OMEGA=OMEGA/GTOR
      PHI=PHI/GTOR
      KAPPA=KAPPA/GTOR
      WRITE(6,320)
320  FORMAT('2. OUTPUT',/,
1     '-----')
      WRITE(6,330) S
330  FORMAT(4X,'SCALE FACTOR = ',F12.4)
      WRITE(6,120) OMEGA,PHI,KAPPA
      WRITE(6,370) TX,TY,TZ

```

```

370 FORMAT(7X,'TX=',F10.2,'          TY=',F10.2,'          TZ=',F10.2)
C   MATRAN(L,VT,MM,1,200,1)
      DO 391 I=1,MM
        VT(1,I)=L(I,1)
391 CONTINUE
C   MATMUL(VT,L,VTV,1,MM,1,1,200,1)
      VTV(1,1)=0.
      DO 392 K=1,MM
        VTV(1,1)=VTV(1,1)+VT(1,K)*L(K,1)
392 CONTINUE
      SO=DSQRT(VTV(1,1)/(MM-7))
      WRITE(6,400) SO
400 FORMAT('STANDARD DEVIATION OF UNIT WEIGHT =',F6.3,' UNITS')
      WRITE(6,410)
410 FORMAT('  TRANSFORMED COORDINATES',/,
1     '  '  '-----')
      WRITE(6,420)
420 FORMAT('POINT',9X,'X',7X,'V(X)',8X,'Y',7X,'V(Y)',9X,'Z',7X,
1     'V(Z)')
C   ----- BLOCK 4 THE TRANSFORMED COORDINATES -----
      IF(MO.NE.0)GOTO 520
      DO 430 I=1,N
        J=3*I-2
        XP1(I)=(S*(M11*XP2(I)+M21*YP2(I)+M31*ZP2(I))+TX+XP1(I))/2.0
        YP1(I)=(S*(M12*XP2(I)+M22*YP2(I)+M32*ZP2(I))+TY+YP1(I))/2.0
        ZP1(I)=(S*(M13*XP2(I)+M23*YP2(I)+M33*ZP2(I))+TZ+ZP1(I))/2.0
        IF(ANS.EQ.'Y') WRITE(4,199) ID1(I),XP1(I),YP1(I),L(J,1),
1     L(J+1,1),L(J+2,1)
199 FORMAT(I4,2F10.0,3F8.0)
430 WRITE(6,440)ID1(I),XP1(I),L(J,1),YP1(I),L(J+1,1),ZP1(I),
1     L(J+2,1)
440 FORMAT(1H ,3X,I5,F13.4,F8.4,F16.4,F8.4,F13.4,F8.4)
      IF(LL.EQ.0) GO TO 490
      DO 480 I=1,LL
        J=N+I
        XP1(J)=S*(M11*XP3(I)+M21*YP3(I)+M31*ZP3(I))+TX
        YP1(J)=S*(M12*XP3(I)+M22*YP3(I)+M32*ZP3(I))+TY
        ZP1(J)=S*(M13*XP3(I)+M23*YP3(I)+M33*ZP3(I))+TZ
        ID1(J)=ID3(I)
        IF(ANS.EQ.'Y') WRITE(4,199) ID1(J),XP1(J),YP1(J),ZP1(J)
        WRITE(6,470) ID1(J),XP1(J),YP1(J),ZP1(J)
480 CONTINUE
520 DO 510 I=1,3
      Q(1,I)=0.
      Q(2,I)=0.
510 CONTINUE
      DO 530 I=1,N
        J=3*I-2
        XT(I)=(S*(M11*XP2(I)+M21*YP2(I)+M31*ZP2(I))+TX+XP1(I))/2.0
        YT(I)=(S*(M12*XP2(I)+M22*YP2(I)+M32*ZP2(I))+TY+YP1(I))/2.0
        ZT(I)=(S*(M13*XP2(I)+M23*YP2(I)+M33*ZP2(I))+TZ+ZP1(I))/2.0
        L(J,1) =XP1(I)-XT(I)
        L(J+1,1)=YP1(I)-YT(I)
        L(J+2,1)=ZP1(I)-ZT(I)
        Q(1,1)= Q(1,1)+L(J,1)**2
        Q(1,2)= Q(1,2)+L(J+1,1)**2
        Q(1,3)=Q(1,3)+L(J+2,1)**2
        WRITE(6,440)ID1(I),XT(I),L(J,1),YT(I),L(J+1,1),ZT(I),
1     L(J+2,1)

```

```

    IF(ANS.EQ.'Y')WRITE(4,199) ID1(I),XT(I),YT(I),L(J,1),
    1L(J+1,1),L(J+2,1)
530 CONTINUE
    WRITE(6,540)
540 FORMAT(//,'THE ROOT MEAN SQUARE ERRORS OF THE GROUND COORDI
    1NATES FOR THE',/, 'CONTROL POINTS IN METRES ARE',/, '=====
    2=====')
    Q(1,1)=DSQRT(Q(1,1)/(N-1))
    Q(1,2)=DSQRT(Q(1,2)/(N-1))
    Q(1,3)=DSQRT(Q(1,3)/(N-1))
    WRITE(6,550) Q(1,1),Q(1,2),Q(1,3)
550 FORMAT('XRMSE=',F6.3,3X,'YRMSE=',F6.3,3X,'ZRMSE=',F6.3,//)
    IF(LL.EQ.0)GO TO 490
    DO 600 I=1,LL
    J=N+I
    XT(J)=S*(M11*XP3(I)+M21*YP3(I)+M31*ZP3(I))+TX
    YT(J)=S*(M12*XP3(I)+M22*YP3(I)+M32*ZP3(I))+TY
    ZT(J)=S*(M13*XP3(I)+M23*YP3(I)+M33*ZP3(I))+TZ
    L(J,1)=XP1(J)-XT(J)
    L(J+1,1)=YP1(J)-YT(J)
    L(J+2,1)=ZP1(J)-ZT(J)
    Q(2,1)=Q(2,1)+L(J,1)**2
    Q(2,2)=Q(2,2)+L(J+1,1)**2
    Q(2,3)=Q(2,3)+L(J+2,1)**2
    WRITE(6,440)ID1(J),XT(J),L(J,1),YT(J),L(J+1,1),ZT(J),
    1L(J+2,1)
    IF(ANS.EQ.'Y') WRITE(4,199) ID1(J),XT(J),YT(J),L(J,1),
    1L(J+1,1),L(J+2,1)
600 CONTINUE
    WRITE(6,610)
610 FORMAT(//,'THE ROOT MEAN SQUARE ERRORS IN THE GROUND COORD
    1INATES FOR THE',/, 'CHECK POINTS IN METRES ARE',/, '=====
    2=====')
    K=ABS(LL-1)
    Q(2,1)=DSQRT(Q(2,1)/K)
    Q(2,2)=DSQRT(Q(2,2)/K)
    Q(2,3)=DSQRT(Q(2,3)/K)
C ----- END OF BLOCK 4 -----
    WRITE(6,550)Q(2,1),Q(2,2),Q(2,3)
470 FORMAT(1H ,3X,I5,F13.4,F20.4,F21.4)
425 FORMAT(1X,I5,3F10.3)
490 IF(ANS.EQ.'Y') CLOSE(UNIT=4)
    WRITE(6,500)
500 FORMAT( )
    STOP
    END

```

B. .2.3 SAMPLE OF INPUT

THREE DIMENSIONAL TRANSFORMATION MODEL 1 SUDAN

55	30	(no. of ckeck and control points respectively)	
12	404190.0000	2186720.0000	820.0000
13	420240.0000	2202570.0000	730.0000
14	436630.0000	2225560.0000	520.0000
24	477650.0000	2187648.0000	650.0000
23	441840.0000	2144620.0000	750.0000
21	411390.0000	2115515.0000	440.0000
31	448350.0000	2093240.0000	560.0000
32	471095.0000	2123800.0000	700.0000

33	504570.0000	2169740.0000	750.0000	
43	519543.0000	2140604.0000	750.0000	
42	494158.0000	2106654.0000	690.0000	
41	482103.0000	2069473.0000	520.0000	
52	550313.0000	2090594.0000	925.0000	(Ground
53	557120.0000	2103770.0000	860.0000	Coordinates)
55	577793.0000	2124805.0000	450.0000	
3515	401300.0000	2161585.0000	570.0000	
3513	409795.0000	2190825.0000	661.0000	
113	435109.0000	2206190.0000	900.0000	
112	412519.0000	2178260.0000	659.0000	
1637	459723.0000	2125986.0000	643.0000	
1632	497377.0000	2129000.0000	700.0000	
114	461495.0000	2108993.0000	670.0000	
115	484500.0000	2140955.0000	720.0000	
116	505140.0000	2169690.0000	690.0000	
1641	519560.0000	2140630.0000	680.0000	
1647	531590.0000	2127288.0000	750.0000	
117	555476.0000	2123185.0000	910.0000	
118	544855.0000	2092757.0000	700.0000	
119	528801.0000	2059150.0000	620.0000	
3514	402860.0000	2160256.0000	580.0000	
1354	399090.0000	2175644.0000	560.0000	
1355	397725.0000	2175950.0000	554.0000	
1358	404900.0000	2186180.0000	588.0000	
1356	406150.0000	2185503.0000	629.0000	
1357	407650.0000	2189584.0000	597.0000	
3516	422220.0000	2207587.0000	540.0000	
1082	441620.0000	2217080.0000	512.0000	
1081	441250.0000	2217045.0000	580.0000	
1359	434160.0000	2198849.0000	440.0000	
3511	424176.0000	2188746.0000	525.0000	
3512	424630.0000	2188200.0000	503.0000	
1351	433727.0000	2189776.0000	712.0000	
1352	433680.0000	2189567.0000	553.0000	
6314	452270.0000	2149758.0000	421.0000	
1635	465030.0000	2123385.0000	532.0000	
1634	467783.0000	2124260.0000	638.0000	
1636	474900.0000	2133360.0000	503.0000	
1631	476045.0000	2138588.0000	660.0000	
6311	494480.0000	2131606.0000	678.0000	
1633	498300.0000	2129000.0000	643.0000	
1638	486287.0000	2118889.0000	740.0000	
1639	483550.0000	2110904.0000	585.0000	
6310	481507.0000	2112045.0000	620.0000	
6312	485210.0000	2109220.0000	640.0000	
6313	484636.0000	2109378.0000	618.0000	
9118	483898.0000	2089186.0000	580.0000	
9114	495579.0000	2098450.0000	668.0000	
9117	508504.0000	2083720.0000	630.0000	
9115	507521.0000	2082131.0000	766.0000	
9113	505490.0000	2079962.0000	750.0000	
9119	478637.0000	2091735.0000	668.0000	
1917	476620.0000	2088779.0000	720.0000	
1911	478795.0000	2084600.0000	588.0000	
1915	485421.0000	2082110.0000	600.0000	
1916	485183.0000	2083530.0000	655.0000	
9121	480640.0000	2079338.0000	680.0000	
1918	475123.0000	2082819.0000	582.0000	

1913	468296.0000	2079125.0000	680.0000	
1912	467577.0000	2075199.0000	440.0000	
1919	460030.0000	2090475.0000	560.0000	
1646	517450.0000	2137600.0000	650.0000	
1645	516620.0000	2137090.0000	690.0000	
1644	521780.0000	2135980.0000	660.0000	
1642	523740.0000	2135380.0000	700.0000	
1643	528898.0000	2130172.0000	727.0000	
1648	531726.0000	2126975.0000	780.0000	
6421	535964.0000	2126661.0000	720.0000	
6416	531182.0000	2113614.0000	886.0000	
6417	533078.0000	2113115.0000	826.0000	
6410	525511.0000	2115060.0000	797.0000	
6415	517420.0000	2114640.0000	750.0000	
6419	510918.0000	2129945.0000	715.0000	
6418	511910.0000	2133195.0000	691.0000	
6481	530528.0000	2109010.0000	810.0000	
6420	529759.0000	2105365.0000	832.0000	
1000.	(Scale Factor)			
	0.0000	0.0000	60.0000	0.0000 0.0000
	(Approx. of Ty, Tz, K, W, O)			
85				
12	52.741	128.865	-89.153	
13	83.745	123.296	-89.203	
14	123.008	123.136	-89.357	
24	112.775	45.987	-89.086	
23	35.037	52.210	-89.154	
21	-22.490	63.543	-89.789	
31	-18.183	3.504	-89.538	
32	34.869	2.225	-89.212	
33	114.059	0.953	-88.902	
43	92.867	-39.463	-88.919	
42	33.857	-37.824	-89.230	
41	-18.143	-53.946	-89.584	
52	60.647	-114.614	-88.702	
53	81.131	-111.782	-88.677	
55	121.621	-118.409	-89.260	
3515	21.787	111.946	-89.613	
3513	61.965	125.801	-89.348	
113	99.747	109.286	-88.918	
112	49.818	112.598	-89.396	
1637	28.235	16.928	-89.360	
1632	61.873	-23.528	-89.124	
114	10.312	1.276	-89.386	
115	65.177	0.703	-89.163	Model
116	114.394	0.247	-88.962	Coordinates
1641	92.900	-39.488	-89.010	
1647	87.406	-63.839	-88.943	
117	101.864	-94.292	-88.672	
118	58.766	-106.674	-88.941	
119	7.550	-115.373	-89.341	
3514	21.627	109.118	-89.501	
1354	36.066	125.731	-89.509	
1355	35.335	127.611	-89.582	
1358	52.768	127.603	-89.409	
1356	52.928	125.632	-89.449	
1357	58.798	127.181	-89.390	
3516	91.031	125.078	-89.367	
1082	117.355	110.604	-89.405	

1081	117.035	110.966	-89.239
1359	90.677	104.458	-89.496
3511	71.094	107.720	-89.528
3512	70.854	106.730	-89.458
1351	79.977	97.707	-89.226
1352	79.731	97.560	-89.361
6314	49.278	44.412	-89.556
1635	29.556	8.767	-89.402
1634	32.692	6.331	-89.343
1636	48.786	5.488	-89.399
1631	55.682	8.458	-89.242
6311	62.552	-18.161	-89.096
1633	62.610	-24.638	-89.139
1638	41.478	-19.012	-89.131
1639	30.222	-22.341	-89.300
6310	29.801	-19.096	-89.344
6312	29.591	-25.619	-89.237
6313	29.323	-24.757	-89.351
9118	5.781	-40.165	-89.368
9114	25.634	-46.015	-89.208
9117	19.269	-72.601	-89.208
9115	16.675	-72.675	-89.111
9113	12.616	-72.142	-89.069
9119	4.386	-32.127	-89.308
1917	-0.585	-32.240	-89.283
1911	-3.565	-37.991	-89.418
1915	-1.058	-47.594	-89.366
1916	0.299	-46.156	-89.313
9121	-8.096	-44.408	-89.280
1918	-8.548	-35.245	-89.427
1913	-18.197	-30.501	-89.336
1912	-23.320	-32.806	-89.677
1919	-11.968	-12.001	-89.487
1646	87.789	-39.513	-89.029
1645	86.553	-38.939	-88.982
1644	89.405	-45.724	-89.037
1642	90.269	-48.443	-88.916
1643	88.516	-58.452	-89.004
1648	87.088	-64.261	-88.871
6421	90.171	-69.391	-88.856
6416	71.510	-74.329	-88.816
6417	72.495	-76.932	-88.804
6410	68.558	-66.740	-88.967
6415	61.609	-57.916	-88.956
6419	73.821	-38.178	-89.085
6418	78.340	-36.727	-89.010
6481	65.705	-77.310	-88.938
6420	60.981	-79.412	-88.818
9999			

B.5.2.4 SAMPLE OF OUTPUT

TYPE INPUT DATA FILE NAME >

/-DATA.ROUT1

DO YOU WANT TO OUTPUT TO A FILE? Y OR N

/-N

THREE DIMENSIONAL COORDINATE TRANSFORMATION

THREE DIMENSIONAL TRANSFORMATION MODEL 1 SUDAN

1. INPUT DATA

SCALE FACTOR = 1000.0000
 OMEGA= 0.000000 PHI= 0.000000 KAPPA= 60.000000
 TX= 0.00 TY= 0.00 TZ= 0.00

POINTS IN MODEL 1 COORDINATE SYSTEM

POINT	X	Y	Z
12	404190.000	2186720.000	820.000
.			
.			

POINTS IN MODEL 2 COORDINATE SYSTEM

POINT	X	Y	Z
12	52.741	128.865	-89.153
.			
.			

2. OUTPUT

SCALE FACTOR = 717.9984
 OMEGA= -0.109000 PHI= 0.165443 KAPPA= 60.898475
 TX= 458129.92 TY=2102544.10 TZ= 64834.45
 STANDARD DEVIATION OF UNIT WEIGHT =23.085 UNITS

TRANSFORMED COORDINATES

POINT	X	V(X)	Y	V(Y)	Z	V(Z)
12	404181.618	8.382	2186712.249	7.750	819.275	0.725
13	420254.974	-14.974	2202581.092	-11.092	721.807	8.192
14	436620.057	9.942	2225562.028	-2.028	520.623	-0.623
24	477647.469	2.530	2187642.188	5.811	662.062	-12.062
23	441833.138	6.861	2144608.578	11.421	771.037	-21.037
21	411380.622	9.378	2115522.939	-7.939	452.527	-12.527
31	448366.450	-16.450	2093227.378	12.621	573.649	-13.649
32	471090.641	4.358	2123807.564	-7.564	704.986	-4.986
33	504585.562	-15.562	2169747.659	-7.659	758.399	-8.399
43	519544.966	-1.966	2140600.353	3.646	757.838	-7.838
42	494162.496	-4.496	2106651.677	2.323	678.228	11.771
41	482106.112	-3.112	2069469.418	3.581	513.642	6.357
52	550312.164	0.835	2090594.225	-0.225	926.072	-1.072
53	557122.843	-2.843	2103777.846	-7.846	882.400	-22.400
55	577780.200	12.799	2124803.005	1.994	423.290	26.709
3515	401295.756	4.243	2161562.589	22.410	554.421	15.578
3513	409791.257	3.742	2190836.874	-11.874	658.926	2.073
113	435110.774	-1.774	2206187.386	2.613	886.761	13.238
112	412513.622	5.377	2178258.964	1.035	647.938	11.061
1637	459718.337	4.662	2125996.154	-10.154	636.255	6.744

1632	497374.219	2.781	2129001.970	-1.970	697.981	2.018
114	461488.201	6.798	2109002.983	-9.983	652.672	17.327
115	484510.265	-10.265	2140962.080	-7.080	700.435	19.564
116	505146.945	-6.945	2169674.837	15.162	706.222	-16.222
1641	519567.543	-7.543	2140617.806	12.193	690.124	-10.124
1647	531590.131	-0.131	2127296.875	-8.875	744.951	5.048
117	555459.092	16.907	2123186.687	-1.687	894.772	15.227
118	544864.302	-9.302	2092766.476	-9.476	732.969	-32.969
119	528792.788	8.211	2059136.990	13.009	599.083	20.916
3514	402872.449	-12.449	2160266.115	-10.115	598.641	-18.641

THE ROOT MEAN SQUARE ERRORS OF THE GROUND COORDINATES FOR THE CONTROL POINTS IN METRES ARE:

=====
 XRMSE= 17.492 YRMSE= 18.630 ZRMSE=29.534

1354	399111.585	-21.585	2175622.884	21.115	595.068	-35.068
1355	397705.844	19.155	2175971.795	-21.795	545.710	8.289
1358	404924.432	-24.432	2186197.822	-17.822	633.656	-45.656
1356	406147.085	2.914	2185476.073	26.927	602.995	26.005
1357	407667.227	-17.227	2189561.436	22.563	634.411	-37.411
3516	422238.883	-18.883	2207604.550	-17.550	582.164	-42.164
1082	441624.264	-4.264	2217061.361	18.638	488.310	23.689
1081	441279.751	-29.751	2217023.592	21.407	608.458	-28.458
1359	434191.330	-31.330	2198864.291	-15.291	473.445	-33.445
3511	424174.015	1.984	2188723.364	22.635	493.865	31.135
3512	424655.738	-25.738	2188172.972	27.027	543.815	-40.815
1351	433725.574	1.425	2189792.698	-16.698	684.048	27.951
1352	433709.786	-29.786	2189587.360	-20.360	587.510	-34.510
6314	452293.907	-23.907	2149726.076	31.923	467.453	-46.453
1635	465048.830	-18.830	2123404.423	-19.423	589.945	-57.945
1634	467775.948	7.051	2124236.603	23.396	623.795	14.204
1636	474929.998	-29.998	2133331.150	28.849	549.424	-46.424
1631	476041.072	3.927	2138606.656	-18.656	650.230	9.769
6311	494503.265	-23.265	2131623.210	-17.210	719.036	-41.036
1633	498327.685	-27.685	2128977.061	22.938	682.754	-39.754
1638	486282.365	4.634	2118905.483	-16.483	737.045	2.954
1639	483577.802	-27.802	2110923.103	-19.103	636.399	-51.399
6310	481499.451	7.548	2112018.774	26.225	608.332	11.667
6312	485240.247	-30.247	2109196.521	23.478	680.269	-40.269
6313	484623.344	12.655	2109395.815	-17.815	599.678	18.321
9118	483922.840	-24.840	2089206.402	-20.402	623.860	-43.860
9114	495570.674	8.325	2098435.020	14.979	692.670	-24.670
9117	508536.742	-32.742	2083699.176	20.823	684.204	-54.204
9115	507506.977	14.022	2082146.599	-15.599	759.185	6.814
9113	505514.741	-24.741	2079985.510	-23.510	798.218	-48.218
9119	478629.271	7.728	2091713.992	21.007	676.404	-8.404
1917	476638.681	-18.681	2088750.441	28.558	704.601	15.398
1911	478779.846	15.153	2084621.990	-21.990	609.175	-21.175
1915	485452.050	-31.050	2082119.440	-9.440	633.456	-33.456
1916	485169.886	13.113	2083510.781	19.218	669.862	-14.862
9121	480670.523	-30.523	2079308.213	29.786	712.444	-32.444
1918	475106.656	16.343	2082834.387	-15.387	615.320	-33.320
1913	468330.552	-34.552	2079135.803	-10.803	704.600	-24.600
1912	467562.580	14.419	2075175.582	23.417	468.538	-28.538
1919	460052.537	-22.537	2090445.741	29.258	598.330	-38.330
1646	517474.849	-24.849	2137596.273	3.726	697.218	-47.218
1645	516626.689	-6.689	2137108.603	-18.603	734.003	-44.003

1644	521787.936	-7.936	2135974.420	5.579	683.042-23.042
1642	523741.098	-1.098	2135356.437	23.562	765.902-65.902
1643	528888.531	9.468	2130186.083	-14.083	698.193 28.806
1648	531706.428	19.571	2126944.626	30.373	791.914-11.914
6421	535992.289	-28.289	2126630.899	30.100	792.084-72.084
6416	531168.124	13.876	2113637.968	-23.968	855.587 30.412
6417	533103.086	-25.086	2113138.850	-23.850	860.029-34.029
6410	525493.352	17.647	2115045.909	14.090	759.505 37.494
6415	517440.311	-20.311	2114619.770	20.229	789.061-39.061
6419	510911.613	6.386	2129952.642	-7.642	687.153 27.846
6418	511930.261	-20.261	2133204.751	-9.751	732.788-41.788
6481	530515.012	12.987	2108998.118	11.881	777.632 32.367
6420	529793.888	34.888	2105356.583	8.416	871.901-39.901

THE ROOT MEAN SQUARE ERRORS IN THE GROUND COORDINATES FOR THE CHECK POINTS IN METRES ARE:

=====
 XRMSE = 20.857 YRMSE = 20.950 ZRMSE = 36.180

B.6 PROGRAM BUNFIX:

This is a simple bundle adjustment program written by Jerry Clark of the Civil Engineering Department of the City of London University. The program applies the solution outlined in Chapter 10. Further explanation can be got from the above mentioned department.

B.7.1 PROGRAM REDUCT

This program was originally developed by Dr. Shortis of the City University of London for on-line comparator measurement reduction of frame photographs. It is used by the Photogrammetry Section of N.E.L. and is installed on the Cromemco System 3 microcomputer which controls its Stecometer. The program was transferred and modified to run on the ICL 2988 mainframe computer of the University to carry out the geometric test of space photography. As explained in Chapter 10, this program carries out the space resection/intersection operation consecutively. After carrying out the resection phase, the ground coordinates of the set of the check points are computed (by space intersection) using the orientation data determined in the resection phase. These computed ground coordinates are then, if desired, compared with the corresponding set of survey data to compute the residuals and the r.m.s.e. values in easting, northing and height. The resection solution is formulated mathematically as explained in Chapter 10. Explanation of each step is given in the form of comment statements. For further explanation, consult Shortis (1980).

In general, the main program calls the following subroutines:

STIO: Carries out the inner orientation; and transforms the comparator coordinates of the measured points into the image coordinate system. Using the calibrated coordinates of the fiducial marks, it computes the transformation parameters which are then used by the TRANSF subroutine to compute the transformed image coordinates. Three choices of transformation procedures are available: linear, affine and deformational transformation.

SINV: Matrix inversion subroutine.

TRANSF: Transformation subroutine which using the set of transformation parameters computed by STION transforms the measured point coordinates to the image coordinate system.

RADIS: Radial lens distortion correction subroutine.


```

      READ(2,70) NF,D,E
70  FORMAT(15,2F10.3)
      WRITE(6,80) D,E
80  FORMAT(/'THE FOCAL LENGTHS OF THE LEFT AND RIGHT CAMERAS ARE',
11X,F10.3,' AND ',F10.3,' RESPECTIVELY.')
      U(1,1,3)=-D/1000.
      U(2,1,3)=-E/1000.

C      READ INITIAL VALUES.

      READ(2,90)A(1),A(2),A(3),W(1),P(1),KA(1)
      READ(2,90) O(1),O(2),O(3),W(2),P(2),KA(2)
90  FORMAT(F10.3,F11.3,4F10.3)

C
C      IF FIDUCIAL COORDS INCLUDED IN CONTROL FILE FC=1 AND
C      IF NOT FC=0
C
      READ(2,70) FC

C
C      PRESET FIDUCIAL IDENTIFIERS TO 1,2,3 & 4.
C
      DO 120 I=1,4
      NC(I)=I
120  CONTINUE
      IM=1
      IF(FC.EQ.0)GO TO 160

C
C      IF CONTROL FILE INCLUDES FIDUCIAL COORDINATES THEN READ THEM.
C
      WRITE(6,130)
130  FORMAT(/' FIDUCIAL MARK COORDINATES'//'      PT',6X,'X',9X,'Y'/)
      DO 150 I=1,NF
      READ(2,360) NC(I),C(I,1),C(I,2)
      WRITE(6,140)NC(I),C(I,1),C(I,2)
140  FORMAT(I6,2F10.3)
150  CONTINUE

C
C      ZERO AL,AV & AC ARRAYS.
C
160  DO 170 I=1,80
      AL(I)=0.
170  CONTINUE
      DO 180 I=1,30
      DO 180 J=1,4
      AV(I,J)=0.
180  AC(J,I)=0.

C
C      OPEN OBSERVATION FILE.
C
      WRITE(6,190)
190  FORMAT(/' TYPE OBSERVATION FILE NAME >')
      READ(5,30) OBSFIL
      OPEN(3,FILE=OBSFIL ,STATUS='OLD',FORM='FORMATTED')
      LU=1

C
C      CALL STIO SUBROUTINE FOR INTERIOR ORIENTATION.
C
      CALL STIO

```

C READ RADIAL LENS DISTORTION CORRECTION PARAMETERS.

C
C READ(2,210) PV
210 FORMAT(7F10.3)

C READ PRINCIPAL POINT'S COORDINATES

C
C READ(2,220)XS,YS
220 FORMAT(2F10.3)
C READ(2,240)NR,ID
240 FORMAT(2I5)
C READ(2,220)SP

C OUTPUT CONTROL POINTS COORDS.

C ONLY THE FIRST 30 CONTROL POINTS ARE READ.

C
C
C
330 WRITE(6,340)
340 FORMAT(//'CONTROL POINT COORDINATES'//'
1,15X,'Z'//)
NCON=1
350 READ(2,361) NC(NCON),(C(NCON,J),J=1,3),IB(NCON)
361 FORMAT(I5,3F13.4,I3)
360 FORMAT(I5,2(1X,F10.3),F10.3,I5)
IF(NC(NCON).EQ.9999) GO TO 400
JJ=IB(NCON)
IF(JJ.EQ.0) GO TO 350
IF(JJ.EQ.1) WRITE(6,370) NC(NCON),C(NCON,3)
IF(JJ.GT.1) WRITE(6,380) NC(NCON),(C(NCON,J),J=1,JJ)
370 FORMAT(I6,30X,2F15.4)
380 FORMAT(I6,4F15.4)
NCON=NCON+1
IF(NCON.LT.31) GO TO 350
WRITE(6,390)
390 FORMAT(//' TOO MANY CONTROL POINTS !?!'//)
400 NCON=NCON-1
WRITE(6,410)
410 FORMAT(1H0)

C
C
C
411 DO 412 I=1,100
NRIS(I)=0
412 CONTINUE
DO 414 I=1,100
DO 414 J=1,3
414 RIS(I,J)=0.
DO 415 J=1,120
DO 415 I=1,3
415 RIST(J,I)=0.
416 FORMAT(7F10.3)
NCO1=1
420 INF=1

C READ CHECK POINTS COODINATES.

C
C
C
421 READ(2, 422) NRIS(INF),(RIS(INF,J),J=1,3)
IF(NRIS(INF).EQ.9999) GOTO 423
INF=INF+1
GOTO 421
422 FORMAT(I5,3F13.4,I3)
C OBSERVATION

C

423 MM=NCON

C

```

K3=-1.*ATAN2(O(2)-A(2),O(1)-A(1))
IF(O(2).EQ.A(2).AND.O(1).LT.A(1))K3=K3-3.141598
DO 424 I=1,3

```

```

424 O(I)=O(I)-A(I)
O(1)=(O(1)*O(1)+O(2)*O(2))**.5
O(2)=0.

```

```

D=A(1)
E=A(2)
T=DCOS(K3)
S=DSIN(K3)
A(1)=D*T-E*S
A(2)= D*S+E*T

```

```

425 DO 426 I=1,30
TN(I)=0.
DO 426 J=1,4
T2(I,J)=0.
TX(I,J)=0.

```

```

426 CONTINUE
LV=-1

```

```

427 READ(3,428,END=436)K,G,H,S,T

```

```

428 FORMAT(I5,4F10.3)
IF(K.EQ.9999)GO TO 436
JJ=0

```

```

DO 429 J=1,MM
IF(NC(J).EQ.K)JJ=J

```

```

429 CONTINUE
IF(JJ.EQ.LV)WRITE(6,430)

```

```

430 FORMAT(/' POINT IS A DUPLICATE -- IGNORED!'/)
IF(JJ.EQ.LV)GO TO 435
IF(JJ.NE.0)GO TO 432
IF(MM.EQ.31)WRITE(6,431)

```

```

431 FORMAT(//)' TOO MANY CONTROL POINTS!?!' )
IF(MM.EQ.30)GO TO 436
MM=MM+1
NC(MM)=K
IB(MM)=0
JJ=MM

```

```

432 VL(1)=G+.5*S
VL(2)=H+.5*T
VL(3)=S
VL(4)=T

```

```

433 DO 434 J=1,4
IF(TN(JJ).EQ.0.)TS(JJ,J)=VL(J)
VL(J)=VL(J)-TS(JJ,J)
TX(JJ,J)=TX(JJ,J)+VL(J)

```

```

434 T2(JJ,J)=T2(JJ,J)+VL(J)**2
TN(JJ)=TN(JJ)+1.0

```

```

435 LV=JJ
GO TO 427

```

```

436 WRITE(6,437)

```

```

437 FORMAT(//'MEAN MEASUREMENTS WITH STD DEVS'//'PT      X',9X,'Y',
18X,'PX',8X,'PY      MEAS'/11X,'SX',8X,'SY',7X,'SPX',7X,'SPY'//)
DO 442 I=1,MM
IF(TN(I).EQ.0.)GO TO 442
DO 438 J=1,4
VL(J)=TX(I,J)/TN(I)

```

```

SX(I,J)=.005
IF(TN(I).GT.1.)SX(I,J)=( (T2(I,J)/TN(I)-VL(J)**2)/(TN(I)-1.))
1**5
IF(SX(I,J).LE.0.)SX(I,J)=.001
438 VL(J)=VL(J)+TS(I,J)
VL(1)=VL(1)-.5*VL(3)
VL(2)=VL(2)-.5*VL(4)
WRITE(6,439)NC(I),(VL(J),J=1,4),TN(I),(SX(I,L),L=1,4)
439 FORMAT(I6,4F10.3,F5.0/6X,4F10.3)
DO 440 J=1,4
440 SX(I,J)=1E-6*SX(I,J)**2
Q(1)=VL(2)+VL(4)
Q(2)=VL(2)
VL(2)=VL(1)+VL(3)
DO 441 J=1,2
NS=J
IX=2*J-1
IY=2*J
X=VL(J)
Y=Q(J)
C CALL TRANSF SUBROUTINE FOLLOWED BY RADIS.

CALL TRANSF(X,Y,NS)
CALL RADIS(X,Y)
U(J,I,1)=X/1000.
U(J,I,2)=Y/1000.
441 U(J,I,3)=U(J,1,3)
442 IF(TN(I).EQ.0.)IB(I)=100+IB(I)
WRITE(6,443)
443 FORMAT(1X)
444 II=0
445 II=II+1
DO 446 I=1,4
446 SQ(I)=0.
I0=0
I1=0
I2=0
S0=0.
WRITE(6,447)II
447 FORMAT('/' RESIDUAL ERRORS FOR ITERATION',I2//' IN METRES
1AT TERRAIN SCALE'//' PT X',15X,'Y',15X,'Z',15X,'PY'//)
DO 449 I=1,2
IF(II.NE.1)GO TO 448
KA(I)=KA(I)/GR
P(I)=P(I)/GR
W(I)=W(I)/GR
448 D=DSIN(KA(I))
E=DCOS(KA(I))
H=DCOS(P(I))
G=DSIN(P(I))
S=DSIN(W(I))
T=DCOS(W(I))
R(I,1,1)=E*H
R(I,1,2)=E*G*S-D*T
R(I,1,3)= E*G*T+D*S
R(I,2,1)= D*H
R(I,2,2)= D*G*S+E*T
R(I,2,3)=D*G*T-E*S
R(I,3,1)=-G

```

```

R(I,3,2)= H*S
449 R(I,3,3)=H*T
DO 500 I=1,78
500 AL(I)=0.
DO 501 I=1,12
501 AY(I)=0.
LL=0
T=DCOS(K3)
S=DSIN(K3)
DO 526 I=1,MM
IF( IB(I).GT.5 )GO TO G=DSIN(P(I))
S=DSIN(W(I))
T=DCOS(W(I))
R(I,1,1)=E*H
R(I,1,2)=E*G*S-D*T
R(I,1,3)= E*G*T+D*S
R(I,2,1)= D*H
R(I,2,2)= D*G*S+E*T
R(I,2,3)=D*G*T-E*S
R(I,3,1)=-G
R(I,3,2)= H*S
449 R(I,3,3)=H*T
DO 500 I=1,78
500 AL(I)=0.
DO 501 I=1,12
501 AY(I)=0.
LL=0
T=DCOS(K3)
S=DSIN(K3)
DO 526 I=1,MM
IF( IB(I).GT.5 )GO TOIN(W(J))*U(J,I,2)+
1DCOS(W(J))*U(J,I,3))
D=MV(1,1)*MV(2,3)-MV(1,3)*MV(2,1)
LM(1)=(O(1)*MV(2,3)-O(3)*MV(2,1))/D
LM(2)=(O(1)*MV(1,3)-O(3)*MV(1,1))/D
X=.5*(LM(1)*MV(1,1)+LM(2)*MV(2,1))
Y=.5*(LM(1)*MV(1,2)+LM(2)*MV(2,2))
Z=.5*(LM(1)*MV(1,3)+LM(2)*MV(2,3))
JJ=IB(I)
IF( IB(I).LT.-5 )JJ=0
IF( JJ.EQ.0 )GO TO 506
IF( IB(I).EQ.1 )GO TO 505
G=C(I,1)*T-C(I,2)*S
H= C(I,1)*S+C(I,2)*T
Q(1)=G-A(1)-.5*O(1)-X
Q(2)=H-A(2)-Y
505 Q(3)=C(I,3)-A(3)-.5*O(3)-Z
F(1)=A(1)-G
F(2)=A(2)-H
F(3)=A(3)-C(I,3)
506 Q(4)=LM(1)*MV(1,2)-LM(2)*MV(2,2)
IF( JJ.EQ.0 )WRITE(6,507)NC(I),Q(4)
507 FORMAT( I6,45X,F15.4)
IF( JJ.EQ.3 )WRITE(6,815)NC(I),(Q(K),K=1,4)
IF( JJ.EQ.2 )WRITE(6,508)NC(I),Q(1),Q(2),Q(4)
508 FORMAT( I6,2F15.4,15X,F15.4)
IF( JJ.EQ.1 )WRITE(6,860)NC(I),Q(3),Q(4)
IF( JJ.EQ.2 )Q(3)=0.
DO 509 J=1,4

```

```

SQ(J)=SQ(J)+Q(J)**2
509 Q(J)=D*Q(J)
AC(1,4)=MV(1,1)*MV(2,3)
AC(3,4)=MV(1,3)*MV(2,3)
AC(2,4)=.5*(MV(1,2)*MV(2,3)+MV(1,3)*MV(2,2))
AC(4,4)=MV(1,3)*MV(2,2)-MV(1,2)*MV(2,3)
AC(1,5)=D*H/GR
AC(2,5)=-D*G/GR
AC(2,6)=-.5*(MV(1,1)*MV(2,2)+MV(1,2)*MV(2,1))
AC(1,6)=-MV(1,1)*MV(2,1)
AC(3,6)=-MV(1,3)*MV(2,1)
AC(4,6)=MV(1,2)*MV(2,1)-MV(1,1)*MV(2,2)
G=F(1)+O(1)
H=F(3)+O(3)
DO 510 J=1,3
AC(J,J)=D
AC(1,J+6)=(CK(1,1,J)*(G*MV(2,3)-O(3)*MV(2,1))-CK(1,3,J)*
1F(1)*MV(2,1))/GR
AC(3,J+6)=(CK(1,1,J)*F(3)*MV(2,3)+CK(1,3,J)*(O(1)*MV(2,3)-
1MV(2,1)*H))/GR
AC(2,J+6)=(CK(1,1,J)*(F(2)*MV(2,3)-.5*O(3)*MV(2,2))+CK(1,2,J)
1*.5*LM(1)*D+CK(1,3,J)*(F(2)*MV(2,1)-F(2)*MV(2,1)))/GR
AC(4,J+6)=(CK(1,3,J)*O(1)-CK(1,1,J)*O(3))*MV(2,2)-CK(1,2,J)
1*LM(1)*D)/GR
AC(1,J+9)=(CK(2,3,J)*G*MV(1,1)-CK(2,1,J)*(O(3)*MV(1,1)+F
1(1)*MV(1,3)))/GR
AC(3,J+9)=(CK(2,3,J)*(F(3)*MV(1,1)+O(1)*MV(1,3))-CK(2,1,J)*H
1*MV(1,3))/GR
AC(2,J+9)=(CK(2,2,J)*.5*LM(2)*D+CK(2,3,J)*(F(2)*MV(1,1)+.5*
1O(1)*MV(1,2))-CK(2,1,J)*(F(2)*MV(1,2)+F(2)*MV(1,3)))/GR
510 AC(4,J+9)=(CK(2,2,J)*LM(2)*D+(CK(2,1,J)*O(3)-CK(2,3,J)*O(1))
1*MV(1,2))/GR
G=O(1)*O(1)
H=(X*X+Y*Y)**2
DO 512 J=1,2
DO 511 K=1,3
MV(J,K)=MV(J,K)**2
511 AV(J,K)=U(J,I,K)**2
AV(3,J)=LM(J)*((MV(J,1)+MV(J,3))/(AV(J,1)+AV(J,3)))**.5
512 AV(4,J)=LM(J)*((MV(J,2)+MV(J,3))/(AV(J,2)+AV(J,3)))**.5
LM(1)=.25*(AV(3,1)+AV(3,2))**2
LM(2)=.25*(AV(4,1)+AV(4,2))**2
VL(10)=G*LM(2)*SX(I,4)/LM(1)+O(3)*O(3)*SX(I,3)*Y*Y/Z/Z
IF(JJ.NE.0)GO TO 513
I0=I0+1
V(4,4)=G/VL(10)/LM(1)/D/D
GO TO 519
513 VL(1)=G*SX(I,1)+X*X*SX(I,3)
VL(2)=X*Y*SX(I,3)
VL(3)=LM(2)*G*SX(I,2)/LM(1)+Y*Y*SX(I,3)
VL(4)=X*Z*SX(I,3)
VL(5)=Y*Z*SX(I,3)
VL(6)=Z*Z*SX(I,3)
VL(7)=-X*Y*O(3)*SX(I,3)/Z
VL(8)=-Y*Y*O(3)*SX(I,3)/Z
VL(9)=-Y*O(3)*SX(I,3)
IF(JJ.EQ.3)GO TO 517
IF(JJ.EQ.1)GO TO 515
VL(4)=VL(7)

```

```

VL(5)=VL(8)
VL(6)=VL(10)
I2=I2+1
DO 514 J=1,12
514 AC(3,J)=AC(4,J)
Q(3)=Q(4)
GO TO 517
515 VL(1)=VL(6)
VL(2)=VL(9)
VL(3)=VL(10)
I1=I1+1
DO 516 J=1,12
AC(1,J)=AC(3,J)
516 AC(2,J)=AC(4,J)
Q(1)=Q(3)
Q(2)=Q(4)
517 KK=JJ+1
CALL SINV(VL, KK)
IF(KK.EQ.0)GO TO 865
DO 518 J=1, KK
DO 518 K=1, KK
JK=J+(K*K-K)/2
IF(J.GT.K)JK=K+(J+J-J)/2
518 V(J,K)=VL(JK)*G/LM(1)/D/D
519 NS=1
IF(JJ.EQ.0)KK=4
IF(JJ.EQ.0)NS=4
DO 520 J=NS, KK
VL(J)=0.
DO 520 K=NS, KK
520 VL(J)=VL(J)+V(J,K)*Q(K)
521 S0=S0+Q(J)*VL(J)
DO 522 J=1,12
DO 522 K=NS, KK
AV(J,K)=0.
DO 522 L=NS, KK
522 AV(J,K)=AV(J,K)+AC(L,J)*V(L,K)
DO 523 J=1,12
DO 523 K=NS, KK
523 AY(J)=AY(J)+AV(J,K)*Q(K)
DO 525 J=1,12
DO 525 K=1,12
IF(J.GT.K)GO TO 525
JK=J+(K*K-K)/2
DO 524 L=NS, KK
524 AL(JK)=AL(JK)+AV(J,L)*AC(L,K)
525 CONTINUE
526 IF(IB(I).GT.5)LL=LL+1
DO 527 I=1,2
527 SQ(I)=(SQ(I)/(MM-I0-LL-I1))**.5
SQ(3)=(SQ(3)/(MM-I0-LL-I2))**.5
SQ(4)=(SQ(4)/(MM-LL))**.5
Z=5.*DABS(SQ(4))
WRITE(6,528)SQ
528 FORMAT('/' RMSE',4F15.4)
S1=4*(MM-LL)-3*I0-2*I1-I2-12
IF(S1.LT.0.)WRITE(6,529)
529 FORMAT('//' NOT ENOUGH CONTROL FOR A SOLUTION!!!!'//)
IF(S1.LT.0.)GO TO 865

```

```

IF(S1.GT.0.)GO TO 531
WRITE(6,530)
530 FORMAT(//' MINIMUM CONTROL FOR A SOLUTION!!'//)
S0=1.
GO TO 532
531 S0=(DABS(S0/S1))**.5
532 WRITE(6,533)
533 FORMAT('/' DO YOU WANT ANOTHER ITERATION ? Y OR N')
READ(5,534)ANS1
534 FORMAT(A1)
N=12
CALL SINV(AL,N)
IF(N.EQ.0)GO TO 865
IF(ANS1.EQ.'N')GO TO 540
LL=0
DO 536 I=1,12
Q(I)=0.
DO 537 J=1,12
JK=I+(J*J-J)/2
IF(I.GT.J)JK=J+(I*I-I)/2
537 Q(I)=Q(I)+AL(JK)*AY(J)
536 IF(DABS(Q(I)).GE..0005)LL=LL+1
B=Q(5)/GR
K3=K3+B
Q(5)=0.
DO 538 I=1,3
A(I)=A(I)+Q(I)
538 O(I)=O(I)+Q(I+3)
P(1)=P(1)+Q(8)/GR
KA(1)=KA(1)+Q(7)/GR
W(1)=W(1)+Q(9)/GR
P(2)=P(2)+Q(11)/GR
KA(2)=KA(2)+Q(10)/GR
W(2)=W(2)+Q(12)/GR
Q(5)=O(1)*B
WRITE(6,539)I1:LL,Q
539 FORMAT(//'AFTER',I3,' ITERATIONS, THERE ARE',I3,'LARGE CORREC
TIONS',//,6X,'AX',8X,'AY',8X,'AZ',8X,'BX',8X,'BY',8X,'BZ'/6F10.
2.4,/6X,'K1',8X,'P1',8X,'O1',8X,'K2',8X,'P2',8X,'O2'/6F10.4//)
GO TO 445
540 CONTINUE
DO 541 I=1,2
KA(I)=KA(I)*GR
P(I)=P(I)*GR
541 W(I)=W(I)*GR
DO 542 I=1,12
J=I*(I+1)/2
542 VL(I)=S0*AL(J)**.5
D=DCOS(K3)
E=DSIN(K3)
B=VL(5)*VL(5)/GR/GR
G=VL(1)*VL(1)+A(2)*A(2)*B
H=VL(2)*VL(2)+A(1)*A(1)*B
VL(1)=(D*D*G+E*E*H)**.5
VL(2)=(E*E*G+D*D*H)**.5
G=VL(4)*VL(4)
H=O(1)*O(1)*B
VL(4)=(D*D*G+E*E*H)**.5
VL(5)=(E*E*G+D*D*H)**.5

```

```

AR(1)=D*A(1)+E*A(2)
AR(2)=D*A(2)-E*A(1)
F(1)= D*O(1)
F(2)=-E*O(1)
AR(3)=A(3)
F(3)=O(3)
DO 550 I=1,3
550 F(I)=AR(I)+F(I)
FLH=F(3)
WRITE(6,560)AR,F,(KA(K),P(K),W(K),K=1,2),SO,VL
560 FORMAT(//'FINAL RELATIVE/ABSOLUTE ORIENTATION PARAMETERS'
1//'LEFT CAMERA X,Y,Z = ',3F15.4/'RIGHT CAMERA X,Y,Z = ',
23F15.4//'2LEFT ROTATIONS K,P,O = ',3F10.4/'RIGHT ROTATIONS
3=' ,3F10.4//'STD DEVIATIONS OF THE PARAMETERS -- SIGMA
4ZERO',F8.2//'LEFT CAMERA X,Y,Z = ',3F10.4/' CAMERA BASE
5X,Y,Z = ',3F10.4//'LEFT ROTATIONS K,P,O = ',3F10.3/' RIGHT
6ROTATIONS K,P,O = ',3F10.3/)
WRITE(6,590)
DO 580 I=1,2
WRITE(6, 610)
DO 570 K=1,3
WRITE(6,600) (R(I,K,J),J=1,3)
570 CONTINUE
580 CONTINUE
590 FORMAT(//,'ROTATION MATRICES ARE:-',//)
600 FORMAT(3F10.6)
610 FORMAT(//,'**',//)
620 WRITE(6,630)
630 FORMAT(//'DO YOU WANT TO ADD/ DISCARD SOME POINTS ? Y OR N')
C
READ(5,534)ANS1
IF(ANS1.EQ.'N')GO TO 735
WRITE(6,640)
640 FORMAT('TYPE THE ID NUMBERS OF THE POINTS TO BE DELETED OR'/
1'RESTORED CHECK EACH RESULT (TERMINATE BY 9999)'/)
650 READ(5,660)J
660 FORMAT(I5)
IF(J.EQ.9999)GO TO 444
JJ=0
DO 670 I=1,MM
670 IF(NC(I).EQ.J)JJ=I
IF(JJ.EQ.0)WRITE(6,680)
680 FORMAT(' NOT FOUND!?!')
IF(JJ.EQ.0)GO TO 650
KK=ABS(IB(JJ))
IF(IB(JJ).GT.5.OR.KK.LT.5)KK=IB(JJ)-100
IF(IB(JJ).EQ.0)KK=100
IF(IB(JJ).LT.-5)KK=200+IB(JJ)
IF(IB(JJ).GT.5)WRITE(6,690)
690 FORMAT(' RESTORED'/)
IF(IB(JJ).LT.5)WRITE(6,700)
700 FORMAT(' DELETED'/)
IB(JJ)=KK
GO TO 650
735 WRITE(6,740)
740 FORMAT(//'DO YOU WANT TO DISPLAY/RECORD TERRAIN COORDS ?
1Y OR N')
READ(5,534)ANS1
IF(ANS1.EQ.'N')GO TO 895

```

```

755 FORMAT(A20)
770 FORMAT(F10.0)
    IF(SPY.EQ.0.)GO TO 775
    Z=SPY
775 WRITE(6,810)
    READ(5,534)ANS2
    IF(ANS2.EQ.'N')GOTO 780
    WRITE(6,880)
    READ(5,755)AZ
    WRITE(6,835)
    WRITE(6,840)
    OPEN(4,FILE=AZ,STATUS='OLD',FORM='FORMATTED')
    GOTO 790
780 WRITE(6,785)
785 FORMAT(/4X,'PT',8X,'X',15X,'Y',15X,'Z',15X,'PY'/)
790 V(1,3)=U(1,1,3)
    V(2,3)=U(2,1,3)
    INM=0
795 READ(3,428)NS,G,H,S,T
    LM(1)=G
    VL(1)=H+T
    LM(2)=G+S
    VL(2)=H
    DO 800 J=1,2
    JK=J
    SUS=LM(J)
    SUB=VL(J)
    CALL TRANSF(SUS,SUB,JK)
    CALL RADIS(SUS,SUB)
    VL(J)=SUB
    LM(J)=SUS
    V(J,1)=LM(J)/1000.
    V(J,2)=VL(J)/1000.
    DO 800 K=1,3
    MV(J,K)=0.
    DO 800 L=1,3
800 MV(J,K)=MV(J,K)+R(J,K,L)*V(J,L)
    B=MV(1,1)*MV(2,3)-MV(1,3)*MV(2,1)
    X=(O(1)*MV(2,3)-O(3)*MV(2,1))/B
    Y=(O(1)*MV(1,3)-O(3)*MV(1,1))/B
    DO 805 J=1,3
805 F(J)=A(J)+.5*(O(J)+X*MV(1,J)+Y*MV(2,J))
    Q(1)=D*F(1)+E*F(2)
    Q(2)=D*F(2)-E*F(1)
    Q(3)=F(3)
    Q(4)=X*MV(1,2)-Y*MV(2,2)
    IF(NS.EQ.9999)GO TO 865
    INM=INM+1
810 FORMAT('/'ARE YOU EXECUTING AN ACCURACY TEST ? Y OR N')
    IF(ANS2.EQ.'Y')GOTO 825
    WRITE(6,815)NS,(Q(J),J=1,4)
815 FORMAT(I6,4F15.4)
    IF(DABS(Q(4)).GT.Z.AND.Z.GT.4E-4)GO TO 820
    IF(ANS2.EQ.'1')WRITE(7,815)NS,(Q(J),J=1,3)
    GOTO 795
820 WRITE(6,855)
    GOTO 795
825 DO 830 N=1,INF
    IF(NRIS(N).NE.NS)GOTO 830

```

```

RIST(INM,1)=RIS(N,1)-Q(1)
RIST(INM,2)=RIS(N,2)-Q(2)
RIST(INM,3)=RIS(N,3)-Q(3)
Q(5)=RIST(INM,1)
Q(6)=RIST(INM,2)
Q(7)=RIST(INM,3)
WRITE(4,845)NS,RIS(N,1),RIS(N,2),Q(5),Q(6),Q(7)
830 CONTINUE
835 FORMAT(1H , 'GROUND COORDS WITH RESIDUALS IN METRES',/,
1 '=====')
840 FORMAT(1H , 'POINT      X          VX          Y          VY
1      Z          VZ')
845 FORMAT(I4,2F10.0,3F8.0)
WRITE(6,850) NS,Q(1),Q(5),Q(2),Q(6),Q(3),Q(7)
850 FORMAT(I6,3(F15.3,F7.3))
GO TO 795
860 FORMAT(I6,20X,2F10.4)
865 IF(ANS2.EQ.'N')GOTO 895
DO 870 J=1,4
Q(J)=0.
870 CONTINUE
DO 875 I=1,INM
Q(6)=0.
Q(1)=Q(1)+(RIST(I,1)**2)
Q(2)=Q(2)+(RIST(I,2)**2)
Q(3)=Q(3)+(RIST(I,3)**2)
875 CONTINUE
Q(1)=DABS((Q(1)/INM)**.5)
Q(2)=DABS((Q(2)/INM)**.5)
Q(3)=DABS((Q(3)/INM)**.5)
Q(4)=Q(3)*1000./FLH
WRITE(6,885)
WRITE(6,890)Q(1),Q(2),Q(3),Q(4)
880 FORMAT('TYPE OUT PUT FILE NAME..>')
885 FORMAT(/, 'THE ROOT MEAN SQUARE ERRORS OF THE DISCREPANCIES'
1,/, 'AT THE GROUND SCALE IN METRES AND THE RMSE AS PER 1000TH'
2,/, 'OF THE FLYING HEIGHT OF THE SENSOR',/, '*****',/)
890 FORMAT(/,1H ,11X, 'X',15X, 'Y',15X, 'Z',14X, 'Z%%FH',/,4F16.3
1,/)
895 CLOSE(UNIT=3)
CLOSE(UNIT=2)
CLOSE(UNIT=4)
STOP
END
C
C *****
C SUBROUTINE SINVA(A ,N)
C *****
C IMPLICIT DOUBLE PRECISION(A-H,O-Z)
C DOUBLE PRECISION A(12)
C JK=0
C DO 8 K=1,N
C JK=JK+K
C IN=JK
C LL=K-1
C DO 8 I=K,N
C E=0.
C IF(LL.EQ.0)GOTO 4
C DO 3 L=1,LL

```

```

J=JK-L
JJ=IN-L
3 E=E+A(J)*A(JJ)
4 E=A(IN)-E
  IF(I-K)7,6,7
6 IF(E.GE.0.0) GOTO 5
  WRITE(6,99)
99 FORMAT(//'***SINGULAR MATRIX!?!?***SOLUTION IMPOSSIBLE***'//)
  N=0
  GOTO 17
5 D=DSQRT(E)
  A(JK)=D
  D=1./D
  GOTO 8
7 A(IN)=E*D
8 IN=IN+I
  JK=N*(N+1)/2
  IN=JK
  DO 13 I=1,N
  D=1./A(JK)
  A(JK)=D
  NS=N
  JJ=I-1
  LL=N-JJ
  IF(JJ.LE.0) GOTO 12
  J=IN
  DO 11 K=1,JJ
  E=0.
  NS=NS-1
  LH=JK
  LV=J
  DO 9 L=LL,NS
  LV=LV+1
  LH=LH+L
  E=E+A(LV)*A(LH)
9 CONTINUE
  A(J)=-E*D
  J=J-NS
11 CONTINUE
12 JK=JK-NS
  IN=IN-1
13 CONTINUE
  DO 16 I=1,N
  JK=JK+I
  J=JK
  DO 16 K=I,N
  E=0.
  LH=J
  DO 14 L=K,N
  LV=LH+K-I
  E=E+A(LH)*A(LV)
14 LH=LH+L
  A(J)=E
16 J=J+K
17 RETURN
  END

```

C
C
C

```

C *****
C SUBROUTINE STIO
C *****
C *=====
C *STIO TRANSFORMS COMPARATOR COORDINATES TO CAMERA FIDUCIAL *
C *MARKS SYSTEM **ORIGIN IS THE INTERSECTION OF THE FIDUCIALS*
C *=====
C
C IMPLICIT DOUBLE PRECISION (A-H,O-Z)
C INTEGER FC
C COMMON /B0/C(30,3),NC(30),U(2,30,3),AC(4,30),AL(80),AY(12),
C 1Q(12),AV(30,4),SQ(4),AQ(30,4),SX(30,4),VL(12),IB(30),NF,FC
C 2/B2/AN(2,8)
C LV=0
C JJ=0
C
C READ COMPARATOR COORDS OF FIDUCIALS **TERMINATE AT 9999**
C
800 READ(3,40,END=801)K,G,H,S,T
40 FORMAT(I5,4F10.3)
IF(K.EQ.9999)GOTO 60
DO 45 J=1,NF
IF(K.EQ.NC(J))JJ=J
45 CONTINUE
IF(JJ.EQ.LV)WRITE(6,46)
46 FORMAT(/'POINT IS A DUPLICATE OR IS NOT RECOGNIZED::IGNORED!
1'/)
IF(JJ.EQ.LV) GOTO 55
VL(1)=G
VL(2)=H+T
VL(3)=G+S
VL(4)=H
DO 50 J=1,4
IF(AL(JJ).EQ.0)AQ(JJ,J)=VL(J)
VL(J)=VL(J)-AQ(JJ,J)
AV(JJ,J)=AV(JJ,J)+VL(J)
50 AC(J,JJ)=AC(J,JJ)+VL(J)**2
AL(JJ)=AL(JJ)+1
55 LV=JJ
GOTO 800
C
C OUTPUT MEAN OBSERVATIONS AND STD DEVIATION OF FIDUCIALS
C
60 WRITE(6,65)
65 FORMAT(//' MEAN MEASUREMENTS WITH STANDARD DEVIATIONS'//'
1PT X1',8X,'Y1',18X,'X2',8X,'Y2 MEAS'/11X,'SX1',7X,'SY1',
37X,'SX2',7X,'SY2'/)
JK=0
DO 85 I=1,NF
IF(AL(I).EQ.0)GOTO 85
JK=JK+1
DO 70 J=1,4
AV(I,J)=AV(I,J)/AL(I)
VL(J)=.005
IF(AL(I).GT.1.0)VL(J)=((AC(J,I)/AL(I)-AV(I,J)**2)/(AL(I)-1))
1**.5
IF(VL(J).LE.0)VL(J)=.001
70 AV(I,J)=AV(I,J)+AQ(I,J)

```

```

WRITE(6,75)NC(I),(AV(I,J),J=1,4),AL(I),(VL(L),L=1,4)
75 FORMAT(I6,4F10.3,F5.0,/6X,4F10.3)
DO 80 J=1,2
DO 80 K=1,2
N=2*J+K-2
IF(JK.EQ.1.AND.FC.EQ.1)AN(J,K)=AV(I,N)-C(I,K)
80 U(J,I,K)=2.5E-5/VL(N)**2
85 IF(AL(I).EQ.0)NC(I)=-999
IF(FC.EQ.0)WRITE(6,901)
901 FORMAT(1X)
IF(FC.EQ.0)GOTO 152
WRITE(6,150)
150 FORMAT('//COMPARATOR COORDS ARE REDUCED TO IMAGE COORDS
1USING:','/, '1- RECTILINEAR, 2- AFFINE, OR 3-DEFORMATIONAL
2TRANSFORMATION'//, 'SELECT 1, 2 OR 3 ?')

```

C

```

READ(5,900) IT
900 FORMAT(I1)
N=2*(IT+1)
152 CONTINUE
DO 224 I=1,2
NS=I
IX=2*I-1
IY=2*I
DO 153 J=4,8
153 AN(I,J)=0.
IF(FC.EQ.0)GOTO 221

```

C
C
C
C

```

TRANSFORMATION:::
=====

AN(I,3)=1
AN(I,6)=1
II=0
DO 155 J=1,36
155 AL(J)=0.
DO 160 J=1,NF
IF(NC(J).EQ.-999)GOTO 160
X=AV(J,IX)
Y=AV(J,IY)
B=X*Y
D=X*X
E=Y*Y
AL(1)=AL(1)+U(I,J,1)
AL(3)=AL(3)+U(I,J,2)
AL(4)=AL(4)+U(I,J,1)*X
AL(8)=AL(8)+U(I,J,2)*X
AL(6)=AL(6)+U(I,J,1)*D
AL(10)=AL(10)+U(I,J,2)*D
AL(11)=AL(11)+U(I,J,1)*Y
AL(13)=AL(13)+U(I,J,1)*B
AL(15)=AL(15)+U(I,J,1)*E
AL(17)=AL(17)+U(I,J,2)*Y
AL(19)=AL(19)+U(I,J,2)*B
AL(21)=AL(21)+U(I,J,2)*E
IF(IT.LT.3)GOTO 160
AL(24)=AL(24)+U(I,J,1)*B*Y
AL(25)=AL(25)-U(I,J,2)*B*X
AL(26)=AL(26)+U(I,J,1)*E*Y

```

```

AL(27)=AL(27)-U(I,J,2)*B*Y
AL(28)=AL(28)+U(I,J,1)*E*E+U(I,J,2)*B*B
AL(31)=AL(31)-U(I,J,1)*B*X
AL(32)=AL(32)+U(I,J,2)*D*X
AL(35)=AL(35)-U(I,J,1)*B*E-U(I,J,2)*B*D
AL(36)=AL(36)+U(I,J,1)*B*B+U(I,J,2)*D*D
160 CONTINUE
IF(IT-2)165,175,170
165 AL(5)=AL(17)
AL(6)=AL(6)+AL(21)
AL(7)=-AL(11)
AL(9)=AL(19)-AL(13)
AL(10)=AL(10)+AL(15)
GOTO 175
170 AL(22)=AL(15)
AL(23)=-AL(19)
AL(29)=-AL(13)
AL(30)=AL(10)
AL(33)=-AL(24)
AL(34)=-AL(25)
175 CALL SINV(AL , N)
IF(N.EQ.0)GOTO 801
180 II=II+1
IF(IT.EQ.1)AN(I,5)=-AN(I,4)
IF(IT.EQ.1)AN(I,6)=AN(I,3)
DO 185 J=1,8
185 AY(J)=0.
DO 190 J=1,NF
IF(NC(J).EQ.-999)GOTO 190
X=AV(J,IX)
Y=AV(J,IY)
D=X
E=Y
CALL TRANSF(D,E,NS)
DX=C(J,1)-D
DY=C(J,2)-E
AY(1)=AY(1)+U(I,J,1)*DX
AY(2)=AY(2)+U(I,J,2)*DY
AY(3)=AY(3)+U(I,J,1)*X*DX
AY(4)=AY(4)+U(I,J,2)*X*DY
AY(5)=AY(5)+U(I,J,1)*Y*DX
AY(6)=AY(6)+U(I,J,2)*Y*DY
AY(7)=AY(7)+DX*U(I,J,1)*Y*Y-DY*U(I,J,2)*X*Y
AY(8)=AY(8)-DX*U(I,J,1)*X*Y+DY*U(I,J,2)*X*X
190 CONTINUE
IF(IT.EQ.1)AY(3)=AY(3)+AY(6)
IF(IT.EQ.1)AY(4)=AY(4)-AY(5)
JK=0
DO 200 J=1,N
Q(J)=0.
DO 195 K=1,N
IJ=J+(K*K-K)/2
IF(J.GT.K)IJ=K+(J*J-J)/2
195 Q(J)=Q(J)+AL(IJ)*AY(K)
AN(I,J)=AN(I,J)+Q(J)
B=DABS(Q(J))
IF(J.GT.2.AND.J.LT.7.AND.B.GT.4E-6)JK=1
200 IF(J.LT.3.AND.B.GT.4E-4.OR.J.GT.6.AND.B.GT.4E-8)JK=1
IF(JK.NE.0.AND.II.LT.10)GOTO 180

```

```

IF(JK.NE.0.AND.II.EQ.10)WRITE(6,201)
201 FORMAT(//'NO CONVERGENCE AFTER 10 ITERATIONS! !????'//)
WRITE(6,205)II,N,I,(AN(I,J),J=1,N)
205 FORMAT(//'AFTER',I3,'ITERATIONS THE',I2,'PARAMETERS FOR
1PHOTOGRAPH NO',I2,'ARE:'//,4(E15.6,/))
B=0.
D=0.
E=0.
WRITE(6,210)
210 FORMAT(//'RESIDUALS AT FIDUCIAL MARKS'//'      PT      X',9X,
1'Y'//)
DO 215 J=1,NF
IF(NC(J).EQ.-999)GOTO 215
SUS=AV(J,IX)
SUB=AV(J,IY)
CALL TRANSF(SUS,SUB,NS)
AV(J,IX)=SUS
AV(J,IY)=SUB
DX=C(J,1)-AV(J,IX)
DY=C(J,2)-AV(J,IY)
D=D+DX*DX
E=E+DY*DY
WRITE(6,27)NC(J),DX,DY
27 FORMAT(I6,6F10.3)
215 IF(NC(J).EQ.-999)B=B+1.
D=(D/(NF-B))**.5
E=(E/(NF-B))**.5
WRITE(6,220) D,E
220 FORMAT(/' RMSE',2F10.3/)
GOTO 902

C
C
C
TRANSLATION ROTATION ONLY

221 D=AV(2,IX)-AV(1,IX)
E=AV(2,IY)-AV(1,IY)
DX=AV(4,IX)-AV(3,IX)
DY=AV(4,IY)-AV(3,IY)
T=.5*(ATAN(D/E)-ATAN(DY/DX))
AN(I,3)=DCOS(T)
AN(I,6)=AN(I,3)
AN(I,4)=DSIN(T)
AN(I,5)=-AN(I,4)
S=D*DY-DX*E
G=AV(2,IX)*AV(1,IY)-AV(1,IX)*AV(2,IY)
H=AV(4,IX)*AV(3,IY)-AV(3,IX)*AV(4,IY)
X=(DX*G-D*H)/S
Y=(DY*G-E*H)/S
AN(I,1)=Y*AN(I,4)-X*AN(I,3)
AN(I,2)=-X*AN(I,4)-Y*AN(I,3)
WRITE(6,222) I
222 FORMAT('TRANSFORMED COORDS FOR PHOTO',I2,/'      PT
1 X',9X,'Y'//)
DO 223 J=1,4
X=AV(J,IX)
Y=AV(J,IY)
CALL TRANSF(X,Y,NS)
223 WRITE(6,27) NC(J),X,Y
WRITE(6,901)
902 PAUSE

```

224 CONTINUE
801 RETURN
END

C
C
C

```
*****  
SUBROUTINE TRANSF(X,Y,I)  
*****  
IMPLICIT DOUBLE PRECISION (A-H,O-Z)  
COMMON /B2/A(2,8)  
XY=X*Y  
D=X  
E=Y  
X=A(I,1)+A(I,3)*D+A(I,5)*E+A(I,7)*E*E-A(I,8)*XY  
Y=A(I,2)+A(I,4)*D+A(I,6)*E-A(I,7)*XY+A(I,8)*D*D  
RETURN  
END
```

C
C
C

```
*****  
SUBROUTINE RADIS(X,Y)  
*****  
IMPLICIT DOUBLE PRECISION (A-H,O-Z)  
COMMON /B1/PV(21),XS,YS,NR,ID,SP  
X=X-XS  
Y=Y-YS  
D=DSQRT(X*X+Y*Y)  
IF(D.LT..001) GOTO 5  
GOTO (2,5),ID  
K=D/SP  
IF(K.EQ.20)E=PV(21)/1000.  
IF(K.LT.20)E=(PV(K+1)+(D-K*SP)*(PV(K+2)-PV(K+1)))/SP/1000.  
GOTO 4  
2 E=0.  
DO 3 I=1,NR  
3 E=E+PV(I)*D**(I-1)  
4 X=X*(1.-E/D)  
Y=Y*(1.-E/D)  
5 RETURN  
END
```

B.7.3 INPUT FILES

INPUT to program REDUCT consists of two files. One is the control file in which the calibration data and ground coordinates of the control and check points are stored and the other is the observation file containing the comparator or image coordinates of the fiducial marks followed by those of the measured points.

B.7.3.1 CONTROL FILE

```
(1)      1
CONTROL FILE FOR RMK A 30/23 MC IN SPACE MAPPING EXPERIMENT
(2)      4      305.128      305.128
(9)      458476.0002102673.36244409.000      0.000      0.000      0.000
          496938.0002163373.00244551.000      0.000      0.000      0.000
(3)      1
          1      -112.996      .046      -113.035      .034
(4)      2          .035      -112.958      -.046      -112.966
          3      113.033      .045      112.958      .035
          4          .034      113.035      -.045      113.033
          0.000      -.210      -1.690      -5.690      -13.490      -26.350      -45.530
(5)      -72.290      -107.914      -153.650      -210.770      -280.530      -364.210      -463.060
          -578.350      -711.350      0.000      0.000      0.000      0.000      0.000
(7)      0.000      -0.000
(8)      16      2
(9)      10.000
          12      404190.0000      2186720.0000      820.0000      3
          13      420240.0000      2202570.0000      730.0000      3
          14      436630.0000      2225560.0000      520.0000      3
          24      477650.0000      2187648.0000      650.0000      3
          23      441840.0000      2144620.0000      750.0000      3
          21      411390.0000      2115515.0000      440.0000      3
          31      448350.0000      2093240.0000      560.0000      3
          32      471095.0000      2123800.0000      700.0000      3 Control point
          33      504570.0000      2169740.0000      750.0000      3 ground coords
          43      519543.0000      2140604.0000      750.0000      3
          42      494158.0000      2106654.0000      690.0000      3
          41      482103.0000      2069473.0000      520.0000      3
          52      550313.0000      2090594.0000      925.0000      3
          53      557120.0000      2103770.0000      860.0000      3
          55      577793.0000      2124805.0000      450.0000      3
          3515      401300.0000      2161585.0000      570.0000      3
          3513      409795.0000      2190825.0000      661.0000      3
          113      435109.0000      2206190.0000      900.0000      3
          112      412519.0000      2178260.0000      659.0000      3
          1637      459723.0000      2125986.0000      643.0000      3
          1632      497377.0000      2129000.0000      700.0000      3
          114      461495.0000      2108993.0000      670.0000      3
          115      484500.0000      2140955.0000      720.0000      3
          116      505140.0000      2169690.0000      690.0000      3
          1641      519560.0000      2140630.0000      680.0000      3
          1647      531590.0000      2127288.0000      750.0000      3
          117      555476.0000      2123185.0000      910.0000      3
          118      544855.0000      2092757.0000      700.0000      3
          119      528801.0000      2059150.0000      620.0000      3
          9999      (end of control points data)
          3514      402860.0000      2160256.0000      580.0000      3
          1354      399090.0000      2175644.0000      560.0000      3
          1355      397725.0000      2175950.0000      554.0000      3
```

1358	404900.0000	2186180.0000	588.0000	3
1356	406150.0000	2185503.0000	629.0000	3
1357	407650.0000	2189584.0000	597.0000	3
3516	422220.0000	2207587.0000	540.0000	3
1082	441620.0000	2217080.0000	512.0000	3
1081	441250.0000	2217045.0000	580.0000	3
1359	434160.0000	2198849.0000	440.0000	3
3511	424176.0000	2188746.0000	525.0000	3
3512	424630.0000	2188200.0000	503.0000	3
1351	433727.0000	2189776.0000	712.0000	3
1352	433680.0000	2189567.0000	553.0000	3
6314	452270.0000	2149758.0000	421.0000	3
1635	465030.0000	2123385.0000	532.0000	3
1634	467783.0000	2124260.0000	638.0000	3
1636	474900.0000	2133360.0000	503.0000	3
1631	476045.0000	2138588.0000	660.0000	3
6311	494480.0000	2131606.0000	678.0000	3
1633	498300.0000	2129000.0000	643.0000	3
1638	486287.0000	2118889.0000	740.0000	3
1639	483550.0000	2110904.0000	585.0000	3
6310	481507.0000	2112045.0000	620.0000	3
6312	485210.0000	2109220.0000	640.0000	3
6313	484636.0000	2109378.0000	618.0000	3
9118	483898.0000	2089186.0000	580.0000	3
9114	495579.0000	2098450.0000	668.0000	3
9117	508504.0000	2083720.0000	630.0000	3
9115	507521.0000	2082131.0000	766.0000	3
9113	505490.0000	2079962.0000	750.0000	3
9119	478637.0000	2091735.0000	668.0000	3
1917	476620.0000	2088779.0000	720.0000	3
1911	478795.0000	2084600.0000	588.0000	3
1915	485421.0000	2082110.0000	600.0000	3
1916	485183.0000	2083530.0000	655.0000	3
9121	480640.0000	2079338.0000	680.0000	3
1918	475123.0000	2082819.0000	582.0000	3
1913	468296.0000	2079125.0000	680.0000	3
1912	467577.0000	2075199.0000	440.0000	3
1919	460030.0000	2090475.0000	560.0000	3
1646	517450.0000	2137600.0000	650.0000	3
1645	516620.0000	2137090.0000	690.0000	3
1644	521780.0000	2135980.0000	660.0000	3
1642	523740.0000	2135380.0000	700.0000	3
1643	528898.0000	2130172.0000	727.0000	3
1648	531726.0000	2126975.0000	780.0000	3
6421	535964.0000	2126661.0000	720.0000	3
6416	531182.0000	2113614.0000	886.0000	3
6417	533078.0000	2113115.0000	826.0000	3
6410	525511.0000	2115060.0000	797.0000	3
6415	517420.0000	2114640.0000	750.0000	3
6419	510918.0000	2129945.0000	715.0000	3
6418	511910.0000	2133195.0000	691.0000	3
6481	530528.0000	2109010.0000	810.0000	3
6420	529759.0000	2105365.0000	832.0000	3
9999	(end of check points data)			

3 Check points
3 ground coords

(1), (2), (3), (4), (5), (6), (7) and (8) are as described above.

(9) Initial approximate values for the camera positions and orientations (X, Y, Z, k, ϕ, w)

o o o

B.7.3.2 OBSERVATION FILE

1	-112.996	.046	.000	.000	
2	.035	-112.958	.000	.000	fiducial marks.
3	113.033	.045	.000	.000	
4	.034	113.033	.000	.000	
9999	(end of fiducial observation data)				
3515	19.575	96.016	-90.397	4.579	
3513	55.716	108.554	-90.479	4.553	
113	89.802	93.814	-90.611	4.581	
112	44.788	96.659	-90.459	4.585	
1637	25.387	10.707	-90.443	4.517	
1632	55.670	-25.651	-90.501	4.480	
114	9.271	-3.359	-90.434	4.505	
115	58.637	-3.868	-90.498	4.506	
116	102.976	-4.258	-90.580	4.478	
1641	83.615	-40.014	-90.541	4.482	
1647	78.686	-61.916	-90.549	4.440	
117	91.775	-89.363	-90.621	4.390	
118	52.903	-100.473	-90.528	4.427	
119	6.789	-108.222	-90.422	4.472	
12	47.450	111.350	-90.528	4.601	
13	75.332	106.347	-90.528	4.549	
14	110.601	106.126	-90.519	4.576	
24	101.481	36.864	-90.559	4.516	
23	31.522	42.449	-90.506	4.518	
21	-20.196	52.548	-90.350	4.501	
31	-16.340	-1.363	-90.403	4.509	Control points.
32	31.365	-2.517	-90.479	4.533	
33	102.692	-3.630	-90.596	4.493	
43	83.608	-39.979	-90.565	4.438	
42	30.453	-38.518	-90.465	4.503	
41	-16.302	-52.978	-90.380	4.502	
52	54.635	-107.707	-90.590	4.454	
53	73.094	-105.116	-90.604	4.377	
55	109.385	-110.942	-90.472	4.500	
11	-19.355	107.979	-90.155	4.808	
12	47.450	111.351	-90.528	4.601	
13	75.332	106.348	-90.528	4.549	
14	110.601	106.136	-90.519	4.576	
24	101.481	36.865	-90.559	4.516	
23	31.522	42.450	-90.506	4.518	
21	-20.196	52.549	-90.350	4.501	
31	-16.340	-1.363	-90.403	4.509	
32	31.365	-2.517	-90.479	4.533	
33	102.692	-3.630	-90.596	4.493	
43	83.608	-39.979	-90.565	4.438	
42	30.453	-38.518	-90.465	4.503	
41	-16.302	-52.978	-90.380	4.502	
51	-8.209	-110.353	-90.383	4.505	
52	54.635	-107.707	-90.590	4.454	
53	73.094	-105.116	-90.604	4.377	
54	113.069	-111.873	-90.334	4.379	
55	109.385	-110.942	-90.472	4.500	
9999	(end of control observation data)				
3514	19.437	93.508	-90.426	4.578	
3515	19.575	96.016	-90.397	4.579	
1354	32.414	108.436	-90.429	4.567	
1355	31.750	110.106	-90.410	4.556	

1358	47.438	110.156	-90.460	4.551
1356	47.577	108.369	-90.449	4.557
1357	52.862	109.763	-90.467	4.588
3513	55.716	108.554	-90.479	4.553
3516	81.847	107.892	-90.490	4.558
1082	105.503	94.875	-90.497	4.548
1081	105.267	95.259	-90.541	4.526
1359	81.498	89.331	-90.450	4.548
3511	63.891	92.256	-90.431	4.544
3512	63.688	91.381	-90.449	4.555
1351	71.938	83.344	-90.513	4.529
1352	71.688	83.173	-90.477	4.539
6314	44.282	35.394	-90.400	4.515
1637	25.387	10.707	-90.443	4.517
1635	26.571	3.377	-90.430	4.504
1634	29.396	1.199	-90.445	4.482
1636	43.860	0.437	-90.432	4.494
1631	50.083	3.107	-90.476	4.499
6311	56.286	-20.819	-90.510	4.468
1632	55.670	-25.651	-90.501	4.480
1633	56.331	-26.645	-90.497	4.474
1638	37.319	-21.596	-90.496	4.487
1639	27.178	-24.583	-90.450	4.489
6310	26.796	-21.664	-90.439	4.491
6312	26.616	-27.540	-90.466	4.499
6313	26.366	-26.749	-90.436	4.484
9118	5.198	-40.600	-90.431	4.475
9114	23.055	-45.863	-90.455	4.464
9117	17.333	-69.786	-90.464	4.469
9115	15.004	-69.874	-90.490	4.471
9113	11.353	-69.401	-90.502	4.466
9119	3.944	-33.396	-90.449	4.508
1917	-0.526	-33.499	-90.457	4.503
1911	-3.205	-38.654	-90.421	4.497
1915	-0.951	-47.292	-90.432	4.496
1916	0.269	-45.998	-90.446	4.481
9121	-7.281	-44.444	-90.458	4.504
1918	-7.684	-36.193	-90.421	4.511
1913	-16.363	-31.938	-90.450	4.511
1912	-20.948	-33.979	-90.362	4.508
1919	-10.757	-15.301	-90.411	4.519
1641	83.615	-40.014	-90.541	4.482
1646	79.011	-40.015	-90.533	4.441
1645	77.909	-39.514	-90.545	4.461
1644	80.463	-45.606	-90.530	4.450
1642	81.270	-48.068	-90.562	4.450
1643	79.671	-57.059	-90.535	4.441
1647	78.686	-61.916	-90.549	4.440
1648	78.416	-62.309	-90.568	4.440
6421	81.196	-66.925	-90.572	4.433
6416	64.400	-71.387	-90.573	4.437
6417	65.289	-73.736	-90.576	4.443
6410	61.714	-64.535	-90.534	4.453
6415	55.460	-56.602	-90.537	4.461
6419	66.428	-38.817	-90.512	4.453
6418	70.510	-37.524	-90.534	4.465
6481	59.151	-74.049	-90.538	4.442
6420	54.917	-75.975	-90.568	4.454
9999	(end of check points observation data)			

Check points.

B.7.4 SAMPLE OF OUTPUT

SPACE PHOTOGRAPHY 3D- REDUCTION TO GROUND SPACE. ALL :
:IMAGE COORDINATES ARE IN MMS. AND ARE READ FROM OBS. FILE:
:

TYPE CONTROL FILE NAME > SUDCON1

CONTROL FILE FOR RMK A 30/23 MC IN SPACE MAPPING EXPERIMENT

THE FOCAL LENGTHS OF THE LEFT AND RIGHT CAMERAS ARE
305.128 AND 305.128 RESPECTIVELY.

FIDUCIAL MARK COORDINATES

PT	X	Y
1	-112.996	0.046
2	0.035	-112.958
3	113.033	0.045
4	0.034	113.035

TYPE OBSERVATION FILE NAME >MCSUD1

MEAN MEASUREMENTS WITH STANDARD DEVIATIONS

PT	X1	Y1	X2	Y2	MEAS
	SX1	SY1	SX2	SY2	
1	-112.996	0.046	-112.996	0.046	1.
	0.005	0.005	0.005	0.005	
2	0.035	-112.958	0.035	-112.958	1.
	0.005	0.005	0.005	0.005	
3	113.033	0.045	113.033	0.045	1.
	0.005	0.005	0.005	0.005	
4	0.034	113.033	0.034	113.033	1.
	0.005	0.005	0.005	0.005	

COMPARATOR COORDS ARE REDUCED TO IMAGE COORDS USING:
1- RECTILINEAR, 2- AFFINE, OR 3-DEFORMATIONAL TRANSFORMATION

SELECT 1, 2 OR 3 ? 2

AFTER 2 ITERATIONS, THE 6 PARAMETERS FOR PHOTOGRAPH NO. 1 ARE:

0.000000E+00
0.499633E-03
0.100000E+01
0.665552E-09

0.000000E+00
0.100001E+01

RESIDUALS AT FIDUCIAL MARKS

PT	X	Y
1	0.000	0.000
2	0.000	0.000
3	0.000	-0.001
4	0.000	0.001
RMSE	0.000	0.001

AFTER 2 ITERATIONS THE 6, PARAMETERS FOR PHOTOGRAPH NO. 2 ARE:

0.000000E+00
0.499633E-03
0.100000E+01
0.665552E-09

0.000000E+00
0.100001E+01

RESIDUALS AT FIDUCIAL MARKS

PT	X	Y
1	0.000	0.000
2	0.000	0.000
3	0.000	-0.001
4	0.000	0.001
RMSE	0.000	0.001

CONTROL POINT COORDINATES

PT	X	Y	Z
12	404190.0000	2186720.0000	820.0000
13	420240.0000	2202570.0000	730.0000
14	436630.0000	2225560.0000	520.0000
.			
.			
.			

MEAN MEASUREMENTS WITH STANDARD DEVIATIONS

PT	X	Y	PX	PY	MEAS
----	---	---	----	----	------

	SX	SY	SPX	SPY	
12	47.450	111.350	-90.528	4.601	1.
	0.005	0.005	0.005	0.005	
13	75.332	106.347	-90.528	4.549	1.
	0.005	0.005	0.005	0.005	
14	110.601	106.126	-90.519	4.576	1.
.					
.					
.					

RESIDUAL ERRORS FOR ITERATION 1

IN METRES AT TERRAIN SCALE

PT	X	Y	Z	PY
.				
.				
.				

DO YOU WANT ANOTHER ITERATION ? Y OR N Y

AFTER 1 ITERATION, THERE ARE 12 LARGE CORRECTIONS

AX	AY	AZ	BX	BY	BZ
-154.0633	720.2634*****		240.6673	16.1943	-104.2105
K1	P1	O1	K2	P2	O2
-3.1488	0.1283	0.0118	-3.1627	0.0674	0.0183

RESIDUAL ERRORS FOR ITERATION 2

IN METRES AT TERRAIN SCALE

PT	X	Y	Z	PY
.				
.				
.				

RESIDUAL ERRORS FOR ITERATION 5

IN METRES AT TERRAIN SCALE

PT	X	Y	Z	PY
.				
.				
.				

DO YOU WANT ANOTHER ITERATION ? Y OR N Y

AFTER 5 ITERATIONS, THERE ARE 0 LARGE CORRECTIONS

AX	AY	AZ	BX	BY	BZ
0.0000	0.0000	0.0000	0.0000	0.0000	0.0000
K1	P1	O1	K2	P2	O2
0.0000	0.0000	0.0000	0.0000	0.0000	0.0000

RESIDUAL ERRORS FOR ITERATION 6

IN METRES AT TERRAIN SCALE

PT	X	Y	Z	PY
12	21.5354	-1.1690	5.9766	16.6460
13	-34.9337	14.5761	18.4658	-24.8296
14	10.7775	-5.0044	-28.4379	-6.4621
24	12.0289	-0.6691	-41.2181	-3.8869
23	27.2298	-2.5393	-31.8123	-9.1014
21	-10.6870	-20.0655	-31.9893	-22.9210
31	-0.0260	35.5340	-34.4475	-0.4501
32	-6.1781	-20.7534	-4.5247	24.8439
33	-31.0295	13.7415	-34.7710	3.4485
43	1.6134	5.3755	-14.5576	-22.8470
42	2.3316	5.6437	30.8308	16.0028
41	2.1335	-0.6444	3.8914	8.5227
52	3.2775	6.2548	6.9396	7.4640
53	-17.3189	7.1808	-32.8136	-46.1566
55	14.3291	-17.2078	20.5398	78.2513
3515	40.1163	22.0940	34.7149	16.4672
3513	-16.2236	-17.8291	12.4030	-18.9371
113	3.3559	6.9302	15.6333	5.1407
112	7.1371	-6.2117	26.3120	16.0616
1637	-10.9091	-23.5703	20.7135	6.7209
1632	0.7195	-10.8951	12.4064	-2.2052
114	-8.3003	-28.2289	39.8724	0.4440
115	-22.9890	5.0461	44.0008	8.5890
116	15.8033	24.1455	-48.5858	-7.4117
1641	11.0968	23.6335	-25.6778	13.1617
1647	-17.0332	-8.6126	12.4068	-11.0653
117	11.1258	-23.5535	30.0425	-34.7012
118	-23.1586	12.7488	-53.0440	-15.1073
119	37.0403	-1.3755	46.4190	4.8064
RMSE	18.2672	15.8687	29.6587	22.1222

DO YOU WANT ANOTHER ITERATION ? Y OR N N

FINAL RELATIVE/ABSOLUTE ORIENTATION PARAMETERS

LEFT CAMERA X,Y,Z = 458412.1573 2102726.8769 244288.1341
 RIGHT CAMERA X,Y,Z = 497016.3782 2163570.1413 244332.3676

LEFT ROTATIONS K,P,O = -3.1122 0.1303 0.0537
 RIGHT ROTATIONS K,P,O = -3.1259 0.0592 0.0701

STD DEVIATIONS OF THE PARAMETERS -- SIGMA ZERO 0.00

LEFT CAMERA X,Y,Z = 0.0058 0.0042 0.0001
 CAMERA BASE X,Y,Z = 0.0002 0.0003 0.0001

LEFT ROTATIONS K,P,O = 0.000 0.000 0.000
 RIGHT ROTATIONS K,P,O = 0.000 0.000 0.000

ROTATION MATRICES ARE:-

**

0.998803 0.048868 0.002002

-0.048866 0.998805 -0.000943
-0.002046 0.000844 0.999998

**

0.998794 0.049082 0.000874
-0.049081 0.998794 -0.001146
-0.000930 0.001102 0.999999

DO YOU WANT TO ADD OR DISCARD SOME POINTS ? Y OR N N

DO YOU WANT TO DISPLAY/RECORD TERRAIN COORDS ? Y OR N Y

DO YOU WANT TO: 1- JUST DISPLAY
OR 2- DISPLAY & RECORD ON A NEW DISC FILE? 1 OR 2 2

ARE YOU EXECUTING AN ACCURACY TEST ? Y OR N Y

TYPE OUT PUT FILE NAME..> SUDOUT1

GROUND COORDS WITH RESIDUALS IN METERES

=====

POINT	X	VX	Y	VY	Z	VZ
3514	402889.669	-29.669	2160275.135	-19.135	613.416	-33.416
1354	399115.723	-25.723	2175621.863	22.137	587.233	-27.233
1355	397710.193	14.807	2175970.502	-20.502	536.562	17.438
1358	404926.220	-26.220	2186197.079	-17.079	623.915	-35.915
1356	406149.104	0.896	2185475.876	27.124	594.415	34.585
1357	407670.412	-20.412	2189559.572	24.428	630.297	-33.297
3516	422240.082	-20.082	2207603.913	-16.913	585.722	-45.722
1082	441625.510	-5.510	2217058.823	21.177	508.218	3.782
1081	441280.540	-30.540	2217022.172	22.828	625.049	-45.049
1359	434191.026	-31.026	2198865.134	-16.134	477.770	-37.770
3511	424173.692	2.308	2188724.110	21.890	489.328	35.672
3512	424654.991	-24.991	2188173.560	26.440	540.067	-37.067
1351	433723.985	3.015	2189794.517	-18.517	680.283	31.717
1352	433708.355	-28.355	2189588.775	-21.775	585.343	-32.343
6314	452289.784	-19.784	2149728.545	29.455	459.084	-38.084
1635	465043.366	-13.366	2123405.653	-20.653	581.331	-49.331
1634	467770.912	12.088	2124237.866	22.134	611.580	26.420
1636	474925.469	-25.469	2133332.844	27.156	539.831	-36.831
1631	476037.022	7.978	2138608.590	-20.590	641.878	18.122
6311	494499.542	-19.542	2131624.888	-18.888	708.915	-30.915
1633	498323.838	-23.838	2128978.675	21.325	673.974	-30.974
1638	486276.946	10.054	2118906.202	-17.202	726.193	13.807
1639	483571.905	-21.905	2110923.485	-19.485	627.065	-42.065
6310	481493.631	13.369	2112019.343	25.657	599.058	20.942
6312	485234.408	-24.408	2109197.272	22.728	672.370	-32.370
6313	484617.439	18.561	2109396.478	-18.478	590.159	27.841
9118	483915.775	-17.775	2089207.595	-21.595	617.664	-37.664
9114	495565.315	13.685	2098433.906	16.094	642.892	25.108
9117	508531.635	-27.635	2083696.665	23.335	675.320	-45.320
9115	507501.811	19.189	2082144.123	-13.123	750.419	15.581
9113	505508.701	-18.701	2079983.359	-21.359	789.428	-39.428
9119	478621.981	15.019	2091716.085	18.915	674.701	-6.701
1917	476631.735	-11.735	2088753.010	25.990	703.874	16.126
1911	478772.676	22.324	2084624.561	-24.561	609.359	-21.359

1915	485444.864	-23.864	2082121.478	-11.478	632.734	-32.734
1916	485162.644	20.356	2083512.224	17.776	666.701	-11.701
9121	480662.977	-22.977	2079311.679	26.321	715.473	-35.473
1918	475099.852	23.148	2082838.487	-19.487	619.477	-37.477
1913	468323.519	-27.519	2079141.893	-16.893	712.652	-32.652
1912	467556.409	20.591	2075183.330	15.670	480.664	-40.664
1919	460046.938	-16.938	2090450.959	24.041	604.376	-44.376
1646	517474.722	-24.722	2137598.918	1.082	694.342	-44.342
1645	516625.827	-5.827	2137110.877	-20.877	733.041	-43.041
1644	521787.827	-7.827	2135976.643	3.357	682.377	-22.377
1642	523741.101	-1.101	2135358.963	21.037	765.825	-65.825
1643	528890.041	7.959	2130187.438	-15.438	696.924	30.076
1648	531708.003	17.997	2126945.338	29.662	789.654	-9.654
6421	535994.974	-30.974	2126631.934	29.066	790.148	-70.148
6416	531170.287	11.713	2113636.491	-22.491	846.030	39.970
6417	533105.285	-27.285	2113136.967	-21.967	852.056	-26.056
6410	525493.586	17.414	2115045.165	14.835	751.631	45.369
6415	517438.991	-18.991	2114618.693	21.307	779.643	-29.643
6419	510909.748	8.252	2129953.875	-8.875	680.065	34.935
6418	511928.232	-18.232	2133206.604	-11.604	728.174	-37.174
6481	530516.400	11.600	2108996.285	13.715	767.528	42.472
6420	529794.689	-35.689	2105353.642	11.358	861.678	-29.678

THE ROOT MEAN SQUARE ERRORS OF THE DISCREPANCIES
 AT THE GROUND SCALE IN METRES AND THE RMSE AS PER 1000TH
 OF THE FLYING HEIGHT OF THE SENSOR

X	Y	Z	Z%%FH
20.039	20.516	35.029	0.143

APPENDIX C

VECTOR PLOTS OF RESIDUALS FOR THE MSS AND TM IMAGES

ENLARGEMENT=X40.

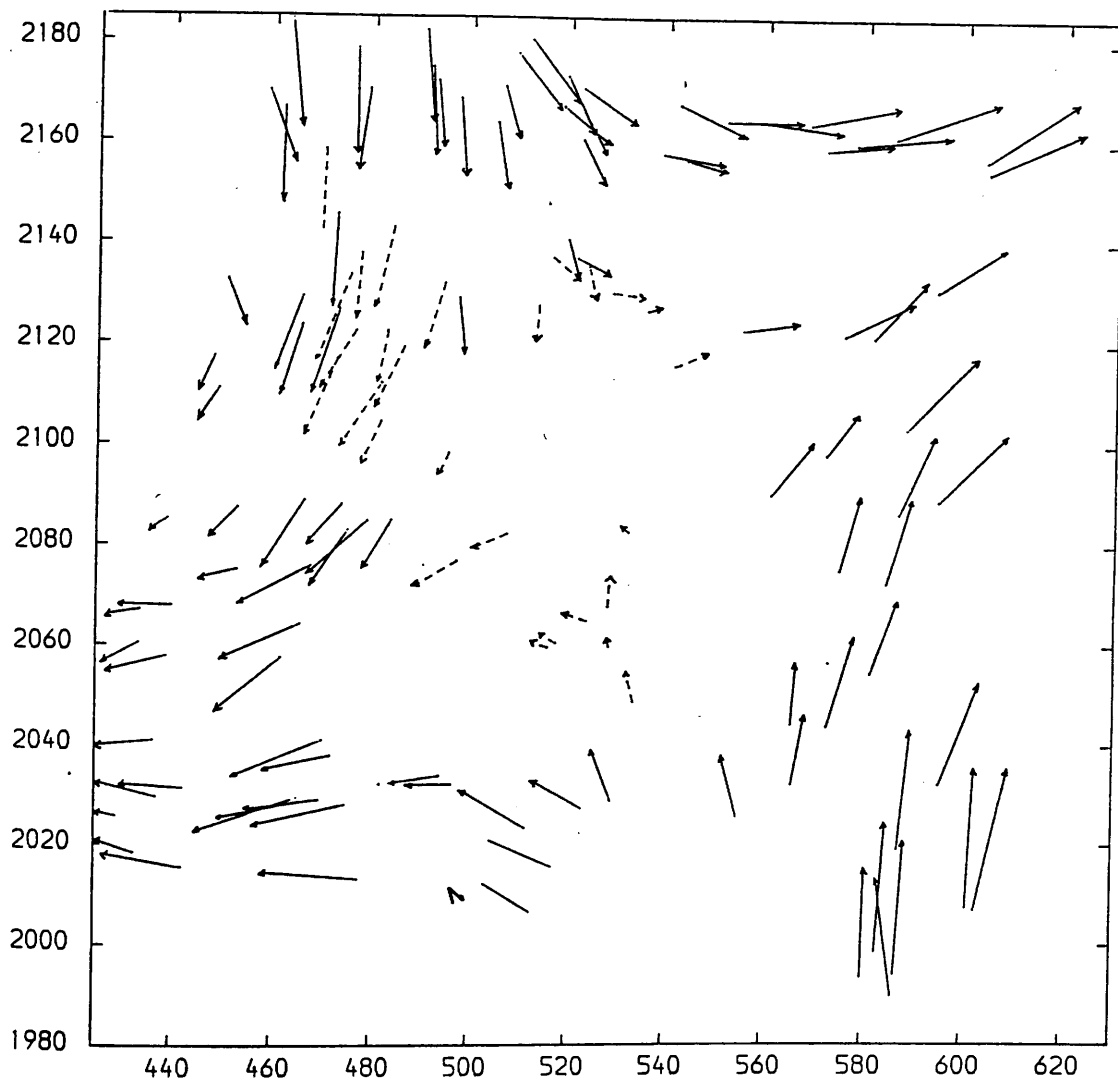


Fig. C.1 Residuals After the Linear Conformal Transformation of the MSS Image Using All Points as Control Points.

ENLARGEMENT=X40.

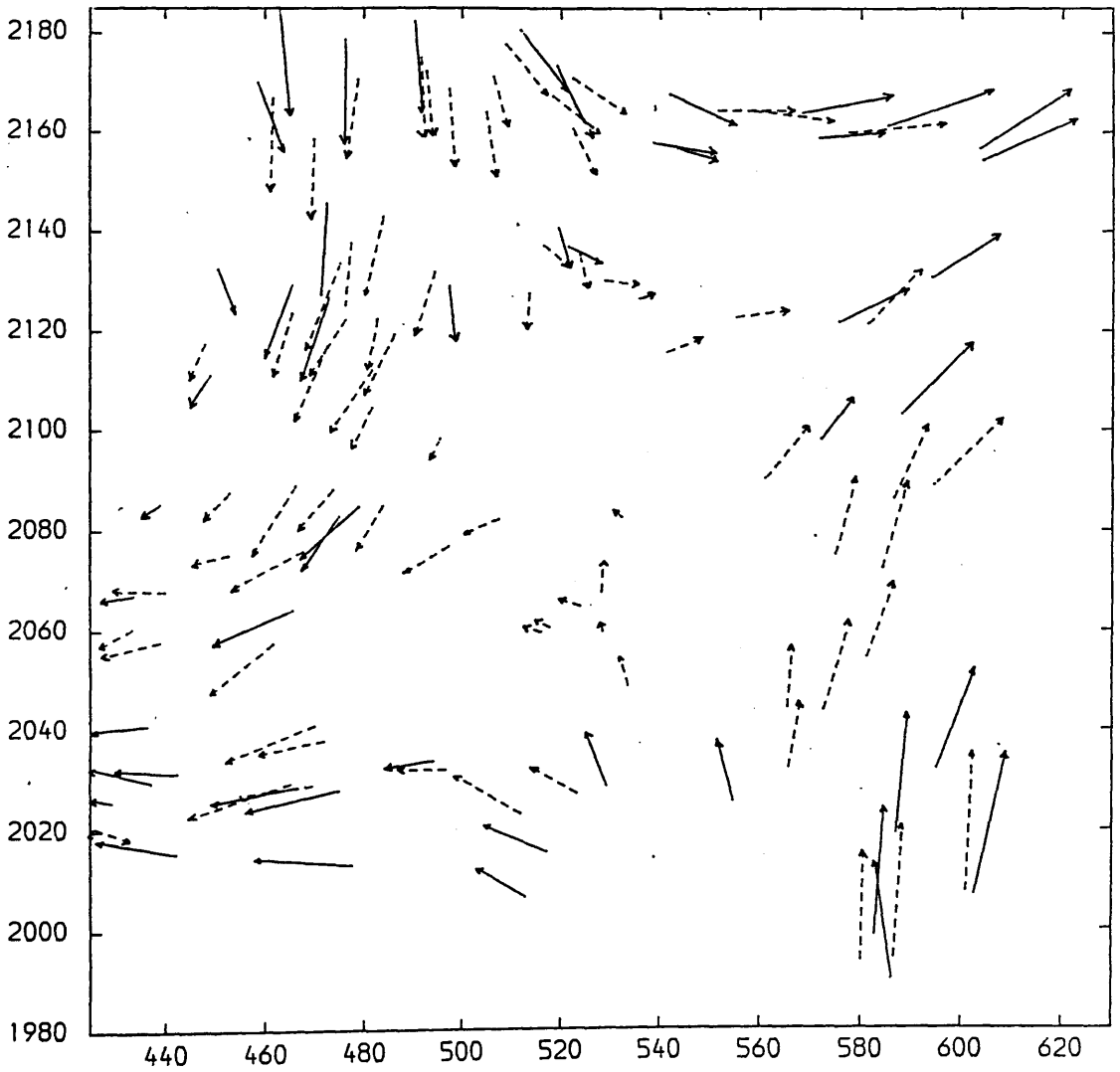


Fig. C.2 Residuals After the Linear Conformal Transformation of the MSS Image Using 50 Control Points.

Control points. ———→

Check Points. - - - ->

ENLARGEMENT=X150.

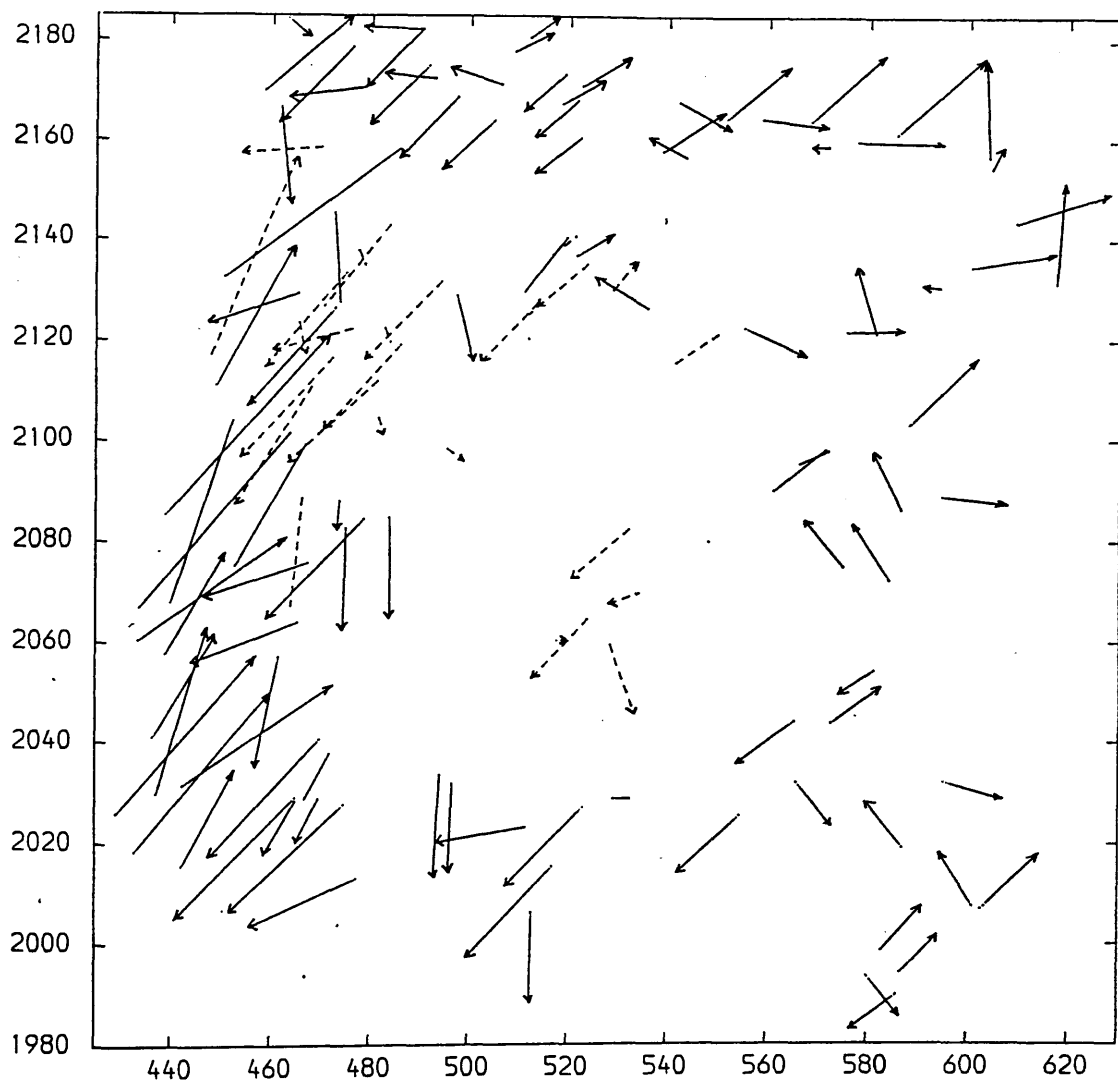


Fig. C.3 Residuals After the Affine Transformation of the MSS Image Using All Points as Control Points.

ENLARGEMENT=x40.

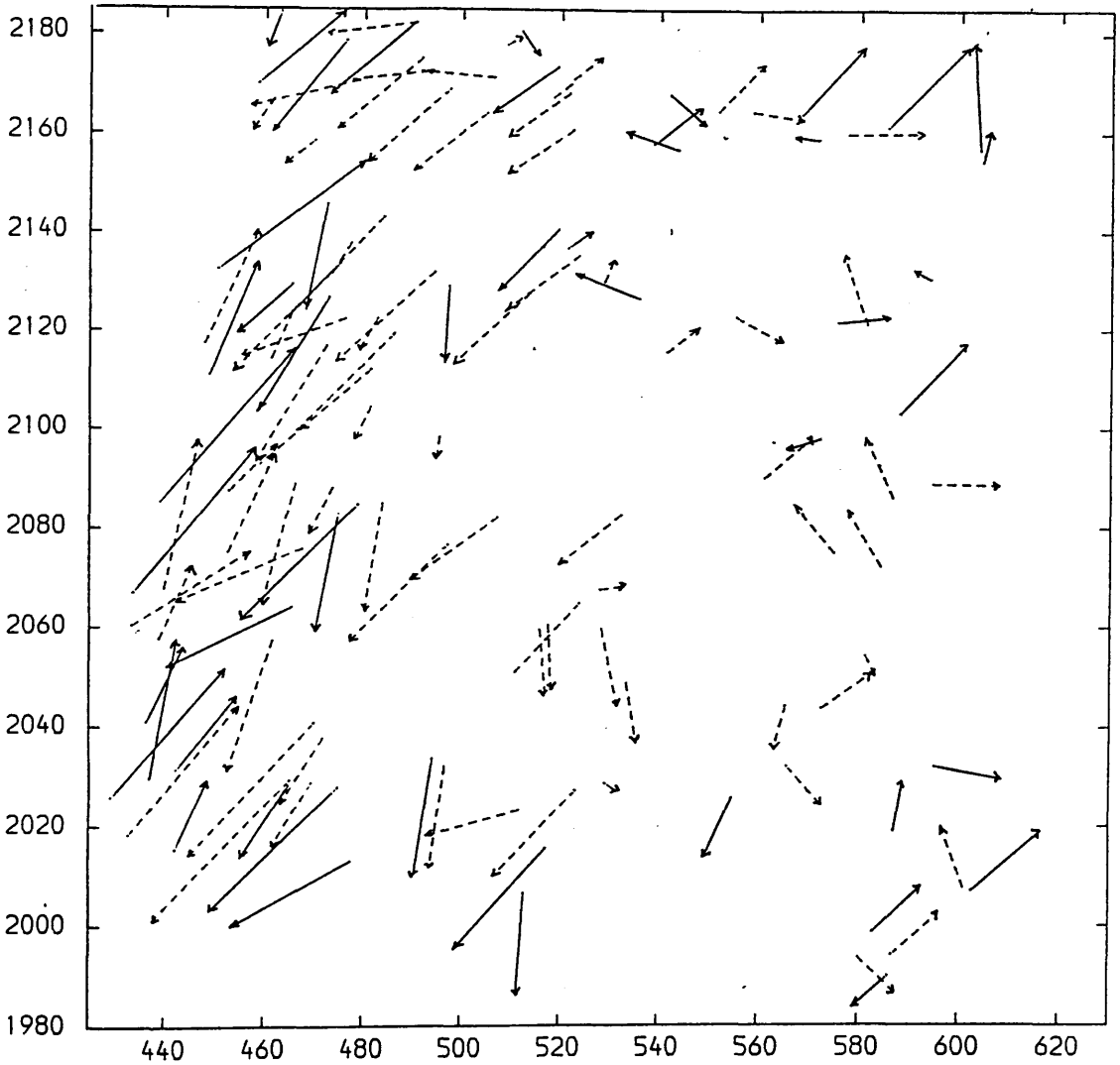


Fig. C.4 Residuals After the Affine Transformation of the MSS Image Using 50 Control Points.

Control Points. —→ Check Points. - - -→

ENLARGEMENT=X150.

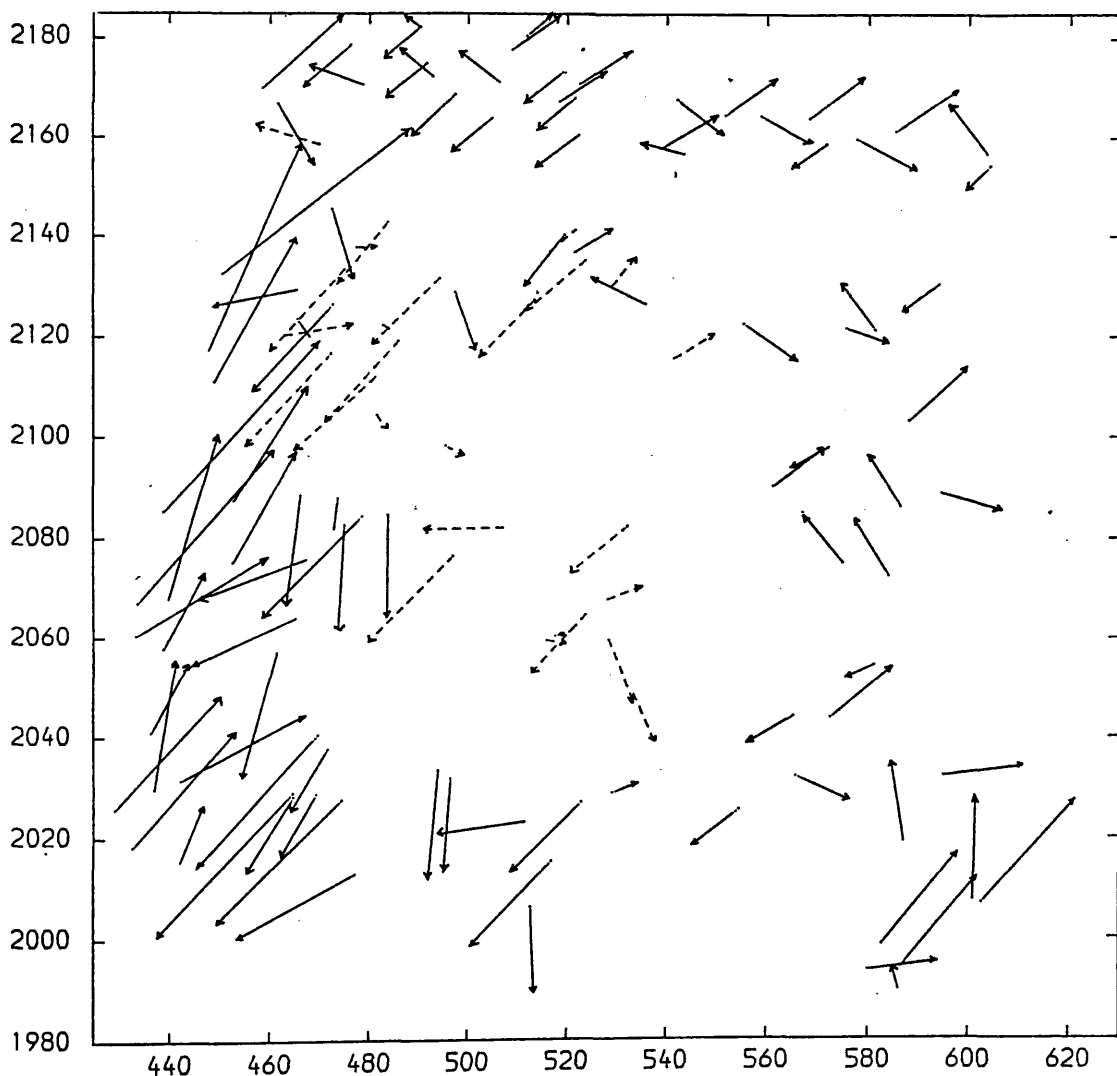


Fig. C.5 Residuals After 4-term Polynomial Transformation of the MSS Image Using All Points as Control Points.

ENLARGEMENT=X150.

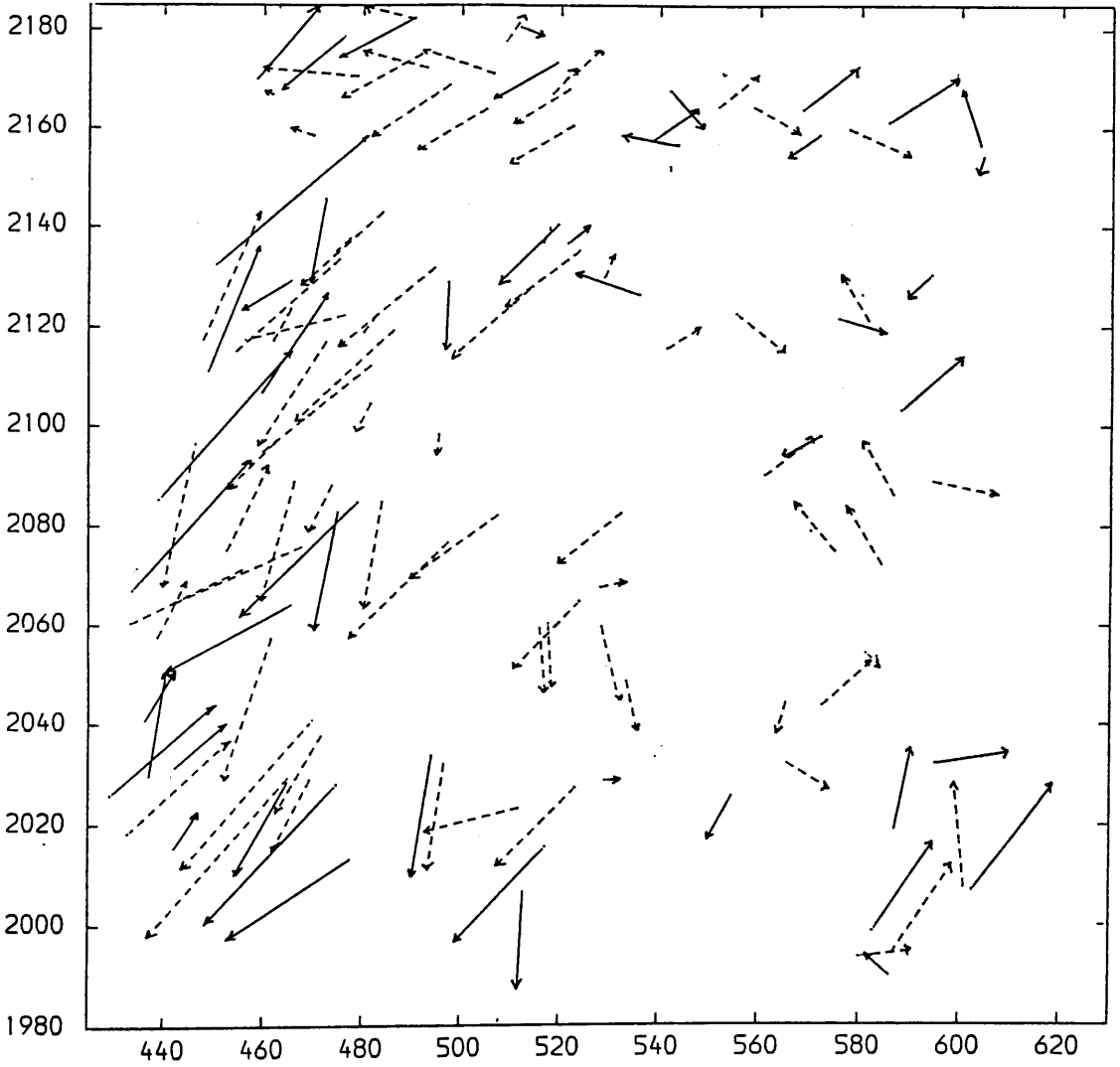


Fig. C.6 Residuals After 4-term Polynomial Transformation of the MSS Image Using 50 Control Points.

Control Points. —→

Check Points. - - -→

ENLARGEMENT=X150.

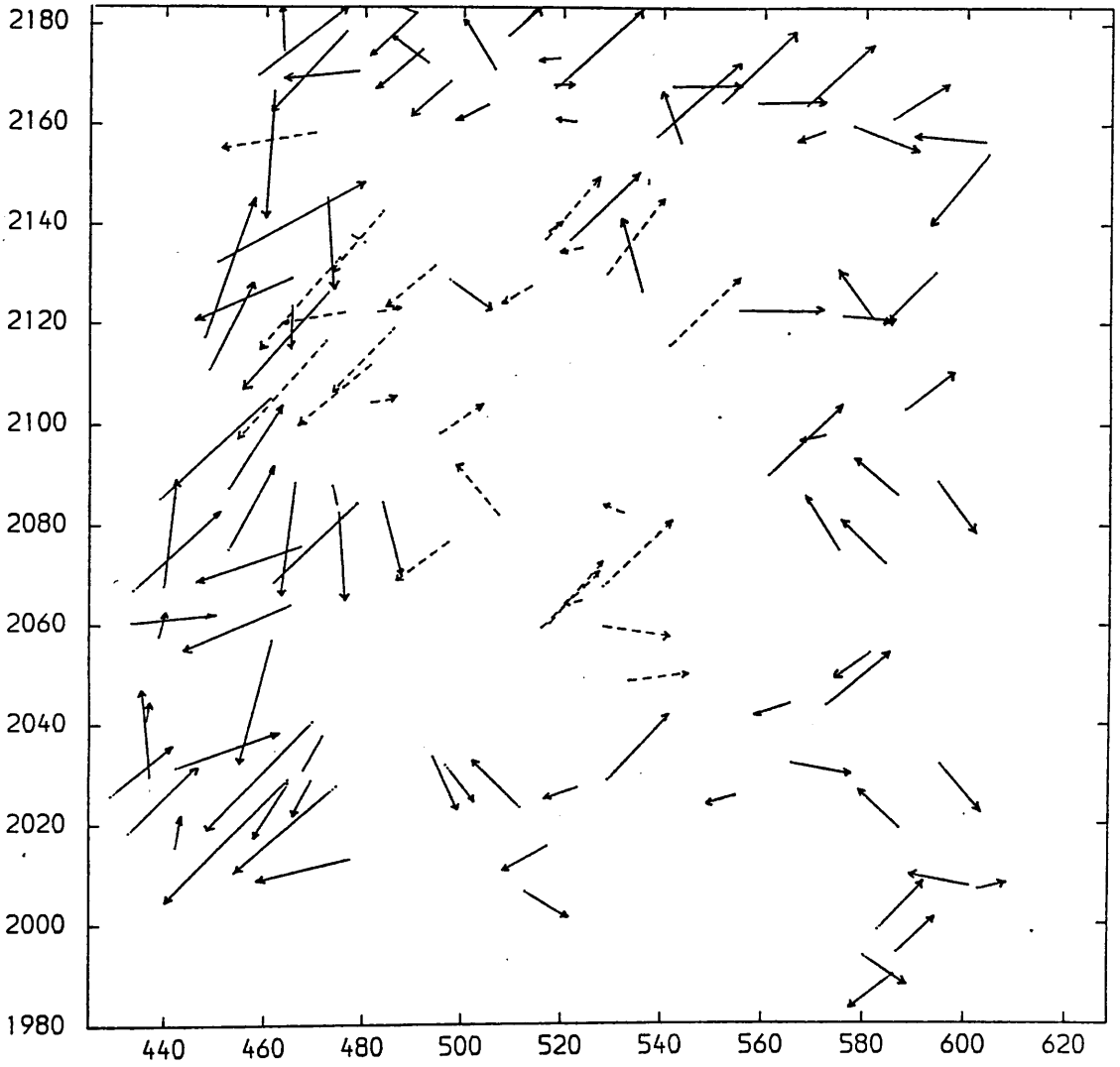


Fig. C.7 Residuals After 6-term Polynomial Transformation of the MSS Image Using All Points as Control Points.

ENLARGEMENT=X150.

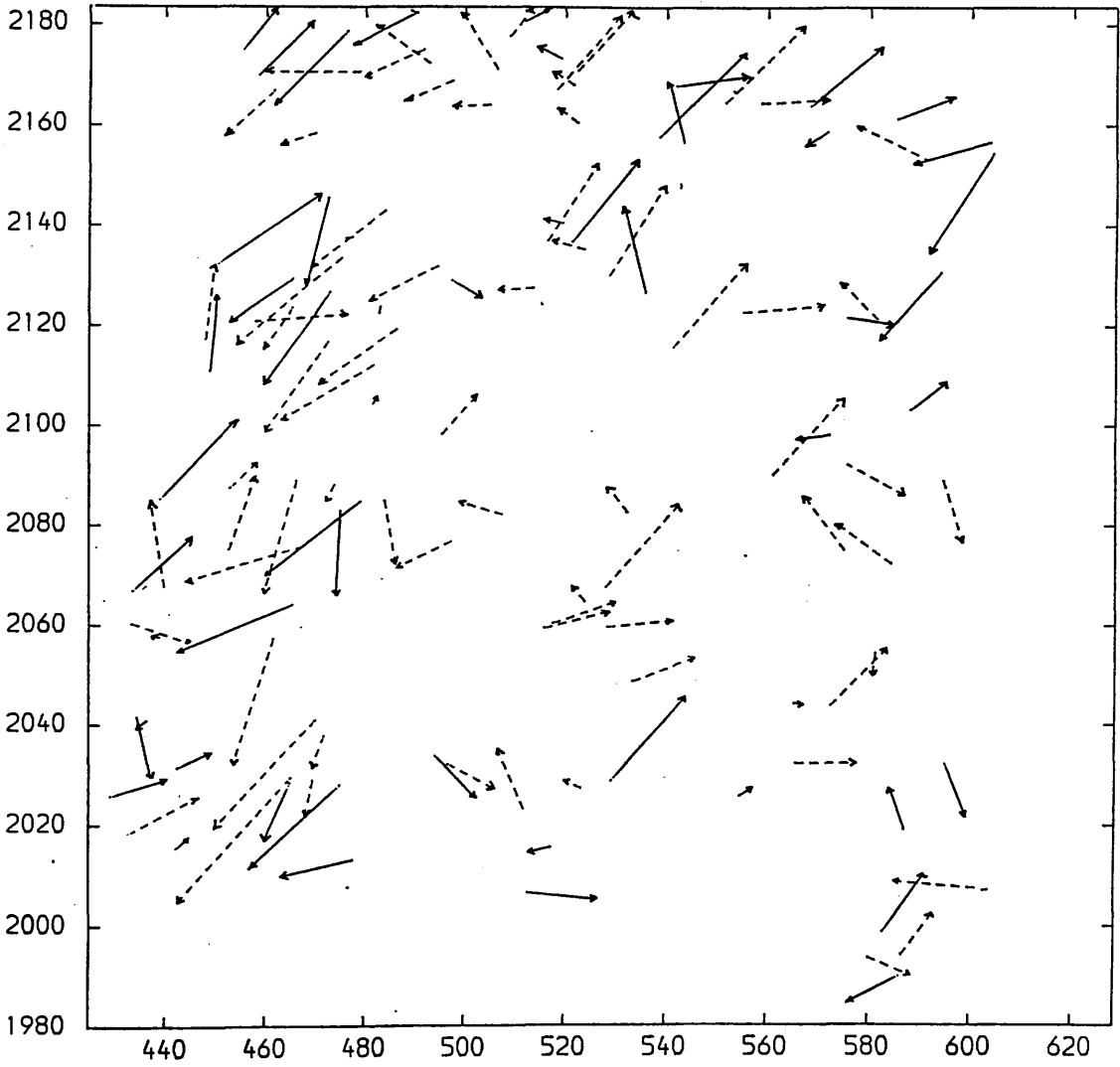


Fig. C.8 Residuals After 6-term Polynomial Transformation of the MSS Image Using 50 Control Points.

ENLARGEMENT=X150.

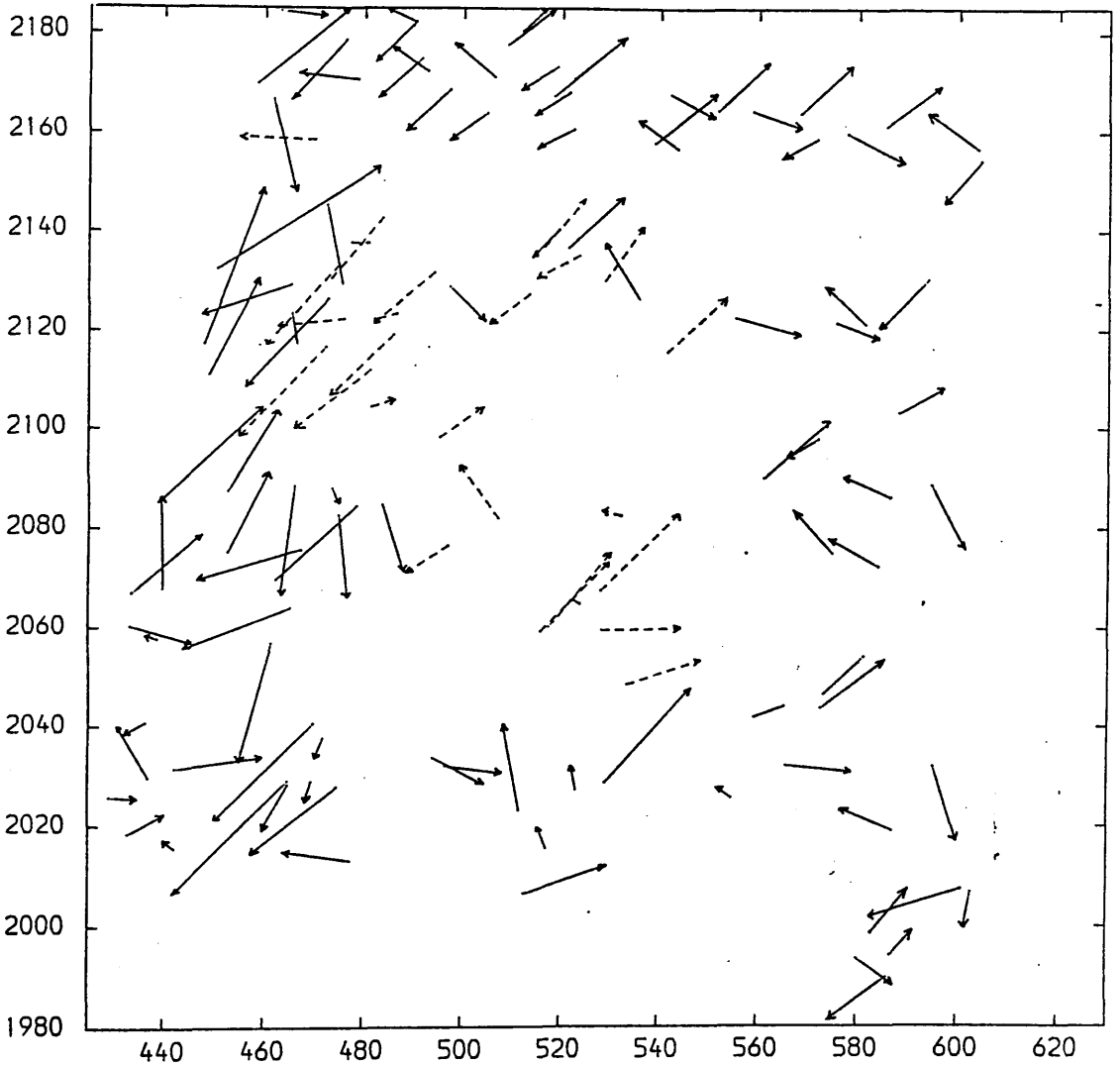


Fig. C.9 Residuals After 8-term Polynomial Transformation of the MSS Image Using All Points as Control Points.

ENLARGEMENT=X150.

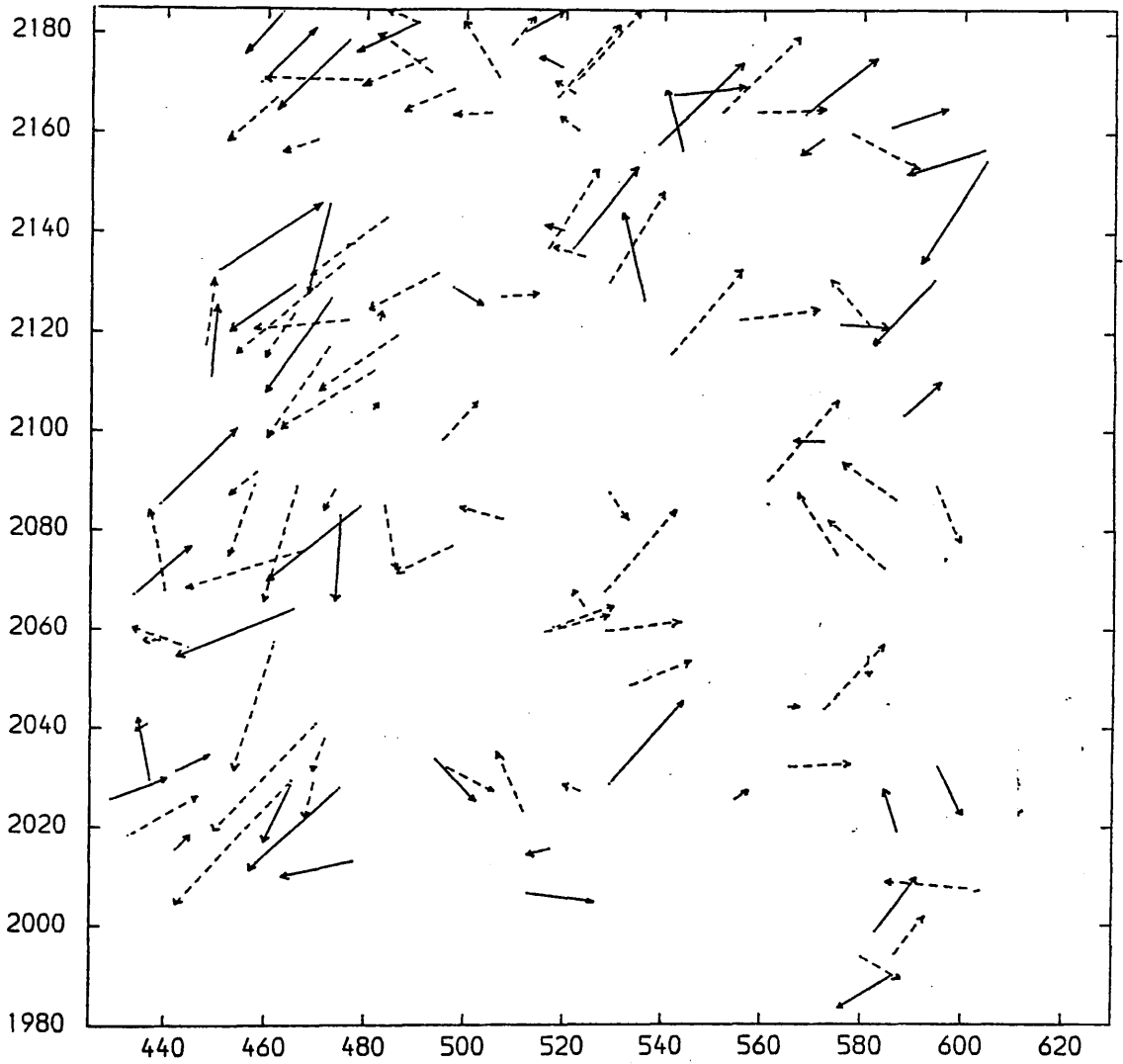


Fig. C.10 , Residuals After 8-term Polynomial Transformation of the MSS Image Using 50 Control Points.

Control Points. —→

Check Points. - - - →

ENLARGEMENT=X150.

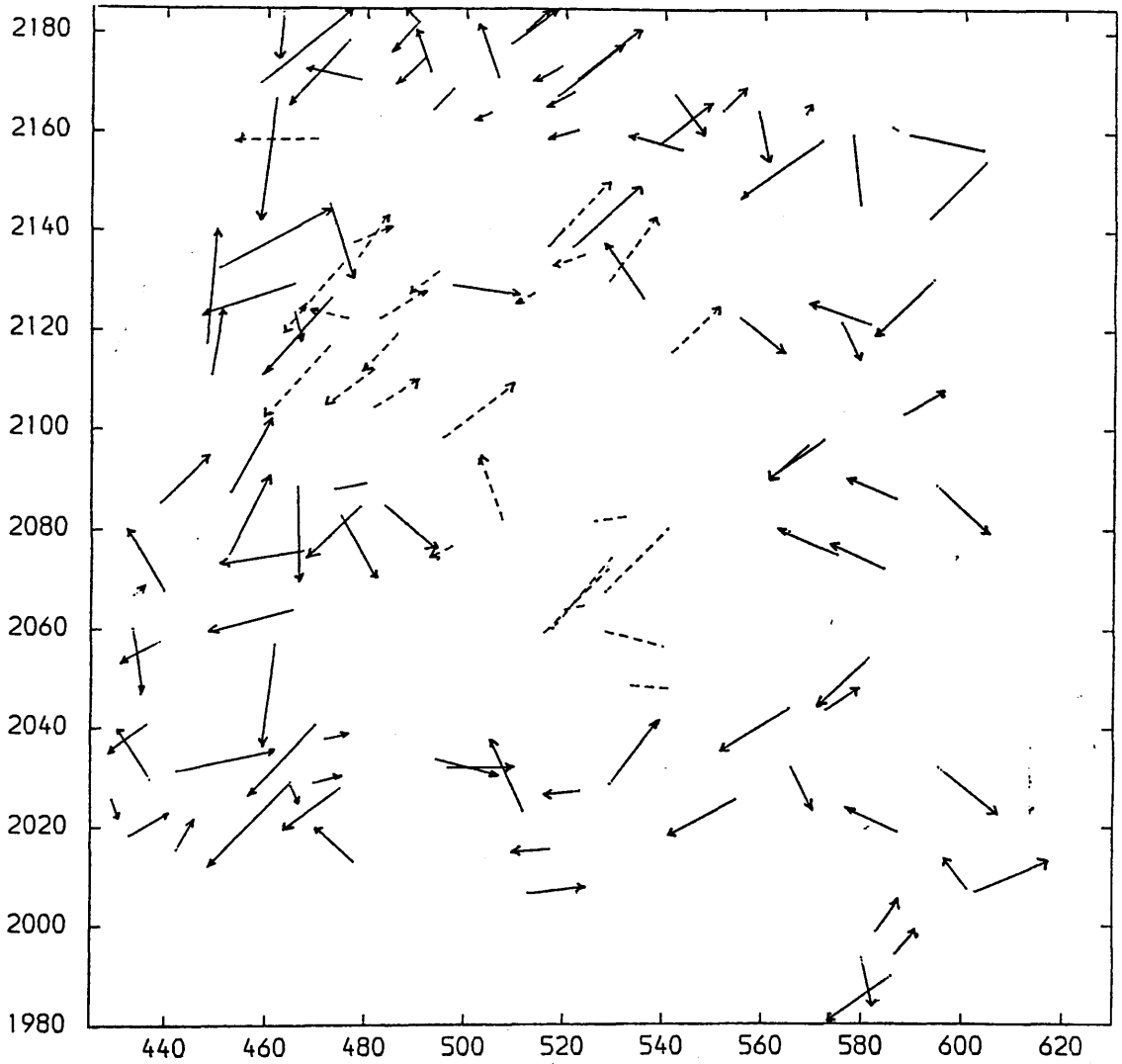


Fig.C.11 Residuals After 10-term Polynomial Transformation of the MSS Image Using All Points as Control Points.

ENLARGEMENT=X150.

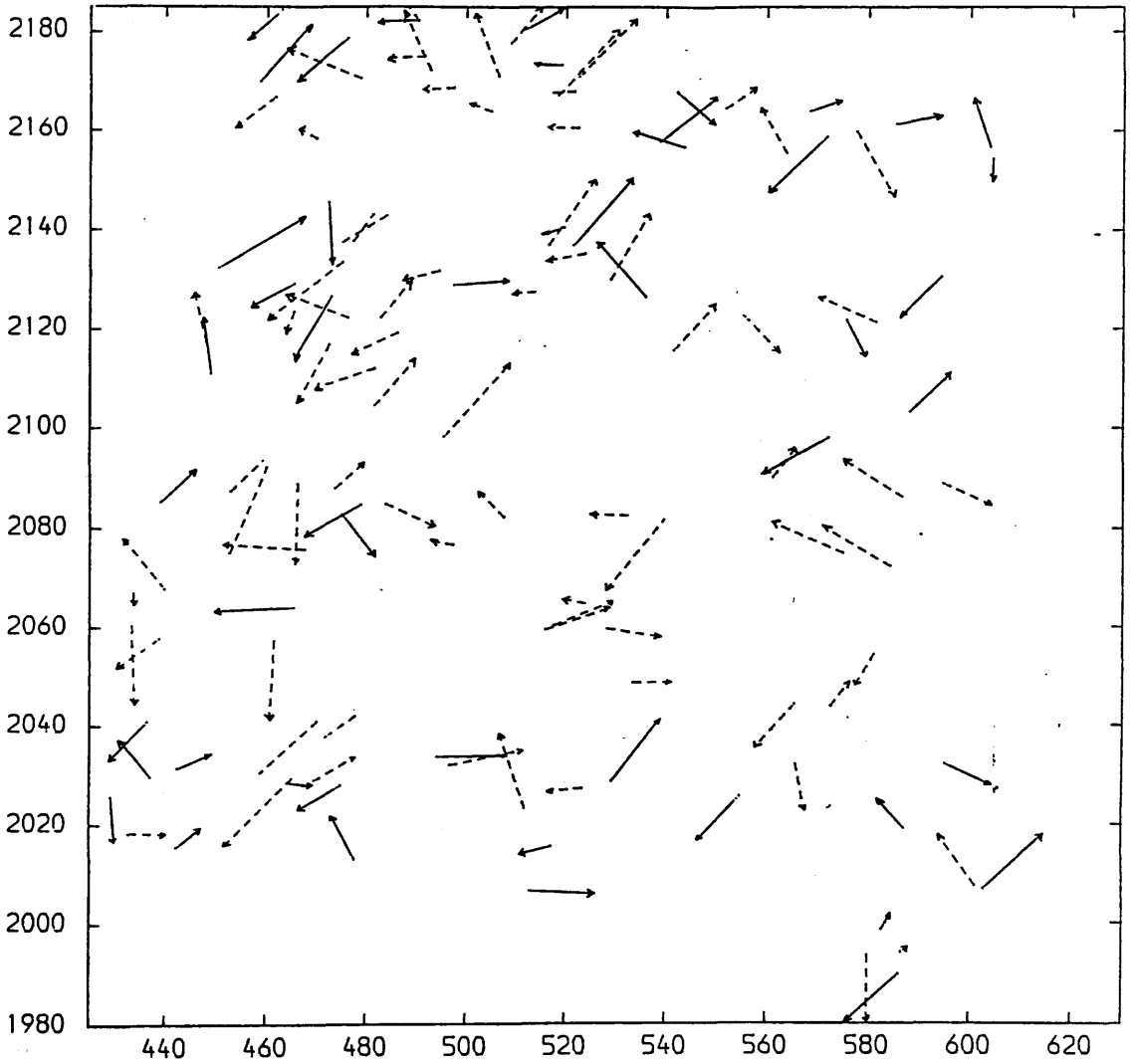


Fig. C.12 Residuals After the 10-term Polynomial Transformation of the MSS Image Using 50 Control Points.

Control Points. —→

Check Points. - - -→

ENLARGEMENT=X150.

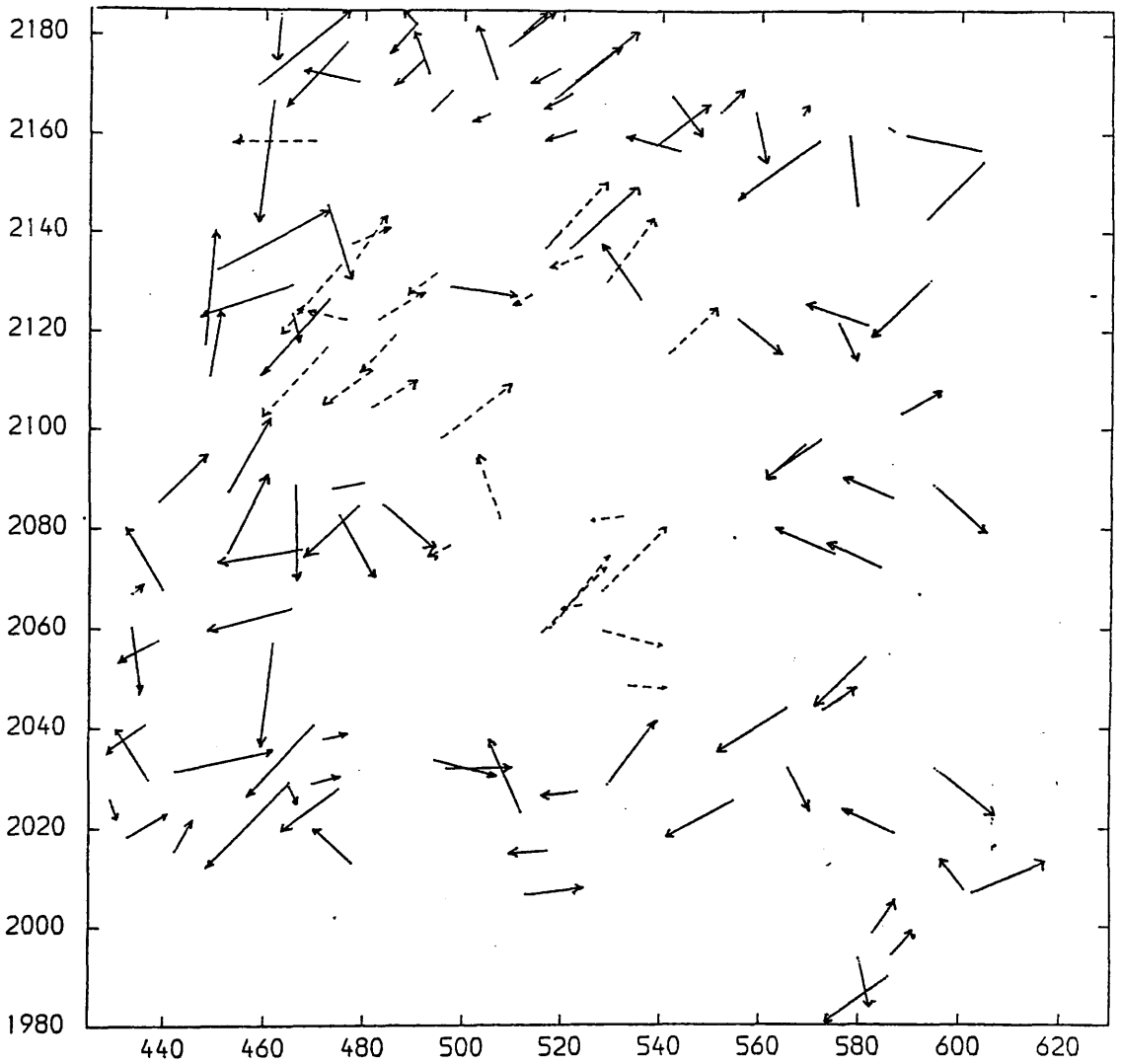


Fig.C.13 Residuals After 14-term Polynomial Transformation of the MSS Image Using All Points as Control Points.

ENLARGEMENT=X150.

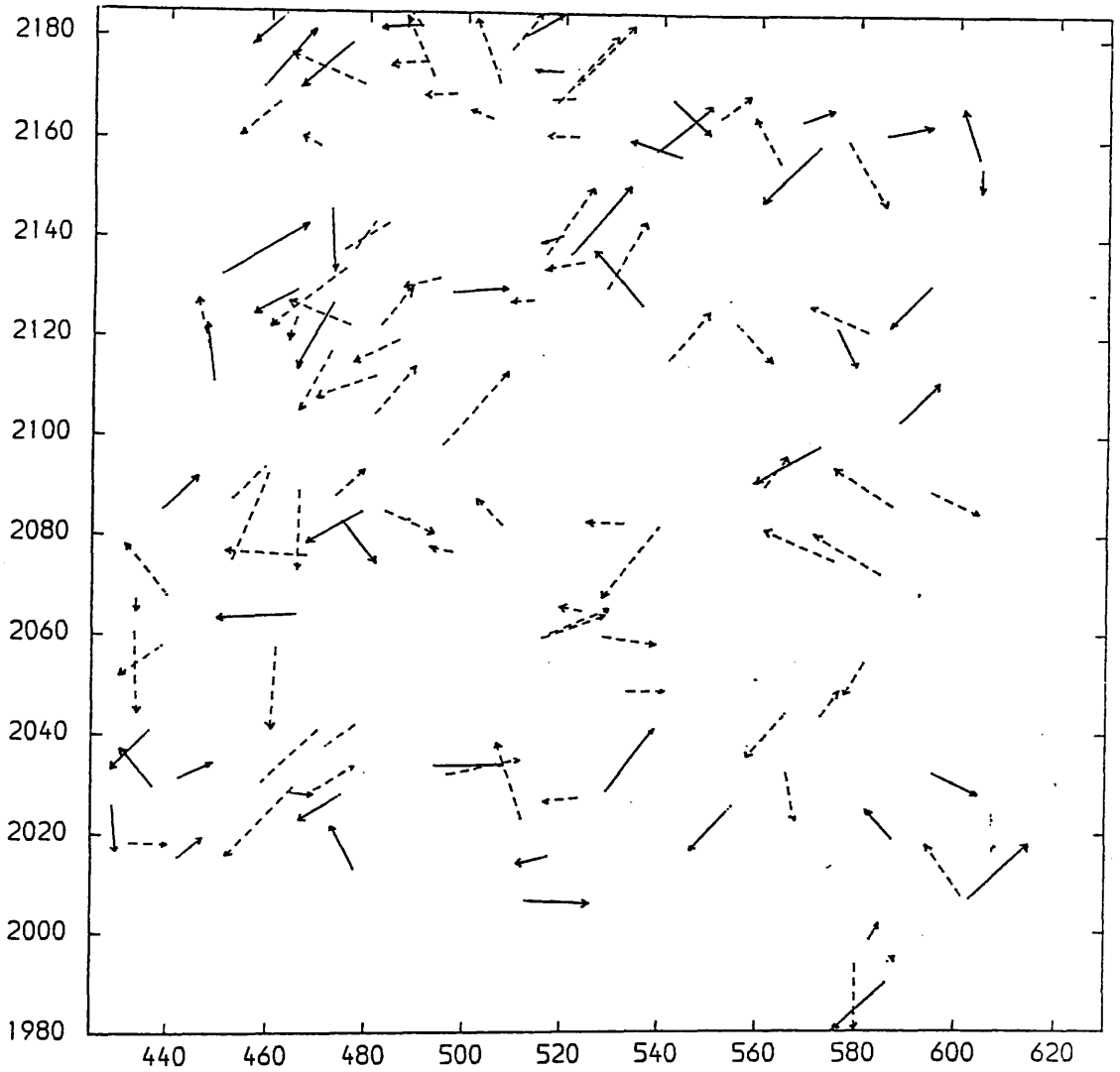


Fig.C.14 Residuals After 14-term Polynomial Transformation of the MSS Image Using 50 Control Points.

Control Points. —→

Check Points. - - - →

ENLARGEMENT=X250.

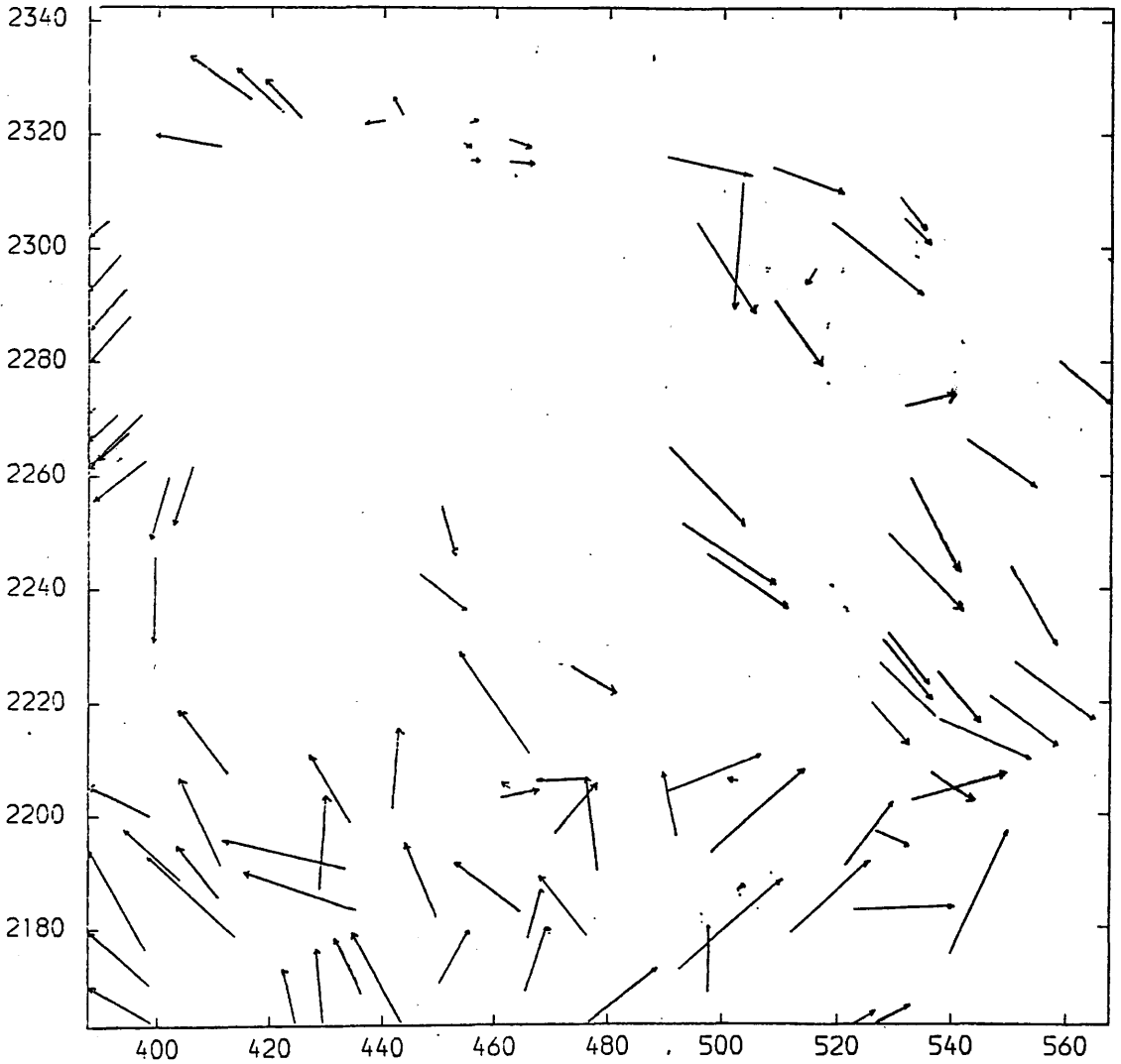


Fig. C.15 Residuals After the Linear Conformal Transformation of the TM Image Using all Points as Control Points.

ENLARGEMENT=X250.

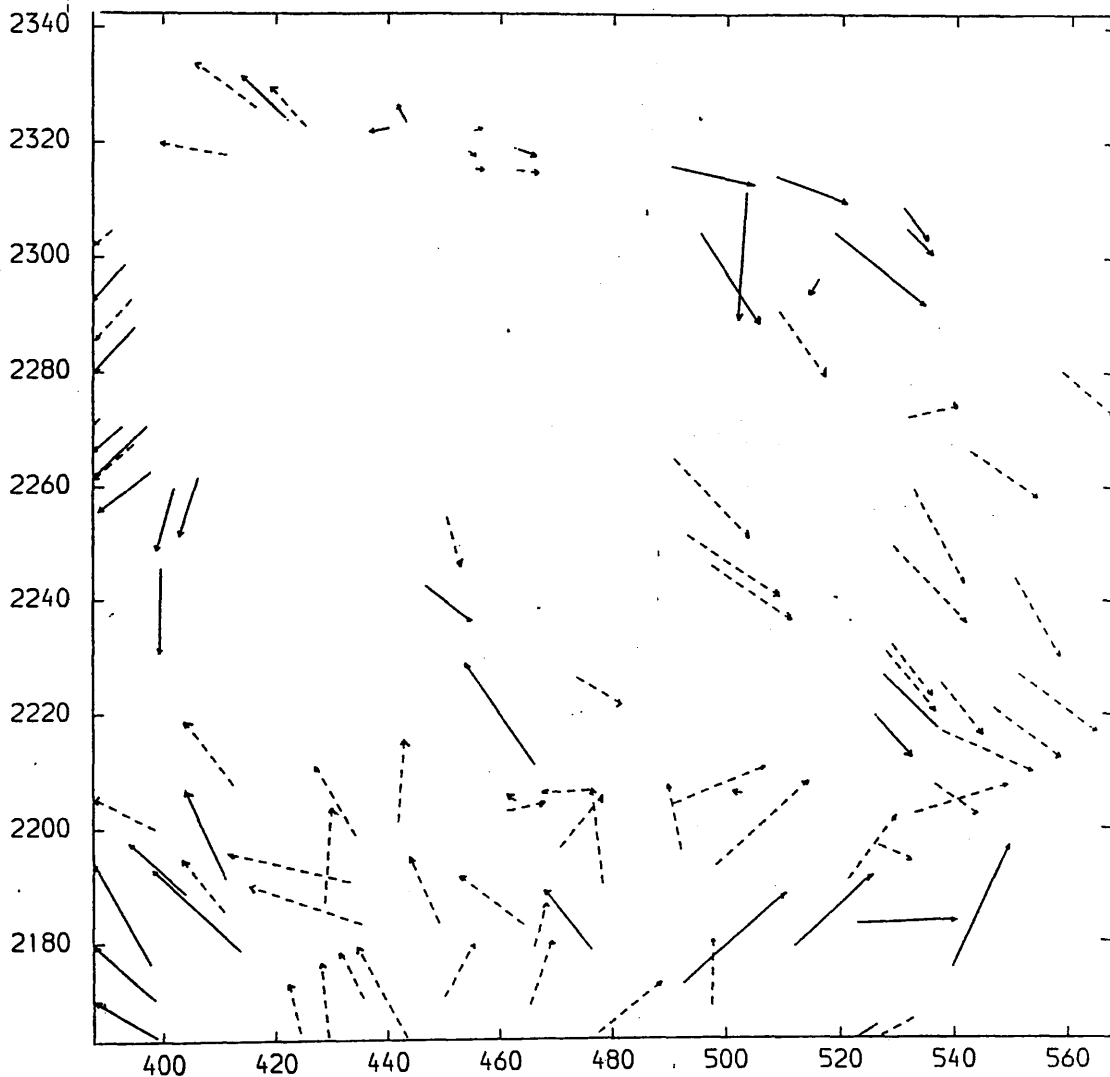


Fig. C.16 Residuals After the Linear Conformal Transformation of the TM Image Using 40 Control Points.

Control Points. —→

Check Points. - - -→

ENLARGEMENT=X250.

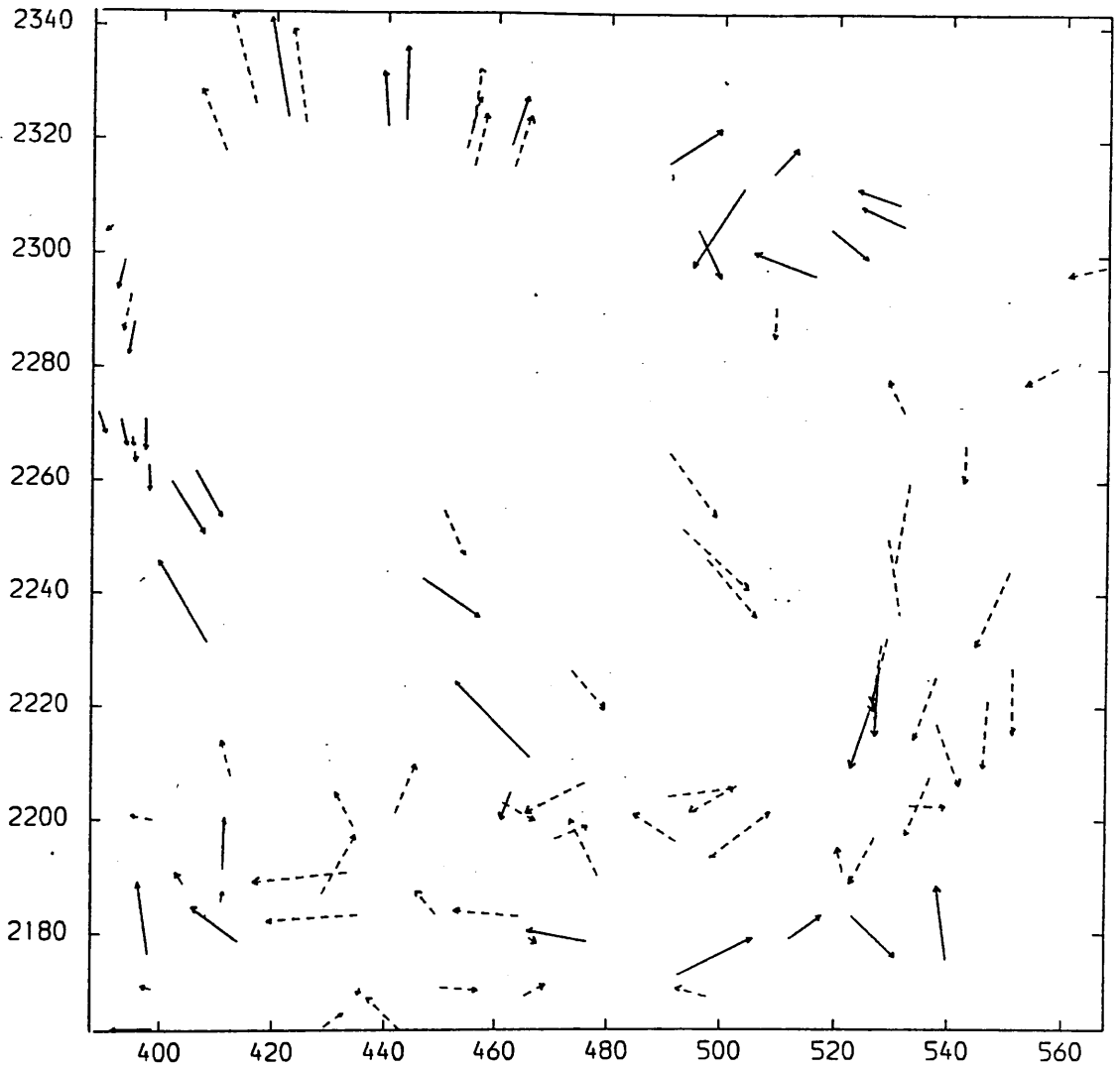


Fig. C.17 Residuals After the Affine Transformation of the TM Image Using 40 Control Points.

Control Points. —→

Check Points. - - - ->

ENLARGEMENT=X250.

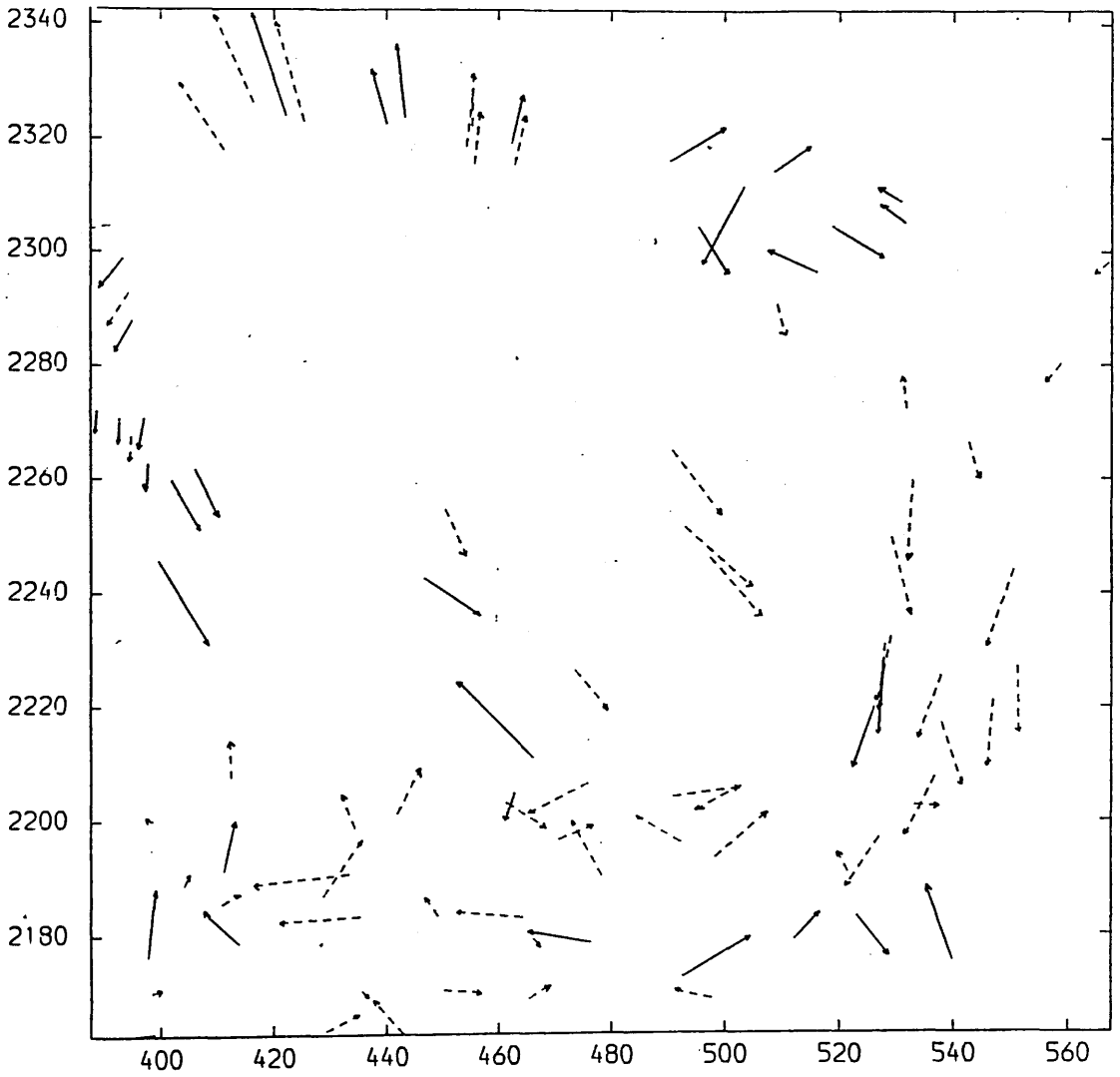


Fig. C.18 Residuals After the 4-term Polynomial Transformation of the TM Image Using 40 Control Points.

Control Points. —→

Check Points. - - -→

ENLARGEMENT=X250.

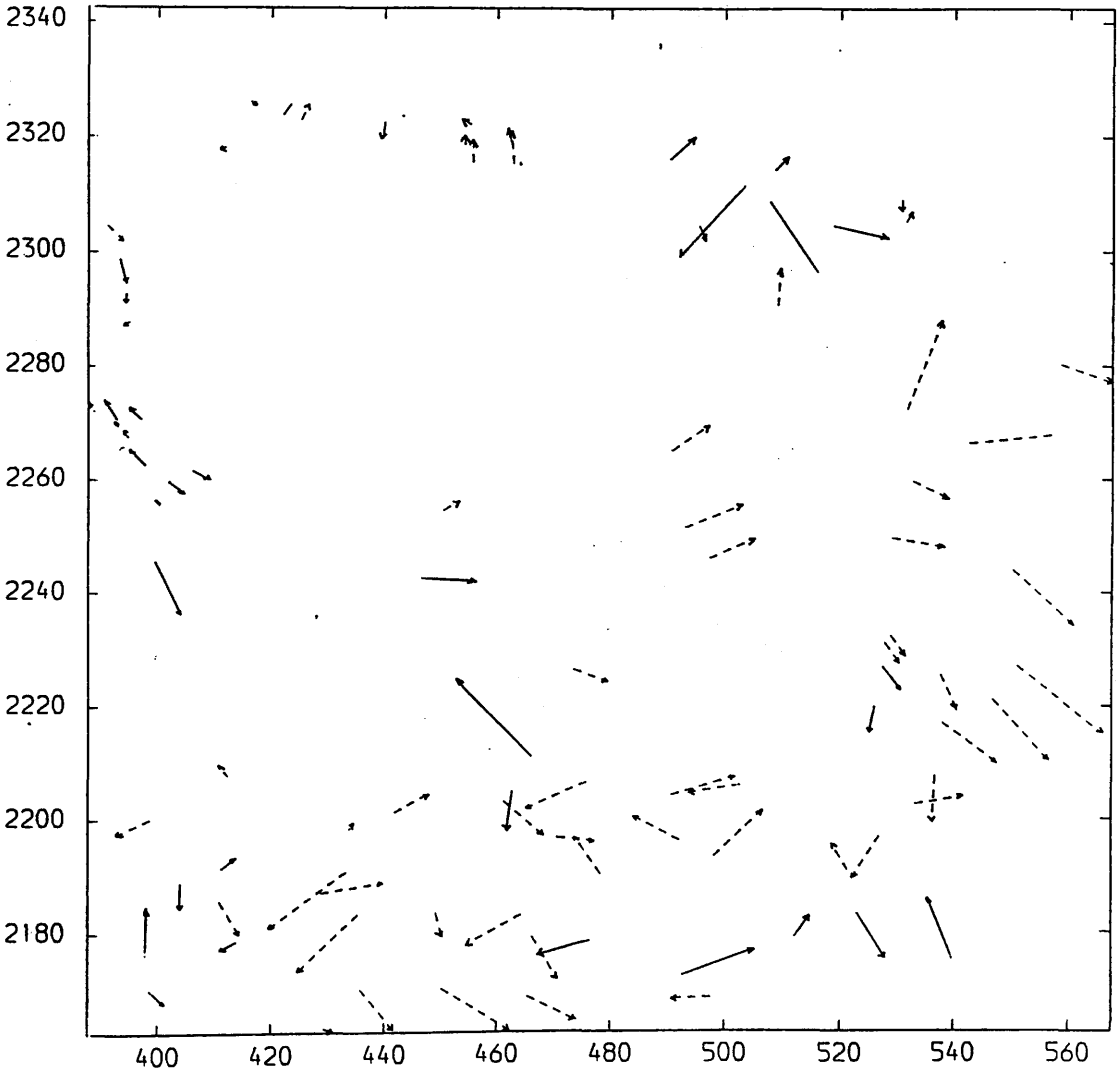


Fig. C.19 Residuals After the 5-term Polynomial Transformation of the TM Image Using 40 Control Points.

Control Points.→

Check Points:---→

ENLARGEMENT=X250.

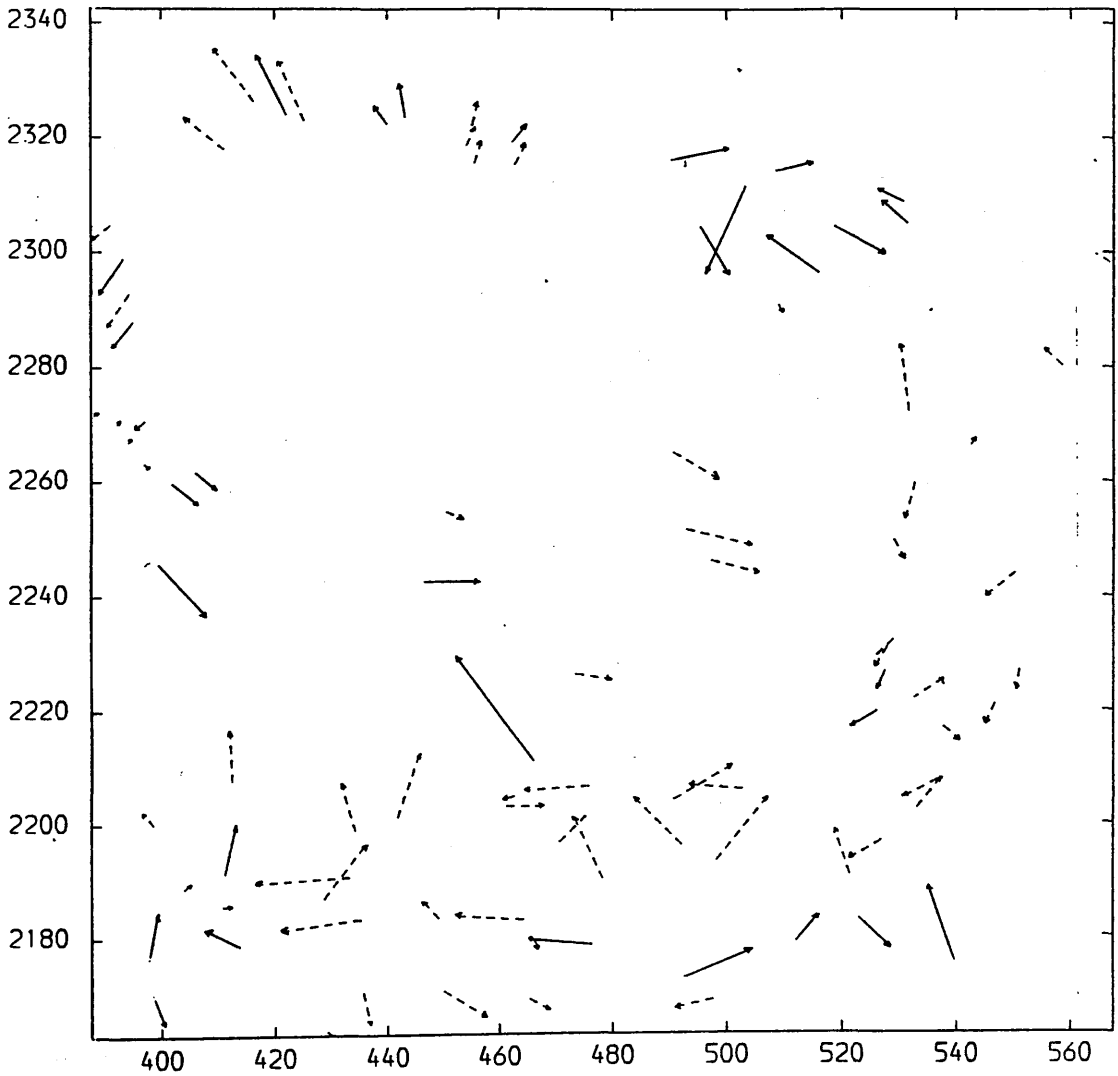


Fig. C.20 Residuals After the 6-term Polynomial Transformation of the TM Image Using 40 Control Points.

Control Points. —→ Check Points. - - - ->

ENLARGEMENT=X250.

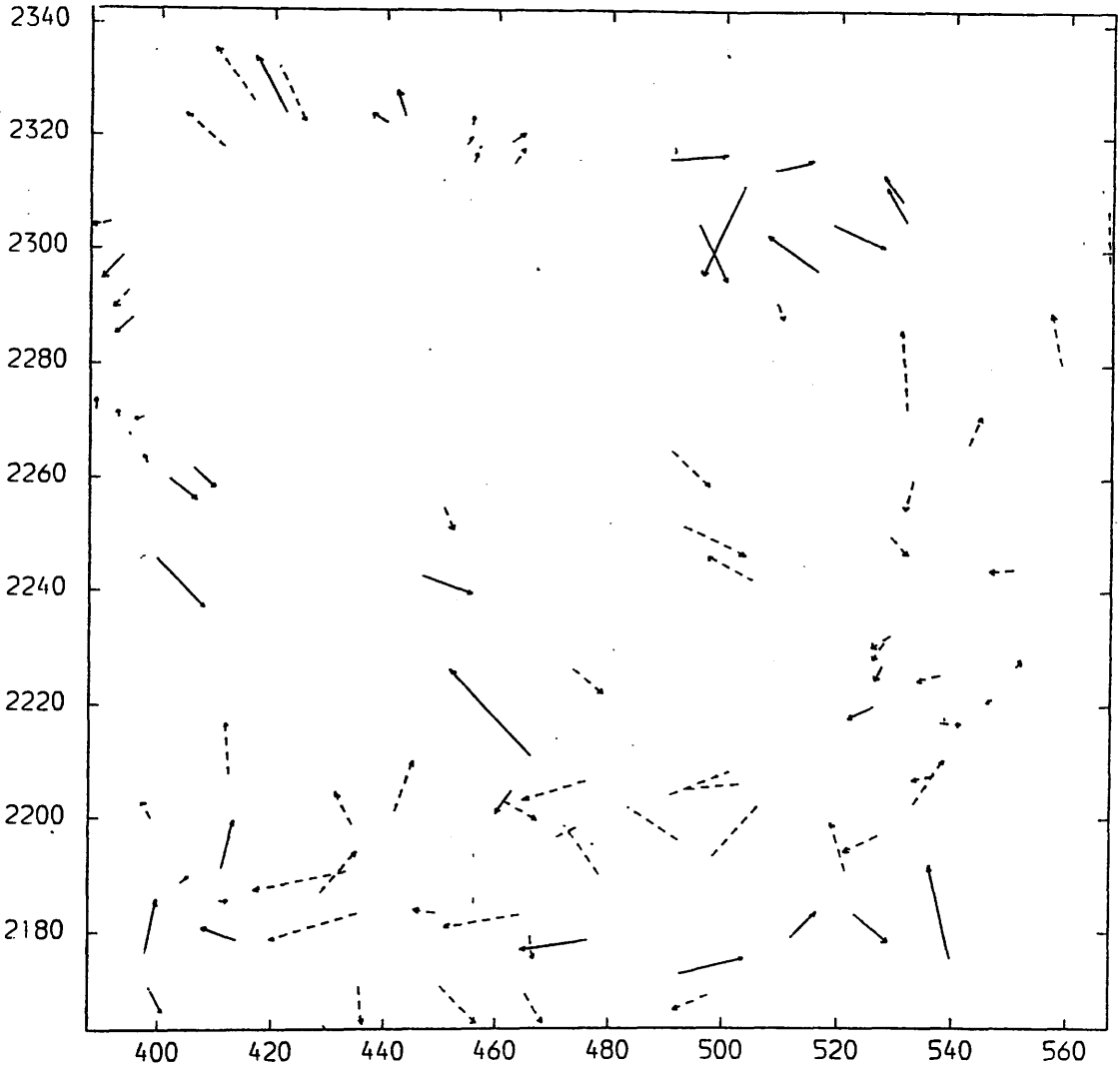


Fig. C.21 Residuals After the 7-term Polynomial Transformation of the TM Image Using 40 Control Points.

Control Points. —→

Check Points. - - - →

ENLARGEMENT=X250.

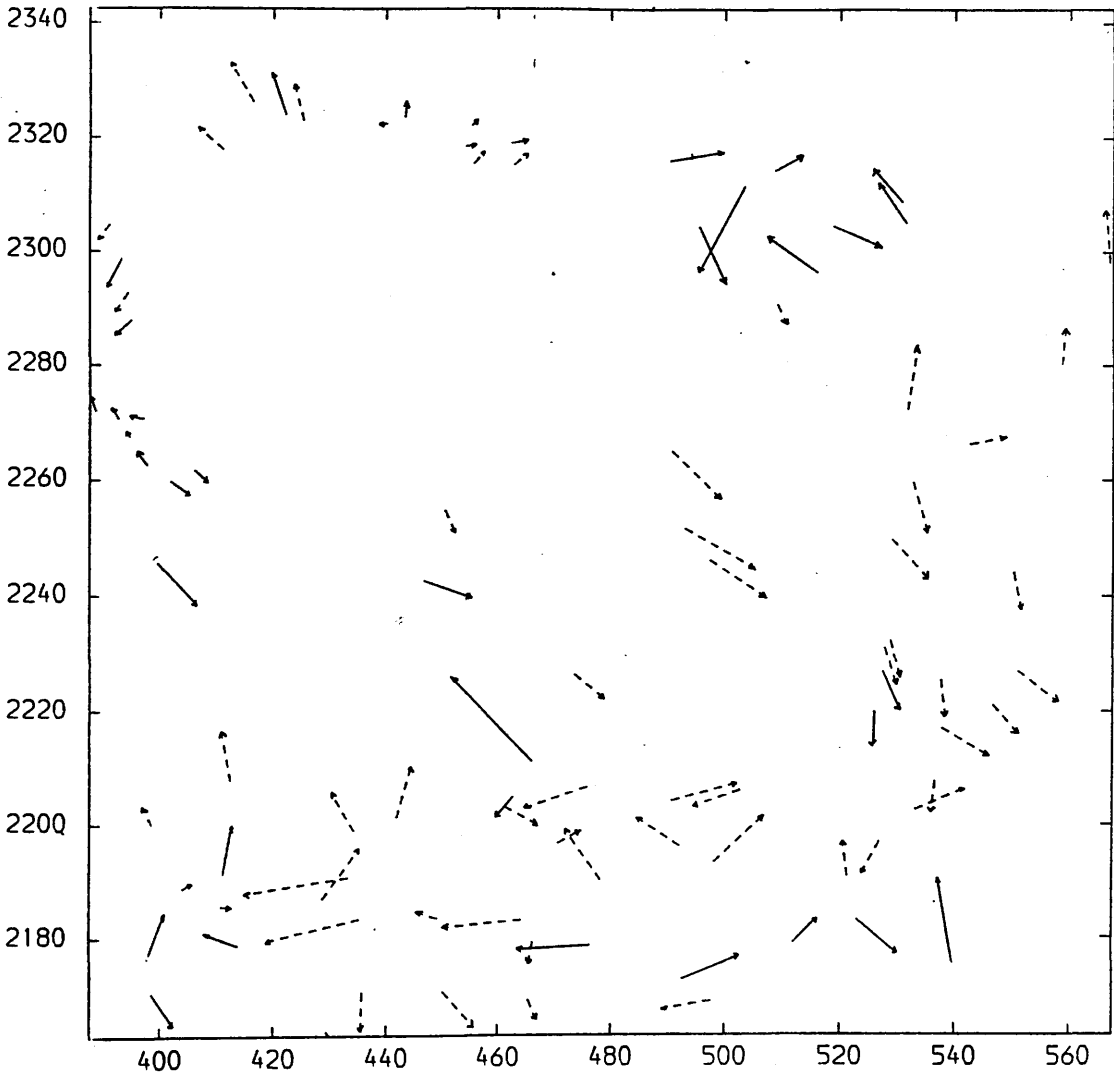


Fig. C.22 Residuals After the 8-term Polynomial Transformation of the TM Image Using 40 Control Points.

Control Points.—→

Check Points.-.-.-→

ENLARGEMENT=X250.

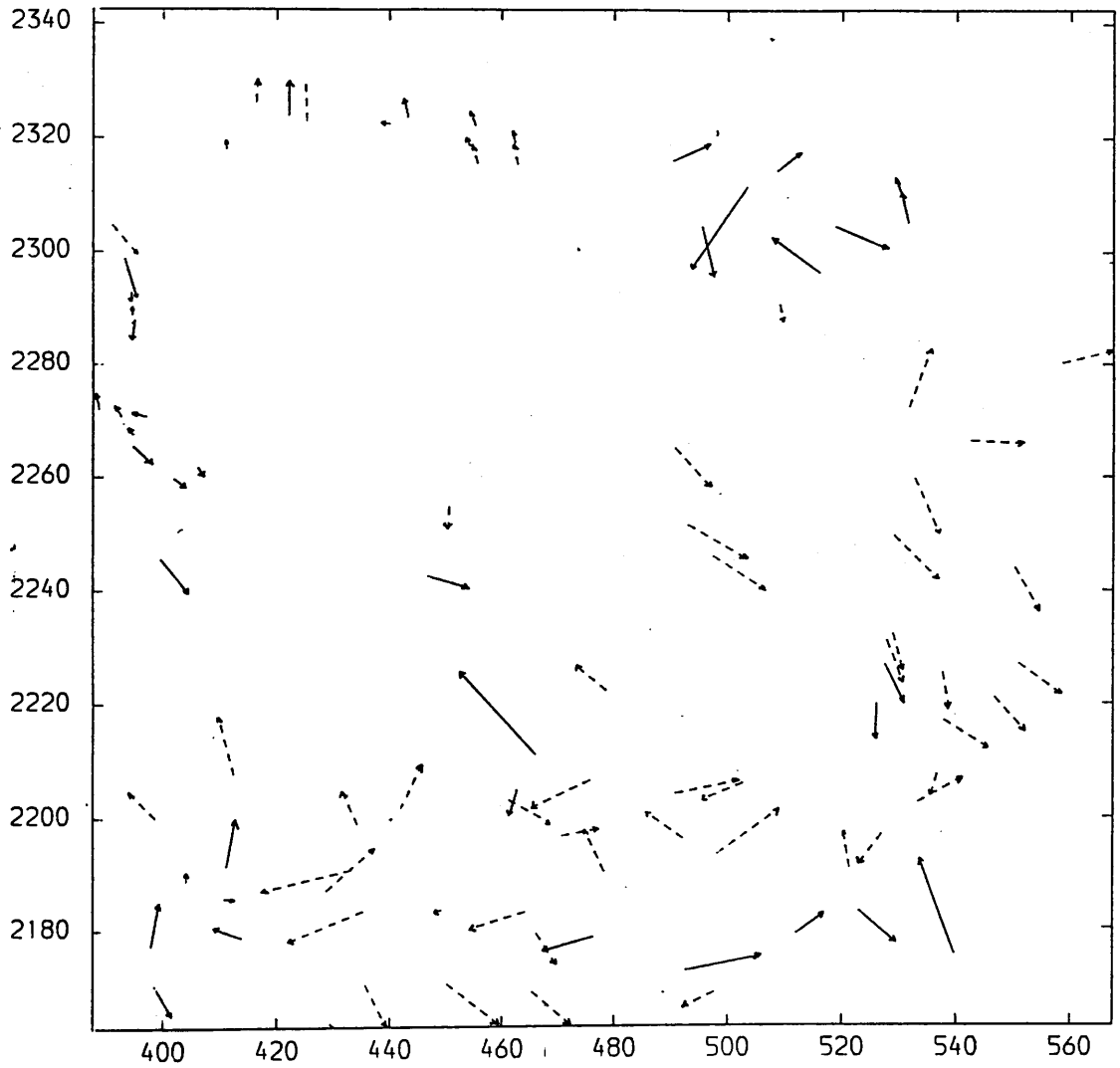


Fig. C.23 Residuals After the 9-term Polynomial Transformation of the TM Image Using 40 Control Points.

Control Points. —→

Check Points. - - - →

ENLARGEMENT=X250.

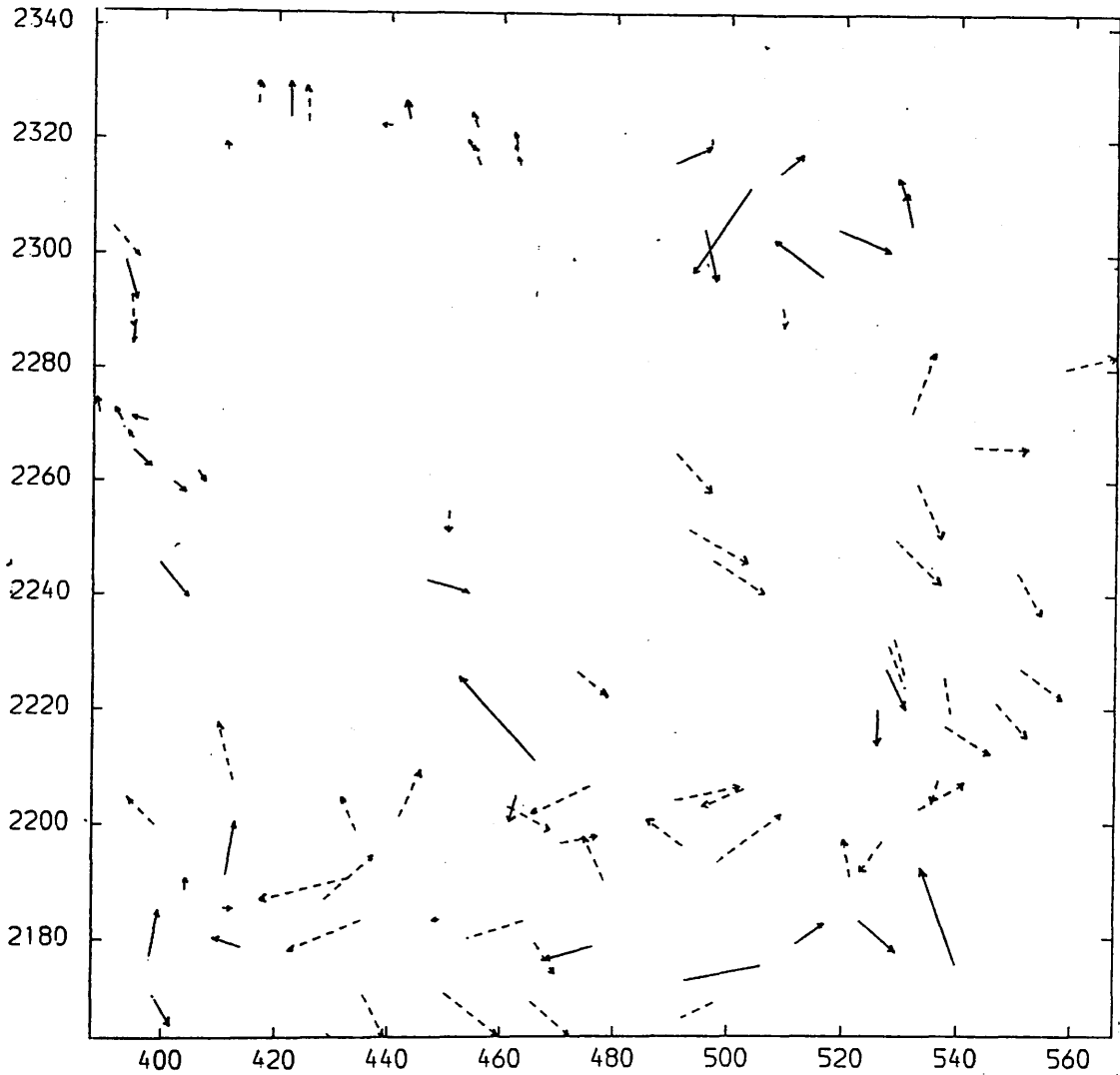


Fig. C.24 Residuals After the 10-term Polynomial Transformation of the TM Image Using 40 Control Points.

Control Points. —→

Check Points. - - - ->

ENLARGEMENT=X250.

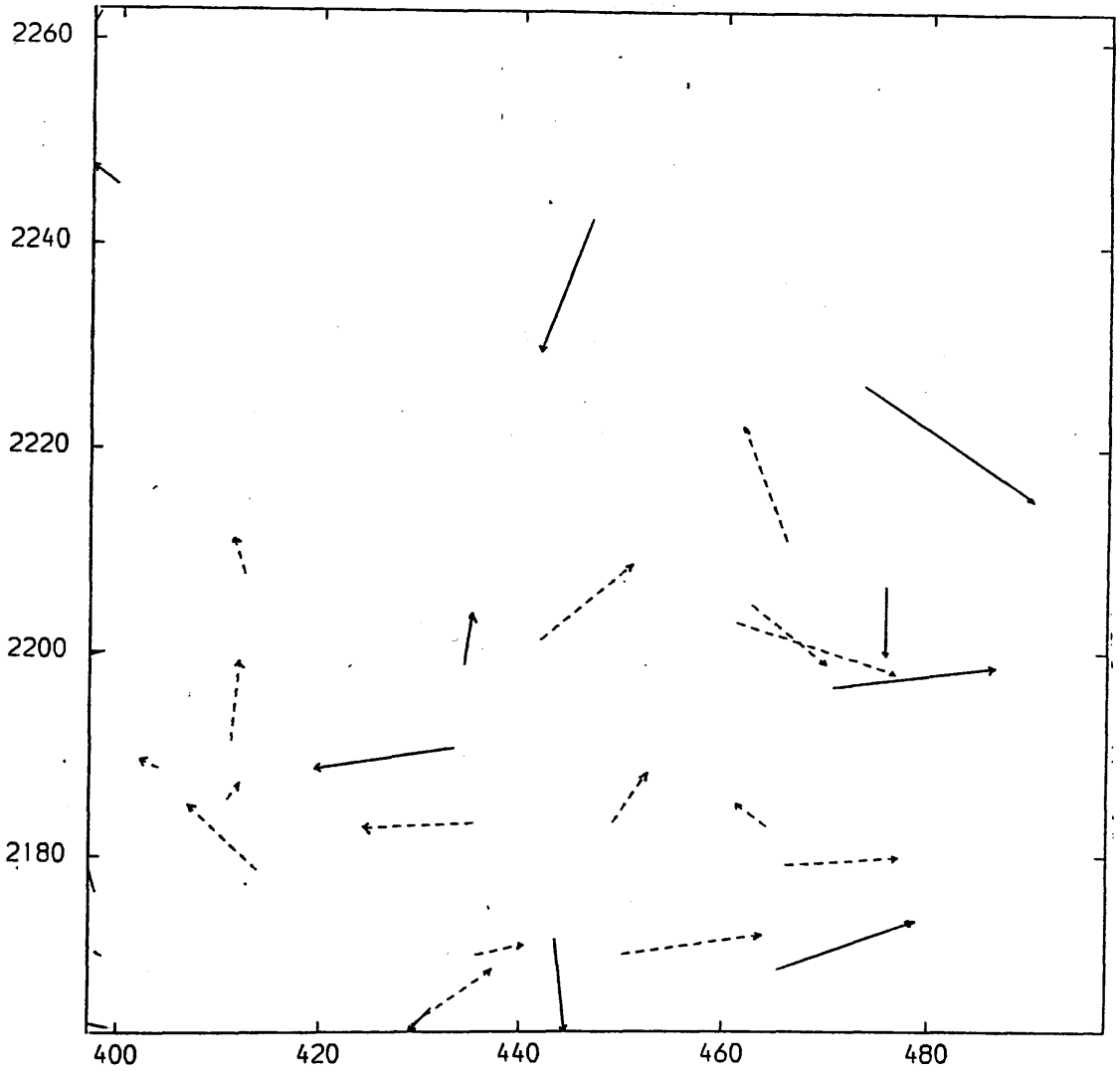


Fig. C.25 Residuals After the Linear Conformal Transformation of the TM Quarter-scene 1.

Control Points. —→ Check Points. - - - ->

ENLARGEMENT=X250.

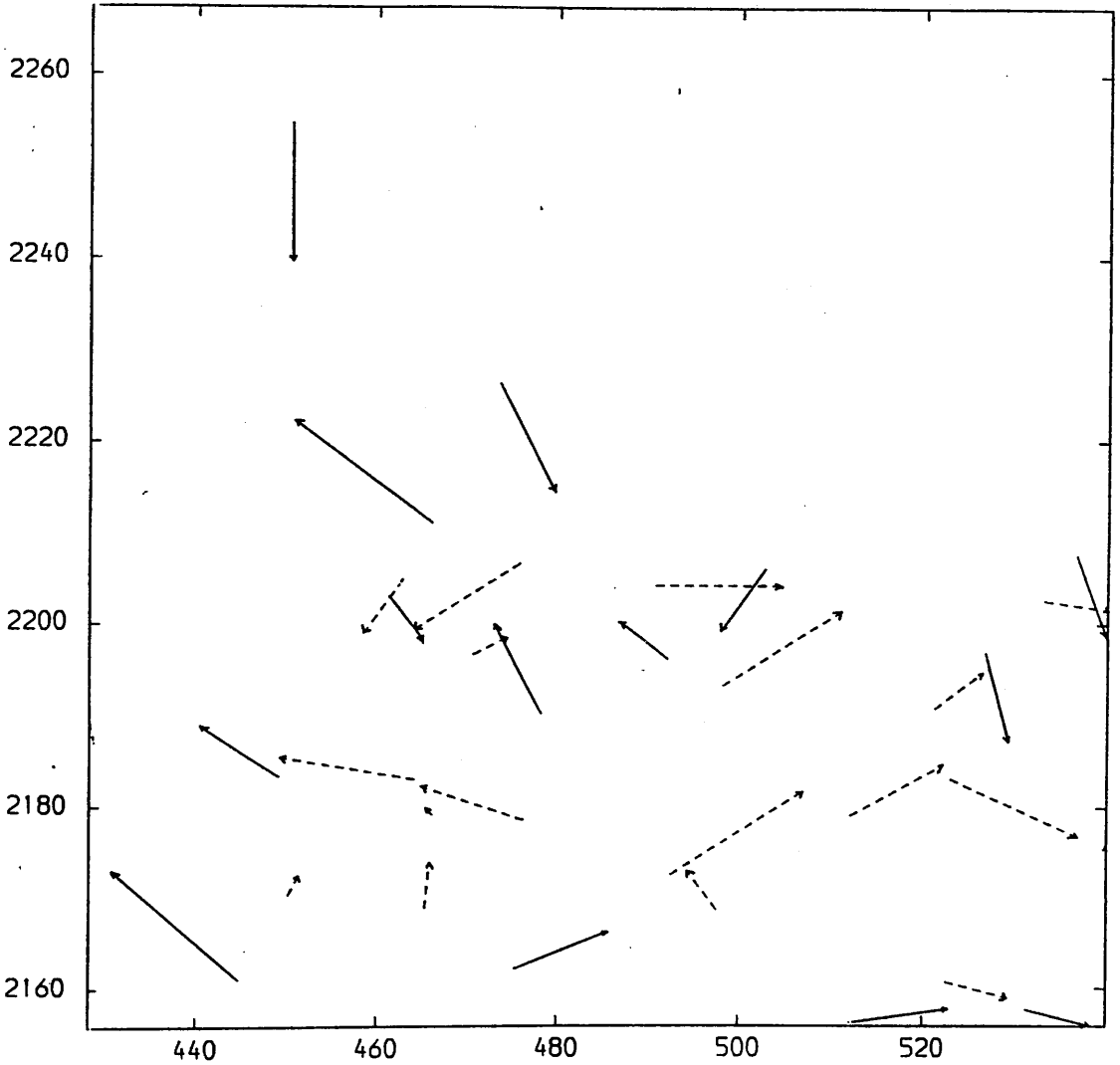


Fig. C.26 Residuals After the Linear Conformal Transformation of the TM Quarter-scene 2.

Control Points. —→

Check Points. - - - ->

ENLARGEMENT=X250.

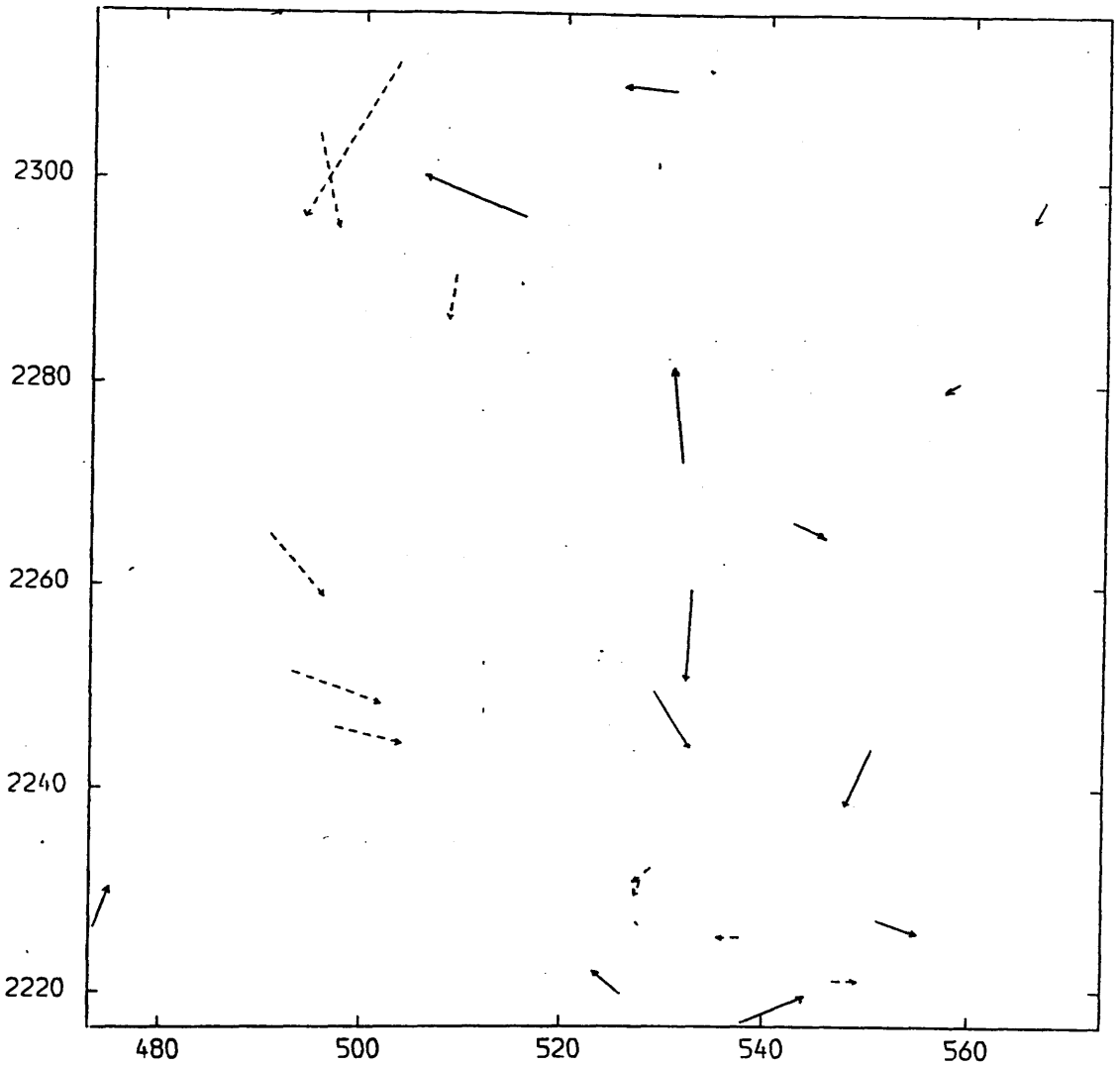


Fig. C.27 Residuals After the Linear Conformal Transformation of the TM Quarter-scene 3.

Control Points. —→

Check Points. - - - →

ENLARGEMENT=X250.

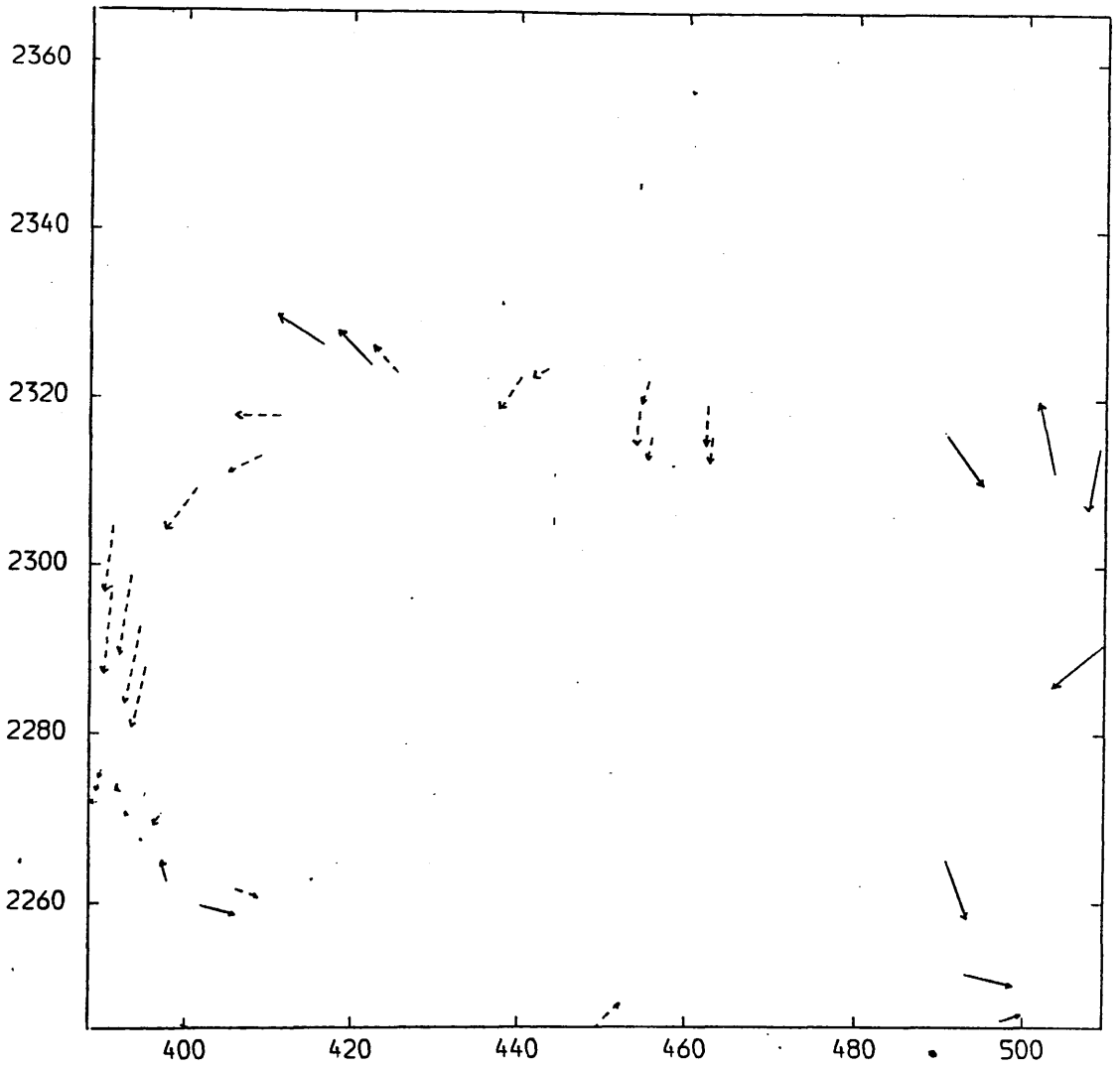


Fig. C.28 Residuals After the Linear Conformal Transformation of the TM Quarter-scene 4.

Control Points. —→

Check Points. - - - ->

ENLARGEMENT=X250.

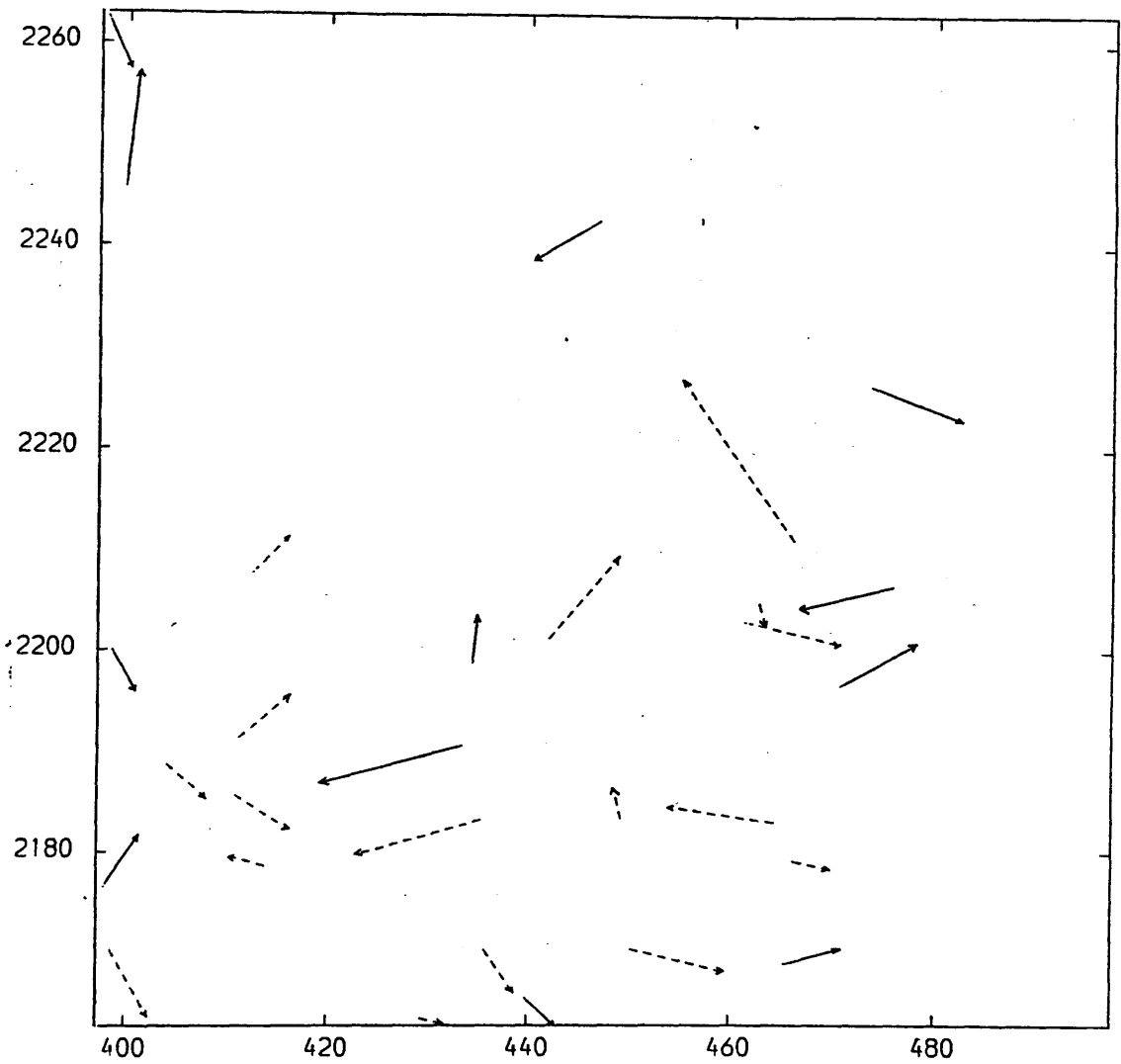


Fig. C.29 Residuals After the Affine Transformation of the TM Quarter-scene 1.

Control Points. —→

Check Points. - - - →

ENLARGEMENT=X250.

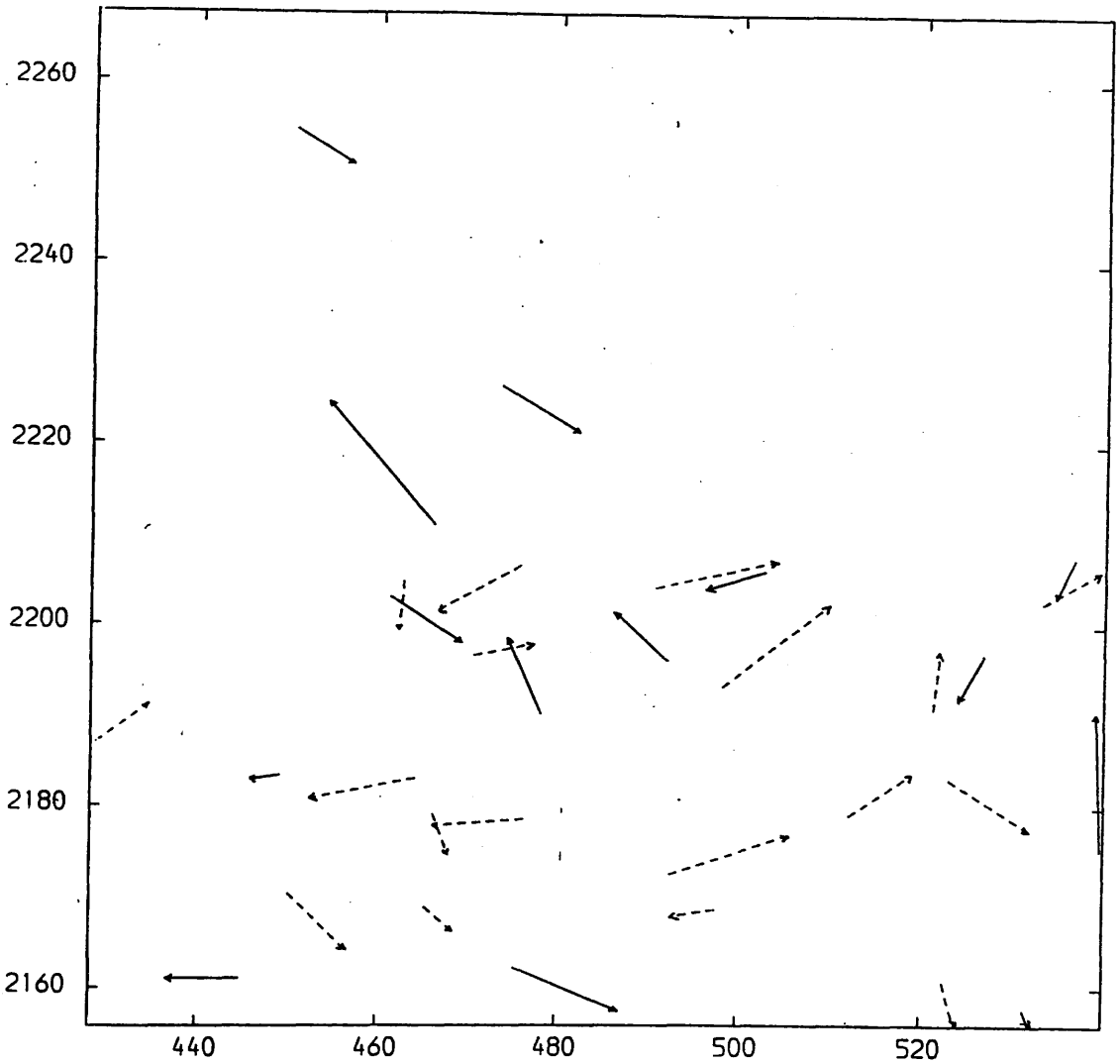


Fig. C.30 Residuals After the Affine Transformation of the TM Quarter-scene 2.

Control Points. —>

Check Points. - - ->

ENLARGEMENT=X250.

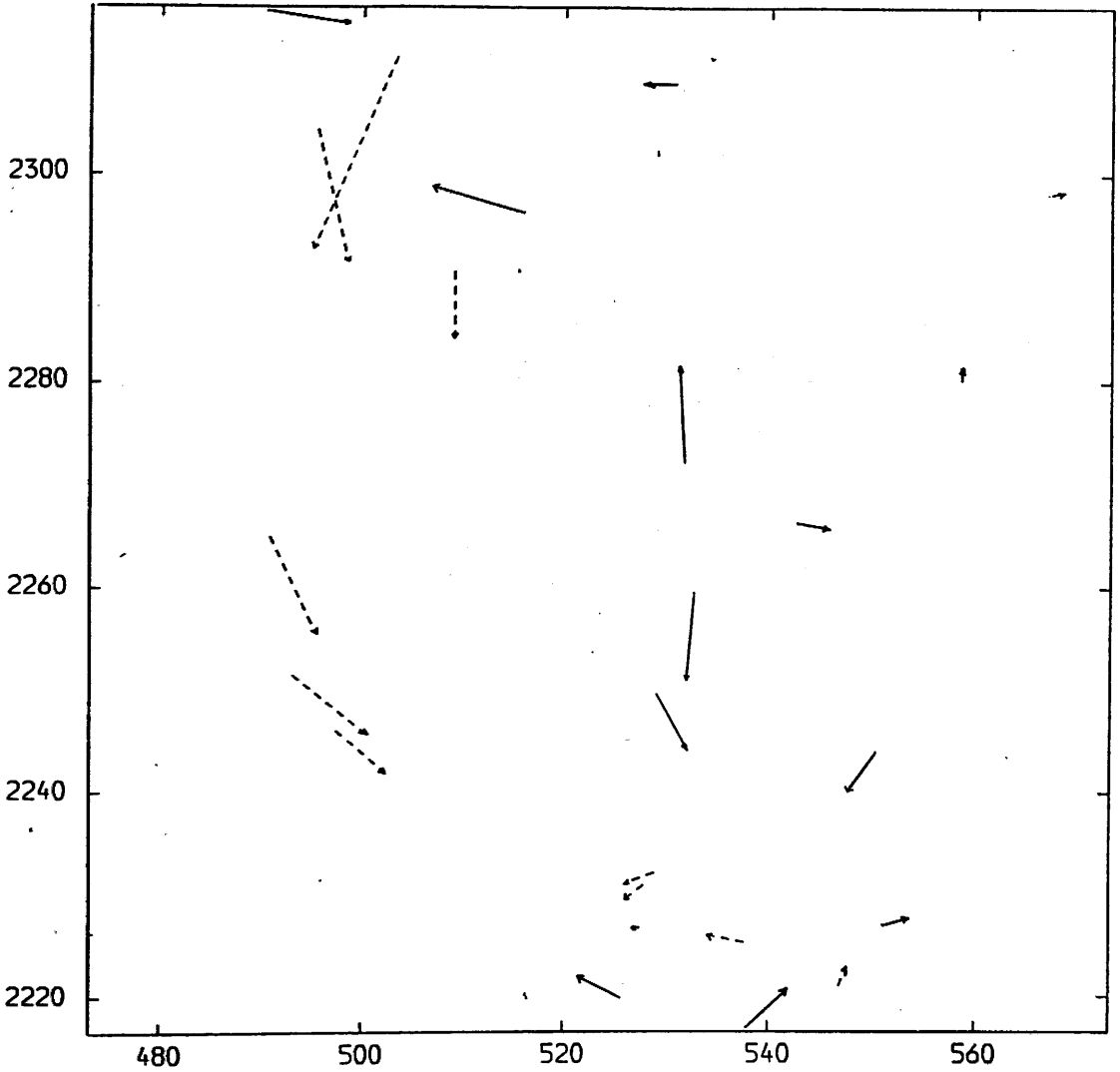


Fig. C.31 Residuals After the Affine Transformation of the TM Quarter-scene 3.

Control Points. —→

Check Points. - - - →

ENLARGEMENT=X250.

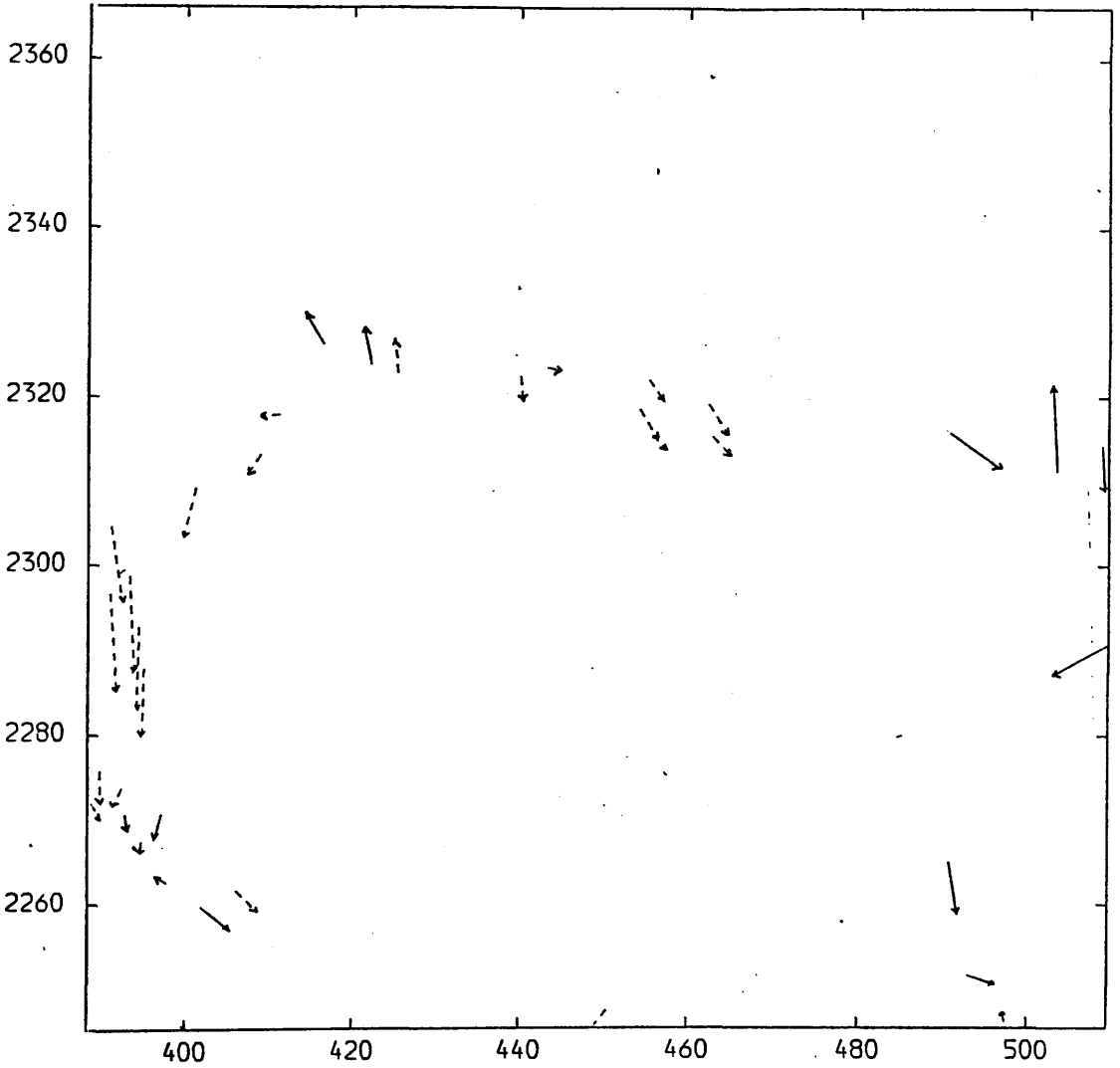


Fig. C.32 Residuals After the Affine Transformation of the TM Quarter-scene 4.

Control Points.—

Check Points.---->

APPENDIX D

VECTOR PLOTS OF THE RESIDUALS FOR MOMS IMAGES

ENLARGEMENT=X0.30

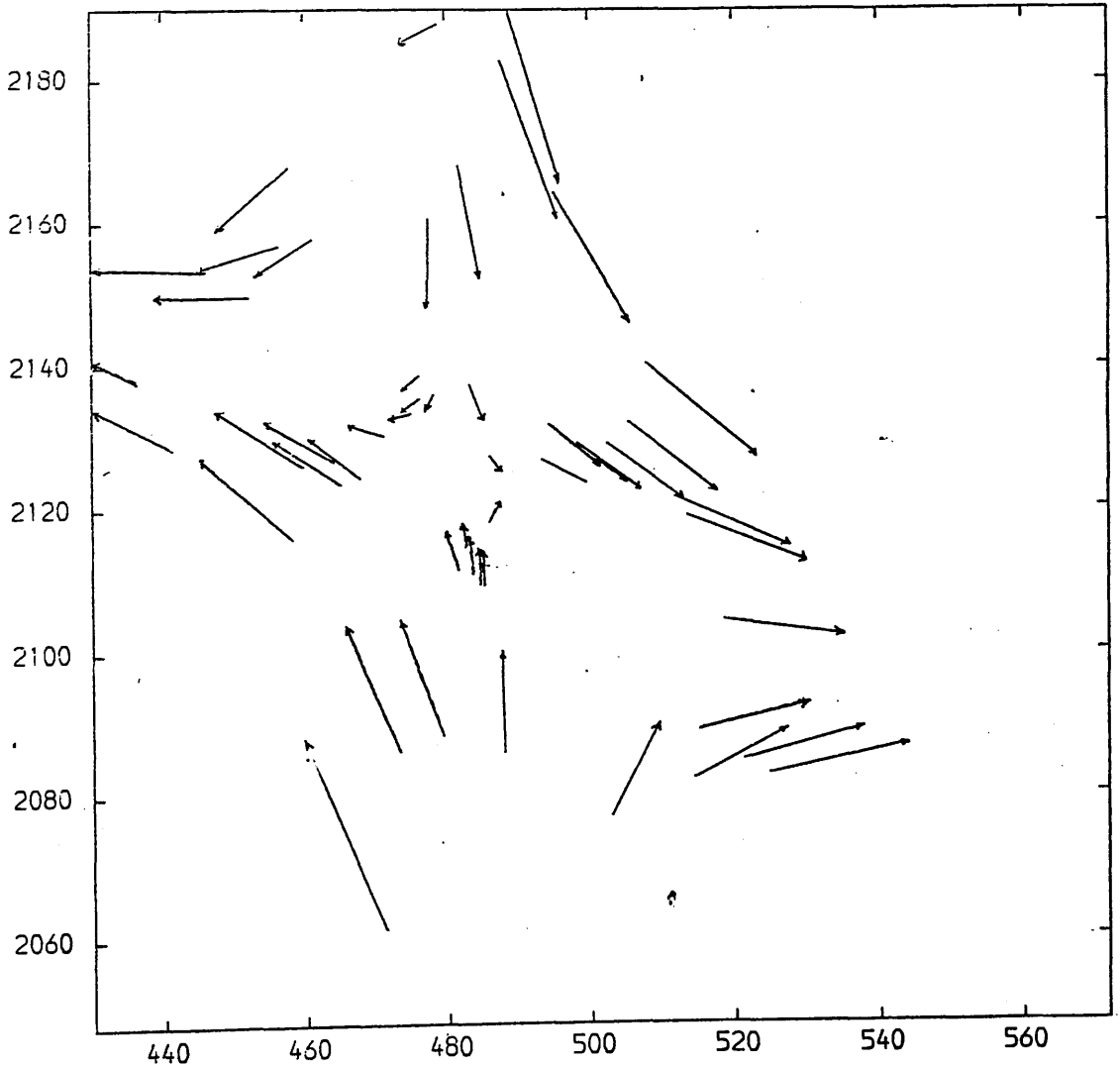


Fig. D.1 Residuals After the Linear Conformal Transformation of the MOMS Image 1 Using All Points as Control Points.

ENLARGEMENT=X0.30

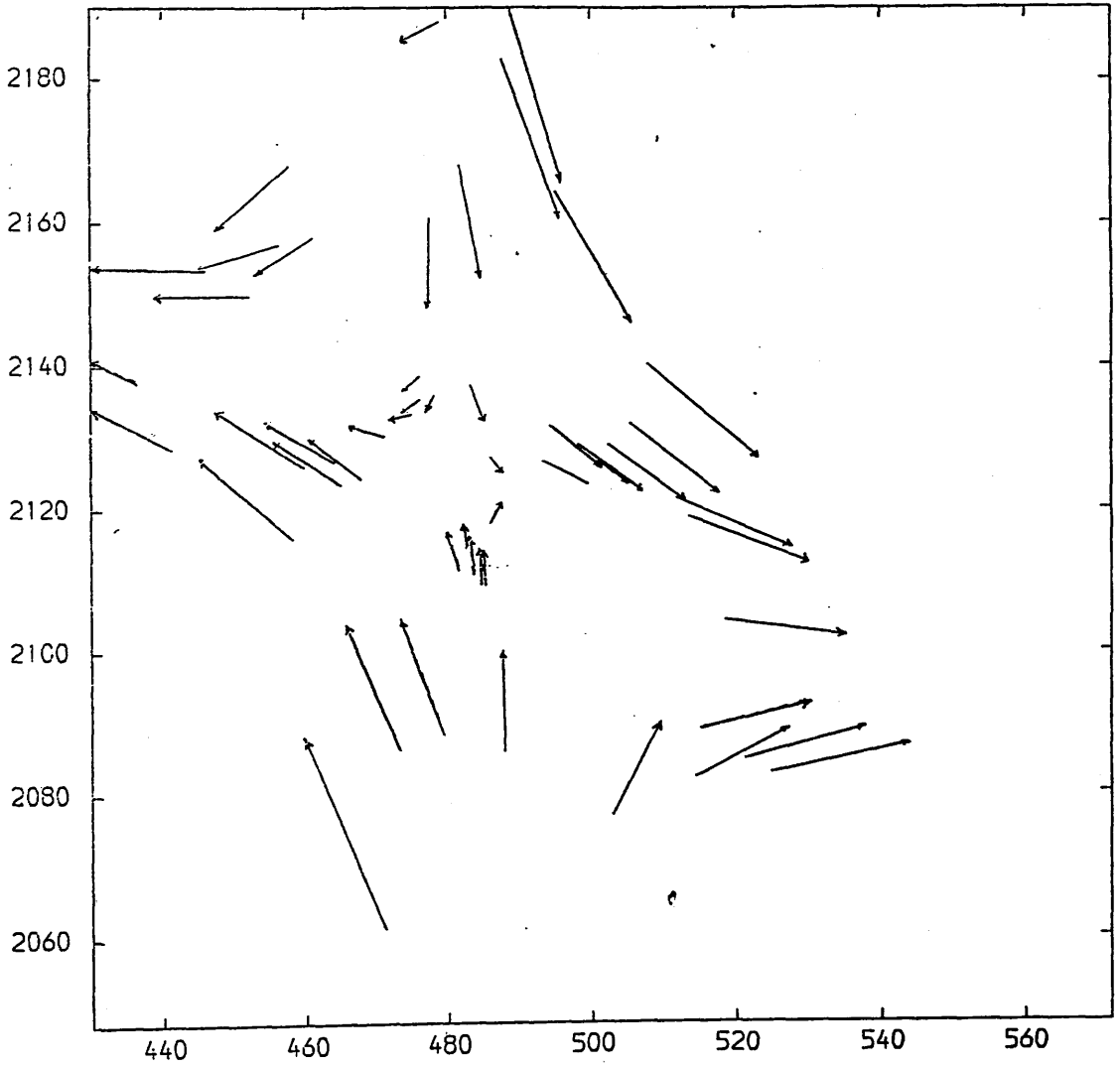


Fig. D.2 Residuals After the Linear Conformal Transformation of the MOMS Image 2 Using All Points as Control Points.

ENLARGEMENT=X0.30

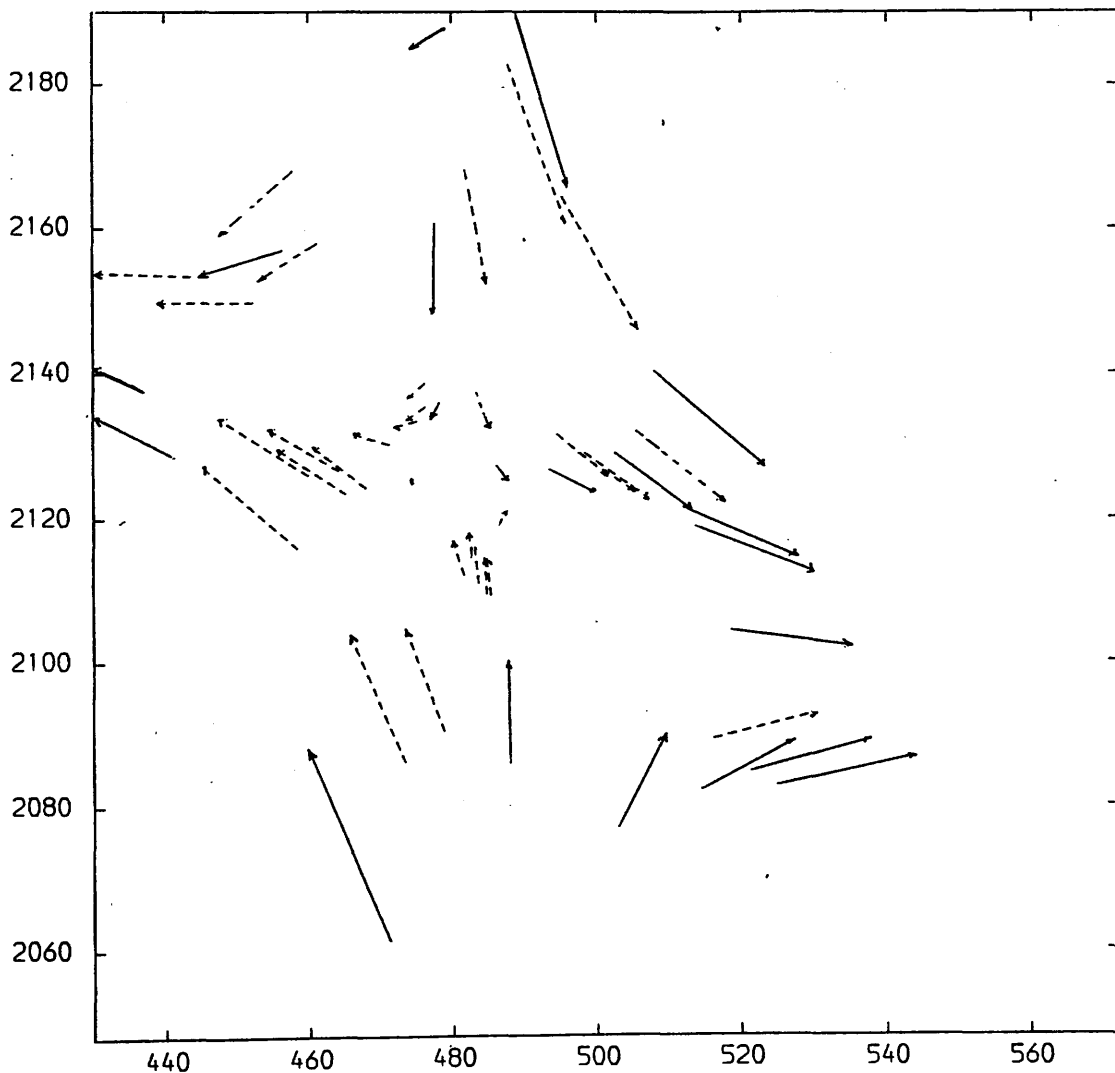


Fig. D.3 Residuals After the Linear Conformal Transformation of the NOMS Image 1 Using 20 Control Points.

Control Points. —→

Check Points. - - - →

ENLARGEMENT=X0.3

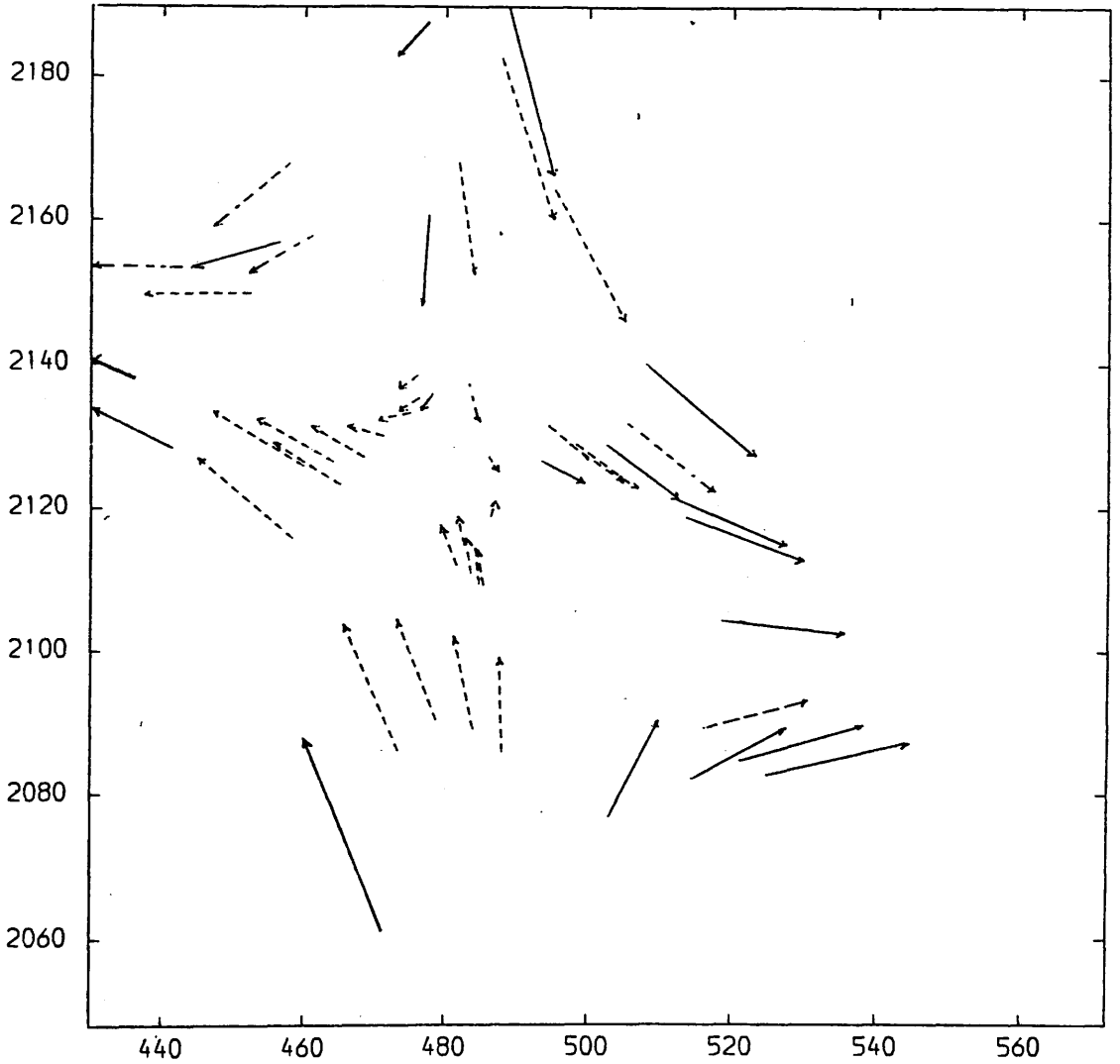


Fig. D.4 Residuals After the Linear Conformal Transformation of the MOMS Image 2 Using 20 Control Points.

Control Points. —→

Check Points. - - - ->

ENLARGEMENT=X300.

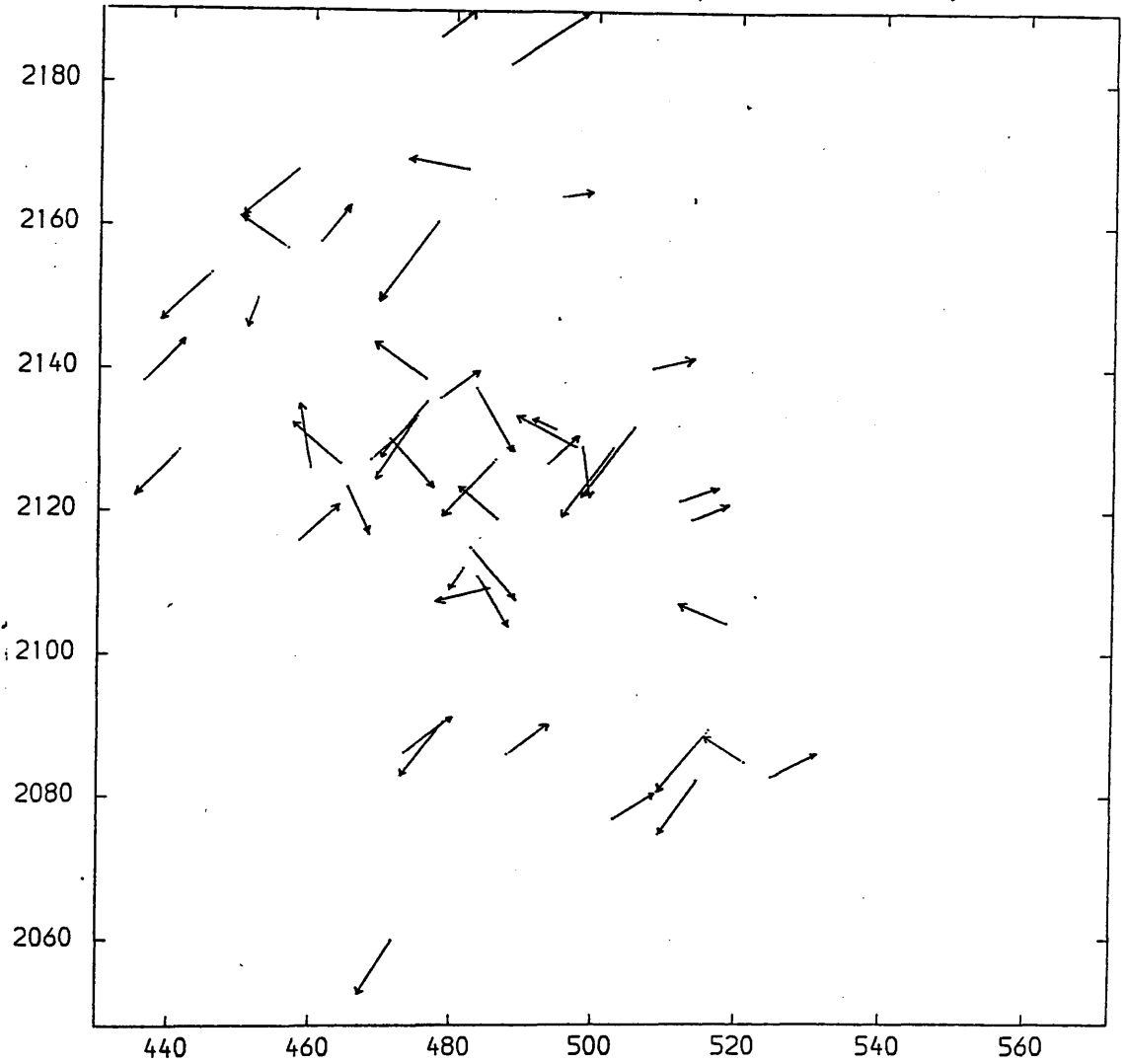


Fig. D.5 Residuals After the Affine Transformation of the MOMS Image 1 Using All Points as Control Points.

ENLAGEMENT=X300.

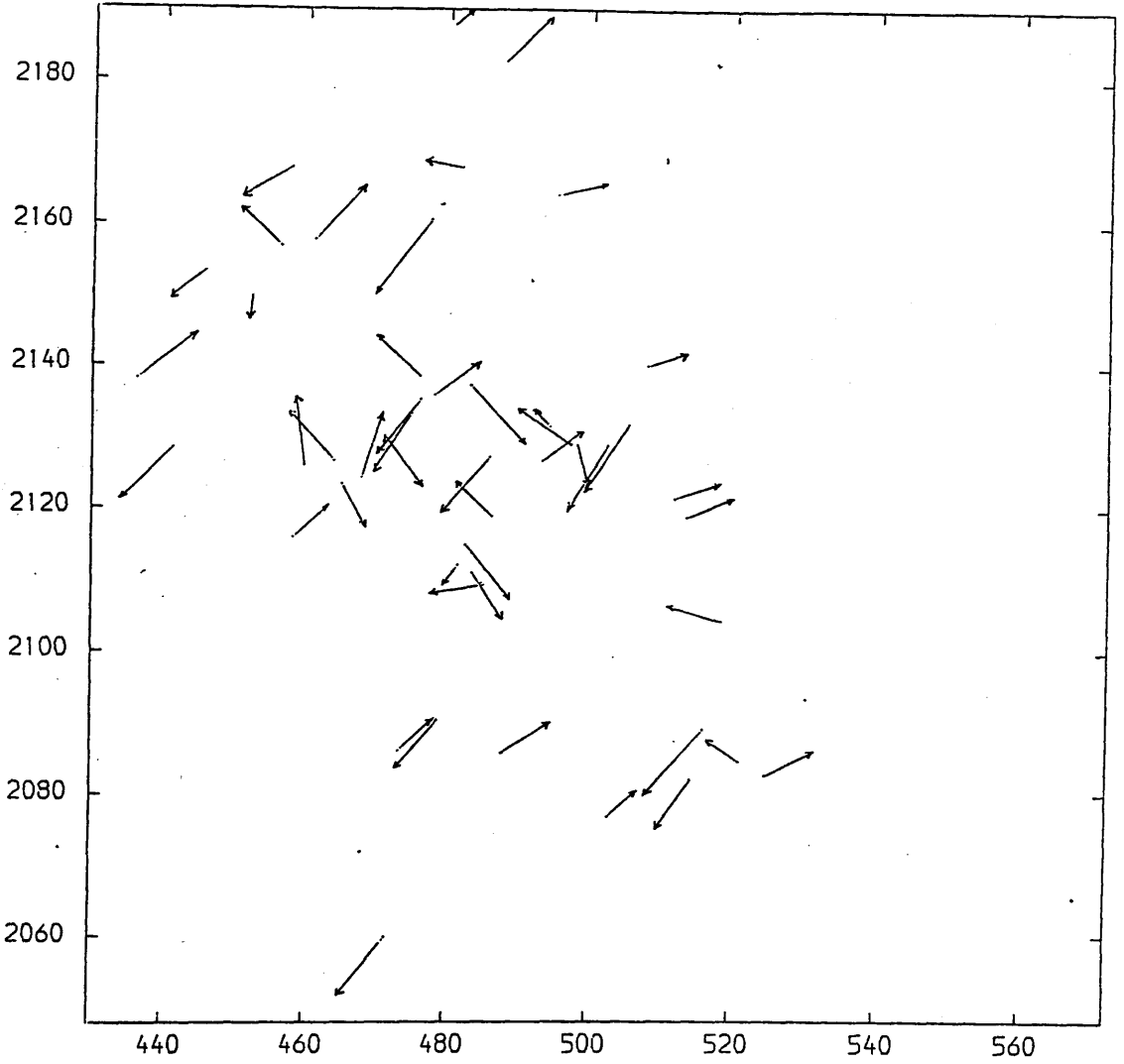


Fig. D.6 Residuals After the Affine Transformation of the MOMS Image 2 Using All Points as Control Points.

ENLARGEMENT=X300.

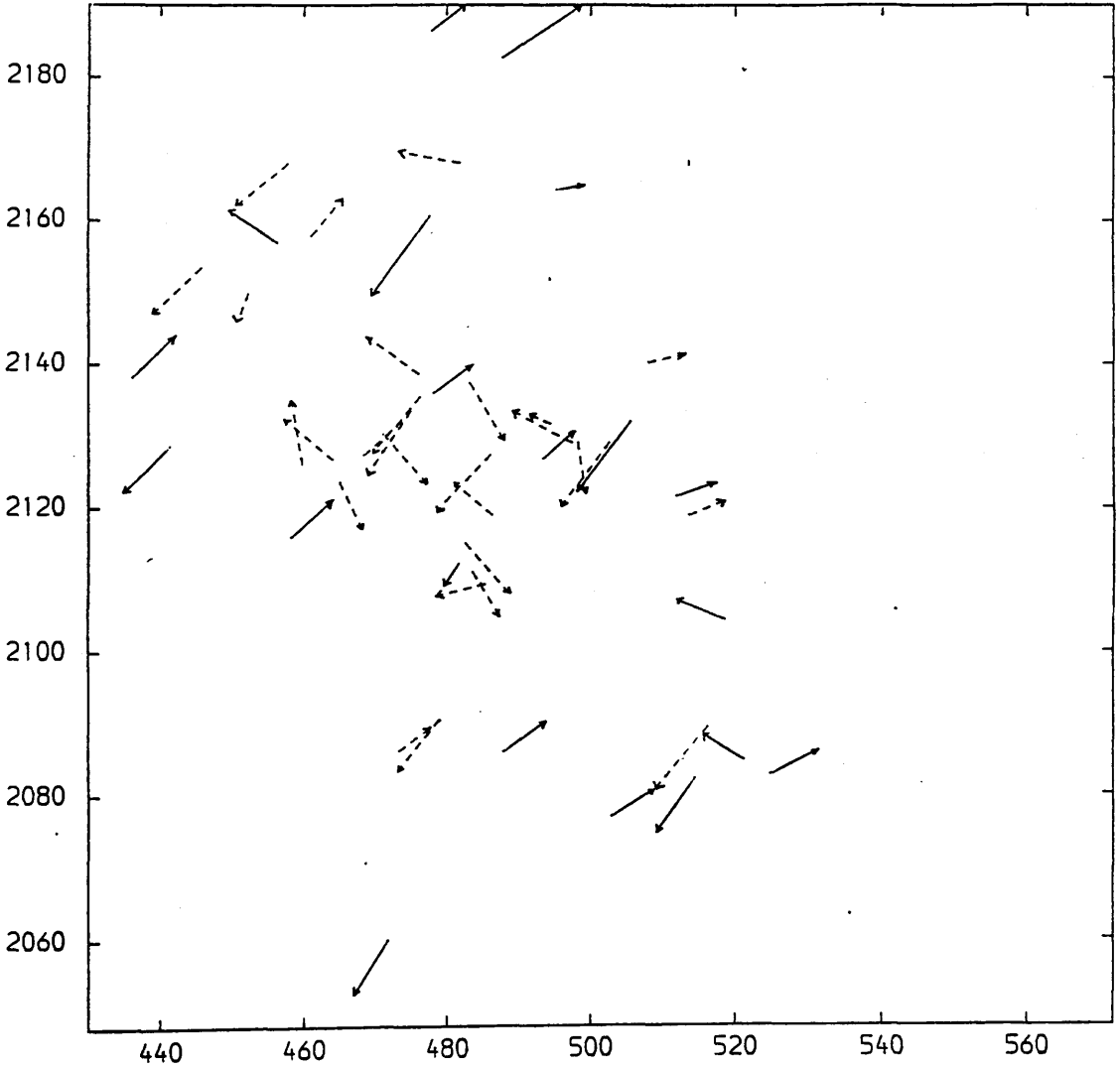


Fig. D.7 Residuals After the Affine Transformation of the MOMS Image 1 Using 20 Control Points.

Control Points. —→

Check Points. - - - →

ENLARGEMENT=X300.

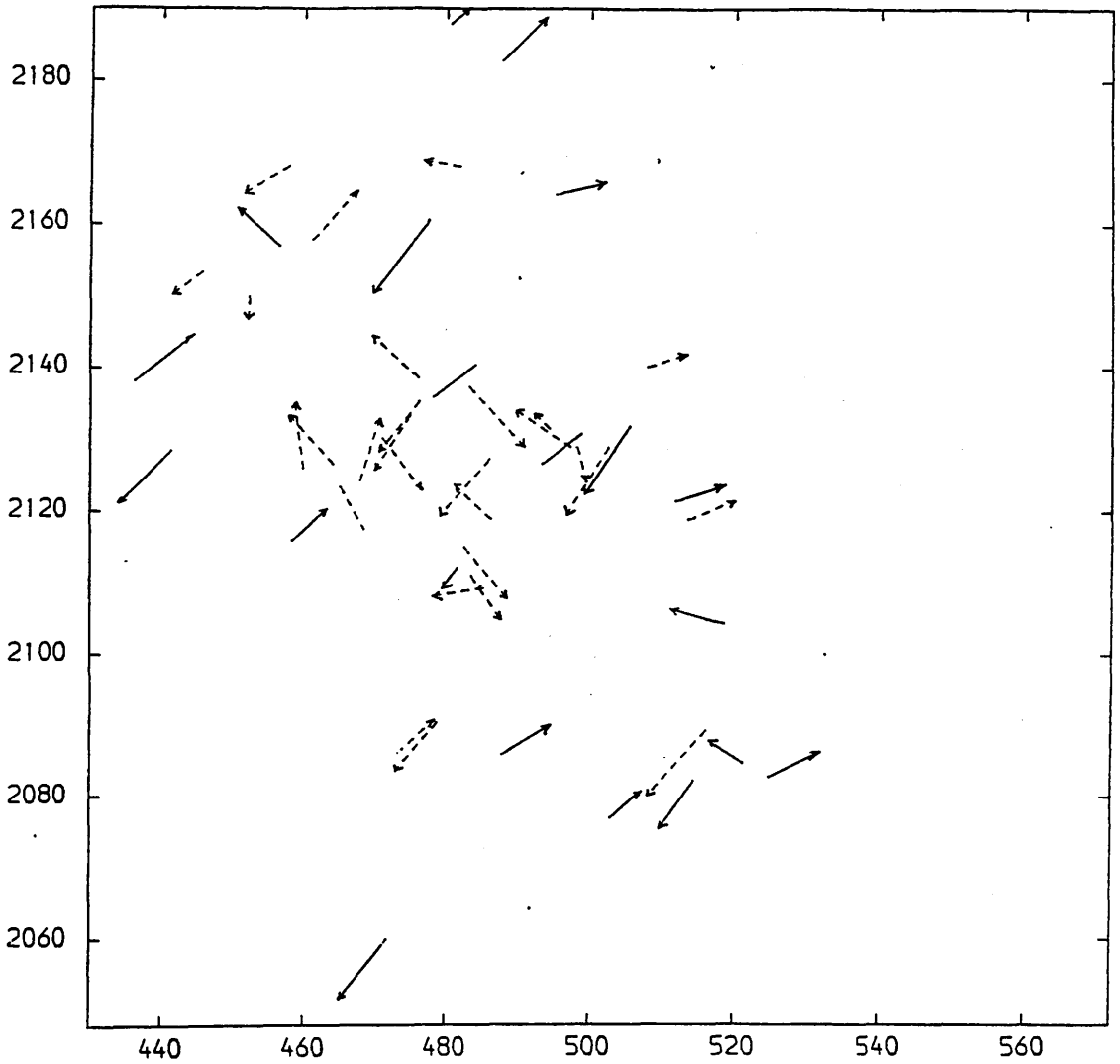


Fig. D.8 Residuals After the Affine Transformation of the MOMS Image 2 Using 20 Control Points.

Control Points. —→

Check Points. - - - →

APPENDIX E

VECTOR PLOTS OF THE RESIDUALS FOR THE RBV IMAGES

ENLARGEMENT=X100.

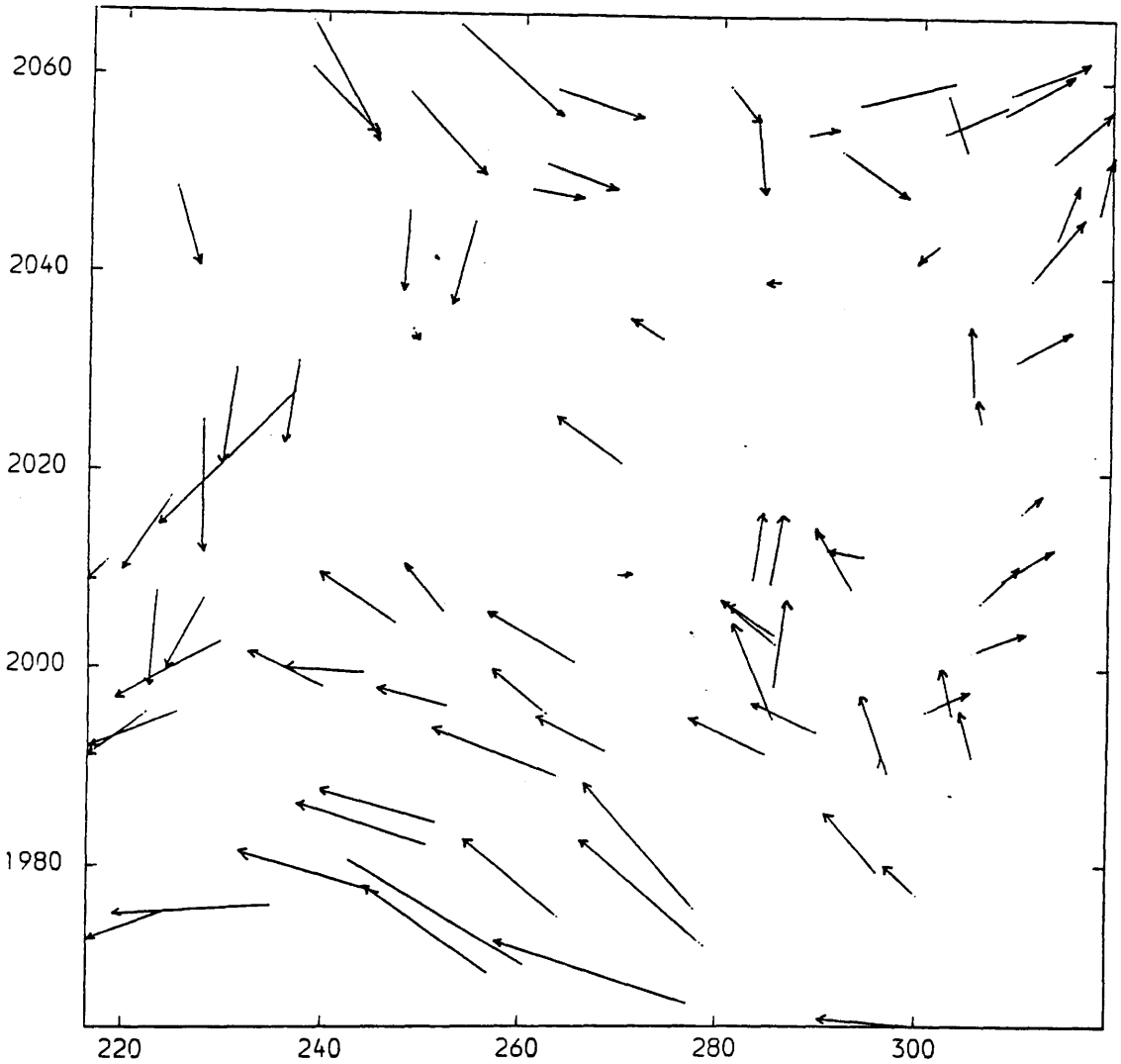


Fig. E.1 Residuals After the Linear Conformal Transformation of the RBV Image of the Red Sea Hills Area Using All Points as Control Points.

ENLARGEMENT=X100.

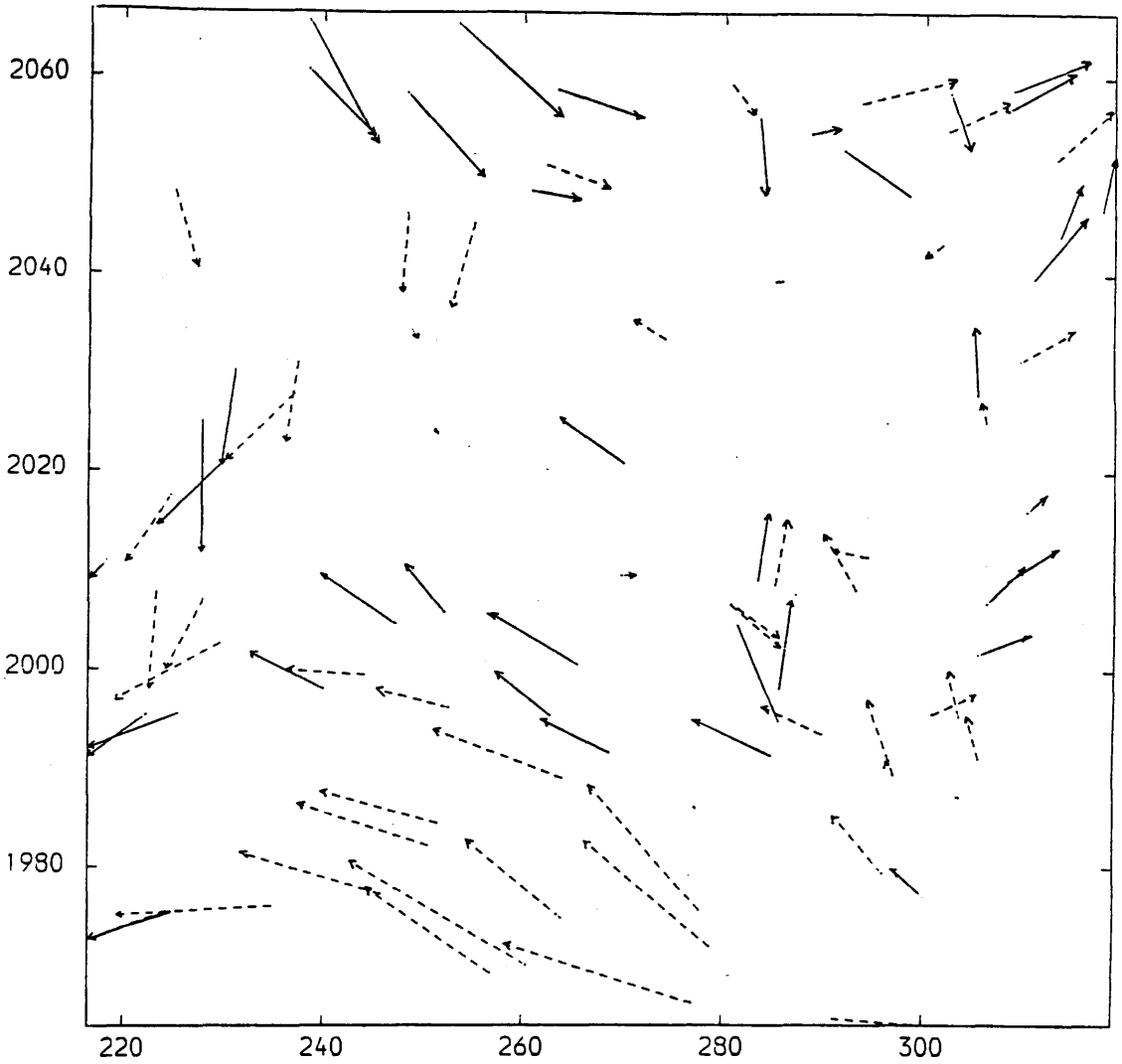


Fig. E.2 Residuals After the Linear Conformal Transformation of the RBV Image of the Red Sea Hills Area Using 40 Control Points.

Control Points ———→

Check Points - - - ->

ENLARGEMENT=X150.

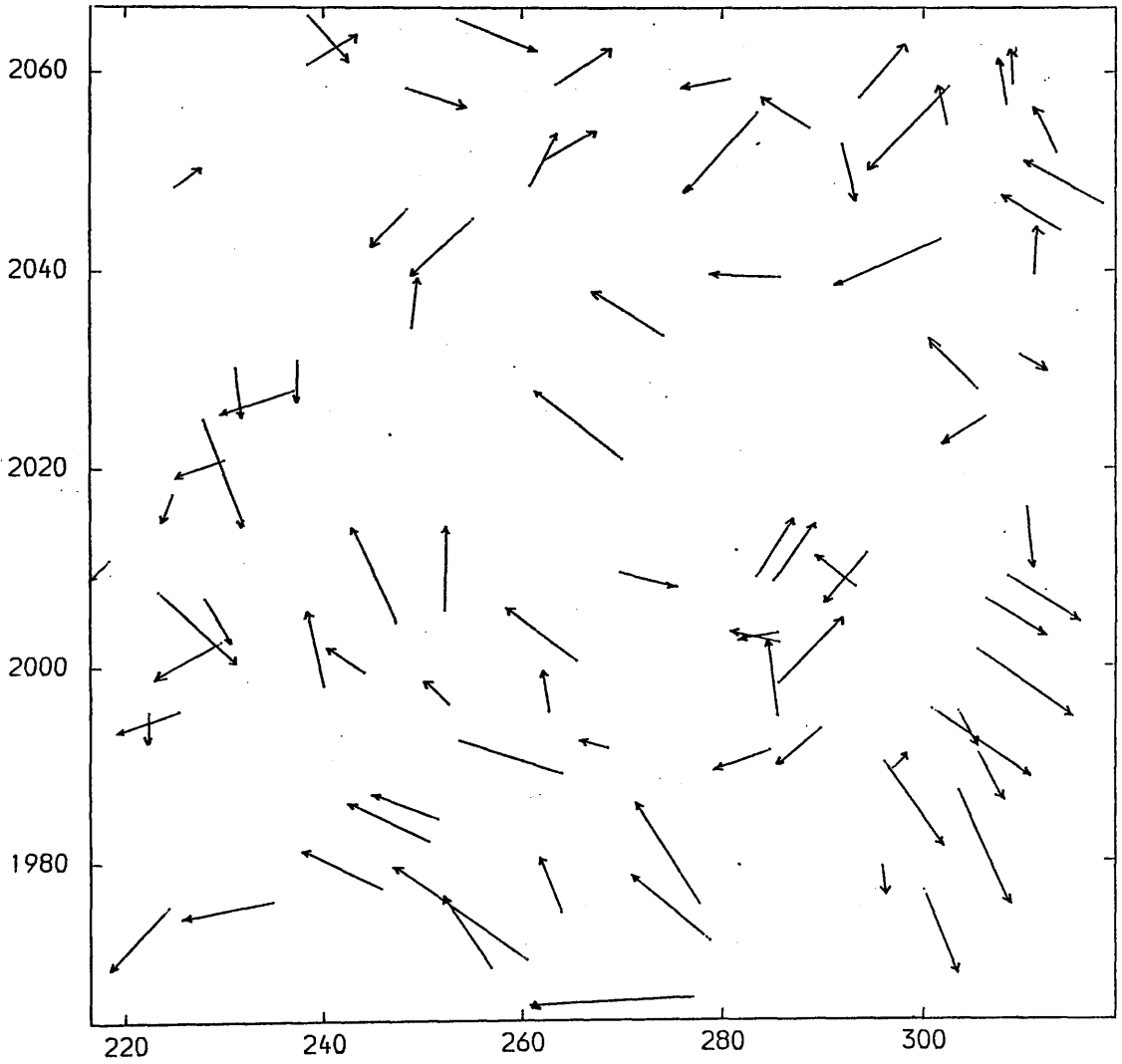


Fig. E.3 Residuals After the Affine Transformation of the RBV Image of the Red Sea Hills Area Using All Points as Control Points.

ENLARGEMENT=X150.

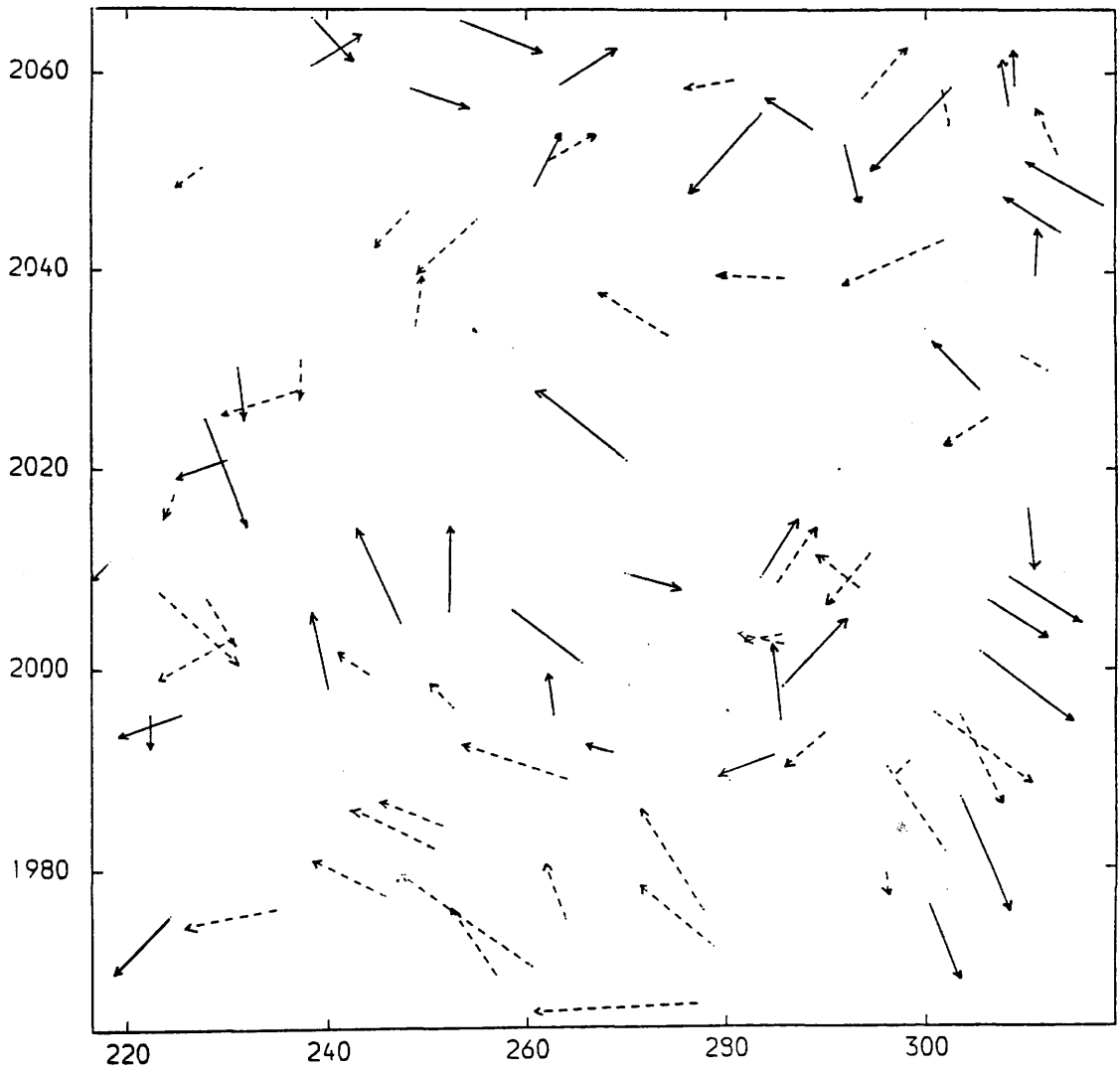


Fig. E.4 Residuals After the Affine Transformation of the RBV Image of the Red Sea Hills Area Using 40 Control Points.

Control Points \longrightarrow

Check Points \dashrightarrow

ENLARGEMENT=X150.

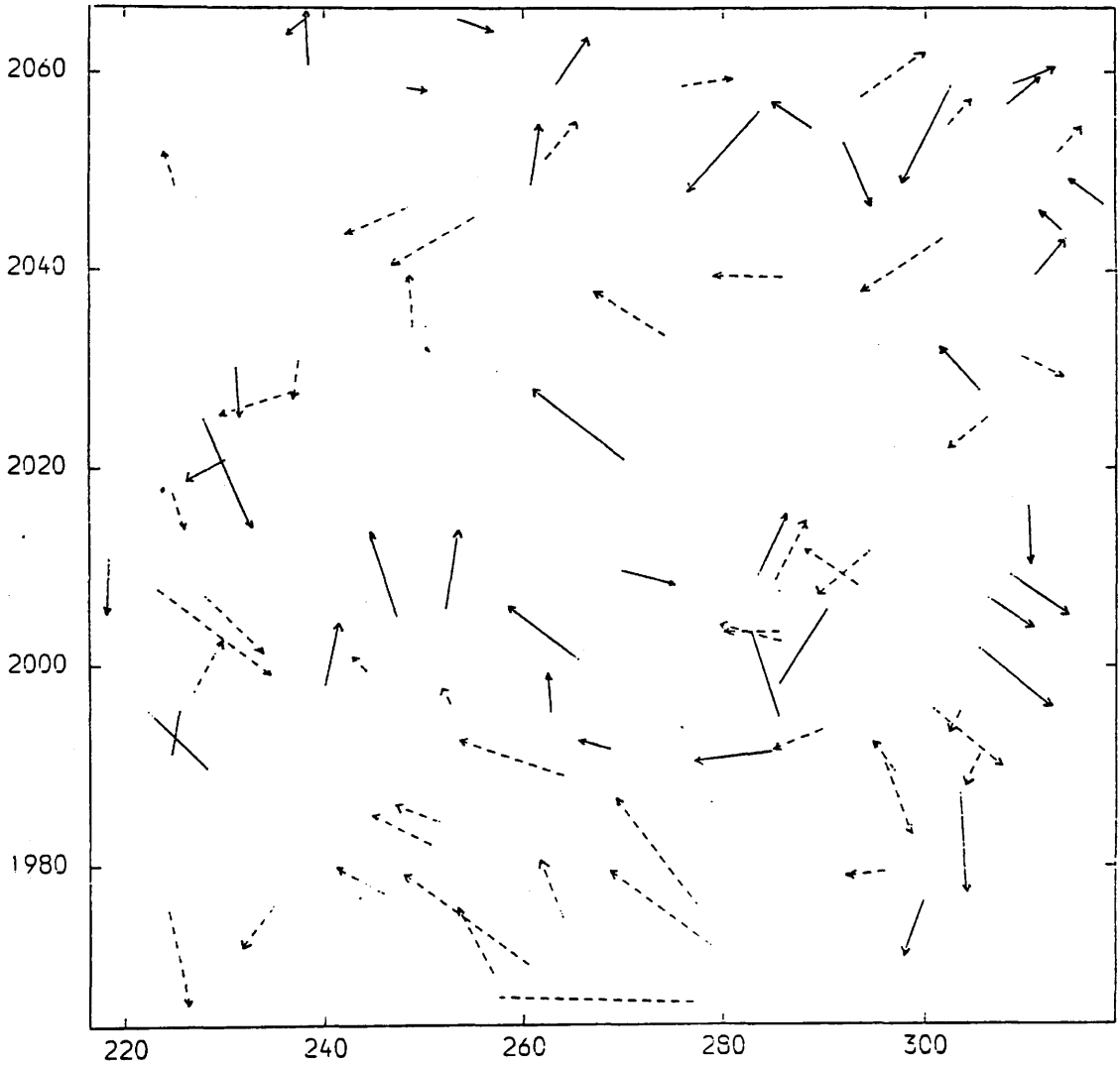


Fig. E.5 Residuals After the 4-term Polynomial Transformation of the RBV Image of the Red Sea Hills Area Using 40 Control Points.

Control Points —→

Check Points - - - →

ENLARGEMENT=X150.

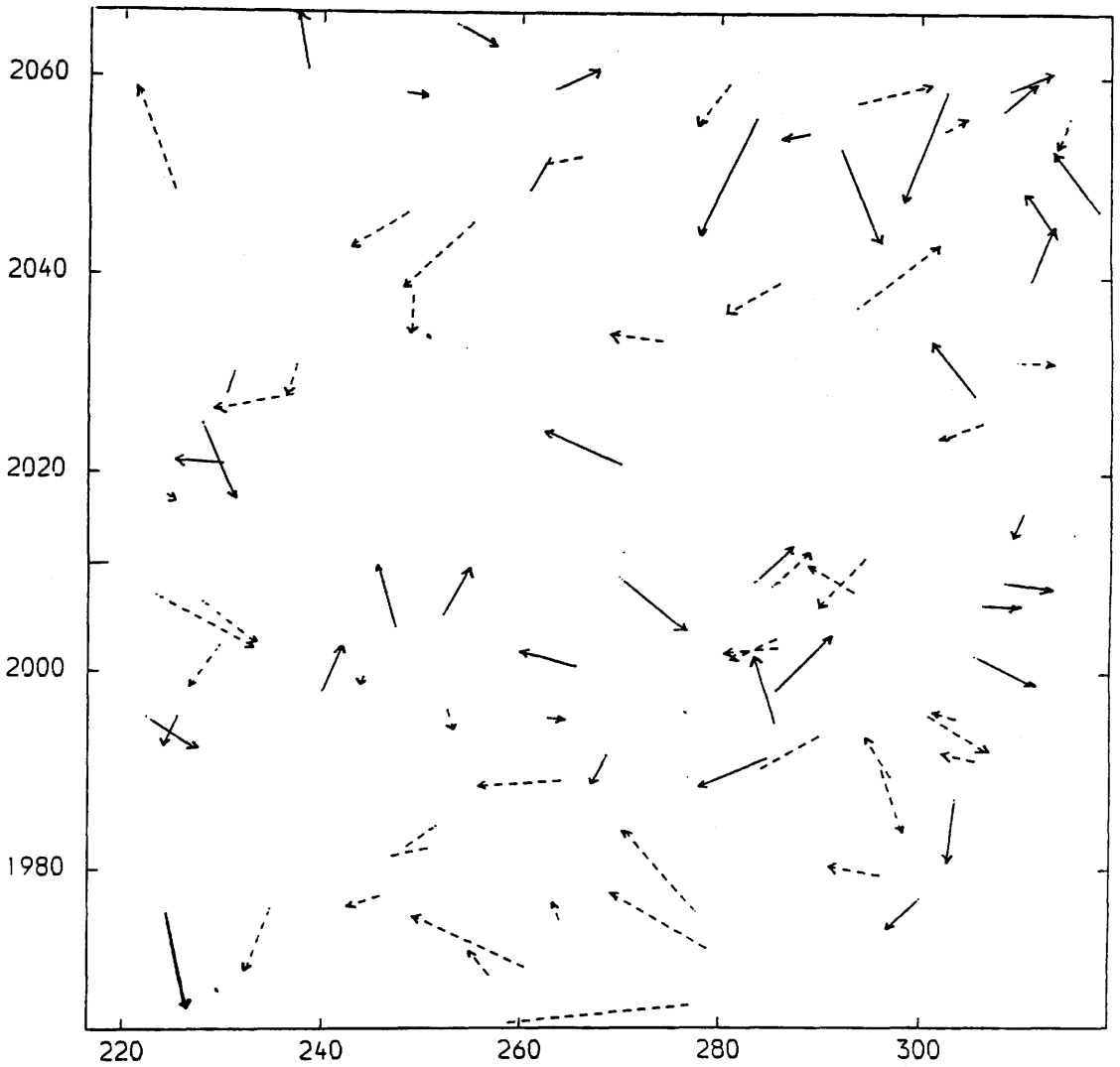


Fig. E.6 Residuals After the 5-term Polynomial Transformation of the RBV Image of the Red Sea Hills Area Using 40 Control Points.

Control Points ———>

Check Points - - - ->

ENLARGEMENT=X150.

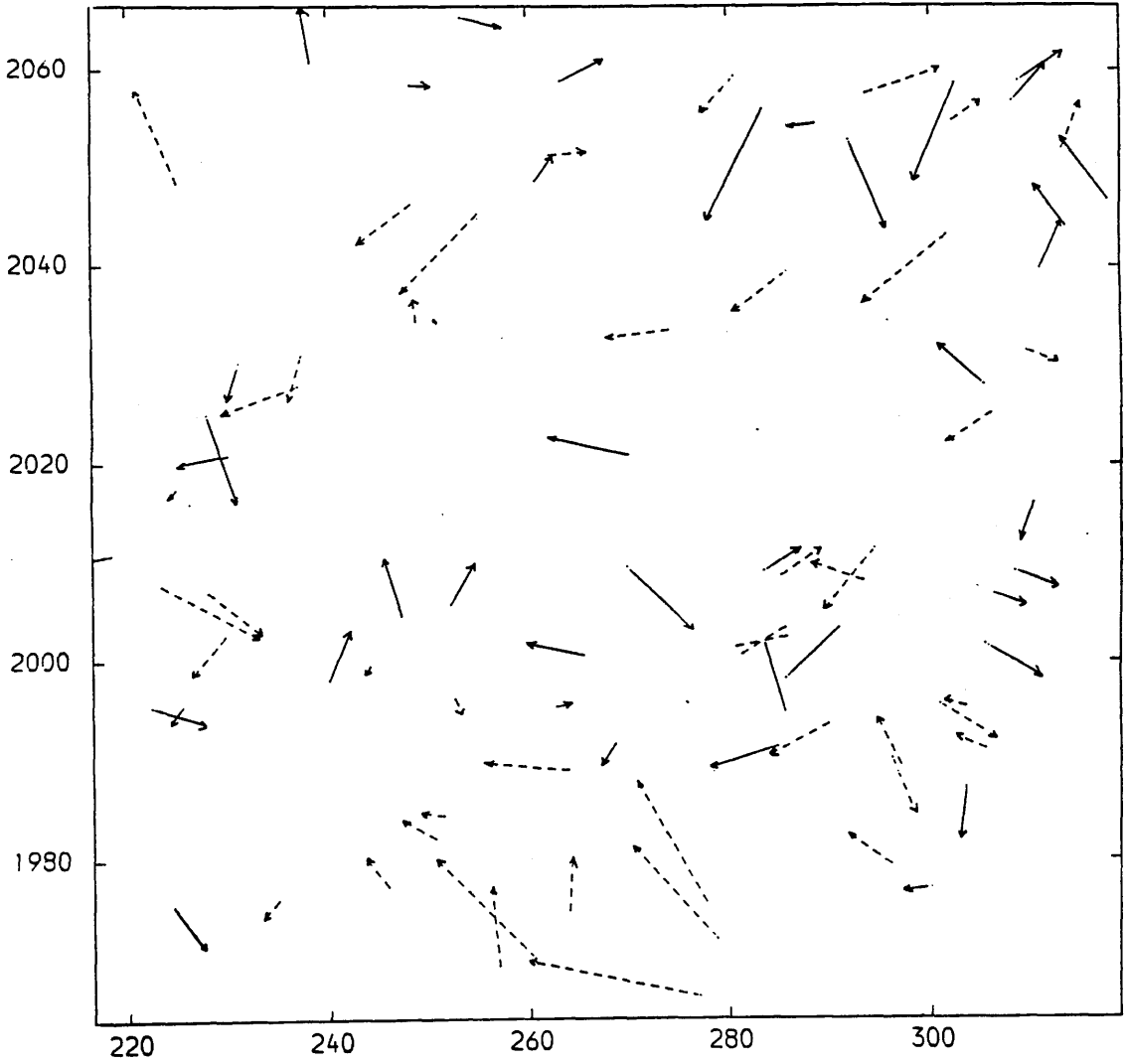


Fig. E.7 Residuals After the 6-term Polynomial Transformation of the RBV Image of the Red Sea Hills Area Using 40 Control Points.

Control Points ———>

Check Points - - - ->

ENLARGEMENT=X150.

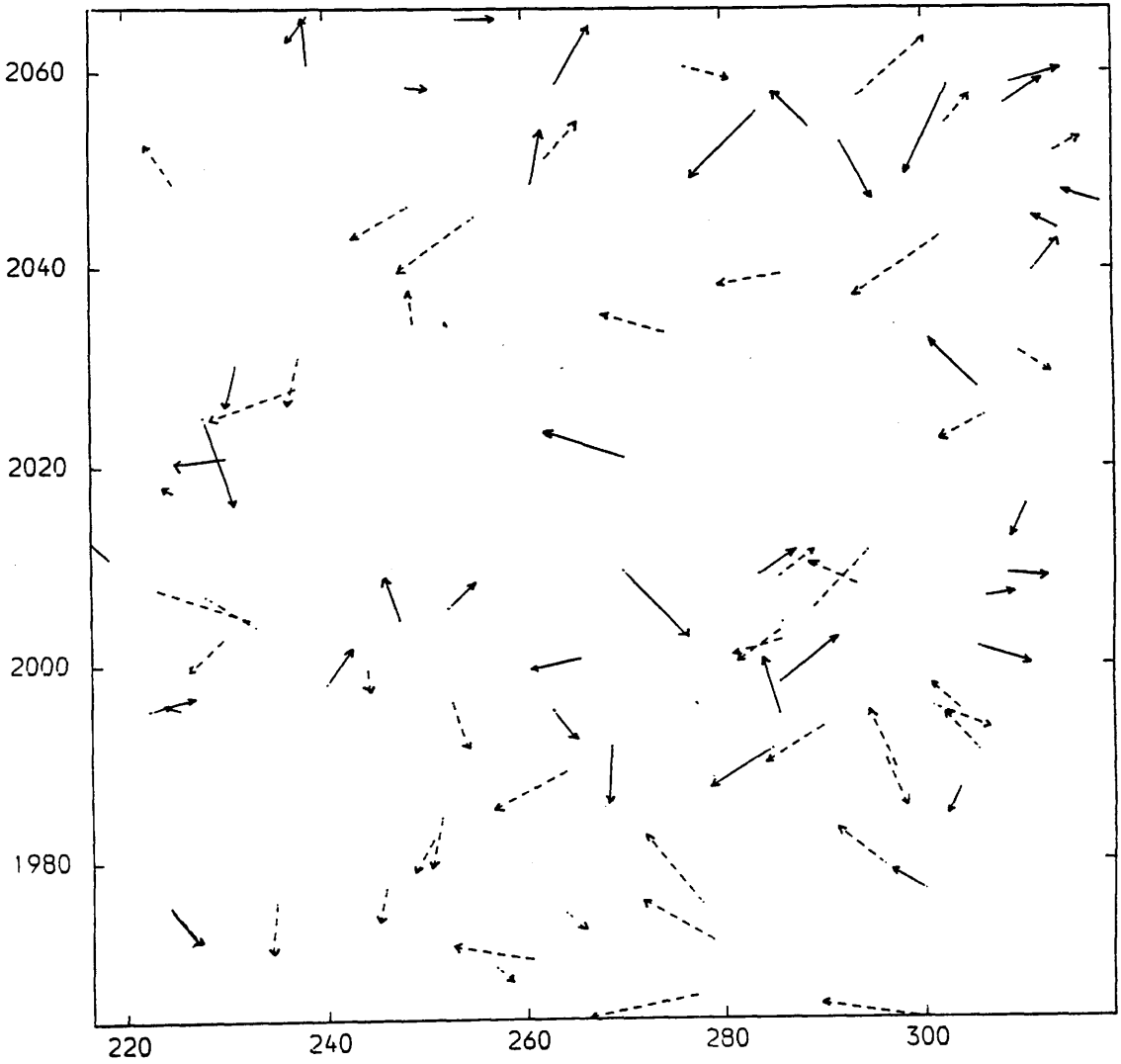


Fig. E.8 Residuals After the 7-term Polynomial Transformation of the RBV Image of the Red Sea Hills Area Using 40 Control Points.

Control Points ———→ Check Points - - - ->

ENLARGEMENT=X150.

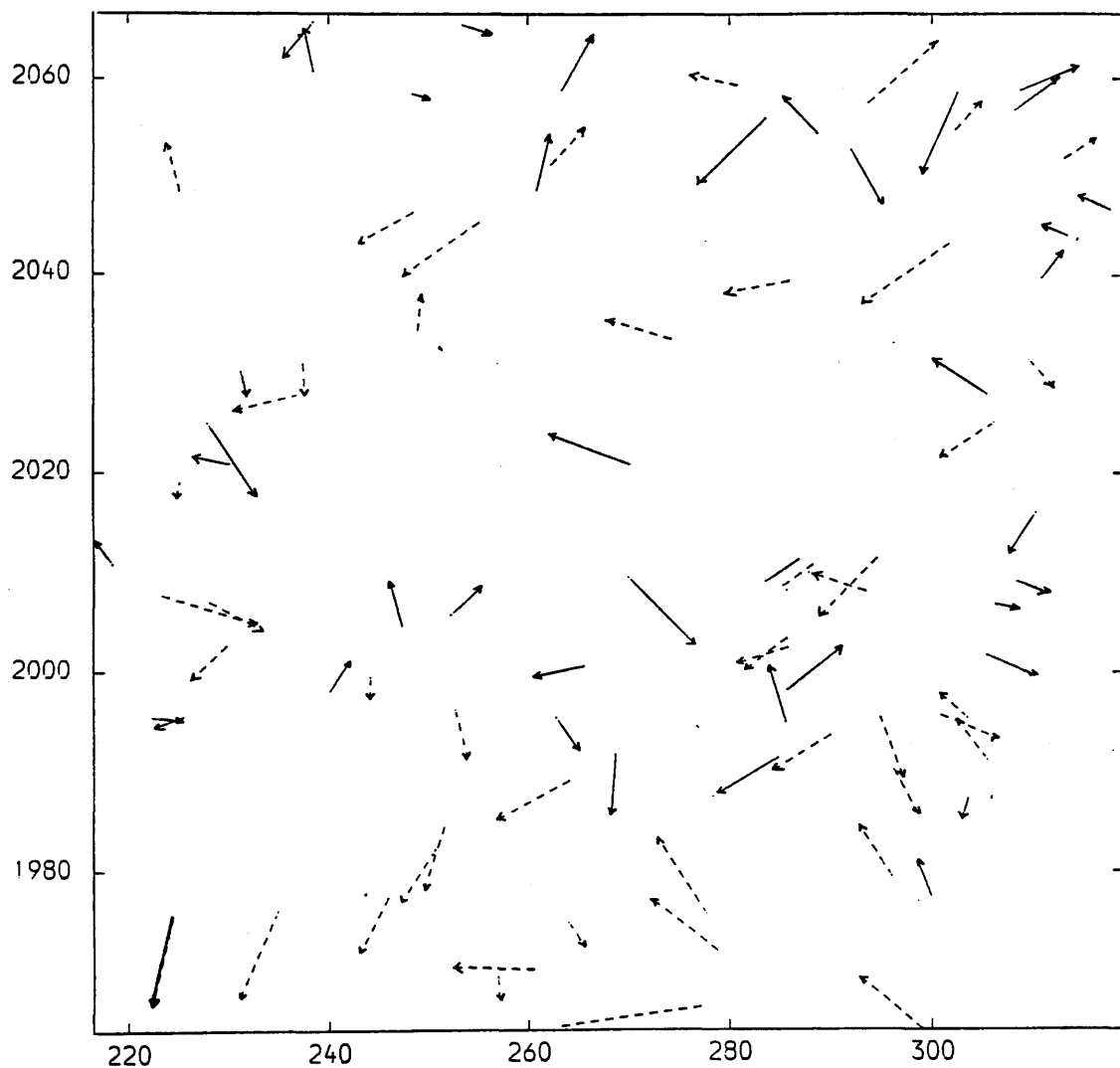


Fig. E.9 Residuals After the 8-term Polynomial Transformation of the RBV Image of the Red Sea Hills Area Using 40 Control Points.

Control Points \longrightarrow

Check Points $-----\longrightarrow$

ENLAGEMENT=X150.

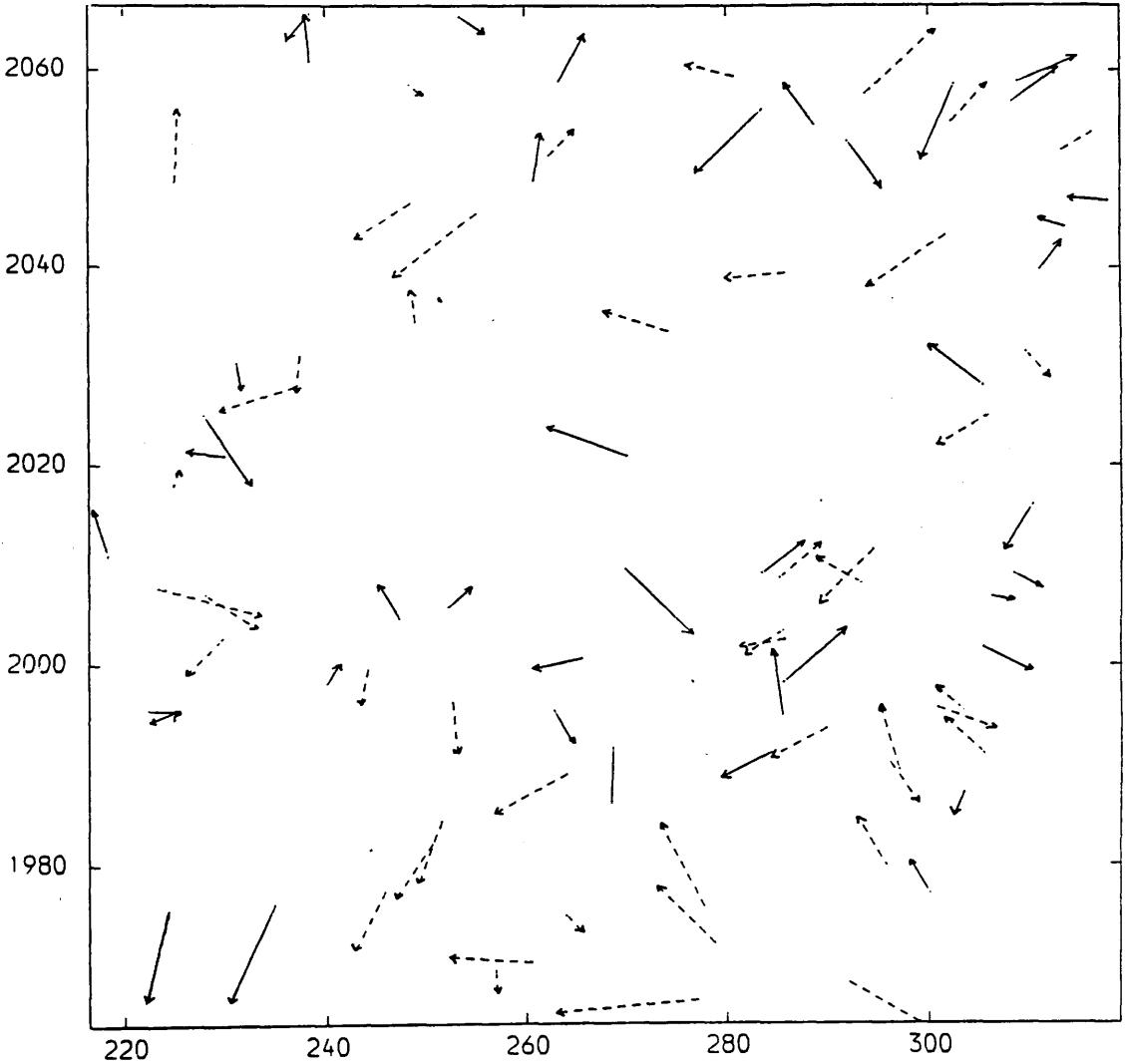


Fig.E.10 Residuals After the 9-term Polynomial Transformation of the RBV Image of the Red Sea Hills Area Using 40 Control Points.

Control Points \longrightarrow

Check Points \dashrightarrow

ENLARGEMENT=X150.

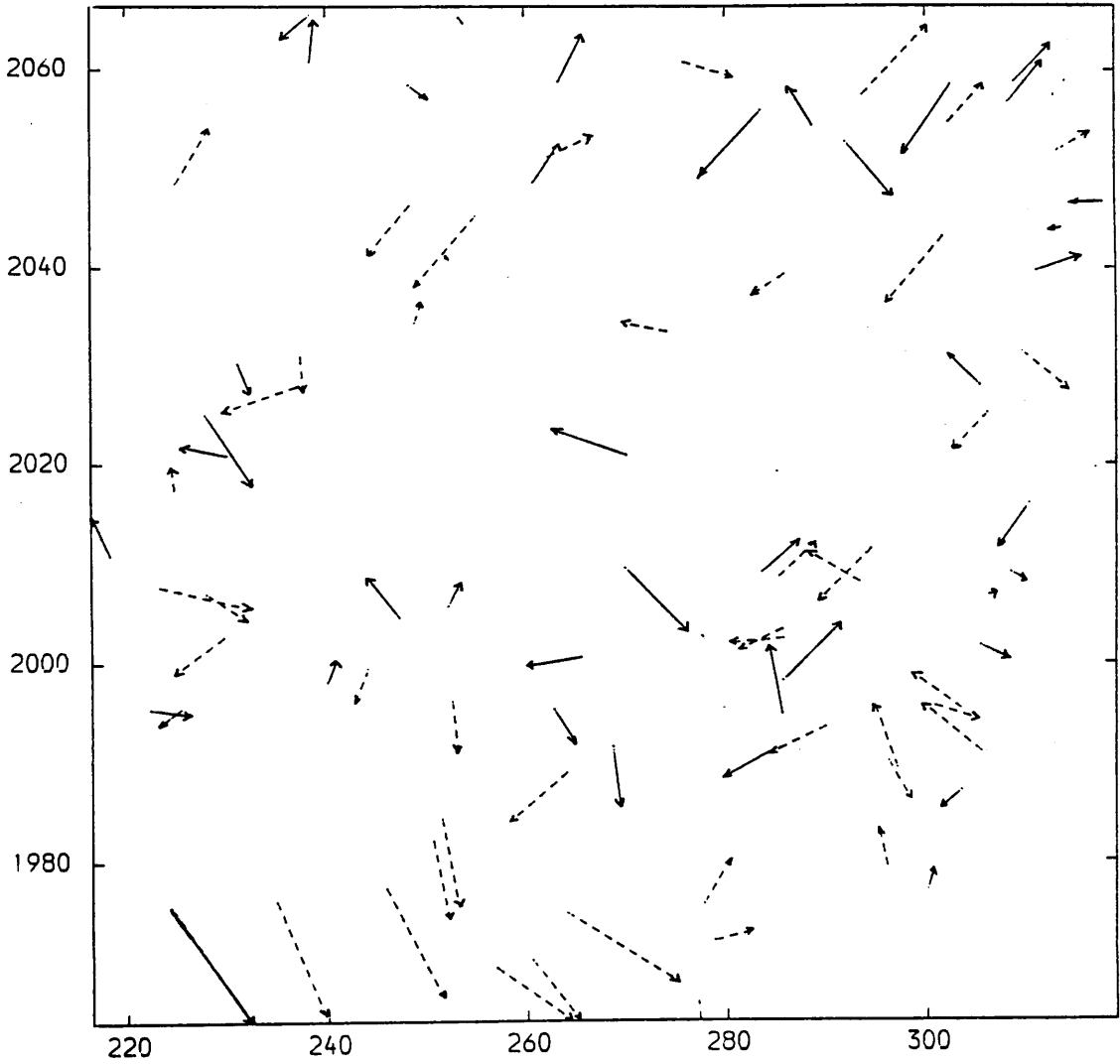


Fig.E.11 Residuals After the 10-term Polynomial Transformation of the RBV Image of the Red Sea Hills Area Using 40 Control Points.

Control Points ———→

Check Points - - - - -→

ENLARGEMENT=X150.

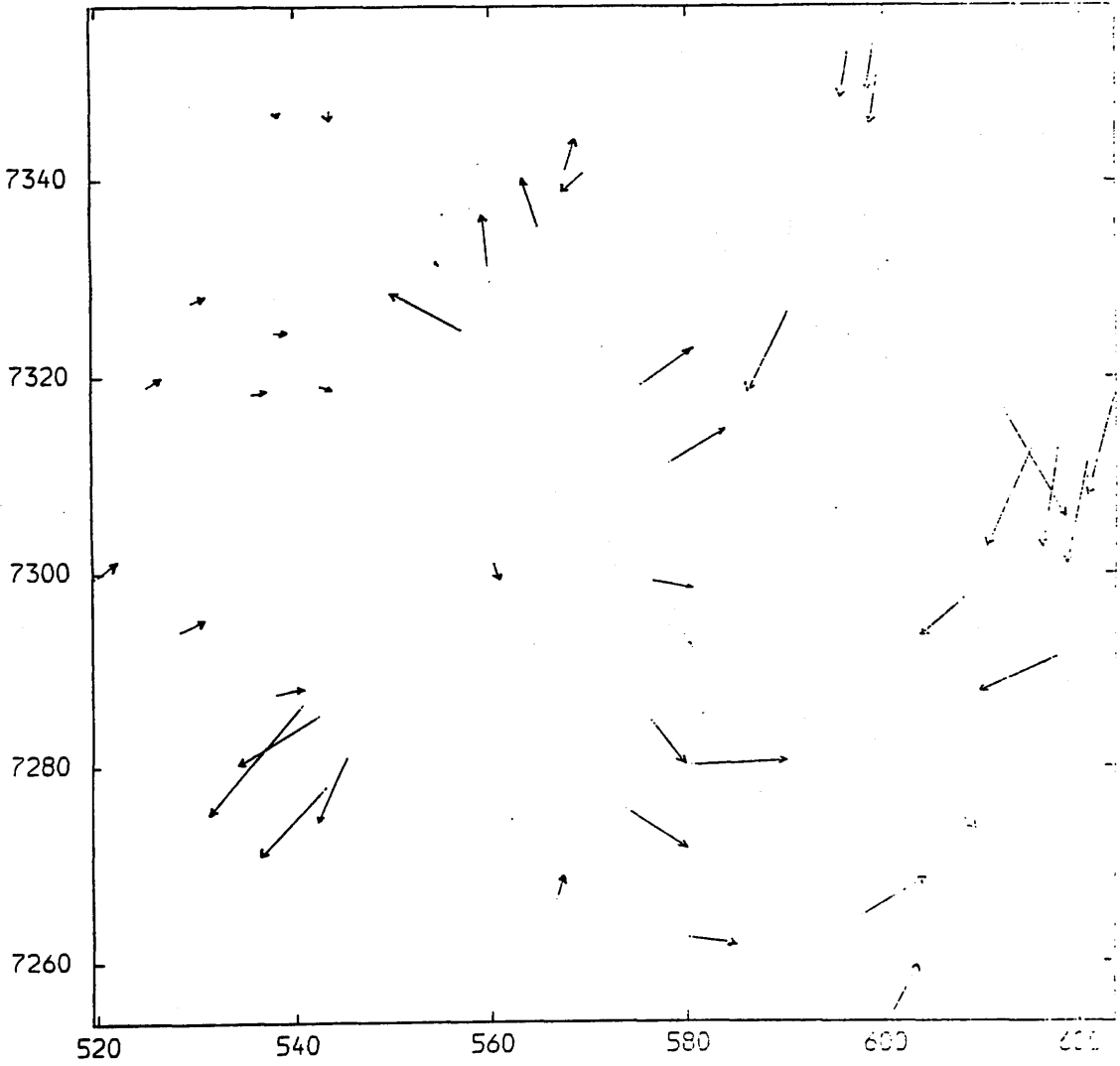


Fig. E.12 Residuals After the Linear Conformal Transformation of the RBV Image 1 of the Alaskan Area Using All Points as Control Points.

ENLARGEMENT=X150.

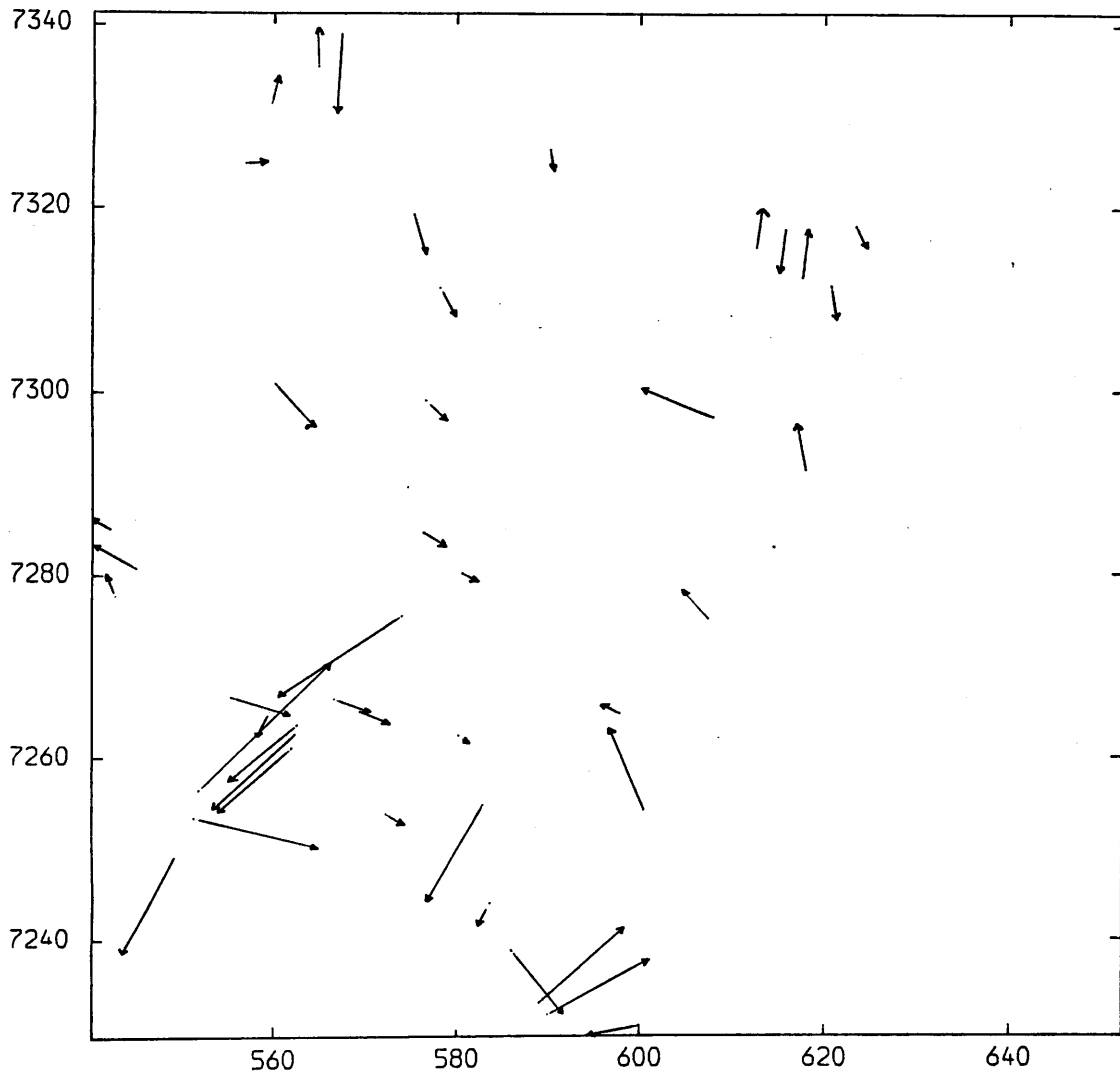


Fig. E.13 Residuals After the Linear Conformal Transformation of the RBV Image 2 of the Alaskan Area Using All Points as Control Points.

ENLAGEMENT=X150.

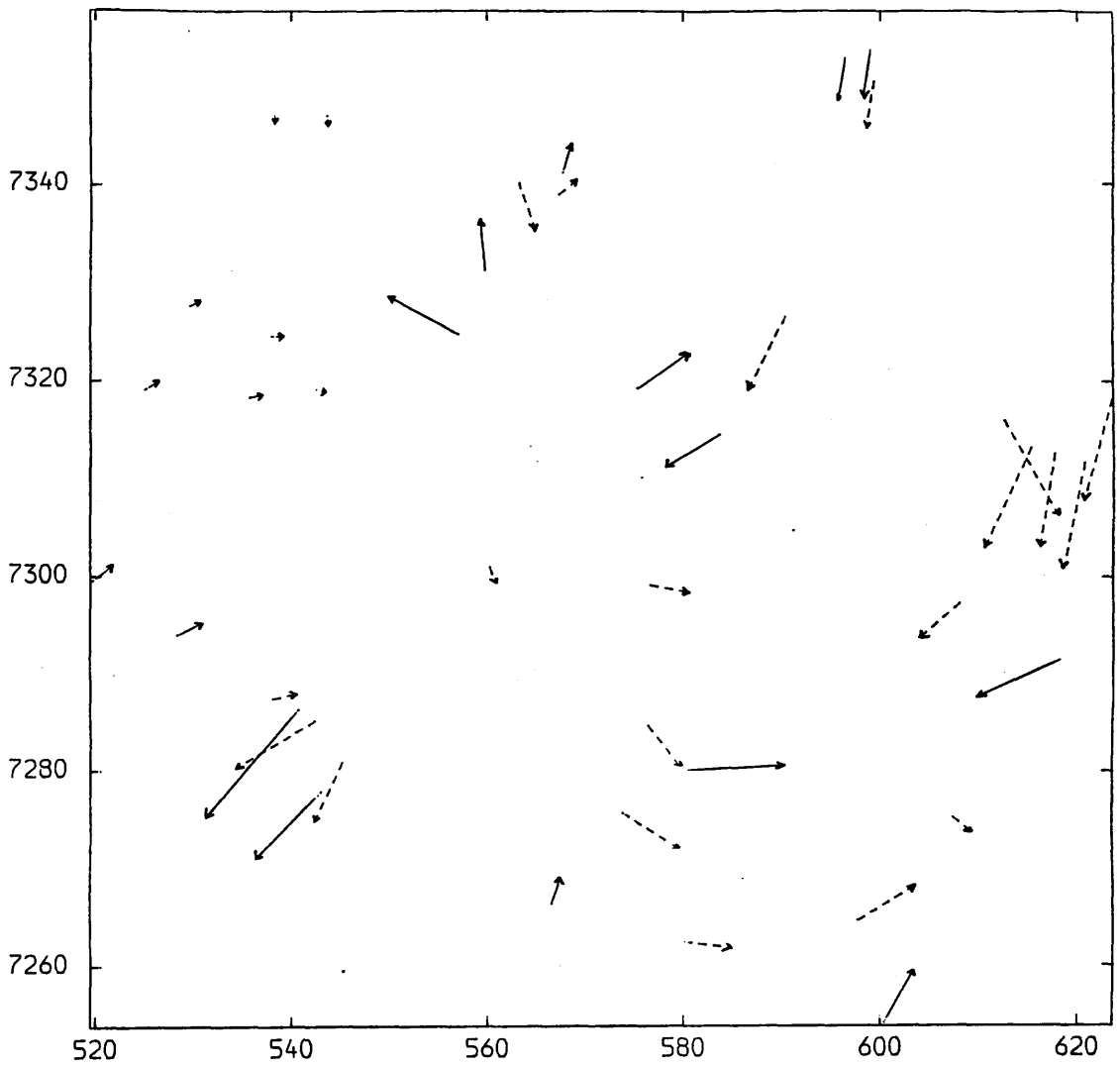


Fig. E.14 Residuals After the Linear Conformal Transformation of the RBV Image 1 of the Alaskan Area Using 20 Control Points.

Control Points —→

Check Points - - - ->

ENLARGEMENT=X150.

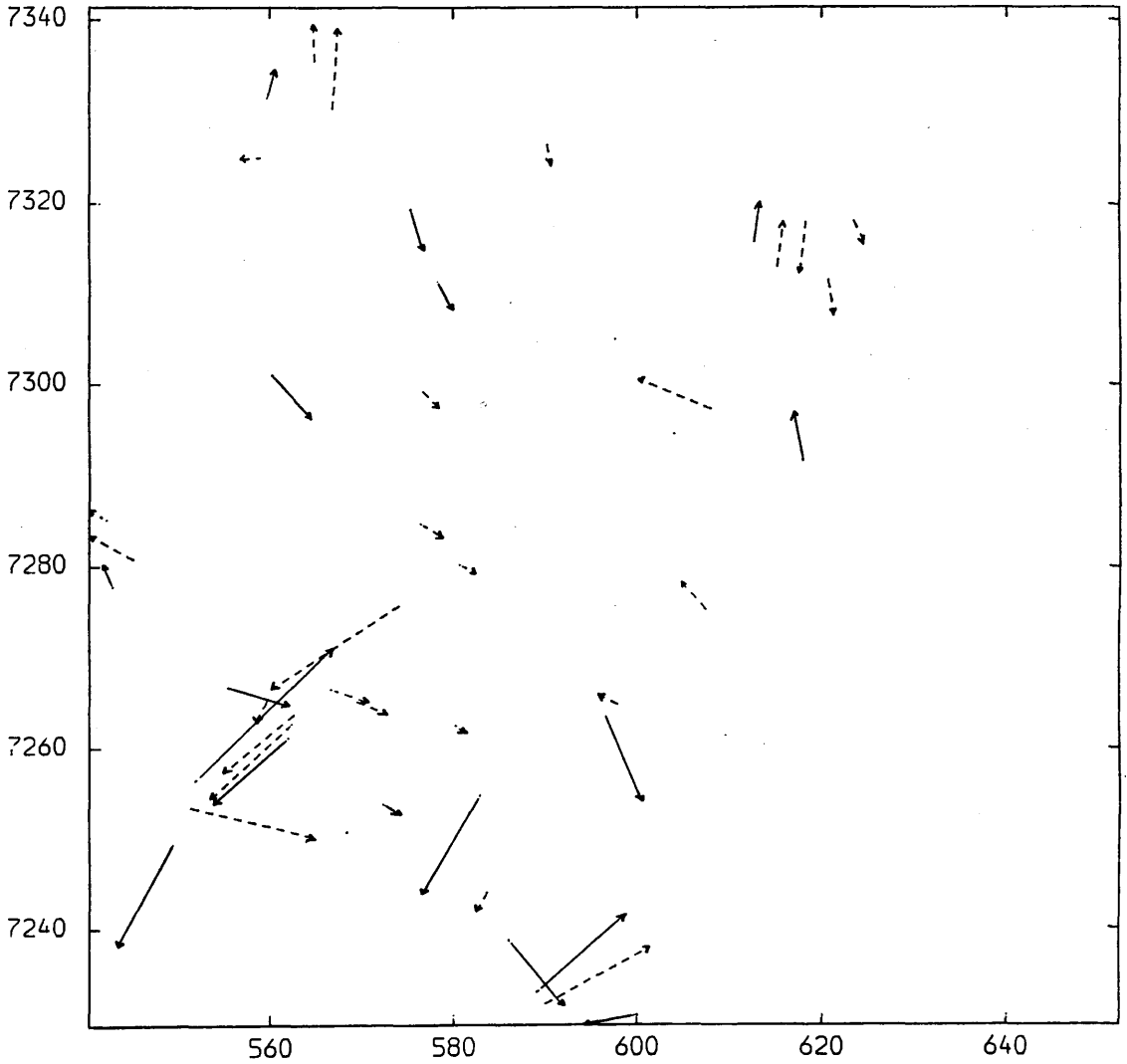


Fig. E.15 Residuals After the Linear Conformal Transformation of the RBV Image 2 of the Alaskan Area Using 20 Control Points.

Control Points —→

Check Points - - - →

ENLARGEMENT=X150.

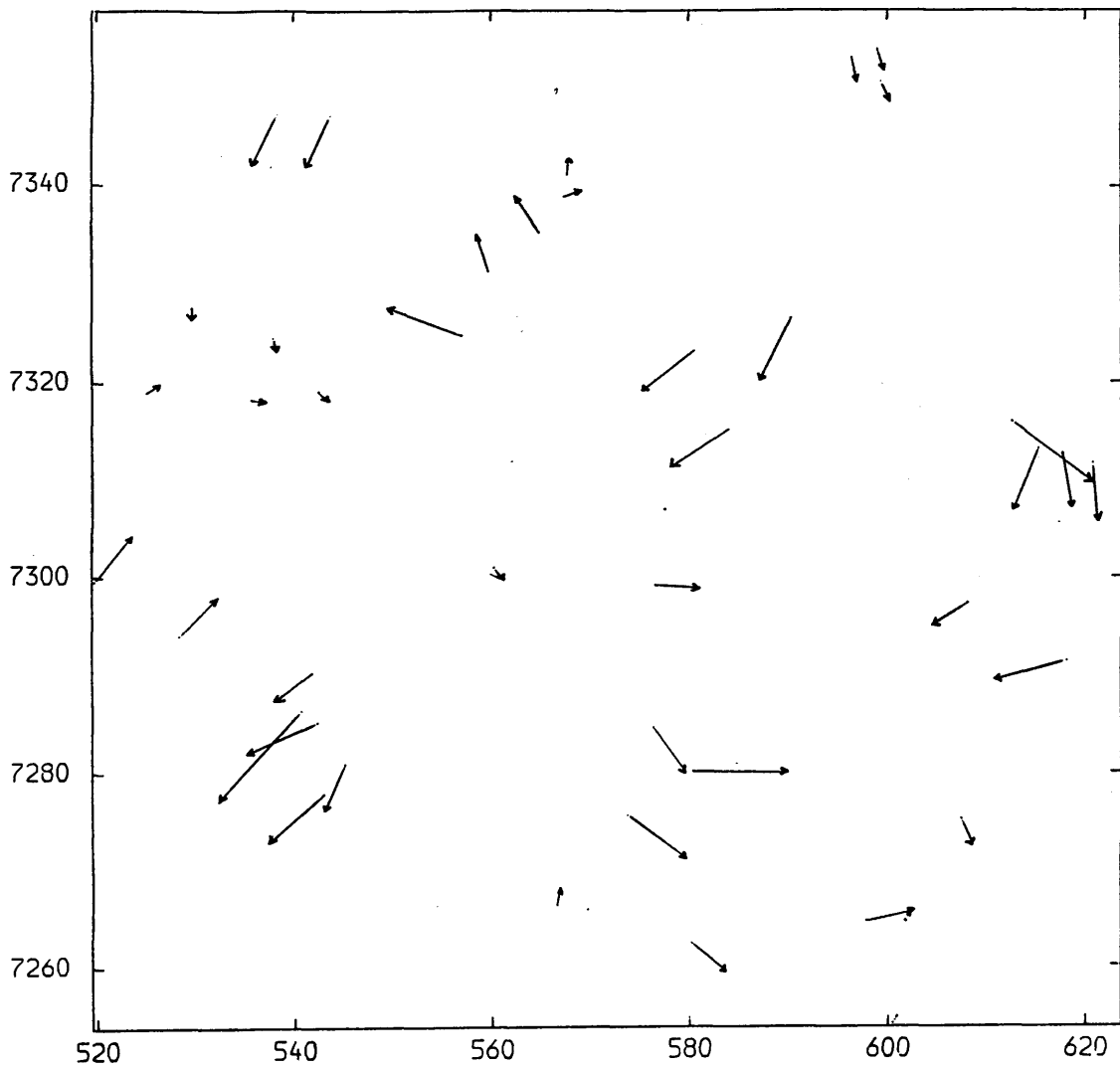


Fig. E.16 Residuals After the Affine Transformation of the RBV Image 1 of the Alaskan Area Using All Points as Control Points.

ENLARGEMENT=X150.

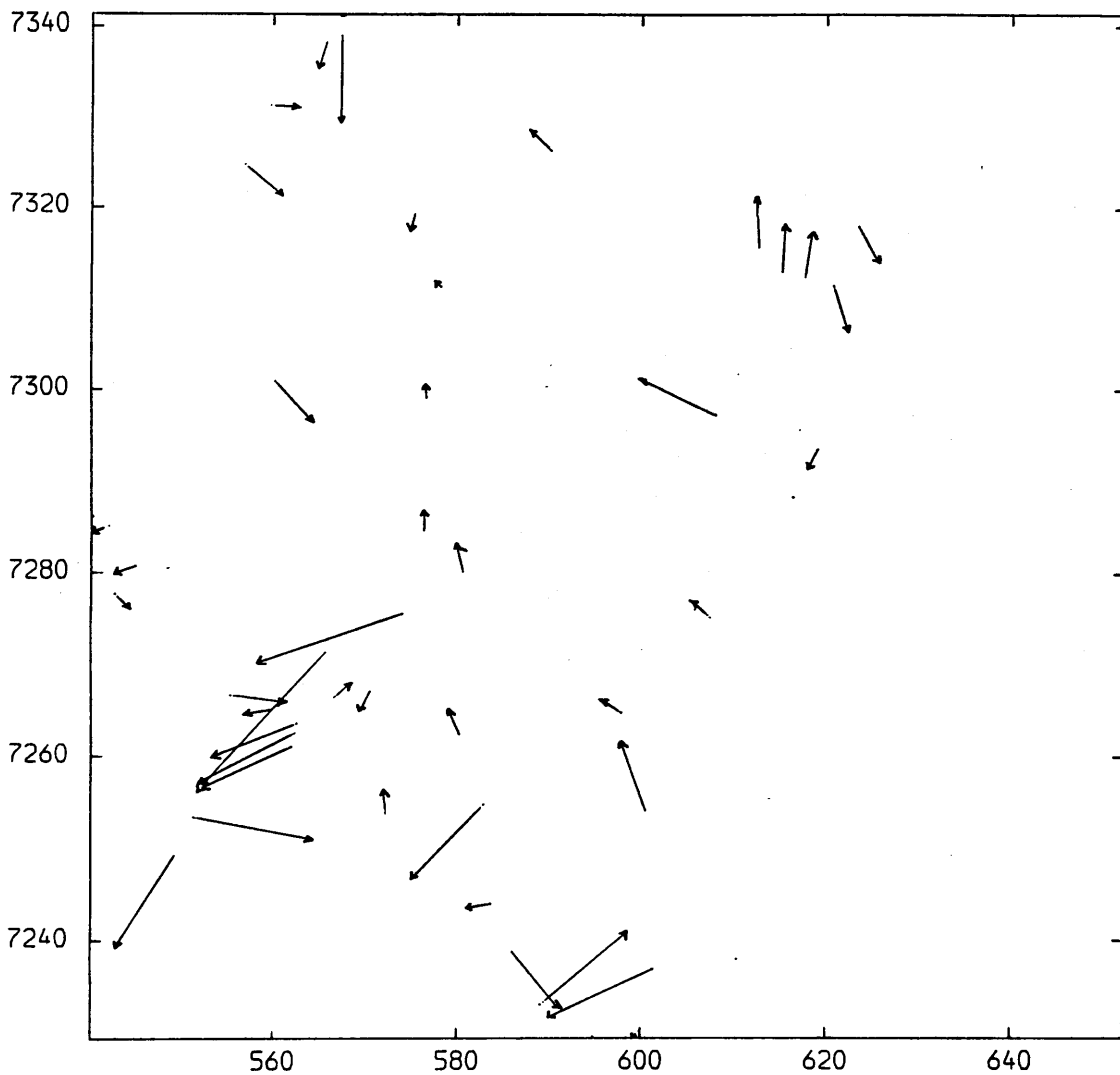


Fig. E.17 Residuals After the Affine Transformation of the RBV Image 2 of the Alaskan Area Using All Points as Control Points.

ENLARGEMENT=X150.

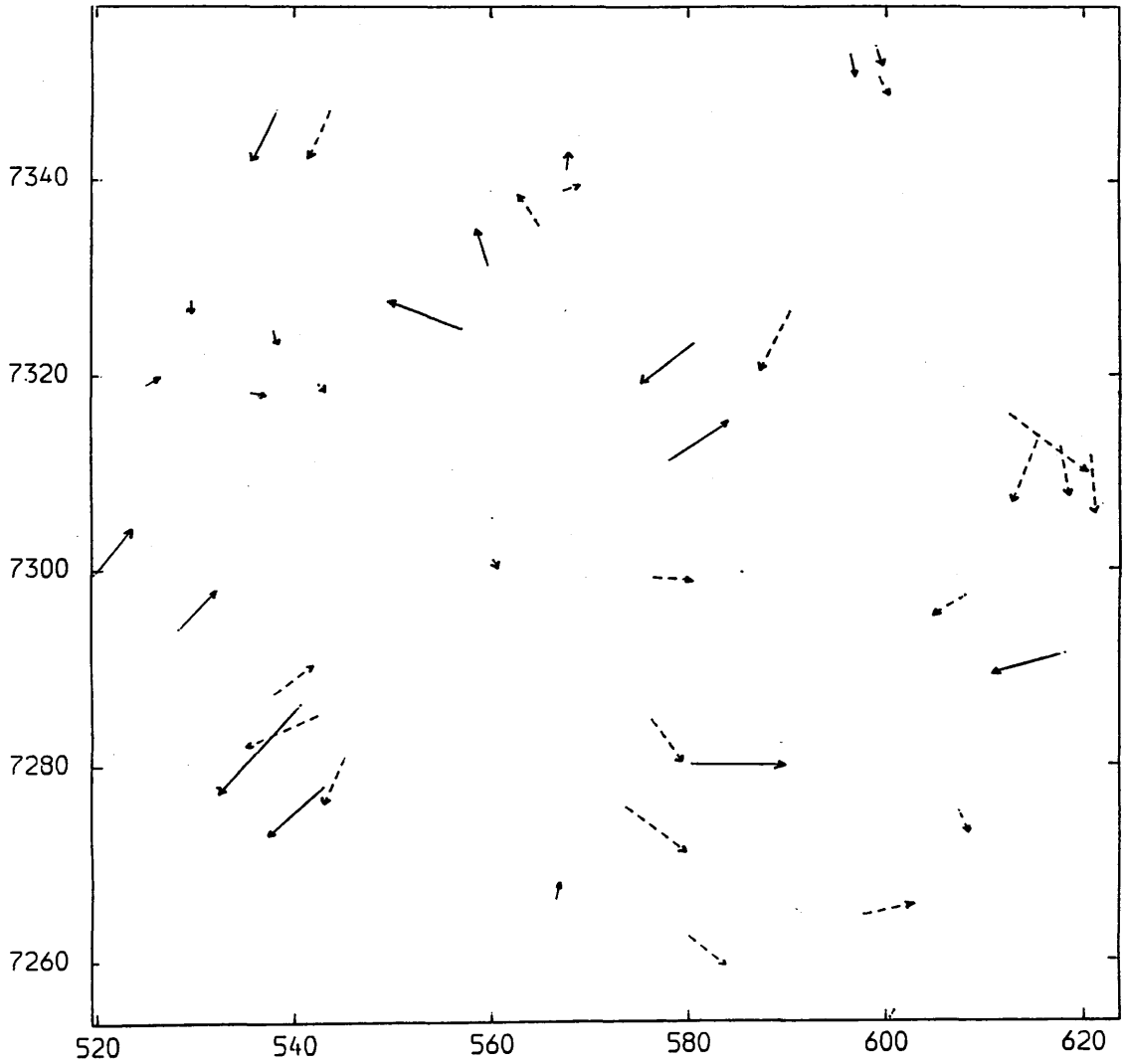


Fig. E.18 Residuals After the Affine Transformation of the RBV Image 1 of the Alaskan Area Using 20 Control Points.

Control Points ———>

Check Points - - - ->

ENLARGEMENT=X150.

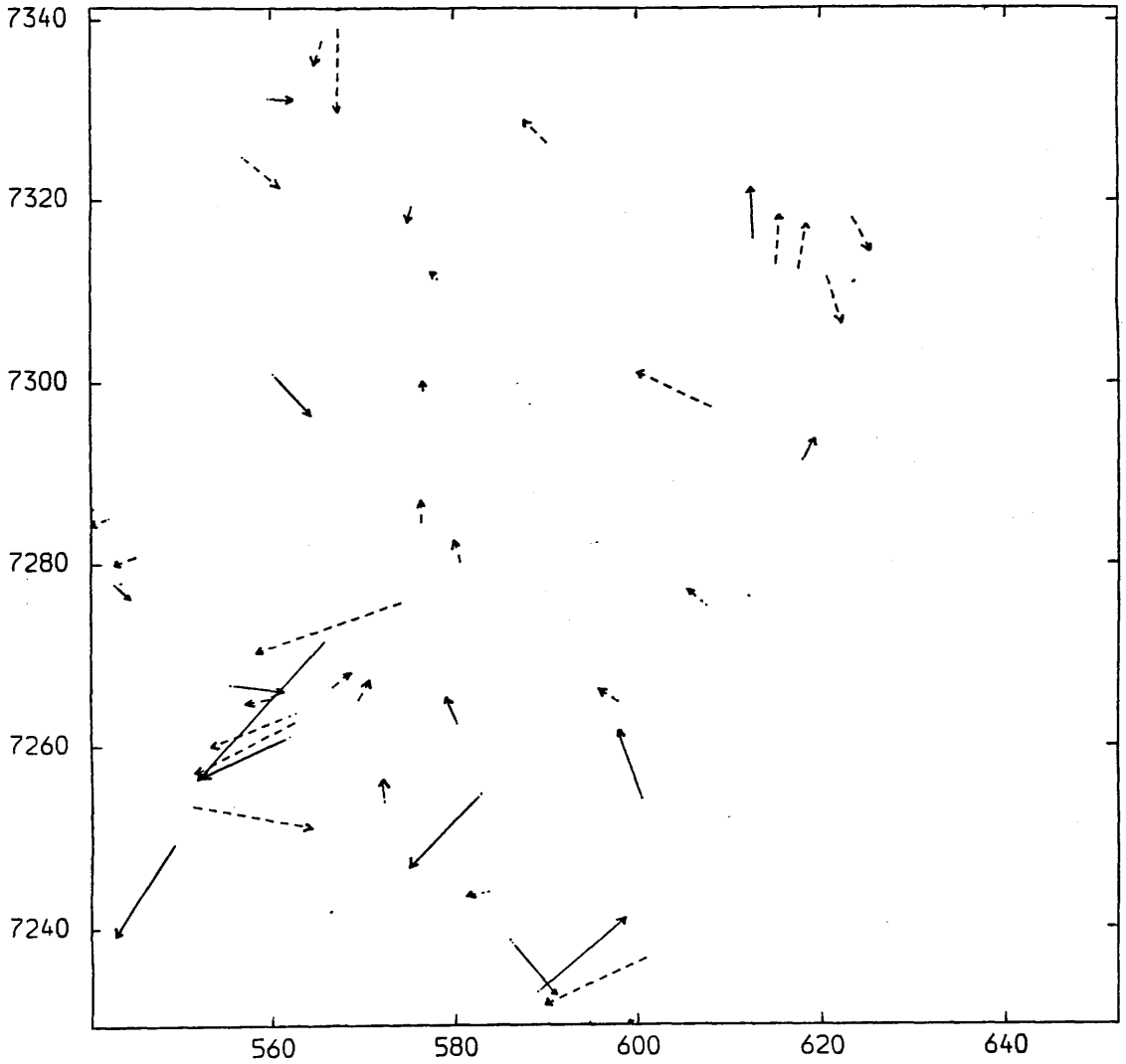


Fig. E.19 Residuals After the Affine Transformation of the RBV Image 2 of the Alaskan Area Using 20 Control Points.

Control Points —

Check Points - - - ->

APPENDIX F

VECTOR PLOTS OF THE RESIDUALS FOR THE MC AND LFC PHOTOGRAPHS

ENLARGEMENT= $\times 150$.

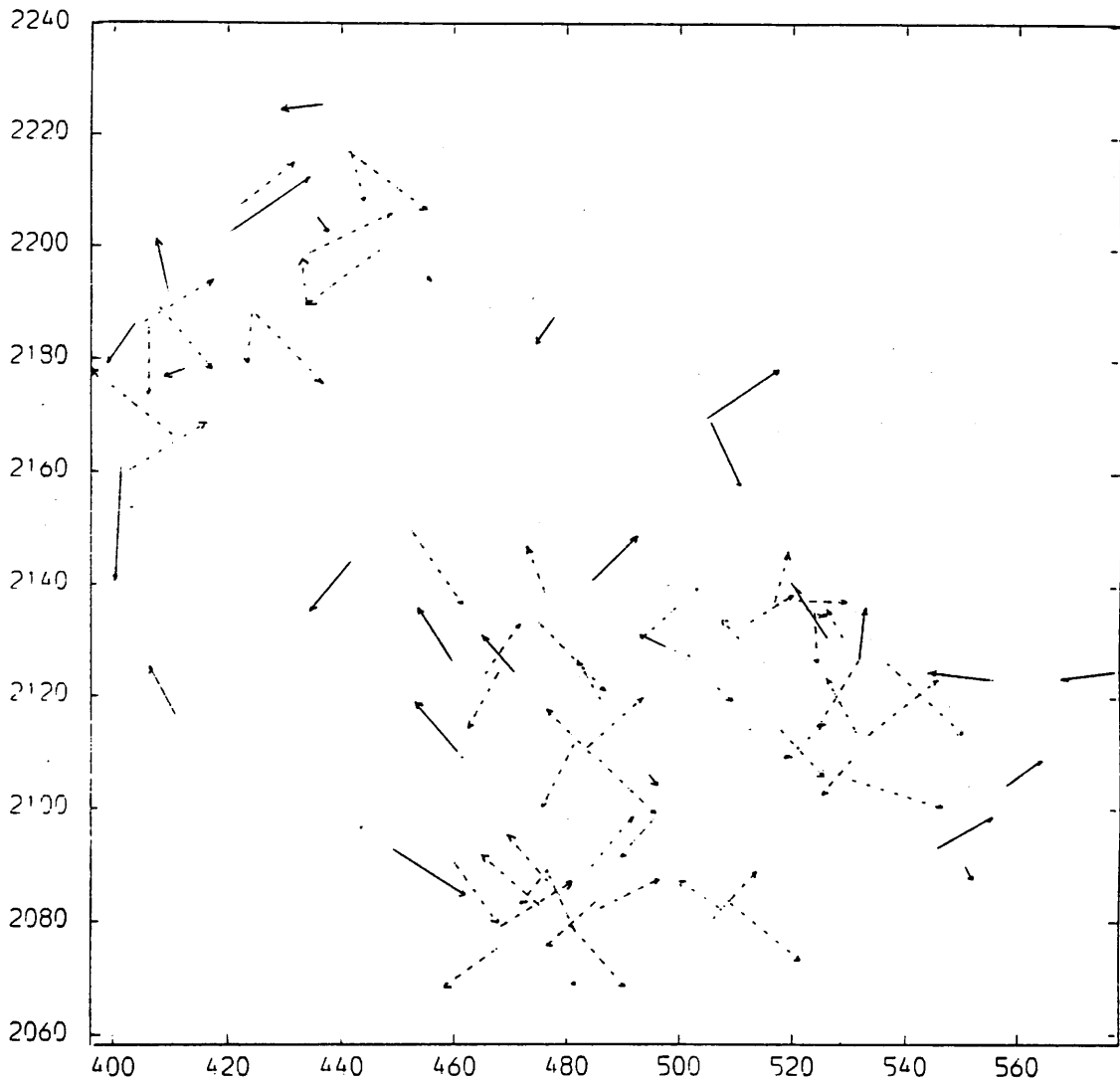


Fig. F.1a Residuals in Planimetry After the Space Resection/Intersection of MC Model 1 (UTM).

Control Points. \longrightarrow Check Points. $\text{-----}\longrightarrow$

ENLARGEMENT=X450.

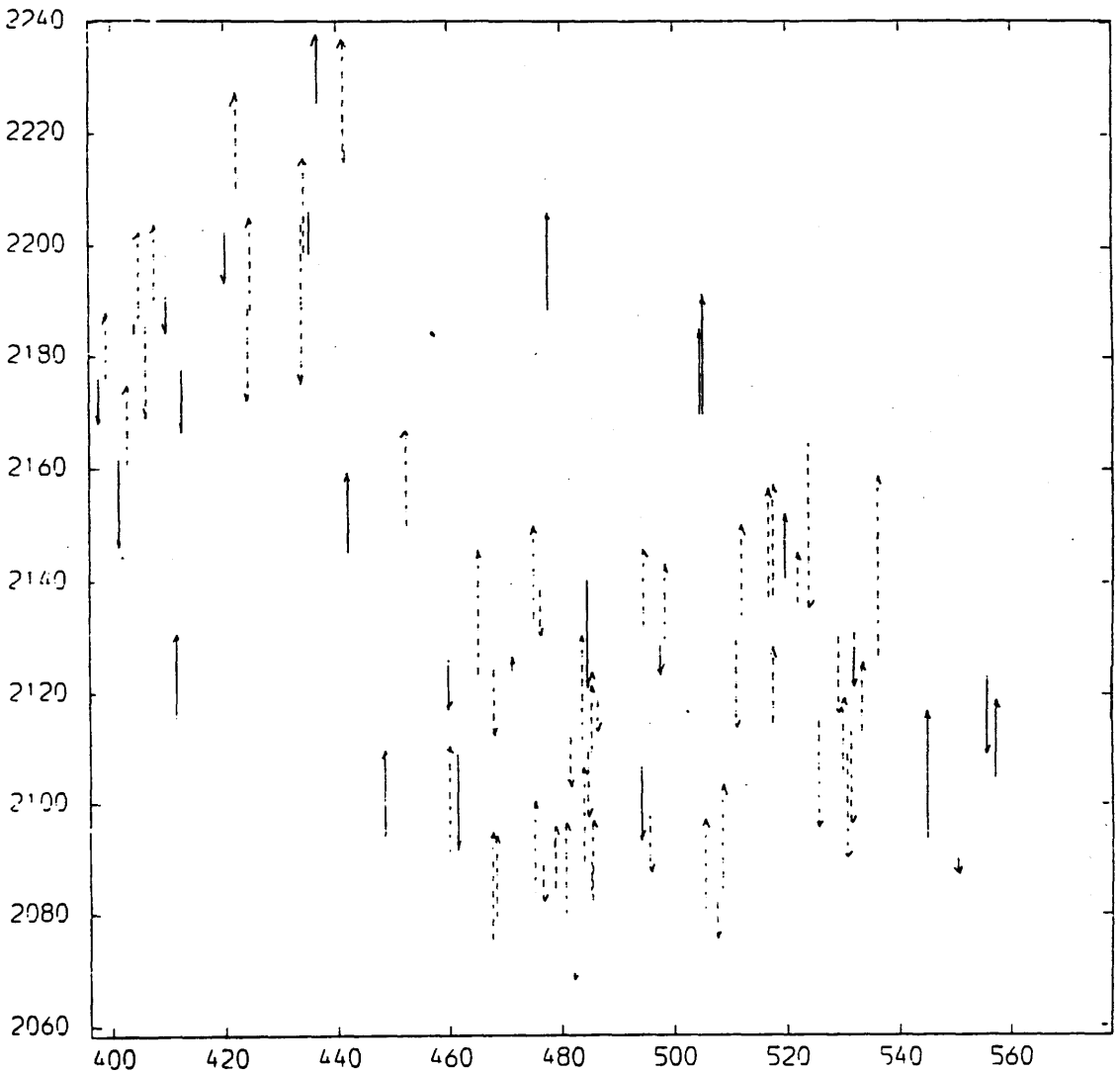


Fig. F.1b Residuals in Height After the Space Resection/Intersection of MC Model 1 (UTM).

Control Points. —>

Check Points. - - ->

ENLARGEMENT=X450.

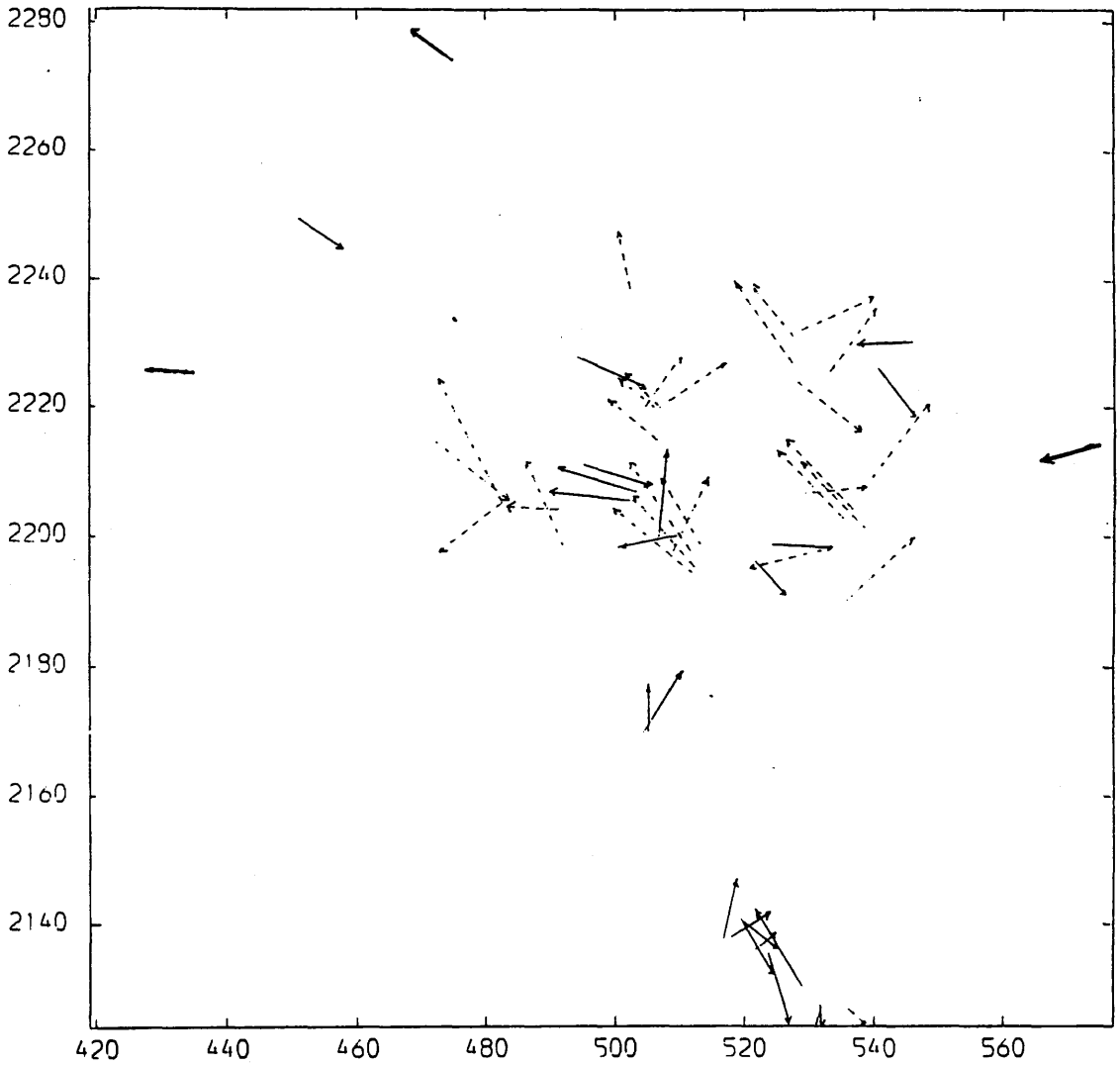


Fig. F.2a Residuals in Planimetry After the Space Resection/Intersection of MC Model 2 (UTM).

Control Points. —→

Check Points. ----→

ENLARGEMENT=X450.

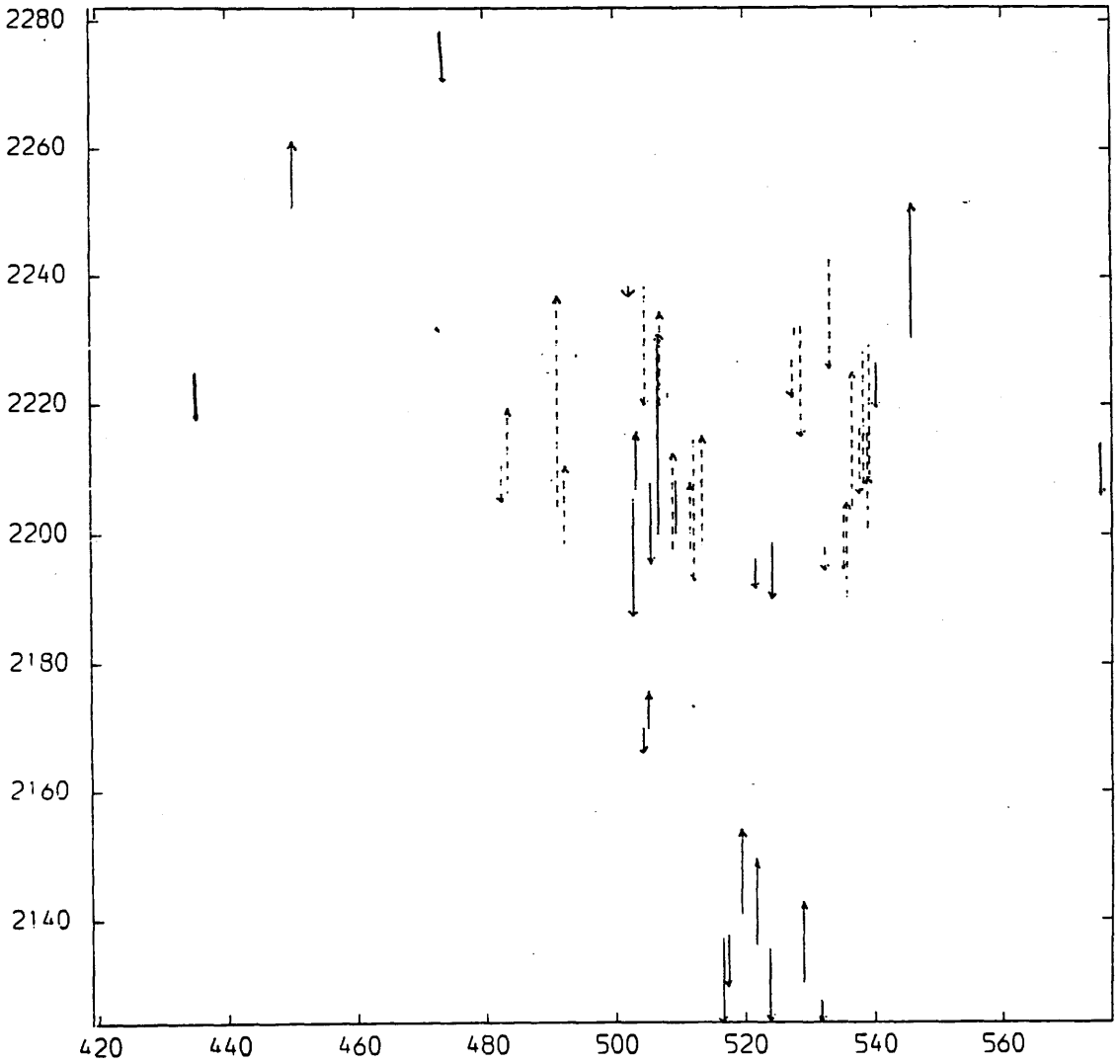


Fig. F.2b Residuals in Height After the Space Resection/Intersection of MC Model 2 (UTM).

Control Points. —→

Check Points. ----→

ENLARGEMENT=X450.

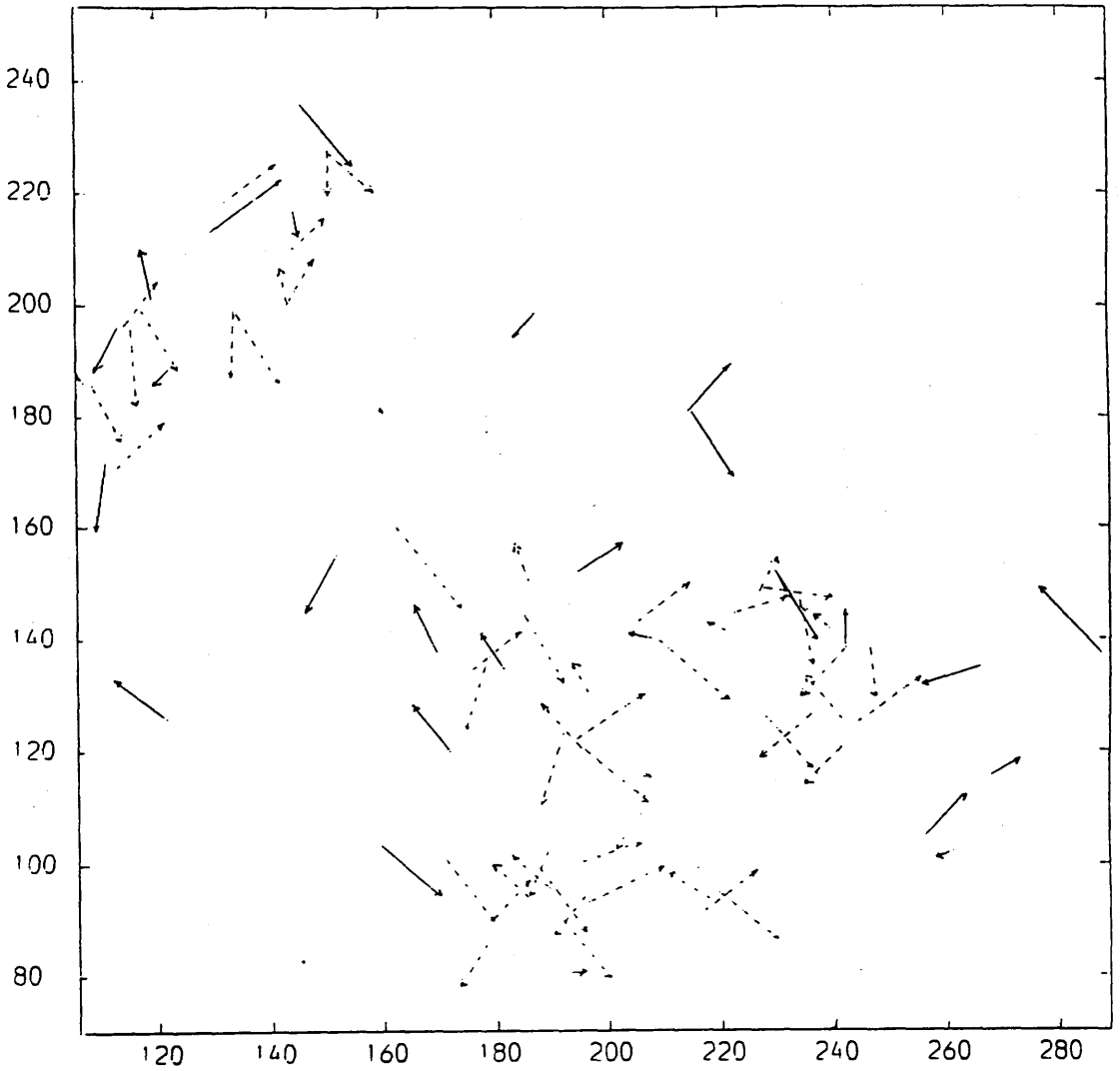


Fig. F.3a Residuals in Planimetry After the Space Resection/Intersection of MC Model 1 (TAN).

Control Points. —→

Check Points. - - - ->

ENLARGEMENT=X450.

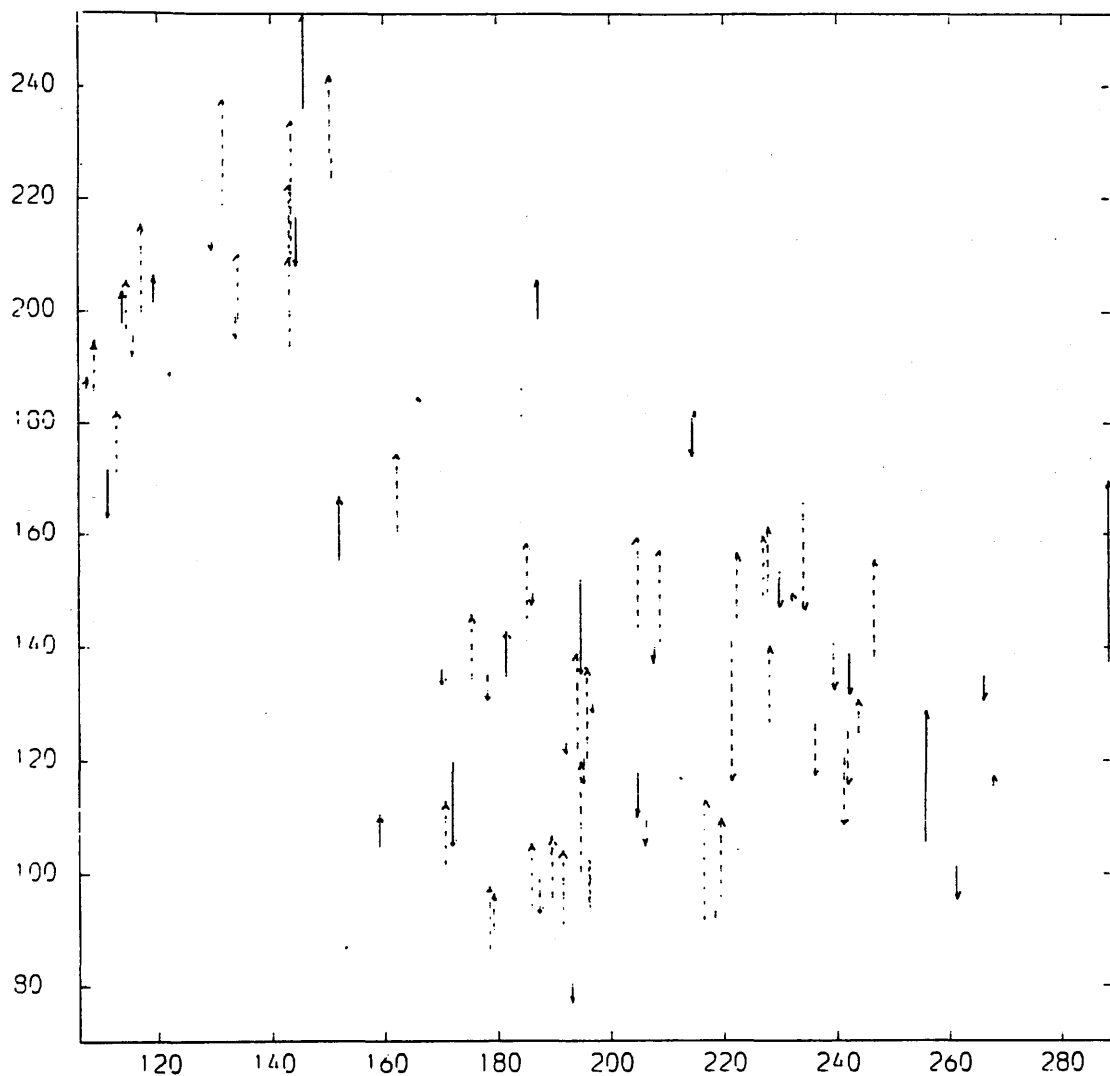


Fig. F.3b Residuals in Height After the Space Resection/Intersection of MC Model 1 (TAN).

Control Points. —→

Check Points. - - - ->

ENLARGEMENT=X450.

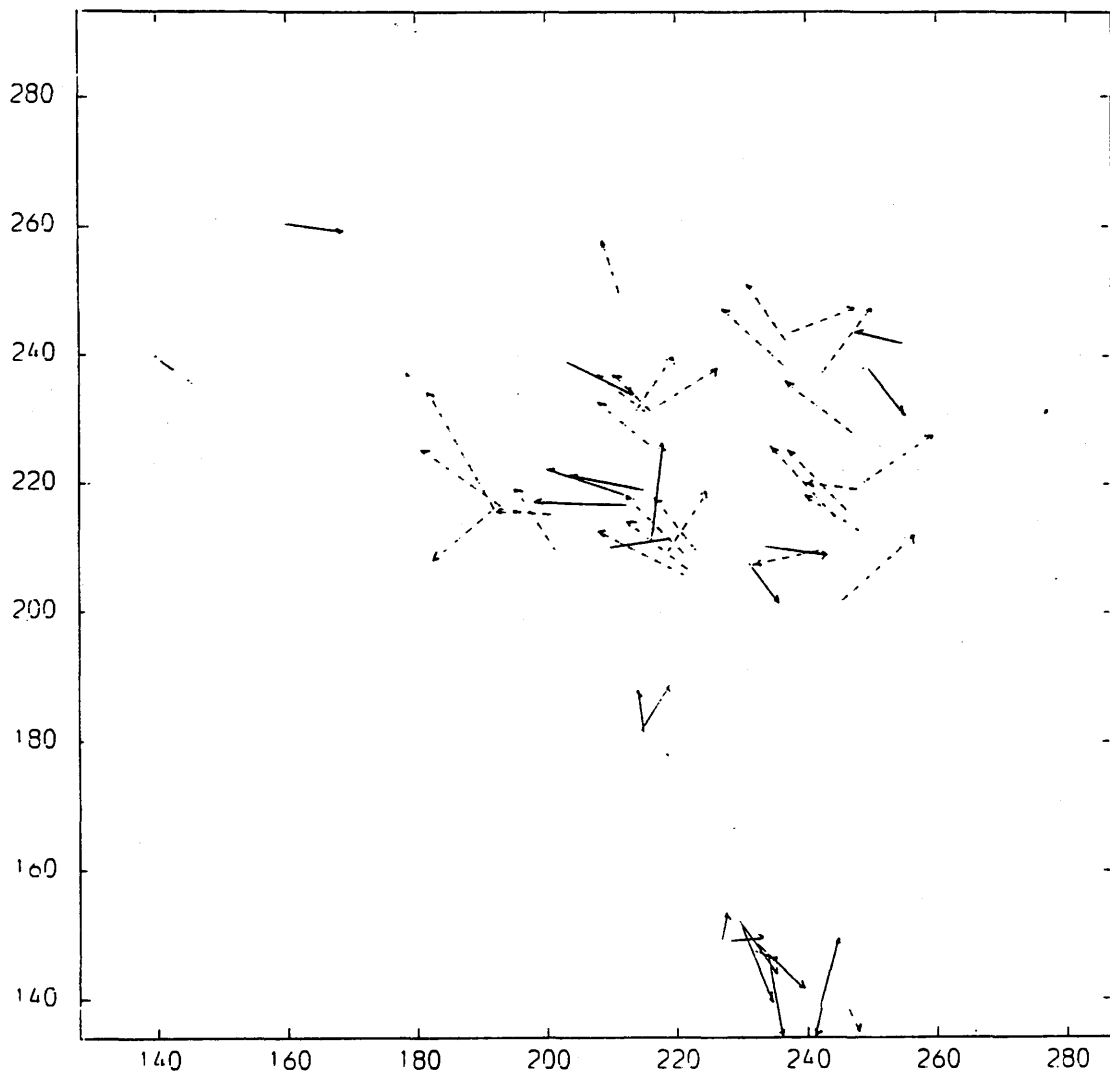


Fig. F.4a Residuals in Planimetry After the Space Resection/Intersection of MC Model 2 (TAN).

Control Points. —→

Check Points. ----→

ENLARGEMENT=X450.

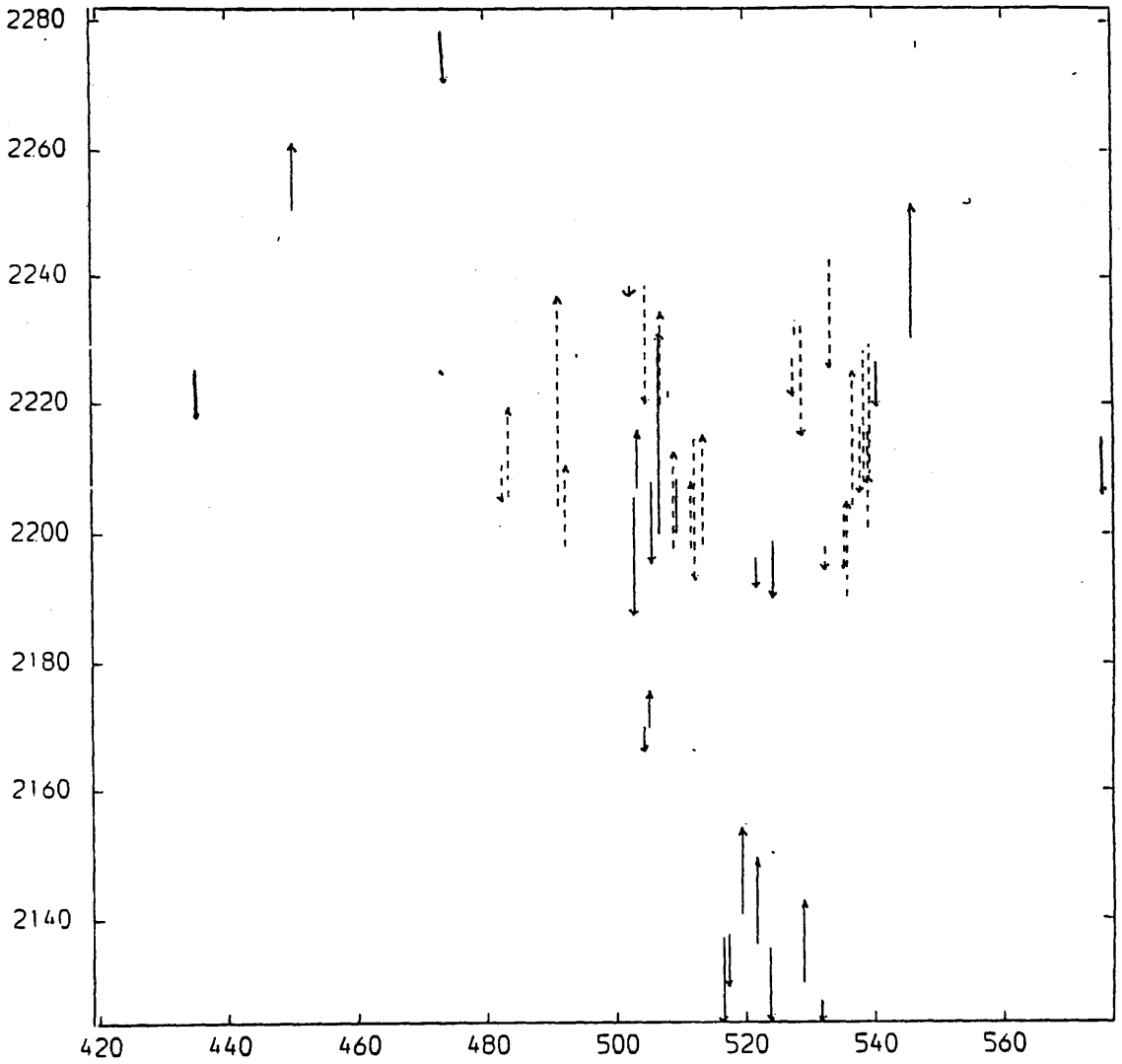


Fig. F.4b Residuals in Height After the Space Resection/Intersection of MC Model 2 (TAN).

Control Points. —→ Check Points. ----→

ENLARGEMENT = X450.

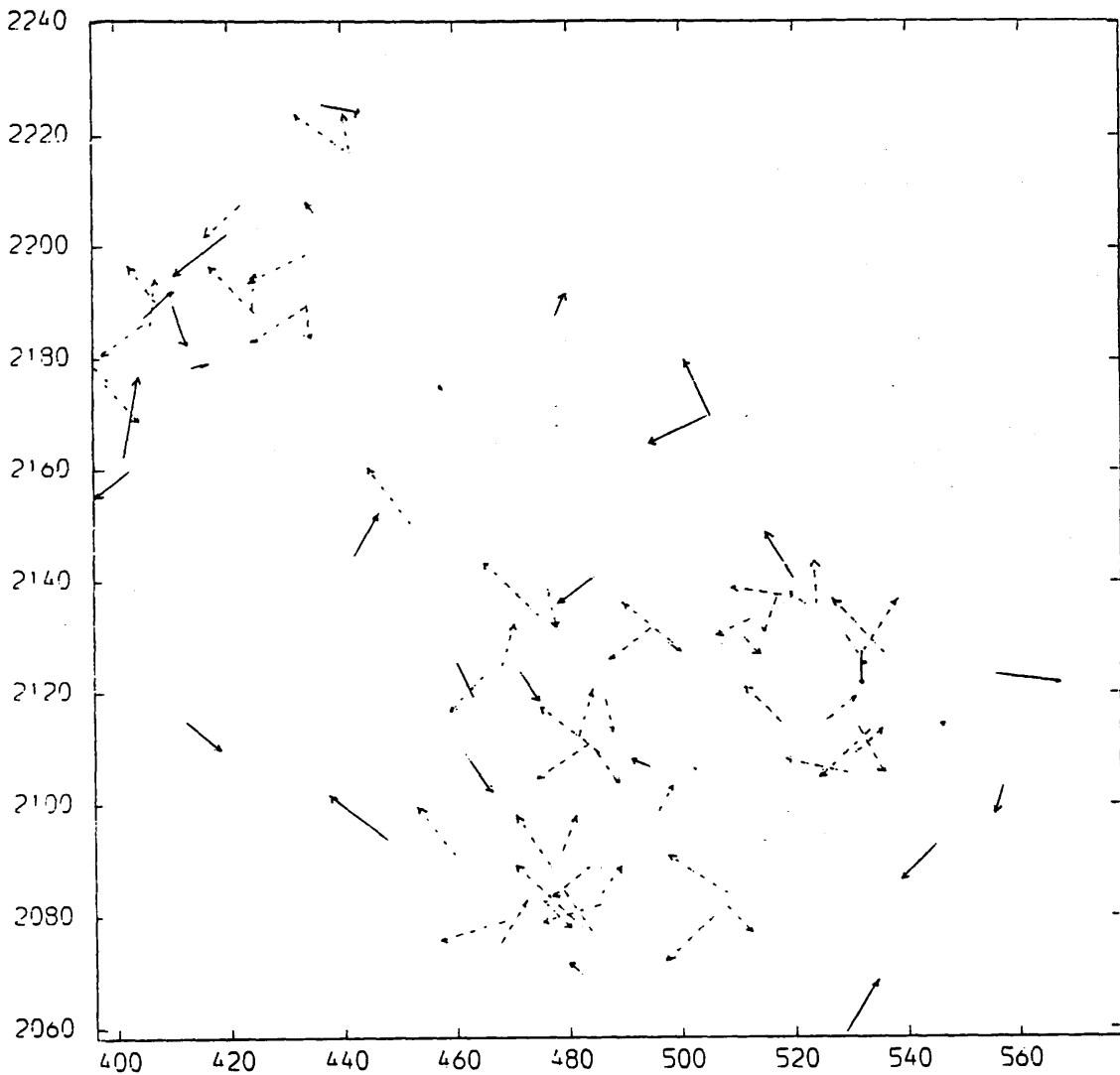


Fig. F.5a Residuals in Planimetry After the Relative/Absolute Orientation of MC Model 1.

Control Points. —→

Check Points. - - -→

ENLARGEMENT=X450.

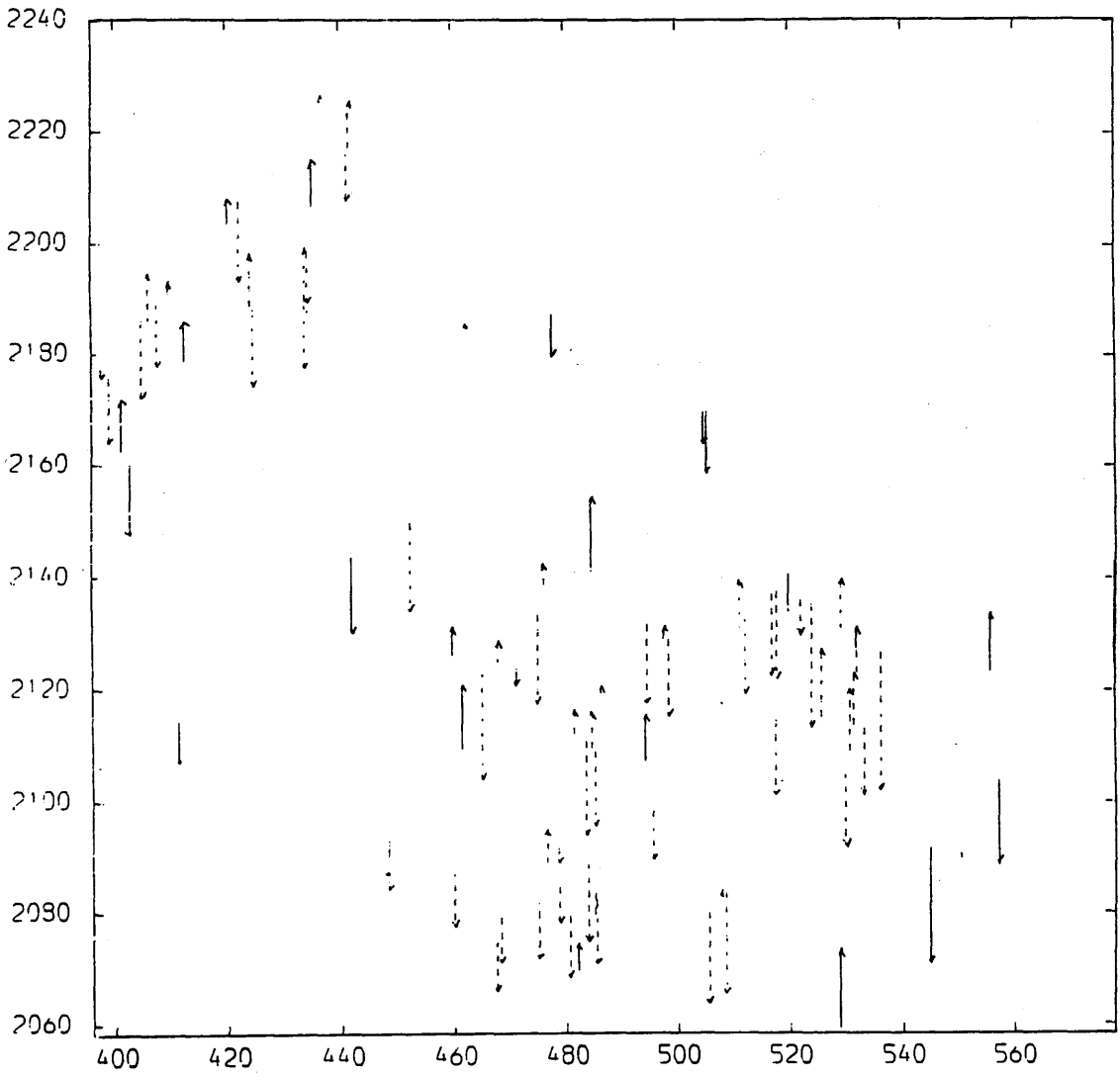


Fig. F.5b Residuals in Height After the Relative/Absolute Orientation of MC Model 1.

Control Points. —→

Check Points. ----→

ENLACEMENT=X450.

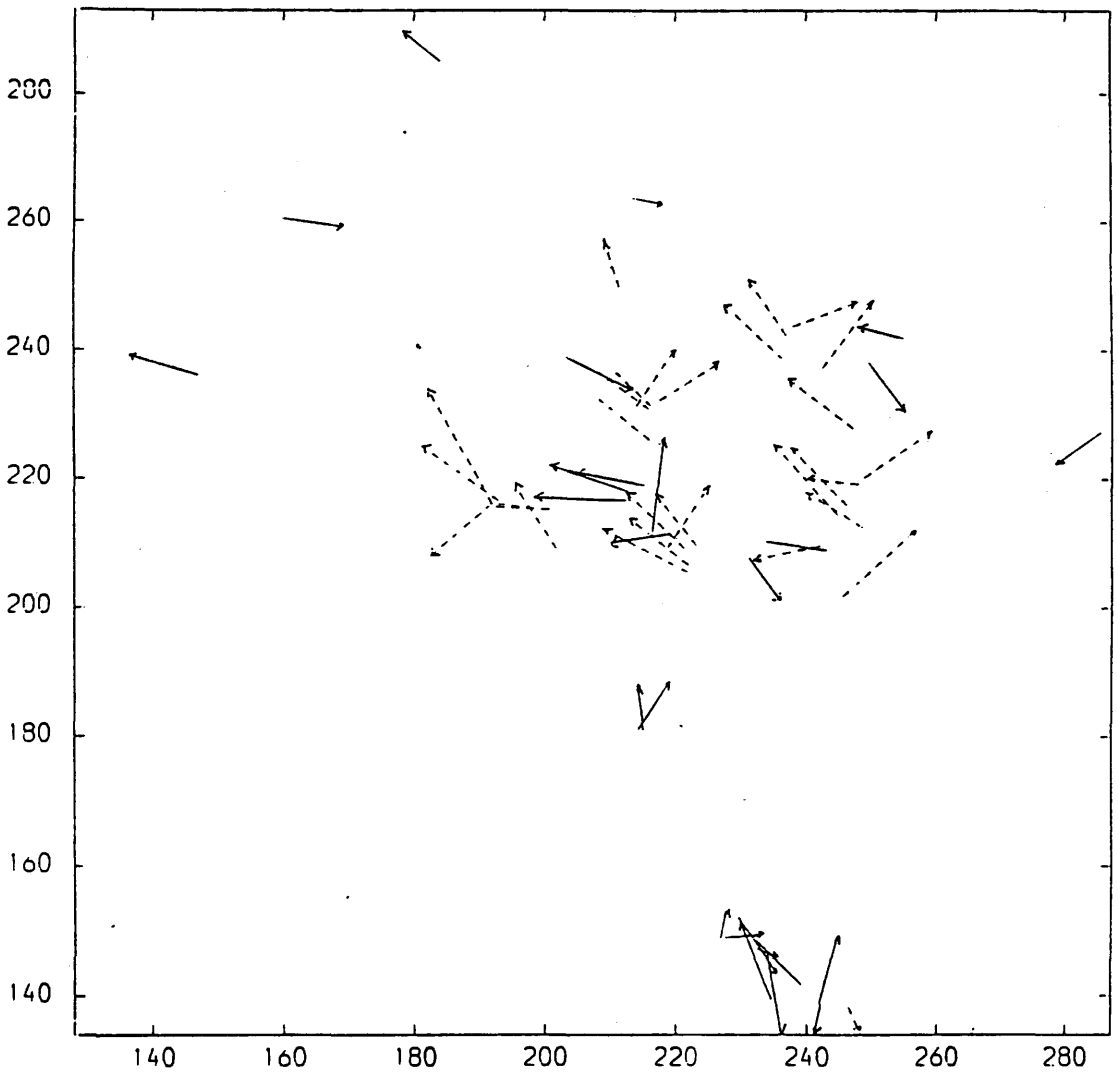


Fig. F.6a Residuals in Planimetry After the Relative/Absolute Orientation of MC Model 2.

Control Points. —→

Check Points. - - - →

ENLARGEMENT=#450.

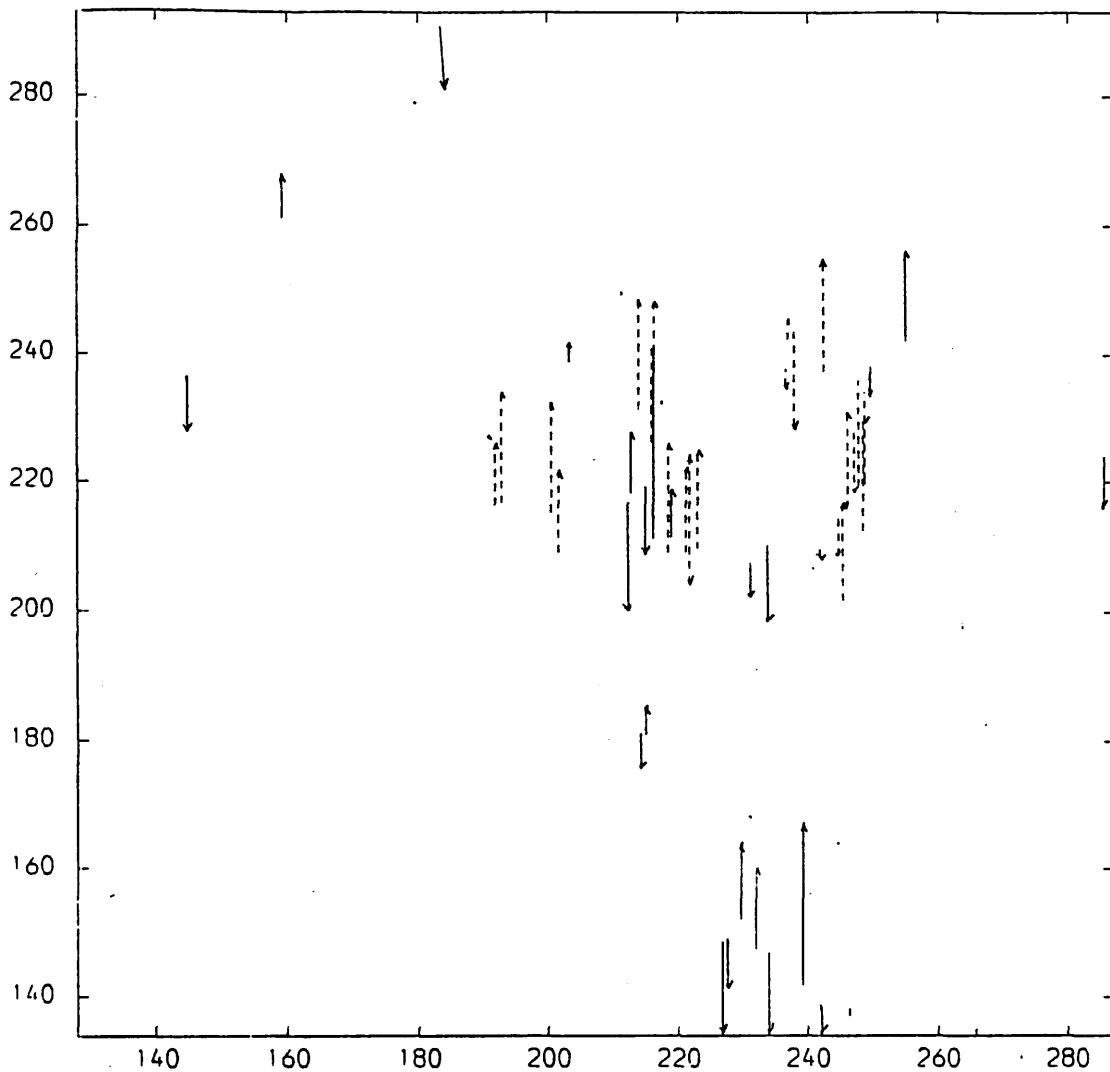


Fig. F.6b Residuals in Height After the Relative/Absolute Orientation of MC Model 2.

Control Points. —→

Check Points. ----→

ENLARGEMENT=X450.

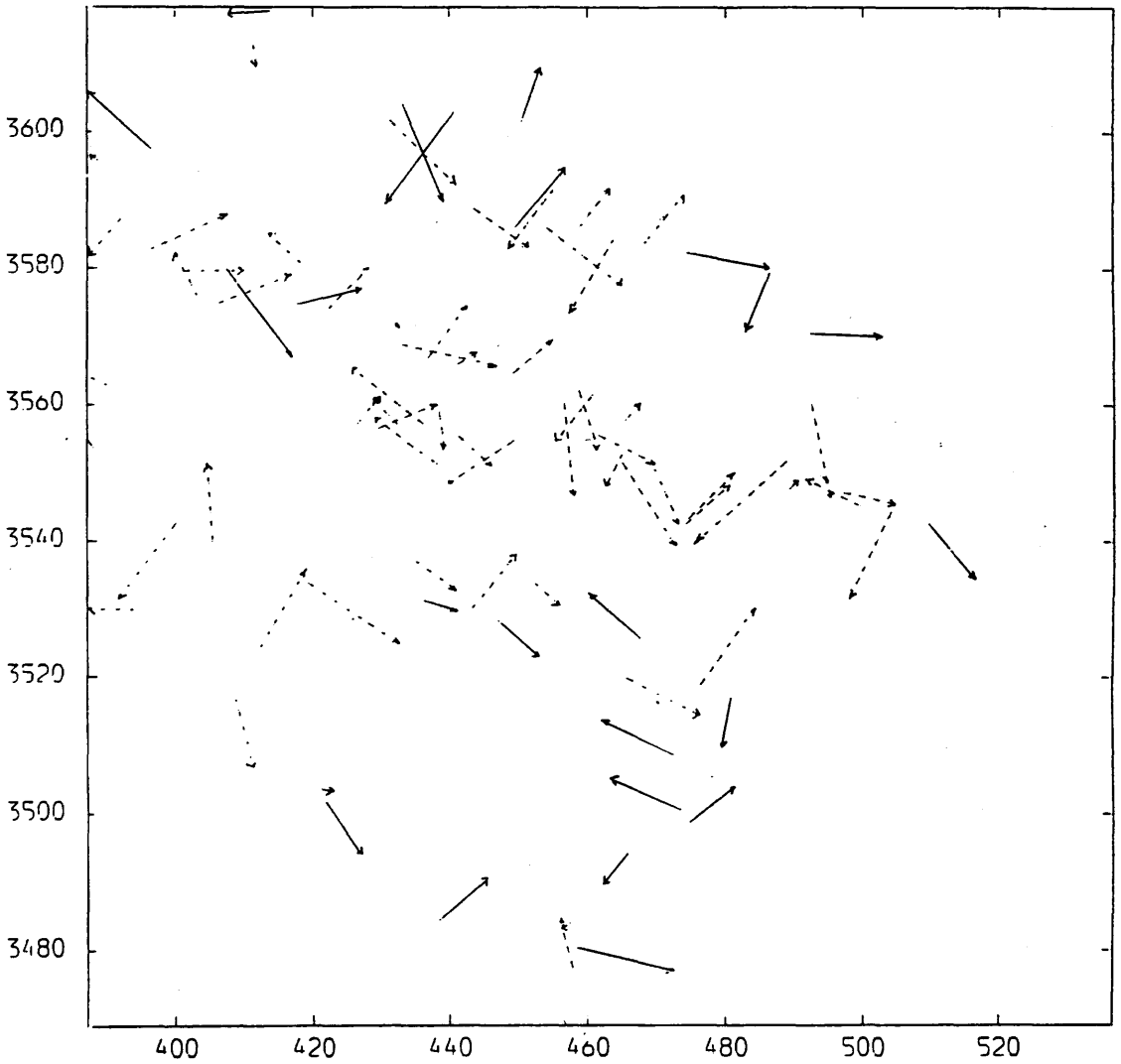


Fig. F.7a Residuals in Planimetry After the Space Resection/Intersection of MC Model 3.

Control Points. —→

Check Points. ----→

ENLARGEMENT=X450.

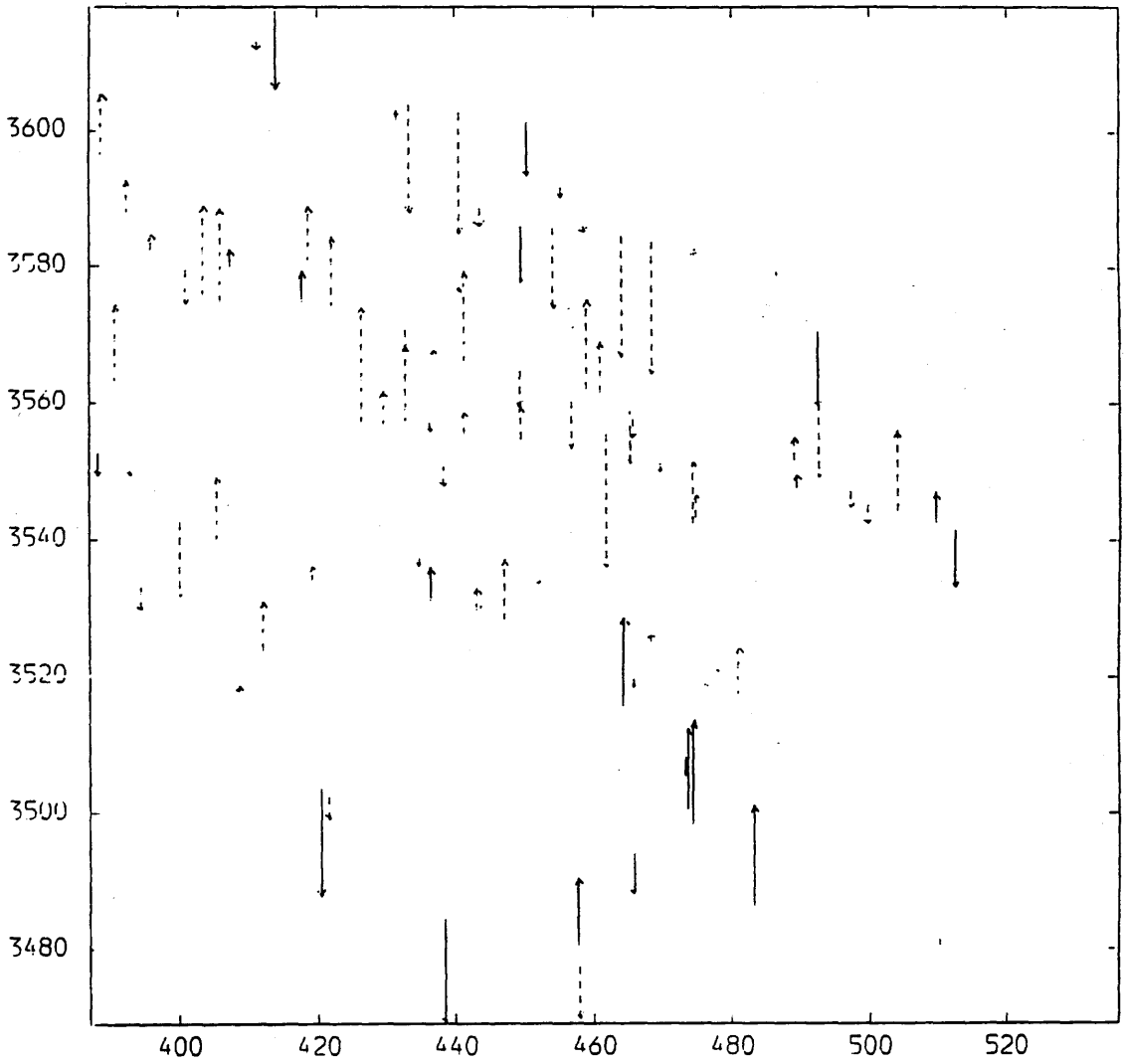


Fig. F.7b Residuals in Height After the Space Resection/Intersection of MC Model 3.

Control Points. ———→ Check Points. - - - - -→

ENLACEMENT=X450.

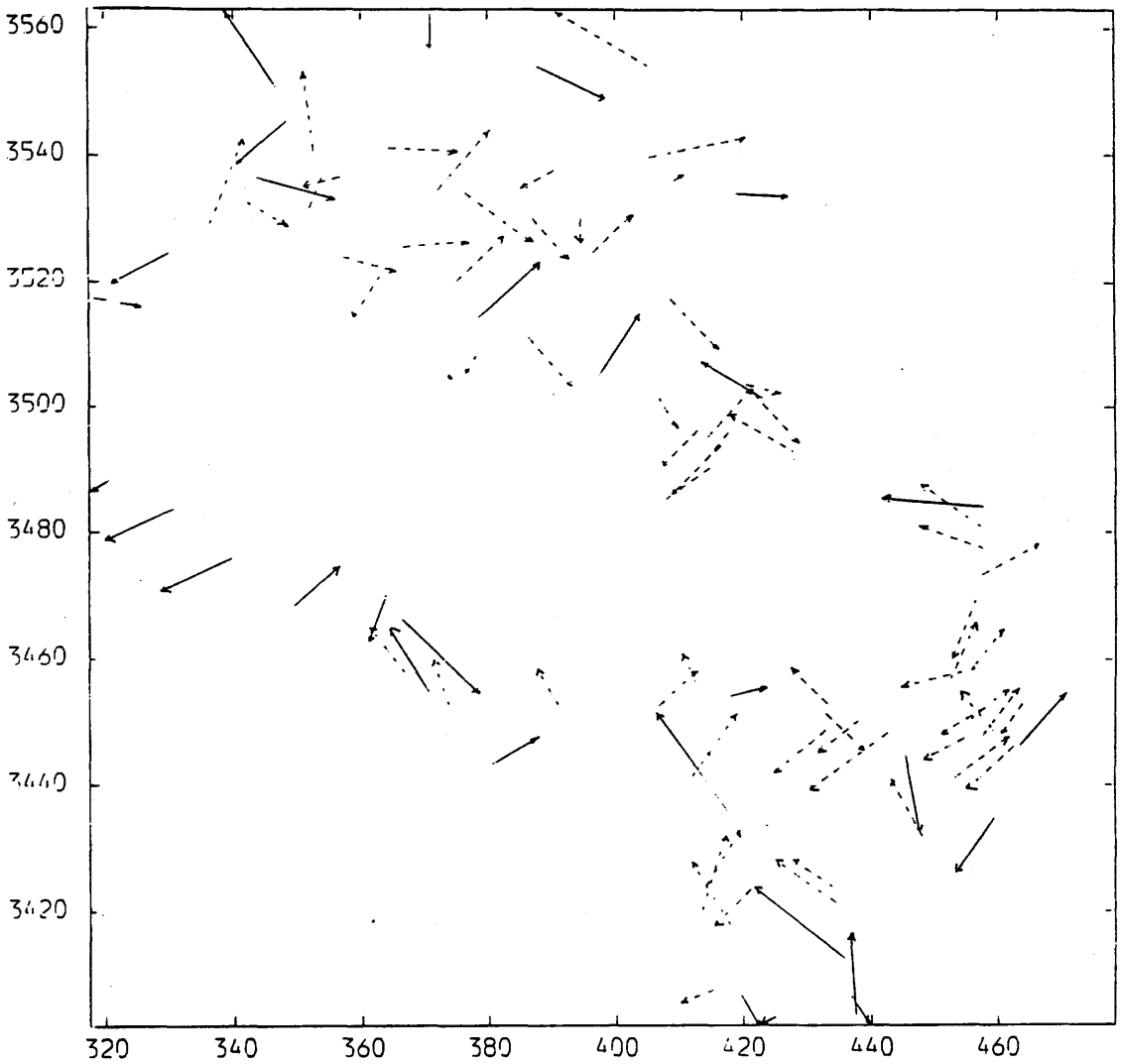


Fig. F.8a Residuals in Planimetry After the Space Resection/Intersection of MC Model 4.

Control Points. —→

Check Points. ----→

ENLARGEMENT=X450.

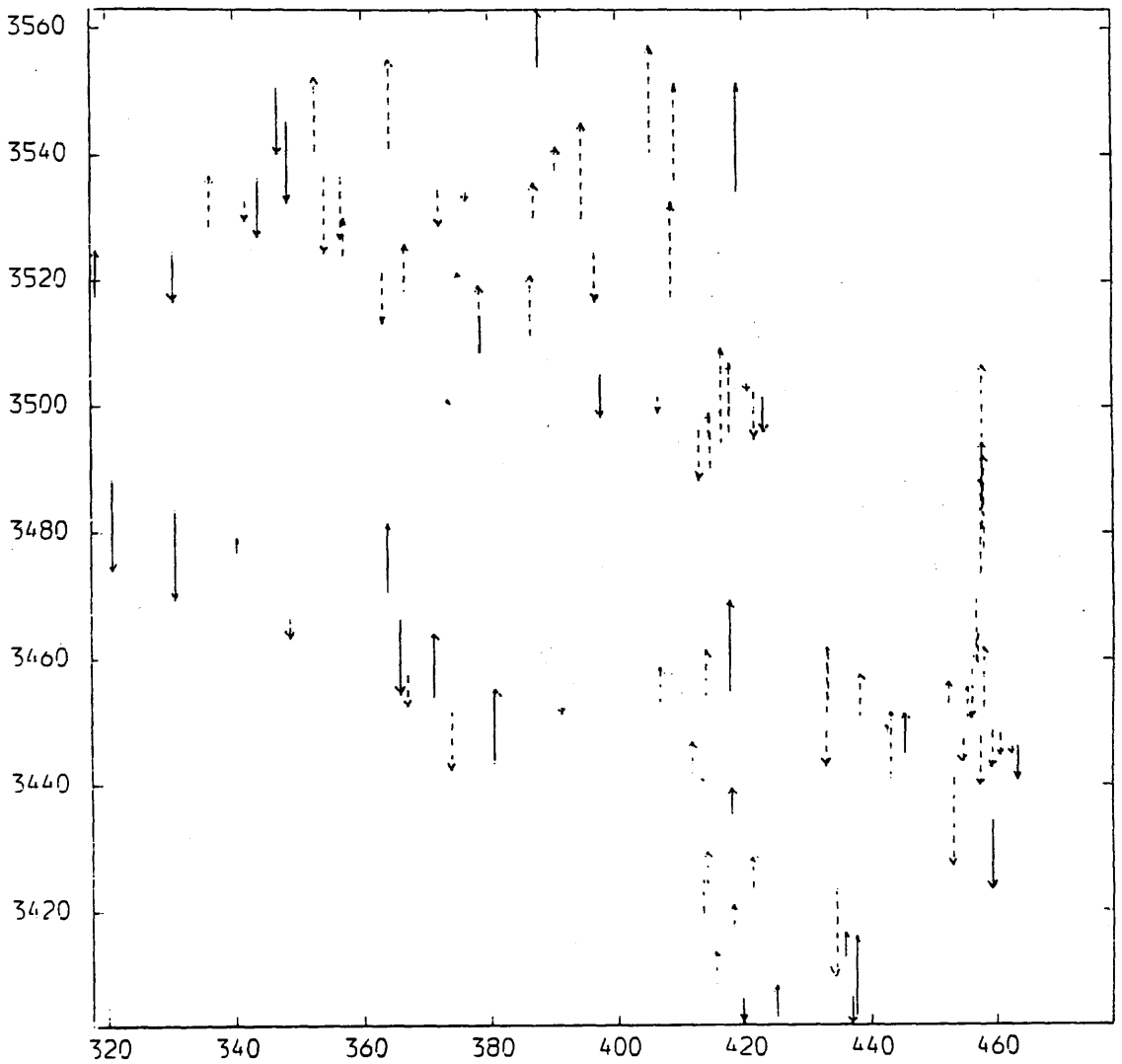


Fig. F.8b Residuals in Height After the Space Resection/Intersection of MC Model 4.

Control Points. —→

Check Points. - - - ->

ENLARGEMENT = X450.

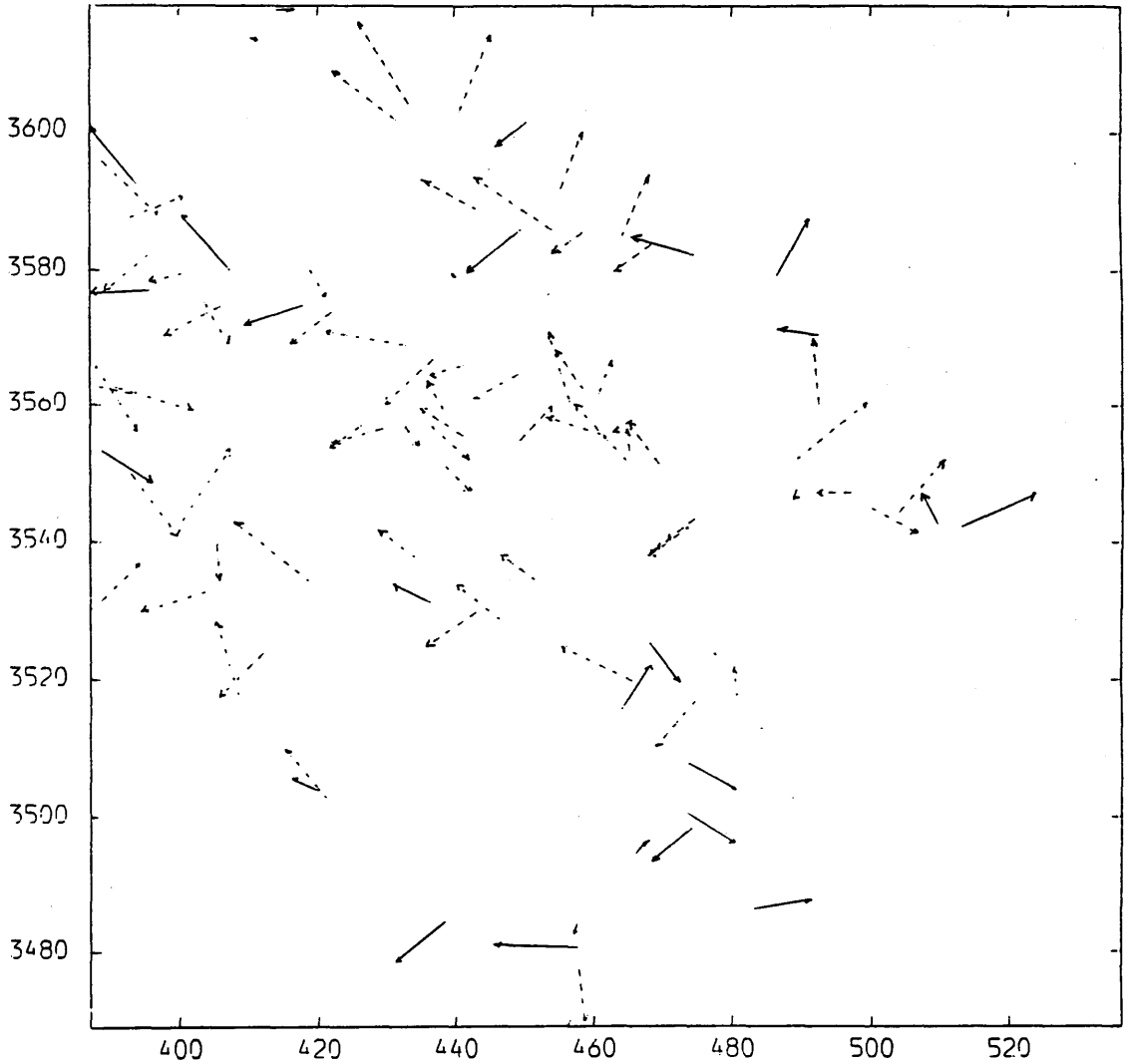


Fig. F.9a Residuals in Planimetry After the Relative/Absolute Orientation of MC Model 3.

Control Points. —→

Check Points. - - - →

ENLARGEMENT=X450.

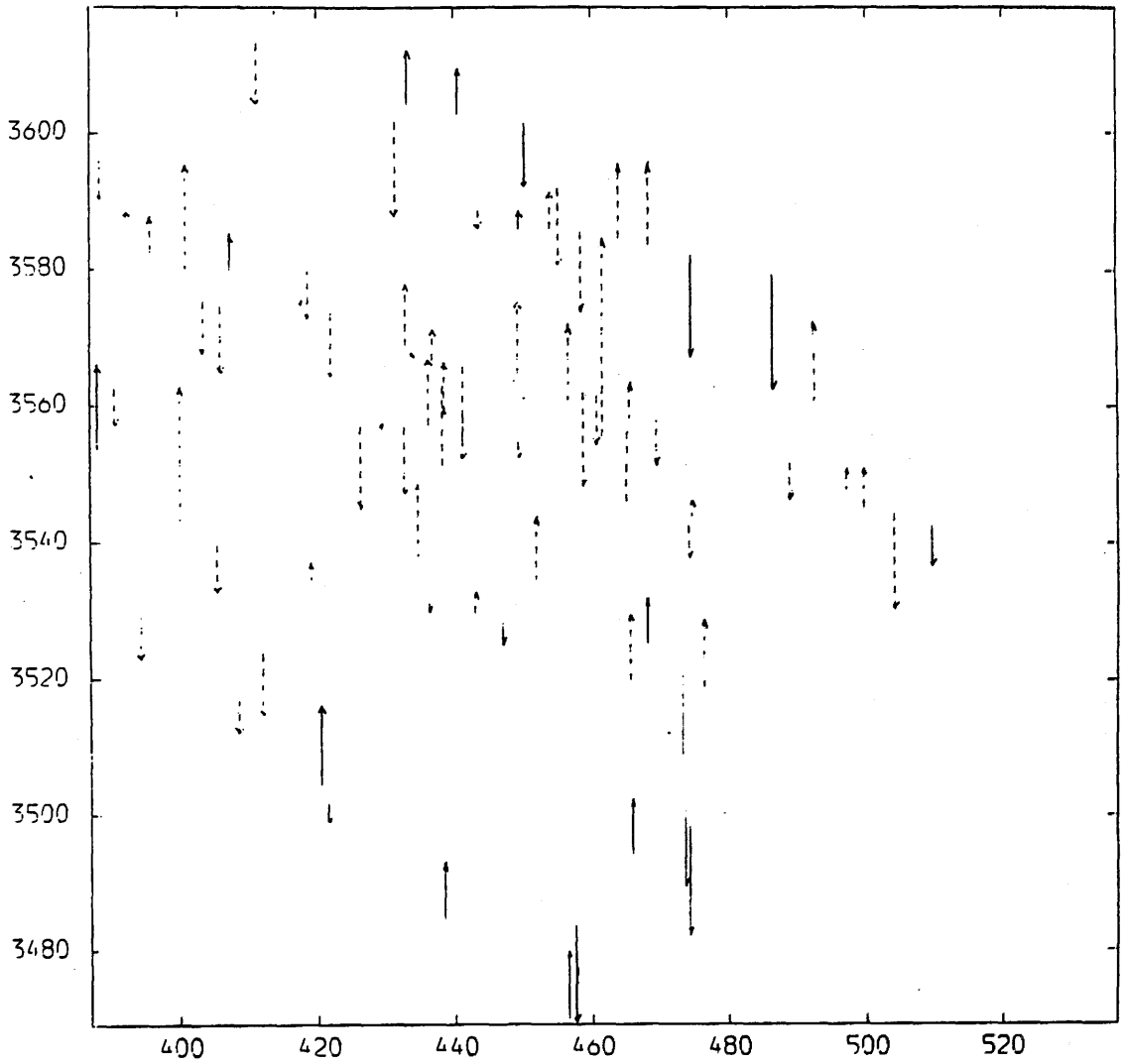


Fig. F.9b Residuals in Height After the Relative/Absolute Orientation of MC Model 3.

Control Points. —→

Check Points. - - - ->

ENLARGEMENT = X450.

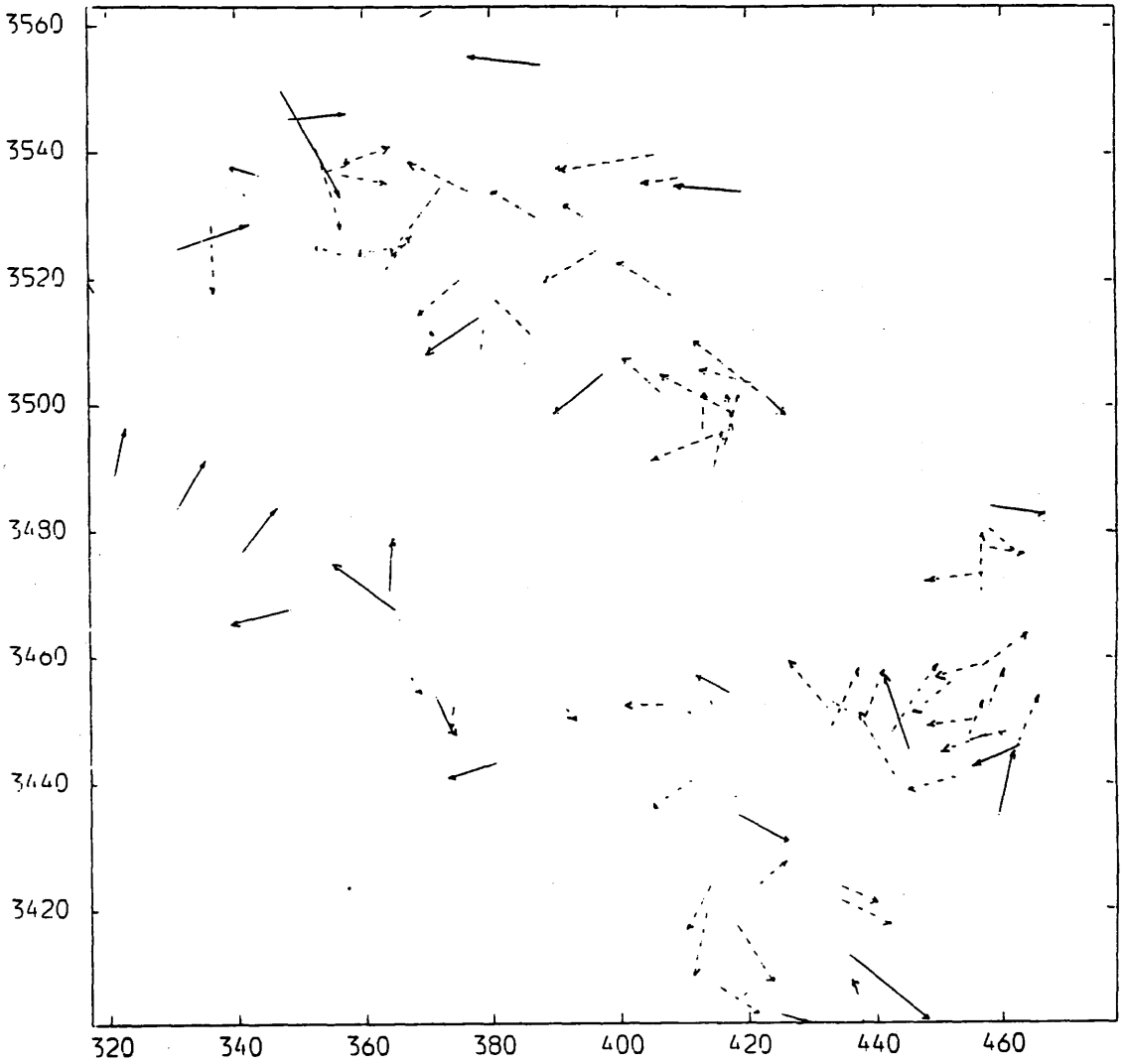


Fig. F.10a Residuals in Planimetry After the Relative/Absolute Orientation of MC Model 4.

Control Points. ———→ Check Points. - - - ->

ENLARGEMENT-x450.

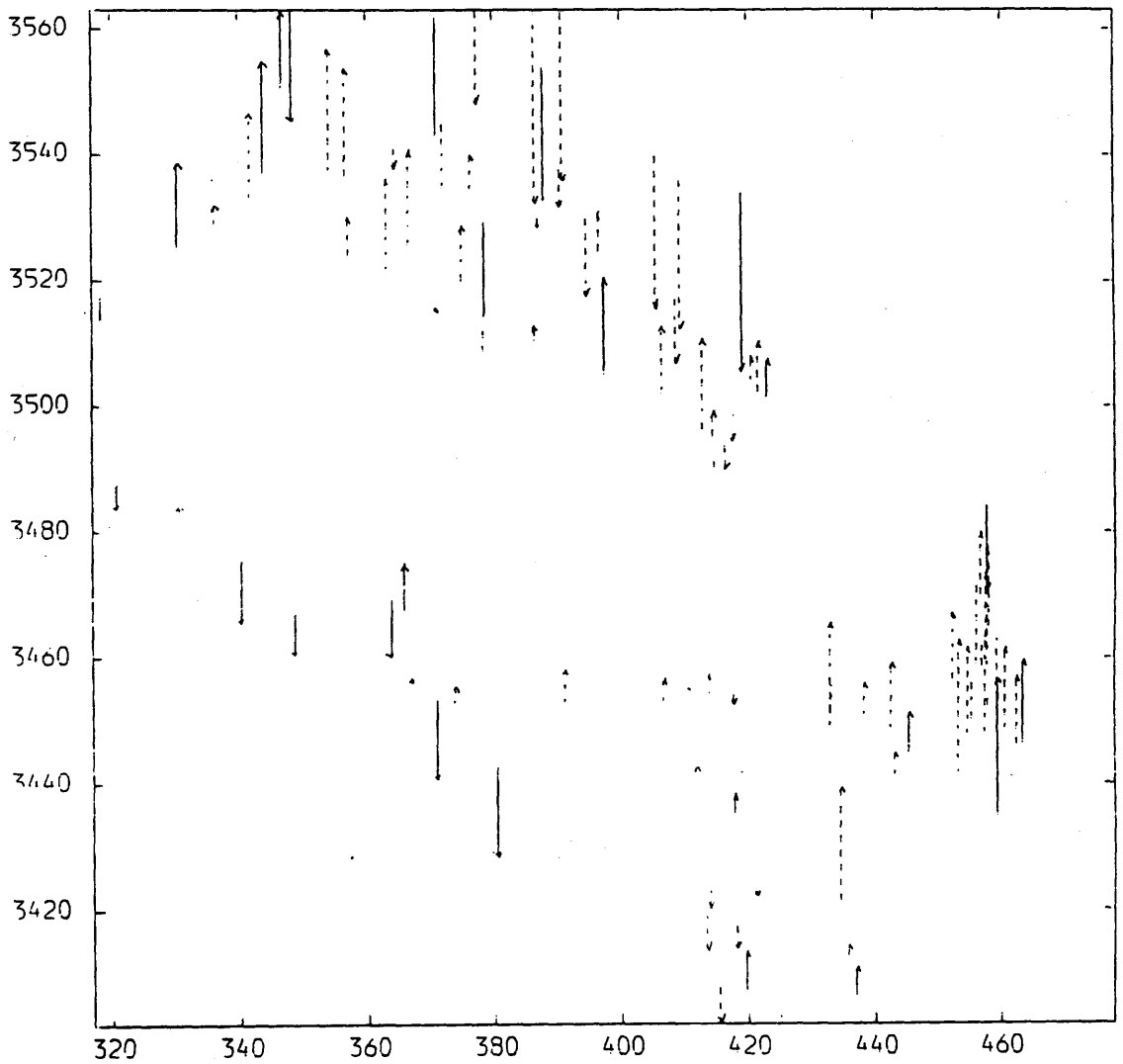


Fig. F.10b Residuals in Height After the Relative/Absolute Orientation of MC Model 4.

Control Points. —→

Check Points. - - - ->

ENLACEMENT=X450

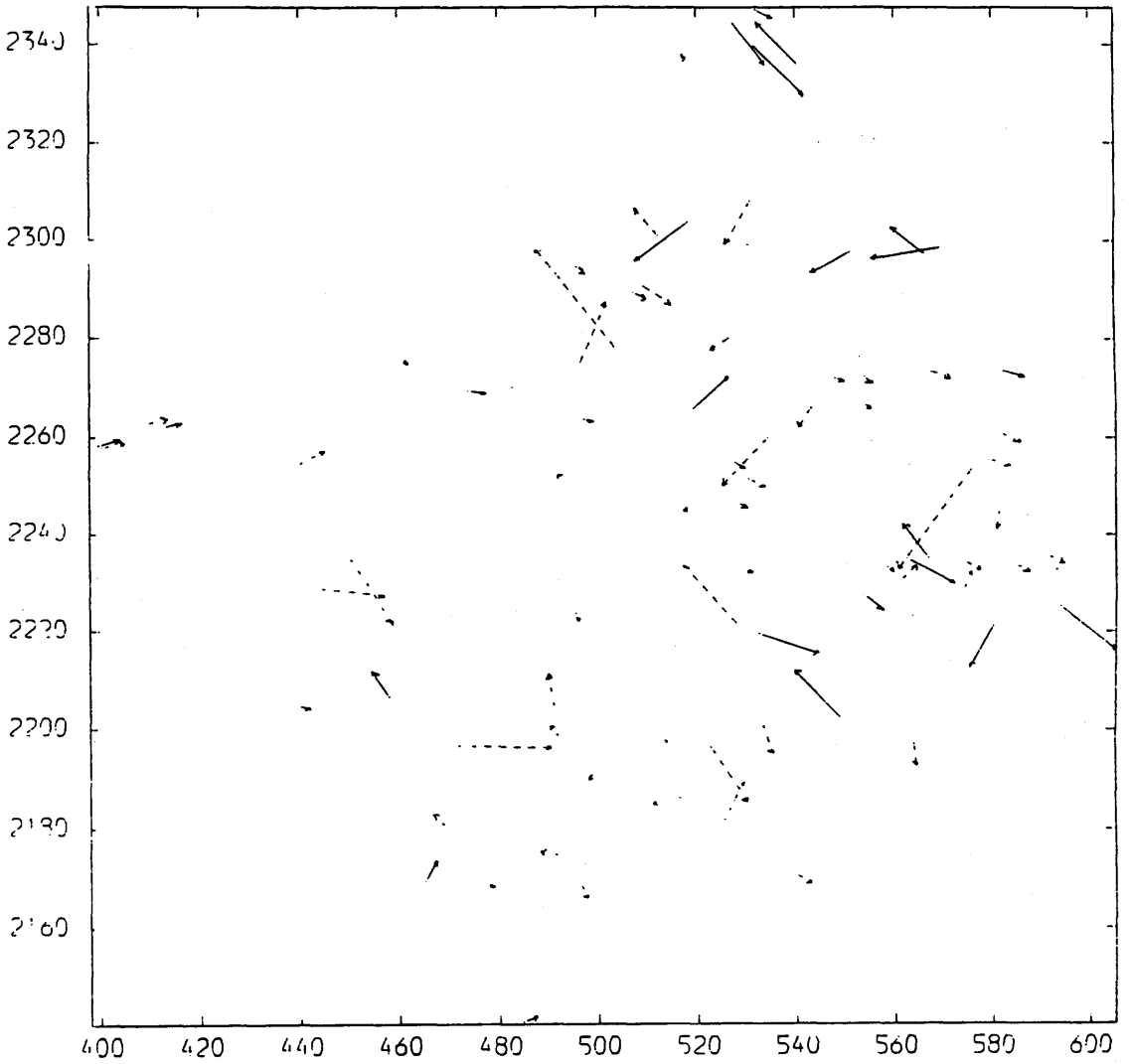


Fig. F.11a Residuals in Planimetry After the Space
Resection/Intersection of LFC Model 1.

Control Points. —→

Check Points. - - -→

ENLARGEMENT=X450

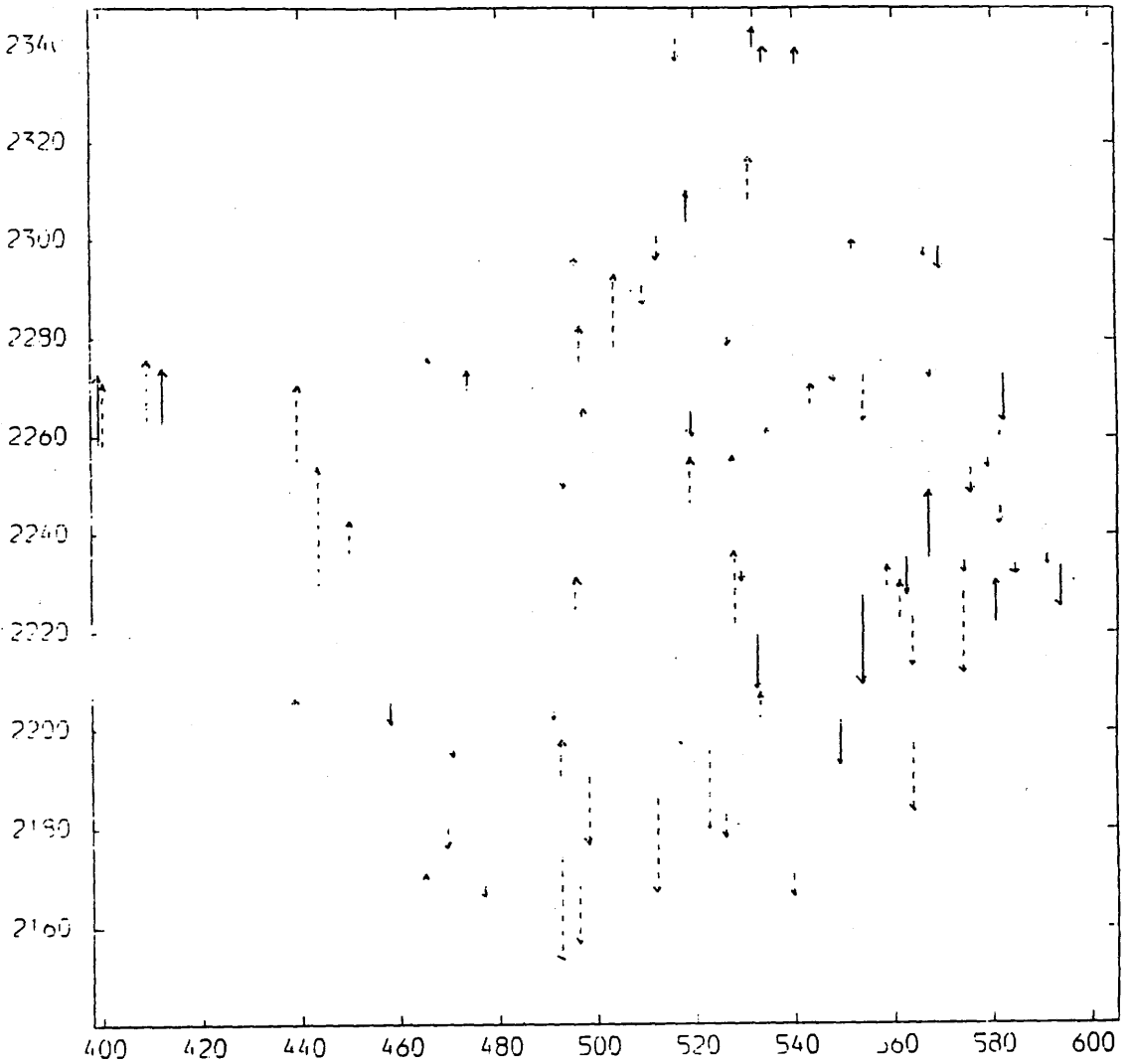


Fig. F.11b Residuals in Height After the Space
Resection/Intersection of LFC Model 1.

Control Points. —→

Check Points. - - - →

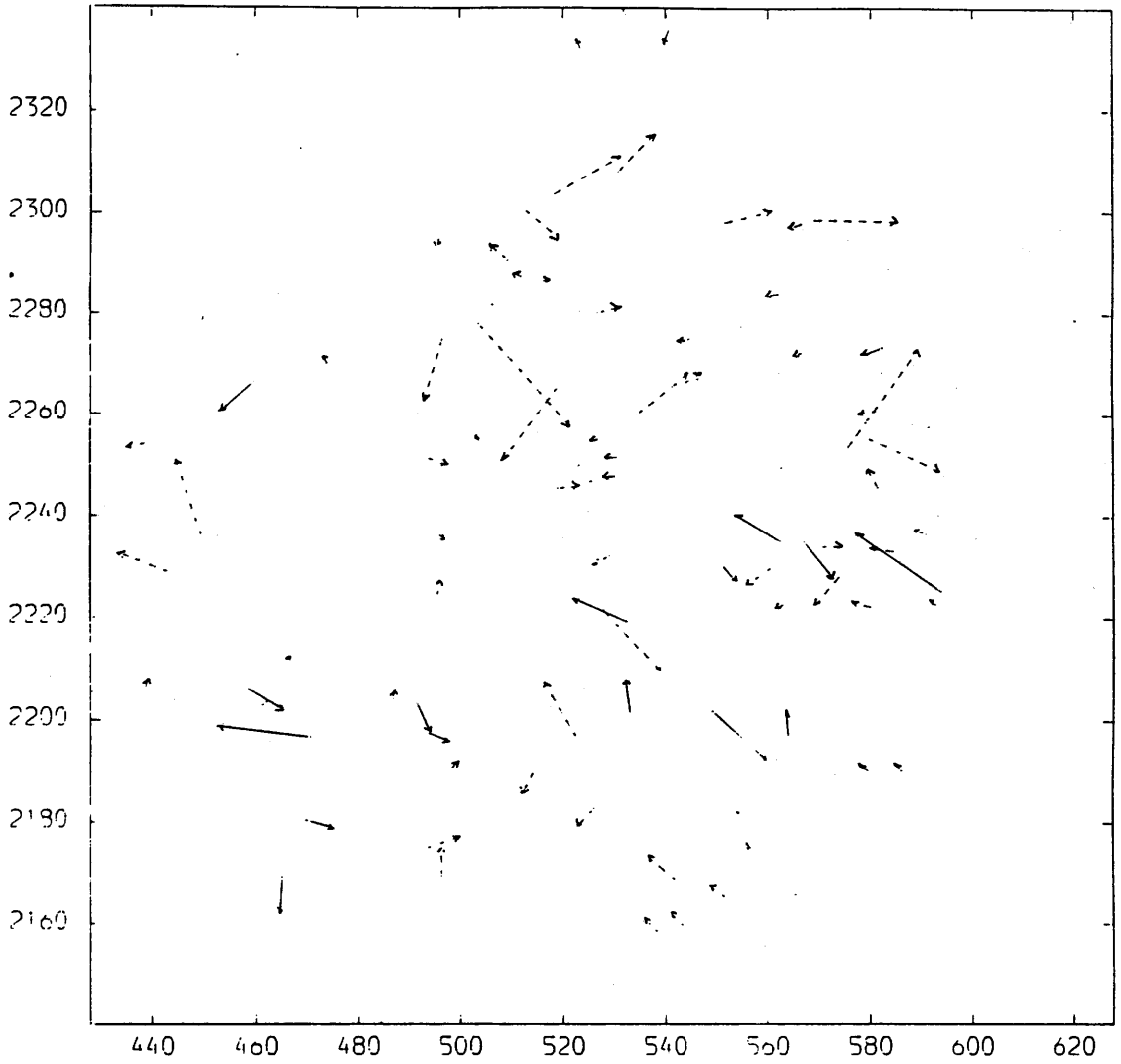


Fig. F.12a Residuals in Planimetry After the Space Resection/Intersection of LFC Model 2.

Control Points. —→ Check Points. - - -→

ENLARGEMENT = X4.50

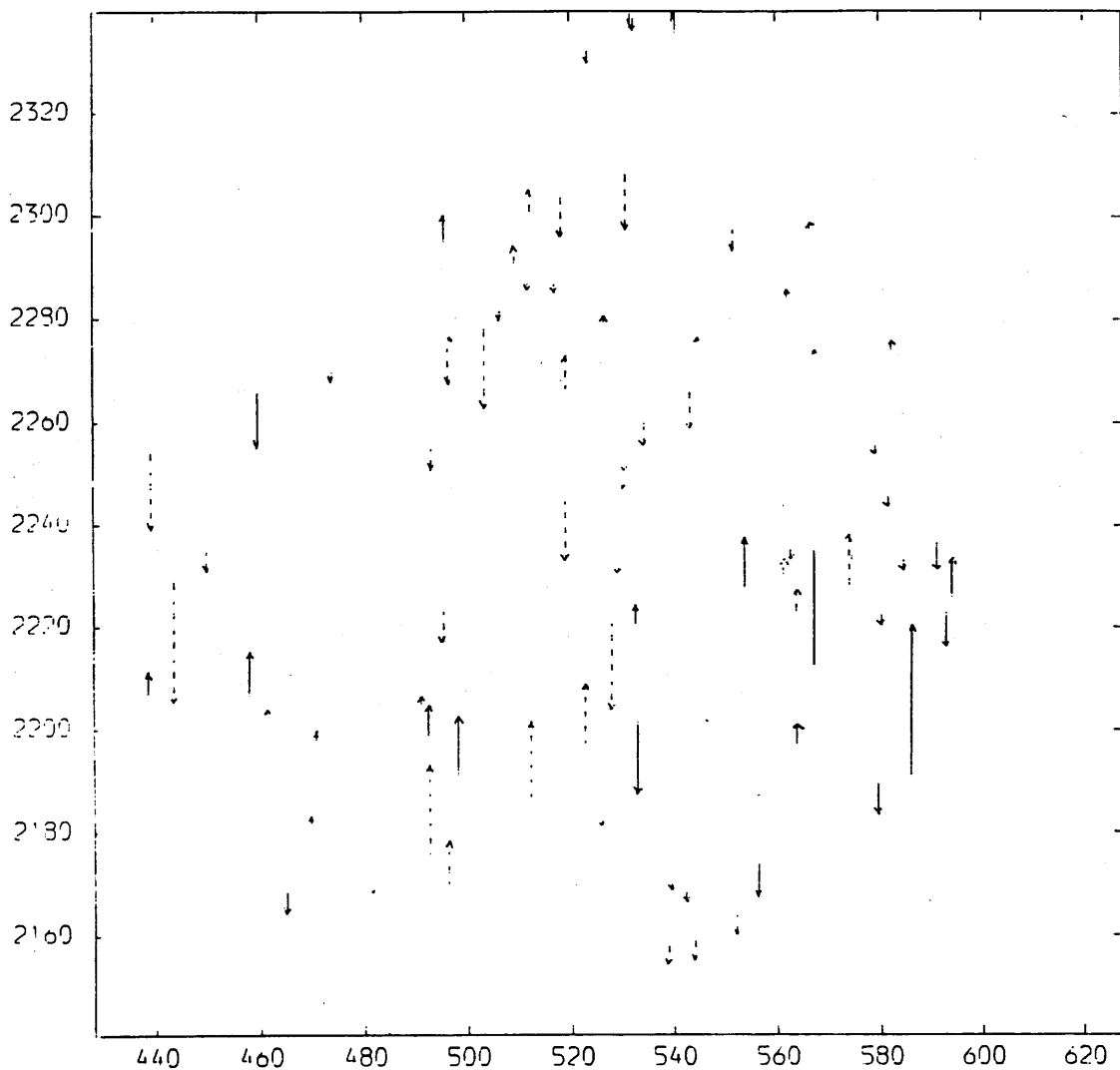


Fig. F.12b Residuals in height After the Space Resection/Intersection of LFC Model 2.

Control Points. ———→ Check Points. - - - ->